PROCEEDINGS

OF THE 6th INTERNATIONAL CONFERENCE ON COMPUTATIONAL MATHEMATICS AND ENGINEERING SCIENCES (CMES-2022)

20-22 May

2022, Ordu – Turkey

Published: 18 December 2022

ISBN

THE SIXTH INTERNATIONAL CONFERENCE ON COMPUTATIONAL MATHEMATICS AND ENGINEERING SCIENCES (CMES-2022), ORDU/TURKEY, MAY 20-22 2022

The **Sixth International Conference on Computational Mathematics and Engineering Sciences (CMES-2022)** was held in Ordu University from **20- to 22 May 2022 in Ordu, Turkey.** It provides an ideal academic platform for researchers and professionals to discuss recent developments in both theoretical, applied mathematics and engineering sciences. This event also aims to initiate interactions among researchers in the field of computational mathematics and their applications in science and engineering, to present recent developments in these areas, and to share the computational experiences of our invited speakers and participants.

The Organizing Committee

Committee Chairs

Hasan Bulut, Firat University, Elazig, Turkey

Zakia Hammouch, Ecole Normale Superierue de Meknes, Moulay Ismail University, Morocco

Mohammed Ouazzani Jamil Universite Privee of fez, Morocco

Carlo Cattani, Tuscia University, Viterbo, Italy

Haci Mehmet Baskonus, Harran University, Sanliurfa, Turkey

MESSAGE FROM THE GENERAL CHAIRS


Dear Conference Attendees,

We are honored to welcome you to the **Sixth International Conference on Computational Mathematics and Engineering Sciences (CMES-2022)** at Ordu University from 20 to 22 May 2022 in Ordu City, Turkey.

CMES, founded in 2016 at Faculty of Science and Techniques Errachidia Moulay Ismail University Morocco is an annual intarnational conference, which was very successful in the past years by providing opportunities to the participants in sharing their knowledge and informations and promoting excellent networking among different international universities. This year, the conference includes 200 extended abstracts, several submissions were received in response to the call for papers, selected by the Program Committee. The program features keynote talks by distinguished speakers such as : **Alissandra Maria Ragusa** from Catania University Italy, **Dumitru Baleanu**, from Institute of Space Sciences, Magurele-Bucharest, Romania, **Juan-Luis García Guirao** from Technical University of Cartagena, Spain, **Oscar Castillo** from Tijuana Institute of Technology, Tijuana, Mexico, **Hossein Jafari** from UNISA South Africa, **Vatan Karakaya** from Ahi Evran University, Turkey, **Ekrem Savas** from Usak University, **Muhammad Reza Safaei** from Florida University USA, **Erhan Coşkun** from Karadeniz Technical University, Turkey and **Hüseyin Merdan** from Tobb University, Turkey. The conference also comprises contributed sessions, posters sessions and various research highlights.

We would like to thank the Program Committee members and external reviewers for volunteering their time to review and discuss submitted abstracts. We would like to extend special thanks to the Honorary, Scientific and Organizing Committees for their efforts in making CMES-2022 a successful event. We would like to thank all the authors for presenting their research studies during our conference. We hope that you will find CMES-2022 interesting and intellectually stimulating, and that you will enjoy meeting and interacting with researchers around the world.

.

***Hasan Bulut**,*

Firat University Elazig, Turkey.

Zakia Hammouch,

École Normale supérieure, Moulay Ismail University of Meknès 50000, Morocco

Thu Dau Mot University, Binh Duong Province, Vietnam

China Medical University Hospital Taichung 40402, Taiwan.

TOPICS

Applied Mathematics,
Financial Mathematics,
Control Theory,
Game Theory
Modeling of Bio-systems for Optimization and Control,
Linear and Nonlinear programming and Dynamics,
Artificial Intelligence,
Geometry and Its Applications,
Analysis and Its Applications,
Statistics and Its Applications,
Mathematics Education and Its Applications,
Algebra and Its Applications.
Engineering Sciences
Computer Science

Information technology
Electrical and Electronic Engineering
Ordinary, Partial, Stochastic and Delay Differential Equations
Chaos and Dynamical Systems
Numerical methods and scientific programming
Fractional Calculus and Applications,
Cryptography and its applications
Computational Fluids mechanics, Heat and Mass Transfers.
Economics and Econometric Studies
Topology and Its Application
Education Sciences
Economics and Econometric Studies
Topology and Its Application

COMMITTEE CHAIRS

Prof.Dr.Hasan Bulut, Firat University Elazig, Turkey
Prof.Dr.Zakia Hammouch, Ecole Normale Supérieure of Meknes, Moulay Ismail University Morocco

COMMITTEE CO-CHAIRS

Prof. Dr. Mohammed Ouazzani Jamil Universite Privee of fez, Morocco
Prof.Dr.Carlo Cattani, Tuscia University, Viterbo, Italy
Prof.Dr.Haci Mehmet Baskonus, Harran University, Sanliurfa, Turkey

HONORARY COMMITTEE

SCIENTIFIC COMMITTEE

Zulqurnain Sabir (Hazara University, Pakistan)
Carla M.A. Pinto (ISEP | Instituto Superior de Engenharia do Porto, Porto – PORTUGAL)
Hossein Jafari (UNISA University Pretoria, South Africa)
Hasan Bulut (Firat University, Turkey)
Haci Mehmet Baskonus (Harran University, Turkey)
Bayram Şahin (Ege University,İzmir ,Turkey)
Dumitru Baleanu (Cankaya University, Turkey)
Eva Kaslik (University of Timisoara, Romania)
Izhar Uddin (Jamia Millia İslamia University. New Delhi)
Ayhan Şerbetçi (Ankara University, Ankara)
Hacer Sengul (Harran University, Sanlıurfa,Turkey)
Ayşe Dilek Maden (Selçuk University, Konya)
Wei Gao (Yunnan Normal University, China.)
Rauf Amirov (Cumhuriyet University, Sivas, Turkey)
Ogün Doğru (Gazi University, Ankara, Turkey)
Hanlar Reşitoğlu (Iğdır University, Turkey)
Erhan Güler (Bartın University, Turkey)
Fethi Bin Muhammad Belgacem (PAAET, Shaamyia, Kuwait)
Omer Kisi (Bartın University, Turkey)
Zhonglong Zhao (North University of China, China)
Bilal Alatas (Firat University, Turkey)
Necati Ozdemir (Balikesir University, Turkey)
Derya Avci (Balikesir University, Turkey)
Firat Evirgen (Balikesir University, Turkey)
Erol YAŞAR (Mersin University, Mersin, Turkey)
Ramadhan A. Mohammed (University of Duhok-Iraq)
Sizar A. Mohammed (University of Duhok-Iraq)
Zanyar Anwer Ameen (University of Duhok-Iraq)
Mehmet Yavuz (Necmettin Erbakan University, Turkey)
Hüseyin Yıldırım (Maraş Sütçü İmam University, K.Maraş)
Filiz Taşcan (Eskişehir Osmangazi University, Eskişehir)
Dursun Irk (Eskişehir Osmangazi University, Eskişehir)
Ali Karcı (İnönü University, Malatya)
Davut Hanbay (İnönü University, Malatya)
Burçin DOĞAN (Malatya Turgut Özal University, Turkey)
Feyza Esra ERDOĞAN (Ege University, İzmir, Turkey)
Fulya ŞAHİN (Ege University, İzmir, Turkey)
Ahmet Bedri ÖZER (Firat University, Elazığ, Turkey)
Ülkü YILMAZ (Malatya Turgut Özal University, Turkey)
Erdal EKİCİ (Çanakkale Onsekiz Mart University, Çanakkale)
Mehmet Akif AKYOL (Bingöl University, Bingöl, Turkey)
Hamza EROL (Mersin University, Mersin, Turkey)
H.Bayram Karadağ (İnönü University, Malatya)

M. Kemal Özdemir (İnönü University, Malatya)
Recep Şahin (Kırıkkale University, Kırıkkale)
M. Baki Yağbasan (Kırşehir Ahi Evran University, Kırşehir)
Mustafa Mikail Özçiloğlu (Kilis 7 Aralık University, Turkey)
Çiğdem İnan (Mersin University, Turkey)
Mustafa Yıldırım (Cumhuriyet University, Turkey)
Mehmet Küçükaslan (Mersin University, Turkey)
Okan Şakar (Bahçeşehir University, Turkey)
Hristos Anastassiu (Int. Hellenic University, Serres, Greece)
Aly Ramadan Seadawy (Taibah University, Saudi Arabia)
İpek A. Turgut (İskenderun Technical University, Turkey)
Mustafa Açıkkar (Adana Science and Tec.University, Turkey)
Bülent Tavlı (TOBB Economics and Tec.University, Turkey)
Halis Yılmaz (Dicle University,Turkey)
Yasin Kaya (Dicle University, Turkey)
Sunil Kumar (National Institute Of Tech. Jamshedpur, India)
Hatun Özlem Güney (Dicle University, Turkey)
Sedat İlhan (Dicle University, Turkey)
Arife Atay (Dicle University, Turkey)
Seçil Yalaz (Dicle University, Turkey)
Özge Kuran (Dicle University, Turkey)
Damla Barlak (Dicle University, Turkey)
Mahmut Isık (Harran University, Sanlıurfa,Turkey)
Tamer Uğur (Ataturk University /Turkey)
Muzaffer Aşkın (Munzur University,Tunceli,Turkey)
Elman Hazar (Igdır University, Turkey)
Serap Şahinkaya (Tarsus University)
Naci Genc (Van Yüzüncü Yıl University, Turkey)
Remzi Tuntas (Van Yüzüncü Yıl University, Turkey)
Kadriye Aydemir (Amasya University,Turkey)
Yadigar Sekerci (Amasya University,Turkey)
Hayati Olgar (Gazi Osman Paşa University,Turkey)
Semih Çavusoglu (Gazi Osman Paşa University,Turkey)
Nagehan Kılınc Gecer (Kırsehir Ahi Evran University,Turkey)
Cem Oguz (Kırsehir Ahi Evran University,Turkey)
Arzu Denk Oguz (Atılım University,Turkey)
Erhan Pişkin (Dicle University,Diyarbakır,Turkey)
Aynur Yalcıner (Selcuk University,Konya,Turkey)
Javid Ali (Aligarh Müslim University,India)
Hamit Mirtagiloğlu (Bitlis Eren University,Bitlis,Turkey)
Heybetkulu Mustafayev (Yüzüncüyıl University, Turkey)
Cesim Temel (Yüzüncüyıl University, Turkey)
Mehmet Mendeş (Canakkale 18 Mart University, Turkey)

Çağrı KARAMAN (Atatürk University – Erzurum, Turkey)
Ceren KINA (Malatya Turgut Özal University, Turkey)
Harun KAYA (Malatya Turgut Özal University, Turkey)
Olha Ivanyshyn (Izmir Instıtute of Technology,Izmir, Turkey)
Ozlem Ertekin (Munzur University, Tunceli, Turkey)
Onur Alp İlhan (Erciyes University, Turkey)
Danyal Soybaş (Erciyes University, Turkey)
Fatma Berna Benli (Erciyes University, Turkey)
Inan Ünal (Munzur University, Turkey)
Kemal Aydın (Selçuk University ,Turkey)
Hakan Şimşek (Kırıkkale University /Turkey)
Bilal Şenol (İnönü University, Malatya)
Sertaç GÖKTAŞ (Mersin University, Mersin, Turkey)
Derya Arslan (Bitlis Eren University, Bitlis, Turkey)
Ali Akgül (Siirt University ,Turkey)
Esra Karataş Akgül (Siirt University ,Turkey)
Abdulkadir Karakaş (Siirt Üniversity,Turkey)
Murat Sat (Erzincan Binali Yıldırım University, Turkey)
İsmail Onur Kıymaz (Ahi Evran University , Turkey)
Ayşegül Çetinkaya (Ahi Evran University , Turkey)
Nergiz (ÖNEN) POYRAZ (Çukurova University, Turkey)
Ozen Ozer (Kırklareli University, Turkey)
Sinan Çalık (Firat Univeristy,Elazıg,Turkey)
Murat Karakaş (Bitlis Eren Univeristy,Bitlis,Turkey)
Ayşe Metin Karakaş (Bitlis Eren Univeristy,Bitlis,Turkey)
Ahmet Yıldız (İnönü Univeristy,Malatya,Turkey)
Aynur Keskin KAYMAKÇI (Selcuk University, Konya)
Nejmi Cengiz (Ataturk University, Turkey)
Abdullah Kopuzlu (Ataturk University, Turkey)
Kürşat Akbulut (Ataturk University, Turkey)
Mesut Karabacak (Ataturk University, Turkey)
Yeşim Saraç (Ataturk University, Turkey)
Sıdıka Şule Şener (Ataturk University, Turkey)
Sait Taş (Ataturk University, Turkey)
Fatma Taşdelen Yeşildal (Ankara University, Turkey)
Şevket Gür (Sakarya Univercity, Turkey)
Serdal Pamuk (Kocaeli Univercity, Turkey)
Fethiye Müge Sakar (Dicle University, Turkey)
Ceren Sultan Elmalı (Erzurum Technical University, Turkey)
Muhammed Yiğider (Erzurum Technical University, Turkey)
Sibel Turanlı (Erzurum Technical University, Turkey)
Hatıra Günerhan (Kafkas University, Turkey)
Murat Çağlar (Erzurum Technical University, Turkey)

Erhan Deniz (Kafkas University, Turkey)
Nizami Mustafa (Kafkas University, Turkey)
Semra Yurttançıkmaz (Ataturk University, Turkey)
Nigar Yıldırım Aksoy (Kafkas University, Turkey)
M. Ali Dokuyucu (Agrı İbrahim Cecen University, Turkey)
Ahmet Ocak Akdemir (Agrı İbrahim Cecen University, Turkey)
Talat Körpinar(Muş Alparslan University, Turkey)
Selçuk Baş (Muş Alparslan University, Turkey)
Rıdvan Cem Demirkol (Muş Alparslan University, Turkey)
Zeliha Körpinar (Muş Alparslan University, Turkey)
Evrim Toklu (Agrı İbrahim Cecen University, Turkey)
Serhan Eker (Agrı İbrahim Cecen University, Turkey)
Kadirhan Polat (Agrı İbrahim Cecen University, Turkey)
Abdullah Çağman (Agrı İbrahim Cecen University, Turkey)
Şebnem Yıldız (Ahi Evran University, Kırşehir, Turkey)
Erhan Set (Ordu University, Turkey)
Esin Ilhan (Kırsehir Ahi Evran University / Turkey)
Hasan Toğrul (Batman University, Batman, Turkey)
İnci Toğrul (Batman University, Batman, Turkey)
Selahaddin Maden (Ordu University, Turkey)
Yıldıray Çelik (Ordu University, Turkey)
Mehmet Korkmaz (Ordu University, Turkey)
Süleyman Şenyurt (Ordu University, Turkey)
Erdal Ünlüyol (Ordu University, Turkey)
Yusuf Pandır (Bozok University – Turkey)
Asıf Yokuş (Fırat University, Elazığ, Turkey)
Hülya Durur(Ardahan University, Ardahan, Turkey)
Cemil İnan (Mardin Artuklu University, Turkey)
Çetin Kürşat Bilir (Ahi Evran University, Turkey)
Alper Ekinci (Bandırma 17 Eylul University, Turkey)
Fatma Sağsöz (Ataturk University, Turkey)
Hayriye Esra Akyüz (Bitlis Eren University,Bitlis,Turkey)
Fahrettin Özbey (Bitlis Eren University,Bitlis,Turkey)
Hatice Kuşak Samancı (Bitlis Eren University,Bitlis,Turkey)
Akbar Barati Chiyaneh (Yüzüncüyıl University,Bitlis,Van)
Ufuk Kaya (Bitlis Eren University,Bitlis,Turkey)
M. Tuncay Gençoğlu (Fırat University, Elazığ, Turkey)
Berivan Polat (Munzur University, Turkey)
Alper Polat (Munzur University, Turkey)
Şükran Konca (İzmir Bakırçay University, İzmir, Turkey)
Ali Çakmak (Bitlis Eren University, Bitlis,Turkey)
Unal İç (Firat Ünİversity, Elazıg)
Seda İğreti Araz (Siirt University, Siirt, Turkey)

Burcu Gürbüz (Johannes Gutenberg-University Mainz, Germany)
Mahir Murat Cengiz (Ataturk University /Turkey)
Nguyen Huy Tuan (Thu Dau Mot university, Vietnam)
Seenith Sivasundaram (Université de Bethune-Cookman, USA)
Agamirza Bashirov (Eastern Mediterranean University, Cyprus)
Lazar Stošić (College for Preschool Teachers, Aleksinac, Serbia)
Alla Belousova (Don State Technical University, Russian Federation)
Aneta Barakoska (Faculty of Philosophy, University St. Cyril Macedonia)
Vera Stojanovska (Faculty of Philosophy, University Ss. Cyril Macedonia)
Irina Abakumova (Don State Technical University, Russian Federation)
Sonja Velickovic (College for Preschool Teachers, Aleksinac, Serbia)
Mohamed Addam (National School of Applied Sciences Hoceima, Morocco)
Luis Manuel Sánchez Ruiz (Technical University of Valencia, Spain)
Roman Chapko(Ivan Franko National University Lviv , Ukraine)
Yarema Savula (Ivan Franko National University Lviv , Ukraine)
Ihor Prokodushyn (Ivan Franko Natıonal University,Lviv,Ukraine)
Zakia Hammouch (Moulay Ismail University, Morocco)
Burçin DOĞAN (Malatya Turgut Özal University, Malatya, Turkey)
Ahmet Bedri ÖZER (Malatya Turgut Özal University, Malatya, Turkey)
Ülkü YILMAZ (Malatya Turgut Özal University, Malatya, Turkey)
Mehmet Atçeken (Tokat Gaziosmanpaşa University, Tokat)
Hristos Anastassiu (International Hellenic University, Serres, Greece)
İpek Abasıkeleş Turgut (İskenderun Technical University, Turkey)
Mustafa Açıkkar (Adana Science and Technology University, Turkey)
Bülent Tavlı (TOBB Economics and Technology University, Turkey)
Salman Khodayifar (Institue for Adv.Studies in Basic Sciences,Iran)
Mehmet Mendeş (Canakkale 18 Mart University Canakkale, Turkey)
Ceren KINA (Malatya Turgut Özal University, Malatya, Turkey)
Harun KAYA (Malatya Turgut Özal University, Malatya, Turkey)
Nergiz (ÖNEN) POYRAZ (Çukurova University, Adana, Turkey)
Mustafa Ali Dokuyucu (Agrı İbrahim Cecen University, Turkey)
Fatma Erdoğan (Firat University, Elazığ)
Gökhan Gökdere (Fırat University, Elazığ)
Yusuf PANDIR (Yozgat Bozok University, Yozgat Turkey)
Yusuf GUREFE (Mersin University, Mersin Turkey)
Şükran Konca (Bitlis Eren University, Bitlis,Turkey)
Hüseyin Merdan(TOBB University of Economics and Technology, Turkey)
Songül Kaya Merdan(Middle East Technical University,Turkey)
Engin Özkan(Erzincan Binali Yıldırım University, Erzincan)
İsrafil Okumuş(Erzincan Binali Yıldırım University, Erzincan)
Bayram Çekim(Gazi University, Turkey)
Gürhan İçöz(Gazi University, Turkey)
Fatma Ayaz(Gazi University, Turkey)

Emel Biçer (Bingöl University, Turkey)
Güven Kaya (Bingöl University, Turkey)
Ramin Najafi (Islamic Azad University, Iran)
Ebru Bozkurt (Ataturk University, Turkey)
Rıdvan Şahin(Gumushane University, Turkey)
İsa Yıldırım (Ataturk University, Turkey)
Halit Orhan (Ataturk University, Turkey)
Arzu Akbulut (Eskisehir Osmangazi University, Turkey)
Erdal Ulualan (Kutahya University, Turkey)
İbrahim Aktaş (Gumushane University, Turkey)
Numan Yalçın (Gumushane University, Turkey)
Muhammet Kamali (Kyrgyz-Turkish Manas University, Kyrgyzstan)
İsmet Altıntaş (Kyrgyz-Turkish Manas University, Kyrgyzstan)
Anargül Urdaletova (Kyrgyz-Turkish Manas University, Kyrgyzstan)
Asan Ömüraliyev (Kyrgyz-Turkish Manas University, Kyrgyzstan)
Avıt Asanov (Kyrgyz-Turkish Manas University, Kyrgyzstan)
Kalışkan Matanova (Kyrgyz-Turkish Manas University, Kyrgyzstan)
Ella Abilayeva (Kyrgyz-Turkish Manas University, Kyrgyzstan)
Peyil Esengül Kızı (Kyrgyz-Turkish Manas University, Kyrgyzstan)

ORGANIZING COMMITTEE

Hasan Bulut (Chair) (Fırat University, Turkey)
Zakia Hammouch (Chair) Ecole Normale Supérieure of Meknes, (Moulay Ismail University Morocco)
Haci Mehmet Baskonus (Co-Chair) (Harran University, Turkey)
Carlo Cattani (Co-Chair) (Tuscia University, Italy)
Fevzi Erdogan (Co-Chair) (Yüzüncüyıl University, Turkey)
Mikail Et (Fırat University, Turkey)
Mehmet Bektaş (Fırat University, Turkey)
Ercan Çelik (Kyrgyz-Turkish Manas University, Kyrgyzstan)
Hemen Dutta (Department of Mathematics, Gauhati University, India)
Alaattin Esen (İnönü University, Turkey)
Mir Sajjad Hashemi (University of Bonab, Iran)
Mahir Murat Cengiz (Ataturk University, Erzurum, Turkey)
Assoc. Prof. Dr. Hasan Hüseyin MUTLU (Ordu University, Ordu, Turkey)
Assoc. Prof. Dr. Sanem TABAK (Ordu University, Ordu, Turkey)
Assoc. Prof. Dr. Erhan YAYLAK (Ordu University, Ordu, Turkey)
Assoc. Prof. Dr. Tolga AKTÜRK (Ordu University, Ordu, Turkey)
Esin İnan Eskitascıoğlu (Yüzüncüyıl University, Turkey)
Bülent Taşel (Final International University, Girne, Cyprus)
M. Giyas Sakar (Yüzüncüyıl University, Van, Turkey)

Onur Saldır (Yüzüncüyıl University, Van, Turkey)
Aysenur Akkılıç (Fırat University, Elazığ, Turkey)
Bahar Acay (Fırat University, Elazığ, Turkey)
Sibel Tarla (Fırat University, Elazığ, Turkey)

LOCAL COMMITTEE

Aytül GÖKÇE (Ordu University, Ordu Turkey)
Gökçe ÇAYLAK KAYATURAN (Ordu University, Ordu Turkey)
Erhan SET (Ordu University, Ordu Turkey)
Cemal BELEN (Ordu University, Ordu Turkey)
Erol TAŞ (Ordu University, Ordu Turkey)
Mehmet KORKMAZ (Ordu University, Ordu Turkey)
Yıldıray ÇELİK (Ordu University, Ordu Turkey)
Meral CANSIZ AKTAŞ (Ordu University, Ordu Turkey)
Hayal YAVUZ MUMCU (Ordu University, Ordu Turkey)
Aslıhan OSMANOĞLU (Ordu University, Ordu Turkey)
Süleyman ŞENYURT (Ordu University, Ordu Turkey)
Erdal ÜNLÜYOL (Ordu University, Ordu Turkey)
Himmet KORKMAZ (Ordu University, Ordu Turkey)
Erdinç YÜCESOY (Ordu University, Ordu Turkey)
Canan ÇİFTÇİ (Ordu University, Ordu Turkey)
İrem EROĞLU (Ordu University, Ordu Turkey)
Abdussamet ÇALIŞKAN (Ordu University, Ordu Turkey)
Fatih SAY (Ordu University, Ordu Turkey)
Ayşe GÜVEN SARIHAN (Ordu University, Ordu Turkey)
Davut CANLI (Ordu University, Ordu Turkey)
Adem TÜRKMEN (Ordu University, Ordu Turkey)
Hayrunnisa AYYILDIZ (Ordu University, Ordu Turkey)
Meral ÇELİKOĞLU (Ordu University, Ordu Turkey)
Hacı Mehmet YEŞİLTAŞ (Ordu University, Ordu Turkey)
Enes ÇİNPOLAT (Ordu University, Ordu Turkey)
Hikmet Kemaloğlu (Fırat University, Elazığ, Turkey)
Çiğdem Bektaş (Fırat University, Elazığ, Turkey)
Handan Öztekin(Fırat University, Elazığ, Turkey)
Alper Osman Öğrenmiş (Fırat University, Elazığ, Turkey)
Yavuz Altın (Fırat University, Elazığ, Turkey)
Reşat Yılmazer (Fırat University, Elazığ, Turkey)
Erdal Baş (Fırat University, Elazığ, Turkey)
Hıfsı Altınok (Fırat University, Elazığ, Turkey)
Mehmet Karay (Final Int. University, Girne, Cyprus)
Gülnür Yel (Final Int.l University, Girne, Cyprus)
Emrah Yılmaz (Fırat University, Elazığ)
Mustafa Yeneroglu (Fırat University, Elazığ, Turkey)
Münevver Tuz (Fırat University, Elazığ, Turkey)
Gülden Altay Suroglu (Fırat University, Elazığ, Turkey)
Pervin Taşel (Final Int.l University, Girne, Cyprus)
Fatma Erdogan (Fırat University, Elazığ, Turkey)
Ebru Cavlak Aslan (Fırat University, Elazığ, Turkey)
Şeyma T. Demiray (Osmaniye Korkut Ata Univ., Turkey)
M. Evren Aydın (Fırat University, Elazığ, Turkey)
Tüba Gülşen (Fırat University, Elazığ, Turkey)
Hatice Aslan (Fırat University, Elazığ, Turkey)
Ahu Ercan (Fırat University, Elazığ, Turkey)
Berat Karaagac (Adıyaman University, Adıyaman, Turkey)
Ezgi Kaya (Igdır University, Igdır, Turkey)
Mahmut İhtiyaroğlu (Van Yüzüncü Yıl Univ., Turkey)
Onur Saldır (Van Yüzüncü Yıl University, Van, Turkey)
Zelal Temel (Van Yüzüncü Yıl University, Van, Turkey)
Şakir İşleyen (Van Yüzüncü Yıl University, Van, Turkey)
Yener Altun (Van Yüzüncü Yıl University, Van, Turkey)
İbrahim Enam İnan (Fırat University, Elazığ, Turkey)
Dilek Günaydın (Fırat University, Elazığ, Turkey)
Betül Demirdağ (ODTÜ University, Ankara, Turkey)
Hajar Farhan Ismael (University of Zakho, Iraq)
Karmina K. Ali (University of Zakho, Iraq)
Sibel Şehriban Ataş (Fırat University, Elazığ, Turkey)
Aysenur Akkılıç (Assistant, Fırat University, Elazığ, Turkey)

LANGUAGE EDITORIAL COMMITTEE

PROCEEDINGS

Full version of submitted papers will be published in Special Volumes of reputed journals. Procedure, Guidelines and Checklist for the preparation and submission of papers to the Proceedings of CMES-2022 can be found in the journals websites. The journals in which selected and peer-reviewed full papers of CMES-2022 will be published are as follows:

1. FRACTAL AND FRACTIONAL [SCI-E],
Selected paper from CMES-2022 will be published in a special issue dedicated to the Conference entitled "New Challenges Arising in Engineering Problems with Fractional and Integer Order-II". https://www.mdpi.com/journal/fractalfract/special_issues/EPFIO2022
This journal is indexed by Clarivate as SCI-E.

2. FRACTALS [SCI-E]
https://www.worldscientific.com/page/fractals/callforpapers.

3. PROCEEDINGS OF THE INSTITUTE OF MATHEMATICS AND MECHANICS [E-SCI]
https://proc.imm.az/special/

4. FULL TEXT PROCEEDING BOOK [FREE]
At the beginning, if Authors submit FULL TEXT PAPERS, then, after getting at least two positive referee reports, FULL TEXT PAPERS will be published in FULL TEXT PROCEEDING BOOK of CMES-2022 with ISBN:77733 number. Therefore, Abstracts of these FULL TEXT PAPERS will NOT be published in ABSTRACT PROCEEDING BOOK of CMES-2022.

1. BOOK OF ABSTRACTS [Free of charge]
If Authors submit ABSTRACT TEXTS, then, after getting referees evaluations for these abstracts, they will be published in ABSTRACT PROCEEDING BOOK of CMES-2022. For FULL TEXT PAPERS, Authors have to submit their FULL TEXT PAPERS online via submission system of CMES-2022. These FULL TEXT PAPERS will be published in FULL TEXT PROCEEDING BOOK of CMES-2022 after getting at least two positive reports.

6. TURKISH JOURNAL OF SCIENCE, [FREE]
"Participants of CMES 2022 can submit their good quality papers to Turkish Journal of Science. After the peer review process, the papers will be published at TJOS. The authors must write "CMES 2022" as comments to the editor.
(Editor in Chief: Dr. Ahmet Ocak AKDEMİR) For on-line submission: https://dergipark.org.tr/tr/pub/tjos

7. TURKISH JOURNAL OF INEQUALITIES, [FREE]
"Participants of CMES 2022 can submit their good quality papers to Turkish Journal of Inequalities. Selected papers will be published at TJI after the peer review process. The participants can send their papers to erhanset@tjinequality.com. The authors must write "CMES 2022" as the subject.
(Editor in Chief: Prof. Dr. Erhan SET)
http://tjinequality.com/

8. MATHEMATICS IN NATURAL SCIENCE (MNS)
*Authors can submit their full text paper directly to the journal by using the following link
https://www.isr-publications.com/mns

9. MATHEMATICS IN ENGINEERING, SCIENCE AND AEROSPACE (MESA), [FREE, SCOPUS]

"Selected papers will be published after peer review in the Journal of Mathematics in Engineering, Science and Aerospace (MESA)"
(Editor in Chief: Prof. Seenith Sivasundaram)
http://nonlinearstudies.com/index.php/mesa

10. APPLIED MATHEMATICS AND NONLINEAR SCIENCES, [SCOPUS]
Participants of CMES 2022 can submit their high quality full text papers to Applied Mathematics and Nonlinear Sciences by selecting CMES-2022 under the Select Article Type Menu.
(https://www.editorialmanager.com/amns/default.aspx)

11. MATHEMATICAL MODELLING AND NUMERICAL SIMULATION WITH APPLICATIONS (MMNSA)
The Special Issue on "Advanced Methods of Modelling and Numerical Computation in Science and Engineering". Authors can submit their full text paper directly to the journal by using the information provided in the following link https://mmnsa.org/index.php/mmnsa/special_issues/SI-CMES2022

12. SPECIAL ISSUE "ADVANCES IN MATRIX TRANSFORMATIONS, OPERATORS AND SYMMETRY"(SCIE)
https://www.mdpi.com/journal/symmetry/special_issues/Advances_Matrix_Transformations_Operators_Symmetry

13. YUZUNCU YIL UNIVERSITY JOURNAL OF THE INSTITUTE OF NATURAL AND APPLIED SCIENCES(The journal indexed by TR-Dizin)
https://dergipark.org.tr/tr/pub/yyufbed

14. PEDAGOGICAL PERSPECTIVE (PEDPER)
Pedagogical Perspective **(PedPer)** is an international, double blind reviwing, non-profit, professional scientific journal. PedPer is a journal that accepts manuscripts related to pedagogy and education.
http://pedagogicalperspective.com/

PLENARY & INVITED TALKS

The interaction of minimizers of functionals and Vanishing Mean Oscillation functions

Maria Alessandra Ragusa

University of Catania, Italy

mariaalessandra.ragusa@unict.it

Abstract We show the advances on some regularity problems related to minimizers

$$u(x) : \Omega \to R^n$$

of some quadratic and non quadratic growth functionals. About the dependence on the variable x is of the integrand function A(x, u, p) of the functionals it belongs to the Vanishing Mean Oscillation class, as a function of x. Then, is pointed out that the continuity of A(x, u, p), with respect to x, is not assumed.

Keyword: Regularity, Minimizers of functionals, Vanishing Mean Oscillation functions.

References

[1] Ragusa M.A., Tachikawa A., Regularity for minimizers for functionals of double phase with variable exponents , Adv. Nonlinear Anal., 9, 710-–728 (2020);

[2] Ragusa M.A., Tachikawa A., Boundary regularity of minimizers of p(x)-energy functionals, Annales de L'Institut Poincarè - Analyse non lineaire, 33, 451--476, (2016).

MODIFIED AND GENERALIZED FRACTIONAL OPERATORS: THEORY AND APPLICATIONS

Dumitru Baleanu
Çankaya University, Turkey and Institute of Space Sciences, Romania
dumitru@cankaya.edu.tr

Abstract

It is wel known that the fractional calculus deals with the study of so-called fractional order integral and derivative operators over real or complex domains, and their applications.In my talk I will present some new trends in the field of modified and generalized fractional operators.Illustrative examples will be presented.

Keywords: fractional calculus, modified fractional operators, generalized fractional operators

REFERENCES

[1] D. Baleanu, K. Diethelm, E. Scalas, J. J. Trujillo, Fractional calculus: models and numerical methods, World Scientific, New York, Second Edition,2016.
[2] M. Caputo and M. Fabrizio, On the singular kernels for fractional derivatives. Some applications to partial differential equations,Progress in Fractional Differentiation and Applications 7, No. 2, 79-82, 2021
[3] R. Nigmatullin, D. Baleanu, A. Fernandez, Balance equations with generalised memory and the emerging fractional kernels, Nonlinear Dynamics, 2021
[4] H. T. Nguyen Huy, D. Baleanu, N. T. Tran Ngoc,D. O'Regan,N. H. Can, Final value problem for nonlinear time fractional reaction-diffusion equation with discrete data, Journal of Computational and Applied Mathematics 376, Article Number: 112883, 2020
[5] D.Baleanu, A.Fernandez, A.Akgul, On a fractional operator combining proportional and classical differintegrals, Mathematics,8(3),Article Number 360,2020
[6] D. Baleanu,, S.S. Samaneh, J. H. Asad, Jihad, A. Jajarmi, Hyperchaotic behaviors, optimal control, and synchronization of a nonautonomous cardiac conduction system, Adv. Differ. Eq., 2021(1), Article Number: 157, 2021.

FIXED POINTS AND COUPLED FIXED POINTS IN B-METRIC SPACES VIA GRAPHICAL CONTRACTIONS

Liliana GURAN

Vasile Goldiș Western University of Arad, Arad, Romania

guran.liliana@uvvg.ro

Abstract

In this paper some existence and stability results for cyclic graphical contractions in complete metric spaces are given. Moreover, we discuss a vectorial case of our main result. Some applications to coupled fixed point problems are also derived.

Keywords: Existence and stability results for cyclic graphical contractions in complete metric spaces

REFERENCES

[1] I.A. Bakhtin, The contraction mapping principle in quasimetric spaces, Funct. Anal., Unianowsk Gos. Ped. Inst. 30(1989) 26-37.

[2] V. Berinde, Generalized contractions in quasimetric spaces, Seminar on Fixed Point Theory, 1993, 3-9.

[3] V. Berinde, Generalized coupled fixed point theorems for mixed monotone mappings in partially ordered metric spaces, Nonlinear Anal. 74 (2011) 7347-7355.

[4] M. Bota, A. Molnar, Cs. Varga, On Ekeland's variational principle in b-metric spaces, Fixed Point Theory, 12(2011), No. 1, 21–28.

[5] S. Czerwik, Contraction mappings in b-metric spaces, Acta Mathematica et Informatica Univ. Ostraviensis 1(1993) 5-11.

A COMPARISON ON SOME INTEGRAL TRANSFORMS

Hossein Jafari[1,2]

[1]Department of Mathematics, University of Mazandaran, Babolsar, Iran

[2]Department of Mathematical Sciences, University of South Africa, UNISA0003, South Africa

jafari.usern@gmail.com,

Abstract

Integral transforms are important to solve real problems. Appropriate choice of integral transforms helps to convert differential equations as well as integral equations into terms of an algebraic equation that can be solved easily.

During last two decades many integral transforms in the class of Laplace transform are introduced such as Sumudu, Elzaki, Natural, Aboodh, Pourreza, Mohand, G_transform, Sawi and Kamal transforms.

In this work, we compare some integral transforms in the class of Laplace transform which are introduced during last few decades. After that we propose a general integral transforms which is covered all of those integral transforms. Also, we discuss about combanition of these integral transforms and decomposition methods.

Keywords: Integral transform; Decomposition methods; Iterative method.

REFERENCES

1. H. Jafari, A new general integral transform for solving fractional integral equation, Journal of Advanced Research, Vol: 32, 133-138, 2021.

MATHEMATICAL METHODS IN INDUSTRIAL MATHEMATICS: A REVIEW FROM RECENT CASE STUDIES

Erhan Coşkun[1]

[1] Department of Mathematics, Karadeniz Technical University, Trabzon, Turkey

erhan@ktu.edu.tr

Abstract In this talk, we describe our experience of identification, mathematical formulation and handling of industrial problems posed by firms having active research and development units. We highlight common features of industrial problems from OECD report of industrial mathematics [1], describe basic mathematical tools and skills needed to engage in problems of industry and discuss some relevant case studies including the ones from the Euro-Asian Study Group with Industry[2] held in Trabzon, Turkey. Our aim is to convince young mathematicians that they can indeed develop their skills to tackle industrial problems, which will not only help industry to gain compatitive advantage but also lead to having original research areas that are more likely to be supported from private and government institutions.

Keywords: Industrial mathematics; mathematical modeling; study groups with industry.

REFERENCES

1. Mathematics in Industry, OECD Global Science Forum report, https://www.oecd.org/science/inno/41019441.pdf
2. Coskun, E. et al., *Gabor Filter Selection and Computational Processing for Emotion Recognition.* Study Group: ESGI 100. 7–11 April, 2014, Oxford, UK. *DOI:* 10.33774/miir-2021-5q5j6.

SHANNON–WHITTAKER–KOTEL’NIKOV’S THEOREM GENERALIZED

JUANLUİS GARCÍA GUİRAO
Technical University of Cartagena, Spain
juan.garcia@upct.es
http://www.jlguirao.es

Abstract The aim of the this talk provide a generalization of the classical Shannon-Whittaker-Katel’niko’s theorem for a class of non band-limited signals which plays a central role in the signal theory, the Gaussian map is the unique function which reachs the minimum of the product of the temporal and frecuential width. This solves a conjecture stated by Boas in 1972.

Keywords: Shannon–Whittaker–Kotel’nikov’s Theorem; recomposi- tion of chemical products, signal theory.

REFERENCES

[1] R.P. Boas Jr., Summation formulas and band--limited signals, Tohoku Math. J., 24, (1972), 121-125.

COMPLEX DYNAMICS OF A RATIO-DEPENDENT POPULATION MODEL: STABILITY, BIFURCATIONS AND CHAOS

HUSEYIN MERDAN
TOBB University of Economics and Technology, Department of Mathematics,
Ankara, Turkey

merdan@etu.edu.tr

Abstract Nonlinear dynamical behaviors of a prey-predator system with Leslie type will be presented. First, the stability analysis will be given. Second, the bifurcations and chaotic behavior of the model will be discussed. Finally, numerical simulations will be shown to support and extend the theoretical results. The results obtained will be interpreted from the biological point of view.

Keywords: Prey-predator model, stability analysis, bifurcations, chaotic behavior

References

[1] E. Karaoglu and H. Merdan, Hopf bifurcations of a ratio-dependent predator-prey model involving two discrete matutaion time delays, Chaos, Soliton and Fractals, 68, 159-168, (2014)

[2] P. Baydemir, H. Merdan, E. Karaoglu and G. Sucu, G, Complex dynamics of a discrete-time prey-predator system with Leslie type: Stability, bifucation analyses and chaos, International Journal of Bifurcation and Chaos, Vol. 30, No. 10, 2050149 (2020).

[3] S. Yildiz, S. Bilazeroglu and H. Merdan, Stability and bifurcation analyses of a discrete Lotka-Volterra type predator-prey system with refuge effect, Preprint, (2022)

[4] S. Wiggins, Introduction to Applied Nonlinear Dynamical Systems and Chaos, Springer-Verlag, New York, (2003)

TYPE-2 FUZZY SYSTEMS AND FUTURE TRENDS FOR TYPE-3: THEORY AND APPLICATIONS

Oscar CASTILLO
Tijuana Institute of Technology, Tijuana, Mexico.
ocastillo@tectijuana.mx

Abstract: Type-2 fuzzy systems are powerful intelligent models based on the theory of fuzzy sets, originally proposed by Prof. Zadeh. Most real-world applications up to now are based on type-1 fuzzy systems, which are built based on the original (type-1) fuzzy sets that extend the concept of classical sets. Type-2 fuzzy sets extend type-1 fuzzy sets by allowing the membership to be fuzzy, in this way allowing a higher level of uncertainty management. Even with the current successful applications of type-1 fuzzy systems, now several papers have shown that type-2 is able to outperform type-1 in control, pattern recognition, manufacturing and other areas. The key challenge in dealing with type-2 fuzzy models is that their design has a higher level of complexity, and in this regard the use of bio-inspired optimization techniques is of great help in finding the optimal structure and parameters of the type-2 fuzzy systems for particular applications, like in control, robotics, manufacturing and others. Finally, the prospects for the future trends and applications of type-3 fuzzy logic will be discussed.

Keywords: Type-2 Fuzzy systems, Type-1 fuzzy systems, Fuzzy Logic.

AN EVALUATION ON THE RELATIONSHIP BETWEEN HUMANITY'S ADVENTURE OF KNOWLEDGE AND HIKMAH

Vatan KARAKAYA
Department of Mathematical Engineering, Yildiz Technical University, Istanbul, Turkey
Ahi Evran University, Kirsehir, Turkey
vkkaya@yahoo.com

Abstract

The main purpose of this study is to investigate the knowledge and wisdom relationship based on the definitions of God and knowledge of certain civilizations within the context of written history. This relationship is tried to be explained under the definitions of God and knowledge derived from eminent thinkers of Ancient Greece, Islamic and Modern Western civilizations. The relationship between knowledge and wisdom in those two civilizations are examined with regard to the concept of 'hikmah' defined in Islamic civilization. After that, a general comparison was made on the topics of God and knowledge definitions of the founder thinkers of these three civilizations. As a result of this comparison, it has been concluded that the definitions of God and knowledge definitions of Ancient Greece and Modern Western civilizations are similar, and these two concepts do not match the content of 'hikmah'. Main reason behind this discrepancy is concluded as the unique conglomeration of tasawwuf, kalam and Aristotelian philosophy in Islamic civilization. In Islamic civilization, these three thought traditions assimilated the thought before them, formed their own tradition and laid the groundwork for the next civilization.

Keywords: Belief in God, definition of knowledge, knowledge and hikmah.

REFERENCES

Abdurrahman, T. (2021). Amel sorunsalı bilim ve düşüncenin pratik temelleri üzerine bir araştırma. (T. Uluç, Çev.). Pınar Yayınları.

Aristoteles. (1999). Metaphysics. A new transalation by Joe Sachs. Green Lion Press. Descartes, R. (2019). Yöntem üzerine konuşma. (Ç. Dürüşken, Çev.). Alfa Yayınları.

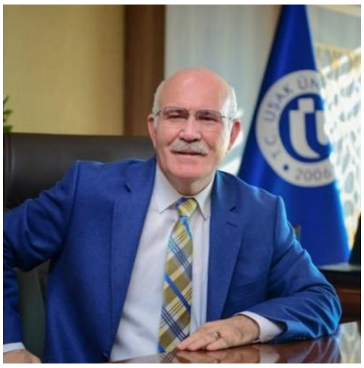

A NEW SEQUENCE SPACE OF WEIGHT g

Ekrem SAVAŞ
Department of Mathematics, Usak University, Usak, Turkey
ekremsavas@yahoo.com

ABSTRACT. Recall that $f : [0,\infty) \to [0,\infty)$ is a modulus function if it satisfies the following properties.

i): $f(x) = 0$ if and only if $x = 0$,

ii): $f(x+y) \leq f(x) + f(y)$,

iii): f is increasing,

iv): f is continuous from the right at 0.

In this paper, we define a new sequence space by using modulus function and also investigate some relations the spaces between $[\hat{V}^g, \lambda, f, t]$ and $\hat{S}_\lambda^g$ where $g : [0,\infty) \times [0,\infty) \to [0,\infty)$, $g((x_{nm}) \to \infty$ for any sequence (x_{nm}) in $[0,\infty) \times [0,\infty)$ with $x_{nm} \to \infty$.

REFERENCES

[1] S. Banach, Théorie des Opérations lieaires, Chelsea Publ. Co., New York, 1955.
[2] S. Bhunia, P. Das and S. K. Pal, Restricting statistical convergence, Acta Math. Hungar. 134 (1-2) (2012), 153-161.
[3] Cakalli, H.; Savas, E. Statistical convergence of double sequences in topological groups. J. Comput. Anal. Appl. 12 (2010), no. 2, 421-426.
[4] R. Colak, Statistical convergence of order α, Modern methods in Analysis and its Applications, New Delhi, India, Anamaya Pub., (2010), 121-129.
[5] R. Colak, Y. Altin, Statistical convergence of double sequences of order α, Journal of Function Spaces, Volume 2013, Article ID 682823.
[6] M. Isik, Y. Altin, and Altin $f(\alpha,\mu)$-statistical convergence of order α for double sequences,J. Ineq. Appl. (2017) 2017:246.
[7] H. Nakano, Modular sequence spaces, Proc. Japan Acad., 27 (1953), 508 - 512.
[8] E. Savaş, Strong almost convergence and almost λ-statistical convergence, Hokkaido Math. J., 29 (3)(2000), 531 - 536.

AUTHORS	TITLES	PAGE
Elif Başkaya	AN APPROXIMATION METHOD FOR THE EIGENVALUE OF A STURM-LIOUVILLE PROBLEM	1
Yasin Bozkurt, Mehmet Tahir Gulluoglu, Haci Mehmet Baskonus	SOME RESULTS FOR A NONLINEAR TRANSMISSION LINE ARISING IN THE ELECTRONIC CIRCUIT	12
Hande Yüzel, Onur Toklu, Senem Şahan Vahaplar, M. Fatih Akay,Sevtap Erdem	BLOCKCHAIN-BASED SERVICE NETWORK PORTAL	23
Adnène Arbi, Najeh Tahri	DYNAMICS OF PSEUDO ALMOST ANTI-PERIODIC SOLUTION OF DELAY DIFFERENTIAL EQUATIONS ON TIME SCALES	31
Gülden Altay Suroğlu ,Yusuf Güzel	ON MODIFIED WEINGARTEN PARALLEL RULED SURFACE	37
Eren Çolak, Ali Keleş, Emre Aslan, İmren Hatay Patır	NUMERICAL INVESTIGATION OF PARTICLE DISTRIBUION IN A CYLINDRICAL CHANNEL	44
Rabia Kevser Yılmaz, Oğuz Yağcı, Recep Şahin	DEGENERATE ARA INTEGRAL TRANSFORM AND ITS APPLICATIONS	52
İnci Çakmak, Aynur Şahin	SOME RESULTS ON THE (p, q)- CALCULUS AND PARTIAL (p, q)-DIFFERENTIAL EQUATIONS	62
Iqbal H. Jebrıl, Iqbal M. Batiha, Abeer A. Al-Nana, Adel Ouannas, Shaher Momani	AN APPLICABLE CONDITION FOR ASSESSING THE STABITLTY OF LINEAR FRACTIONAL DIFFERENTIAL SYSTEMS	74
Mustafa Özdemir, Eralp Osman Erdoğan	FORMULATION OF A 7-DOF HALF-CAR MODEL WITH NONLINEAR SPRINGS AND DAMPERS FOR RIDE COMFORT ANALYSIS OF IN-WHEEL-MOTOR ELECTRIC VEHICLES	83
Oğuzhan Taş, Amani Yahyaoui	MACHINE LEARNING BASED INTRUSION DETECTION SYSTEM USING GREY WOLF OPTIMIZATION FOR FEATURE SELECTION	93
Yasemin Akgün	THERMAL INSULATION PERFORMANCES OF FOAMED MORTARS CONTAINING BENTONITE BLENDED CEMENTS	102
Arzu Bal, Numan Yalçın and Mutlu Dedetürk	ON SOLUTIONS OF INTEGRAL EQUATIONS IN GEOMETRIC ANALYSIS	111
Zeynep Kübra Kazan, Sevda Türkiş, Elif Çil	A DOCUMENT ANALYSIS ON THE EFFECT OF FINLAND AND TURKISH EDUCATION SYSTEMS ON PISA SUCCESS	124
Mustafa Mutlu and Çetin Kurnaz	RECTANGULAR MICROSTRIP ANTENNA DESIGN FOR WIRELESS TECHNOLOGIES	136
Mustafa Kara	SCATTERED GEOMETRICAL OPTICS FIELD BY A PERFECTLY CONDUCTING HALF PLANE BETWEEN TWO ISOREFRACTIVE MEDIA	152
Hayatem Hamal, Pembe Sabancıgil	KANTOROVICH TYPE (p,q) GENERALIZATION OF BERNSTEIN OPERATORS	159
Ilhame Amirali and Ece Eroglu	A BRIEFSURVEYONNUMERICAL SOLUTIONS OFSINGULARLY PERTURBEDPROBLEMS	166

Serkan ÖZDEMİR, Ecir Uğur KÜÇÜKSİLLE, Serkan GÜLSOY, Özdemir ŞENTÜRK, Mehmet Güvenç NEGİZ, Halil SÜEL, Ahmet MERT, Kürşad ÖZKAN	MODELING OF SPECIES DISTRIBUTIONS WITH DEEP LEARNING METHOD	180
Fatih Coşkun, Beytullah Topçu, M. Fatih Akay	DEVELOPMENT OF A NATIONAL SMART METER SYSTEM	191
Özlem Kırcı	ANALYSIS OF THE SOLUTIONS OF A SPACE-TIME FRACTIONAL MATHEMATICAL MODEL WITH AN ANALYTICAL METHOD	198
Gökhan Kaplan, Oğuzhan Çelebi, Ali Öz, Haluk Görkem Alcan, Barış Bayrak, Abdulkadir Cüneyt Aydın	INVESTIGATION OF MECHANICAL AND MICROSCOPIC PROPERTIES OF RECYCLED CONCRETE BASED ON GEOPOLYMER POWDER CONTAINING LIME AND METAKAOLIN	210
Ali Öz, Oğuzhan Çelebi, Gökhan Kaplan, Barış Bayrak, Haluk Görkem Alcan, Abdulkadir Cüneyt Aydın	THE EFFECT OF POLYVINYL ALCOHOL FIBER ON THE MECHANICAL PROPERTIES OF HIGH STRENGTH GEOPOLYMER CONCRETES	221
Ayşe Kabataş	AN EIGENVALUE PROBLEM WITH A SPECTRAL PARAMETER IN BOUNDARY CONDITIONS	231
Gül Deniz Çaylı	A NEW CONSTRUCTION METHOD FOR TRIANGULAR NORMS AND TRIANGULAR CONORMS ON BOUNDED LATTICES	240
Ümmügülsün Akbaba, Ali Hikmet Değer, Tolga Berber	AN ALGORITHM FOR THE VERTICES ON THE PATHS OF MINIMAL LENGTH IN THE SUBORBITAL GRAPHS	250
Çimen Gül Kuluşaklı, Mustafa Birinci	FINE GRINDING OF MARBLE WASTE: PRELIMINARY TEST RESULTS	256
Derya Deniz and Mücahit Saydam	ON THE SOLUTION PAVLOV EQUATION BY THE VARIATIONAL ITERATION METHOD	263
Pakize Uygun	ON P-SASAKIAN MANIFOLDS SATISFYING CERTAIN CURVATURE CONDITIONS	270
Oğuzhan Çelebi, Barış Bayrak, Mahmut Kılıç, Abdulkadir Cüneyt Aydın	INVESTIGATION OF THE EFFECTS OF AMBIENT VIBRATIONS FILTERED AT DIFFERENT FREQUENCY RANGE ON THE DYNAMIC BEHAVIOR OF THE BUILDING	277
Furkan Şimşek, Şükrü Kitiş	ARDUINO BASED DIGITAL TACHOMETER WITH TRACKING PROGRAM	287
İnci Çilingir Süngü, Emre Aydın	ON THE SEMI-ANALYTICAL METHODS FOR THE FIFTH ORDER NONLINEAR KdV EQUATIONS	298
Esma Kurban, Fatmanur Büyükbayraktar	OPINIONS OF PRE-SERVICE SCIENCE TEACHERS ABOUT VIRTUAL TOURS TO SCIENCE CENTERS	312
Hicran Gümüşbaş, Ulas Vural	SEGMENTATION OF ELECTRICITY SUBSCRIBERS BASED ON THE CONSUMPTION PATTERNS	321
Oğuzhan Çelebi, Barış Bayrak, Mahmut Kılıç, Abdulkadir Cüneyt Aydın	ENERGY BASED EVALUATION OF REINFORCED CONCRETE STRUCTURE AFFORDABLE BY FAR FIELD EARTHQUAKE	329
Erdem Türkeli	THE WIND LOAD CALCULATION OF A MASONRY MINARET BY USING DIN1056 STANDARD	351

Ömer Akgüller, Mehmet Ali Balcı	DISTRIBUTION OF DISCRETE GEODESICS ON ALPHA COMPLEXES	359
Yusuf Ziya Yüksel, Şeref Doğuşcan Akbaş	STRESS ANALYSIS OF MULTI-LAYERED SOIL MEDIUM BY USING FINITE AND INFINITE ELEMENTS	366
Afrah Said, Hanife Göker	AUTISM SPECTRUM DISORDER DETECTION USING MACHINE LEARNING ALGORITHMS	376
Yusuf Ziya Yüksel , Şeref Doğuşcan Akbaş	STATIC RESPONSES OF A CAVITY IN A HALF-SPACE BY USING FINITE ELEMENT METHOD	387
Elham Sefıdgarı, Ercan Çelik, Babak Shırı	COMPLEX TRANSFORM METHOD FOR SYSTEM OF FRACTIONAL DIFFERENTIAL EQUATIONS AND APPLICATIONS	397
Sefa Yıldırım, Beyza Canbolat, M. Enes Güngör, Şahin Akdoğan, Lokman Kuzu	COCO ANTENNA DESIGN AND MANUFACTURING	406
M.Taher Omar, Shelan Saied Ismaeel	COMPARE K-NEAREST NEIGHBOR METHOD WITH KERNEL MODEL IN NONPARAMETRIC FUNCTIONAL REGRESSION	412
Betül Turanoğlu Şirin	A MULTI CRITERIA DECISION MAKING APPROACH BASED ON ENTROPY AND MOORA METHOD FOR THE MASK SELECTION PROBLEM	417
Mesut Tartuk, Furkan Taha Nurdağ, Vedat Acar, Mehmet Fatih Akay, Fatih Abut	CALL ASSISTANT APPLICATION FOR CALL CENTERS	424
Damla Okulu, Fatih Selimefendigil, Hakan F. Öztop	SIMULATION OF THERMOELECTRIC ENERGY CONVERSION FOR DIFFERENT THERMOELECTRIC DEVICE INSTALLATIONS IN A CHANNEL FLOW OPERATING WITH AIR AND HYBRID NANOFLUIDS	434
Oguzhan Karahan, Hasan Karcı, Ali Tangel	TIME OPTIMAL TRAJECTORY GENERATION IN JOINT SPACE FOR 6R INDUSTRIAL SERIAL ROBOTS USING CUCKOO SEARCH ALGORITHM	455

AN APPROXIMATION METHOD FOR THE EIGENVALUE OF A STURM-LIOUVILLE PROBLEM

Elif BAŞKAYA [1]

[1] Department of Mathematics, Karadeniz Technical University, Trabzon, Turkey

elifbekar@ktu.edu.tr,

Abstract

In this paper, we approximate the eigenvalues of a Sturm-Liouville problem includes the spectral parameter in a boundary condition by associating the problem with Riccati equation. The potential of the problem is real valued, continuous, monoton and symmetric.

Keywords: Sturm-Liouville problem; Asymptotic eigenvalues; Continuous potential.

1. INTRODUCTION

This manuscript includes the following boundary value problem

$$y''(t)+\{\lambda-q(t)\}y(t)=0, \quad t\in[0,a], \tag{1}$$

$$\alpha_1 y(0)-\alpha_2 y'(0)=\lambda\left[\alpha_1' y(0)-\alpha_2' y'(0)\right], \tag{2}$$

$$y(a)\cos\beta+y'(a)\sin\beta=0, \quad \beta\in[0,\pi), \tag{3}$$

where λ is a real parameter; $q(t)$ is a real-valued function; $\alpha_i,\ \alpha_i'\in\mathbb{R}$ for $i=1,2$. Also we assume that $q(t)$ is continuous, monoton and symmetric in the related interval. [10] proves that this problem is self-adjoint problem if the relation $\alpha_1'\alpha_2-\alpha_1\alpha_2'>0$. In [7], it is given that the type of this boundary value problems arises from the method of separation of variables applied to mathematical models for physical and this problem has been studied by many researchers before. Some of them are [3]-[6], [9]. Besides, (1) is equal to one-dimensional Schrödinger equation and especially in recent years, since quantum mechanic has gained importance, there are a lot of studies on eigenvalues of Hill' s equation and Schrödinger' s operator with symmetric single well potential [1], [3] and [9]. In this paper, our potential is symmetric single well potential on [0,a] is defined as symmetric with respect to the midpoint a/2 and nonincreasing on [0, a/2]. The eigenvalues of these equations represent excitation energy and eigenfunctions are named as wavefunction in physics. The purpose of this paper is to obtain asymptotic approximations for the eigenvalues of (1)-(3).

2. GENERAL PROPERTIES OF METHOD

First of all, we can say that $q'(t)$ exists because a monotone function on an interval is differentiable almost everywhere on that interval [8].

We use the similar method to [2]. We associate (1) with its Riccati equation

$$v'(t,\lambda) = -\lambda + q - v^2$$

and we identify the following functions

$$S(t,\lambda) := \mathrm{Re}\left[v(t,\lambda)\right], \tag{4}$$

$$T(t,\lambda) := \mathrm{Im}\left[v(t,\lambda)\right]. \tag{5}$$

[2] says that any real-valued solution of (1) is in the form

$$y(t,\lambda) = R(t,\lambda)\cos\theta(t,\lambda) \tag{6}$$

with

$$S(t,\lambda) = \frac{R'(t,\lambda)}{R(t,\lambda)}, \tag{7}$$

$$T(t,\lambda) = \theta'(t,\lambda). \tag{8}$$

We remark that we use the last equation to calculate asymptotic eigenvalues of the problem, thus we have

$$\theta(a,\lambda) - \theta(0,\lambda) = \int_0^a T(x,\lambda)\,dx. \tag{9}$$

We suppose that there exist functions $A(t)$ and $\eta(\lambda)$ so that

$$\left|\int_t^a e^{2i\lambda^{1/2}x} q'(x)\,dx\right| \le A(t)\eta(\lambda), \quad t \in [0,a]$$

where

i) $A(t) := \int_t^a |q'(x)|\,dx$ is a decreasing function of t,

ii) $A(.) \in L[0,a]$,

iii) $\eta(\lambda) \to 0$ as $\lambda^{1/2} \to \infty$.

For $q' \in L[0,a]$ the existence of the A and η functions may be established for λ positive as follows. We note that, avoiding the trivial case $\int_t^a |q'(x)| dx = 0$. $\left|\int_t^a e^{2i\lambda^{1/2}x} q'(x)\,dx\right| \le \int_t^a |q'(x)| dx < \infty$ so, if we define

$$F(t,\lambda) := \begin{cases} \left|\int_t^a e^{2i\lambda^{1/2}x} q'(x)\,dx\right| / \int_t^a |q'(x)| dx, & \text{if } \int_t^a |q'(x)| dx \ne 0, \\ 0 & , \text{ if } \int_t^a |q'(x)| dx = 0, \end{cases} \tag{10}$$

then $0 \le F(t,\lambda) \le 1$ and we set $\eta(\lambda) := \sup_{0 \le t \le a} F(t,\lambda)$. $\eta(\lambda)$ is well defined by (10) and $\lambda^{-1/2}\eta(\lambda) \to 0$ as $\lambda \to \infty$ [2].

Our method of approximating a solution of Riccati equation $v'(t,\lambda) = -\lambda + q - v^2$ on $[0,a]$ is similar to [2], so we set

$$v(t,\lambda) := i\lambda^{1/2} + \sum_{n=1}^{\infty} v_n(t,\lambda). \tag{11}$$

When we put this serie into the Riccati equation and solve differential equations, we hold

$$\begin{aligned} v_1(t,\lambda) &= -e^{-2i\lambda^{1/2}t} \int_t^a e^{2i\lambda^{1/2}x} q(x)\,dx, \\ v_2(t,\lambda) &= e^{-2i\lambda^{1/2}t} \int_t^a e^{2i\lambda^{1/2}x} v_1^2(x,\lambda)\,dx, \\ v_n(t,\lambda) &= e^{-2i\lambda^{1/2}t} \int_t^a e^{2i\lambda^{1/2}x} \left[v_{n-1}^2(x,\lambda) + 2v_{n-1}(x,\lambda) \sum_{m=1}^{n-2} v_m(x,\lambda) \right] dx, \quad n \ge 3. \end{aligned} \tag{12}$$

Also if we consider (9) with (5) and (11), we have

$$\theta(a,\lambda) - \theta(0,\lambda) = \int_0^a \left[\lambda^{1/2} + \operatorname{Im} \sum_{n=1}^{\infty} v_n(x,\lambda) \right] dx,$$

thus

$$\theta(a,\lambda) - \theta(0,\lambda) = \lambda^{1/2} a + \sum_{n=1}^{\infty} \operatorname{Im} \int_0^a v_n(x,\lambda)\,dx. \tag{13}$$

Theorem 1. [2] If $v(t,\lambda)$ as in (11), as $\lambda \to \infty$

$$v(t,\lambda)=i\lambda^{1/2}+v_1(t,\lambda)+O\left(\lambda^{-1}\eta^2(\lambda)\right)$$

where

$$v_1(t,\lambda)=-\frac{1}{2}\lambda^{-1/2}q(a)\sin 2\lambda^{1/2}(a-t)+\frac{1}{2}\lambda^{-1/2}\int_t^a\left[\sin 2\lambda^{1/2}(x-t)\right]q'(x)dx$$
$$+i\left\{\frac{1}{2}\lambda^{-1/2}q(a)\cos 2\lambda^{1/2}(a-t)-\frac{1}{2}\lambda^{-1/2}q(t)-\frac{1}{2}\lambda^{-1/2}\int_t^a\left[\cos 2\lambda^{1/2}(x-t)\right]q'(x)dx\right\}$$

and $\eta(\lambda)$ is defined with (10).

After some calculations by using the last theorem, with (4) we can write

$$S(t,\lambda)=-\frac{1}{2}\lambda^{-1/2}q(a)\sin 2\lambda^{1/2}(a-t)+\frac{1}{2}\lambda^{-1/2}\left(\cos 2\lambda^{1/2}t\right)\int_t^a\left[\sin 2\lambda^{1/2}x\right]q'(x)dx$$
$$-\frac{1}{2}\lambda^{-1/2}\left(\sin 2\lambda^{1/2}t\right)\int_t^a\left[\cos 2\lambda^{1/2}x\right]q'(x)dx+O\left(\lambda^{-1}\eta^2(\lambda)\right).$$

Let use the following notations:

$$\sin\xi_t:=\int_t^a\left[\cos 2\lambda^{1/2}x\right]q'(x)dx,$$

$$\cos\xi_t:=\int_t^a\left[\sin 2\lambda^{1/2}x\right]q'(x)dx,$$

so we can express $S(t,\lambda)$ as

$$S(t,\lambda)=-\frac{1}{2}\lambda^{-1/2}q(a)\sin 2\lambda^{1/2}(a-t)+\frac{1}{2}\lambda^{-1/2}\cos\left(2\lambda^{1/2}t+\xi_t\right)+O\left(\lambda^{-1}\eta^2(\lambda)\right). \tag{14}$$

Similarly, with (5) we gain $T(t,\lambda)$ as

$$T(t,\lambda)=\lambda^{1/2}+\frac{1}{2}\lambda^{-1/2}q(b)\cos 2\lambda^{1/2}(b-t)-\frac{1}{2}\lambda^{-1/2}q(t)-\frac{1}{2}\lambda^{-1/2}\sin\left(2\lambda^{1/2}t+\xi_t\right)$$
$$+O\left(\lambda^{-1}\eta^2(\lambda)\right). \tag{15}$$

Also, by using integration by part to (12), we determine

$$\int_a^b v_1(x,\lambda)dx=\frac{i}{2\lambda^{1/2}}\int_t^b e^{2i\lambda^{1/2}(x-a)}q(x)dx$$

and again with integration by part

$$\int_a^b v_1(x,\lambda)dx = \frac{i}{2}\lambda^{-1/2}e^{-2i\lambda^{1/2}a}\left[\frac{q(x)e^{2i\lambda^{1/2}x}}{2i\lambda^{1/2}}\Bigg|_{x=a}^{b} - \frac{1}{2i\lambda^{1/2}}\int_a^b e^{2i\lambda^{1/2}x}q'(x)dx\right]$$

$$= \frac{1}{4}\lambda^{-1}e^{2i\lambda^{1/2}(b-a)}q(b) - \frac{1}{4}\lambda^{-1}q(a) - \frac{1}{4}\lambda^{-1}e^{-2i\lambda^{1/2}a}\int_a^b e^{2i\lambda^{1/2}x}q'(x)dx$$

$$= \frac{1}{4}\lambda^{-1}q(b)\left[\cos 2\lambda^{1/2}(b-a) + i\sin 2\lambda^{1/2}(b-a)\right] - \frac{1}{4}\lambda^{-1}q(a)$$

$$-\frac{1}{4}\lambda^{-1}\int_a^b\left[\cos 2\lambda^{1/2}(x-a) + i\sin 2\lambda^{1/2}(x-a)\right]q'(x)dx,$$

so

$$\operatorname{Im}\int_a^b v_1(x,\lambda)dx = \frac{1}{4}\lambda^{-1}q(b)\sin 2\lambda^{1/2}(b-a) - \frac{1}{4}\lambda^{-1}\cos(2\lambda^{1/2}a + \xi_a).$$

We also have from equation (12),

$$\int_a^b v_2(x,\lambda)dx = \frac{i}{2\lambda^{1/2}}\int_a^b\left[1 - e^{2i\lambda^{1/2}(x-a)}\right]v_1^2(x,\lambda)dx$$

and for $n \geq 3$

$$\int_a^b v_n(x,\lambda)dx = \frac{i}{2\lambda^{1/2}}\int_a^b\left[1 - e^{2i\lambda^{1/2}(x-a)}\right]\left[v_{n-1}^2(x,\lambda) + 2v_{n-1}(x,\lambda)\sum_{m=1}^{n-2}v_m(x,\lambda)\right]dx.$$

Thus, with the last equations

$$\int_a^b\sum_{n=1}^{\infty}\operatorname{Im}\{v_n(x,\lambda)\}dx = \sum_{n=1}^{\infty}\operatorname{Im}\left\{\int_a^b v_n(x,\lambda)dx\right\}$$

$$= \frac{1}{4}\lambda^{-1}q(b)\sin 2\lambda^{1/2}(b-a) - \frac{1}{4}\lambda^{-1}\cos(2\lambda^{1/2}a + \xi_a) \tag{16}$$

$$+O\left(\lambda^{-3/2}\eta^2(\lambda)\right).$$

We take advantage of the main results of [2] which finds the results by writing (6) for boundary conditions by using (7), (8) and their asymptotic expansion (14), (15), and also (16) in (13). So if we rearrange Theorem 2.1 and Theorem 2.2 of [2] according to our interval, we easily gain the following asymptotic expansions:

Theorem 2 The eigenvalues λ_n of (1)-(3) satisfy as $n \to \infty$,

i) if $\alpha_2' \neq 0$ and $\beta \neq 0$,

$$\lambda_n^{1/2}=\frac{(n+1)\pi}{a}+\frac{1}{(n+1)\pi}\left\{\cot\beta+\frac{\alpha_1'}{\alpha_2'}-\frac{a}{4(n+1)\pi}\int_0^a\left[\sin\frac{2(n+1)\pi x}{a}\right]q'(x)dx\right.$$

$$+\frac{\alpha_1'}{2\alpha_2'}\frac{a^2}{(n+1)^2\pi^2}\left[q(a)-q(0)-\frac{2\left(3\alpha_1'\alpha_2'\alpha_2+3\alpha_1'[\alpha_2']^2+[\alpha_1']^3\right)}{3\alpha_1'[\alpha_2']^2}-\frac{2\alpha_2'}{3\alpha_1'}\cot^3\beta\right]$$

$$\left.+\frac{\alpha_1'}{2\alpha_2'}\frac{a^2}{(n+1)^2\pi^2}\int_0^a\left[\cos\frac{2(n+1)\pi x}{a}\right]q'(x)dx\right\}+O\left(n^{-4}\eta(n)\right)+O\left(n^{-3}\eta^2(n)\right),$$

ii) if $\alpha_2'\neq 0$ and $\beta=0$,

$$\lambda_n^{1/2}=\frac{(2n+3)\pi}{2a}+\frac{1}{(2n+3)\pi}\left\{\frac{2\alpha_1'}{\alpha_2'}-\frac{a}{(2n+3)\pi}\int_0^a\left[\sin\frac{(2n+3)\pi x}{a}\right]q'(x)dx\right.$$

$$+\frac{4\alpha_1'}{\alpha_2'}\frac{a^2}{(2n+3)^2\pi^2}\left[q(a)+q(0)+\frac{2\left(3\alpha_1'\alpha_2'\alpha_2-3\alpha_1[\alpha_2']^2-[\alpha_1']^3\right)}{3\alpha_1'[\alpha_2']^2}\right]$$

$$\left.+\frac{4\alpha_1'}{\alpha_2'}\frac{a^2}{(2n+3)^2\pi^2}\int_0^a\left[\cos\frac{(2n+3)\pi x}{a}\right]q'(x)dx\right\}+O\left(n^{-4}\eta(n)\right)+O\left(n^{-3}\eta^2(n)\right).$$

Theorem 3 The eigenvalues λ_n of (1)-(3) satisfy as $n\to\infty$,

i) if $\alpha_2'=0$ and $\beta\neq 0$,

$$\lambda_n^{1/2}=\frac{(2n+3)\pi}{2a}+\frac{1}{(2n+3)\pi}\left\{2\cot\beta+\frac{2\alpha_2}{\alpha_1'}+\frac{a}{(2n+3)\pi}\int_0^a\left[\sin\frac{(2n+3)\pi x}{a}\right]q'(x)dx\right.$$

$$-\frac{4\alpha_2}{\alpha_1'}\frac{a^2}{(2n+3)^2\pi^2}\left[q(a)+q(0)+\frac{2\left(1-\dfrac{3\alpha_1'\alpha_1}{\alpha_2^2}\right)}{3\left[\dfrac{\alpha_1'}{\alpha_2}\right]^2}-\frac{2}{3}\cot^3\beta\right]$$

$$\left.-\frac{4\alpha_2}{\alpha_1'}\frac{a^2}{(2n+3)^2\pi^2}\int_0^a\left[\cos\frac{(2n+3)\pi x}{a}\right]q'(x)dx\right\}+O\left(n^{-4}\eta(n)\right)+O\left(n^{-3}\eta^2(n)\right),$$

ii) if $\alpha_2'=0$ and $\beta=0$,

$$
\begin{aligned}
\lambda_n^{1/2} = {} & \frac{(n+2)\pi}{a} + \frac{1}{(n+2)\pi}\left\{\frac{\alpha_2}{\alpha_1'} + \frac{a}{4(n+2)\pi}\int_0^a \left[\sin\frac{2(n+2)\pi x}{a}\right] q'(x)\,dx \right. \\
& -\frac{\alpha_2}{2\alpha_1'}\frac{a^2}{(n+2)^2\pi^2}\left[q(a)-q(0)+\frac{2\left(1-\frac{3\alpha_1'\alpha_1}{\alpha_2^2}\right)}{3\left[\frac{\alpha_1'}{\alpha_2}\right]^2}\right] \\
& \left. -\frac{\alpha_2}{2\alpha_1'}\frac{a^2}{(n+2)^2\pi^2}\int_0^a \left[\cos\frac{2(n+2)\pi x}{a}\right] q'(x)\,dx \right\} + O\left(n^{-4}\eta(n)\right) + O\left(n^{-3}\eta^2(n)\right).
\end{aligned}
$$

3. RESULTS

We assume without loss of generality that $q(t)$ has mean value zero. That is $\int_a^b q(t)\,dt = 0$. Our potential is symmetric single well, so we can write $q(t)=q(a-t)$. We will use this trueness, calculate integral terms Theorem 2 and Theorem 3. Firstly, let us consider the following lemma:

Lemma 1 If $q(t)$ is a symmetric single well potential, then

i) $\int_0^a \left[\sin\frac{2(n+1)\pi x}{a}\right] q'(x)\,dx = 2\int_0^{a/2} \left[\sin\frac{2(n+1)\pi x}{a}\right] q'(x)\,dx,$

ii) $\int_0^a \left[\sin\frac{(2n+3)\pi x}{a}\right] q'(x)\,dx = 0,$

iii) $\int_0^a \left[\sin\frac{2(n+2)\pi x}{a}\right] q'(x)\,dx = 2\int_0^{a/2} \left[\sin\frac{2(n+2)\pi x}{a}\right] q'(x)\,dx,$

iv) $\int_0^a \left[\cos\frac{2(n+1)\pi x}{a}\right] q'(x)\,dx = 0,$

v) $\int_0^a \left[\cos\frac{(2n+3)\pi x}{a}\right] q'(x)\,dx = 2\int_0^{a/2} \left[\cos\frac{(2n+3)\pi x}{a}\right] q'(x)\,dx,$

vi) $\int_0^a \left[\cos\frac{2(n+2)\pi x}{a}\right] q'(x)\,dx = 0.$

Proof i) Because $q(t)$ is a symmetric single well potential, $q'(t)$ exists and

$$\int_0^a \left[\sin\frac{2(n+1)\pi x}{a}\right] q'(x)\,dx = \int_0^{a/2} \left[\sin\frac{2(n+1)\pi x}{a}\right] q'(x)\,dx + \int_{a/2}^{a} \left[\sin\frac{2(n+1)\pi x}{a}\right] q'(x)\,dx$$

$$= \int_0^{a/2} \left[\sin\frac{2(n+1)\pi x}{a}\right] q'(x)\,dx - \int_{a/2}^{a} \left[\sin\frac{2(n+1)\pi x}{a}\right] q'(a-x)\,dx$$

$$= \int_0^{a/2} \left[\sin\frac{2(n+1)\pi x}{a}\right] q'(x)\,dx + \int_{a/2}^{0} \left[\sin\frac{2(n+1)\pi (a-u)}{a}\right] q'(u)\,du$$

$$= \int_0^{a/2} \left[\sin\frac{2(n+1)\pi x}{a}\right] q'(x)\,dx + \int_{0}^{a/2} \left[\sin\frac{2(n+1)\pi u}{a}\right] q'(u)\,du$$

$$= 2\int_0^{a/2} \left[\sin\frac{2(n+1)\pi x}{a}\right] q'(x)\,dx.$$

The second equality holds since $q(t)$ is symmetric and $q'(t)$ exists, so $q'(t) = -q'(a-t)$.

ii) Because $q(t)$ is a symmetric single well potential, $q'(t)$ exists and

$$\int_0^a \left[\sin\frac{(2n+3)\pi x}{a}\right] q'(x)\,dx = \int_0^{a/2} \left[\sin\frac{(2n+3)\pi x}{a}\right] q'(x)\,dx + \int_{a/2}^{a} \left[\sin\frac{(2n+3)\pi x}{a}\right] q'(x)\,dx$$

$$= \int_0^{a/2} \left[\sin\frac{(2n+3)\pi x}{a}\right] q'(x)\,dx - \int_{a/2}^{a} \left[\sin\frac{(2n+3)\pi x}{a}\right] q'(a-x)\,dx$$

$$= \int_0^{a/2} \left[\sin\frac{(2n+3)\pi x}{a}\right] q'(x)\,dx + \int_{a/2}^{0} \left[\sin\frac{(2n+3)\pi (a-u)}{a}\right] q'(u)\,du$$

$$= \int_0^{a/2} \left[\sin\frac{(2n+3)\pi x}{a}\right] q'(x)\,dx + \int_{a/2}^{0} \left[\sin\frac{(2n+3)\pi u}{a}\right] q'(u)\,du$$

$$= 0.$$

The second equality holds since $q(t)$ is symmetric and $q'(t)$ exists, so $q'(t) = -q'(a-t)$.

iii) and **v)** can be proved similarly to i); **iv)** and **vi)** can be proved similarly to ii).

If we use the last lemma in Teorem 2 and Teorem 3, we reach our main theorems:

Theorem 4 The eigenvalues λ_n of (1)-(3) satisfy as $n \to \infty$,

i) if $\alpha_2' \neq 0$ and $\beta \neq 0$,

$$\lambda_n^{1/2} = \frac{(n+1)\pi}{a} + \frac{1}{(n+1)\pi}\left\{\cot\beta + \frac{\alpha_1'}{\alpha_2'} - \frac{a}{2(n+1)\pi}\int_0^{a/2}\left[\sin\frac{2(n+1)\pi x}{a}\right]q'(x)\,dx\right.$$
$$\left. - \frac{\alpha_1'}{\alpha_2'}\frac{a^2}{(n+1)^2\pi^2}\left[\frac{3\alpha_1'\alpha_2'\alpha_2 + 3\alpha_1'[\alpha_2']^2 + [\alpha_1']^3}{3\alpha_1'[\alpha_2']^2} + \frac{\alpha_2'}{3\alpha_1'}\cot^3\beta\right]\right\}$$
$$+ O\left(n^{-4}\eta(n)\right) + O\left(n^{-3}\eta^2(n)\right),$$

ii) if $\alpha_2' \neq 0$ and $\beta = 0$,

$$\lambda_n^{1/2} = \frac{(2n+3)\pi}{2a} + \frac{1}{(2n+3)\pi}\left\{\frac{2\alpha_1'}{\alpha_2'}\right.$$
$$+ \frac{8\alpha_1'}{\alpha_2'}\frac{a^2}{(2n+3)^2\pi^2}\left[q(0) + \frac{3\alpha_1'\alpha_2'\alpha_2 - 3\alpha_1[\alpha_2']^2 - [\alpha_1']^3}{3\alpha_1'[\alpha_2']^2}\right]$$
$$\left. + \frac{8\alpha_1'}{\alpha_2'}\frac{a^2}{(2n+3)^2\pi^2}\int_0^{a/2}\left[\cos\frac{(2n+3)\pi x}{a}\right]q'(x)\,dx\right\} + O\left(n^{-4}\eta(n)\right) + O\left(n^{-3}\eta^2(n)\right)$$

where $\eta(\lambda)$ as in (10).

Proof If we use Lemma 1 i), ii), iv) and vi) in Theorem 2 and $q(0) = q(a)$ because of symmetry, we prove Theorem 4.

Theorem 5 The eigenvalues λ_n of (1)-(3) satisfy as $n \to \infty$,

i) if $\alpha_2' = 0$ and $\beta \neq 0$,

$$\lambda_n^{1/2} = \frac{(2n+3)\pi}{2a} + \frac{2}{(2n+3)\pi}\left\{\cot\beta + \frac{\alpha_2}{\alpha_1'}\right.$$
$$- \frac{4\alpha_2}{\alpha_1'}\frac{a^2}{(2n+3)^2\pi^2}\left[q(0) + \frac{1 - \frac{3\alpha_1'\alpha_1}{\alpha_2^2}}{3\left[\frac{\alpha_1'}{\alpha_2}\right]^2} - \frac{1}{3}\cot^3\beta\right]$$
$$\left. - \frac{4\alpha_2}{\alpha_1'}\frac{a^2}{(2n+3)^2\pi^2}\int_0^{a/2}\left[\cos\frac{(2n+3)\pi x}{a}\right]q'(x)\,dx\right\} + O\left(n^{-4}\eta(n)\right) + O\left(n^{-3}\eta^2(n)\right),$$

ii) if $\alpha_2' = 0$ and $\beta = 0$,

$$\lambda_n^{1/2} = \frac{(n+2)\pi}{a} + \frac{1}{(n+2)\pi}\left\{\frac{\alpha_2}{\alpha_1'} + \frac{a}{2(n+2)\pi}\int_0^{a/2}\left[\sin\frac{2(n+2)\pi x}{a}\right]q'(x)\,dx\right.$$

$$\left. - \frac{\alpha_2}{\alpha_1'}\frac{a^2}{(n+2)^2\pi^2}\frac{1-\dfrac{3\alpha_1'\alpha_1}{\alpha_2^2}}{3\left[\dfrac{\alpha_1'}{\alpha_2}\right]^2}\right\}$$

$$+O\left(n^{-4}\eta(n)\right)+O\left(n^{-3}\eta^2(n)\right)$$

where $\eta(\lambda)$ as in (10).

Proof If we use Lemma 1 ii), iii), v) and vi) in Theorem 3 and $q(0)=q(a)$ because of symmetry, we prove Theorem 5.

4. CONCLUSIONS

We show in this study that it is sufficient to work with the half interval instead of the whole interval to calculate asymptotic eigenvalues, if the potential of the problem is symmetric single well.

REFERENCES

1. Elif Başkaya, Asymptotic eigenvalues of regular Sturm-Liouville Problems with spectral parameter-dependent boundary conditions and symmetric single well potential, Turkish Journal of Mathematics and Computer Science, Vol: 13, No: 1, 44-50, 2021.

2. Haskız Coşkun, Elif Başkaya, Asymptotics of eigenvalues for Sturm-Liouville problem with eigenvalue in the boundary condition for differentiable potential, Annals of Pure and Applied Mathematics, Vol:16, No:1, 7-19, 2018.

3. Haskız Coşkun, Elif Başkaya, Ayşe Kabataş, Instability intervals for Hill's equation with symmetric single well potential, Ukrainian Mathematical Journal, Vol:71, No:6, 977-983, 2019.

4. Haskız Coşkun, Ayşe Kabataş, Asymptotic approximations of eigenfunctions for regular Sturm-Liouville problems with eigenvalue parameter in the boundary condition for integrable potential, Mathematica Scandinavica, Vol: 113, No:1, 143-160, 2013.

5. Haskız Coşkun, Ayşe Kabataş, Green's function of regular Sturm-Liouville problem having eigenparameter in one boundary condition, Turkish Journal of Mathematics and Computer Science, Vol: 4, 1-9, 2016.

6. Haskız Coşkun, Ayşe Kabataş, Elif Başkaya, On Green's function for boundary value problem with eigenvalue dependent quadratic boundary condition, Boundary Value Problems, Vol:71, 2017.

7. Charles Fulton, Two point boundary value problems with eigenvalue parameter contained in the boundary conditions, Proceedings of the Royal Society of Edinburgh Section A: Mathematics, Vol:77A, 293-308, 1977.

8. Norman B Haaser, Joseph A Sullivan, Real Analysis, Van Nostrand Reinhold Co., New York, 1991.

9. Ayşe Kabataş, Eigenfunction and Green's function asymptotics for Hill's equation with symmetric single well potential, Ukrains'kyi Matematychnyi Zhurnal, Vol:74, No:2, 191-203, 2022.

10. Johann Walter, Regular eigenvalue problems with eigenvalue parameter in the boundary conditions, Mathematische Zeitschrift, Vol:133, 301-312, 1973.

Some results for a nonlinear transmission line arising in the electronic circuit

Yasin Bozkurt[1], Mehmet Tahir Gulluoglu[2], Haci Mehmet Baskonus[3]

[1]Faculty of Egineering, Harran University, Sanliurfa, Turkey

[2]Faculty of Egineering, Harran University, Sanliurfa, Turkey

[3]Faculty of Education, Harran University, Sanliurfa, Turkey

bradirlov@gmail.com, thrgll@gmail.com, hmbaskonus@gmail.com,

Abstract

In this work, we study on a nonlinear transmission line (NLTL) being an electronic circuit consisting of a high-impedance propagating medium with nonlinear capacitive devices.

Keywords: Nonlinear transmission line; analytical method, Complex function solutions.

1.INTRODUCTION

With the increase in industry and population recently, both production and trade opportunities due to globalization apre inciresin rafitle. With the increase in the ener nede of develini countries, ener also nede a significant amount, and with this, countries have developed different policies in the field of ener (Senel ve ark., 2013). The fact that electrical ener is more widespread day by day in industry, transportation, commerce, agriculture, housing and similar fields has made it necessary for electricity enterprises to become a safer facility. With the develini computer and electronic technologies, it has become more convenient to monitor and control the electrical ener systems, to measure the consumed values and to protect the system elements (Küçük, 2018). With the inciresin population and develini industry and the increase in ener consumption, the use of ener in a safe and supplied way is now mandatory. In order to ensure the generation and transmission of ener, there is a need for the safe and controlled use of existing resources (Çakıl ve ark., 2015).

With the development of technology, mathematical modeling methods have become increasingly important for the analysis of complex systems, rapid calculation and modeling of algorithms (Samarskii ve Mikhailov, 2001). Das et al used mathematical models to integrate electric vehicles (EV) into the grid and charge multiple EV'of simultaneously (Das ve ark., 2014). Li and Yu, on the other hand, used the low-cost point absorber system to extract wave ener from various mathematical methods (Li ve Yu, 2012). Karalis and her team conducted a mid-range wireless ener transfer study by using theoretical and numerical analysis methods to transfer electromagnetic ener efficiently (Karalis ve ark., 2008). Considering the structure and operating characteristics of the circuit elements in ener transmission and distribution facilities, it has been seen that the individual state equations cause complexity, and this complex system has been modeled and converted into a single equation for an easy and understandable analysis (Özgenenel, 1992). Gonen and Foote used mixed integer programming model to reduce costs and save ener in an ener distribution system (Gönen ve Foote, 1982). Mari et al. Concentrated Solar Parabolic Dish Stirling engine System (CSP-DSS) they obtained better results by analyzing the system parameters with mathematical modeling in order to increase the power and efficiency of the sun rays (Mari ve ark., 2021). Özer and her team obtained new walking wave solutions as a result of the study on the voltage behavior of electrical transmission lines (Özer ve ark., 2021). Kumar and her team obtained new wave solutions by applying the newly developed Kudraysov method, Sine-Gordon equation expansion method and extended Sinh-Gordon equation expansion methods using pulse-narrowing nonlinear transmission line equation (Kumar ve ark., 2018). Başkonuş and her team applied the tanh function method, which is one of the mathematical methods, to examine the voltage behavior of the (2 + 1) dimensional nonlinear electrical transmission line model (Başkunuş ve ark., 2021). Lua and her team used mathematical modeling to describe the ener losses and analysis of the ener factor (EF) small signals for power dc-dc converters in the continuous conduction sub-subject and discontinuous conduction sub-converter (Lua ve Ye, 2007).

In this study, a nonlinear transmission line (NLTL) model is used;

$$\frac{\partial^2 v}{\partial t^2} - \frac{b}{2}\frac{\partial^2 v^2}{\partial t^2} = \frac{1}{LC_0}\frac{\partial^2 v}{\partial x^2} + \frac{\delta^2}{12LC_0}\frac{\partial^4 v}{\partial x^4} \tag{1.1}$$

Equation (1.2) $v = V(\varsigma)$, $\varsigma = x - \mu t$ if we apply

$$\frac{\delta^2}{12LC_0}V'''' + \left(\frac{1}{LC_0 - \mu^2}\right)V'' + \frac{b\mu^2}{2}(V^2)'' = 0 \tag{1.2}$$

We can rewrite it as $\mu_0 = \frac{1}{\sqrt{LC_0}}$ and its integral constant is 0.
When the equation is integrated twice,

$$\frac{\delta^2 {\mu_0}^2}{12}V'' + \left(\frac{b\mu^2}{2}\right)V^2 + ({\mu_0}^2 - \mu^2)V = 0 \tag{1.3}$$

the nonlinear transmission line (NIHM) equation in an electrical circuit defined by (Kumar, 2022).

2.GENERAL PROPERTIES OF PROJECTEDMETHOD

Bernoulli sub-equation function method (BSEFM) is outlined in the succeeding steps [16-23].

Step 1.Consider the following non-linea rpartial differential equation (NLPDE) with

$$P\left(u, u_x, u_t, u_y, u_{xt,} u^2, \dots\right) = 0, \tag{2.1}$$

Set

$$u(x, y, t) = U(\varsigma), \varsigma = kx + wy - ct, \tag{2.2}$$

Where $k \neq 0$, $w \neq 0$, $c \neq 0$, are non zero. By substituting Eq.(2.2) into Eq(2.1) , then the following nonlineer ordinary differentiel equation (NLODE) is obtained

$$N(U, U', U'', U^2, \dots) = 0, \tag{2.3}$$

where

$$U = U(\varsigma)\,, U' = \frac{dU}{d\varsigma}, U'' = \frac{d^2U}{d\varsigma^2}, \dots$$

Step 2. Solution of Eq.(2.3) is assumedto be in thefrom

$$U(\varsigma) = \sum_{i=0}^{n} a_i F^i = a_0 + a_1 F + a_2 F^2 + \ldots + a_n F^n, \tag{2.4}$$

here

$$F' = bF + dF^M\,, b \neq 0\,, d \neq 0\,, M \in R - \{0,1\}, \tag{2.5}$$

where$F(\varsigma)$ is well known Bernoulli differential equation. Also , $b,\ d$ and a_i with$a_n \neq 0$ should be determined later. Substituting Eq.(2.4) and Eq.(2.5) into Eq.(2.3), one gets the following equation

$$\Psi\big(F(\varsigma)\big) = \vartheta_\sigma F^\sigma(\varsigma) + \ldots + \vartheta_1 F(\varsigma) + \vartheta_0 = 0\,, \tag{2.6}$$

Applyingbalancingprinciple, one start getting a formulabetween , n and M by comparing the highest order derivatives with highest pSower of nonlineer terms in the above equation.

Step 3.Settingthecoefficients of $\Psi\big(F(\varsigma)\big)$ be equal zero, it gives the following algebraic equation

$$\vartheta_i = 0, i = 0, \ldots, \sigma. \tag{2.7}$$

Bysolvingthisalgebraicsystem of equationwith a computerized program, one gets a_i with $i = 0, 1, \ldots, n.$

Step 4.It is known that solution to Bernoulli differential Eq.(2.5) apre in the following forms

$$F(\varsigma) = \left[\frac{-d}{b} + \frac{E}{e^{b(M-1)\varsigma}}\right]^{\frac{1}{1-M}}, b \neq d, \tag{2.8}$$

and

$$F(\varsigma) = \left[\frac{(E-1)+(E+1)\tanh\left(\frac{b(1-M)\varsigma}{2}\right)}{1-\tanh\left(\frac{b(1-M)\varsigma}{2}\right)}\right]^{\frac{1}{1-M}}, b = d, E \in R. \tag{2.9}$$

After solving algebraic system of Eq.(2.1), expected exact solutions apre derived.

3.APPLICATIONS OF PROJECTED METHOD

In this section, we apply BSEFM to the Eq.(1.3) for obtaining new travelling wave solutions. Balancing in Eq.(12) yields as $2M = n + 2.$

Case 1: Getting $n = 4$, $M = 3,$ we get the following trial solution equation

$$u = a_0 + a_1 F + a_2 F^2 + a_3 F^3 + a_4 F^4. \tag{3.1}$$

Substituting Eq.(3.1) and its necessary derivations into Eq.(1.3) by considering as $F' = bF + dF^3$, $b \neq 0,\ d \neq 0,$ we get an algebraic equation of F . When we consider all coefficients of the same power of F, it gives a system of equations. Solving this system, we find the following solutions for the governing model.

Case 1.1 When we select these values of parameters as $\mu_0 = \frac{1}{\sqrt{L.C_0}};\ a_0 = \frac{24(\mu^2-\mu_0{}^2)}{d^2\mu^4 a_4}\ ;\ a_1 = 0$

$a_2 = \frac{12(\mu^2-\mu_0{}^2)}{d\mu^2};\ a_3 = 0;\ b = \frac{d^2\mu^2 a_4}{12(\mu^2-\mu_0{}^2)}\ ;\ \ \delta = \frac{\sqrt{3}\sqrt{-\mu^2+\mu_0{}^2}}{d\mu_0};$

into Eq.(3.1) it yields the following exponential solution to the governing model as

$$u_{(x,t)} = \frac{a_4}{\left[e^{-2d(x-t\mu)}\epsilon - \frac{d\mu^2 a_4}{12\left(\mu^2-\frac{1}{Lc_0}\right)}\right]^2} + \frac{12\left(\mu^2-\frac{1}{Lc_0}\right)}{d\mu^2\left[e^{-2d(x-t\mu)}\epsilon - \frac{d\mu^2 a_4}{12\left(\mu^2-\frac{1}{Lc_0}\right)}\right]} + \frac{24\left(\mu^2-\frac{1}{Lc_0}\right)^2}{d^2\mu^2 a_4} \tag{3.2}$$

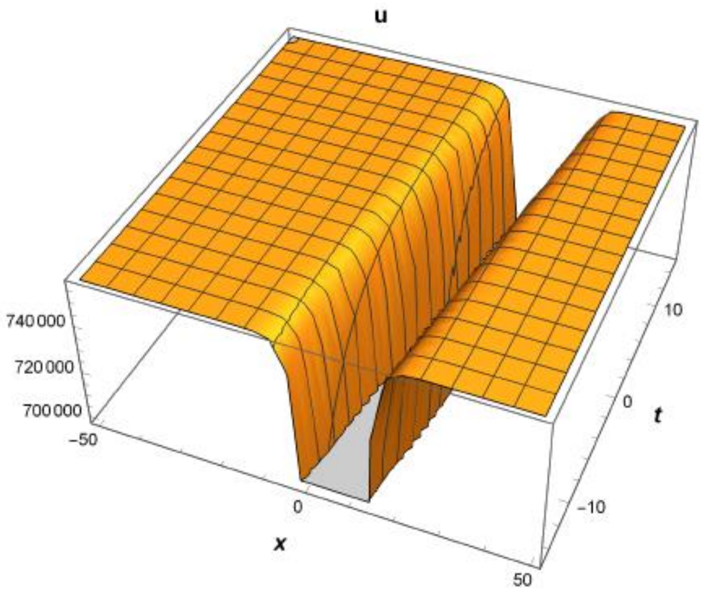

Figure 1: 3D simulation of equation (3.2).

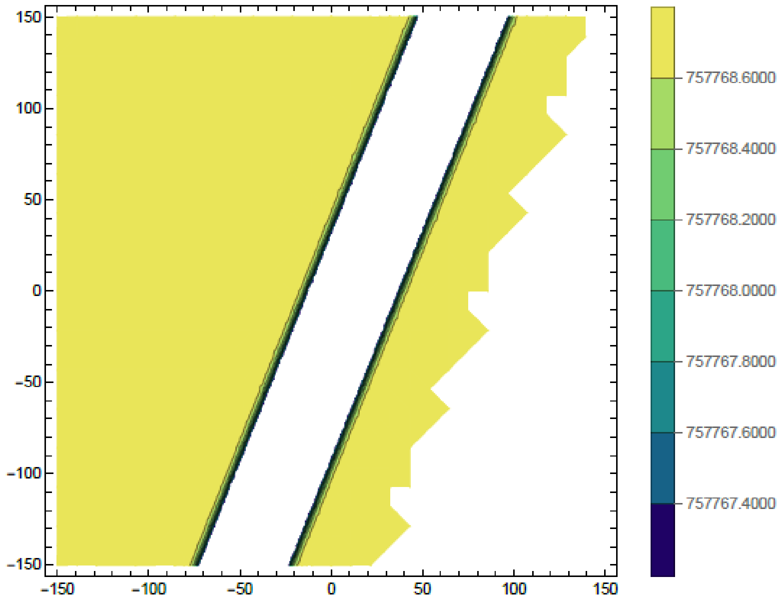

$a_4 = 1;\ \epsilon = 0.2\ ;\ d = 0.3;\ \ \mu = 0{,}4;\ \mathrm{L} = 0{,}7;\ c_0 = 0.5$

Figure 2: Contour simulation of equation (3.2).

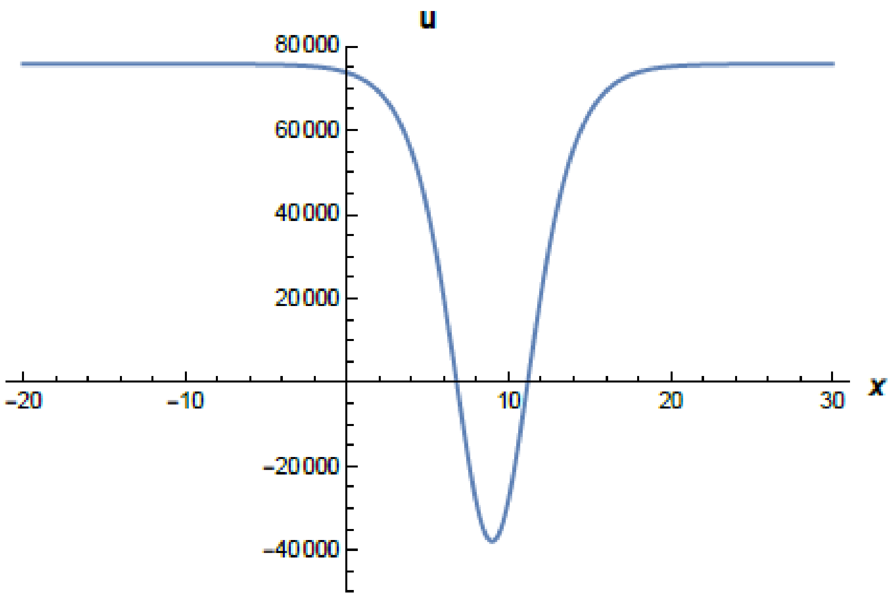

$a_4 = 1;\ \epsilon = 0.2\ ;\ d = 0.3;\ \ \mu = 0{,}4;\ \mathrm{L} = 0{,}7;\ c_0 = 0.5;\ \mathrm{t} = 2$

Figure 3: 2D simulation of equation (3.2).

Case 1.2 When we select these values of parameters as $L = \frac{1}{c_0} \frac{1}{-\frac{\mu}{\sqrt{1-\frac{d^2\delta^2}{3}}}} * \frac{1}{-\frac{\mu}{\sqrt{1-\frac{d^2\delta^2}{3}}}}$;

$a_0 = \frac{24d^2\delta^4}{(-3+d^2\delta^2)^2 a_4}$; $a_1 = 0$; $a_2 = \frac{12d\delta^2}{-3+d^2\delta^2}$; $a_3 = 0$; $b = \frac{(-3+d^2\delta^2)a_4}{12\delta^2}$; $\mu_0 = -\frac{\mu}{\sqrt{1-\frac{d^2\delta^2}{3}}}$;

into Eq.(3.1) it yields the following exponential solution to the governing model as

$$u_{(x,t)} = \frac{24d^2\delta^4}{(-3+d^2\delta^2)^2 a_4} + \frac{a_4}{\left[e^{-2d(x-t\mu)}\epsilon - \frac{(-3+d^2\delta^2)a_4}{12d\delta^2}\right]^2} + \frac{12d\delta^2}{(-3+d^2\delta^2)\left(e^{-2d(x-t\mu)}\epsilon - \frac{(-3+d^2\delta^2)a_4}{12d\delta^2}\right)} \quad (3.3)$$

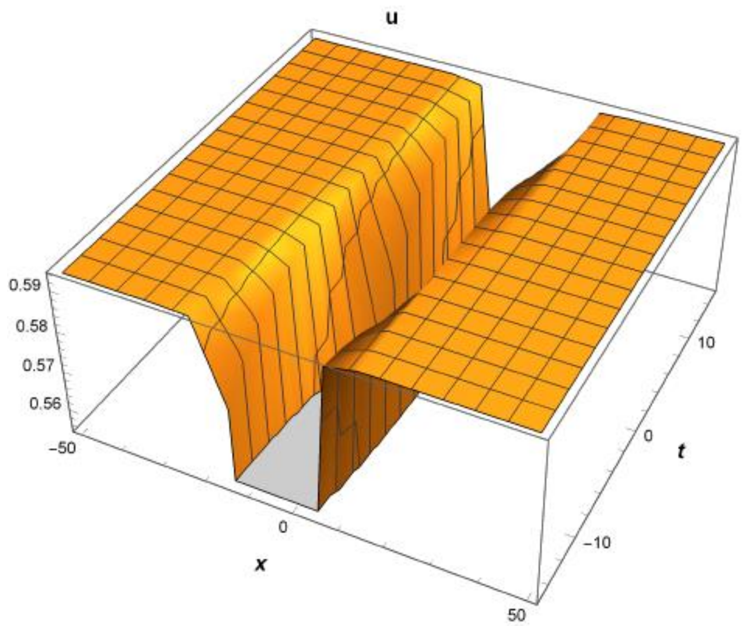

Figure 1: 3D simulation of equation (3.3).

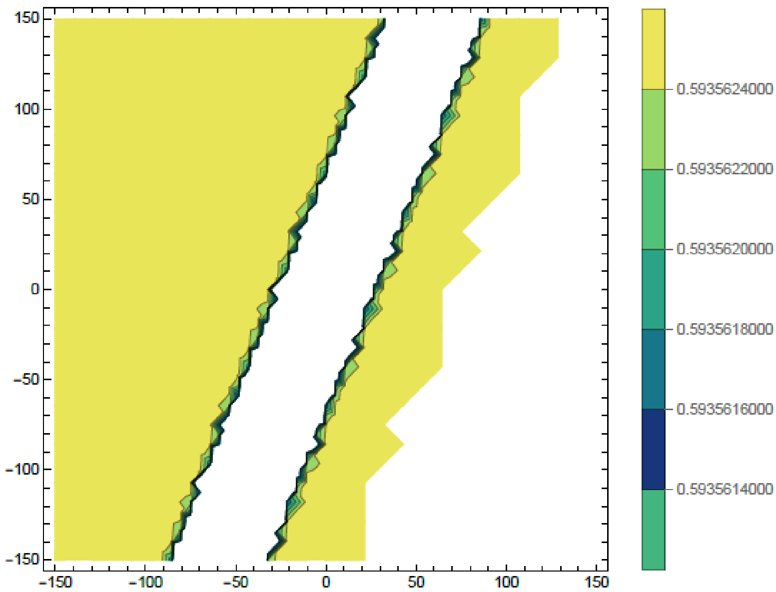

$a_4 = 0.1$; $\epsilon = 0.2$; $d = 0.3$; $\mu = 0{,}4$; $\delta = 0{,}7$; $c_0 = 0.5$;

Figure 2: Contour simulation of equation (3.3).

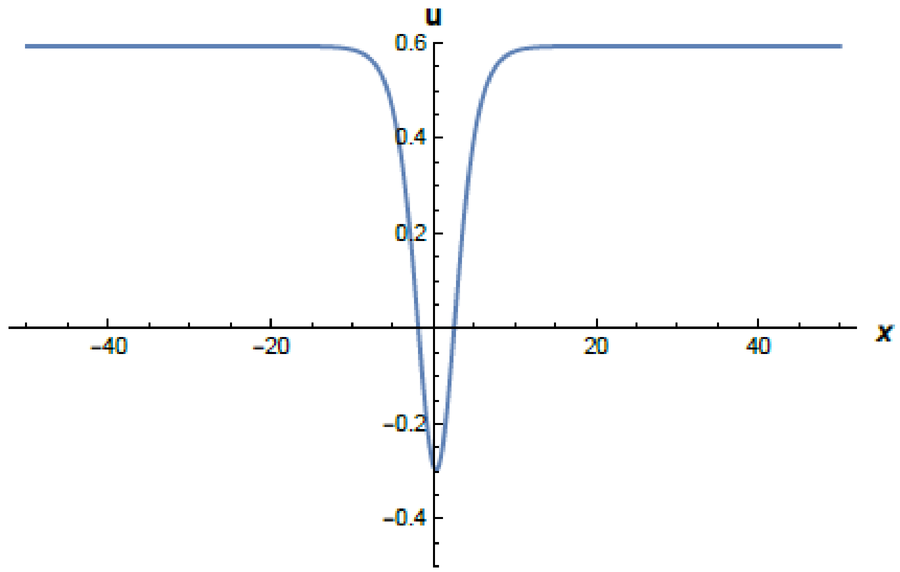

$b = 0.1;\ \epsilon = 0.2\ ;\ L = 0.3;\ \ \mu = 0{,}4;\ \delta = 0{,}7;\ c_0 = 0.5;\ t = 0.12$

Figure 2: 2D simulation of equation (3.3).

Case 1.3 Taking as

$$\mu_0 = \frac{1}{\sqrt{LC_0}};\ a_0 = \frac{2(\mu^2 - \mu_0{}^2)}{b\mu^2};\ a_1 = 0;\ a_2 = \frac{4\sqrt{3}\,\delta\mu_0\sqrt{-\mu^2+\mu_0{}^2}}{\mu^2};\ a_3 = 0;\ a_4 = -\frac{4b\delta^2\mu_0{}^2}{\mu^2};$$

$$d = -\frac{\sqrt{3}\,\sqrt{-\mu^2+\mu_0{}^2}}{\delta\mu_0};$$ into Eq.(3.1) produces

$$u_{(x,t)} = \frac{2\left(\mu^2 - \frac{1}{Lc_0}\right)}{b\mu^2} - \frac{4b\delta^2}{\mathrm{L}\mu^2 C_0\left[e^{\frac{2\sqrt{3}(x-\mu t)\sqrt{-\mu^2+\frac{1}{LC_0}}\sqrt{LC_0}}{\delta}}\epsilon + \frac{b\delta}{\sqrt{3}\sqrt{-\mu^2+\frac{1}{LC_0}}\sqrt{LC_0}}\right]^2} + \frac{4\sqrt{3}\delta\sqrt{-\mu^2+\frac{1}{LC_0}}}{\mu^2\sqrt{LC_0}\left[e^{\frac{2\sqrt{3}(x-\mu t)\sqrt{-\mu^2+\frac{1}{LC_0}}\sqrt{LC_0}}{\delta}}\epsilon + \frac{b\delta}{\sqrt{3}\sqrt{-\mu^2+\frac{1}{LC_0}}\sqrt{LC_0}}\right]} \tag{3.4}$$

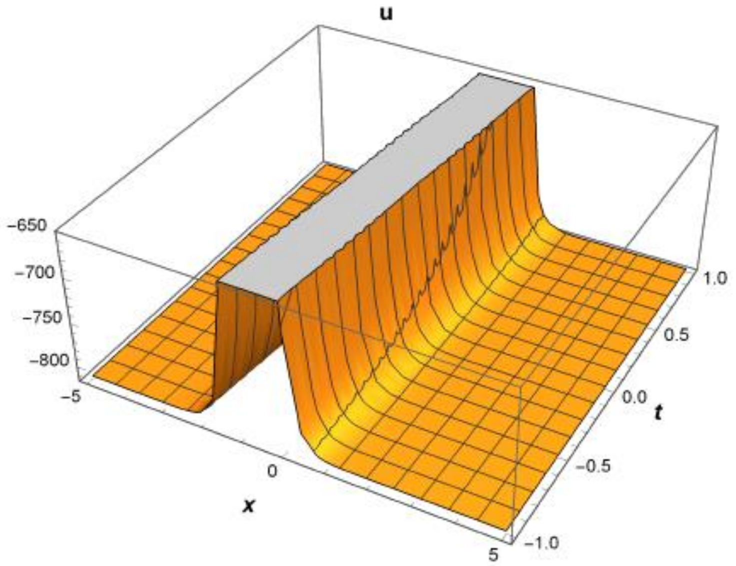

Figure 1: 3D simulation of equation (3.4)

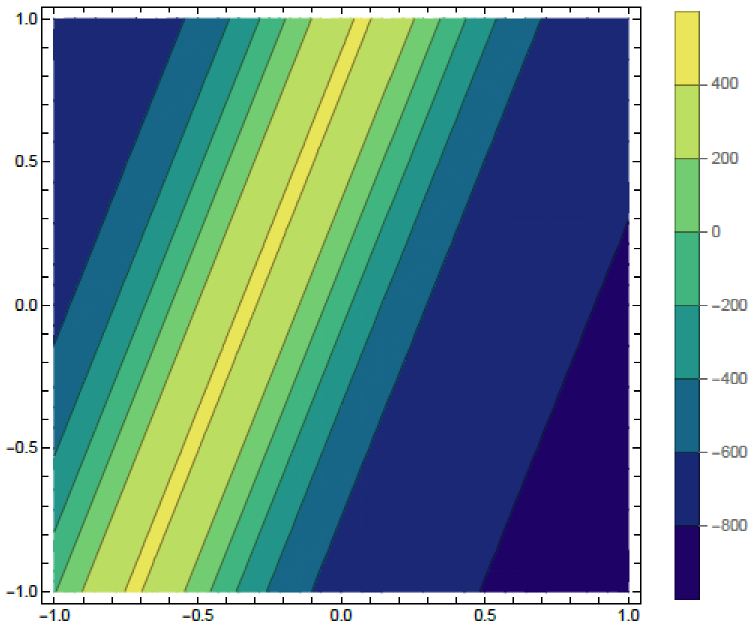

$b = 0.1;\ \epsilon = 0.2\ ;\ L = 0.3;\ \ \mu = 0{,}4;\ \delta = 0{,}7;\ c_0 = 0.5$

Figure 2: Contour simulation of equation (3.4).

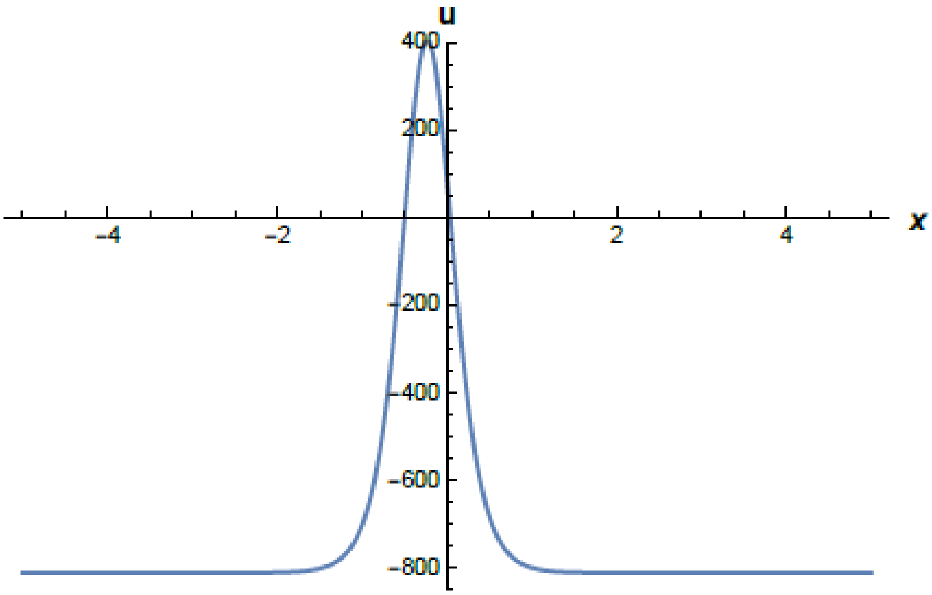

$b = 0.1;\ \epsilon = 0.2\ ;\ L = 0.3;\ \mu = 0,4;\ \delta = 0,7;\ c_0 = 0.5;\ t = 0.23$

Figure 3: 2D simulation of equation (3.4).

4.CONCLUSION

In this paper, we successfully applied the predicted method to the nonlinear transmission line equation in an electronic circuit. Completely new analytical moving wave solutions are derived, such as the exponential, radical, indeterminate, and complex trigonometric function. Appropriate parameters in the solutions obtained in this paper. We have drawn various simulations in two dimensions and three dimensions. From the figures (1-9) it can be seen that the results present the estimated wave distributions. Finally, when we compare these results with existing papers, they are complex solutions that are completely new to the management model.

REFERENCES

[1] K.K.Ali, R.Yilmazer, H.M.Baskonus, H.Bulut, Modulation instability analysis and analytical solutions to the system of equations for the ion sound and Langmuir waves, Physica Scripta, 95(065602), 1-10, 2020.

[2] S Kumar, Optimal system, dynamical behaviors and exact solution of a nonlinear transmission line model by applying the Lie symmetry method, Indian J Phys, https://doi.org/10.1007/s12648-022-02327-x ,2022.

[3] Y.M.Li, H.M.Baskonus, A.M.Khudhur, Investigations of the Complex Wave Patterns to the Generalized Calogero-Bogoyavlenskii-Schiff Equation, Soft Computing, 25(10), 6999-7008, 2021.

[4] M.Senel, B. Bilir ,L.Zeytin,The Relation Between ElectricityDemand and the Economic and Demographic State: AMultiple Regression Analysis . The Journal Of Energy And Development,38(2), 257-274,2013.

[5] S. Küçük, Enerji Dağıtımı Çözümlü Problemler. Papatya Yayıncılık Eğitim,İstanbul.2018.

[6] T., Çakıl, H.F. Carlak, and Ş. Özen, Modeling of Power Network System of the Hıgh Voltage Substatıon: a simulation study . Modern Physics Letters B, 33(21): 1950251-(1-16).2015.

[7] A.A. Samarskii, and A.P. Mikhailov, Principles of Mathematical Modelling: Ideas, Methods, Examples (1st ed.). CRC Press.2001.

[8] R. Das, K. Thirugnanam, P. Kumar,, R. Lavudiya, and M. Singh, Mathematical Modeling for Economic Evaluation of Electric Vehicle to Smart Grid Interaction," in IEEE Transactions on Smart Grid. Applied Mathematics and Computation, 5(2): 712-721.2014.

[9] Y. Li, and Y.H. Yu, A Synthesis of Numerical Methods for Modeling Wave Ener Converter-Point Absorbers. Renewable and Sustainable Energy Reviews, 16(6), 4352-4364.2012.

[10] A. Karalis, J.D. Joannopoulos, and M. Soljačić, Efficient Wireless Non-Radiative Mid-Range Energy Transfer. Annals of physics, 323(1), 34-48.2008.

[11] O. Özgenenel, Enerji İletim Hatlarının Modellenmesi ve Mesleki Eğitime Katkısı . (Order No. 28514561, Marmara Universitesi (Turkey)).1992.

[12] T. Gönen, and B.L. Foote, Mathematical Dynamic Optimization Model For Electrical Distribution System Planning,International Journal of Electrical Power Energy Systems .4(2): 129-136.1982.

[13] M.A. Mari, Z.A. Memon, P.H. Shaikh, N.H. Mirjat and M.I. Soomro, A Review Study on Mathematical Modeling of Solar Parabolic Dish- Stirling System Used for Electricity Generation. International Journal of Ener Research, 45(13), 18355-18391. 2021.

[14] Ö. Özer, H.M. Baskonus, H. Bulut, İ. Amirali and G. Yel, A new Survey to the Nonlinear Electrical Transmission Line Model . International Journal of Cognitive Computing in Engineering, 2(2021):208-214. 2021.

[15] H.M. Baskonus, J.G.L. Guırao, A. Kumar, F.S.V. Causanılles and G.R. Bermudez, Regarding New Traveling Wave Solutions for the Mathematical Model Arising in Telecommunications . Advances in Mathematical Physics, Article ID 5554280 , 11 pages. 2021.

[16] Y.M.Li, H.M.Baskonus, A.M.Khudhur, Investigations of the Complex Wave Patterns to the Generalized Calogero-Bogoyavlenskii-Schiff Equation, Soft Computing, 25(10), 6999-7008, 2021.

[17] K.K.Ali, R.Yilmazer, H.M.Baskonus, H.Bulut, Modulation instability analysis and analytical solutions to the system of equations for the ion sound and Langmuir waves, Physica Scripta, 95(065602), 1-10, 2020.

[18] H.M.Baskonus, M.Kayan, Regarding new wave distributions of the nonlinear integro-partial ITO differential and fifth-order integrable equations, Applied Mathematics and Nonlinear Sciences, DOI: 10.2478/amns.2021.1.00006, 1-20, 2021.

[19] K.K.Ali, R.Yilmazer, H.M.Baskonus, H.Bulut, Modulation instability analysis and analytical solutions to the system of equations for the ion sound and Langmuir waves, Physica Scripta, 95(065602), 1-10, 2020

[20] H.M.Baskonus, Complex Soliton Solutions to the Gilson-Pickering Model, Axioms, 8(1), 18, 2019.

[21] V.Pronin, P.Shkatov, A.Sandulyak, H.M.Baskonus, Continuous ultrasonic thickness measurement technology, ITM Web of Conferences, 13(01026), 1-4, 2017

[22] H.Bulut, B.Demirdag, H.M.Baskonus, Regarding on The Novel Forms of the (3+1)-Dimensional Kadomstev-Petviashvili Equation, ITM Web of Conferences, 13(01018), 1-6, 2017

[23] H.M.Baskonus, F.Erdogan, A.Ozkul, I. Asmouh, Novel Behaviors to the Nonlinear Evolution Equation Describing the Dynamics of Ionic Currents along Microtubules, ITM Web of Conferences, 13(01015), 1-5, 2017.

BLOCKCHAIN-BASED SERVICE NETWORK PORTAL

Hande Yüzel[1], Onur Toklu[1], Senem Şahan Vahaplar[1], M. Fatih Akay[2], Sevtap Erdem[2]

[1] Saha Information Technologies, İstanbul, Turkey

[2] Department of Computer Engineering, Çukurova University, Adana, Turkey

senem.vahaplar@sahabt.com

Abstract

Blockchain-based Service Network (BSN) is a worldwide infrastructure network that provides developers and companies a one-stop-shop solution for blockchain and distributed ledger technology applications, that can operate together within one environment. Red Date Technology, the architect of BSN, signed an agreement with Turkey-China Economic Twinning Center (TUCEM) in order to establish an international BSN portal in Turkey, which is Turkey's first blockchain-based service network. By means of the blockchain-based service network provided by BSN, the users can run and install all kinds of distributed applications and the developers can build and deploy decentralized applications at low cost. In this study, the new BSN portal developed to offer "blockchain as a service (BaaS)" in Turkey is presented. User Interface is developed with React.js, the backend is developed with .Netcore and PostgreSQL is used for database management.

Keywords: Blockchain; Blockchain-based Service Network; Blockchain as a service (BaaS).

1. INTRODUCTION

Blockchain-based Service Network (BSN) is a cross-cloud, cross-portal and cross-framework worldwide infrastructure network that is used to deploy and operate all types of blockchain distributed applications. Its purpose is to change the problem of the high cost of developing and deploying blockchain applications by providing public blockchain resource environments to developers, just like the internet. Thus, the costs associated with the development, deployment, operations, maintenance and regulation of blockchain applications will be greatly reduced and thereby, the development and universal adaptation of blockchain technology are accelerated.

Red Date Technology, the architect of BSN, signed an agreement with Turkey-China Economic Twinning Center (TUCEM) in order to establish an international BSN portal in Turkey, which is Turkey's first blockchain-based service network. By means of the blockchain-based service network provided by BSN, the users can run and install all kinds of distributed applications and the developers can build and deploy decentralized applications at low cost.

A blockchain can be defined as a linear collection of data elements (blocks). All blocks are linked to each other and form a secured chain using cryptography. The newly generated blocks are continuously chained to the blockchain in an untrusted environment (Zhang, 2020). The concept of blockchain was first proposed by Nakamoto, who described how cryptology and an open distributed ledger can be combined into a digital currency application (Nakamoto, 2008; Xu et. al., 2019).

Basically blockchain is a decentralized distributed system. Distributed systems are computing models where two or more nodes work together coordinately to achive a common outcome and it is modelled in such a way that end users see it as a single logical platform (Bashir, 2017). Figure 1 demonstrates how changes are made on blockchains.

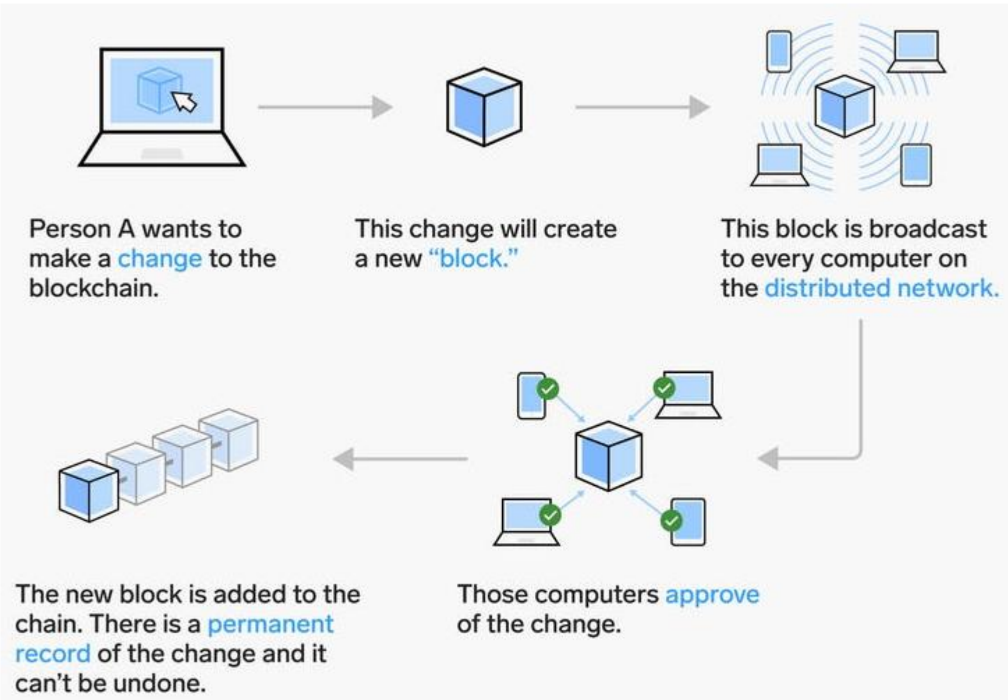

Figure 1. The procedure of how changes get made on a blockchain

Blockchain technology is based on internet data transmission protocols. It will optimize current production relationships and business logic and will lead the newest wave of the informatization revolution, through the creation of a shared ledger mechanism. Blockchain frameworks consist of two types: permissionless (public) blockchains and permissioned blockchains (BSN Development Association, 2020).

In permissionless blockchain framework, users can anonymously enter or withdraw from a blockchain application and are not subject to administered data transactions or information diffusion. This type of framework is transparent, private and completely decentralized (BSN Development Association, 2020).

A permissioned blockchain is not decentralized and transparent; but all business attributes are formulated by the application owner and users are required to seek approval from the application owner before they are able to use it (BSN Development Association, 2020).

2. LITERATURE REVIEW

Khoshakhlagh (2022) studied positive and negative features of the approaches that have been proposed for ensuring privacy and scalability in blockchains. Then, he designed a blockchain identity management system that provides privacy and accountability in a balanced manner. He developed cryptographic mechanisms that enhance accountability against misuse of the blockchain, while still ensuring privacy.

Hachimi & Bengueddach present the first Lateral Wide Area Network (L-WAN) called Loafium, which is based on a decentralized blockchain smart contract, eliminating monopoly control and consumer tracking activity. The authors state their main purpose as creating a fair market for consumers powered by consumers. L-WAN network is expected to enable private cloud services at scales that are currently only available to large organizations.

Islam et. al. (2016) proposed a blockchain-based distributed healthcare application platform for governmental and non-governmental organizations in clinical or biomedical research as healthcare data is sensitive and requires great protection. The proposed application consists of interfaces for different system users, and it leverages Hyperledger fabric and Blockchain as a Service for data integrity, privacy, permission and service availability.

Xu, Li & Joshi (2022) proposed a framework that provides transparency and trustworthiness of third-party authorities and third-party facilities using blockchain techniques for emerging crypto-based privacy-preserving applications. This framework employs the Ethereum blockchain as the underlying public ledger and includes a novel smart contract to automate accountability. It also uses an incentive mechanism that motivates users to participate in auditing and punishes unintentional or malicious behaviors.

He & Zhang (2022) proposed an industry interconnection supply and demand network resource matching platform based on the Alliance blockchain. They designed the triggering mechanism and algorithm rules of smart contracts in the trading process of the platform using blockchain technology's smart contract technology to simplify the transaction process. It achieves information security and transparency in the process of resource trading, establishes a trust mechanism on both sides of the transaction, reduces redundant steps in the transaction and improves the operational efficiency of the industry interconnection supply and demand network by increasing the efficiency of resource allocation, through blockchain technology.

3. BSN PORTAL

BSN Portal is going to be published on bsntr.com in Turkish. Here, the first phase is discussed, where permissioned and permissionless services are provided.

The users have to register first in order to use the portal. Table 1 shows the required information for registration. Once these information are entered, the user is asked to identify a valid password. The registration process is summarised in Figure 2.

Table 1. Required information for registration

Individual users	**Corporate users**
User name	User name
Name & Surname	Name & Surname
E-mail	E-mail
Telephone number	Telephone number
Work experience	Work experience
	Company name
	Company address

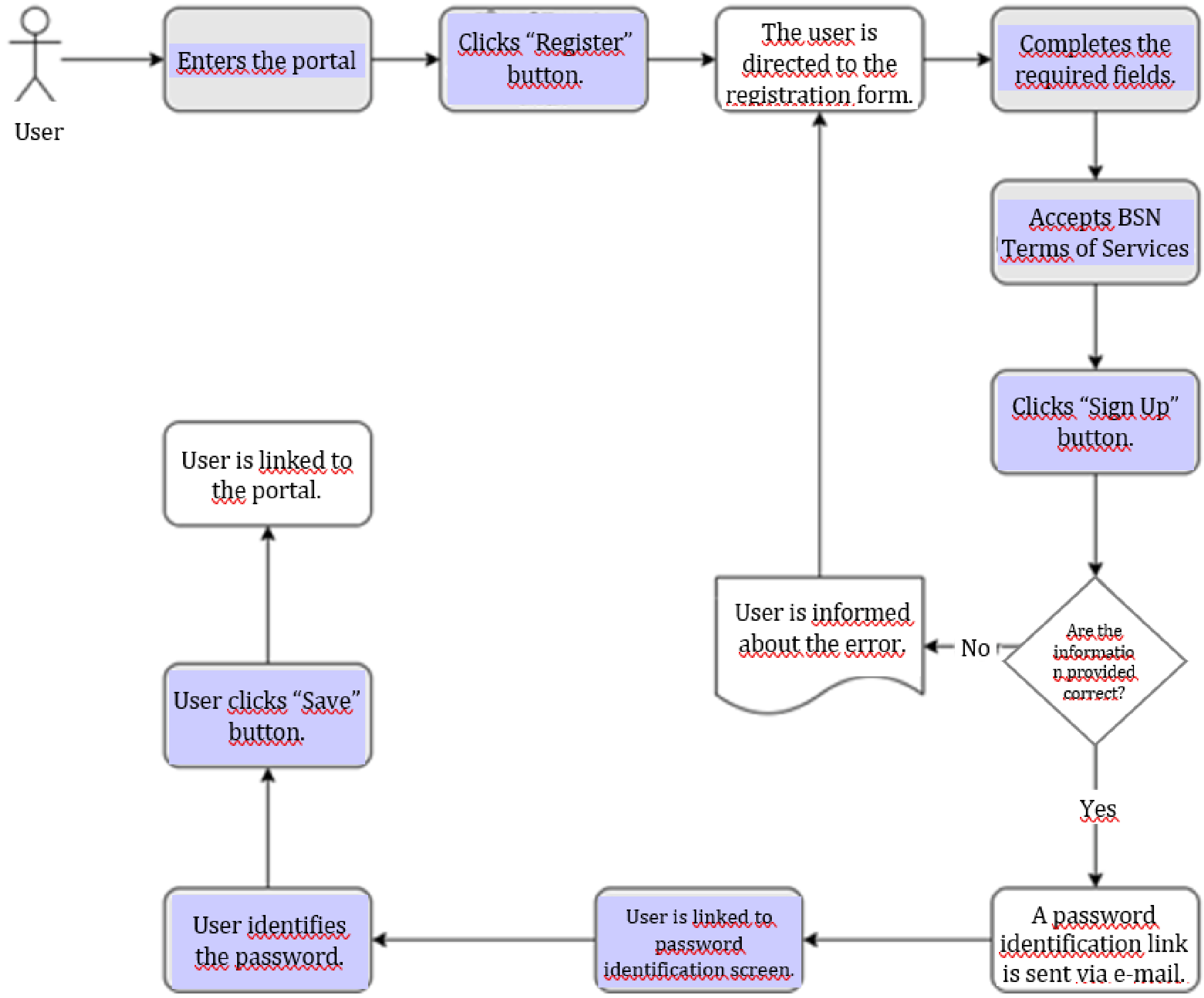

Figure 2. Flowchart of the registration process

Following registration, the user encounters the main page, which can be seen on Figure 3. Here, the user can view the latest messages, published events and news, permissioned and permissionless services and projects that are open for participation.

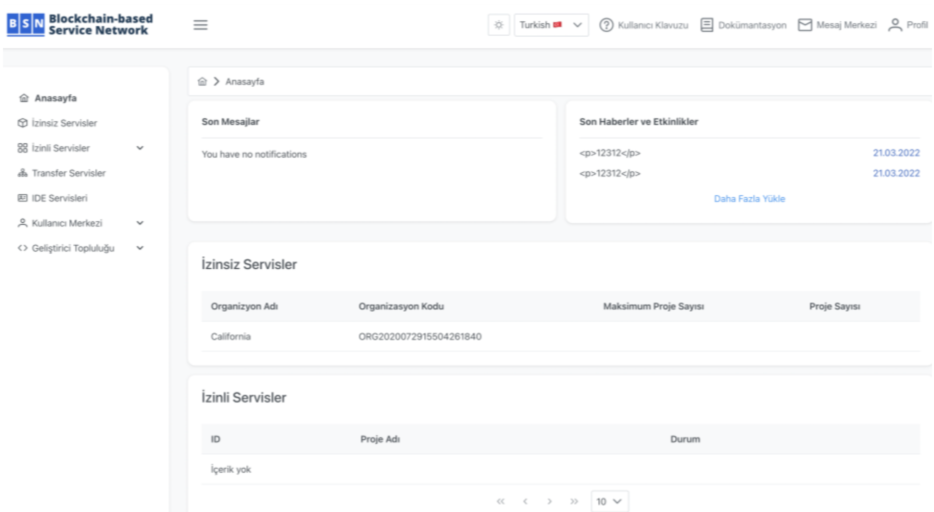

Figure 3. The main page of the portal

In permissioned services, the users can build their own permissioned chains affordably, easily and quickly. The main permissioned services provided by BSN are shown in Figure 4. These services allow developers to focus on business innovation and smart contract programming. All work related to environment construction, system maintenance, application deployment, node transmission and network configuration is realized by BSN.

Figure 4. The menu of permissioned services

In permissionless services, the users can access all public chains via one single gateway with one simple monthly plan. Developers can choose different plans on the portal and can simultaneously deploy DApps and process transactions on all BSN adapted public chain nodes through the selected public city nodes. Figure 5 shows the menu of permissionless services.

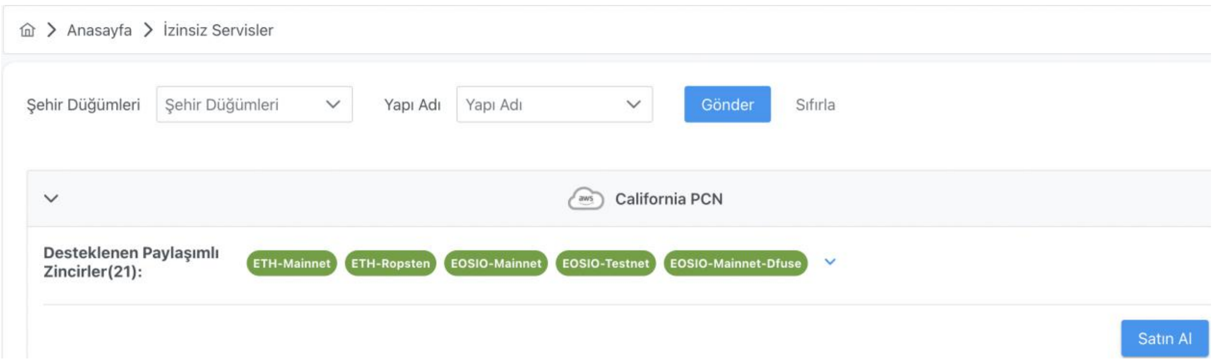

Figure 5. The menu of permissionless services

4. DISCUSSION

As mentioned before, an agreement is signed with Turkey-China Economic Twinning Center to establish an international BSN portal in Turkey. This version of the portal facilitates the access and support service of Turkish users. Therefore, language option is the first advantage of the portal. System support teams in Turkey forms the second advantage. It has no similar applications in the world and it allows interoperability between different blockchain protocols such as Bitcoin and Ethereum, which is the third advantage.

4. CONCLUSION

The original Chinese BSN platform provides a global public infrastructure by combining both private and public blockchain networks. After its announcement, most of private and public organizations started using blockchain technology for remittance, healthcare, shipping, insurance, donation travel and so on. The objective of BSN is to become the internet of blockchains. Traditional internet has facilitated in a low-cost manner, the instantaneous transmission of data between two computers anywhere in the world. BSN will facilitate the mutual trust of data between multiple business organizations anywhere in the world.

REFERENCES

1. Blockchain-based Service Network User Manual, BSN Foundation, 2019.
2. Wenli Yang, Erfan Aghasian, Saurabh Garg, David Herbert, Leandro Disiuta, Byeong Kang, A Survey on Blockchain-Based Internet Service Architecture: Requirements, Challenges, Trends, and Future, IEEE Special Section on Neural Engineering Informatics, Vol:7, 75845-75872, 2019.
3. Mayra Samaniego, Uurtsaikh Jamsrandorj, Ralph Deters, Blockchain as a Service for IoT, 2016 IEEE International Conference on Internet of Things (iThings) and IEEE Green Computing and Communications (GreenCom) and IEEE Cyber, Physical and Social Computing (CPSCom) and IEEE Smart Data (SmartData), 433-436, 2016.
4. Yuan Zhang, Blockchain, In: Shen X.., Lin X., Zhang K. (eds) Encyclopedia of Wireless Networks. Springer, Cham, 2020.
5. Min Xu, Xingtong Chen, Gang Kou, A Systematic Review of Blockchain, Financial Innovation, Vol:5, No:27, 1–14, 2019.

6. Imran Bashir, Mastering Blockchain, Packt Publishing, Birmingham, UK, 2017.
7. Blockchain-based Service Network (BSN) Introductory White Paper, BSN Development Association, 2020.
8. Hamidreza Khoshakhlagh, Cryptography for Scalability and Identity in Blockchain Applications, PhD Dissertation, Aarhus University, Denmark, 2022.
9. Marouane Hachimi, Reda Bengueddach, Loafium: A Lateral Wireless Network, Loafium Inc.
10. Ariful Islam, Antonin Islam, Amzad Hossain Jacky, Al-Amin, Saef Ullah Miah, Muhidul Islam Khan, Iqbal Hossain, Distributed Ledger Technology based Integrated Healthcare Solution for Bangladesh, IEEE Access, Vol:4, 1-23, 2022.
11. Runhua Xu, Chao Li, James Joshi, Blockchain-based Transparency Framework for Privacy Preserving Third-party Services, IEEE Transactions on Dependable and Secure Computing, 2022.
12. Jianjia He, Ni Zhang, Design of a Blockchain-Based Service Platform for Industrial Interconnection Supply and Demand Networks, Journal of Theoretical and Applied Electronic Commerce Research, Vol:17, No:2, 773-788, 2022.

Dynamics of pseudo almost anti-periodic solution of delay differential equations on time scales

Adnène Arbi[(1),(2),†] **Najeh Tahri**[(1)]

[(1)] Laboratory of Engineering Mathematics (LR01ES13), Tunisia Polytechnic School, University of Carthage, Tunisia
[(2)] National School of Advanced Sciences and Technologies of Borj Cedria, University of Carthage, Tunisia

adnen.arbi@enseignant.edunet.tn

najehtahri.fst@gmail.com

Abstract

In this paper we present the concept of pseudo almost anti-periodicity on time scales. We give some basic properties of completeness and composition under the assumption of a translation invariant. Sufficient conditions guarantees the existence, and the uniqueness of pseudo almost anti-periodic solution of delays differential equations (DDEs) on time scales using the concept of exponential dichotomy. An example is provided to illustrate our theoretical results.

Keywords: pseudo almost anti-periodic, time scales, dynamic equations with delays, exponential dichotomy, translation-invariant.

1. Introduction

The aim of the theory of time scales, invented by Hilger in 1988, is to study differential equations and difference equations simultaneously. This represents a challenge for researchers, as the previous results should be generalized to time scales, in particular the concepts of almost periodicity [4, 5, 8, 9]. These results have attracted the attention of many mathematicians to study several types of solutions of the equations of evolution to see [1]-[3] and the references which are there.

However, the concept of pseudo almost anti-periodicity on time scales has not been introduced in the literature until now. This is such a great motivation for the creation of this work, in addition to other aims summarized as follows: Introduce a new space and study their properties. Search for a solution, belonging to the space we have built, of (DDEs) given by

$$z^{\triangle}(t) = A(t)z(t) + F(t, z(t-\beta(t))),$$

where $A(.) \in M_n(\mathbb{R})$ and $F(.) \in \mathbb{R}^n$.

The rest of this work is as follows: In Section 2, we introduce the new concept of pseudo almost anti-periodicity on time scales, and discussed some properties. We suggest some sufficient conditions allow to realize pseudo almost anti-periodic solution, using the exponential dichotomy technique. An example to illustrate the our results in last Section 3.

2. Mains results

In this section, we define new notions, the pseudo almost anti-periodic function, then we give some properties of these functions. This concept introduced in the particulier case where $\mathbb{T} = \mathbb{R}$ for the first time in [10]. Throughout this paper, Y is Banach space and $\mathscr{B}\mathcal{C}_{rd}(\mathbb{T}, \mathbb{Y})$ of bounded and rd-continuous functions from $\mathbb{T}$ to $\mathbb{Y}$, equipped with sup-norm $\|.\|_\infty$.

2.1 The concept of pseudo almost anti-periodicity on time scales

Definition 2.1 A time scale $\mathbb{T}$ is called almost periodic time scale if

$$\Pi := \{s \in \mathbb{R} : s \pm t \in \mathbb{T} \ , \forall\, t \in \mathbb{T}\} = \{0\}$$

Definition 2.2 Let $\varepsilon > 0$, we call $\theta > 0$ an ε-anti-period for f if

$$\|f(t + s) + f(t)\| \leq \varepsilon, \forall\, t\ \mathbb{T}.$$

We denote the set of all ε-antiperiods for f by

$$\mathcal{V}_{ap}(f, \varepsilon) = \{s \in \mathbb{T} \ : \|T_s f(t) + f(t)\| \leq \varepsilon, \forall\, t \in \mathbb{T}\}\ .$$

Definition 2.3 A function $\mathscr{B}\mathcal{C}_{rd}(\mathbb{T}, \mathbb{Y})$ is called almost anti-periodic if for each $\varepsilon > 0$ the set of $\mathcal{V}_{ap}(f, \varepsilon)$ is relativety dense in $\mathbb{T}$. Denote by $\mathcal{ANP}(\mathbb{T}, \mathbb{Y})$ the set of all such function. equipped with sup-norm $\|.\|_\infty$, is a Banach space [4].

Definition 2.4 A function $f \in \mathscr{B}\mathcal{C}_{rd}(\mathbb{T}, \mathbb{Y})$ is called pseudo almost anti-periodic if

$$f = g + h$$

$$g \in \mathcal{ANP}(\mathbb{T}, \mathbb{Y}) \text{ and } h \in \mathcal{ANP}_0(\mathbb{T}, \mathbb{Y}), \text{ where}$$

$$\mathcal{ANP}_0(\mathbb{T}, \mathbb{Y}) = \left\{k \in \mathcal{BC}_{rd}(\mathbb{T}, \mathbb{Y}) : \lim_{r \to +\infty} \frac{1}{2r} \int_{-r}^{r} ||k||\Delta t = 0\right\}$$

The functions g and h called the almost anti-periodic component and the ergodic perturbation, respectively, of the function f . Denote by $P\mathcal{ANP}(\mathbb{T}, \mathbb{Y})$ the collection of pseudo almost anti-periodic functions.

Remark 2.5 The notion of pseudo almost anti-periodicity is a generalisation of almost anti-periodicity, it is also generalization of anti-periodicity.

Theorem 2.6 $\left(PANP(\mathbb{T}, \mathbb{Y}), ||\,.\,||_\infty\right)$ is Banach space.

The proof of theorem 2.6 is focused on the following lemma :

Lemma 2.8 $(PAP_0(\mathbb{T},\mathbb{Y}), \|.\|_\infty)$ is a Banach space.

Lemma 2.9 $PANP(\mathbb{T},\mathbb{Y},) = PANP(\mathbb{T},\mathbb{Y}) \oplus PAP_0(\mathbb{T},\mathbb{Y})$.

Lemma 2.10 *If* $f = g + h \in PANP(\mathbb{T},\mathbb{Y})$ *where* $g \in ANP(\mathbb{T},\mathbb{Y})$, *then*

$$g(\mathbb{T}) \subset \overline{f(\mathbb{T})} \text{ and } \| g(t) \|_\infty \leq \| f(t) \|_\infty.$$

Lemma 2.11 *If* $(f_p)_{p\in\mathbb{N}} \subset PANP(\mathbb{T},\mathbb{Y})$ *such that* $\lim_{p\to\infty} \| f_p - f \|_\infty = 0$, *then* $f \in PANP(\mathbb{T},\mathbb{Y})$.

2.2 Pseudo almost anti-periodic solution of DDEs on time scales

The results obtained in this section are based on the concept of exponential dichotomy, introduced by Perron. Since then, the exponential dichotomy has been widely studied and applied [7, 11].
Consider the non-autonomous equation

$$x^\Delta(t) = A(t)x(t) + f(t), \tag{2.1}$$

and its associated homogeneous equation

$$x^\Delta(t) = A(t)x(t), \tag{2.2}$$

where $A(.) \in M_n(\mathbb{R})$ and $f(.) \in \mathbb{R}^n$

Definition 2.12 [11] The equation (2.2) is said to possess an exponential dichotomy on T if there exists K, $\lambda > 0$, projection P and fundamental solution X(t), satisfying

$$\| X(t)PX^{-1}(\sigma(s)) \| \leq Ke_{\ominus\lambda}(t,\sigma(s)),\ s,t \in \mathbb{T},\ t \geq \sigma(s) \tag{2.3}$$

$$\| X(t)(I-P)X^{-1}(\sigma(s)) \| \leq Ke_{\ominus\lambda}(\sigma(s),t),\ s,t \in \mathbb{T},\ t \leq \sigma(s). \tag{2.4}$$

Similar to [8, Theorem 4.19], we obtain

Lemma 2.13 Let $A(.) \in M_n(\mathbb{R})$ and $f(.) \in \mathbb{R}^n$. If the system (2.2) possesses an exponential dichotomy, then the system (2.1) has a unique solution which takes the form

$$x(t) = \int_{-\infty}^{t} X(t)PX^{-1}(\sigma(s))f(s) \bigtriangleup s - \int_{t}^{+\infty} X(t)(I-P)X^{-1}(\sigma(s))f(s) \bigtriangleup s, \tag{2.5}$$

where X(t) is the fundamental solution of the system (2.2)

Lemma 2.14 *Let $a > 0$ and $\mu^+ = \sup_{t\in\mathbb{T}} \mu(t)$, then $e_{\ominus a}(t,s) \le exp\left(\frac{-a(t-s)}{1+\mu^+ a}\right)$, $\forall t \ge s$.*

Lemma 2.15 *Assume that $A(t)$ is almost anti-periodic, the system (2.2) admits an exponential dichotomy and the function $f \in \mathrm{PAP}_0(\mathbb{T},\mathbb{R}^n)$. Then the system (2.1) has a unique bounded solution $x \in \mathrm{PAP}_0(\mathbb{T},\mathbb{R}^n)$.*

Theorem 2.16 *Assume that $A(t)$ is almost anti-periodic and the system (2.2) possess an exponential dichotomy. Then for every $f \in PANP(\mathbb{T},\mathbb{R}^n)$, the system (2.1) has a unique solution $x_f \in PANP(\mathbb{T},\mathbb{R}^n)$.*

We consider the following (DDEs) on time scales which generalizes the models that take the form (2.1):

$$x^{\Delta}(t) = A(t)x(t) + F(t, x(t-\beta(t))), \tag{2.6}$$

where $t - \beta_i(t) \in \mathbb{T}$ for all $t \in \mathbb{T}$.

To obtain the main results, we need the following assumptions. Assume that:

$(\mathcal{P}_1)$: $A(.) \in M_n(\mathbb{R})$ and $F(.) \in \mathbb{R}^n$, β is periodic function.

$(\mathcal{P}_2)$: $x^{\Delta}(t) = A(t)x(t)$ admits an exponential dichotomy on T with positive constants K and a.

$(\mathcal{P}_3)$: There exists $L < \frac{a}{K(2+\mu^+ a)}$ such that $\| F(t,x) - F(t,y) \| \le L \| x - y \|$ for all $t \in \mathbb{T}$, $x,y \in \mathbb{R}^n$.

Theorem 2.17 Suppose that assumptions $(\mathcal{P}_1) - (\mathcal{P}_3)$are fulfilled. Then, the system (2.6) has a unique pseudo almost anti-periodic solution.

Proof. The system (2.6) has a unique solution $T_x \in PANP(\mathbb{T},\mathbb{R}^n)$which takes the following form

$$T_x(t) = \int_{-\infty}^{t} X(t)PX^{-1}(\sigma(s))F(s,x(s)) \,\triangle s - \int_{t}^{+\infty} X(t)(I-P)X^{-1}(\sigma(s))F(s,x(s)) \,\triangle s.$$

Define a mapping

$$\begin{array}{rccc} T & : & \mathrm{PANP}(\mathbb{T},\mathbb{R}^n,u) & \longrightarrow & \mathrm{PANP}(\mathbb{T},\mathbb{R}^n,u) \\ & & x & \longmapsto & T_x \end{array}$$

From $(\mathcal{P}_2)$, we have

$$\begin{aligned} \| T_x(t) - T_y(t) \| &\le \int_{-\infty}^{t} X(t)PX^{-1}(\sigma(s)) \| F(s,x(s)) - F(s,y(s)) \| \triangle s \\ &\quad - \int_{t}^{+\infty} X(t)(I-P)X^{-1}(\sigma(s)) \| F(s,x(s)) - F(s,y(s)) \| \triangle s \\ &\le \left(\int_{-\infty}^{t} K e_{\ominus\lambda}(t,\sigma(s)) \,\triangle s + \le \int_{-\infty}^{t} K e_{\ominus\lambda}(\sigma(s),t) \,\triangle s\right) L \| x - y \| \\ &\le \frac{K(2+\mu^+ a)}{a} L \| x - y \|. \end{aligned}$$

From $(\mathcal{P}_3)$, T is a contractive operator. The proof is achieved.

From (P_3), T is a contractive operator.

3. **Illustrative example**

$$x^{\triangle}(t) = A(t)x(t) + f(t, x(t - \beta(t))), \qquad (3.1)$$

where

$$A(t) = \begin{pmatrix} \sin t + \sin\sqrt{2}t & 0 \\ 0 & \cos t + \cos\sqrt{2}t \end{pmatrix},$$

It's clear that $A(t) \in \mathrm{ANP}(\mathbb{R}, M_2(\mathbb{R}))$.
On the other hand, the function f takes the form $f = g + h$, where

$$g(t) = \begin{pmatrix} \sin t + \sin\sqrt{2}t \\ \cos(t) \end{pmatrix} \in \mathrm{ANP}(\mathbb{R}, \mathbb{R}^2),\ h(t) = \begin{pmatrix} \frac{\sin x}{t\sigma(t)} \\ \frac{\cos x}{t\sigma(t)} \end{pmatrix} \in \mathrm{ANP}_0(\mathbb{T}, \mathbb{R}^2)$$

and

$$\lim_{r\to+\infty} \frac{1}{2r} \int_{[t_0 - r, t_0 + r]} \| h(t) \| \triangle t = 0,$$

which indicates $f \in \mathcal{PAP}(\mathbb{R}, \mathbb{R}^2, v)$, and the assumption $(\mathcal{P}_1)$ is satisfied.
From [6, Lemma5.2], the system (3.1) possess an exponential dichotomy because the matrix $-A$ is diagonal and positively regressive, which proves that the assumption $(\mathcal{P}_2)$ is satisfied.
The third assumption $(\mathcal{P}_3)$ is easy to have.

References

1. Arbi A and Cao J. Pseudo-almost periodic solution on time-space scales for a novel class of competitive neutral-type neural networks with mixed time-varying delays and leakage delays. Neural Processing Letters, 46(2), 719-745; 2017.

2. Arbi A. Dynamics of BAM neural networks with mixed delays and leakage time varying delays in the weighted pseudo almost periodic on time space scales. Mathematical Methods in the Applied Sciences, 41(3), 1230-1255; 2018.

3. Arbi A, Guo Y, and Cao J. Convergence analysis on time scales for HOBAM neural networks in the Stepanov-like weighted pseudo almost automorphic space. Neural Computing and Applications, 1-15; 2020.

4. Arbi A, Tahri N, Chaker J, Huang C, Cao J. Almost Anti-periodic Solution of Inertial Neural Networks with Leakage and Time-Varying Delays on Timescales. Circuits, Systems, and Signal Processing, 1-17, 2021.

5. Arbi A, Tahri N. Stability analysis of Inertial Neural Networks: a case of almost anti-periodic environment. *Mathematical Methods in the Applied Sciences*.

6. Bohner M. and Peterson A. Dynamic Equations on Time Scales: An introduction with applications. Birkhuser: Basel; 2001.

7. Coppel WA. Dichotomies in Stability Theory. Lecture Notes in Mathematics, vol. 629, Springer-Verlag, Berlin, New York; 1978.

8. Li YK and Wang C. Uniformly almost periodic functions and almost periodic solutions to dynamic equations on time scales. In *Abstract and Applied Analysis* (Vol. 2011). Hindawi.

9. Li YK and Wang C. Pseudo almost periodic functions and pseudo almost periodic solutions to dynamic equations on time scales. Adv. Difference Equ. (77), 1-24; 2012.

10. Zhang CY. Pseudo almost periodic solutions of some differential equations. Journal of Mathematical Analysis and Applications, 62âĂ˘S¸ 76, 1994.

11. Zhang J, Fan M and Zhu H. Existence and roughness of exponential dichotomies of linear dynamic equations on time scales. Computers Mathematics with Applications, vol. 59, no. 8, pp. 2658âĂ˘S¸ 2675; 2010.

On Modified Weingarten Parallel Ruled Surface

Gülden Altay Suroğlu , Yusuf Güzel
Department of Mathematics, University of Firat, Elazig, Turkey
galtay@firat.edu.tr, ysfgzl023@gmail.com

Abstract

In this paper, we obtain some new characterization for Weingarten parallel ruled surface according to Modified frame.

Keywords: Modified frame; ruled surface; Weingarten surface.

Introduction

In differential geometry, ruled surface is a special type of surface which can be defined by choosing a curve and a line along that curve. The ruled surfaces are one of the easiest of all surfaces to parametrize. That surface was found and investigated by Gaspard Monge who established the partial differential equation that satisfies all ruled surfaces.

A parallel ruled surface is a surface represented by points which are at a constant distance along the normal vector of a ruled surface. As it is well known, both ruled surfaces and parallel surfaces have some applications in many industrial processes such as manufacturing for toolpath generation in sculptured surface machining and also in rapid prototyping, to fabricate additively a solid object or assembly from CAD models by using 3D printing technologies such as laser sintering, stereolithography, and laminated object manufacturing. Ruled surfaces have been widely applied in designing cars, ships, manufacturing of products and many other areas such as motion analysis and simulation of rigid body and model-based object recognition systems. Modern surface modeling systems include ruled surfaces. The geometry of ruled surfaces is essential for studying kinematical and positional mechanisms in $\mathbb{E}^3$ and $\mathbb{E}^3_1$.

A surface in three dimensional Euclidean space is called a Weingarten surface if there is some relation between its two principal curvature K and H are not independent of one another, that is, if there is a smooth function of two variables such that $\Phi(H, K) = 0$. Weingarten surface is a classical topic in differential geometry, as introduced by Weingarten, ((Weingarten 1861), (Weingarten 1863),). E. Beltrami and U. Dini proved that a helicoidal ruled surface is the only nondevelopable Weingarten ruled surface in three dimensional Euclidean space , ((Beltrami 1865-1866), (Dini 1865-1866)). This result is later reproved by W. Kühnel, (Kühnel 1994). It has been obtained that parallel surfaces of a ruled Weingarten surface are also Weingarten surfaces. It has been shown that the parallel surfaces of a developable ruled surface are ruled Weingarten surfaces, (Ziya Savcı 2011).

In [], they investigate the evolution of space curves and the special ruled surfaces with modified orthogonal frame. They determine the first and second fundamental forms, the Gaussian and mean curvatures of the tangent, normal, and binormal ruled surfaces according to the modified frame. Finally they obtain the characterizations of the minimal and developable ruled surfaces based on modified orthogonal frame.

In this paper, we obtain some characterization for Weingarten parallel ruled surface according to Modified frame.

2. Preliminaries

In Euclidean 3-space, Euclidean inner product is given by $\langle , \rangle = dx_1^2 + dx_2^2 + dx_3^2$ where $x = (x_1, x_2, x_3) \in \mathbb{E}^3$.The norm of a vector $x \in \mathbb{E}^3$ $\|x\| = \sqrt{|\langle x, x\rangle|}$. For any curve, if $\|\alpha'(s)\| = 1$, then curve is unit speed curve in Euclidean space. The most well-known and used Frenet frame on a curve plays an important role in di erential geometry. Let be a space curve with respect to the arc-length s in $\mathbb{E}^3$. t, n and b are tangent, principal normal and binormal unit vectors at each point $\alpha(s)$ of a curve , respectively. Then there exists an orthogonal frame $\{t, n, b\}$ which satisfies the Frenet-Serret equation

$$\begin{aligned} t' &= \kappa n, \\ n' &= -\kappa t + \tau b, \\ b' &= -\tau n \end{aligned} \tag{2.1}$$

where κ is the curvature, τ is the torsion.

The fundamental theorem of regular curves states that if $\kappa > 0$ and are differentiable functions then there exists a unit speed curve whose curvature and torsion are κ and τ, respectively. However, the principal normal and binormal vectors are discontinuous at zero points of the curvature in general and the curvature is not always differentiable even if the curve is analytic. In that case, the formulation of the Frenet frame of a space curve generally established causes ambiguity for an analytical space curve at a point where the curvature vanishes.

This problem was considered by Hord and Sasai for analytic space curves of which the curvatures have discrete zero points. With a simple but convenient approach, an orthogonal frame was introduced by Sasai. Although this modified orthogonal frame seems like a Frenet frame with scaled normal and binormal vectors, it allows to use a new formula corresponding to the Frenet-Serret equation for the aforementioned case and is also useful for investigating analytic curves with singularities.

Let α be an analytic curve of which curvature has discrete zero points in Euclidean 3-space. Under the assumption $\kappa(s)$ of is not identically zero, the elements of modified orthogonal frame are given by

$$T = \frac{d\alpha}{ds},\ N = \frac{dT}{ds},\ B = T \times N \tag{2.2}$$

where s is the arc-length parameter and $T \times N$ is the vector product of T and N. The relations between the Frenet frame $\{t, n, b\}$ and modified orthogonal frame $\{T, N, B\}$ at non-zero points of κ are

$$T = t,\ N = \kappa n,\ B = \kappa b. \tag{2.3}$$

this orthogonal frame is called the modified orthogonal frame, bükçü.

The modified orthogonal frame $\{T, N, B\}$ satisfies

$$\langle T, T\rangle = 1, \langle N, N\rangle = \langle B, B\rangle = \kappa^2, \langle T, N\rangle = \langle T, B\rangle = \langle N, B\rangle = 0. \tag{2.4}$$

Then we have

$$\begin{aligned} T'(s) &= N(s), \\ N'(s) &= -\kappa^2 T(s) + \frac{\kappa_s}{\kappa} N(s) + \tau B(s), \\ B'(s) &= -\tau N(s) + \frac{\kappa_s}{\kappa} B(s). \end{aligned} \tag{2.5}$$

Here, the essential quantities κ^2 and are analytic.

3. Weingarten Parallel Ruled Surface According to Modified Frame

In this section, we will give characterization of Weingarten parallel ruled surface.with modified orthogonal frame. Let $\alpha(u)$ a curve on three dimensional Euclidean space and $\theta(u, v)$ a ruled surface which is parametrized as

$$\theta(u, v) = \alpha(u) + v\mathbf{T}(u). \tag{3.1}$$

Then, parallel surfaces of the ruled surface is

$$\varphi(u, v) = \theta(u, v) + a\mathbf{U}(u, v) \tag{3.2}$$

3

where a is a constant and $\mathbf{U}(u,v)$ is unit normal vector field of the ruled surface $\theta(u,v)$. So, it parameterized as

$$\varphi(u,v) = \alpha(u) + vT(u) - \frac{v}{k}B \tag{3.3}$$

Theorem 1. Let $\varphi(u,v)$ be a parallel ruled surface which is given by (3.3) in three dimensional Euclidean space. Then, $\varphi(u,v)$ is a minimal surface according to modified orthogonal frame, if

$$\begin{aligned} &-v^2\kappa^3\tau + v^2\tau^2 + \kappa^2(-1+v^2-2v^2\tau^2) \\ &+\kappa(2(-1+v^2)\tau - v^2\tau^3 + v(\kappa'+\tau') = 0. \end{aligned} \tag{3.4}$$

Proof. If we take derivatives of the surface, which is given with the parametrization (3.3), we have

$$\begin{aligned} \varphi_u &= N(v+\frac{v\tau}{\kappa})+T, \\ \varphi_v &= \frac{-B}{\kappa}+T. \end{aligned} \tag{3.5}$$

Then, components of the first fundamental form of the surface are

$$\begin{aligned} E &= 1+\kappa^2(v+\frac{v\tau}{\kappa})^2, \\ F &= 1, \\ G &= 2. \end{aligned} \tag{3.6}$$

The unit normal vector field of the $\varphi(u,v)$ is

$$\mathbf{U} = \frac{1}{A}\left(\frac{N}{\kappa} + B(-v-\frac{v\tau}{\kappa}) + T(\frac{-v}{\kappa}-\frac{v\tau}{\kappa^2})\right). \tag{3.7}$$

where

$$A = \sqrt{\kappa + (\frac{-v}{\kappa}-\frac{v\tau}{\kappa^2})^2(\frac{\kappa^2-1}{\kappa})}.$$

components of the second fundamental form of the surface are

$$\begin{aligned} h_{11} &= \frac{1}{A}(-v^2\kappa^3\tau + v^2\tau^2 + \kappa^2(1+v^2-2v^2\tau^2) \\ &\quad +v\kappa(2v\tau - v\tau^3 + \kappa' + \tau'), \\ h_{12} &= \frac{1}{A}(\kappa+\tau), \\ h_{22} &= 0. \end{aligned} \tag{3.8}$$

4

Then the mean curvature of the surface $\varphi(u,v)$

$$\begin{aligned} H &= \frac{1}{A^{3/2}}(-v^2\kappa^3\tau + v^2\tau^2 + \kappa^2(-1+v^2-2v^2\tau^2) \\ &\quad +\kappa(2(-1+v^2)\tau - v^2\tau^3 + v(\kappa' + \tau')) \end{aligned} \tag{3.9}$$

Corollary 2. Let $\varphi(u,v)$ be parallel ruled surface in three dimensional Euclidean space. Then, points of the surface $\varphi(u,v)$ are hyperbolic points.

Proof. From 3.8 the Gauss curvature of the surface $\varphi(u,v)$

$$K = -\frac{1}{A^2}(\kappa+\tau)^2. \tag{3.10}$$

So the proof is complete.

Corollary3. Let $\varphi(u,v)$ be parallel ruled surface in three dimensional Euclidean space. If $\varphi(u,v)$ developable , then $\kappa = -\tau$

Corollary 4. Let $\varphi(u,v)$ be parallel ruled surface in three dimensional Euclidean space. Then, $\varphi(u,v)$ is a Weingarten parallel ruled surface.with modified orthogonal frame, if $\alpha(u)$ is a cylindrical helix.

Proof. Let a, b and $c \in \mathbb{R}$. If we think derivatives of equations 3.9 and 3.10 in

$$aH + bK = c,$$

we have $\alpha(u)$ is a cylindrical helix.

References

1. A. A. Akdemir, Eğrilik ile modifiye edilmiş ortogonal çatıda eğriler, yüksek lisans tezi, Kayseri, 2021.

2. D. W. Yoon, Some Properties of Parallel Surfaces in Euclidean 3-Spaces, Honam Mat. J., 30, 4, 637-641, 2018.

3. K. Eren, Hidayet Huda Kosal, Evolution of space curves and the special ruled surfaces with modified orthogonal frame, AIMS Mathematics, 5, 3, 2027–2039, 2020.

4. M. T. Sariaydin, T. Körpinar and V. Asil, On Parallel p-equidistant Ruled Surfaces by Using Mofied Orthogonal Frame with Curvature in E 3, Bol. Soc. Paran. Mat, 40, 1-7, 2022.

5. S. Baş, T. Körpınar, Modified Roller Coaster Surface in Space, Mathematics, 7, 5, 2019.

6. U. Z. Savcı, A. Görgülü, C. Ekici, Parallel surfaces of ruled Weingarten surfaces, 3, 4, 237-246, 2015.

7. Y. Ünlütürk, M. Cimdiker, C. Ekici, Characteristic properties of the parallel ruled surfaces with Darboux frame in Euclidean 3- space,Communication in Mathematical Modeling and Applications, 1, 1, 26-43, 2016.

8. S. Şenyurt, A. Çalışkan, B-Scroll Weıngarten Surface, Ordu Üniv. Bil. Tek. Dergisi, 6, 2, 220-231, 2016.

9. J. Weingarten, über eine Klasse auf einander abwickelbarer Fläachen, J Reine AngewMath, 59, 382–393, 1861.

10. J. Weingarten, Über eine flächen, derer normalen eine gegebene flächeberühren, Journal für die Reine und Angewandte Mathematik, 62, 61-63, 1863.

11. B. van–Brunt, K. Grant, Potential applications of Weingarten surfaces in CAGD. I: Weingarten surfaces and surface shape investigation, Comput Aided Geom Des, 13 , 569–582, 1996.

12. E. Beltrami, Risoluzione di un Problema Relativo alla Teoria delle Superficie Gobbe, Ann. Mat. Pura Appl., 7, 139–150, 1865.

13. U. Dini, Sulle Superficie Gobbe nelle quali uno dei due Raggi di Curvatura Principale é una Funzione Dell'altro, Ann. Mat. Pura Appl., 7, 205– 210, 1865.

14. Z. Savcı, On the Parallel Ruled Weingarten Surfaces in 3–dimensional Euclid Space, PhD Thesis, Osmangazi University, Eskişehir, 2011.

15. W. Kühnel, Ruled W–surfaces, Arch. Math., 62, 475–480, 1994.

16. W. Kühnel, M. Steller, On Closed Weingarten Surfaces, Monatsh. Math., 146, 113–126, 2005

17. R. A. Hord, Torsion at an inflection point of a space curve, Am. Math. Mon., 79, 371–374, 1972.

18. T. Sasai, The fundamental theorem of analytic space curves And apparent singularities of Fuchsian differential equations, Tohoku Math. J., 36, 17–24, 1984.

19. T. Sasai, Geometry of analytic space curves with singularities and regular singularities of differential equations, Funkcial. Ekvac., 30 , 283–303, 1987.

20. B. Bükçü, M. K. Karacan, On the modified orthogonal frame with curvature and torsion in 3- Space, Math. Sci. Appl. E-Notes, 4 , 184–188, 2016.

21.T. Mert, Timelike ruled surface in de-Sitter 3-Space, Turkish Journal of Mathematics and Computer Science, 2 (12), 166-175, 2020.

22. T. Mert, M. Atçeken, Special ruled surfaces in de-Sitter 3- space, Fundamental Journal of Mathematics and Applications, 4 (3), 195-209, 2021.

23. T. Mert, M. Atçeken, Spacelike ruled surfaces in de-Sitter 3-space, Asian Journal of Maths. And Computer Research, (2020), 37-53.

7

Numerical Investigation of Particle Distribution in a Cylindrical Channel

Eren Çolak[1-2], Ali Keleş[1], Emre Aslan[3], İmren Hatay PATIR[4]

GKE Energy R&D Center, Milas[1],

Department of Mechanical Engineering, Hacettepe University, Ankara, Turkey[2]

Department of Biochemistry, Selcuk University, Konya, Turkey[3]

Department of Biotechnology, e Selcuk University, Konya, Turkey[4]

eren.colak@gke.com.tr,

Abstract Particle distributions in a continuous media is an important research subject for thermo-fluid and computational science. In this study particle-laden flow of the nano sized particles in a channel investigated with different flow rates (corresponds to Reynolds number 500, 1000, 1500), different particle diameters (1e-5<d<-9e-5), and different particle densities (1500, 2100, 3000 kg/m3). For this purpose, water as a continuous phase (Eulerian) used as an inert species to advect the nanoparticles, different particle shapes (spherical, cube, tetrahedron, disk). Distribution of these particles in a cylindrical domain is investigated with different flow rates, different particle diameters and different particle densities.

Keywords: FVM, CFD, Particle-laden flow, OpenSource

1.INTRODUCTION

Particle-laden flow has many examples in nature and industry, such as human sneezing [1], cyclone separator [2], fuel injection [3], and rain droplets [4] etc. Due to the complex physics of the particle-laden flow, modelling this phenomenon involves semi-empirical models and relies on experimental data [5]. Although in this study particles are modelled as rigid solid particles, it is possible to calculate the break-up (particles can divide into smaller particles) of the particles [6], which usually happens when liquid droplets modelled as particles. By employing Eulerian-Lagrangian approach to model the particle transport in continuous media, particle aggregation thickness, particle distribution, and solid cloud heigh are investigated by many researchers in past [7-10]. In this study, particle shape, particle density, and flow rate effects on the particle distribution and aggregate thickness will be investigated to understand the solid-liquid flow phenomenon. For this purpose, different flow conditions (500<Re<1500), different particle shapes (cubical, spherical, tetrahedral, disk), and particle density (1500<rho<3000) will be used to conduct the simulations. Overall, in order to determine how homogenously distributed the particles are, the particle and the flow properties are important parameters. Particles need to be homogenously distributed, because homogenous distribution of the particles can be used to determine other important phenomenon such as radiation, and heterogenous catalytic reactions.

2.GENERAL PROPERTIES OF METHOD

Continuity and Momentum equations for fluid motion [11] are given in Eq. 1-2, and equation of motion for solid particles are given in Eq. 3-4. In Eq. 2, there is an additional force term, namely F_p which includes the drag, buoyancy and gravitational forces on the particle to the fluid domain.

$$\nabla.\vec{u} = 0 \tag{1}$$

$$\rho\frac{\partial\vec{u}}{\partial t} + \rho(\vec{u}\nabla.\vec{u}) = -\nabla P + \mu\nabla^2\vec{u} + F_P \tag{2}$$

$$\frac{\mathrm{d}}{\mathrm{dt}}\mathrm{x_p} = \overrightarrow{u_p} \tag{3}$$

$$m_p\frac{d}{dt}\overrightarrow{u_p} = \sum\vec{F_i} \tag{4}$$

Drag coefficient can be calculated with Eq. 5 [5], with respect to particle shape factor Ø, and the drag force can be calculated with Eq. 6. Gravitational and buoyancy force can be calculated with Eq. 7, and overall force on the particle can be expressed with Eq. 8, where F_g corresponds to the gravity and buoyancy force on individual particles, and the overall force on the particle can be expressed with Eq. 9.

$$C_D = \frac{24}{Re}[1 + \exp(2.3288 - 6.4581\emptyset + 2.4486\emptyset^2)\ Re^{(0.0964+0.5565\emptyset)} + \frac{Re*\exp(4.905-13.8944\emptyset+18.4222\emptyset^2-10.2599\emptyset^3)}{Re+\exp(1.4681+12.2584\emptyset-207322\emptyset^2+15.8855\emptyset^3} \tag{5}$$

$$F_D = \frac{3}{4}\frac{\rho\, m_p}{\rho_p\, d_p}C_D(u - u_p)|u - u_p| \tag{6}$$

$$F_B + F_G = (\rho_p - \rho)\frac{\pi d_p^3}{6}g \tag{7}$$

$$F_p = F_D + F_B + F_G \tag{8}$$

Reynolds number, expressed in Eq. 9 quantifies the inertia forces over viscous forces, where μ is dynamic viscosity (Pa.s), and D is the channel diameter (m). Since channel flows can be assumed turbulent when Re>2300, it is an important parameter in fluid mechanics. In this study, Reynolds number range kept under 2300 to ensure flow conditions stays under laminar regime.

$$Re = \frac{\rho UD}{\mu} \tag{9}$$

Semi-implicit method for pressure linked equations (SIMPLE) algorithm used to solve these equation sets with 2nd order spatial and temporal discretization. OpenFOAM [12], an open source FVM library used for this application. Computational domain constructed with structural grid (Fig. 1) and the grid independency study shown in Fig. 2. Overall, 70000 structural elements used to represent the fluid domain, which has a cylindrical shape.

Particles are inserted to the domain from the inlet with fixed total mass. Particle diameters varies between 1e-5 < d_p < 9e-5 m. Density of the particles selected as 1500, 2100, and 3000 kg/m3 respectively for different case studies. Flow conditions are controlled with Reynolds number.

Selected Reynolds numbers for this study are 500, 1000, and 1500, which ensures the flow is laminar and no additional treatments to the momentum equation is necessary. Different shaped particles are used Fig.1 shows the computational domain, and Fig. 2 shows the grid independency study. Relative error between velocities along the diameter are lower than the 0.6% if 70000 grid is used. Maximum skewness of the grid is 0.48, and the maximum non-orthogonality is 22.68, which ensures computational grid is suitable for calculations.

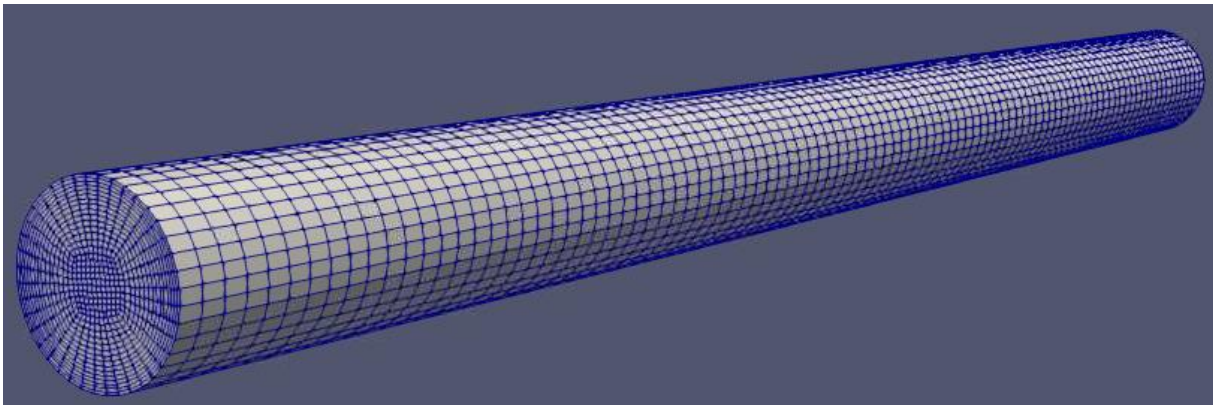

Fig. 1 Computational Domain

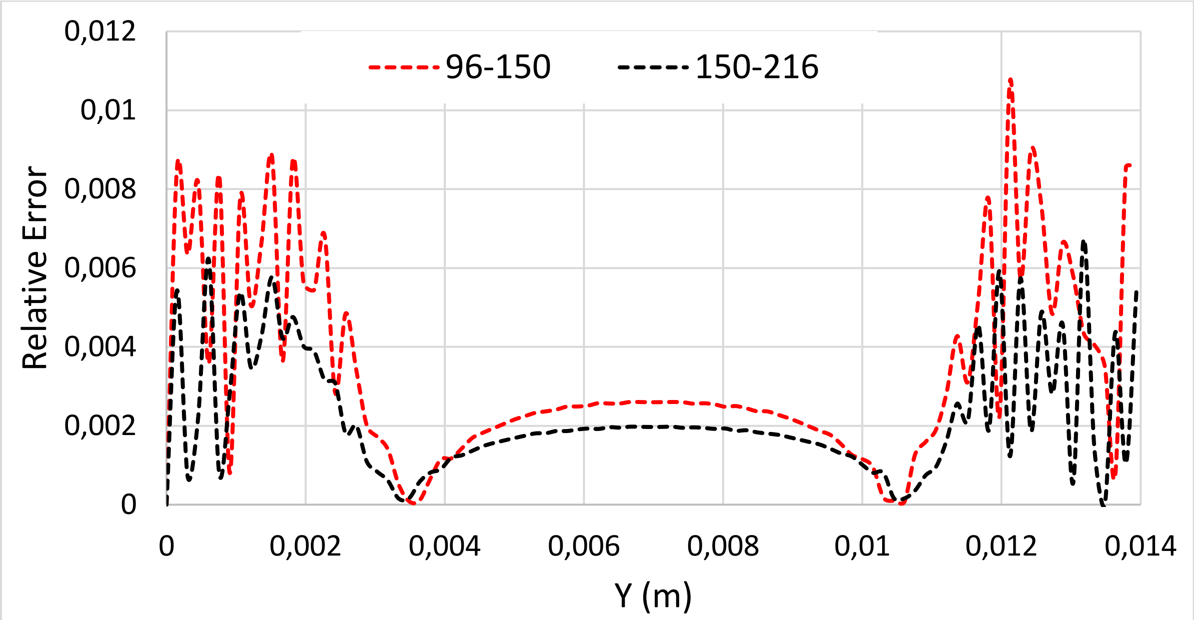

Fig. 2 Grid independency study

3.APPLICATIONS

Fig. 3 shows the particle volume fraction on the continuous media for different Reynolds numbers. It is obvious that when Reynolds number increases, inertia forces also increase, i.e. velocity increases in the continuous phase. When velocity increases, it tends to transport particles more, and gravitational force that causes particles to aggregate becomes less effective. Therefore, increasing Reynolds number decreases the aggregation of the particles as it can be seen from the Fig. 3.

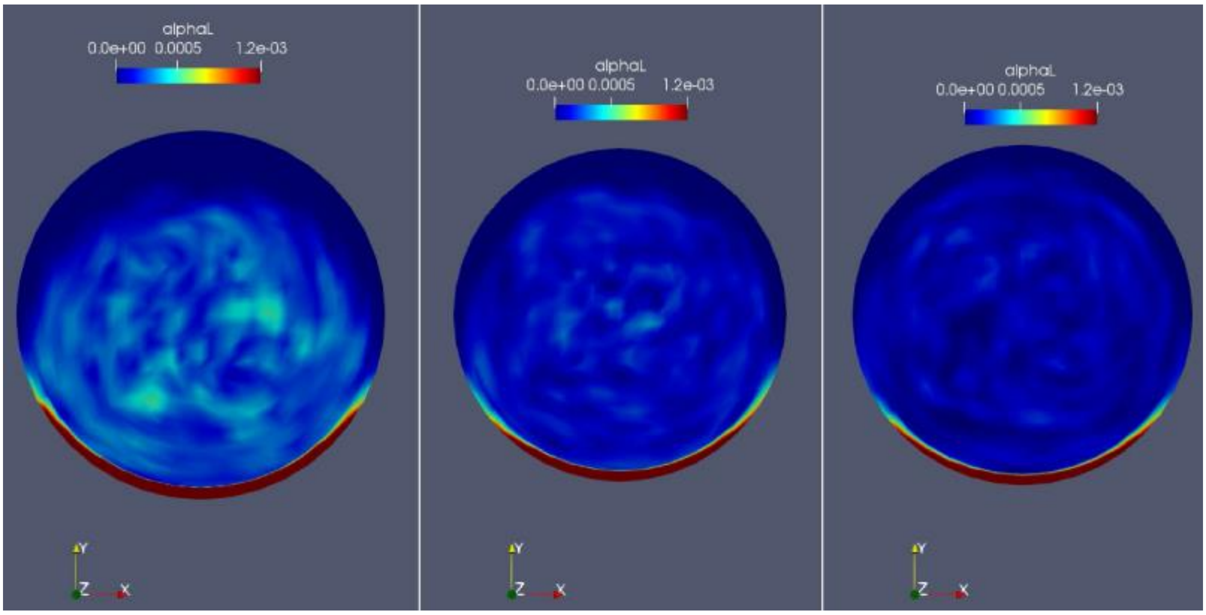

Fig. 3 Reynolds number effect on particle distribution (from left to the right: Re=500, 1000, 1500)

Particle shape effect on the Lagrangian volume fraction can be seen from Fig. 4, and numerical data can be seen from Fig. 5. Cubical, spherical, and tetrahedral particles show similar behavior under same flow conditions (Re=1000), but disk-shaped particles aggregates at much lower rate. In the bottom of the domain Lagrangian volume fraction is 0.0025 for disk shaped particles whereas it is between 0.0065-0.007 for different shaped particles. This means drag force on the disk-shaped particles much less than the other particles due to the lower surface area of the disk-shaped particles.

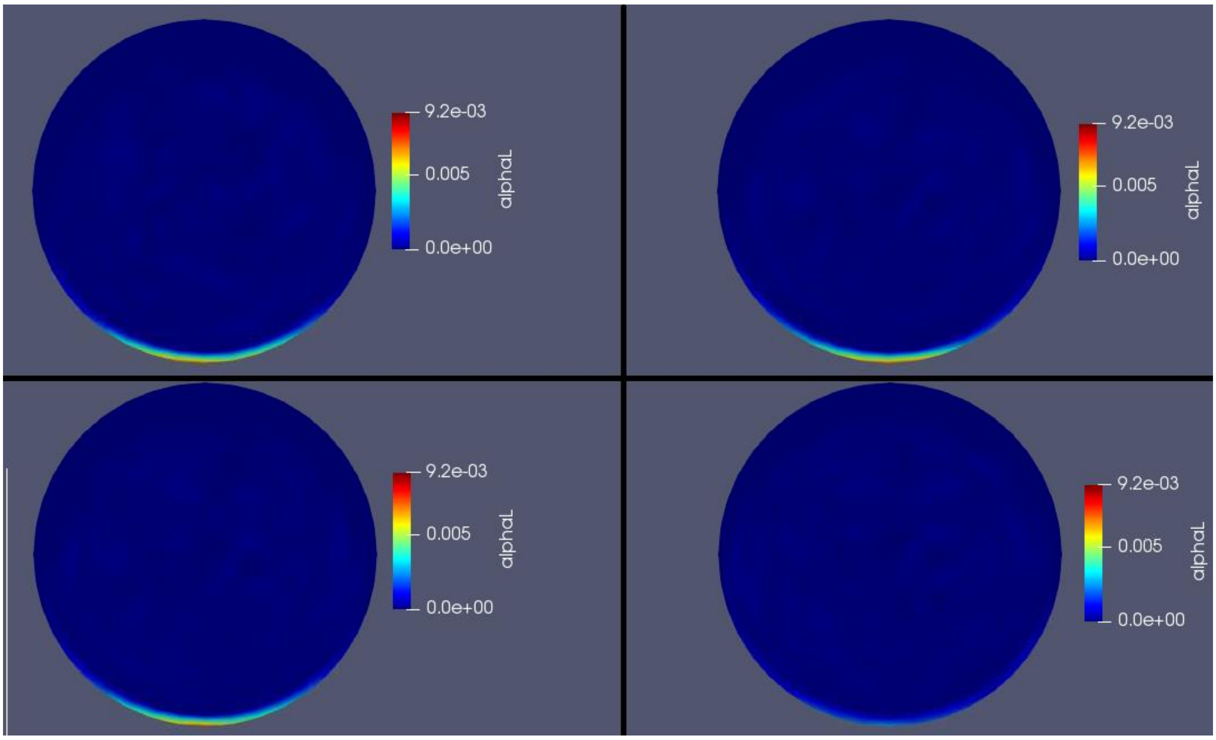

Fig. 4 Particle volume fraction with respect to particle shape (left top: spherical, left bottom: tetrahedral, right top: cubical, right bottom: disk)

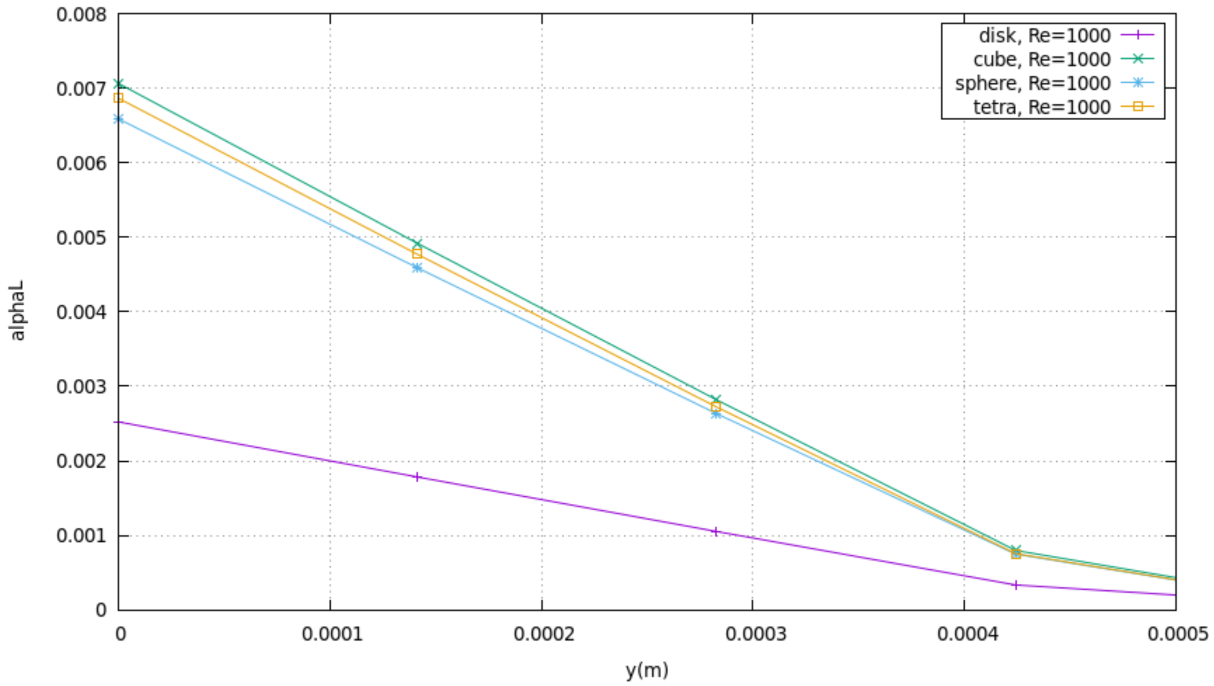

Fig. 5 Particle volume fractions with different shaped particles

Effect of the particle density on the Lagrangian volume fraction can be seen from Fig. 8. It is obvious that increasing density will directly affect the forces on the particles as its shown in Eq. 6-7. Due to increased forces on the particles, aggregation thickness of the Lagrangian particles increases as the density increases. Particle distribution is more homogenous when particle density is 1000 kg/m^3, and when particle density is 2100 kg/m^3. In all three cases, Lagrangian volume fraction is zero at the top of the channel, but the thickness of this particle free layer gets larger as the density increases.

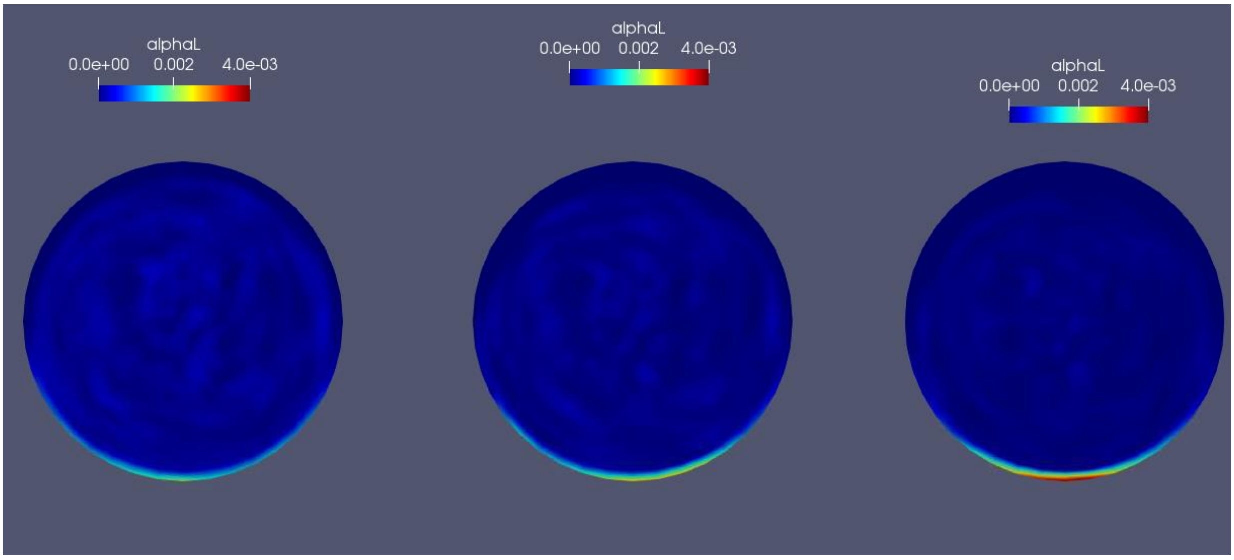

Fig. 6 Particle volume fraction with respect to different densities at Re=1000 (from left to right, ρ=1000, 2100, 3000 kg/m^3)

Fig. 7 shows the Reynolds number and density effects on the disk-shaped particles. The highest Lagrangian volume fraction is 0.005 with Re=500, and ρ= 3000 kg/m^3 case, and the lowest Lagrangian volume fraction is 0.0012 with Re=1500 and ρ= 1500 kg/m^3 case. General trend shows aggregate thickness decreases at y=4e-4 m

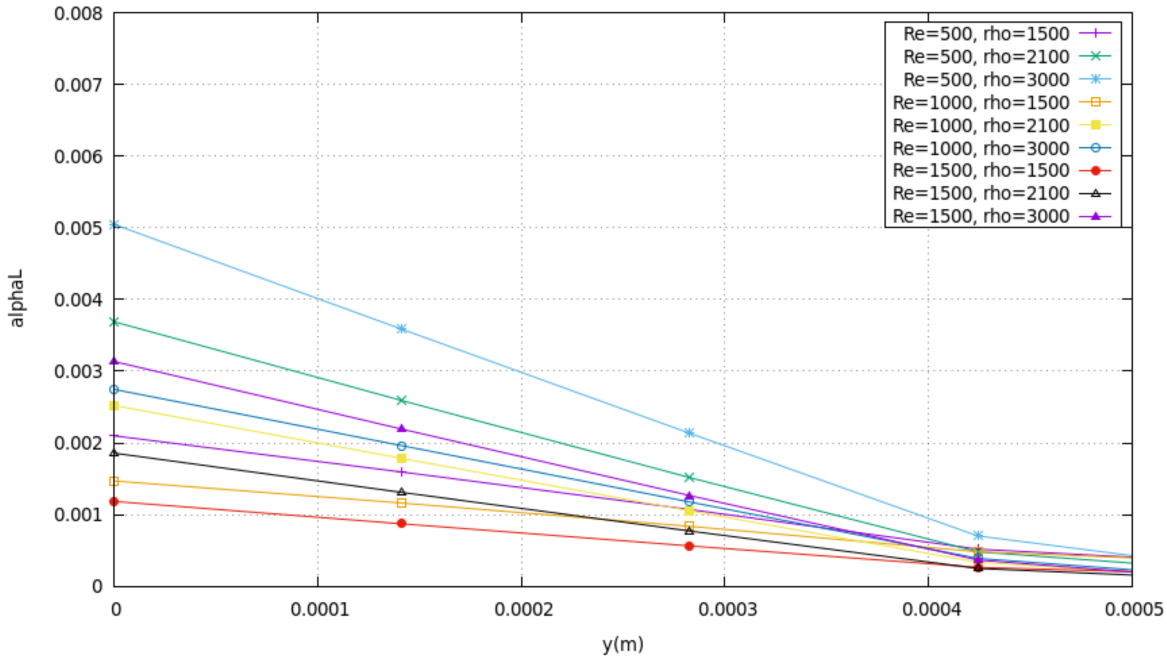

Fig. 7 particle volume fraction under different flow conditions and densities

The highest volume fraction list shown in Table 1. Which indicates that density has the highest effect on the Lagrangian volume fraction than the Reynolds number. Although both inertia of the fluid and the density has direct effect on the forces on the particles, particle forces are calculated with difference between fluid and particle velocity, and increasing fluid velocity also increases the particle velocity, whereas increasing density directly increases the forces on the particles.

Table 1 The Highest volume fraction list of the cases for disk shaped particles

Volume Fraction*10^3	Re	ρ (kg/m^3)
5.05	500	3000
3.7	500	2100
3.14	1500	3000
2.75	1000	3000

4.CONCLUSIONS

In this study particle density, Reynolds number, and particle shape parameters are investigated to understand the particle distribution in a channel. It is observed that as the Reynolds number increases particles aggregates less, and higher density particles tends to aggregate more. Particle shape is an important factor, because it is directly related with the drag force on the particles, and aggregation percent with respect to particles can be placed in descended order as: cubical, tetrahedral, spherical, and disk. Although difference between cubical, spherical, and tetrahedral particles are small, aggregation thickness of the disk-shaped particles approximately 2.6 times less than the different shaped particles. Overall, the highest aggregation thickness observed on Re=500 and ρ=3000 kg/m^3 particles, and lowest aggregation thickness observed on Re=1500, and ρ= 1500 kg/m^3 particles. Forces on the particles are directly affected by density, therefore density has the highest effect on the Lagrangian volume fraction.

ACKNOWLEDGEMENT

This study supportes by the Scientific and Technological Research Council of Turkey with project number 3211037 of the 1501 Industrial R&D Projects Support Program (TÜBİTAK). The authors are thankful for the funding from TÜBİTAK.

REFERENCES

1. Mariam, Magar, A., Joshi, M., Rajagopal, P., Khan, A., Rao, M. and Sapra, B., 2021. CFD Simulation of the Airborne Transmission of COVID-19 Vectors Emitted during Respiratory Mechanisms: Revisiting the Concept of Safe Distance. *ACS Omega*, 6(26), pp.16876-16889.
2. Katare, P., Krupan, A., Dewasthale, A., Datar, A. and Dalkilic, A., 2021. CFD analysis of cyclone separator used for fine filtration in separation industry. *Case Studies in Thermal Engineering*, 28, p.101384.
3. Hii, W. and Michalek, D., 2002. Development of a Transient CFD Model of an SI Fuel Injector. *Design, Operation, and Application of Modern Internal Combustion Engines and Associated Systems*,.
4. Raghavan, V., Joo, P., Pao-Hsiung, C., Kubilay, A. and Allegrini, J., 2017. Determination of Optimal Parameters for Wind Driven Rain CFD Simulation for Building Design in the Tropics. *Procedia Engineering*, 180, pp.1345-1354.
5. Haider, A. and Levenspiel, O., 1989. Drag coefficient and terminal velocity of spherical and nonspherical particles. *Powder Technology*, 58(1), pp.63-70.
6. Brinckman, Kevin & Hosangadi, Ashvin & Ahuja, Vineet & Dash, Sanford & Feldman, G.M.. 2008. A CFD Methodology for Liquid Jet Breakup and Vaporization Predictions of Compressible Flows. 46th AIAA Aerospace Sciences Meeting and Exhibit. 10.2514/6.2008-1023.
7. A. Barresi, G. Baldi, Solids suspension in an agitated vessel, Chem. Eng. Sci. 42(12) (1987) 2949–2956.
8. T.N.H. Zwietering, Suspending of solids particle in liquid by agitators, Chem. Eng. Sci. 8 (1958) 244–253.
9. K.J. Bittorf, S.M. Kresta, Prediction of cloud height for solid suspensions in stirred tanks, Chem. Eng. Res. Des. 81(A5) (2003) 568–577.
10. W. Bujalski, K. Takenmaka, S. Paolini, M. Jahoda, A. Paghanti, K. Takahashi, A. Nienow, A.W. Etchells,. Suspension, homogenization in high solids concentration stirred chemical reactors, Tran. Inst. Chem. Eng. 77A (1999) 241–247.
11. Kundu, P., Cohen, I., Dowling, D. and Tryggvason, G., 2016. *Fluid mechanics*. Amsterdam: Elsevier.

12. Weller, H., Tabor, G., Jasak, H. and Fureby, C., 1998. A tensorial approach to computational continuum mechanics using object-oriented techniques. *Computers in Physics*, 12(6), p.620.

DEGENERATE ARA INTEGRAL TRANSFORM AND ITS APPLICATIONS

RABIA KEVSER YILMAZ , OĞUZ YAĞCI AND RECEP ŞAHIN

Abstract. In [1] (Russ. J. Math. Phys. 2017, 24, 241-248), Kim-Kim defined and introduced the degenerate Laplace transform, also investigated some of their several properties. In this study, we first define and introduce the degenerate ARA transform and establish several properties and relations. We attain degenerate ARA transforms of power functions, degenerate sine, degenerate cosine, degenerate hyperbolic sine, degenerate hyperbolic cosine, degenerate exponential function, and function derivatives. Furthermore, we present that the degenerate ARA transform is the theoretical dual transform to the degenerate Sumudu transform and the degenerate Laplace transform.

1. INTRODUCTION, PRELIMINARIES AND DEFINITIONS

Throughout this paper, we use the notations

$$\mathbb{N}_0 = \{0, 1, 2, ...\}\ , \quad \mathbb{N} = \{1, 2, 3, ...\}\,.$$

The classical gamma function can be defined [7, 8] by

$$\Gamma(\omega) = \int_0^\infty t^{\omega-1} \exp(-t)\, dt, \quad \Re(\omega) > 0. \tag{1.1}$$

Also, the classical Beta function can be defined [7, 8] by

$$\mathfrak{B}(\mu, \nu) = \int_0^1 t^{\mu-1}(1-t)^{\nu-1} dt, \quad \Re(\mu),\, \Re(\nu) > 0,$$

or

$$\mathfrak{B}(\mu, \nu) = \int_0^\infty \frac{u^{\mu-1}}{(1+u)^{\mu+\nu}}\, du, \quad \Re(\mu),\, \Re(\nu) > 0. \tag{1.2}$$

Also, the following relationship between classical Gamma function (1.1) and the Beta function (1.2) is given as follows [7, 8]:

$$\mathfrak{B}(\mu, \nu) = \frac{\Gamma(\mu)\Gamma(\nu)}{\Gamma(\mu+\nu)} \quad \Re(\mu), \Re(\nu) > 0. \tag{1.3}$$

For $\beta \in \mathbb{C}$, the Pochhammer symbol $(\beta)_\nu$ is defined by

$$(\beta)_\upsilon = \begin{cases} \prod\limits_{k=0}^{\nu-1} (\beta + k) = \frac{\Gamma(\beta+\nu)}{\Gamma(\beta)}, & \nu \geq 1 \\ \quad\quad 1 & , \quad \nu \leq 0. \end{cases}$$

2000 *Mathematics Subject Classification.* Primary 33C20.

Key words and phrases. Degenerate exponential function, degenerate Gamma function, degenerate Laplace transform, degenerate Sumudu transform, Laplace transform, Sumudu transform, ARA transform.

The Pochhammer symbol $(\alpha)_n$ is also known as the rising factorial, see [17, 18, 19, 20, 21] and closely related references therein.

For $\lambda \in (0, \infty)$ and $\xi \in \mathbb{R}$, degenerate exponential function e_λ^ξ was defined [1] as

$$e_\lambda^\xi = (1 + \lambda\xi)^{1/\lambda}. \tag{1.4}$$

Kim and Kim defined in [1] degenerate Gamma function $\Gamma_\lambda(z)$ as:

$$\Gamma_\lambda(z) = \int_0^\infty e_\lambda^{-\xi} \xi^{z-1} d\xi, \qquad 0 < \Re(z) < \frac{1}{\lambda}, \tag{1.5}$$

where the degenerate exponential function e_λ^ξ defined in (1.4). In addition to these, the following relationship betweenn degenerate Gamma function (1.5) and Beta function (1.2) holds true:

$$\Gamma_\lambda(s) = \lambda^{-s} \mathfrak{B}\left(s, \frac{1}{\lambda} - s\right). \tag{1.6}$$

Also, the degenerate Laplace transform is introduced and studied by Kim-Kim in [1] as follows:

$$\mathfrak{L}_\lambda \{f(\xi)\} = \mathfrak{F}_\lambda(s) = \int_0^\infty e_\lambda^{-s\xi} f(\xi) d\xi, \tag{1.7}$$

if the integral converges.

In 2020, Saadeh *et al.* [6] defined the ARA integral transform by

$$G_n [g(t)](s) = G(n, s) = s \int_0^\infty t^{n-1} e^{-st} g(t) dt, \quad s > 0, \tag{1.8}$$

provided that the integrals involved are convergent [6].

The main goal of this paper is to define and investigate a degenerate ARA transform by using degenerate exponential function e_λ^ξ defined in (1.4). A great number of integral transforms are available in the literature $[1, 4 - 16]$. The paper is organized as follows: In Sec. (2.1), we introduce the degenerate ARA transform. In Sec. (2.2), the degenerate ARA transform is given the theoretical dual transform to the degenerate Sumudu transform and the degenerate Laplace transform. In Sec. (2.3), we investigate some properties for degenerate special functions using the degenerate ARA transform. In Sec. (3), we investigate several interesting examples for finding degenerate ARA transform for several functions.

2. GENERAL PROPERTIES OF METHOD

2.1. Degenerate ARA Integral Transform

Here, we present the degenerate ARA transform and investigate several of their properties.

Definition 2.1. *Let $\lambda \in (0, \infty)$ and the degenerate ARA integral transform of order n of the continuous function $g(t)$ on the interval $(0, \infty)$ is defined as:*

$$G_{n,\lambda} [g(t)](s) = G_\lambda(n, s) = s \int_0^\infty t^{n-1} e_\lambda^{-st} g(t) dt \qquad s > 0, \tag{2.1}$$

if the integral converges.

We note that

$$\lim_{\lambda \longrightarrow 0^+} G_{n,\lambda}\left[g(t)\right](s) = G_n\left[g(t)\right](s).$$

Theorem 2.1. *The sufficient condition for the existence of degenerate ARA transform. If the function $g(t)$ is piecewise continuous in every finite interval $0 \leq t \leq \alpha$ and satisfies:*

$$\left|t^{n-1}g(t)\right| \leq \mathbb{K}e_{\lambda}^{\rho t} \tag{2.2}$$

then, degenerate ARA transform exists for all $s-\rho > \lambda$.

Proof. We obtain □

$$s\int_0^\infty t^{n-1}e_{\lambda}^{-st}g(t)dt = s\int_0^\alpha t^{n-1}e_{\lambda}^{-st}g(t)dt + s\int_\alpha^\infty t^{n-1}e_{\lambda}^{-st}g(t)dt$$

since the function $g(t)$ is piecewise continuous then the first integral on the right side exists. And the second integral on the right side converges because:

$$\left|s\int_\alpha^\infty e_{\lambda}^{-st}t^{n-1}g(t)dt\right| \leq s\int_\alpha^\infty e_{\lambda}^{-st}\left|t^{n-1}g(t)\right|dt \leq s\int_\alpha^\infty e_{\lambda}^{-st}\mathbb{K}e_{\lambda}^{\rho t}dt$$

$$= s\mathbb{K}\int_\alpha^\infty e_{\lambda}^{-(s-\rho)t}dt = \frac{s\mathbb{K}}{s-\rho-\lambda}\left(1+\lambda\alpha\right)^{-\frac{s-\rho-\lambda}{\lambda}},$$

and, this improper integral is convergent for all $s-\rho > \lambda$. Thus, $G_{n+1,\lambda}\left[g\left(t\right)\right](s)$ exists.

2.2. Duality Between Some Degenerate Integral Transform

In this section, we will give duality between some degenerate integral transforms. First of all, we will present duality between degenerate ARA and degenerate Laplace transforms. Putting $n=0$ and $n=1$, respectively, in the equation (2.1), then the following equations hold true:

$$G_{0,\lambda}\left[g(t)\right](s) = G_{\lambda}(0,s) = s\int_0^\infty t^{-1}e_{\lambda}^{-st}g(t)dt = s\mathfrak{L}_{\lambda}\left\{\frac{g(t)}{t}\right\}, \tag{2.3}$$

$$G_{1,\lambda}\left[g(t)\right](s) = G_{\lambda}(1,s) = s\int_0^\infty e_{\lambda}^{-st}g(t)dt = s\mathfrak{L}_{\lambda}\left\{g(t)\right\}, \tag{2.4}$$

where $\mathfrak{L}_{\lambda}\left\{g(t)\right\}$ is the degenerate Laplace transform (1.7).

Now, we will present duality between degenerate ARA and degenerate Sumudu transform. Putting $n=1$ in the equation (2.1), then using the duality between degenerate Laplace and degenerate Sumudu transform, we have

$$G_{1,\lambda}\left[g(t)\right](s) = G_{\lambda}(1,s) = s\mathfrak{L}_{\lambda}\{g(t)\} = s\mathfrak{F}_{\lambda}(s) = \mathfrak{G}_{\lambda}\left(\frac{1}{s}\right) \tag{2.5}$$

where the degenerate Sumudu transform [4],[5] is

$$\mathfrak{G}_{\lambda}(u) = S_{\lambda}[f(t)] = \frac{1}{u}\int_0^{\infty} e_{\lambda}^{-\frac{t}{u}} f(t)dt. \tag{2.6}$$

Finally, we will attain duality between degenerate ARA and degenerate Elzaki transform. Putting $n = 1$ in the equation (2.1), then taking consideration the duality between degenerate Laplace and degenerate Elzaki transform, we have

$$G_{1,\lambda}\left[g(t)\right](s) = G_{\lambda}(1,s) = s\mathfrak{L}_{\lambda}\{g(t)\} = s\mathfrak{F}_{\lambda}(s) = s^2\,\mathfrak{T}_{\lambda}\left(\frac{1}{s}\right), \tag{2.7}$$

where the degenerate Elzaki transform [16] is

$$\epsilon_{\lambda}[f(t)] = \mathfrak{T}_{\lambda}(s) = s^2\int_0^{\infty} e_{\lambda}^{-t} f(st)dt. \tag{2.8}$$

2.3. Some Properties Of Degenerate ARA Transform

Now, we will present some properties of the degenerate ARA transform.

Let $f(t)$ and $g(t)$ are continuous function on the interval $(0, \infty)$ and $\alpha, \beta \in \mathbb{R}$ then, the degenerate ARA transform is a linear transform,

$$\begin{aligned} G_{n,\lambda}\left[\alpha f(t) + \beta g(t)\right](s) &= s\int_0^{\infty} t^{n-1} e_{\lambda}^{-st}\left[\alpha f(t) + \beta g(t)\right]dt \\ &= \alpha s\int_0^{\infty} t^{n-1} e_{\lambda}^{-st} f(t)dt + \beta s\int_0^{\infty} t^{n-1} e_{\lambda}^{-st} g(t)dt \\ &= \alpha G_{n,\lambda}\left[f(t)\right](s) + \beta G_{n,\lambda}\left[g(t)\right](s). \end{aligned}$$

Using the definition of degenerate ARA transform (2.1) for $g(at)$, and a setting of $u = at$ in (2.2), we get the following property:

$$G_{n,\lambda}\left[g(at)\right](s) = \frac{1}{a^{n-1}} G_{\lambda}\left(n, \frac{s}{a}\right).$$

Taking consideration of equation (2.1) for $g(t) = e_{\lambda}^{-ct} g(t)$, and we have the shifting in $s - Domain$ property as follows:

$$\begin{aligned} G_{n,\lambda}\left[e_{\lambda}^{-ct} g(t)\right](s) &= s\int_0^{\infty} t^{n-1} e_{\lambda}^{-(s+c)t} g(t)dt \\ &= \frac{s}{s+c}(s+c)\int_0^{\infty} t^{n-1} e_{\lambda}^{-(s+c)t} g(t)dt \\ &= \frac{s}{s+c} G_{\lambda}\left(n, s+c\right). \end{aligned}$$

Now, applying similarly for $g(t) = t^m g(t)$ in (2.1), then the following equality holds true:

$$G_{n,\lambda}\left[t^m g(t)\right](s) = s\int_0^{\infty} t^{n-1} e_{\lambda}^{-st} t^m g(t)dt = G_{\lambda}(n+m, s).$$

Applying the definition of (2.1) for $u_c(t)\,g(t-c)$, and a setting of $t-c=\mu$, we attain the following property:

$$G_{n,\lambda}\left[u_c(t)g(t-c)\right](s)=e_\lambda^{-sc}G_{1,\lambda}\left[g(\mu)(\mu+c)^{n-1}\right],$$

where $u_c(t)\,g(t-c)$ is named as shifted (delayed) unit function, and defined as follows:

$$u_c(t)=\begin{cases}0, & t<c\\ 1, & t\geq c.\end{cases}$$

In the degenerate ARA transformation expressed in the definition in (2.1), when the derivative is applied once according to the parameter s, we have

$$\frac{d}{ds}G_{n,\lambda}\left[f(t)\right](s)=\frac{G_{n,\lambda}\left[f(t)\right](s)}{s}-\lambda^{-1}G_{n,\lambda}\left[\log(1+\lambda t)\,f(t)\right](s). \tag{2.9}$$

Then, taking the derivative according to s again in the above expression (2.9), we get

$$\begin{aligned}\left(\frac{d}{ds}\right)^2G_{n,\lambda}\left[f(t)\right](s) &= (-1).2.\lambda^{-1}\frac{G_{n,\lambda}\left[\log(1+\lambda t)\,f(t)\right](s)}{s}\\ &\quad+(-1)^2\lambda^{-2}G_{n,\lambda}\left[\left(\log(1+\lambda t)\right)^2f(t)\right](s).\end{aligned} \tag{2.10}$$

Finally, taking the derivative $(m-2)$ times according to s in (2.10), the following general expression can be obtained:

$$\begin{aligned}\left(\frac{d}{ds}\right)^mG_{n,\lambda}\left[f(t)\right](s) &= (-1)^{m-1}m\lambda^{-m+1}\frac{G_{n,\lambda}\left[\left(\log(1+\lambda t)\right)^{m-1}f(t)\right](s)}{s}\\ &\quad+(-1)^m\lambda^{-m}G_{n,\lambda}\left[\left(\log(1+\lambda t)\right)^mf(t)\right](s).\end{aligned} \tag{2.11}$$

Taking the derivative with respect to in the definition (2.1), we get

$$\begin{aligned}G_{n,\lambda}\left[\frac{d}{dt}g(t)\right](s) &= s\int_0^\infty t^{n-1}(1+\lambda t)^{-\frac{s}{\lambda}}g'(t)dt=st^{n-1}(1+\lambda t)^{-\frac{s}{\lambda}}g(t)\Big|_0^\infty\\ &\quad-s(n-1)\int_0^\infty t^{n-2}(1+\lambda t)^{-\frac{s}{\lambda}}g(t)dt+s^2\int_0^\infty t^{n-1}(1+\lambda t)^{-\frac{s+\lambda}{\lambda}}g(t)dt,\end{aligned}$$

then, putting $n=1$ in the definition (2.1) and, using the relationship in the equation (2.4), we obtain

$$G_{1,\lambda}\left[\frac{d}{dt}g(t)\right](s)=s\mathfrak{L}_\lambda\left\{g'(t)\right\}=-sg(0)+s^2\mathfrak{L}_\lambda\left\{(1+\lambda t)^{-1}g(t)\right\}. \tag{2.12}$$

Taking the derivative $(m-1)$ times with respect to in the above equation (2.12), we can be state the following equality:

$$
\begin{aligned}
G_{1,\lambda}\left[\left(\frac{d}{dt}\right)^m g(t)\right](s) &= s\mathfrak{L}_\lambda\left\{g^{(m)}(t)\right\} \qquad (2.13)\\
&= s^2(s+\lambda)(s+2\lambda)...(s+(m-1)\lambda)\mathfrak{L}_\lambda\left\{(1+\lambda t)^{-m} g(t)\right\}\\
&\quad -s\sum_{i=0}^{m-1} g^{(i)}(0)\left(\prod_{k=1}^{m-i-1} s+(k-1)\lambda\right),
\end{aligned}
$$

where $\mathfrak{L}_\lambda$ is the degenerate Laplace transforms defined in [1].

3. APPLICATIONS

Now, we investigate several interesting examples for finding degenerate ARA transform for several functions.

Example 1: Let $\lambda \in (0,\infty)$ and putting $g(t) = 1$ in equation (2.1), we get

$$
G_{n,\lambda}[1](s) = s\int_0^\infty t^{n-1}e_\lambda^{-st}dt = s\mathfrak{L}_\lambda\left\{t^{n-1}\right\} = \frac{1}{s^{n-1}}\Gamma_{\frac{\lambda}{s}}(n) \qquad (3.1)
$$

where $\Gamma_\lambda(n)$ is the degenerate Gamma function in (1.5). Then, using the relationship (1.6) in the above equation, we can be derive the following equation:

$$
G_{n,\lambda}[1](s) = \lambda^{-n}s\mathfrak{B}\left(n, \frac{s}{\lambda}-n\right). \qquad (3.2)
$$

Also, taking consideration the relationship between Gamma function and Beta function (1.3) in the above equation, we obtain:

$$
G_{n,\lambda}[1](s) = \lambda^{-n}s\frac{\Gamma(n)\Gamma\left(\frac{s}{\lambda}-n\right)}{\Gamma\left(\frac{s}{\lambda}\right)}.
$$

Example 2: For $g(t) = t^m$ in equation (2.1), and $m \in \mathbb{N}$, we have

$$
\begin{aligned}
G_{n,\lambda}[t^m](s) &= s\int_0^\infty t^{m+n-1}e_\lambda^{-st}dt = s\mathfrak{L}_\lambda\left\{t^{m+n-1}\right\} \qquad (3.3)\\
&= \frac{1}{s^{m+n-1}}\Gamma_{\frac{\lambda}{s}}(m+n).
\end{aligned}
$$

Example 3: For $g(t) = e_\lambda^{-at}$, e_λ^{at}, e_λ^{-ait}, e_λ^{ait} , respectively, in equation (2.1), $n \in \mathbb{N}$ and $s > n\lambda - a$, we get

$$
G_{n,\lambda}\left[e_\lambda^{-at}\right](s) = s\int_0^\infty t^{n-1}e_\lambda^{-(s+a)t}dt = \frac{s}{(s+a)^n}\Gamma_{\frac{\lambda}{s+a}}(n). \qquad (3.4)
$$

Also, taking consideration the relationship (1.6) in the above equation, we obtain

$$
G_{n,\lambda}\left[e_\lambda^{-at}\right](s) = s\lambda^{-n}\mathfrak{B}\left(n, \frac{s+a}{\lambda}-n\right) = s\lambda^{-n}\frac{\Gamma(n)\Gamma\left(\frac{s+a}{\lambda}-n\right)}{\Gamma\left(\frac{s+a}{\lambda}\right)},
$$

$$
G_{n,\lambda}\left[e_\lambda^{at}\right](s) = s\int_0^\infty t^{n-1}e_\lambda^{-(s-a)t}dt = \frac{s}{(s-a)^n}\Gamma_{\frac{\lambda}{s-a}}(n), \qquad (3.5)
$$

$$G_{n,\lambda}\left[e_{\lambda}^{-ait}\right](s)=s\int_{0}^{\infty}t^{n-1}e_{\lambda}^{-(s+ai)t}dt=\frac{s}{(s+ai)^{n}}\Gamma_{\frac{\lambda}{s+ai}}(n),\tag{3.6}$$

$$G_{n,\lambda}\left[e_{\lambda}^{ait}\right](s)=s\int_{0}^{\infty}t^{n-1}e_{\lambda}^{-(s-ai)t}dt=\frac{s}{(s-ai)^{n}}\Gamma_{\frac{\lambda}{s-ai}}(n)\tag{3.7}$$

where $\Gamma_{\lambda}(n)$ is the degenerate Gamma function in (1.5).

Example 4: For $g(t)=t^{m}e_{\lambda}^{at}$ in equation (2.1), $m\in\mathbb{N}$ and $s>(m+n)\lambda+a$, we obtain

$$G_{n,\lambda}\left[t^{m}e_{\lambda}^{at}\right](s)=s\int_{0}^{\infty}t^{m+n-1}e_{\lambda}^{-(s-a)t}dt=\frac{s}{(s-a)^{m+n}}\Gamma_{\frac{\lambda}{s-a}}(m+n).\tag{3.8}$$

Example 5: For $g(t)=\cos_{\lambda}(at)=\frac{e_{\lambda}^{ait}+e_{\lambda}^{-ait}}{2}$ in equation (2.1), we have

$$\begin{aligned}G_{n,\lambda}\left[\cos_{\lambda}(at)\right](s) &= G_{n,\lambda}\left[\frac{e_{\lambda}^{ait}+e_{\lambda}^{-ait}}{2}\right](s)\\ &= \frac{1}{2}G_{n,\lambda}\left[e_{\lambda}^{ait}\right](s)+\frac{1}{2}G_{n,\lambda}\left[e_{\lambda}^{-ait}\right](s)\\ &= \frac{1}{2}\left[\frac{s}{(s-ai)^{n}}\Gamma_{\frac{\lambda}{s-ai}}(n)+\frac{s}{(s+ai)^{n}}\Gamma_{\frac{\lambda}{s+ai}}(n)\right]\end{aligned}\tag{3.9}$$

where $\cos_{\lambda}(at)$ is the degenerate cos function defined by Kim-Kim [1].

Example 6: For $g(t)=\sin_{\lambda}(at)=\frac{e_{\lambda}^{ait}-e_{\lambda}^{-ait}}{2i}$ in equation (2.1), we get

$$\begin{aligned}G_{n,\lambda}\left[\sin_{\lambda}(at)\right](s) &= G_{n,\lambda}\left[\frac{e_{\lambda}^{ait}-e_{\lambda}^{-ait}}{2i}\right](s)\\ &= \frac{1}{2i}G_{n,\lambda}\left[e_{\lambda}^{ait}\right](s)-\frac{1}{2i}G_{n,\lambda}\left[e_{\lambda}^{-ait}\right](s)\\ &= \frac{1}{2i}\left[\frac{s}{(s-ai)^{n}}\Gamma_{\frac{\lambda}{s-ai}}(n)-\frac{s}{(s+ai)^{n}}\Gamma_{\frac{\lambda}{s+ai}}(n)\right]\end{aligned}\tag{3.10}$$

where $\sin_{\lambda}(at)$ is the degenerate sin function defined by Kim-Kim [1].

Example 7: For $g(t)=\cosh_{\lambda}(at)=\frac{e_{\lambda}^{at}+e_{\lambda}^{-at}}{2}$ in equation (2.1), we derive

$$\begin{aligned}G_{n,\lambda}\left[\cosh_{\lambda}(at)\right](s) &= G_{n,\lambda}\left[\frac{e_{\lambda}^{at}+e_{\lambda}^{-at}}{2}\right](s)\\ &= \frac{1}{2}G_{n,\lambda}\left[e_{\lambda}^{at}\right](s)+\frac{1}{2}G_{n,\lambda}\left[e_{\lambda}^{-at}\right](s)\\ &= \frac{1}{2}\left[\frac{s}{(s-a)^{n}}\Gamma_{\frac{\lambda}{s-a}}(n)+\frac{s}{(s+a)^{n}}\Gamma_{\frac{\lambda}{s+a}}(n)\right],\end{aligned}\tag{3.11}$$

and then, using the relationship (1.6) in the above equation, we get

$$G_{n,\lambda}\left[\cosh_\lambda(at)\right](s) = \frac{s}{2}\lambda^{-n}\left[\mathfrak{B}(n,\frac{s-a}{\lambda}-n)+\mathfrak{B}(n,\frac{s+a}{\lambda}-n)\right]$$
$$= \frac{s}{2}\lambda^{-n}\Gamma(n)\left[\frac{\Gamma\left(\frac{s-a}{\lambda}-n\right)}{\Gamma\left(\frac{s-a}{\lambda}\right)}+\frac{\Gamma\left(\frac{s+a}{\lambda}-n\right)}{\Gamma\left(\frac{s+a}{\lambda}\right)}\right] \tag{3.12}$$

where $\cosh_\lambda(at)$ is the degenerate cosh function defined by Kim-Kim in [1].

Example 8: For $g(t)=\sinh_\lambda(at)=\frac{e_\lambda^{at}-e_\lambda^{-at}}{2}$ in equation (2.1), we have

$$\begin{aligned} G_{n,\lambda}\left[\sinh_\lambda(at)\right](s) &= G_{n,\lambda}\left[\frac{e_\lambda^{at}-e_\lambda^{-at}}{2}\right](s) \\ &= \frac{1}{2}G_{n,\lambda}\left[e_\lambda^{at}\right](s)-\frac{1}{2}G_{n,\lambda}\left[e_\lambda^{-at}\right](s) \\ &= \frac{1}{2}\left[\frac{s}{(s-a)^n}\Gamma_{\frac{\lambda}{s-a}}(n)-\frac{s}{(s+a)^n}\Gamma_{\frac{\lambda}{s+a}}(n)\right], \end{aligned} \tag{3.13}$$

and also, we obtain

$$G_{n,\lambda}\left[\sinh_\lambda(at)\right](s) = \frac{s}{2}\lambda^{-n}\left[\mathfrak{B}\left(n,\frac{s-a}{\lambda}-n\right)-\mathfrak{B}\left(n,\frac{s+a}{\lambda}-n\right)\right]$$
$$= \frac{s}{2}\lambda^{-n}\Gamma(n)\left[\frac{\Gamma\left(\frac{s-a}{\lambda}-n\right)}{\Gamma\left(\frac{s-a}{\lambda}\right)}-\frac{\Gamma\left(\frac{s+a}{\lambda}-n\right)}{\Gamma\left(\frac{s+a}{\lambda}\right)}\right] \tag{3.14}$$

where $\sinh_\lambda(at)$ is the degenerate sinh function defined by Kim-Kim [1].

Example 9: For $g(t)=e_\lambda^{-at}\cos_\lambda(bt)$ in equation (2.1), we get

$$\begin{aligned} &G_{n,\lambda}\left[e_\lambda^{-at}\cos_\lambda(bt)\right](s) \\ =\ &\frac{s}{2}\left[\frac{1}{(s+a-bi)^n}\Gamma_{\frac{\lambda}{s+a-bi}}(n)+\frac{1}{(s+a+bi)^n}\Gamma_{\frac{\lambda}{s+a+bi}}(n)\right]. \end{aligned} \tag{3.15}$$

Example 10: For $g(t)=e_\lambda^{-at}\sin_\lambda(bt)$ in equation (2.1), we have

$$\begin{aligned} &G_{n,\lambda}\left[e_\lambda^{-at}\sin_\lambda(bt)\right](s) \\ =\ &\frac{s}{2i}\left[\frac{1}{(s+a-bi)^n}\Gamma_{\frac{\lambda}{s+a-bi}}(n)-\frac{1}{(s+a+bi)^n}\Gamma_{\frac{\lambda}{s+a+bi}}(n)\right]. \end{aligned} \tag{3.16}$$

Example 11: For $g(t)=e_\lambda^{-at}\cosh_\lambda(bt)$ in equation (2.1), we get

$$\begin{aligned} &G_{n,\lambda}\left[e_\lambda^{-at}\cosh_\lambda(bt)\right](s) \\ =\ &\frac{s}{2}\left[\frac{1}{(s+a-b)^n}\Gamma_{\frac{\lambda}{s+a-b}}(n)+\frac{1}{(s+a+b)^n}\Gamma_{\frac{\lambda}{s+a+b}}(n)\right]. \end{aligned} \tag{3.17}$$

Example 12: For $g(t)=e_\lambda^{-at}\sinh_\lambda(bt)$ in equation (2.1), we obtain

$$\begin{aligned} &G_{n,\lambda}\left[e_\lambda^{-at}\sinh_\lambda(bt)\right](s) \\ =\ &\frac{s}{2}\left[\frac{1}{(s+a-b)^n}\Gamma_{\frac{\lambda}{s+a-b}}(n)-\frac{1}{(s+a+b)^n}\Gamma_{\frac{\lambda}{s+a+b}}(n)\right]. \end{aligned} \tag{3.18}$$

4. CONCLUSIONS

In our present paper, we first demonstrated the degenerate ARA transform by considering degenerate exponential function. Then by means of newly defined integral transform, we demonstrated a degenerate special functions. We make an observation limitting $\lambda \to 0^+$, then the result derived in this paper will be reduced to the classical ARA integral transform. Moreover, we show that the degenerate ARA transform is the theoretical dual transform to the degenerate Laplace transform, degenerate Sumudu transform and degenerate Elzaki transform.

In addition to all this, using the relationship of the ARA integral transform between other integral transforms [6]. It gives us the opportunity to identify new degenerate integral transformations and investigate their interesting properties. For example, taking $n = 1$ in the equation (2.1), then we can be introduced degenerate Laplace-Carson transform as given:

$$G_{1,\lambda}\left[g(t)\right](s) = \mathfrak{L}_{\lambda,*}\left[g(t)\right] = s\int_0^\infty e_\lambda^{-st} g(t)dt$$

where taking limit $\lambda \to 0^+$ for $\mathfrak{L}_{\lambda,*}\left[g(t)\right]$, we have the classical Laplace-Carson transform [22].

Also, setting $n = 1$ and multiplying both sides $\frac{1}{s^2}$ in the equation (2.1), then we can be introduced degenerate Aboodh transform as follows:

$$\frac{1}{s^2}G_{1,\lambda}\left[g(t)\right](s) = \mathfrak{A}_\lambda\left[g(t)\right] = \frac{1}{s}\int_0^\infty e_\lambda^{-st} g(t)dt$$

where taking limit $\lambda \to 0^+$ for $\mathfrak{A}_\lambda\left[g(t)\right]$, we get the classical Aboodh transform [23].

Finally, putting $n = 1$ and multiplying both sides s in the equation (2.1), then we can be introduced degenerate Mohand transform as given:

$$sG_{1,\lambda}\left[g(t)\right](s) = \mathfrak{M}_\lambda\left[g(t)\right] = s^2\int_0^\infty e_\lambda^{-st} g(t)dt$$

where taking limit $\lambda \to 0^+$ for $\mathfrak{M}_\lambda[g(t)]$, we get the classical Mohand transform [24].

References

[1] T. Kim, D. S. Kim, Degenerate Laplace transform and degenerate Gamma function, Russian Journal of Mathematical Physics, 24(2), 241-248, 2017.

[2] T. Kim, D. S. Kim, Note on the degenerate Gamma function, Russian Journal of Mathematical Physics, 27(3), 352-358, 2020.

[3] YunJae Kim, Byung Moon Kim, Lee-Chae Jang, Jongkyum Kwon, Note on modified degenerate Gamma and Laplace transformation, Symmetry, 10(10), 471, 2018.

[4] Uğur Duran, Degenerate Sumudu transform and its properties, Filomat, 35(14), 4731-4741, 2021.

[5] Oğuz Yağcı, Recep Şahin, Degenerate Pochhammer symbol, degenerate Sumudu transform, and degenerate hypergeometric function with applications, Hacettepe Journal of Mathematics and Statistics, 1-18, 2021.

[6] Rania Saadeh, Ahmad Qazza, Aliaa Burqan, A new integral transform: ARA transform and its properties and applications, Symmetry, 12(6), 925, 2020.

[7] Hari Mohan Srivastava, H. Manocha, Treatise on generating functions, John Wiley Sons, Inc., 605 Third Ave., New York, NY 10158, USA, 500, 1984.

[8] Hari Mohan Srivastava, Per W. Karlsson, Multiple Gaussian hypergeometric series, E. Horwood, 1985.

[9] Lokenath Debnath, Integral Transforms and Their Applications, CRC Press, Florida, 1995.
[10] Alexander D. Poularikas, The Transforms and Applications Handbook, The Electrical Engineering Handbook Series, CRC Press, Florida, 1996.
[11] Mohd Saif, Faisal Khan, Kottakkaran Sooppy Nisar, Serkan Araci, Modified Laplace transform and its properties, Journal of Mathematics and Computer Science, 21, 127135, 2020.
[12] G. K. Watugala, Sumudu transform: A new integral transform to solve differential equations and control engineering problems, International Journal of Mathematical Education in Science and Technology 24, 3543, 1993.
[13] G. K. Watugala, The Sumudu transform for functions of two variables, Mathematical Engineering in Industry, 8, 293302, 2002.
[14] Lalit Mohan Upadhyaya, On the degenerate Laplace transform-I, Bulletin of Pure and Applied Sciences-Mathematics and Statistics, 37(1), 1-8, 2018.
[15] Lalit Mohan Upadhyaya, On the degenerate laplace transform III, International Journal of Engineering, Science and Mathematics, 7(1), 400-410, 2018.
[16] A. Kalavathi, T. Kohila, Lalit Mohan Upadhyaya, On the degenerate Elzaki transform, Bull. Pure Appl. Sci. Sect. E Math. Stat. E, 40, 99-107, 2021.
[17] Feng Qi, Bai-Ni Guo, Relations among Bell polynomials, central factorial numbers, and central Bell polynomials, Math. Sci. Appl. E-Notes 7 (2019), no. 2, 191–194; available online at https://doi.org/10.36753/mathenot.566448.
[18] Feng Qi, Da-Wei Niu, Dongkyu Lim, and Bai-Ni Guo, Closed formulas and identities for the Bell polynomials and falling factorials, Contrib. Discrete Math. 14 (2019), no. 2, in press; available online at https://doi.org/10.13140/RG.2.2.34679.52640.
[19] Feng Qi, Da-Wei Niu, Dongkyu Lim, and Yong-Hong Yao, Special values of the Bell polynomials of the second kind for some sequences and functions, HAL preprint (2018), available online at https://hal.archives-ouvertes.fr/hal-01766566.
[20] Feng Qi, Xiao-Ting Shi, and Fang Fang Liu, Several identities involving the falling and rising factorials and the Cauchy, Lah, and Stirling numbers, Acta Univ. Sapientiae Math. 8 (2016), no. 2, 282–297; available online at https://doi.org/10.1515/ausm-2016-0019.
[21] Feng Qi, Guo-Sheng Wu, and Bai-Ni Guo, An alternative proof of a closed formula for central factorial numbers of the second kind, Turkish J. Anal. Number Theory 7 (2019), no. 2, 56–58; available online at https://doi.org/10.12691/tjant-7-2-5.
[22] Sudhanshu Aggarwal, Anjana Rani Gupta, Swarg Deep Sharma, Raman Chauhan, and Nidhi Sharma, Mahgoub transform (Laplace-Carson transform) of error function, International Journal of Latest Technology in Engineering, Management and Applied Science, 8(4), 92-98, 2019.
[23] Sudhanshu Aggarwal, and G. P. Singh, Aboodh transform of error function, Universal Review, 10(6), 137-150, 2019.
[24] Sudhanshu Aggarwal, Anjana Rani Gupta, and Deepak Kumar, Mohand transform of error function, International Journal of Research in Advent Technology, 7(5), 224-231, 2019.

Department of Mathematics, University of Kirikkale, Kirikkale, Turkey
Rabia Kevser Yılmaz (rabia.kyilmaz05@gmail.com)
Oğuz Yağcı (oguzyagci26@gmail.com)
Recep Şahin (recepsahintr@gmail.com)

SOME RESULTS ON THE (p,q)- CALCULUS AND PARTIAL (p,q)-DIFFERENTIAL EQUATIONS

İnci Çakmak[1] **and Aynur Şahin**[2]

[1,2] Department of Mathematics, Sakarya University, 54050, Sakarya, Türkiye

incicakmak13113@gmail.com, ayuce@sakarya.edu.tr

Abstract

Recently, Jafari et al. (Rom. Journ. Phys. 59, 399-407, 2014) presented the reduced q-differential transform method for solving partial q-differential equations. In this paper, we define the concept of partial (p,q)-derivative for a multivariable function and generalize the method of Jafari et al. to partial (p,q)-differential equations. Also, we give some examples to discover the effectiveness and performance of the proposed method.

Mathematics Subject Classification: 05A30; 35A25; 35N20.

Keywords: q -calculus; (p,q)-calculus; Partial differential equation; Initial value problem.

1. INTRODUCTION AND PRELIMINARIES

The q-calculus (or recalled the quantum calculus) appeared as a connection between mathematics and physics (see [1-7]). It has many applications in different mathematical areas, such as number theory, combinatorics, orthogonal polynomials, and other sciences: quantum theory, mechanics, and theory of relativity. Further, there is the possibility of extension of the q -calculus to post-quantum calculus denoted by the (p,q) -calculus. When the case $p=1$, the (p,q)-calculus reduces to the q-calculus (see [8-10]).

The (p,q)-number is defined as

$$[n]_{p,q}=\frac{p^n-q^n}{p-q},\quad p\neq q.$$

The (p,q)- binomial coefficients given by

$$\begin{bmatrix} n \\ k \end{bmatrix}_{p,q}=\frac{[n]_{p,q}!}{[n-k]_{p,q}!\,[k]_{p,q}!},\quad n\geq k$$

and the (p,q)-factorial given by

$$[n]_{p,q}!=[n]_{p,q}[n-1]_{p,q}\dots[2]_{pq}[1]_{p,q},\quad n\in\mathbb{N}$$

are also known from [10] and [11].

Let $f:\mathbb{R}\to\mathbb{R}$ then the (p,q)-derivative of a function f, denoted by $D_{p,q}f$, is defined as

$$D_{p,q}f(x)=\frac{f(px)-f(qx)}{(p-q)x},\qquad x\neq 0,\qquad p\neq q$$

and

$$(D_{p,q}f)(0)=f'(0),$$

provided that f is differentiable at 0.

Note that for $p=1$, the (p,q)-derivative reduces to the q-derivative given by

$$D_q f(x)=\frac{f(x)-f(qx)}{(1-q)x},\quad x\neq 0,\ q\neq 1;$$

also for $q\to 1=p$, the (p,q)-derivative reduces to the ordinary derivative named as $Df(x)$ if $f(x)$ is differentiable.

As with the q-derivative and the ordinary derivative, the action of applying the (p,q)-derivative of any function is a linear operator, see [10].

Example 1: (see [9,10]) The following equation holds

$$D_{p,q}(x^n)=\frac{(px)^n-(qx)^n}{px-qx}=[n]_{p,q}x^{n-1},\ \ n\in\mathbb{Z}^+.$$

By induction on n, it follows from the (p,q)-analog of the Leibniz rule [8,9]

$$D_{p,q}^n(fg)(x)=\sum_{k=0}^{n}\begin{bmatrix}n\\k\end{bmatrix}_{p,q}D_{p,q}^k(f)(xp^{n-k})D_{p,q}^{n-k}(g)(xq^k),$$

where $D_{p,q}^n=\frac{d_{p,q}^n}{d_{p,q}x^n}$.

Now the (p,q)-Taylor formula for polynomials is given as follows.

Theorem 1: (see [10]) For any polynomial $f(x)$ of degree N, and any number a , the following (p,q)-Taylor expansion holds

$$f(x)=\sum_{k=0}^{N}p^{-\binom{k}{2}}\frac{(D_{p,q}^k f)(ap^{-k})}{[k]_{p,q}!}(x\ominus a)_{p,q}^k$$

where $(x\ominus a)_{p,q}^k=(x-a)(px-aq)\ldots(p^{k-2}x-aq^{k-2})(p^{k-1}x-aq^{k-1})$.

Note that in the above equality, N can be taken to be ∞ with the condition that the infinite series obtained is convergent. Then, the formula becomes

$$f(x)=\sum_{k=0}^{\infty}p^{-\binom{k}{2}}\frac{(D_{p,q}^k f)(ap^{-k})}{[k]_{p,q}!}(x\ominus a)_{p,q}^k.$$

In the following parts of the paper, we calculus the (p,q)-derivatives of some functions and present the (p,q)-differential transform method for solving some partial (p,q)-differential equations. Our results provide a generalization of the results of Jafari et al. [12].

2. (p,q)-DERIVATIVES OF SOME STANDARD FUNCTIONS

Following the procedure for computing the (p,q)-derivative, we now obtain some results for the (p,q)-derivative of standard functions, such as $\sin x$, e^x and $\ln x$.

Let us recall that $\sin x = \sum_{n=0}^{\infty}(-1)^n \frac{x^{2n+1}}{(2n+1)!}$, $e^x = \sum_{n=0}^{\infty}\frac{x^n}{n!}$ and $\ln x = \sum_{n=1}^{\infty}(-1)^{n-1}\frac{(x-1)^n}{n}$.

2.1. (p,q)-Derivative of the Function $f(x) = \sin x$

By the definition of (p,q)-derivative, we have

$$D_{p,q}\sin x = \frac{\sin(px) - \sin(qx)}{(p-q)x}$$

$$= \frac{\left(px - \frac{(px)^3}{3!} + \frac{(px)^5}{5!} - \frac{(px)^7}{7!} + \cdots\right) - \left(qx - \frac{(qx)^3}{3!} + \frac{(qx)^5}{5!} - \frac{(qx)^7}{7!} + \cdots\right)}{(p-q)x}$$

$$= 1 - \frac{1}{3!}x^2\frac{p^3-q^3}{p-q} + \frac{1}{5!}x^4\frac{p^5-q^5}{p-q} - \frac{1}{7!}x^6\frac{p^7-q^7}{p-q} + \cdots$$

Using the fact that

$$\frac{p^r-q^r}{p-q} = p^{r-1} + p^{r-2}q + \cdots + pq^{r-2} + q^{r-1},$$

we obtain

$$D_{p,q}\sin x = 1 - \frac{1}{3!}x^2(p^2+pq+q^2) + \frac{1}{5!}x^4(p^4+p^3q+p^2q^2+pq^3+q^4)$$
$$- \frac{1}{7!}x^6(p^6+p^5q+p^4q^2+p^3q^3+p^2q^4+pq^5+q^6) + \cdots$$

If we take $p=1$ and the limit as $q \to 1 = p$ in this equation, then we get the q-derivative and the ordinary derivative of the function $\sin x$

$$D_q\sin x = 1 - \frac{1}{3!}x^2(1+q+q^2) + \frac{1}{5!}x^4(1+q+q^2+q^3+q^4)$$
$$- \frac{1}{7!}x^6(1+q+q^2+q^3+q^4+q^5+q^6) + \cdots$$

and

$$D\sin x = 1 - \frac{1}{3!}x^2(3) + \frac{1}{5!}x^4(5) - \frac{1}{7!}x^6(7) + \cdots$$

$$= 1 - \frac{1}{2!}x^2 + \frac{1}{4!}x^4 - \frac{1}{6!}x^6 + \cdots = \cos x,$$

respectively.

2.2. (p,q)-Derivative of the Function $f(x)=e^x$

We have by the definition of (p,q)-derivative

$$D_{p,q}e^x=\frac{e^{px}-e^{qx}}{(p-q)x}=\frac{e^x(e^{-x(1-p)}-e^{-x(1-q)})}{(p-q)x}.$$

Since

$$e^{-x(1-p)}=\sum_{n=0}^{\infty}\frac{\left(-x(1-p)\right)^n}{n!}=\sum_{n=0}^{\infty}\frac{(-1)^n(1-p)^n x^n}{n!}$$

$$=1-(1-p)x+(1-p)^2\frac{x^2}{2!}-(1-p)^3\frac{x^3}{3!}+\cdots+(-1)^k(1-p)^k\frac{x^k}{k!}+\cdots$$

and

$$e^{-x(1-q)}=\sum_{n=0}^{\infty}\frac{\left(-x(1-q)\right)^n}{n!}=\sum_{n=0}^{\infty}\frac{(-1)^n(1-q)^n x^n}{n!}$$

$$=1-(1-q)x+(1-q)^2\frac{x^2}{2!}-(1-q)^3\frac{x^3}{3!}+\cdots+(-1)^k(1-q)^k\frac{x^k}{k!}+\cdots,$$

then we have

$$D_{p,q}e^x=\frac{e^x}{(p-q)x}\Big[(p-q)x-[(1-q)^2-(1-p)^2]\frac{x^2}{2!}+[(1-q)^3-(1-p)^3]\frac{x^3}{3!}+\cdots+(-1)^k[(1-q)^k-(1-p)^k]\frac{x^k}{k!}+\cdots\Big].$$

Using the fact that

$$\frac{(1-q)^r-(1-p)^r}{p-q}=(1-q)^{r-1}+(1-q)^{r-2}(1-p)+\cdots+(1-q)(1-p)^{r-2}+(1-p)^{r-1},$$

we obtain

$$\begin{aligned}D_{p,q}e^x=e^x\Bigg[&1-[(1-q)+(1-p)]\frac{x}{2!}+[(1-q)^2+(1-q)(1-p)+(1-p)^2]\frac{1}{3!}x^2\\&+\cdots+(-1)^k[(1-q)^{k-1}+(1-q)^{k-2}(1-p)+\cdots+(1-q)(1-p)^{k-2}\\&+(1-p)^{k-1}]\frac{x^{k-1}}{k!}+\cdots\Bigg].\end{aligned}$$

If we take $p=1$ and the limit as $q\to 1=p$ in this equation, then we get the q-derivative and the ordinary derivative of the function e^x

$$D_q e^x=e^x\left[1-(1-q)\frac{x}{2!}+(1-q)^2\frac{1}{3!}x^2+\cdots+(-1)^k(1-q)^{k-1}\frac{x^{k-1}}{k!}+\cdots\right]$$

and

$De^x = e^x$,

respectively.

2.3. (p, q)-Derivative of the Function $f(x) = \ln x$

By the definition of (p, q)-derivative, we have

$$D_{p,q}\ \ln x = \frac{\ln px - \ln qx}{(p-q)x}$$

$$= \frac{(px-1) - \frac{(px-1)^2}{2} + \frac{(px-1)^3}{3} + \cdots + (-1)^{k-1}\frac{(px-1)^k}{k} + \cdots}{(p-q)x}$$

$$- \frac{(qx-1) - \frac{(qx-1)^2}{2} + \frac{(qx-1)^3}{3} + \cdots + (-1)^{k-1}\frac{(qx-1)^k}{k} + \cdots}{(p-q)x}$$

$$= 1 - \tfrac{1}{2}[(px-1) + (qx-1)] + \tfrac{1}{3}[(px-1)^2 + (px-1)(qx-1) + (qx-1)^2] + \cdots$$

$$+ \frac{(-1)^{k-1}}{k}[(px-1)^{k-1} + (px-1)^{k-2}(qx-1) + \cdots + (qx-1)^{k-1}] + \cdots$$

If we take $p = 1$ and the limit as $q \to 1 = p$ in this equation, then we get the q-derivative and the ordinary derivative of the function $\ln x$

$$D_q\ \ln x = 1 - \frac{1}{2}[(x-1) + (qx-1)] + \frac{1}{3}[(x-1)^2 + (x-1)(qx-1) + (qx-1)^2] + \cdots$$

$$+ \frac{(-1)^{k-1}}{k}[(x-1)^{k-1} + (x-1)^{k-2}(qx-1) + \cdots + (qx-1)^{k-1}] + \cdots$$

and

$$D\ln x = 1 - \frac{1}{2}.2.(x-1) + \frac{1}{3}.3.(x-1)^2 + \cdots + \frac{(-1)^{k-1}}{k}.k.(x-1)^{k-1} + \cdots$$

$$= \textstyle\sum_{n=1}^{\infty}(-1)^{n-1}(x-1)^{n-1} = \sum_{n=0}^{\infty}(-1)^n (x-1)^n = \frac{1}{x},$$

respectively.

We remark that the (p, q)-derivatives of other standard functions can be obtained similarly.

3. PARTIAL (p, q)-DERIVATIVE OF A MULTIVARIABLE FUNCTION

Firstly, we define the partial (p, q)-derivative of a multivariable real continuous function $f(x_1, x_2, \ldots, x_n)$ for a variable x_i

$$D_{p,q,x_i}f(x) = \frac{(\varepsilon_{p,x_i} f)(x) - (\varepsilon_{q,x_i} f)(x)}{(p-q)x_i}, \qquad x_i \neq 0, \qquad p \neq q$$

$$\left[D_{p,q,x_i} f(x)\right]_{x_i=0} = \lim_{x_i \to 0} D_{p,q,x_i} f(x)$$

where $\left(\varepsilon_{p,x_i} f\right)(x) = f(x_1, x_2, \dots, px_i, \dots, x_n)$ and $\left(\varepsilon_{q,x_i} f\right)(x) = f(x_1, x_2, \dots, qx_i, \dots x_n)$.

After the definition of partial (p,q)-derivative, we can give the following theorem for the functions of two variables (compare with [6,12]).

Theorem 2: Suppose that the function $f(x,t)$ has continuous partial (p,q)-derivatives of all orders. Then

$$f(x,t) = \sum_{k=0}^{\infty} \frac{p^{-\binom{k}{2}}}{[k]_{p,q}\,!} \left(\frac{\partial_{p,q}^{k}}{\partial_{p,q} t^{k}} f(x,t) \right)_{t=ap^{-k}} (t \ominus a)_{p,q}^{k}.$$

In this theorem, we set $a = 0$, then

$$(t \ominus 0)_{p,q}^{k} = (t - 0)(pt - 0q) \dots (p^{k-2}t - 0q^{k-2})(p^{k-1}t - 0q^{k-1})$$

$$= t.pt \dots p^{k-2}t.p^{k-1}t = t^k p^{1+2+\dots+k-1} = t^k p^{\binom{k}{2}}.$$

Hence, we obtain

$$f(x,t) = \sum_{k=0}^{\infty} \frac{1}{[k]_{p,q}\,!} \left(\frac{\partial_{p,q}^{k}}{\partial_{p,q} t^{k}} f(x,t) \right)_{t=0} t^k.$$

Definition 1: Suppose that the function $u(x,t)$ has continuous partial (p,q)-derivatives of all orders. t-dimensional (p,q)-differential transform of function $u(x,t)$ is defined as follows:

$$U_k(x) = \frac{p^{-\binom{k}{2}}}{[k]_{p,q}\,!} \left(\frac{\partial_{p,q}^{k}}{\partial_{p,q} t^{k}} u(x,t) \right)_{t=ap^{-k}}. \tag{1}$$

In the equation (1), $u(x,t)$ is the original function and $U_k(x)$ is the transformed function.

Definition 2: The t-dimensional (p,q)-differential inverse transform of $U_k(x)$ is defined as follows:

$$u(x,t) = \sum_{k=0}^{\infty} U_k(x)(t \ominus a)_{p,q}^{k}. \tag{2}$$

In fact, from the equations (1) and (2), we obtain

$$u(x,t) = \sum_{k=0}^{\infty} \frac{p^{-\binom{k}{2}}}{[k]_{p,q}\,!} \left(\frac{\partial_{p,q}^{k}}{\partial_{p,q} t^{k}} u(x,t) \right)_{t=ap^{-k}} (t \ominus a)_{p,q}^{k}$$

which implies that the concept of t-dimensional (p,q)-differential transform is derived from (p,q)- Taylor formula given in Theorem 2.

In the following theorems, we set $a = 0$ then we have

$$u(x,t) = \sum_{k=0}^{\infty} \frac{1}{[k]_{p,q}\,!} \left(\frac{\partial_{p,q}^{k}}{\partial_{p,q} t^{k}} u(x,t) \right)_{t=0} t^k$$

and so

$$U_k(x) = \frac{1}{[k]_{p,q}\,!}\left(\frac{\partial^k_{p,q}}{\partial_{p,q}t^k}u(x,t)\right)_{t=0}. \qquad (3)$$

Theorem 3: If $W_k(x), U_k(x)$ and $V_k(x)$ are the t-dimensional (p,q)-differential transforms of functions $w(x,y), u(x,t)$ and $v(x,t)$ at point $t=0$ respectively, the following results hold.

(i) If $w(x,t) = \alpha u(x,t) \mp v(x,t)$ then $W_k(x) = \alpha U_k(x) \mp V_k(x)$ where α is a real constant.

(ii) If $w(x,y) = x^m t^n$ then $W_k(x) = x^m \delta(k-n)$ where

$$\delta(k-n) = \begin{cases} 1 & k = n \\ 0 & k \neq n. \end{cases}$$

Proof: By the linearity of the (p,q)-derivative, we can easily obtain the result *(i)*.

(ii) By Definition 2 and the equation (3), we have

$$W_k(x) = \frac{1}{[k]_{p,q}\,!}\left(\frac{\partial^k_{p,q}}{\partial_{p,q}t^k}w(x,t)\right)_{t=0}$$

$$= \frac{1}{[k]_{p,q}\,!}\left(\frac{\partial^k_{p,q}(x^m t^n)}{\partial_{p,q}t^k}\right)_{t=0}$$

$$= \frac{x^m}{[k]_{p,q}\,!}\left(\frac{\partial^k_{p,q}(t^n)}{\partial_{p,q}t^k}\right)_{t=0}$$

$$= \begin{cases} \dfrac{x^m}{[k]_{p,q}\,!}.[k]_{p,q}\,! = x^m, & k = n \\ \dfrac{x^m}{[k]_{p,q}\,!}.\ [n]_{p,q}\,[n-1]_{p,q} \ldots [n-k-1]_{p,q}t^{n-k}\big|_{t=0} = 0, & k < n \\ \dfrac{x^m}{[k]_{p,q}\,!}.0 = 0, & k > n \end{cases}$$

$$= x^m \delta(k-n).$$

Theorem 4: If $w(x,t) = \frac{\partial_{p,q}}{\partial_{p,q}x}u(x,t)$, then $W_k(x) = \frac{\partial_{p,q}}{\partial_{p,q}x}U_k(x)$.

Proof: $W_k(x) = \frac{1}{[k]_{p,q}\,!}\left[\frac{\partial^k_{p,q}}{\partial_{p,q}t^k}\left(\frac{\partial_{p,q}}{\partial_{p,q}x}u(x,t)\right)\right]_{t=0}$

$$= \frac{1}{[k]_{p,q}\,!}\left[\frac{\partial_{p,q}}{\partial_{p,q}x}\left(\frac{\partial^k_{p,q}}{\partial_{p,q}t^k}u(x,t)\right)\right]_{t=0}$$

$$= \frac{\partial_{p,q}}{\partial_{p,q}x}\left[\frac{1}{[k]_{p,q}\,!}.\frac{\partial^k_{p,q}}{\partial_{p,q}t^k}u(x,t)\right]_{t=0}$$

$= \frac{\partial_{p,q}}{\partial_{p,q}x} U_k(x).$

Theorem 5: If $w(x,t) = \frac{\partial_{p,q}^r}{\partial_{p,q}t^r} u(x,t)$, then

$$W_k(x) = [k+1]_{p,q}\, [k+2]_{p,q} \dots [k+r]_{p,q} U_{k+r}(x).$$

Proof: $W_k(x) = \frac{1}{[k]_{p,q}\,!} \cdot \left[\frac{\partial_{p,q}^k}{\partial_{p,q}t^k}\left(\frac{\partial_{p,q}^r}{\partial_{p,q}t^r} u(x,t)\right)\right]_{t=0}$

$$= \frac{1}{[k]_{p,q}\,!} \cdot \frac{[k+r]_{p,q}!}{[k+r]_{p,q}!} \cdot \left[\frac{\partial_{p,q}^{k+r}}{\partial_{p,q}t^{k+r}} u(x,t)\right]_{t=0}$$

$$= \frac{[k+r]_{p,q}!}{[k]_{p,q}\,!} \cdot \frac{1}{[k+r]_{p,q}!} \left[\frac{\partial_{p,q}^{k+r}}{\partial_{p,q}t^{k+r}} u(x,t)\right]_{t=0}$$

$= \ [k+1]_{p,q}\, [k+2]_{p,q} \dots [k+r]_{p,q} U_{k+r}(x).$

Example 2: Suppose we want to solve the (p,q)-diffusion equation

$$\frac{\partial_{p,q}}{\partial_{p,q}t} u(x,t) = \frac{\partial_{p,q}^2}{\partial_{p,q}x^2} u(x,t)$$

subject to the initial condition

$$u(x,0) = e_{p,q}^x$$

where $e_{p,q}^x$ is the (p,q)-exponential function given as [9]

$$e_{p,q}^x = \sum_{k=0}^{\infty} p^{\binom{k}{2}} \frac{x^k}{[k]_{p,q}\,!}$$

and have the (p,q)-derivative

$$\frac{\partial_{p,q}}{\partial_{p,q}x} e_{p,q}^x = e_{p,q}^{px}.$$

By using the t-dimensional (p,q)-differential transform of (p,q)-diffusion equation, we write the following recursion

$$[k+1]_{p,q}\, U_{k+1}(x) = \frac{\partial_{p,q}^2}{\partial_{p,q}x^2} U_k(x), \ \ k = 0,1,2,\dots \tag{4}$$

Then the initial data is written as

$$U_0(x) = u(x,0) = e_{p,q}^x. \tag{5}$$

Now, substituting (5) into (4), we obtain the following $U_k(x)$ values successively

$$U_1(x) = \frac{p}{[1]_{p,q}!} e_{p,q}^{p^2x}$$

$$U_2(x) = \frac{p^6}{[2]_{p,q}!} e_{p,q}^{p^4 x}$$

$$U_3(x) = \frac{p^{15}}{[3]_{p,q}!} e_{p,q}^{p^6 x}$$

$$\vdots$$

$$U_k(x) = \frac{p^{k(2k-1)}}{[k]_{p,q}!} e_{p,q}^{p^{2k} x}.$$

Hence we get the solution of (p,q)-diffusion equation as follows

$$u(x,t) = \sum_{k=0}^{\infty} U_k(x) t^k = \sum_{k=0}^{\infty} \frac{p^{k(2k-1)}}{[k]_{p,q}!} e_{p,q}^{p^{2k} x} t^k.$$

For $p = 1$, this result is also the same in Example 4.1 of [12].

Example 3: Consider the following partial (p,q)- differential equation

$$\frac{\partial_{p,q}}{\partial_{p,q} t} u(x,t) = \frac{\partial^2}{\partial x^2} u(x,t) + \frac{\partial}{\partial x}(xu(x,t)) \tag{6}$$

with the initial condition

$u(x,0) = 2x^2.$

By using the t-dimensional (p,q)-differential transform of equation (6), we have

$$[k+1]_{p,q} U_{k+1}(x) = \frac{\partial^2}{\partial x^2} U_k(x) + \frac{\partial}{\partial x}(xU_k(x)) \tag{7}$$

where

$$U_0(x) = 2x^2. \tag{8}$$

Solving (7) with the initial condition (8), we successively achieve the values $U_k(x)$ as follows:

$$U_1(x) = \frac{4 + 6x^2}{[1]_{p,q}} = \frac{2.(3^1 - 1) + 2.3^1\, x^2}{[1]_{p,q}!}$$

$$U_2(x) = \frac{16 + 18x^2}{[1]_{p,q}[2]_{p,q}} = \frac{2.(3^2 - 1) + 2.3^2\, x^2}{[2]_{p,q}!}$$

$$U_3(x) = \frac{52 + 54x^2}{[1]_{p,q}[2]_{p,q}[3]_{p,q}} = \frac{2.(3^3 - 1) + 2.3^3\, x^2}{[3]_{p,q}!}$$

$$\vdots$$

$$U_k(x) = \frac{2.(3^k - 1) + 2.3^k\, x^2}{[k]_{p,q}!}$$

Substituting all $U_k(x)$ into (2), we have the required solution of the partial (p,q)-differential equation to be

$$u(x,t) = 2x^2 + (4+6x^2)\frac{t}{[1]_{p,q}!} + (16+18x^2)\frac{t^2}{[2]_{p,q}!} + \cdots$$
$$+ (2.(3^k - 1) + 2.3^k\, x^2)\frac{t^k}{[k]_{p,q}!} + \cdots$$

$$= \sum_{n=0}^{\infty} (2.(3^n - 1) + 2.3^n\, x^2)\frac{t^n}{[n]_{p,q}!}.$$

To prove the next theorem, we will use the following lemmas.

Lemma 1.

$$D_{p,q}^n(fg)(x,t) = \sum_{k=0}^{n} \begin{bmatrix} n \\ k \end{bmatrix}_{p,q} D_{p,q,t}^k(f)(x,tp^{n-k}) D_{p,q,t}^{n-k}(g)(x,tq^k).$$

Proof. The lemma can easily be proved by applying the principle of mathematical induction as in [9, Lemma 3.2.1].

Lemma 2.

$$f(x,p^n t) = \sum_{k=0}^{n} \begin{bmatrix} n \\ k \end{bmatrix}_{p,q} t^k p^{\binom{k}{2}} (p-q)^k D_{p,q,t}^k f(x,t).$$

Proof. The lemma can easily be proved by using divided differences as in [8, Theorem 4].

Theorem 6: If $w(x,t) = u(x,t)v(x,t)$, then

$$W_k(x) = \sum_{n=0}^{k} U_n(x) V_{k-n}(x).$$

Proof: $W_k(x) = \frac{1}{[k]_{p,q}!}\left[D_{p,q,t}^k(u(x,t)v(x,t))\right]_{t=0}$

$$= \frac{1}{[k]_{p,q}!}\left[\sum_{n=0}^{k} \begin{bmatrix} k \\ n \end{bmatrix}_{p,q} D_{p,q,t}^n u(x,tp^{k-n})\; D_{p,q,t}^{k-n} v(x,tq^n)\right]_{t=0}$$

$$= \sum_{n=0}^{k} \frac{1}{[k-n]_{p,q}!\,[n]_{p,q}!} \left[\begin{array}{l} \sum_{r=0}^{k-n} \begin{bmatrix} k-n \\ r \end{bmatrix}_{p,q} t^r p^{\binom{r}{2}} (p-q)^r D_{p,q,t}^{n+r} u(x,t) \\ * \sum_{s=0}^{n} \begin{bmatrix} n \\ s \end{bmatrix}_{p,q} t^s q^{\binom{s}{2}} (p-q)^s D_{p,q,t}^{k-n+s} v(x,t) \end{array}\right]_{t=0}$$

$$= \sum_{n=0}^{k} \frac{1}{[k-n]_{p,q}!\,[n]_{p,q}!} D_{p,q,t}^n u(x,t) D_{p,q,t}^{k-n} v(x,t)$$

$$= \sum_{n=0}^{k} \frac{1}{[n]_{p,q}!} D_{p,q,t}^{n} u(x,t) \frac{1}{[k-n]_{p,q}!} D_{p,q,t}^{k-n} v(x,t)$$

$$= \sum_{n=0}^{k} U_n(x) V_{k-n}(x).$$

Example 4: Consider the following nonlinear partial (p,q)- differential equation

$$\frac{\partial_{p,q}}{\partial_{p,q} t} u(x,t) = u^2(x,t) + \frac{\partial_{p,q}}{\partial_{p,q} x} u(x,t) \tag{9}$$

with the initial condition

$u(x,0) = 1 + 4x.$

By taking the t-dimensional (p,q)-differential transform of equation (9) and using Theorems 5 and 6, we have

$$[k+1]_{p,q} U_{k+1}(x) = \sum_{n=0}^{k} U_n(x) U_{k-n}(x) + \frac{\partial_{p,q}}{\partial_{p,q} x} U_k(x), \qquad k = 0,1,2,\ldots$$

From the initial equation, we obtain

$U_0(x) = u(x,0) = 1 + 4x.$

Starting with $k = 0$, the values of $U_k(x)$ are successively computed as follows.

$$[1]_{p,q} U_1(x) = U_0(x) U_0(x) + \frac{\partial_{p,q}}{\partial_{p,q} x} U_0(x) = (1+4x)^2 + 4$$

$$\Longrightarrow U_1(x) = 16x^2 + 8x + 5,$$

$$[2]_{p,q} U_2(x) = 2U_0(x) U_1(x) + \frac{\partial_{p,q}}{\partial_{p,q} x} U_1(x)$$
$$= 2(1+4x)(16x^2 + 8x + 5) + (16(p+q)x + 8)$$

$$\Longrightarrow U_2(x) = \frac{128x^3 + 96x^2 + [56 + 16(p+q)]x + 18}{p+q},$$

$\vdots$

Substituting all $U_k(x)$ in (2), we obtain the series solution as

$$u(x,t) = 1 + 4x + (16x^2 + 8x + 5)t + \frac{128x^3 + 96x^2 + [56 + 16(p+q)]x + 18}{p+q} t^2 + \cdots.$$

REFERENCES

1. Jackson, F. H., On q-functions and a certain difference operator, Trans. R. Soc. Edinb. **46**, 253-281, 1909.
2. Jackson, F. H., A q-form of Taylor's theorem. Messenger Math., **38**, 62-64, 1909.

3. Jackson, F. H., On q-definite integrals, Quarterly J. Pure Appl. Math., **41**, 193-203, 1910.
4. Ernst, T., The history of q-calculus and a new method, Licentiate Thesis, Report 2000:16, Department of Mathematics, Uppsala University, Uppsala, Accessed 2 March 2001.
5. Kac, V., Cheung, P., Quantum Calculus, New York, Springer, 2002.
6. El-Shahed, M., Gaber, M., Two-dimensional q-differential transformation and its application, App. Math. Comput., **217**, 9165-9172, 2011.
7. Akça, H., Benbourenane J., Eleuch, H., The q-derivative and differential equation, Journal of Physics: Conference Series, 1411:012002, 2019.
8. Aracı, S., Duran, U., Açıkgöz, M., Srivastava, H. M., A certain (p,q)-derivative operator and associated divided differences, J. Ineq. Appl., 2016:301, 2016.
9. Duran, U., Post quantum calculus, Master Thesis, Department of Mathematics, Gaziantep University, Gaziantep, Türkiye, 2016.
10. Sadjang, P. N., On the fundamental theorem of (p,q)-calculus and some (p,q)-Taylor formulas, Results Math., **73**:39, 2018.
11. Corcino, R. B., On P,Q-binomial coefficients, Electron. J. Comb. Number Theory, **8**, Article ID A29, 2008.
12. Jafari, H., Haghbin, A., Hesam, S., Baleanu, D., Solving partial q-differential equations within reduced q-differential transform method, Rom. Journ. Phys., **59**(5-6), 399-407, 2014.

AN APPLICABLE CONDITION FOR ASSESSING THE STABITLTY OF LINEAR FRACTIONAL DIFFERENTIAL SYSTEMS

[1]IQBAL H. JEBRIL, [2,3]IQBAL M. BATIHA, [4]ABEER A. Al-NANA, [5]ADEL OUANNAS, [2,6]SHAHER MOMANI

[1]Department of Mathematics, Faculty of Science and Technology, Al-Zaytoonah University of Jordan, Amman Jordan.

[2]Department of Mathematics, Faculty of Science and Technology, Irbid National University, 2600 Irbid, Jordan.

[3]Nonlinear Dynamics Research Center (NDRC), Ajman University, Ajman 346, United Arab Emirates.

[4]International Center for Scientific Research and Studies (ICSRS), Irbid, Jordan.

[5]Department of Mathematics, Faculty of Science, Larbi Ben M'hidi University, Ouam El Bouaghi, Algeria.

[6]Department of Mathematics, Faculty of Science, The University of Jordan, Amman 11942, Jordan.

[1]i.jebril@zuj.edu.jo, [2,3]ibatiha@inu.edu.jo, [4]mathabeer@yahoo.com, [5]dr.ouannas@gmail.com, [6]s.momani@ju.edu.jo

Abstract

This paper aims to discuss the stability of linear fractional-order differential systems formulated in the sense of Caputo fractional-order derivative operator. In particular, a new applicable condition for assessing the stability of those systems is established through introducing a new theoretical result with the help of Fubini's Theorem.

Keywords: Stability, Linear fractional-order differential system, Caputo fractional-order derivative operator.

1. INTRODUCTION

More than three centuries ago, interest in classical fractional calculus began. In the past few decades, it has been observed that many scientists have developed many fractional-order differential systems due to their importance and the well-known potential in solving many intractable problems, as well as designing models based on their constructions, such as viscoelastic systems, signal processing, diffusion processes, control processing, etc.

On the other hand, the stability of the fractional-order differential systems has attracted increasing attention due to their significance in control theory. It was appeared for the first time in mechanics during the investigation of an equilibrium state of a system by Matignon [1] who studied the stability of linear fractional-order differential systems in 1996. Next, many researchers have studied further on the stability of linear fractional-order differential systems. In [2], Yan Li et al. presented the Mittag-Leffler stability of fractional-order nonlinear dynamic systems and proposed Lyapunov direct method to check the stability of the fractional-order nonlinear dynamic systems. Moreover, the stability analysis of Hilfer fractional-order differential systems is displayed in [3]. In addition, a description of the asymptotical stability of the nonlinear fractional differential system with Caputo derivative has been considered in [4]. Wen et al. [5] and Zhou et al. [6] considered the stability of nonlinear fractional differential systems. In [7], Zhang et al. proposed a single state adaptive-feedback controller for stabilization three-dimensional fractional-order chaotic systems. Faieghi et al. [8] proposed a simple controller for stabilization a class of fractional-order chaotic systems based on the theory of Linear Matrix Inequality (LMI). For further details, the reader may back to the references [9, 10, 11, 12, 13,14]

In this work, we concern with the stability of the linear system of fractional-order differential equations that has the following form:

$$D^{\alpha}x(t) = f\big(t, x(t)\big) \qquad (1)$$

where $x(t) = [x_1(t)\, x_2(t) \dots x_m(t)\,]^T$ is its solution, $0 < \alpha < 1$ and $f = [f_1\ f_2 \dots f_m(t)\,]^T \in C[\mathbb{R}^+ \times \mathbb{R}^n, \mathbb{R}^{n+}]$ which is the set of all continuous positive functions defined on a given finite interval. In addition, a new theoretical result establishing a sufficient condition for judging the stability of the solution of the above system is stated and proved for sufficient cause.

2. PRELIMINARIES

In this part, certain necessary definitions and basic facts related to fractional calculus, fractional-order differential systems and the stability of their solutions are presented for completeness.

Definition 2.1 [6, 7]: Let $f(t)$ be an integrable piecewise continuous function on any finite subinterval of $(0\,, +\infty)$, then the fractional integral of $f(t)$ of order α is defined as:

$$J^{\alpha}f(t):=\frac{t^{\alpha-1}}{\Gamma(\alpha)}\star f(t)=\frac{1}{\Gamma(\alpha)}\int_0^t (t-\tau)^{\alpha-1}f(\tau)d\tau, \quad (2)$$

where $t>0, \alpha>0$ and $\star$ denotes the convolution product in which

$$(f\star g)(t)=\int_0^t f(t-\tau)\,g(\tau)d\tau, \qquad (3)$$

and $f\star g$ denotes the convolution operator. For instance, we have:

$$J^{\alpha}t^{\mu}=\frac{\Gamma(\mu+1)}{\Gamma(\mu+\alpha+1)}t^{\mu+\alpha}, \qquad (4)$$

where $\alpha>0, \mu>-1, t>0$.

Definition 2.2 [6, 7]: The Caputo fractional-order derivative operator is defined as:

$$D^{\alpha}f(t)=\frac{1}{\Gamma(M-\alpha)}\int_0^t \frac{f^{M}(\tau)}{(t-\tau)^{\alpha+1-M}}d\tau, \quad (5)$$

where $\Gamma(\cdot)$ is the Gamma function and $f^{M}(\tau)=\frac{d^{M}f(\tau)}{d\tau^{M}}$ such that $M-1\le\alpha<M,\ M\in\mathbb{N}$.

Definition 2.4 [15]: The solution $x(t)$ of system (1) is said to be stable on a finite time interval, if for a given $\varepsilon>0$ and $t_0\in\mathbb{R}^{+}$, there exist $\delta>0$ such that $\|y_0-x_0\|<\delta$ implies $\|y(t)-x(t)\|<\varepsilon$, for all $t>t_0$, where $y(t)$ is any solution of system (1) with another initial condition y_0.

Definition 2.5 [16]: Let $1\le p<\infty$ and $\Omega\subset\mathbb{R}^{+}$. System (1) is said to be an L^{p}-stable if the solution $x(t)\in L^{p}(\Omega)$.

Definition 2.5 [17,18]: The convolution kernel K_{α} of order α for fractional integrals is defined:

$$K_{\alpha}(t)=\frac{{t_{+}}^{\alpha-1}}{\Gamma(\alpha)}\in L^{1}(\mathbb{R}^{+}), \qquad \alpha>0 \qquad (6)$$

where

$${t_{+}}^{\alpha-1}=\begin{cases} t^{\alpha-1}, & t>0\\ 0\ , & t\le 0\end{cases} \qquad (7)$$

3. STABILITY RESULT

A numerical approximation is reportedly stable if the numerical solution can be bounded from above by the data that is supplied to the problem with a constant that does not depend on the discretization parameters. Stability is often shown by using norms of the solution. In this section, we concern with the stability of the linear system of fractional-order on a finite-time interval. This task will be carried out by establishing a sufficient condition for such stability. To this aim, we consider system (1) again. That is;

$$D^{\alpha}x(t) = f\big(t, x(t)\big), \qquad (8a)$$

with initial condition

$$x(0) = v \qquad (8b)$$

where $x(t) = [x_1(t)\ x_2(t)\ \ldots\ x_m(t)\ ]^T$ is the solution of the system, $0 < \alpha < 1$, and $f = [f_1\ \ f_2\ \ldots\ f_m\ ]^T \in C[\mathbb{R}^+ \times \mathbb{R}^n, \mathbb{R}^{n+}]$ that represents the set of all continuous positive functions defined on a finite interval. Applying J^{α} on both sides of system (8a) yields:

$$x(t) = x(0) + J^{\alpha} f\big(t, x(t)\big) \qquad (9)$$

Without loss of generality, assume $x(0) = 0$, then (9) becomes:

$$x(t) = \frac{1}{\Gamma(\alpha)} \int_0^t (t-s)^{\alpha-1} f\big(s, x(s)\big).ds \qquad (10)$$

That is; system (10) can be then written as the convolution like:

$$x(t) = \frac{t^{\alpha-1}}{\Gamma(\alpha)} \star f\big(t, x(t)\big) \qquad (11)$$

Suppose that $I = [0,\ t^*]$, where t^* is a finite appropriate positive number. Define the following norm $\|\cdot\|_0^{t^*}$ on $C[\mathbb{R}^+ \times \mathbb{R}^n, \mathbb{R}^{n+}]$ by:

$$\|x(t)\|_0^{t^*} = \sum_{i=1}^{m} \|x_i(t)\|_0^{t^*} = \sum_{i=1}^{m} \left[\int_0^{t^*} |x_i(t)|.dt\right] \quad (12)$$

Now, in order to study the stability of the solution of system (8), we should prove that $x_i(t)$ is bounded for all $i = 1, 2, 3, \ldots, m$. In other words, we should prove

$$\|x_i(t)\|_0^{t^*} < \infty, \qquad i = 1, 2, 3, \dots, m \tag{13}$$

In fact, the solution given in (11) can be written using the convolution operator in the following form

$$x(t) = K_\alpha \star f\big(t, x(t)\big), \tag{14}$$

where K_α is the convolution kernel defined in (6). That is:

$$x_i(t) = (K_\alpha \star f_i)(t), \quad i = 1, 2, 3, \dots, m \tag{15}$$

Now, for reaching to our goal (i.e. (13) should be hold), we state and prove the following theorem.

Theorem 3.1: Let $K_\alpha, f_i \in C[\mathbb{R}^+, \mathbb{R}^+] \cap L^1[0,\ t^*]$, $\forall\, i = 1, 2, 3, \dots, m$, where t^* is a finite positive number. If

$$\left|\frac{t^\alpha}{\Gamma(\alpha+1)}\right| < \varepsilon, \quad \varepsilon > 0. \tag{16}$$

Then the solution of system (8) is stable.

Proof: Using the definition of the norm $\|\cdot\|_0^{t^*}$ given in (12), one might get

$$\|x_i(t)\|_0^{t^*} = \int_0^{t^*} |x_i(t)|.\, dt, \tag{17}$$

where $i = 1, 2, \dots, m$. By substituting (15) in (17) and considering the assumptions on K_α and f_i, we obtain:

$$\|x_i(t)\|_0^{t^*} = \int_0^{t^*} K_\alpha \star f_i(t, x_i(t)).\, dt\,, \tag{18}$$

where $i = 1, 2, 3, \dots, m$. Since K_α is a convolution kernel, then (18) can be written as

$$\|x_i(t)\|_0^{t^*} = \int_0^{t^*} \int_0^{t} K_\alpha(t-s)\, f_i(s, x_i(s)).\, dsdt\,, \tag{19}$$

where $i = 1, 2, 3, \dots, m$. Now, using Fubini's Theorem for positive functions, one can get:

$$\|x_i(t)\|_0^{t^*} = \int_0^{t^*} \int_s^{t} K_\alpha(t-s)\, f_i(s, x_i(s)).\, dtds\,, \tag{20}$$

where $i = 1, 2, 3, \dots, m$. Changing of variables, $u = t - s$, in (20) yields:

$$\|x_i(t)\|_0^{t^*} = \int_0^{t^*} f_i(s, x_i(s)) \left(\int_0^{t^*-s} K_\alpha(t-s)\,.\,dt \right) ds$$

$$= \int_0^{t^*} f_i(s, x_i(s)) \left(\int_0^{t^*-s} K_\alpha(u)\,.\,du \right) ds \qquad (21)$$

That is;

$$\|x_i(t)\|_0^{t^*} = \int_0^{t^*} f_i(s, x_i(s)) \left(\int_0^{t^*-s} K_\alpha(t)\,.\,dt \right) ds \qquad (22)$$

where $i = 1, 2, 3, \dots, m$. Since K_α is positive, we have:

$$\int_0^{t^*-s} K_\alpha(t)\,.\,dt \le \int_0^{t^*} K_\alpha(t)\,.\,dt \qquad (23)$$

Thus, (22) becomes:

$$\|x_i(t)\|_0^{t^*} \le \left(\int_0^{t^*} K_\alpha(t)\,.\,dt \right) \left(\int_0^{t^*} f_i(s, x_i(s))\,.\,ds \right)$$

$$= \left(\int_0^{t^*} \frac{t^{\alpha-1}}{\Gamma(\alpha)}.\,dt \right) \left(\int_0^{t^*} f_i(s, x_i(s))\,.\,ds \right)$$

$$= \frac{(t^*)^\alpha}{\Gamma(\alpha+1)} \left(\int_0^{t^*} f_i(s, x_i(s))\,.\,ds \right) \qquad (24)$$

Since t^* is a finite positive number, then the right-hand side of the above inequality given in (24) will converge, provided that the condition (16) is satisfied. That is;

$$\|x_i(t)\|_0^{t^*} \le \left| \frac{(t^*)^\alpha}{\Gamma(\alpha+1)} \right| \left(\int_0^{t^*} f_i(s, x_i(s)) ds \right) < \infty, (25)$$

where $i = 1, 2, 3, \dots, m$. Hence, $\|x(t)\|_0^{t^*}$ is bounded.

Now, suppose $x(t)$ and $y(t)$ are two solutions of system (8) with different initial conditions x_0 and y_0, respectively, such that $|y_0 - x_0| < \delta$. In the same manner for $\|y(t) - x(t)\|_0^{t^*}$, one can get:

$$\|y(t)-x(t)\|_0^{t^*}=\sum_{i=1}^{m}\|y_i(t)-x_i(t)\|_0^{t^*}=\sum_{i=1}^{m}\left[\int_0^{t^*}|y_i(t)-x_i(t)|.dt\right] \quad (26)$$

In particular,

$$\|y_i(t)-x_i(t)\|_0^{t^*}=\int_0^{t^*}|y_i(t)-x_i(t)|.dt$$

$$=\int_0^{t^*}K_\alpha*\Big(f_i\big(t,y_i(t)\big)-f_i\big(t,x_i(t)\big)\Big).dt$$

$$=\int_0^{t^*}\int_0^{t}K_\alpha(t-s)\Big(f_i\big(t,y_i(t)\big)-f_i\big(t,x_i(t)\big)\Big).dsdt$$

$$=\int_0^{t^*}\int_s^{t}K_\alpha(t-s)\Big(f_i\big(t,y_i(t)\big)-f_i\big(t,x_i(t)\big)\Big).dtds$$

$$=\int_0^{t^*}\Big(f_i\big(t,y_i(t)\big)-f_i\big(t,x_i(t)\big)\Big)\left(\int_0^{t^*-s}K_\alpha(t).dt\right)ds$$

That is;

$$\|y_i(t)-x_i(t)\|_0^{t^*}$$
$$=\left(\int_0^{t^*-s}K_\alpha(t).dt\right)\left(\int_0^{t^*}\Big(f_i\big(t,y_i(t)\big)-f_i\big(t,x_i(t)\big)\Big).ds\right), \quad (27)$$

where $i=1,2,3,\dots,m$. Using (23), then (27) becomes

$$\|y_i(t)-x_i(t)\|_0^{t^*}$$

$$\leq\left(\int_0^{t^*}K_\alpha(t).dt\right)\left(\int_0^{t^*}\Big(f_i\big(t,y_i(t)\big)-f_i\big(t,x_i(t)\big)\Big).ds\right)$$

$$=\frac{(t^*)^\alpha}{\Gamma(\alpha+1)}\left(\int_0^{t^*}\Big(f_i\big(t,y_i(t)\big)-f_i\big(t,x_i(t)\big)\Big).ds\right) \quad (28)$$

For the same reason that is t^* is a finite positive number, we conclude that the last term in (28) is converge and bounded providing that condition (16) is satisfied. That is;

$$\|y_i(t)-x_i(t)\|_0^{t^*}\leq\left|\frac{(t^*)^\alpha}{\Gamma(\alpha+1)}\right|\left(\int_0^{t^*}\Big(f_i\big(t,y_i(t)\big)-f_i\big(t,x_i(t)\big)\Big).ds\right)<\infty, \quad (29)$$

where $i = 1, 2, 3, \dots, m$. Therefore, $\|y(t) - x(t)\|_0^{t^*}$ is bounded which completes the proof. ■

CONCLUSION

The stability of solutions for the linear systems of the fractional-order differential equations has been investigated and discussed. A sufficient condition for assessing the stability of such systems has been dedicated via a new theoretical result.

REFERENCES

1. Matignon D. Stability results for fractional differential equations with applications to control processing, in Proceedings of the IMACS-SMC, 2: 963–968, 1996.

2. Li Y, Chen Y, Podlubny I. Stability of fractional-order nonlinear dynamic systems: Lyapunov direct method and generalized Mittag–Leffler stability, Computers & Mathematics with Applications, 59: 1810-1821, 2010.

3. Zhang R, Tian G, Yang S, Cao H. Stability analysis of a class of fractional order nonlinear systems with order lying in (0, 2). ISA transactions, 56: 102-110, 2015.

4. Li C, Chen G. Chaos in the fractional order Chen system and its control. Chaos Solitons Fractals, 22:549-554, 2004.

5. Wen X, Wu Z, Lu J. Stability analysis of a class of nonlinear fractional order systems, IEEE Transactions on Circuits and Systems II, 55: 1178–1182, 2008.

6. Zhou X, Hu L, Liu S, Jiang W, Stability criterion for a class of nonlinear fractional differential system, Appl. Math. Lett., 28: 25-29, 2014.

7. Zhang R, Yang S. Stabilization of fractional-order chaotic system via a single state adaptive-feedback controller, Nonlinear Dyn., 68: 45-51, 2012.

8. Faieghi M, Kuntanapreeda S, Delavari H, Baleanu D. LMI-based stabilization of a class of fractional-order chaotic systems, Nonlinear Dyn., 72: 301-309, 2013.

9. Batiha I M, Ouannas A, Emwas J A. A stabilization approach for a novel chaotic fractional-order discrete neural network, Journal of Mathematical and Computational Science, 11: 5514-5524, 2021.

10. Batiha I M, Albadarneh R B, Momani S, Jebril I H. Dynamics analysis of fractional-order Hopfield neural networks, International Journal of Biomathematics, 13: 2050083, 2020.

11. Albadarneh R B, Alomari A K, Tahat N, Batiha I M. Analytic solution of nonlinear singular BVP with multi-order fractional derivatives in electrohydrodynamic flows, Turkish World Mathematical Society Journal of Applied and Engineering Mathematics, 11: 1125-1137, 2021.

12. Khennaoui A A, Ouannas A, Momani S, Batiha I M, Dibi Z, Grassi G. On dynamics of a fractional-order discrete system with only one nonlinear term and without fixed points, Electronics, 9: 2179, 2020.

13. Djenina N, Ouannas A, Batiha I M, Grassi G, Pham V T. On the stability of linear incommensurate fractional-order difference systems, Mathematics, 8: 1754, 2020.

14. Batiha I M, Oudetallah J, Ouannas A, Al-Nana A A, Jebril I H. Tuning the Fractional-order PID-Controller for Blood Glucose Level of Diabetic Patients, International Journal of Advances in Soft Computing and its Application, 13: 2, 1-10. 2021.

15. Çiçek M, Coskun Y, Bülent O. Stability, boundedness, and Lagrange stability of fractional differential equations with initial time difference, The Scientific World Journal, 2014: Article ID 939027, 2014.

16. Ladaci S, Moulay E. Lp-stability analysis of a class of nonlinear fractional differential equations, Journal of Automation and Systems Engineering, 2: 40-46, 2008.

17. Matignon D. Stability properties for generalized fractional differential systems, ESAIM: Proc., 5: 145-158, 1998.

18. Dababneh A., Hammad M.A., Zreqat A., Albarmawi B., Abrikah S.A. Conformable Fractional of Euler Type Equation, 2021 International Conference on Information Technology, ICIT 2021 - Proceedings, pp. 19–20, 9491675, 2021.

FORMULATION OF A 7-DOF HALF-CAR MODEL WITH NONLINEAR SPRINGS AND DAMPERS FOR RIDE COMFORT ANALYSIS OF IN-WHEEL-MOTOR ELECTRIC VEHICLES

Mustafa Özdemir[1], **Eralp Osman Erdoğan**[2]

[1] Department of Mechanical Engineering, Faculty of Engineering, Marmara University, Recep Tayyip Erdoğan Campus, 34854 Maltepe, Istanbul, Turkey
E-mail: mustafa.ozdemir@marmara.edu.tr
ORCID iD: https://orcid.org/0000-0002-4981-9573

[2] Department of Mechanical Engineering (English), Institute of Pure and Applied Sciences, Marmara University, Göztepe Campus, 34722 Kadıköy, Istanbul, Turkey
E-mail: eralp.osman@marun.edu.tr
ORCID iD: https://orcid.org/0000-0002-6273-5964

Corresponding author: Mustafa Özdemir

Abstract

In this paper, we formulate a seven-degree-of-freedom half-car model for ride comfort analysis of electric vehicles with in-wheel motors. All the springs and dampers in the model are considered to exhibit cubic nonlinearities in addition to their linear characteristics. In this manner the nature of the corresponding vehicle components is described realistically. The equations of motion are obtained by using the Lagrangian method. The resulting system of ordinary differential equations can be numerically integrated to simulate vibrations due to road irregularities and unbalance of rotating parts.

Keywords: Electric vehicle; Half-car model; Vehicle dynamics.

1. INTRODUCTION

When compared to their conventional counterparts with internal combustion engines, electric vehicles have notable advantages such as reducing air pollution, global warming, and petroleum consumption [1]. Increasing environmental awareness of societies has started to reflect positively on sales shares of electric cars. Nevertheless, one of the most important aspects affecting consumers' automobile choices is the ride quality. This makes the suspension system an essential component of automobiles. However, ride comfort analysis of in-wheel-motor electric vehicles is different than that of traditional internal combustion-engined ones due to vertical unbalance forces of the motors and due to varying battery locations from vehicle model to vehicle model.

Car vibration models generally use linear springs and dampers to describe the constitutive relations for the suspension elements. This modelling approach is commonly applied to simplify computations [2]. But real springs and dampers always exhibit nonlinearities to a certain extent [3]. The present paper formulates a seven-degree-of-freedom

(DOF) half-car pitch-plane model of in-wheel-motor electric vehicles with all the springs and dampers being of linear-plus-cubic characteristics. Each wheel of the vehicle is assumed to be driven by its own in-wheel motor. The dynamic equations of the model are obtained by using the Lagrangian method.

2. DESCRIPTION OF THE MODEL

In the present paper, the electric vehicle is modeled by adapting the bicycle vibrating model [4]. The bicycle model is a standard 4-DOF model (also known in the literature as the half-car model) used to simulate the vertical translation and pitch rotation of the vehicle body and the vertical translations of the front and rear axles in the presence of road disturbance [5]. This model is modified in accordance with the studies conducted by Quynh et al. [6], Wang [7], and Huang and Nguyen [8] to include the front and rear in-wheel motors and motor suspensions. In addition, as suggested by Haug and Arora [9], the driver and driver seat are also added together with the stiffness and damping properties of the seat to the model. Moreover, all the springs in the model are considered to be Duffing springs. Similarly, all the dampers are taken as providing both linear and cubic damping. The prescribed 7-DOF nonlinear half-vehicle model is shown in Figure 1. Here, the masses are denoted by m's with subscripts, whereas the k's (c's) having both subscripts and superscripts stand for the spring (damping) coefficients. The origin of the right-handed, orthogonal, Cartesian coordinate system xyz is located at the center of gravity (CG) of the vehicle. I_{yb} is the mass moment of inertia of the half-vehicle body about the y-axis. The pitch angular displacement of the vehicle body is θ_b and the z's with subscripts represent the vertical displacements. All displacements are measured from the undeformed state. The bar representing the half-vehicle body is rigid and z_b is the heave of its center of gravity.

The subscript letters used in the notation are explained in Table 1. The subscript $seat$ refers to the driver's seat. For the springs and dampers, the superscripts 1 and 3 in parentheses are employed to indicate respectively the linear and cubic coefficients. It is worth noting that the vehicle body is assumed to be symmetric about the xz-plane. In other words, m_b and I_{yb} are respectively halves of the mass and the centroidal pitch moment of inertia of the full vehicle body [4]. Also note that m_d is the total mass of the driver and the driver's seat [9].

Table 1. Subscript letters used in the parameters and variables of the model.

Symbol	Definition
b	half-vehicle body
d	driver and driver's seat
f	front
g	ground or road surface
m	in-wheel motor
r	rear
s	vehicle suspension
t	tire
u	unsprung mass

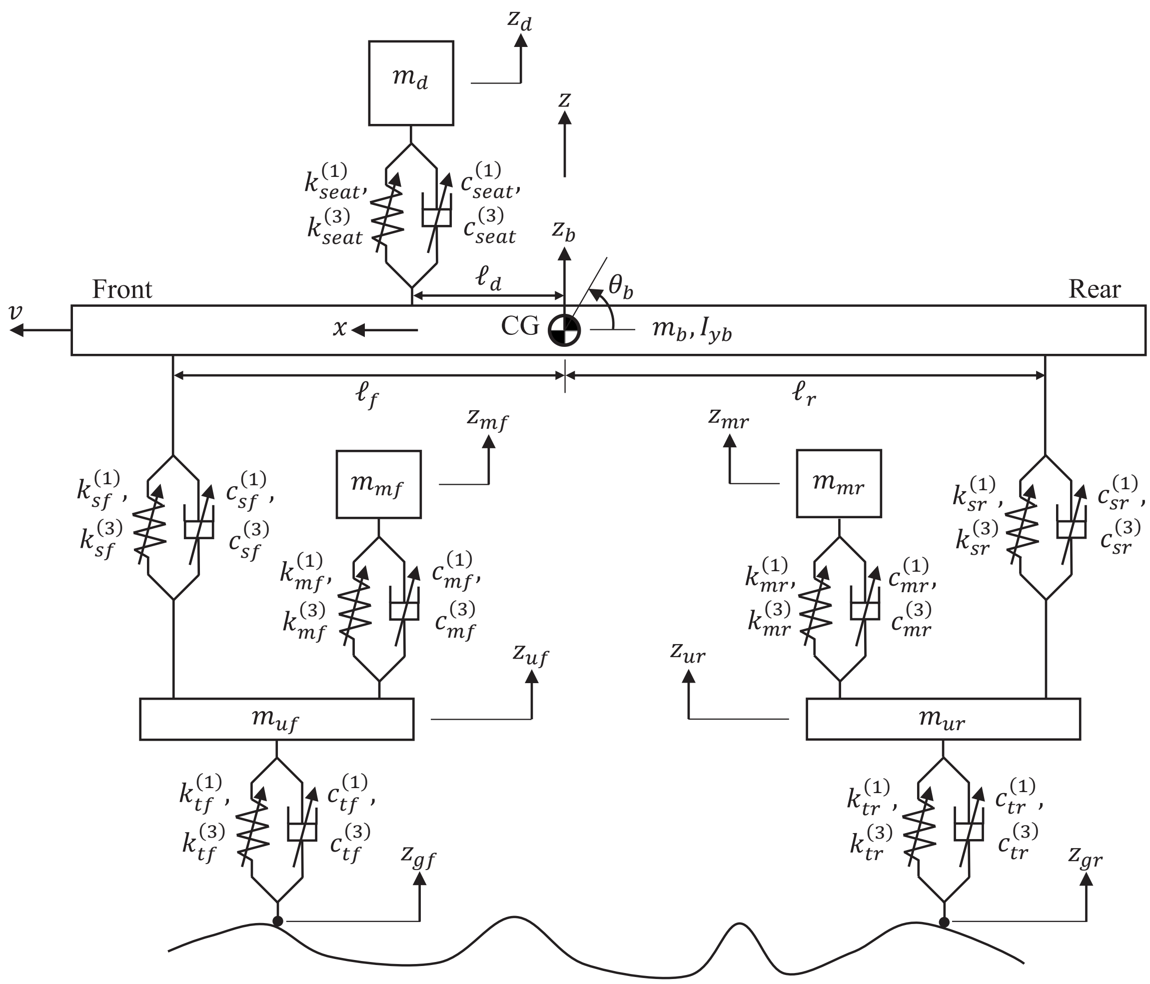

Figure 1. The 7-DOF nonlinear half-car model for in-wheel-motor electric vehicles.

3. MODEL EQUATIONS

In the below formulations, the overdot represents the derivative with respect to time t. The generalized coordinates are as follows:

$$q_1 = z_d, \quad q_2 = z_b, \quad q_3 = \theta_b, \quad q_4 = z_{mf}, \quad q_5 = z_{uf}, \quad q_6 = z_{mr}, \quad q_7 = z_{ur} \tag{1}$$

The total kinetic energy of the system is

$$E_K = \frac{1}{2}m_d\dot{z}_d{}^2 + \frac{1}{2}m_b\dot{z}_b{}^2 + \frac{1}{2}I_{yb}\dot{\theta}_b{}^2 + \frac{1}{2}m_{mf}\dot{z}_{mf}{}^2 + \frac{1}{2}m_{uf}\dot{z}_{uf}{}^2 + \frac{1}{2}m_{mr}\dot{z}_{mr}{}^2 + \frac{1}{2}m_{ur}\dot{z}_{ur}{}^2 \tag{2}$$

its total potential energy is

$$
\begin{aligned}
E_P = {} & \frac{1}{2}k_{seat}^{(1)}\{z_d - [z_b - \ell_d \sin(\theta_b)]\}^2 + \frac{1}{4}k_{seat}^{(3)}\{z_d - [z_b - \ell_d \sin(\theta_b)]\}^4 \\
& + \frac{1}{2}k_{sf}^{(1)}\left[z_b - \ell_f \sin(\theta_b) - z_{uf}\right]^2 \\
& + \frac{1}{4}k_{sf}^{(3)}\left[z_b - \ell_f \sin(\theta_b) - z_{uf}\right]^4 + \frac{1}{2}k_{mf}^{(1)}\left(z_{mf} - z_{uf}\right)^2 \\
& + \frac{1}{4}k_{mf}^{(3)}\left(z_{mf} - z_{uf}\right)^4 + \frac{1}{2}k_{tf}^{(1)}\left(z_{uf} - z_{gf}\right)^2 \\
& + \frac{1}{4}k_{tf}^{(3)}\left(z_{uf} - z_{gf}\right)^4 + \frac{1}{2}k_{sr}^{(1)}[z_b + \ell_r \sin(\theta_b) - z_{ur}]^2 \\
& + \frac{1}{4}k_{sr}^{(3)}[z_b + \ell_r \sin(\theta_b) - z_{ur}]^4 + \frac{1}{2}k_{mr}^{(1)}(z_{mr} - z_{ur})^2 \\
& + \frac{1}{4}k_{mr}^{(3)}(z_{mr} - z_{ur})^4 + \frac{1}{2}k_{tr}^{(1)}\left(z_{ur} - z_{gr}\right)^2 \\
& + \frac{1}{4}k_{tr}^{(3)}\left(z_{ur} - z_{gr}\right)^4 + m_d g z_d + m_b g z_b + m_{mf} g z_{mf} \\
& + m_{uf} g z_{uf} + m_{mr} g z_{mr} + m_{ur} g z_{ur} + U_0
\end{aligned}
\tag{3}
$$

and the dissipation function is

$$
\begin{aligned}
D = {} & \frac{1}{2}c_{seat}^{(1)}\left\{\dot{z}_d - \left[\dot{z}_b - \ell_d \dot{\theta}_b \cos(\theta_b)\right]\right\}^2 \\
& + \frac{1}{4}c_{seat}^{(3)}\left\{\dot{z}_d - \left[\dot{z}_b - \ell_d \dot{\theta}_b \cos(\theta_b)\right]\right\}^4 \\
& + \frac{1}{2}c_{sf}^{(1)}\left[\dot{z}_b - \ell_f \dot{\theta}_b \cos(\theta_b) - \dot{z}_{uf}\right]^2 \\
& + \frac{1}{4}c_{sf}^{(3)}\left[\dot{z}_b - \ell_f \dot{\theta}_b \cos(\theta_b) - \dot{z}_{uf}\right]^4 + \frac{1}{2}c_{mf}^{(1)}\left(\dot{z}_{mf} - \dot{z}_{uf}\right)^2 \\
& + \frac{1}{4}c_{mf}^{(3)}\left(\dot{z}_{mf} - \dot{z}_{uf}\right)^4 + \frac{1}{2}c_{tf}^{(1)}\left(\dot{z}_{uf} - \dot{z}_{gf}\right)^2 \\
& + \frac{1}{4}c_{tf}^{(3)}\left(\dot{z}_{uf} - \dot{z}_{gf}\right)^4 + \frac{1}{2}c_{sr}^{(1)}\left[\dot{z}_b + \ell_r \dot{\theta}_b \cos(\theta_b) - \dot{z}_{ur}\right]^2 \\
& + \frac{1}{4}c_{sr}^{(3)}\left[\dot{z}_b + \ell_r \dot{\theta}_b \cos(\theta_b) - \dot{z}_{ur}\right]^4 + \frac{1}{2}c_{mr}^{(1)}(\dot{z}_{mr} - \dot{z}_{ur})^2 \\
& + \frac{1}{4}c_{mr}^{(3)}(\dot{z}_{mr} - \dot{z}_{ur})^4 + \frac{1}{2}c_{tr}^{(1)}\left(\dot{z}_{ur} - \dot{z}_{gr}\right)^2 \\
& + \frac{1}{4}c_{tr}^{(3)}\left(\dot{z}_{ur} - \dot{z}_{gr}\right)^4
\end{aligned}
\tag{4}
$$

where g is the gravitational acceleration acting in the negative z-direction and U_0 is a constant that depends on the datum of the gravitational potential energy. The vertical displacement inputs from the road surface to the front and rear tires are denoted by z_{gf} and z_{gr}, respectively. In this study, it is assumed that the vehicle is moving forward with a constant speed of v. So, we have

$$
z_{gr}(t) = z_{gf}(t - \tau) \tag{5}
$$

with

$$\tau = \frac{\ell_f + \ell_r}{v} \tag{6}$$

The Lagrangian of the system is defined as

$$L = E_K - E_P \tag{7}$$

The equations of motion of the model can be obtained by using the Lagrangian and the dissipation function as follows:

$$\frac{d}{dt}\left(\frac{\partial L}{\partial \dot{q}_j}\right) - \frac{\partial L}{\partial q_j} + \frac{\partial D}{\partial \dot{q}_j} = Q_j, \quad j = 1, 2, \dots, 7 \tag{8}$$

where Q_j is the generalized nonconservative force, excluding the damping forces, associated with the jth generalized coordinate q_j. The partial derivatives of the Lagrangian with respect to the generalized coordinates are given below.

$$\frac{\partial L}{\partial z_d} = -k_{seat}^{(1)}[z_d - z_b + \ell_d \sin(\theta_b)] - k_{seat}^{(3)}[z_d - z_b + \ell_d \sin(\theta_b)]^3 - m_d g \tag{9}$$

$$\begin{aligned}\frac{\partial L}{\partial z_b} = {} & k_{seat}^{(1)}[z_d - z_b + \ell_d \sin(\theta_b)] + k_{seat}^{(3)}[z_d - z_b + \ell_d \sin(\theta_b)]^3 \\ & - k_{sf}^{(1)}\left[z_b - \ell_f \sin(\theta_b) - z_{uf}\right] - k_{sf}^{(3)}\left[z_b - \ell_f \sin(\theta_b) - z_{uf}\right]^3 \\ & - k_{sr}^{(1)}[z_b + \ell_r \sin(\theta_b) - z_{ur}] - k_{sr}^{(3)}[z_b + \ell_r \sin(\theta_b) - z_{ur}]^3 \\ & - m_b g\end{aligned} \tag{10}$$

$$\begin{aligned}\frac{\partial L}{\partial \theta_b} = {} & -k_{seat}^{(1)}\ell_d \cos(\theta_b)\,[z_d - z_b + \ell_d \sin(\theta_b)] \\ & - k_{seat}^{(3)}\ell_d \cos(\theta_b)\,[z_d - z_b + \ell_d \sin(\theta_b)]^3 \\ & + k_{sf}^{(1)}\ell_f \cos(\theta_b)\left[z_b - \ell_f \sin(\theta_b) - z_{uf}\right] \\ & + k_{sf}^{(3)}\ell_f \cos(\theta_b)\left[z_b - \ell_f \sin(\theta_b) - z_{uf}\right]^3 \\ & - k_{sr}^{(1)}\ell_r \cos(\theta_b)\,[z_b + \ell_r \sin(\theta_b) - z_{ur}] \\ & - k_{sr}^{(3)}\ell_r \cos(\theta_b)\,[z_b + \ell_r \sin(\theta_b) - z_{ur}]^3\end{aligned} \tag{11}$$

$$\frac{\partial L}{\partial z_{mf}} = -k_{mf}^{(1)}\left(z_{mf} - z_{uf}\right) - k_{mf}^{(3)}\left(z_{mf} - z_{uf}\right)^3 - m_{mf} g \tag{12}$$

$$\begin{aligned}\frac{\partial L}{\partial z_{uf}} = {} & k_{sf}^{(1)}\left[z_b - \ell_f \sin(\theta_b) - z_{uf}\right] + k_{sf}^{(3)}\left[z_b - \ell_f \sin(\theta_b) - z_{uf}\right]^3 \\ & + k_{mf}^{(1)}\left(z_{mf} - z_{uf}\right) + k_{mf}^{(3)}\left(z_{mf} - z_{uf}\right)^3 - k_{tf}^{(1)}\left(z_{uf} - z_{gf}\right) \\ & - k_{tf}^{(3)}\left(z_{uf} - z_{gf}\right)^3 - m_{uf} g\end{aligned} \tag{13}$$

$$\frac{\partial L}{\partial z_{mr}} = -k_{mr}^{(1)}(z_{mr} - z_{ur}) - k_{mr}^{(3)}(z_{mr} - z_{ur})^3 - m_{mr} g \tag{14}$$

$$\frac{\partial L}{\partial z_{ur}} = k_{sr}^{(1)}[z_b + \ell_r \sin(\theta_b) - z_{ur}] + k_{sr}^{(3)}[z_b + \ell_r \sin(\theta_b) - z_{ur}]^3 + k_{mr}^{(1)}(z_{mr} - z_{ur}) + k_{mr}^{(3)}(z_{mr} - z_{ur})^3 - k_{tr}^{(1)}(z_{ur} - z_{gr}) - k_{tr}^{(3)}(z_{ur} - z_{gr})^3 - m_{ur}g \tag{15}$$

The partial derivatives of the Lagrangian with respect to the generalized velocities are as follows:

$$\frac{\partial L}{\partial \dot{z}_d} = m_d \dot{z}_d \tag{16}$$

$$\frac{\partial L}{\partial \dot{z}_b} = m_b \dot{z}_b \tag{17}$$

$$\frac{\partial L}{\partial \dot{\theta}_b} = I_{yb} \dot{\theta}_b \tag{18}$$

$$\frac{\partial L}{\partial \dot{z}_{mf}} = m_{mf} \dot{z}_{mf} \tag{19}$$

$$\frac{\partial L}{\partial \dot{z}_{uf}} = m_{uf} \dot{z}_{uf} \tag{20}$$

$$\frac{\partial L}{\partial \dot{z}_{mr}} = m_{mr} \dot{z}_{mr} \tag{21}$$

$$\frac{\partial L}{\partial \dot{z}_{ur}} = m_{ur} \dot{z}_{ur} \tag{22}$$

Equations (16) – (22) can be differentiated with respect to time to get

$$\frac{d}{dt}\left(\frac{\partial L}{\partial \dot{z}_d}\right) = m_d \ddot{z}_d \tag{23}$$

$$\frac{d}{dt}\left(\frac{\partial L}{\partial \dot{z}_b}\right) = m_b \ddot{z}_b \tag{24}$$

$$\frac{d}{dt}\left(\frac{\partial L}{\partial \dot{\theta}_b}\right) = I_{yb} \ddot{\theta}_b \tag{25}$$

$$\frac{d}{dt}\left(\frac{\partial L}{\partial \dot{z}_{mf}}\right) = m_{mf} \ddot{z}_{mf} \tag{26}$$

$$\frac{d}{dt}\left(\frac{\partial L}{\partial \dot{z}_{uf}}\right) = m_{uf} \ddot{z}_{uf} \tag{27}$$

$$\frac{d}{dt}\left(\frac{\partial L}{\partial \dot{z}_{mr}}\right) = m_{mr} \ddot{z}_{mr} \tag{28}$$

$$\frac{d}{dt}\left(\frac{\partial L}{\partial \dot{z}_{ur}}\right) = m_{ur}\ddot{z}_{ur} \tag{29}$$

Differentiating the dissipation function with respect to the generalized velocities yields

$$\frac{\partial D}{\partial \dot{z}_d} = c_{seat}^{(1)}\left[\dot{z}_d - \dot{z}_b + \ell_d\dot{\theta}_b\cos(\theta_b)\right] + c_{seat}^{(3)}\left[\dot{z}_d - \dot{z}_b + \ell_d\dot{\theta}_b\cos(\theta_b)\right]^3 \tag{30}$$

$$\begin{aligned}\frac{\partial D}{\partial \dot{z}_b} = &-c_{seat}^{(1)}\left[\dot{z}_d - \dot{z}_b + \ell_d\dot{\theta}_b\cos(\theta_b)\right] - c_{seat}^{(3)}\left[\dot{z}_d - \dot{z}_b + \ell_d\dot{\theta}_b\cos(\theta_b)\right]^3 \\ &+ c_{sf}^{(1)}\left[\dot{z}_b - \ell_f\dot{\theta}_b\cos(\theta_b) - \dot{z}_{uf}\right] \\ &+ c_{sf}^{(3)}\left[\dot{z}_b - \ell_f\dot{\theta}_b\cos(\theta_b) - \dot{z}_{uf}\right]^3 \\ &+ c_{sr}^{(1)}\left[\dot{z}_b + \ell_r\dot{\theta}_b\cos(\theta_b) - \dot{z}_{ur}\right] \\ &+ c_{sr}^{(3)}\left[\dot{z}_b + \ell_r\dot{\theta}_b\cos(\theta_b) - \dot{z}_{ur}\right]^3\end{aligned} \tag{31}$$

$$\begin{aligned}\frac{\partial D}{\partial \dot{\theta}_b} = &\; c_{seat}^{(1)}\ell_d\cos(\theta_b)\left[\dot{z}_d - \dot{z}_b + \ell_d\dot{\theta}_b\cos(\theta_b)\right] \\ &+ c_{seat}^{(3)}\ell_d\cos(\theta_b)\left[\dot{z}_d - \dot{z}_b + \ell_d\dot{\theta}_b\cos(\theta_b)\right]^3 \\ &- c_{sf}^{(1)}\ell_f\cos(\theta_b)\left[\dot{z}_b - \ell_f\dot{\theta}_b\cos(\theta_b) - \dot{z}_{uf}\right] \\ &- c_{sf}^{(3)}\ell_f\cos(\theta_b)\left[\dot{z}_b - \ell_f\dot{\theta}_b\cos(\theta_b) - \dot{z}_{uf}\right]^3 \\ &+ c_{sr}^{(1)}\ell_r\cos(\theta_b)\left[\dot{z}_b + \ell_r\dot{\theta}_b\cos(\theta_b) - \dot{z}_{ur}\right] \\ &+ c_{sr}^{(3)}\ell_r\cos(\theta_b)\left[\dot{z}_b + \ell_r\dot{\theta}_b\cos(\theta_b) - \dot{z}_{ur}\right]^3\end{aligned} \tag{32}$$

$$\frac{\partial D}{\partial \dot{z}_{mf}} = c_{mf}^{(1)}\left(\dot{z}_{mf} - \dot{z}_{uf}\right) + c_{mf}^{(3)}\left(\dot{z}_{mf} - \dot{z}_{uf}\right)^3 \tag{33}$$

$$\begin{aligned}\frac{\partial D}{\partial \dot{z}_{uf}} = &-c_{sf}^{(1)}\left[\dot{z}_b - \ell_f\dot{\theta}_b\cos(\theta_b) - \dot{z}_{uf}\right] - c_{sf}^{(3)}\left[\dot{z}_b - \ell_f\dot{\theta}_b\cos(\theta_b) - \dot{z}_{uf}\right]^3 \\ &- c_{mf}^{(1)}\left(\dot{z}_{mf} - \dot{z}_{uf}\right) - c_{mf}^{(3)}\left(\dot{z}_{mf} - \dot{z}_{uf}\right)^3 + c_{tf}^{(1)}\left(\dot{z}_{uf} - \dot{z}_{gf}\right) \\ &+ c_{tf}^{(3)}\left(\dot{z}_{uf} - \dot{z}_{gf}\right)^3\end{aligned} \tag{34}$$

$$\frac{\partial D}{\partial \dot{z}_{mr}} = c_{mr}^{(1)}(\dot{z}_{mr} - \dot{z}_{ur}) + c_{mr}^{(3)}(\dot{z}_{mr} - \dot{z}_{ur})^3 \tag{35}$$

$$\begin{aligned}\frac{\partial D}{\partial \dot{z}_{ur}} = &-c_{sr}^{(1)}\left[\dot{z}_b + \ell_r\dot{\theta}_b\cos(\theta_b) - \dot{z}_{ur}\right] - c_{sr}^{(3)}\left[\dot{z}_b + \ell_r\dot{\theta}_b\cos(\theta_b) - \dot{z}_{ur}\right]^3 \\ &- c_{mr}^{(1)}(\dot{z}_{mr} - \dot{z}_{ur}) - c_{mr}^{(3)}(\dot{z}_{mr} - \dot{z}_{ur})^3 + c_{tr}^{(1)}\left(\dot{z}_{ur} - \dot{z}_{gr}\right) \\ &+ c_{tr}^{(3)}\left(\dot{z}_{ur} - \dot{z}_{gr}\right)^3\end{aligned} \tag{36}$$

By substituting equations (9) – (15), (23) – (29) and (30) – (36) into equations (8), we obtain the equations of motion of the model as follows:

$$
\begin{aligned}
m_d\ddot{z}_d + c_{seat}^{(1)}\left[\dot{z}_d - \dot{z}_b + \ell_d\dot{\theta}_b\cos(\theta_b)\right] + c_{seat}^{(3)}\left[\dot{z}_d - \dot{z}_b + \ell_d\dot{\theta}_b\cos(\theta_b)\right]^3 \\
+ k_{seat}^{(1)}[z_d - z_b + \ell_d\sin(\theta_b)] + k_{seat}^{(3)}[z_d - z_b + \ell_d\sin(\theta_b)]^3 \\
+ m_d g = 0
\end{aligned} \tag{37}
$$

$$
\begin{aligned}
m_b\ddot{z}_b - c_{seat}^{(1)}\left[\dot{z}_d - \dot{z}_b + \ell_d\dot{\theta}_b\cos(\theta_b)\right] - c_{seat}^{(3)}\left[\dot{z}_d - \dot{z}_b + \ell_d\dot{\theta}_b\cos(\theta_b)\right]^3 \\
+ c_{sf}^{(1)}\left[\dot{z}_b - \ell_f\dot{\theta}_b\cos(\theta_b) - \dot{z}_{uf}\right] \\
+ c_{sf}^{(3)}\left[\dot{z}_b - \ell_f\dot{\theta}_b\cos(\theta_b) - \dot{z}_{uf}\right]^3 \\
+ c_{sr}^{(1)}\left[\dot{z}_b + \ell_r\dot{\theta}_b\cos(\theta_b) - \dot{z}_{ur}\right] \\
+ c_{sr}^{(3)}\left[\dot{z}_b + \ell_r\dot{\theta}_b\cos(\theta_b) - \dot{z}_{ur}\right]^3 \\
- k_{seat}^{(1)}[z_d - z_b + \ell_d\sin(\theta_b)] - k_{seat}^{(3)}[z_d - z_b + \ell_d\sin(\theta_b)]^3 \\
+ k_{sf}^{(1)}\left[z_b - \ell_f\sin(\theta_b) - z_{uf}\right] + k_{sf}^{(3)}\left[z_b - \ell_f\sin(\theta_b) - z_{uf}\right]^3 \\
+ k_{sr}^{(1)}[z_b + \ell_r\sin(\theta_b) - z_{ur}] + k_{sr}^{(3)}[z_b + \ell_r\sin(\theta_b) - z_{ur}]^3 \\
+ m_b g = 0
\end{aligned} \tag{38}
$$

$$
\begin{aligned}
I_{yb}\ddot{\theta}_b + c_{seat}^{(1)}\ell_d\cos(\theta_b)\left[\dot{z}_d - \dot{z}_b + \ell_d\dot{\theta}_b\cos(\theta_b)\right] \\
+ c_{seat}^{(3)}\ell_d\cos(\theta_b)\left[\dot{z}_d - \dot{z}_b + \ell_d\dot{\theta}_b\cos(\theta_b)\right]^3 \\
- c_{sf}^{(1)}\ell_f\cos(\theta_b)\left[\dot{z}_b - \ell_f\dot{\theta}_b\cos(\theta_b) - \dot{z}_{uf}\right] \\
- c_{sf}^{(3)}\ell_f\cos(\theta_b)\left[\dot{z}_b - \ell_f\dot{\theta}_b\cos(\theta_b) - \dot{z}_{uf}\right]^3 \\
+ c_{sr}^{(1)}\ell_r\cos(\theta_b)\left[\dot{z}_b + \ell_r\dot{\theta}_b\cos(\theta_b) - \dot{z}_{ur}\right] \\
+ c_{sr}^{(3)}\ell_r\cos(\theta_b)\left[\dot{z}_b + \ell_r\dot{\theta}_b\cos(\theta_b) - \dot{z}_{ur}\right]^3 \\
+ k_{seat}^{(1)}\ell_d\cos(\theta_b)[z_d - z_b + \ell_d\sin(\theta_b)] \\
+ k_{seat}^{(3)}\ell_d\cos(\theta_b)[z_d - z_b + \ell_d\sin(\theta_b)]^3 \\
- k_{sf}^{(1)}\ell_f\cos(\theta_b)\left[z_b - \ell_f\sin(\theta_b) - z_{uf}\right] \\
- k_{sf}^{(3)}\ell_f\cos(\theta_b)\left[z_b - \ell_f\sin(\theta_b) - z_{uf}\right]^3 \\
+ k_{sr}^{(1)}\ell_r\cos(\theta_b)[z_b + \ell_r\sin(\theta_b) - z_{ur}] \\
+ k_{sr}^{(3)}\ell_r\cos(\theta_b)[z_b + \ell_r\sin(\theta_b) - z_{ur}]^3 = 0
\end{aligned} \tag{39}
$$

$$
\begin{aligned}
m_{mf}\ddot{z}_{mf} + c_{mf}^{(1)}\left(\dot{z}_{mf} - \dot{z}_{uf}\right) + c_{mf}^{(3)}\left(\dot{z}_{mf} - \dot{z}_{uf}\right)^3 + k_{mf}^{(1)}\left(z_{mf} - z_{uf}\right) \\
+ k_{mf}^{(3)}\left(z_{mf} - z_{uf}\right)^3 + m_{mf}g = F_{mf}(t)
\end{aligned} \tag{40}
$$

$$
\begin{aligned}
m_{uf}\ddot{z}_{uf} - c_{sf}^{(1)}\left[\dot{z}_b - \ell_f\dot{\theta}_b\cos(\theta_b) - \dot{z}_{uf}\right] - c_{sf}^{(3)}\left[\dot{z}_b - \ell_f\dot{\theta}_b\cos(\theta_b) - \dot{z}_{uf}\right]^3 \\
- c_{mf}^{(1)}\left(\dot{z}_{mf} - \dot{z}_{uf}\right) - c_{mf}^{(3)}\left(\dot{z}_{mf} - \dot{z}_{uf}\right)^3 + c_{tf}^{(1)}\left(\dot{z}_{uf} - \dot{z}_{gf}\right) \\
+ c_{tf}^{(3)}\left(\dot{z}_{uf} - \dot{z}_{gf}\right)^3 - k_{sf}^{(1)}\left[z_b - \ell_f\sin(\theta_b) - z_{uf}\right] \\
- k_{sf}^{(3)}\left[z_b - \ell_f\sin(\theta_b) - z_{uf}\right]^3 - k_{mf}^{(1)}\left(z_{mf} - z_{uf}\right) \\
- k_{mf}^{(3)}\left(z_{mf} - z_{uf}\right)^3 + k_{tf}^{(1)}\left(z_{uf} - z_{gf}\right) + k_{tf}^{(3)}\left(z_{uf} - z_{gf}\right)^3 \\
+ m_{uf}g = 0
\end{aligned} \tag{41}
$$

$$
\begin{aligned}
m_{mr}\ddot{z}_{mr} + c_{mr}^{(1)}(\dot{z}_{mr} - \dot{z}_{ur}) + c_{mr}^{(3)}(\dot{z}_{mr} - \dot{z}_{ur})^3 + k_{mr}^{(1)}(z_{mr} - z_{ur}) \\
+ k_{mr}^{(3)}(z_{mr} - z_{ur})^3 + m_{mr}g = F_{mr}(t)
\end{aligned} \tag{42}
$$

$$
\begin{aligned}
m_{ur}\ddot{z}_{ur} - c_{sr}^{(1)}\left[\dot{z}_b + \ell_r\dot{\theta}_b\cos(\theta_b) - \dot{z}_{ur}\right] - c_{sr}^{(3)}\left[\dot{z}_b + \ell_r\dot{\theta}_b\cos(\theta_b) - \dot{z}_{ur}\right]^3 \\
- c_{mr}^{(1)}(\dot{z}_{mr} - \dot{z}_{ur}) - c_{mr}^{(3)}(\dot{z}_{mr} - \dot{z}_{ur})^3 + c_{tr}^{(1)}\left(\dot{z}_{ur} - \dot{z}_{gr}\right) \\
+ c_{tr}^{(3)}\left(\dot{z}_{ur} - \dot{z}_{gr}\right)^3 - k_{sr}^{(1)}[z_b + \ell_r\sin(\theta_b) - z_{ur}] \\
- k_{sr}^{(3)}[z_b + \ell_r\sin(\theta_b) - z_{ur}]^3 - k_{mr}^{(1)}(z_{mr} - z_{ur}) \\
- k_{mr}^{(3)}(z_{mr} - z_{ur})^3 + k_{tr}^{(1)}\left(z_{ur} - z_{gr}\right) + k_{tr}^{(3)}\left(z_{ur} - z_{gr}\right)^3 \\
+ m_{ur}g = 0
\end{aligned} \tag{43}
$$

where $F_{mf}(t)$ and $F_{mr}(t)$ are the vertical unbalance forces of the front and rear in-wheel motors, respectively.

4. CONCLUSIONS

This paper develops the equations of motion of a 7-DOF vibration model of electric vehicles driven by in-wheel motors. In order to ensure a realistic model, all the springs and dampers in the model are considered to be of linear-plus-cubic type. The formulations are based on the Lagrangian method. The resulting system of seven second-order differential equations can be transformed into a system of 14 first-order differential equations. Then the solution can be approximated by using the Runge-Kutta method for systems of differential equations [10].

ACKNOWLEDGEMENTS

This paper is based on a part of the Master of Science Thesis of the second author (Eralp Osman Erdoğan), which is in preparation in the Department of Mechanical Engineering (English) at Marmara University Institute of Pure and Applied Sciences under the supervision of the first author (Assoc. Prof. Dr. Mustafa Özdemir).

REFERENCES

1. Mehrdad Ehsani, Yimin Gao, Ali Emadi, Modern Electric, Hybrid Electric, and Fuel Cell Vehicles: Fundamentals, Theory, and Design, 2nd Edition, CRC Press, Boca Raton, FL, USA, 2010.

2. S. Narayanan, S. Senthil, Stochastic optimal active control of a 2-DOF quarter car model with non-linear passive suspension elements, Journal of Sound and Vibration, vol. 211, no. 3, pp. 495–506, 1998.

3. Ernest O. Doebelin, System Dynamics: Modeling, Analysis, Simulation, Design, Marcel Dekker, New York, USA, 1998.

4. Reza N. Jazar, Vehicle Dynamics: Theory and Application, 2nd Edition, Springer, New York, USA, 2014.

5. Jinhui Jiang, Mohammed Seaid, M Shadi Mohamed, Hongqiu Li, Inverse algorithm for real-time road roughness estimation for autonomous vehicles, Archive of Applied Mechanics, vol. 90, no. 6, pp. 1333–1348, 2020.

6. Le Van Quynh, Bui Van Cuong, Nguyen Van Liem, Le Xuan Long, Pham Thi Thanh Dung, Effect of in-wheel motor suspension system on electric vehicle ride comfort, Vibroengineering PROCEDIA, vol. 29, pp. 148–152, 2019.

7. Peiling Wang, Effect of electric battery mass distribution on electric vehicle movement safety, Vibroengineering PROCEDIA, vol. 33, pp. 78–83, 2020.

8. Shuting Huang, Vanliem Nguyen, Influence of dynamic parameters of electric-vehicles on the ride comfort under different operation conditions, Journal of Mechanical Engineering, Automation and Control Systems, vol. 2, no. 1, pp. 1–8, 2021.

9. Edward J. Haug, Jasbir S. Arora, Applied Optimal Design: Mechanical and Structural Systems, Wiley, New York, USA, 1979.

10. Richard L. Burden, J. Douglas Faires, Numerical Analysis, 9th Edition, Brooks/Cole, Cengage Learning, Boston, MA, USA, 2011.

Machine Learning based Intrusion Detection System using Grey Wolf Optimization for Feature Selection

Oğuzhan Taş[1], Amani Yahyaoui[2]

[1] **Department of Computer Engineering, Istanbul Sabahattin Zaim University**

[2] **Department of Software Engineering, Istanbul Sabahattin Zaim University**

oguzhantas@gmail.com , amani.yahyaoui@izu.edu.tr

Abstract

In the age of information and technology, heterogeneous connected devices share information between applications and generate significant data traffic. It is essential to ensure that this traffic, which is critical for the digital workflow, is not disrupted and that cybersecurity is necessary. Network-based attacks are an indispensable part of cybersecurity issues. Since conventional signature-based intrusion detection systems cannot detect zero-day attacks, it is essential to use machine learning to detect attacks in a large amount of flowing data.

This paper proposes a model using the AdaBoost ensemble classifier and grey wolf optimization algorithm for feature selection to detect attacks that threaten network security. The experimental results show that the proposed Adaboost-GWO algorithm improves the IDS performance and accuracy, up to 89.21%.

***Keywords**:* Intrusion detection, Network Security, Machine Learning, Grey Wolf Optimization

1.INTRODUCTION

The Internet and network technologies, an indispensable part of our lives, are increasing daily. While 4.1 billion people (or 54 percent of the world's population) used the Internet in 2019, users increased by 782 million in 2021, reaching 4.9 billion people and 63 percent of the world's population[1]. The rapid increase in internet users worldwide has brought along some security problems. Data theft, loss, modification, and service interruptions are the most common security problems. Tas et al.[2] presented that the attacks that threaten the security of wireless sensor networks and IoT devices are examined and classified according to network layers, and they proposed defense techniques.

Furthermore, intrusion detection systems prevent network and host-based security problems. An intrusion detection system analyzes a computer system or network activity by observing movements when there are signs of computer security policies, user policies, and standard security practices. As another definition, an Intrusion Detection System(IDS) is software that automates intrusion detection[3].

First-time detection of abnormal activities in the system was made by Anderson[4] in 1980. IDS systems can be classified into two main groups. The first group, Signed intrusion detection systems (SIDS), are a type of IDS where the detected attack signatures are stored in a database and make decisions based on these signatures only. The intrusion detection system is also called Misuse-based Detection. One of the advantages is that when a known attack activity is identified, the user can examine the signature database and find it immediately, or software can automatically search for this signature pattern in the database[5]. Another advantage is that the false alarm rate is relatively low. The disadvantage of SIDS is that it is only effective in known attack types and cannot detect new attacks, so it is ineffective in zero-day attacks[6]. An example of signature-based intrusion detection tools is SNORT[7].

The second group is anomaly-based intrusion detection(AIDS), which can be a statistical-based and machine learning-based technique. AIDS has more modern detection systems than signature-based systems in detecting zero-day attacks. In AIDS, the system issues a warning when a deviation between the observed and modeled behavior is detected. The AIDS system can detect zero-day attacks as an advantage. However, it may give a high false alarm rate and consumes many system resources.

Feature selection is essential in AIDS systems using machine learning techniques. In a survey paper published by Thavallaee et al.[8] determined that only 24% of researchers who examined some studies published on IDS between 2000-2008 used feature selection in their studies. Another result obtained from this study is that the IDS performance depends on the used dataset, the characteristics of the experiments, and performance measures. Ingre et al.[9] proposed an intrusion detection model using Correlation Feature Selection(CFS) subset evaluation for feature selection on the NSL-KDD dataset with the Decision Tree algorithm. They stated that feature selection improves prediction performance in Decision Tree-based IDS.

In recent years, researchers working in security and artificial intelligence have developed IDS systems by applying hybrid methods consisting of multiple algorithms in the form of multi-layer classification of machine learning algorithms and have achieved more successful results. Miah et al.[10] proposed a hybrid multi-layer classification method for attack detection. Firstly, the Cluster-based Algorithm classifies the incoming data as attack/leakage or normal. If the system detects an attack, it classifies it according to the sub-attack type. Using Random Forest and KDD99 dataset, they achieved a detection rate of 98% on highly imbalanced big data. In another hybrid intrusion detection approach, Li et al. Firstly used C4.5 Algorithm to classify the attack. After, they use the kNN algorithm in the second step on the NSL-KDD dataset. With this combination, they obtained better results than Artificial Neural Network(ANN), kNN, Random Forest(RF), and Naive Bayes(NB) algorithms.

Furthermore, to make feature selection in Machine Learning algorithms, Optimization algorithms are also used for hyperparameter selection to obtain more efficient results. Bamakan et al.[11] presented Particle Swarm Optimization(PSO) based on Multiple Criteria Linear Programming(MCLP) to get better accuracy results and lower false alarm rate(FAR) according to Support Vector Machine and C 5.0 algorithms in attack detection. MCLP is an optimization-based classification algorithm; they use KDDCup99 dataset to evaluate the model performance.

This paper used the Gray Wolf Optimization algorithm for feature selection, and the AdaBoost Algorithm consists of a combination of many learning algorithms to increase performance. Making feature selection with the Gray Wolf optimization algorithm, the accuracy rate of the model increases, and overfitting decreases[12].

The rest of the paper is organized as follows. In Section 2, basic concepts are introduced, past studies are reviewed, the Grey wolf algorithm and the AdaBoost ensemble learning algorithm are explained in detail, and the proposed approach is presented. In Section 3, the experimental results of the proposed model are presented. The conclusion of the research and the discussion are in Section 4.

2. GENERAL PROPERTIES OF METHOD

2.1. AdaBoost Algorithm

AdaBoost Algorithm, developed by Freund and Schapire, is the first practical boosting algorithm applied to many different fields and won the Gödel award. Boosting Algorithms combine many weak and inaccurate rules and make predictions with high accuracy[13][14][15]. Each model or learner tries to correct the previous one in the boosting logic. The weights are assigned to each model or learner. The weights are updated with the next classifier and trained again, and a prediction is made on the training set again, then it continues in this way. Classifier algorithms can be SVM, ANN, Decision Tree, or kNN.

If we look at Algorithm 1; For each instance, initially the w_i *(1,2,3,…,N)* weight values are set equally as *1/m (m=1,2,3,…M, number of instances*). The first classifier is trained by $G_m(x)$ and the weighted error rate errm is calculated. Here the term errm is the most important term for finding and updating weights. The *I* function in the formula returns 1 for misclassified instances and 0 for correctly classified instances. After the errm is calculated, the weight of the estimator, α_m, is calculated with 2.1. The value of α_m here is the weight of the new tree consisting of all the classifiers combined. In the formula in 2.1, η is the learning rate hyperparameter and defaults to 1, which will be higher for more accurate prediction.

$$\alpha_m = \eta log\,(\frac{(1-err_m)}{err_m}) \qquad (2.1)$$

Finally, AdaBoost algorithm will give a weighted sum of classifier votes; G(x) value for AdaBoost Algorithm binary classification will be obtained as -1 or +1.

Algorithm 1. Pseudo-code of AdaBoost Algorithm

1. Initialize the observation weights $w_i=1/N$*, i=1,2, 3,…,N*
2. ***for*** *m=1 to M* ***do***

(a) Fit a classifier Gm(x) to the training data using weight w_i

(b) Compute $err_m = \frac{\sum_{i=1}^{N} w_i I(y_i \neq G_m(x_i))}{\sum_{i=1}^{N} w_i}$

(c) Compute $\alpha_m = \eta log\,(\frac{(1-err_m)}{err_m})$

(d) Update weights for $i = 1,2,3, \dots,$ N

$w_i \leftarrow w_i \cdot exp[\alpha_m \cdot I(y_i \neq G_m(x_i)]$

3. Output G(x) = $[\sum_{m=1}^{M} \alpha_m G_m(x)]$

2.2. Grey Wolf Optimization Algorithm

Gray Wolf Optimization Algorithm(GWO) is a metaheuristic algorithm developed by Mirjalili[16], inspired by the hunting strategies of wolves. In the GWO algorithm, Populations are divided into four groups Alpha(α), Beta(β), Delta(δ), and Omega(ω). Gray wolves move hierarchically in tracking, surrounding, and attacking prey. The alpha wolf is in the top echelon and occupies a leading position. Alpha wolf; hunting, choosing a sleeping place, waking, etc., situations are decisive.

On the other hand, Beta wolves are in the lower echelon of the alpha wolf and help the alpha wolf; in case the alpha wolf dies or gets old, the new alpha wolf is chosen among these wolves. Omega wolves are at the lowest level in the hierarchy; they have no authority and eat the last prey. The mathematical model of encircling behavior is as follows.

$$\vec{D} = \left|\vec{C} - \overrightarrow{X_p}(t) - \overrightarrow{X(t)}\right| \qquad (2.2)$$

$$\vec{X}(t+1) = \vec{X}_p(t) - \vec{A}.\vec{D} \qquad (2.3)$$

where t indicates current iteration, $\vec{A}$ and $\vec{C}$ are coefficient vectors, $\overrightarrow{X_p}$ is the position vector of the prey, and $\vec{X}$ indicates the position vector of a grey wolf.

$$\vec{A} = 2\vec{a}.\vec{r}_1 - \vec{a} \qquad (2.4)$$

$$\vec{C} = 2.\vec{r}_2 \qquad (2.5)$$

where $\vec{a}$ variable is linearly decreased from 2 to 0 during the each loop step and $\vec{r}_1$ and $\vec{r}_2$ are random values between 0 and 1. The mathematical model of the hunting phase is as follows. At this stage, alpha is the best solution candidate, beta and delta have better knowledge of the prey's position, respectively.

$$\overrightarrow{D_\alpha} = \left|\overrightarrow{C_1}.\overrightarrow{X_\alpha} - \vec{X}\right| \qquad (2.6)$$

$$\overrightarrow{D_\beta} = \left|\overrightarrow{C_2}.\overrightarrow{X_\beta} - \vec{X}\right| \qquad (2.7)$$

$$\overrightarrow{D_\delta} = \left|\overrightarrow{C_3}.\overrightarrow{X_\delta} - \vec{X}\right| \qquad (2.8)$$

Here $\overrightarrow{C_1}, \overrightarrow{C_2}$ ve $\overrightarrow{C_3}$ are random vectors, $\overrightarrow{X_\alpha}$, $\overrightarrow{X_\beta}$ and $\overrightarrow{X_\delta}$ are the positions of alpha, beta and delta worms, respectively. $\vec{X}$ is the position of the current solution.

$$\overrightarrow{X_1} = \overrightarrow{X_\alpha} - \overrightarrow{A_1}.\overrightarrow{D_\alpha} \qquad (2.9)$$

$$\overrightarrow{X_2} = \overrightarrow{X_\beta} - \overrightarrow{A_2}.\overrightarrow{D_\beta} \qquad (2.10)$$

$$\overrightarrow{X_3} = \overrightarrow{X_\delta} - \overrightarrow{A_3}.\overrightarrow{D_\delta} \qquad (2.11)$$

$$\vec{X}(t+1) = \frac{\overrightarrow{X_1} + \overrightarrow{X_2} + \overrightarrow{X_3}}{3} \qquad (2.12)$$

According to the above equations, the position of alpha, beta, and delta search agents is determined in the 2D search space. In other words, alpha, beta, and delta wolves change their positions according to the predicted prey position, while other wolves randomly update their positions around the prey.

Furthermore, attacking the prey is the last stage of the algorithm, when the prey remains motionless. In the mathematical model, $\vec{a}$ value decreases in each iteration, so the $\vec{A}$ value depending on this value also decreases. While $\vec{a}$ value decreases from 2 to 0, $\vec{A}$ value takes random values in the range [-2a, 2a]. If $|A| < 1$ the wolves attack the prey, if $|A| > 1$ the wolves move away from the prey. The pseudo code of the GWO algorithm is as follows.

Algorithm 2. Pseudo code of the GWO Algorithm

Initalize the grey wolf population Xi (i=1,2,...,n)
Initialize a, A, and C
Calculate the fitness of each search agent
X_α=the best search agent
X_β=the second search agent
X_δ=the third best search agent
***while** (t<Max number of iterations)*
    for** each search agent **do
        Update the position of the current search agent by equation
    end for
    Update a, A, and C
    Calculate the fitness of all search agents
    Update X_α, X_β and X_δ
    t=t+1
end while
return X_α

3. EXPERIMENT AND RESULT

The performance of classification algorithms is evaluated according to many criteria. In this study, Accuracy, Precision, Recall, and Sensitivity values were examined, and the proposed method was compared with the traditional AdaBoost. These metrics are used to measure the model's success calculated with the following equations. The equivalents of TP(True Positive), FN(False Negative), TN(True Negative), and FP(False Positive) values in intrusion detection systems are as follows.

- True Positive(TP): Attack data that is correctly classified as an attack.
- False Positive(FP): Normal data that is incorrectly classified as an attack.
- True Negative(TN): Normal data that is correctly classified as normal.
- False Negative(FN): Attack data that is incorrectly classified as normal.

$$Accuracy = \frac{(TP+TN)}{(TP+TN+FP+FN)} \quad (3.1)$$

$$Precision = \frac{TP}{TP+FP} \quad (3.2)$$

$$Recall(Sensivity) = \frac{TP}{(TP+FN)} \quad (3.3)$$

$$F1 - Score = 2 * \frac{Precision*Recall}{Precision+Recall} \quad (3.4)$$

3.1. Intrusion Detection Dataset

The NSL KDD[17] dataset is an improved version of KDDCup99[18]. NSL-KDD data set was created by deleting the redundant data in the KDD data set and providing a homogeneous distribution. Redundant connection records (Connection records-136.489 records) and connection records (connection records-136.497 records) were removed from the test data. Thus, a more suitable data set for machine learning algorithms has been obtained. Figure 1 shows the transformation of datasets from DARPA to KDDCup99 and then to NSL KDD.

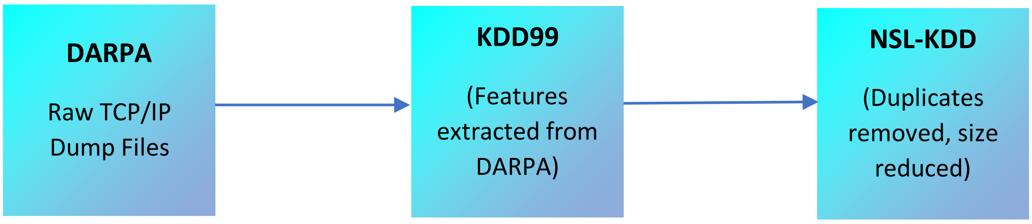

Figure 1. NSL KDD Dataset

NSL-KDD Dataset is labeled and contains 42 features; these features are grouped under four different categories as DoS, Probe, U2L, and R2L. In Table 1, the attack categories of the NSL-KDD data set can be seen.

Table 1. Training and Testing records from NSL-KDD dataset.

NSL-KDD	Train	Test
Normal	67,343	9,711
DoS	45,927	7,460
Probe	11,656	2,421
R2L	995	2,885
U2R	52	67
Total	**125,973**	**22,544**

Table 2. Attack categories of NSL-KDD dataset

Class	Subclass	Description
Normal	**Normal**	**Benign**
DoS	apache2, back, land, neptune, mailbomb, pod, processtable, smurf, teardrop, udpstorm, worm	In a DoS attack, the attacker aims to down/block the a machine or network resources.
Probe	Nmap, Ipsweep, Portsweep, Satan, Mscan, Saint	It is an attack to obtain detailed statistical information about the system and network.
R2L	httptunnel, ftp_write, guess_passwd, snmpguess, snmpgetattack, imap, spy, warezclient, warezmaster, multihop, phf, imap, named, sendmail, xlock, xsnoo, snmpgettattack	Unauthorized Access from a remote machine, e.g. guessing password
U2R	Ps, buffer_overflow, perl, rootkit, loadmodule, xterm, sqlattack, httptunnel	Unauthorized Access to root privileges, e.g., various "buffer overflow" attacks

3.2. Preprocessing

First, 43 features were selected from the NSL-KDD set, then the difficulty_level field, whose result could not be affected, was removed. Later, the attacks were classified according to the categories of Benign, Dos, Probe, R2L and U2R. Then, numerical data are selected and normalized with the fit_transform method in the StandardScalar() class. Then, the protocol_type field, which consists of data such as tcp, udp, has undergone one-hot encoding. If the binary classification is to be made as there is an attack / no attack, the attack category is divided into two as Normal/Abnormal. It is then encoded as 0 or 1 with Label Encoding.

3.3. Results

The algorithm is implemented on an Intel i7-7700HQ computer with a 2.8 GHz CPU and 16 GB RAM using an Anaconda environment (Python +Scikit Learn Library). After the classification was made, the study's success was evaluated according to the following criteria of the model.

Table 3. Experimental Results

	Accuracy	Precision	Recall	F1-Score
AdaBoost	77.67%	76.37%	50.05%	51.77%
AdaBoost+GWO	89.21%	79.50%	53.07%	53.87%

When the Confusion Matrices of both algorithms are compared, it is seen that the Probe attack gives better results in the proposed model and other attack categories close values, especially in R2L and DoS attacks. Furthermore, as we expect in the U2R category, both algorithms have a low prediction rate because it has less data than other categories.

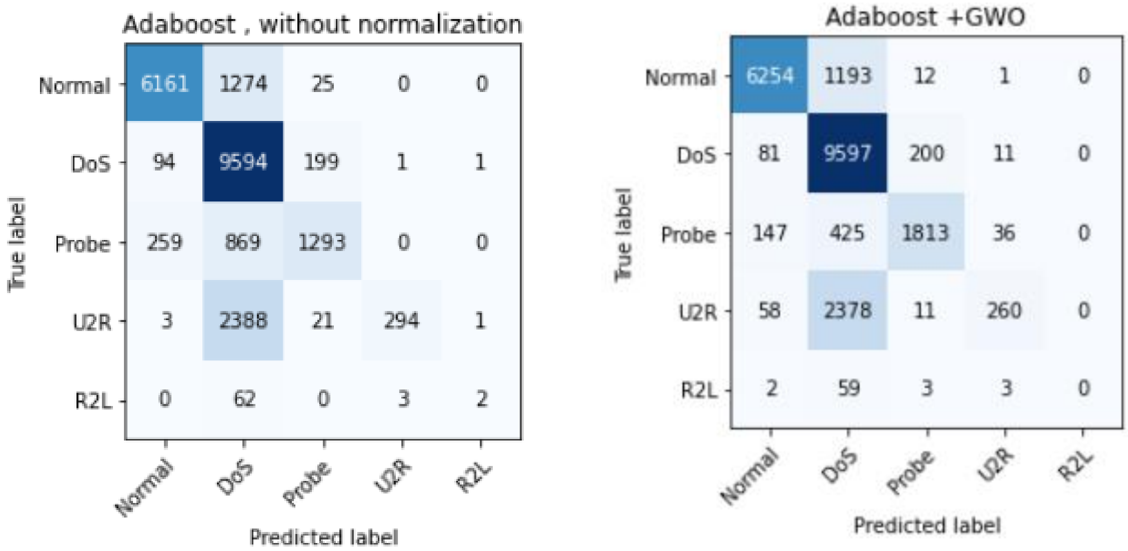

Figure 2. Confusion Matrix of Algorithms.

4. CONCLUSIONS

The following striking conclusions can be drawn from the experimental results. As a result of the feature selection made in the Gray Wolf Optimization and AdaBoost Boosting Algorithm, even if there are hundreds of features in the data set, the most useful ones are selected among these features providing benefits in terms of both time and computation. If we look at the experimental results, the performance values are higher than the standard AdaBoost algorithm. While it was 77.81% in normal AdaBoost, it increased to 89.21% in the proposed AdaBoost+GWO approach.

REFERENCES

[1] "Facts and figures 2021." https://www.itu.int/itu-d/reports/statistics/2021/11/15/internet-use/ (accessed May 17, 2022).

[2] O. Taş and F. Kiani, "Nesnelerin İnterneti (IoT) ve Kablosuz Algılayıcı Ağların Güvenliğine Yapılan Saldırıların Tespit Edilmesi ve Önlenmesi," *J. Polytech.*, vol. 24, no. 1, pp. 219–235, Mar. 2021, doi: 10.2339/politeknik.627825.

[3] K. Scarfone and P. Mell, "Intrusion Detection and Prevention Systems," 2001.

[4] D. Anderson, T. Frivold, and A. Valdes, "Next-generation Intrusion Detection Expert System (NIDES) A Summary 1," 1995.

[5] A. Khraisat, I. Gondal, P. Vamplew, and J. Kamruzzaman, "Survey of intrusion detection systems: techniques, datasets and challenges," *Cybersecurity*, vol. 2, no. 1, pp. 1–22, Dec. 2019, doi: 10.1186/s42400-019-0038-7.

[6] H. Holm, "Signature based intrusion detection for zero-day attacks: (Not) A closed chapter?," *Proc. Annu. Hawaii Int. Conf. Syst. Sci.*, pp. 4895–4904, 2014, doi: 10.1109/HICSS.2014.600.

[7] Snort, "Snort - Network Intrusion Detection & Prevention System," *Snort.Org*, 2016. https://www.snort.org/ (accessed Jun. 29, 2020).

[8] M. Tavallaee, N. Stakhanova, and A. A. Ghorbani, "Toward credible evaluation of anomaly-based intrusion-detection methods," *IEEE Trans. Syst. Man Cybern. Part C Appl. Rev.*, vol. 40, no. 5, pp. 516–524, Sep. 2010, doi: 10.1109/TSMCC.2010.2048428.

[9] B. Ingre, A. Yadav, and A. K. Soni, "Decision Tree Based Intrusion Detection System for NSL-KDD Dataset," *Smart Innov. Syst. Technol.*, vol. 84, pp. 207–218, 2018, doi: 10.1007/978-3-319-63645-0_23.

[10] M. O. Miah, S. S. Khan, S. Shatabda, and D. M. Farid, "Improving Detection Accuracy for Imbalanced Network Intrusion Classification using Cluster-based Under-sampling with Random Forests," *1st Int. Conf. Adv. Sci. Eng. Robot. Technol. 2019, ICASERT 2019*, May 2019, doi: 10.1109/ICASERT.2019.8934495.

[11] S. M. H. Bamakan, B. Amiri, M. Mirzabagheri, and Y. Shi, "A New Intrusion Detection Approach Using PSO based Multiple Criteria Linear Programming," *Procedia Comput. Sci.*, vol. 55, pp. 231–237, Jan. 2015, doi: 10.1016/J.PROCS.2015.07.040.

[12] E. O. Abiodun, A. Alabdulatif, O. I. Abiodun, M. Alawida, A. Alabdulatif, and R. S. Alkhawaldeh, "A systematic review of emerging feature selection optimization methods for optimal text classification: the present state and prospective opportunities," *Neural Comput. Appl. 2021 3322*, vol. 33, no. 22, pp. 15091–15118, Aug. 2021, doi: 10.1007/S00521-021-06406-8.

[13] R. E. Schapire, "Explaining AdaBoost," *Empir. Inference Festschrift Honor Vladimir N. Vapnik*, pp. 37–52, Jan. 2013, doi: 10.1007/978-3-642-41136-6_5.

[14] O. Sagi and L. Rokach, "Ensemble learning: A survey," *Wiley Interdiscip. Rev. Data Min. Knowl. Discov.*, vol. 8, no. 4, Jul. 2018, doi: 10.1002/widm.1249.

[15] H. Tyralis and G. Papacharalampous, "Boosting algorithms in energy research: a systematic review," *Neural Comput. Appl. 2021 3321*, vol. 33, no. 21, pp. 14101–14117, Apr. 2021, doi: 10.1007/S00521-021-05995-8.

[16] S. Mirjalili, S. M. Mirjalili, and A. Lewis, "Grey Wolf Optimizer," *Adv. Eng. Softw.*, vol. 69, pp. 46–61, Mar. 2014, doi: 10.1016/J.ADVENGSOFT.2013.12.007.

[17] "NSL-KDD | Datasets | Research | Canadian Institute for Cybersecurity | UNB." https://www.unb.ca/cic/datasets/nsl.html (accessed Dec. 17, 2020).

[18] "KDD Cup 1999 Data." http://kdd.ics.uci.edu/databases/kddcup99/kddcup99.html (accessed Dec. 17, 2020).

THERMAL INSULATION PERFORMANCES OF FOAMED MORTARS CONTAINING BENTONITE BLENDED CEMENTS

Yasemin Akgün [1]

[1] Department of Renewable Energy, Institue of Science, Ordu University, Ordu, Türkiye

ysmakgun@gmail.com

Abstract

The construction sector, which has intense energy consumption, has an important place in the solutions of world energy security problems. Blended cement production and/or using materials with high thermal performance in terms of insulation in buildings are some of these solutions. Bentonite is an alternative material for blended cement production. On the other hand, thermal performances of foamed mortars/concretes are quite high. The main purpose of this study is to determine how the thermal performance and mechanical properties of foamed mortar are affected by blended cements containing bentonite as alternative material. For this purpose, foamed mortar plates containing bentonite blended cements were produced. Bentonite replacement ratios of blended cements were 0, 5, 10, 15 wt.%. In the study, the strengths and thermal performances of foamed mortars containing bentonite blended cements were determined as experimental. The experiment results were compared among themselves and with each other. From the experiment results, it was concluded that the thermal performances of the foamed mortars containing bentonite blended cements could be improved up to 15% replacement ratio without compromising the strength.

Keywords: Thermal insulation; Foamed mortar; Bentonite; Blended cement.

1. INTRODUCTION

According to the world population expectation report published by the United Nations in 2019 [1], it is predicted that the world population will increase approximately 45% at the end of the century. With the increase in energy demand due to this rapid increase in the world population, some problems occur due to the limited energy resources and costly production. To solve these problems, it has become necessary to use energy optimally and to turn to sustainable alternative energy sources. On the other hand, according to the report published by the International Energy Agency (IEA) in 2020 [2], on a sectoral basis, 21% of the world's energy consumption is consumed by the building sector. This sector which has a higher ratio in energy consumption and CO_2 emissions compared to other sectors has important responsibilities in terms of energy efficiency and environmental awareness. A significant portion of the energy used in buildings is consumed for heating-cooling-ventilation systems to provide indoor air comfort conditions. For this reason, recently, studies on building materials with high thermal performances that will help the management of thermal comfort to control building energy consumption have become widespread.

Foamed concrete is one of these building materials. Foamed concrete is a light-weight concrete, in which air voids are trapped in mortar by a suitable foaming agent [3]. Foamed concrete has excellent thermal insulation properties due to its low self-weight. Depending on the amount of foam that will enter the mixture, foamed concrete can be obtained at different densities (400-1600 kg/m^3). Due to the positive thermal insulation properties of foamed concrete, it is seen as a suitable building material in wall-panel manufacturing and concrete blocks.

On the other hand, one of the important components of concrete, which is used extensively in building construction, is Portland cement (PC). Cement production requires high energy consumption, and it has ecologically harmful CO_2 emissions during production process. To overcome these problems the most convenient and easy solution is to use mineral additives which have positive properties for replacement with cement clinker. In addition, the strength and durability performances of mortars/concretes produced with blended cements containing mineral additives are also improved.

Also many researchers have studied the use of pozzolanic mineral additives to produce foamed concrete due to its contribution to long-term strength [4-7]. However, there are very few detailed studies on the use of bentonite as a cement replacement material in foamed concrete production [8-9]. Clays containing predominantly montmorillonite, formed as a result of chemical weathering of volcanic ash, tuff and lava rich in aluminum and magnesium, are defined as bentonite. The general chemical formula of bentonite, which is a type of clay minerals; (Na, Ca) (Al, Mg) 6(Si4 O_{10}) 6 n.H2 O.Na bentonite, which has a high swelling capacity, swells 8-10 times its own volume in contact with water. Swelling with water disappears after 600°C. Bentonite calcined at the appropriate temperature has pozzolanic properties. Turkey has bentonite deposits spread over wide areas. Approximately 70% of Turkey's bentonite reserves are found in the Çankırı region. Bentonite deposits in different places in the region along the North Anatolian Fault zone, in Tokat-Reşadiye, Çanakkale-Ayvacık, Kütahya- Başören, Eskişehir-Mihalıççık, Ordu-Ünye and Fatsa regions have developed depending on the fault systems.

The main purpose of this study is to determine how the thermal insulation performance and mechanical properties of foamed mortar are affected by blended cements containing bentonite as alternative material, to create data for the technical literature with results obtained from tests performed on the foamed concretes containing bentonite blended cement to reduce the production costs of foamed concrete used in the market and to increase using efficiency of its in terms of thermal performance. For these purposes, foamed mortar plates containing bentonite blended cements were produced. Bentonite replacement ratios of blended cements were 0, 5, 10 and 15 wt.%. In the study, the strengths and thermal insulation performances of foamed mortars containing bentonite blended cements were determined as experimental. The experiment results were compared among themselves and with each other.

2. MATERIALS AND METHODS

The material replaced with Portland cement (PC) was bentonite (Figure 1a). The bentonite (B) was obtained from Ordu/Fatsa regions of Turkey. It is natural pozzolan with volcanic tuff origin. Bentonite, also known as montmorillonite, volcanic clay, soap clay and amargosite, is a soft, plastic, light-colored, porous rock consisting largely of colloidal silica. Composed mainly of clay minerals, it swells extensively when wet. In the study, bentonite was used by calcined at 900 ^{0}C in mixtures to eliminate swelling and to produce pozzolanic properties. The physical and chemical properties of bentonite are given in Table 1. The cement used in tests was CEM I 42.5 R type of PC produced in accordance with EN 197-1 [10]. Physical, chemical and mechanical properties of PC are given in Table 2. In addition, CEN Standard sand in accordance with TS EN 196-1 [11] standard was used in the production of mortars (Figure 1b). The foaming agent used in the study is in protein-based and liquid form. It is obtained by the hydrolysis of animal proteins. And it is named as "Neopor" (Figure 1c). The physical properties of the foaming agent are given in Table 3. In production of all samples, the water that does not contain organic substances, harmful minerals or salts was used. In the test program of this study, it was planned four test series with 0%, 5%, 10% and 15% replacement ratios. The samples produced for the planned series are 20x60x150 mm mortar plates for thermal insulation performance tests (Figure 2), and 150x150x150 mm standard cubes for strength tests (Figure 3). The explanatory information about these test series is given in Table 4.

Table 1. The physical and chemical properties of bentonite

Chemical components	**Mass (%)**
SiO_2	67.5
Al_2O_3	15.6
Fe_2O_3	1.1
TiO_2	0.12
CaO	2.3
MgO	3.8
Na_2O	1.0
K_2O	1.1
Loss Of Ignition	7.4
Physical properties	
Density, (g/cm^3)	2.58

Table 2. The physical, chemical and mechanical properties of Portland cement

Chemical	**Mass (%)**	**Physical and mechanical properties**	
SiO_2	19.68	Density, (g/cm^3)	3.11
Al_2O_3	5.37	Initial set, min.	162
Fe_2O_3	3.36	Final set, min.	268
CaO	62.57	Volume expansion, mm	1.00
MgO	0.96	Blaine specific surface (cm^2/g)	3313
SO_3	2.70	Strength of 2 days, MPa	32.10
Loss of Ignition	4.14	Strength of 7 days, MPa	41.30
		Strength of 28 days, MPa	48.70

Table 3. The physical properties of the foaming agent

Physical properties	
Density	1.09 ± 0.01 g/cm³
pH	6.00 ± 0.5
Viscosity	< 20 cps
Sedimentation v/v %	< 0.10
Freezing point	≤ -5.00 °C

Table 4. The explanatory information of test series

Labels of test series	The explanatory information of test series
MB0	0% mortar containing bentonite
MB5	5% mortar containing bentonite
MB10	10% mortar containing bentonite
MB15	15% mortar containing bentonite

Figure 1. Bentonite (a), CEN Standard Sand (b) and Foaming Agent (c)


Figure 2. Plate molds


Figure 3. Standard cube molds

Compositions of foamed mortar mixtures (for 1 m^3) are given in Table 5. In Table 5, the water/cement ratio; 0.40, cement/sand ratio; 1:1, foaming agent/water ratio;1:30. All of the samples were produced in accordance with TS EN 196-1. The mini-slump and spread values of foamed mortar mixtures are on average in the range of 20-25mm and 140-150mm, respectively. Foamed mortar is produced by adding preformed stable foam (a mixture of foaming agent and water) to the cement mortar mixture.

Table 5. Component amounts of foamed mortar (for 1m^3)

Components	**MB0**	**MB5**	**MB10**	**MB15**
Portland Cement (kg/m^3)	500	450	350	250
Bentonite (kg/m^3)	0	50	150	250
Water (kg/m^3)	200			
CEN Sand (kg/m^3)	500			
Foaming Agent (kg/m^3)	4			
Water (kg/m^3)*	120			

*The amount of water used to activate the foaming agent

The samples were first kept in molds for 2 days in a laboratory environment at 23±2ºC. The samples removed from the molds were kept in air for 1 day. Then it was kept in water cure for 4 days. The samples removed from the water cure were subjected to air curing for 21 days until the experiment. The samples were 28 days old at the time of the test. The compressive strengths of the produced foamed mortar cube samples were determined with compression press. To determine the thermal insulation performances of the produced foamed mortar plates, the thermal conductivity coefficients (k) were measured with an ISOMET brand 2104 model device as specified in TS EN ISO 8990 [12] and ISO 6946 [13]. standards in the Laboratory of the Department of Mining Engineering, Faculty of Architecture and Engineering, Dicle University (Figure 4). The measurements were made at room temperature and were determined by taking the arithmetic average of the results obtained from 5 different points on the sample.

Figure 4. The device used for thermal insulation performance measurements

To determine thermal insulation performance of solid materials, the density (ρ), thermal conductivity (λ) are important parameters. Density (ρ) is calculated by Eq. (1).

$$\rho = m/V \tag{1}$$

where m is mass of the material and V volume of the material. The thermal conductivity coefficient (λ) is calculated by Eq. (2).

$$\lambda = q(\Delta L/\Delta T) \tag{2}$$

where q is heat flow through section A, ΔT temperature difference at ΔL. The smaller the thermal conductivity coefficient (λ) of a material, the better the insulation.

3. RESULTS AND DISCUSSIONS

This study includes results of preliminary tests performed on foamed mortars containing bentonite blended cement. A view of the foamed mortar samples produced in the study is given in the Figure 5. Saturated density, dry density, compressive strength and thermal conductivity test results of the test samples are shown in Table 6-7, and the variation graphs of theirs are shown in Figure 6-8.

Figure 5. A view of the foamed mortar samples

Table 6. The density and compressive strength of the foamed mortar samples

Labels of test series	Saturated density(g/cm³) (28 days)	Dry density(g/cm³) (28 days)	Strengths (MPa) (28 days)
MB0	0.551	0.470	2.25
MB5	0.538	0.463	2.12
MB10	0.529	0.457	1.98
MB15	0.514	0.436	1.73

Table 7. Thermal conductivity coefficients of foamed mortar samples in a dry state

Labels of test series	Dry density(g/cm³) (ρ)	Thermal conductivity coefficient (k) (W/mK)	Temperature (°C)
MB0	0.470	0.195	23.73
MB5	0.463	0.151	25.45
MB10	0.457	0.134	23.52
MB15	0.436	0.112	24.97

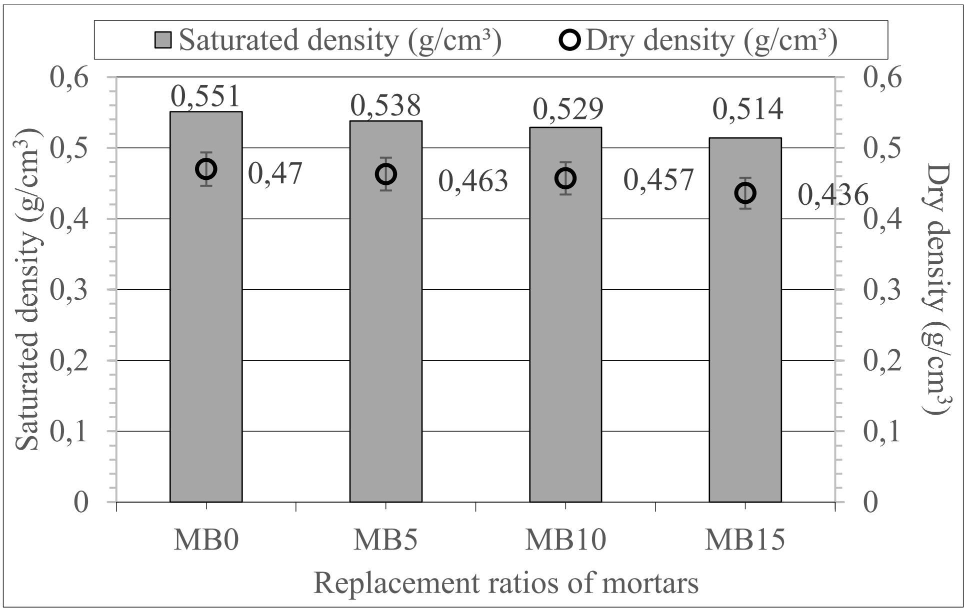

Figure 6. Saturated-dry densities of foamed mortar samples

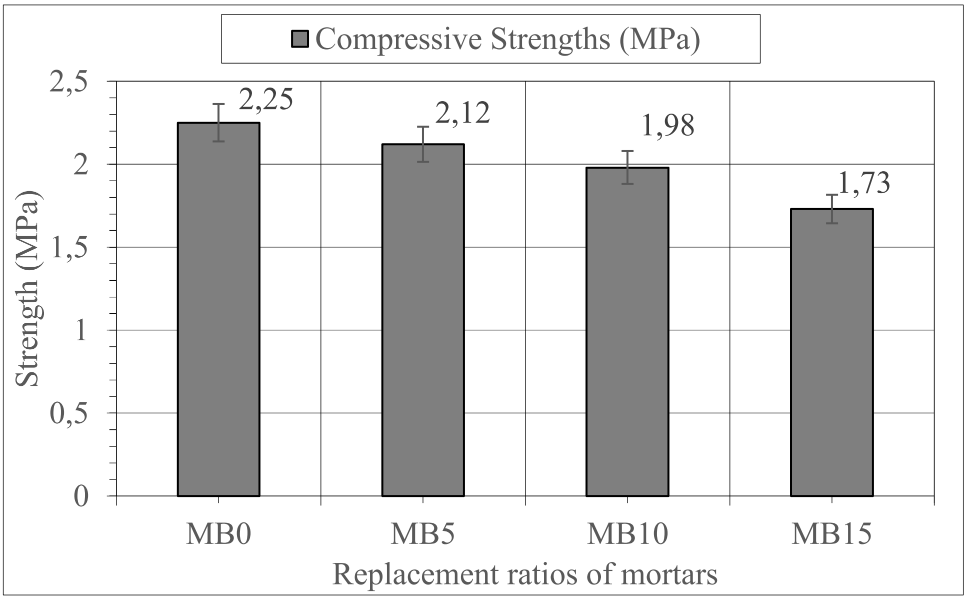

Figure 7. Strengths of foamed mortar samples

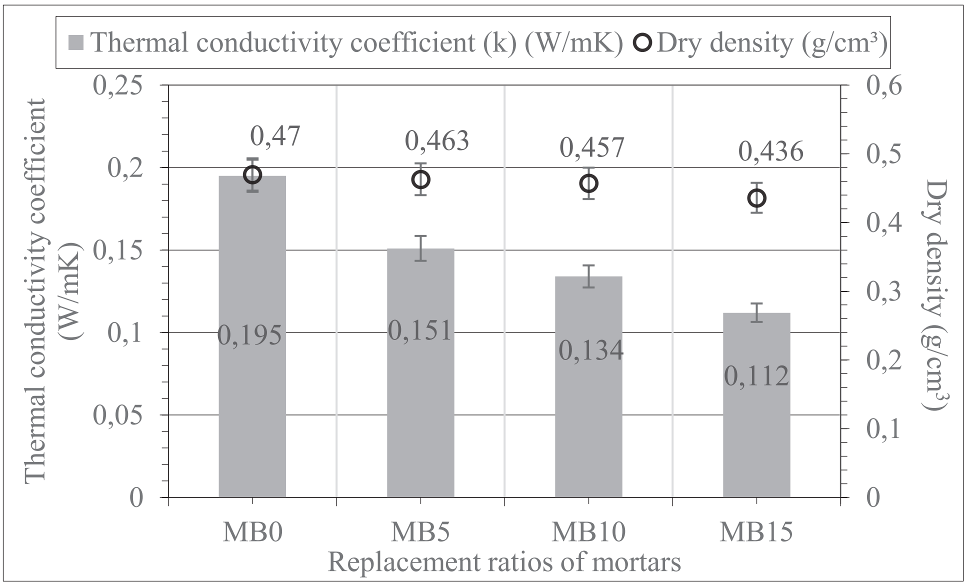

Figure 8. Dry densities and thermal conductivity coefficients of foamed mortar samples

Saturated and dry densities of foamed mortar samples (MB5, MB10, MB15) containing bentonite blended cements decreased with the increase of replacement ratios (Table 6). Because density of bentonite is lower as 17.04% than that of Portland cement.

The compressive strengths of the foamed mortars containing the blended cements were lower than that of the mortars containing Portland cement. Compressive strengths of foam mortar samples are in range of 1.73-2.25 MPa (Table 6). The test results are compatible with the 1.5 MPa limit value given in TS EN 13655 [14] for foamed concretes.

The thermal conductivity of mortars decreased with the increase of bentonite replacement ratio. This decrease could be mainly attributed to the fact that the density of mortars containing bentonite decreased with the increase of bentonite content due to the lower density of bentonite. The thermal conductivity of mortars containing PC is higher than that of mortars containing bentonite. This is related to the cited lower density mechanism. As seen, bentonite additive improved the thermal insulation ability of mortars.

Thermal conductivities of mortars with 15% bentonite replacement ratios were approximately 42.56% lower than those of mortars containing PC. In terms of thermal insulation ability and satisfying strength values, it could be concluded that the mortars containing bentonite with optimum 15% replacement ratio can be accepted as a preferable option in building applications.

4. CONCLUSIONS

The compressive strengths of foamed mortars containing bentonite blended cements decreased with the increase of replacement ratios of additive. Although there is a decrease in the compressive strengths of mortars containing bentonite additives, the strength of mortars was at acceptable levels with up to 15% replacement ratio.

In summary, according to the results of this experimental study, when it is simultaneously evaluated in terms of strength, thermal insulation performance, cost and environmental awareness at applications of foamed concrete which are becoming increasingly common in the market for especially in energy efficient building designs, it is seen that thermal insulation performances of foamed concretes produced by using bentonite blended cement could be improved up to 15% replacement ratio.

This study includes only preliminary test results. Therefore, in future studies, it is recommended to do durability and later ages strength tests on bentonites obtained from different origins.

REFERENCES

1. World Population Prospects 2019. United Nations, New York, (Date of access: 18.05.2022), https://population.un.org/wpp/
2. Global Energy Review 2021, (Date of access: 18.05.2022), https://iea.blob.core.windows.net/assets/d0031107-401d-4a2f-a48b-9eed19457335/GlobalEnergyReview2021.pdf
3. Mayur Madhukar Maske1, Dr. Nandkumar Krishnarao Patil, Dr. Amey Deepak Katdare, Review of application of plain and calcined bentonite as a cement blending material in concrete and mortar, Psychology And Education, Vol: 58, No: 1, 5873-5878, 2021.
4. Yue Xie, Jun Li, Zhongyuan Lu, Jun Jiang, Yunhui Niu, Preparation and properties of ultra-lightweight EPS concrete based on pre-saturated bentonite, Construction and Building Materials, Vol: 195, 505–514, 2019.
5. Xiao Zhao, Siong-Kang Lim, Cher-Siang Tan, Bo Li, Tung-Chai Ling, Runqiu Huang and Qingyuan Wang, Properties of Foamed Mortar Prepared with Granulated Blast-Furnace Slag, *Materials,* Vol:*8*, 462-473, 2015.
6. Yasemin Akgün, Talha Yılmaz, Thermal performance of mortars/concretes containing analcime, Journal of Thermal Analysis and Calorimetry Vol: 146,47–60, 2021.
7. Khamphee Jitchaiyaphum, Theerawat Sinsiri, Chai Jaturapitakkul, and Prinya Chindaprasirt, Cellular lightweight concrete containing high-calcium fly ash and natural zeolite, International Journal of Minerals, Metallurgy and Materials, Vol: 20, No:5, 462, 2013.
8. Noureddine Mesboua, Khaled Benyounes, Abdelbaki Benmounah, Study of the impact of bentonite on the physicomechanical and flow properties of cement grout, Cogent Engineering, Vol: 5, 2018.
9. Sajan K. Jose, Mini Soman & Sheela Evangeline Y, Ecofriendly building blocks using foamed concrete with ground granulated blast furnace slag, International Journal of Sustainable Engineering, Vol: 14, No: 4, 776-784, 2021.
10. CEN EN 197–1 Cement Part 1: Composition, specification and conformity criteria for common cements. European Committee for Standardization. Brussels, Belgium; 2012.
11. CEN EN 196–1 Methods of testing cement—Part 1: Determination of strength. European Committee for Standardization. Brussels, Belgium; 2016.
12. CEN EN ISO 8990 Thermal insulation—Determination of steady-State thermal transmission properties-Calibrated and guarded hot box. European Committee for Standardization. Brussels, Belgium;1989.
13. CEN EN ISO 6946 Building components and building elements-Thermal resistance and thermal transmittance-Calculation methods. European Committee for Standardization. Brussels, Belgium; 2017.
14. TS EN 13655. (2015). Kâgir birimler-Özellikler-Köpük beton kâgir birimler. TürkStandardları Enstitüsü (TSE), Ankara.

ON SOLUTIONS OF INTEGRAL EQUATIONS IN GEOMETRIC ANALYSIS

Arzu Bal[1], Numan Yalçın[2] and Mutlu Dedetürk[1]

[1] Department of Mathematical Engineering, University of Gumushane, Gümüşhane, Turkey

arzucavusculubal@gmail.com,

mutludedeturk@gumushane.edu.tr,

[2]Gumushane Vocational School, Department of Electronics and Automation, University of Gumushane, Gümüşhane, Turkey

numan@gumushane.edu.tr,

Abstract

In this paper, we will give definitions of types of integral equations on geometric analysis. And solutions of different types of integral equations in geometric analysis via multiplicative power series method will be examined.

Keywords: Multiplicative integral equation; Multiplicative Fredholm integral equation; Multiplicative Volterra integral equation; Multiplicative Volterra-Fredholm integral equation.

1. INTRODUCTION

Integral equations have been used since the 18th century for the solution of many problems in applied mathematics, mathematical physics and engineering. Integral equations have started to be used in the field of engineering and other basic sciences and have gained an important place because they can be used in applications of differential equations. Since integral equations have a very wide field of research, it is not possible to establish a theory that covers all integral equations. For this reason, integral equations are examined separately according to their properties. Considering these separate examinations, it is divided into two as Volterra and Fredholm Integral Equations. In the end of 19th century Volterra and in the beginning of 20th century I. Fredholm, D. Hilbert, E. Schmidt contributed to the development of a general theory of integral equations.

It is not so easy to explain some problems in mathematics with known classical concepts and to find analytical solutions. For the solution of such problems, geometric (multiplicative) analysis including multiplicative derivative and multiplicative integral has been developed as an alternative. It has been seen that geometric analysis brings ease of application to some problems and in some cases gives more effective and faster results than classical analysis. In this study, the solution of multiplicative integral equations is investigated by using the definition and properties of multiplicative integral. These solutions are found with the help of the multiplicative power series method.

2. MULTIPLICATIVE INTEGRAL EQUATIONS AND MULTIPLICATIVE POWER SERIES METHOD

Definition 2.1. Suppose $g(x)$ and $K(x,t)$ are given functions and b is a given positive real number. Then the equation

$$\psi(x) = g(x) * \int_0^b \psi(t)^{K(x,t)dt}$$

is called the multiplicative Fredholm integral equation (MFIE) of the second kind.

Definition 2.2. Suppose $g(x)$ and $K(x,t)$ are given functions and b is a given positive real number. Then the equation

$$\psi(x) = g(x) * \int_0^x \psi(t)^{K(x,t)dt}$$

is called a multiplicative Volterra integral equation (MVIE) of the second kind.

Definition 2.3. Suppose $g(x)$ and $K_1(x,t), K_2(x,t)$ are given functions and b is a given positive real number. Then the equation

$$\psi(x) = g(x) * \int_0^x \psi(t)^{K_1(x,t)dt} * \int_0^b \psi(t)^{K_2(x,t)dt}$$

is called a multiplicative Volterra-Fredholm integral equation (MVFIE) of the second kind.

3. MULTIPLICATIVE FREDHOLM INTEGRAL EQUATION (MFIE)

3.1. Solution of the MFIE with Kernel $K(x,t) = 1$

Theorem 3.1. Suppose the MFIE

$$\psi(x) = g(x) * \int_0^b \psi(t)^{dt}$$

is given. Here $b \in (0,\infty) \setminus \{1\}$. Also let $g(x) = \prod_{i=0}^{\infty}(c_i)^{x^i}$ be the multiplicative power series (MPS) of $g(x)$. Then the multiplicative power series solution

$$\psi(x) = \prod_{n=0}^{\infty}(a_i)^{x^i}$$

has bases $a_i,\ i \geq 0$ which can be calculated by the below formulas.

$$a_i = c_i\,, \qquad i \geq 1$$

$$a_0 = \left[c_0 \cdot \prod_{k=1}^{\infty}(a_k)^{b^{k+1}/(k+1)}\right]^{\frac{1}{(1-b)}}$$

Proof.

$$\psi(x) = g(x) * \int_0^b \psi(t)^{dt}$$

$$\prod_{i=0}^{\infty}(a_i)^{x^i} = \prod_{i=0}^{\infty}(c_i)^{x^i} \cdot * \int_0^b \left[\prod_{k=0}^{\infty}(a_k)^{t^k}\right]^{dt}$$

$$\prod_{i=0}^{\infty}(a_i)^{x^i} = \prod_{i=0}^{\infty}(c_i)^{x^i} \cdot \prod_{k=0}^{\infty} * \int_0^b \left[(a_k)^{t^k}\right]^{dt}$$

$$\prod_{i=0}^{\infty}(a_i)^{x^i} = \prod_{i=0}^{\infty}(c_i)^{x^i} \cdot \prod_{k=0}^{\infty}(a_k)^{\left(\frac{t^{k+1}}{k+1}\right)_{t=0}^{b}}$$

$$\prod_{i=0}^{\infty}(a_i)^{x^i} = c_0 \cdot \prod_{i=1}^{\infty}(c_i)^{x^i} \cdot \prod_{k=0}^{\infty}(a_k)^{\frac{b^{k+1}}{k+1}}$$

$$a_0 \cdot \prod_{i=1}^{\infty}(a_i)^{x^i} = \left[c_0 \cdot \prod_{k=0}^{\infty}(a_k)^{\frac{b^{k+1}}{k+1}}\right] \cdot \prod_{i=1}^{\infty}(c_i)^{x^i}$$

From here we have

$a_i = c_i\,, \qquad i \geq 1$

and

$$a_0 = c_0 \cdot \prod_{k=0}^{\infty}(a_k)^{\left(\frac{b^{k+1}}{k+1}\right)}$$

$$a_0 = c_0 \cdot (a_0)^b \cdot \prod_{k=1}^{\infty}(a_k)^{\left(\frac{b^{k+1}}{k+1}\right)}$$

$$(a_0)^{1-b} = c_0 \cdot \prod_{k=1}^{\infty}(a_k)^{\left(\frac{b^{k+1}}{k+1}\right)}$$

Thus we get

$a_i = c_i\,, \qquad i \geq 1$

$$a_0 = \left[c_0 \cdot \prod_{k=1}^{\infty}(a_k)^{\left(\frac{b^{k+1}}{k+1}\right)}\right]^{\frac{1}{(1-b)}}$$

3.2. Solution of The MFIE with Kernel $K(x)$ Depending Only on The Variable x

Below, we will give the solution of MFIE with the Kernel $K(x)$ depending only on the variable x.

Theorem 3.2. Suppose the MFIE

$$\psi(x) = g(x) * \int_0^b \psi(t)^{K(x)dt}$$

$$\psi(x) = g(x) \cdot \left[* \int_0^b \psi(t)^{dt}\right]^{K(x)}$$

is given. Also, let $g(x) = \prod_{i=0}^{\infty}(c_i)^{x^i}$ be the multiplicative power series of $g(x)$ and $K(x) = \sum_{i=0}^{\infty} k_i x^i$ be the additive power series of $K(x)$. Here $b > 0$. Then the multiplicative power series solution

$$\psi(x) = \prod_{i=0}^{\infty}(a_i)^{x^i}$$

have bases $a_i,\ i \geq 0$ which can be calculated by the below formulas.

$$a_i = \left[\left(\prod_{j=0}^{\infty}(c_j)^{\left(\frac{b^{j+1}}{j+1}\right)}\right)^{1/\left[1-\sum_{j=0}^{\infty} k_j \cdot \frac{b^{j+1}}{j+1}\right]}\right]^{k_i} \cdot c_i$$

Proof.

$$\psi(x) = g(x) * \int_0^b \psi(t)^{K(x)dt}$$

$$\psi(x) = g(x) \cdot \left[* \int_0^b \psi(t)^{dt}\right]^{K(x)}$$

Let us say $A =* \int_0^b \psi(t)^{dt}$, then we have

$$\psi(x) = g(x) \cdot \left[* \int_0^b \psi(t)^{dt}\right]^{K(x)}$$

$$\prod_{i=0}^{\infty}(a_i)^{x^i} = \prod_{i=0}^{\infty}(c_i)^{x^i} \cdot A^{K(x)}$$

$$\prod_{i=0}^{\infty}(a_i)^{x^i} = \prod_{i=0}^{\infty}(c_i)^{x^i} \cdot A^{\sum_{i=0}^{\infty} k_i x^i}$$

$$\prod_{i=0}^{\infty}(a_i)^{x^i} = \prod_{i=0}^{\infty}(c_i)^{x^i} \cdot \prod_{i=0}^{\infty}(A^{k_i})^{x^i}$$

and let us define $b_i = (A)^{k_i}$. Then we can write

$$\prod_{i=0}^{\infty}(a_i)^{x^i} = \prod_{i=0}^{\infty}(c_i)^{x^i} \cdot \prod_{i=0}^{\infty}(b_i)^{x^i}$$

$$\prod_{i=0}^{\infty}(a_i)^{x^i} = \prod_{i=0}^{\infty}(b_i \cdot c_i)^{x^i} \Rightarrow a_i = (b_i \cdot c_i)$$

$$\psi(t) = \prod_{i=0}^{\infty}(b_i \cdot c_i)^{t^i}$$

Now we will find the value of A

$$A =* \int_0^b \psi(t)^{dt} \Rightarrow A =* \int_0^b \left[\prod_{n=0}^{\infty}(b_i \cdot c_i)^{t^i}\right]^{dt}$$

$$A=\prod_{i=0}^{\infty}(b_i\cdot c_i)^{\int_0^b t^i dt} \Rightarrow A=\prod_{i=0}^{\infty}(b_i\cdot c_i)^{\frac{b^{i+1}}{(i+1)}}$$

$$A=\prod_{i=0}^{\infty}(A^{k_i}\cdot c_i)^{\frac{b^{i+1}}{(i+1)}}$$

$$A=\left[\prod_{i=0}^{\infty}(A)^{k_i\cdot\frac{b^{i+1}}{(i+1)}}\right]\cdot\left[\prod_{i=0}^{\infty}(c_i)^{\frac{b^{i+1}}{(i+1)}}\right]$$

$$A=\left[(A)^{\sum_{i=0}^{\infty}k_i\cdot\frac{b^{i+1}}{(i+1)}}\right]\cdot\left[\prod_{i=0}^{\infty}(c_i)^{\frac{b^{i+1}}{(i+1)}}\right]$$

Putting the powers of A to the same side, we write

$$(A)^{1-\sum_{i=0}^{\infty}k_i\cdot\frac{b^{i+1}}{(i+1)}}=\prod_{i=0}^{\infty}(c_i)^{\frac{b^{i+1}}{(i+1)}}$$

$$A=\left[\prod_{i=0}^{\infty}(c_i)^{\frac{b^{i+1}}{(i+1)}}\right]^{\frac{1}{1-\sum_{i=0}^{\infty}k_i\cdot\frac{b^{i+1}}{(i+1)}}}$$

So we have

$$\psi(x)=\prod_{i=0}^{\infty}(a_i)^{x^i}=\prod_{i=0}^{\infty}(b_i\cdot c_i)^{x^i}=\prod_{i=0}^{\infty}(A^{k_i}\cdot c_i)^{x^i}$$

$$\prod_{i=0}^{\infty}(a_i)^{x^i}=\prod_{i=0}^{\infty}\left\{\left[\left(\prod_{j=0}^{\infty}(c_j)^{(b^{j+1}/j+1)}\right)^{1/\left[1-\sum_{j=0}^{\infty}k_j\cdot\frac{b^{j+1}}{j+1}\right]}\right]^{k_i}\cdot c_i\right\}^{x^i}$$

$$a_i=\left[\left(\prod_{j=0}^{\infty}(c_j)^{(b^{j+1}/j+1)}\right)^{1/\left[1-\sum_{j=0}^{\infty}k_j\cdot\frac{b^{j+1}}{j+1}\right]}\right]^{k_i}\cdot c_i$$

3.3. Solution of The MFIE with Kernel $K(t)$ Depending Only on The Variable t

Theorem 3.3. Suppose the MFIE

$$\psi(x)= g(x)*\int_0^b \psi(t)^{K(t)dt}$$

is given. Also, let $g(x)=\prod_{i=0}^{\infty}(c_i)^{x^i}$ be the multiplicative power series of $g(x)$ and $K(x)=\sum_{j=0}^{\infty}k_j t^j$ be the additive power series of $K(t)$. Here $b>0$. Then the multiplicative power series solution

$$\psi(x)=\prod_{i=0}^{\infty}(a_i)^{x^i}$$

have bases $a_i,\ \ i\geq 0$ which can be calculated by the below formulas.

$$\begin{cases} a_i = c_i, \qquad i \geq 1 \\ a_0 = \left[c_0 \cdot \prod_{n=1}^{\infty} (a_n)^{\sum_{j=0}^{\infty}\left(k_j \cdot \frac{b^{n+j+1}}{n+j+1}\right)} \right]^{\frac{1}{1-\sum_{j=0}^{\infty}\left(k_j \cdot \frac{b^{j+1}}{j+1}\right)}} . \end{cases}$$

Proof.

$$\psi(x) = g(x) * \int_0^b \psi(t)^{K(t)dt}$$

$$\prod_{i=0}^{\infty} (a_i)^{x^i} = \prod_{i=0}^{\infty} (c_i)^{x^i} \cdot * \int_0^b \left[\prod_{n=0}^{\infty} (a_n)^{t^k \cdot \sum_{j=0}^{\infty} k_j \cdot t^j} \right]^{dt}$$

$$\prod_{i=0}^{\infty} (a_i)^{x^i} = \prod_{i=0}^{\infty} (c_i)^{x^i} \cdot \prod_{n=0}^{\infty} (a_n)^{\int_0^b t^k \cdot \sum_{j=0}^{\infty} k_j \cdot t^j dt}$$

$$\prod_{i=0}^{\infty} (a_i)^{x^i} = \prod_{i=0}^{\infty} (c_i)^{x^i} \cdot \prod_{n=0}^{\infty} (a_n)^{\sum_{j=0}^{\infty} \int_0^b k_j \cdot t^{n+j} dt}$$

and we get

$$\prod_{i=0}^{\infty} (a_i)^{x^i} = \prod_{i=0}^{\infty} (c_i)^{x^i} \cdot \prod_{n=0}^{\infty} (a_n)^{\sum_{j=0}^{\infty}\left(k_j \cdot \frac{t^{n+j+1}}{n+j+1}\right)}$$

$$\prod_{i=0}^{\infty} (a_i)^{x^i} = \prod_{i=0}^{\infty} (c_i)^{x^i} \cdot \prod_{n=0}^{\infty} (a_n)^{\sum_{j=0}^{\infty}\left(k_j \cdot \frac{t^{n+j+1}}{n+j+1}\right)_{t=0}^{b}}$$

$$\prod_{i=0}^{\infty} (a_i)^{x^i} = \prod_{i=0}^{\infty} (c_i)^{x^i} \cdot \prod_{n=0}^{\infty} (a_n)^{\sum_{j=0}^{\infty}\left(k_j \cdot \frac{b^{n+j+1}}{n+j+1}\right)}$$

$$a_0 \cdot \prod_{i=1}^{\infty} (a_i)^{x^i} = \left[c_0 \cdot \left(\prod_{n=0}^{\infty} (a_n)^{\sum_{j=0}^{\infty}\left(k_j \cdot \frac{b^{n+j+1}}{n+j+1}\right)} \right) \right] \cdot \prod_{i=1}^{\infty} (c_i)^{x^i}$$

From here we have

$a_i = c_i$, $\qquad i \geq 1$

and

$$a_0 = c_0 \cdot \prod_{n=0}^{\infty} (a_n)^{\sum_{j=0}^{\infty}\left(k_j \cdot \frac{b^{n+j+1}}{n+j+1}\right)}$$

$$a_0 = c_0 \cdot (a_0)^{\sum_{j=0}^{\infty}\left(k_j \cdot \frac{b^{j+1}}{j+1}\right)} \cdot \prod_{n=1}^{\infty} (a_n)^{\sum_{j=0}^{\infty}\left(k_j \cdot \frac{b^{n+j+1}}{n+j+1}\right)}$$

$$a_0 = \left[c_0 \cdot \prod_{n=1}^{\infty} (a_n)^{\sum_{j=0}^{\infty}\left(k_j \cdot \frac{b^{n+j+1}}{n+j+1}\right)} \right]^{\frac{1}{1-\sum_{j=0}^{\infty}\left(k_j \cdot \frac{b^{j+1}}{j+1}\right)}}$$

4. MULTIPLICATIVE VOLTERRA INTEGRAL EQUATION (MVIE)

Theorem 4.1. Suppose the below MVIE is given

$$\psi(x) = g(x) * \int_0^x \psi(t)^{K(x,t)dt}$$

And also let's assume that $\psi(x) = \prod_{i=0}^{\infty}(a_i)^{x^i}$ and $g(x) = \prod_{i=0}^{\infty}(c_i)^{x^i}$ are multiplicative power series of the unknown function $\psi(x)$ and the given function $g(x)$, respectively and let $K(x,t) = \sum_{n=0}^{\infty}\sum_{j=0}^{\infty} k_{n,j} \cdot x^n t^j$ be the additive power series of $K(x,t)$. Then the solution of the above equation is given as:

$$\psi(x) = \prod_{i=0}^{\infty}(a_i)^{x^i}$$

Where

$$\begin{cases} a_0 = c_0 \\ a_i = c_i \cdot \prod_{n=0}^{i-1}(a_n)^{\sum_{j=0}^{i-1-n}\frac{k_{i-1-n-j,j}}{n+j+1}}, \quad i \geq 1 \end{cases}$$

Proof.

$$\psi(x) = g(x) \cdot * \int_0^x \psi(t)^{K(x,t)dt}$$

$$\prod_{i=0}^{\infty}(a_i)^{x^i} = \prod_{i=0}^{\infty}(c_i)^{x^i} \cdot * \int_0^x \left[\prod_{i=0}^{\infty}(a_i)^{t^i}\right]^{\sum_{n,j=0}^{\infty} k_{n,j}\cdot x^n t^j dt}$$

$$\prod_{i=0}^{\infty}(a_i)^{x^i} = \prod_{i=0}^{\infty}(c_i)^{x^i} \cdot \prod_{i=0}^{\infty} * \int_0^x (a_i)^{t^i \cdot \sum_{n,j=0}^{\infty} k_{n,j}\cdot x^n t^j dt}$$

$$\prod_{i=0}^{\infty}(a_i)^{x^i} = \prod_{i=0}^{\infty}(c_i)^{x^i} \cdot \prod_{i=0}^{\infty}(a_i)^{\int_0^x \sum_{n=0}^{\infty} x^n \cdot \sum_{j=0}^{\infty} k_{n,j}\cdot t^{i+j}dt}$$

$$\prod_{i=0}^{\infty}(a_i)^{x^i} = \prod_{i=0}^{\infty}(c_i)^{x^i} \cdot \prod_{i=0}^{\infty}(a_i)^{\sum_{n=0}^{\infty} x^n \cdot \sum_{j=0}^{\infty} k_{n,j}\cdot \int_0^x t^{i+j}dt}$$

$$\prod_{i=0}^{\infty}(a_i)^{x^i} = \prod_{i=0}^{\infty}(c_i)^{x^i} \cdot \prod_{i=0}^{\infty}(a_i)^{\sum_{n=0}^{\infty} x^n \cdot \sum_{j=0}^{\infty} k_{n,j}\cdot \left(\frac{t^{i+j+1}}{i+j+1}\right)_{t=0}^{x}}$$

Consequently, we write

$$\prod_{i=0}^{\infty}(a_i)^{x^i} = \prod_{i=0}^{\infty}(c_i)^{x^i} \cdot \prod_{i=0}^{\infty}(a_i)^{\sum_{n=0}^{\infty} x^n \cdot \sum_{j=0}^{\infty} k_{n,j}\cdot \left(\frac{x^{i+j+1}}{i+j+1}\right)}$$

$$\prod_{i=0}^{\infty}(a_i)^{x^i} = \prod_{i=0}^{\infty}(c_i)^{x^i} \cdot \prod_{i=0}^{\infty}(a_i)^{\sum_{n=0}^{\infty}\sum_{j=0}^{\infty}\left(\frac{k_{n,j}}{i+j+1}\cdot x^{i+n+j+1}\right)}$$

$$\prod_{i=0}^{\infty}(a_i)^{x^i} = \prod_{i=0}^{\infty}(c_i)^{x^i} \cdot \prod_{i=0}^{\infty}(a_i)^{\sum_{n=0}^{\infty}\sum_{j=0}^{n}\left(\frac{k_{n-j,j}}{i+j+1}\cdot x^{i+n+1}\right)}$$

$$\prod_{i=0}^{\infty}(a_i)^{x^i} = \prod_{i=0}^{\infty}(c_i)^{x^i} \cdot \prod_{i=0}^{\infty}(a_i)^{\sum_{n=0}^{\infty}\sum_{j=0}^{n}\left(\frac{k_{n-j,j}}{i+j+1}\right)\cdot x^{i+n+1}}$$

$$\prod_{i=0}^{\infty}(a_i)^{x^i} = \prod_{i=0}^{\infty}(c_i)^{x^i} \cdot \prod_{i=0}^{\infty}\prod_{n=0}^{\infty}\left[(a_i)^{\sum_{j=0}^{n}\left(\frac{k_{n-j,j}}{i+j+1}\right)\cdot x^{i+n+1}}\right]$$

Here we define

$$D_{i,n} = (a_i)^{\sum_{j=0}^{n}\left(\frac{k_{n-j,j}}{i+j+1}\right)}$$

and we have

$$\prod_{i=0}^{\infty}(a_i)^{x^i} = \prod_{i=0}^{\infty}(c_i)^{x^i} \cdot \prod_{i=0}^{\infty}\prod_{n=0}^{\infty}\left[\left(D_{i,n}\right)^{x^{i+n+1}}\right]$$

$$\prod_{i=0}^{\infty}(a_i)^{x^i} = \prod_{i=0}^{\infty}(c_i)^{x^i} \cdot \prod_{i=0}^{\infty}\left[\prod_{n=0}^{i}\left(D_{i-n,n}\right)^{x^{i+1}}\right]$$

$$\prod_{i=0}^{\infty}(a_i)^{x^i} = \prod_{i=0}^{\infty}(c_i)^{x^i} \cdot \prod_{i=0}^{\infty}\left[\prod_{n=0}^{i}\left(D_{i-n,n}\right)\right]^{x^{i+1}}$$

$$\prod_{i=0}^{\infty}(a_i)^{x^i} = \prod_{i=0}^{\infty}(c_i)^{x^i} \cdot \prod_{i=1}^{\infty}\left[\prod_{n=1}^{i-1}\left(D_{i-n-1,n}\right)\right]^{x^i}$$

$$\prod_{i=0}^{\infty}(a_i)^{x^i} = c_0 \cdot \prod_{i=1}^{\infty}\left[c_i \cdot \prod_{n=1}^{i-1}\left(D_{i-n-1,n}\right)\right]^{x^i}$$

$$a_0 \cdot \prod_{i=1}^{\infty}(a_i)^{x^i} = c_0 \cdot \prod_{i=1}^{\infty}\left[c_i \cdot \prod_{n=1}^{i-1}\left(D_{n,i-n-1}\right)\right]^{x^i}$$

and thus

$$a_0 = c_0$$

$$a_i = c_i \cdot \prod_{n=1}^{i-1}\left(D_{n,i-n-1}\right), \qquad i \geq 1$$

At this point calculating $D_{n,i-n-1}$

$$D_{u,v} = (a_u)^{\left(\sum_{j=0}^{u} \frac{k_{u-j,j}}{u+j+1}\right)}$$

$$D_{n,i-n-1} = (a_u)^{\left(\sum_{j=0}^{i-n-1} \frac{k_{i-n-1-j,j}}{n+j+1}\right)}$$

and using its worth we have

$$a_i = c_i \cdot \prod_{n=1}^{i-1}\left(D_{n,i-n-1}\right)$$

$$a_i = c_i \cdot \prod_{n=1}^{i-1}(a_n)^{\left(\sum_{j=0}^{i-n-1} \frac{k_{i-n-1-j,j}}{n+j+1}\right)}, \qquad i \geq 1$$

Hence the solution $\psi(x) = \prod_{i=0}^{\infty}(a_i)^{x^i}$ has bases

$$
\begin{cases}
a_0 = c_0 \\
a_i = c_i \cdot \prod_{n=0}^{i-1} (a_u)^{\sum_{j=0}^{i-n-1} \frac{k_{i-n-1-j,j}}{n+j+1}}, \quad i \geq 1
\end{cases}
$$

5. Multiplicative Volterra-Fredholm Integral Equation (MVFIE)

5.1 Solution of the MVFIE with Kernel $\boldsymbol{K_1(x,t) = K_2(x,t) = 1}$

Theorem 5.1. Suppose the MVFIE

$$
\psi(x) = g(x) * \int_0^x \psi(t)^{dt} \cdot * \int_0^b \psi(t)^{dt}
$$

is given. Here $b \in (0,\infty) \setminus \{1\}$. Also, let $g(x) = \prod_{i=0}^{\infty} (c_i)^{x^i}$ be the multiplicative power series of $g(x)$. Then the multiplicative power series solution

$$
\psi(x) = \prod_{i=0}^{\infty} (a_i)^{x^i}
$$

has bases a_i, $i \geq 0$ which can be calculated by the below formulas.

$$
a_i = \left(\prod_{k=1}^{i} (c_k)^{k!/i!} \right) \cdot (a_0)^{\frac{1}{i!}}, \qquad i \geq 1
$$

$$
a_0 = \left\{ \left(c_0 \cdot (c_1)^{b^2/2} \right) \cdot \prod_{i=2}^{\infty} \left[\prod_{k=1}^{i} (c_k)^{k!/i!} \right]^{\frac{b^{i+1}}{i+1}} \right\}^{\frac{1}{1-b-e^b}}
$$

Proof. Let

$$
\psi(x) = \prod_{i=0}^{\infty} (a_i)^{x^i}
$$

$$
g(x) = \prod_{i=0}^{\infty} (c_i)^{x^i}
$$

be the multiplicative power series of $\psi(x)$ and $g(x)$, respectively.

$$
\psi(x) = g(x) \cdot \left(* \int_0^x \psi(t)^{dt} \right) \cdot \left(* \int_0^b \psi(t)^{dt} \right)
$$

$$
\prod_{i=0}^{\infty} (a_i)^{x^i} = \prod_{i=0}^{\infty} (c_i)^{x^i} \cdot \left[* \int_0^x \left(\prod_{i=0}^{\infty} (a_i)^{t^i} \right)^{dt} \right] \cdot \left[* \int_0^b \left(\prod_{i=0}^{\infty} (a_i)^{t^i} \right)^{dt} \right]
$$

$$
\prod_{i=0}^{\infty} (a_i)^{x^i} = \left[\prod_{i=0}^{\infty} (c_i)^{x^i} \right] \cdot \prod_{i=0}^{\infty} \left[* \int_0^x \left([a_i]^{t^i} \right)^{dt} \right] \cdot \prod_{i=0}^{\infty} \left[* \int_0^b \left([a_i]^{t^i} \right)^{dt} \right]
$$

$$
\prod_{i=0}^{\infty} (a_i)^{x^i} = \left[\prod_{i=0}^{\infty} (c_i)^{x^i} \right] \cdot \left[\prod_{i=0}^{\infty} (a_i)^{\frac{x^{i+1}}{i+1}} \right] \cdot \left[\prod_{i=0}^{\infty} (a_i)^{\frac{b^{i+1}}{i+1}} \right]
$$

$$\prod_{i=0}^{\infty}(a_i)^{x^i}=\left[\prod_{i=0}^{\infty}(c_i)^{x^i}\right]\cdot\left[\prod_{i=1}^{\infty}(a_{i-1})^{\frac{x^i}{i}}\right]\cdot\left[\prod_{i=0}^{\infty}(a_i)^{\frac{b^{i+1}}{i+1}}\right]$$

$$a_0\cdot\prod_{i=1}^{\infty}(a_i)^{x^i}=\left\{c_0\cdot\prod_{i=0}^{\infty}(a_i)^{\frac{b^{i+1}}{i+1}}\right\}\cdot\prod_{i=1}^{\infty}\left[c_i\cdot(a_{i-1})^{\frac{1}{i}}\right]^{x^i}$$

Thus we have

$$a_0=c_0\cdot\prod_{i=0}^{\infty}(a_i)^{\frac{b^{i+1}}{i+1}}\quad and\quad a_i=c_i\cdot(a_{i-1})^{\frac{1}{i}},\qquad i\geq 1$$

$$a_0=c_0\cdot(a_0)^b\cdot\prod_{i=1}^{\infty}(a_i)^{\frac{b^{i+1}}{i+1}}$$

$$(a_0)^{1-b}=c_0\cdot\prod_{i=1}^{\infty}(a_i)^{\frac{b^{i+1}}{i+1}}$$

$$a_0=\left\{c_0\cdot\prod_{i=1}^{\infty}(a_i)^{\frac{b^{i+1}}{i+1}}\right\}^{\frac{1}{1-b}}$$

First we will a_n with respect to a_0

$$a_i=c_i\cdot(a_{i-1})^{\frac{1}{i}}$$

$a_1=c_1\cdot a_0$	$a_1=(c_1)^{\frac{1!}{1!}}\cdot(a_0)^{\frac{1}{1!}}$
$a_2=c_2\cdot(a_1)^{1/2}=c_2\cdot(c_1\cdot a_0)^{\frac{1}{2}}$	
$a_2=c_2\cdot(c_1)^{\frac{1}{2}}\cdot(a_0)^{\frac{1}{2}}$	$a_2=(c_2)^{\frac{2!}{2!}}\cdot(c_1)^{\frac{1!}{2!}}\cdot(a_0)^{\frac{1}{2}}!$
$a_3=c_3\cdot(c_2)^{\frac{1}{3}}\cdot(c_1)^{\frac{1}{3!}}\cdot(a_0)^{\frac{1}{3!}}$	$a_3=(c_3)^{\frac{3!}{3!}}\cdot(c_2)^{\frac{2!}{3!}}\cdot(c_1)^{\frac{1!}{3!}}\cdot(a_0)^{\frac{1}{3!}}$
$a_4=c_4\cdot(a_3)^{\frac{1}{4}}$	
$a_4=c_4\cdot(c_3)^{\frac{1}{4}}\cdot(c_2)^{\frac{1}{3\cdot 4}}\cdot(c_1)^{\frac{1}{4!}}\cdot(a_0)^{\frac{1}{4!}}$	$a_4=(c_4)^{\frac{4!}{4!}}\cdot(c_3)^{\frac{3!}{4!}}\cdot(c_2)^{\frac{2!}{4!}}\cdot(c_1)^{\frac{1!}{4!}}\cdot(a_0)^{\frac{1}{4!}}$

So we have

$$a_i=\left(\prod_{k=1}^{i}(c_k)^{\frac{k!}{i!}}\right)\cdot(a_0)^{\frac{1}{i!}},\qquad i\geq 1$$

Then let's find a_0

$$a_i=\left(\prod_{k=1}^{i}(c_k)^{\frac{k!}{i!}}\right)\cdot(a_0)^{\frac{1}{i!}},\qquad i\geq 1$$

$$a_0=\left\{c_0\cdot\prod_{i=1}^{\infty}(a_i)^{\frac{b^{i+1}}{i+1}}\right\}^{\frac{1}{1-b}}$$

$$a_0=\left\{c_0\cdot\prod_{i=1}^{\infty}\left[\left(\prod_{k=1}^{i}(c_k)^{\frac{k!}{i!}}\right)\cdot(a_0)^{\frac{1}{i!}}\right]^{\frac{b^{i+1}}{i+1}}\right\}^{\frac{1}{1-b}}$$

$$a_0^{(1-b)}=c_0\cdot\prod_{i=1}^{\infty}\left[\left(\prod_{k=1}^{i}(c_k)^{\frac{k!}{i!}}\right)\cdot(a_0)^{\frac{1}{i!}}\right]^{\frac{b^{i+1}}{i+1}}$$

$$a_0^{(1-b)}=c_0\cdot\prod_{i=1}^{\infty}\left(\prod_{k=1}^{i}(c_k)^{\frac{k!b^{i+1}}{(i+1)!}}\right)\cdot\prod_{i=1}^{\infty}(a_0)^{\frac{b^{i+1}}{(i+1)!}}$$

$$a_0^{(1-b)}=c_0\cdot\prod_{i=1}^{\infty}\left(\prod_{k=1}^{i}(c_k)^{\frac{k!b^{i+1}}{(i+1)!}}\right)\cdot(a_0)^{\sum_{i=1}^{\infty}\frac{b^{i+1}}{(i+1)!}}$$

$$a_0^{(1-b)}=c_0\cdot\prod_{i=1}^{\infty}\left(\prod_{k=1}^{i}(c_k)^{\frac{k!b^{i+1}}{(i+1)!}}\right)\cdot(a_0)^{\sum_{i=2}^{\infty}\frac{b^{i}}{i!}}$$

$$a_0^{(1-b)}=c_0\cdot\prod_{i=1}^{\infty}\left(\prod_{k=1}^{i}(c_k)^{\frac{k!b^{i+1}}{(i+1)!}}\right)\cdot a_0{}^{(e^b-1-b)}$$

$$a_0^{(2-e^b)}=c_0\cdot\prod_{i=1}^{\infty}\left(\prod_{k=1}^{i}(c_k)^{\frac{k!b^{i+1}}{(i+1)!}}\right)$$

$$a_0=\left[c_0\cdot\prod_{i=1}^{\infty}\left(\prod_{k=1}^{i}(c_k)^{\frac{k!b^{i+1}}{(i+1)!}}\right)\right]^{1/(2-e^b)}$$

6. CONCLUSIONS

In this work, the definitions of types of integral equations on geometric analysis is given. The multiplicative power series method is presented for finding solutions of different types of integral equations in geometric analysis. Multiplicative Fredholm integral equations, multiplicative Volterra integral equations and multiplicative Fredholm-Volterra integral equations with different kernels are investigated.

REFERENCES

1. Fredholm, Erik I. (1903), "Sur une classe d'equations fonctionnelles" (PDF), Acta Mathematica, 27: 365–390, doi:10.1007/bf02421317.
2. Volterra, V., & Hostinsky, B. (1938). Opérations Infinitésimales linéares, Herman.
3. Lovitt, W.V.: Linear Integral Equations. Dover Publications Inc.,New York (1950).
4. Smithies, F.: Integral Equations. Cambridge University Press, London (1958).
5. Krasnov, M., Kiselev, K., Makarenko, G.: Problems and Exercises in Integral Equation. Mır Publishers, Moscow (1971).
6. Kiselev, A., Makeronko, G., Krasnov, M., (Cevdet Cerit trans.), Problems and Exercises in Integral Equations, Alfa Yayınları, ˙Istanbul, 1976.
7. Delves, L.V., Mohamed, J.L.: Computational Methods for Integral Equations. Cambridge University Press, New York (1985).
8. Upadhyay, S., Integral equation. 10.13140/RG.2.1.2854.8569. (2015).
9. Brunner, Hermann (2017). Volterra Integral Equations: An Introduction to Theory and Applications. Cambridge Monographs on Applied and Computational Mathematics. Cambridge, UK: Cambridge University Press. ISBN 978-1107098725.
10. Durmaz, H. (2019). Çarpımsal integral denklemler ve çarpımsal integral denklemlerin çarpımsal diferansiyel denklemler ile arasındaki ilişkisi (Master's thesis, Gümüşhane Üniversitesi).
11. GÜNGÖR, N., & DURMAZ, H. Multiplicative Volterra Integral Equations And The Relationship Between Multiplicative Differential Equations. Ikonion Journal of Mathematics, 2(2), 9-25.
12. Yalçın, N., & Dedeturk, M. (2021). Solutions of multiplicative ordinary differential equations via the multiplicative differential transform method. Aims Mathematics, 6(4), 3393-3409.
13. Yalçın, N., Dedeturk, M. Solutions of Multiplicative Linear Differential Equations via the Multiplicative Power Series Method., (In press).
14. Bashirov, A. E., Kurpınar, E. M., & Özyapıcı, A. (2008). Multiplicative calculus and its applications. Journal of mathematical analysis and applications, 337(1), 36-48.

15. Bashirov, A. E., Mısırlı, E., Tandoğdu, Y., & Özyapıcı, A. (2011). On modeling with multiplicative differential equations. Applied Mathematics-A Journal of Chinese Universities, 26(4), 425-438.
16. Çevik, C., & Özeken, Ç. C. (2016). Completion of Multiplicative Metric Spaces. Gazi University Journal of Science, 29(3).
17. Yalçın, N. (2021). The solutions of multiplicative Hermite differential equation and multiplicative Hermite polynomials. Rendiconti del Circolo Matematico di Palermo Series 2, 70(1), 9-21.
18. YALÇIN, N., & ÇELİK, E. Çarpımsal Cauchy-Euler ve Legendre Diferansiyel Denklemi. Gümüşhane Üniversitesi Fen Bilimleri Enstitüsü Dergisi, 9(3), 373-382.
19. Grossman, M., Katz, R.: Non-Newtonian calculus Lee Press, Pigeon Cove, MA, (1972).
20. Misirli, E., & Gurefe, Y. (2011). Multiplicative adams bashforth–moulton methods. Numerical Algorithms, 57(4), 425-439.
21. Misirli, E., & Ozyapici, A. (2009). Exponential approximations on multiplicative calculus. In Proc. Jangjeon Math. Soc (Vol. 12, No. 2, pp. 227-236).
22. Stanley, D. (1999). A multiplicative calculus. Problems, Resources, and Issues in Mathematics Undergraduate Studies, 9(4), 310-326.
23. Yalcin, N., Celik, E., & Gokdogan, A. (2016). Multiplicative Laplace transform and its applications. Optik, 127(20), 9984-9995.
24. Yalçın, N., & Çelik, E. (2018). The solution of multiplicative non-homogeneous linear differential equations. J. Appl. Math. Comput, 2(1), 27-36.
25. Yalcin, N., & Celik, E. (2018). Solution of multiplicative homogeneous linear differential equations with constant exponentials. New Trends in Mathematical Sciences, 6(2), 58-67.

A DOCUMENT ANALYSIS ON THE EFFECT OF FINLAND AND TURKISH EDUCATION SYSTEMS ON PISA SUCCESS

Zeynep Kübra Kazan[1], Sevda Türkiş[2], Elif Çil[3]
[1,2,3] Department of Mathematics and Science Education, Faculty of Education, Ordu University, Ordu Turkey

kazanzeynepkubra@gmail.com, sevdaturkis@odu.edu.tr, elifcil@odu.edu.tr

Abstract

The aim of the study examines the differences between the Finnish and Turkish education models and their impact on PISA success. By considering the factors behind the success in PISA exams, the similarities and differences between the two education models were determined with the document review method. It was aimed to make suggestions for increasing the success of PISA. A holistic approach is aimed at the Finnish curriculum, while a constructivist approach is aimed at the Turkish education model. Since 2018, it has been supported by the spiral approach in the Turkish curriculum. With the spiral approach, repetitive acquisitions and explanations at the different subject and grade levels are included, and learning outcomes that are holistic aim to be gained at once. It is planned to evaluate the effect of the Turkish education model, the constructivist approach model, and the Finnish education model on the science literacy of the Pisa exams.

Keywords: Finnish education system, Turkish education system, science literacy

1.INTRODUCTION

The development and welfare of countries is directly related to education, so education should be carried out meticulously and efficiency should be ensured. Each country aims at success by determining its own education policy. A country's educational success is measured by the international PISA Exam, which is evaluated on the same scale.

In the PISA application, it is evaluated not only how well students can remember what they have learned, but also how much they can benefit from their knowledge and skills in order to be able to use the knowledge and skills they have gained, to analyze and understand new situations they will encounter, and to make correct predictions on subjects they do not know (MEB, 2016).
Pisa exam is a qualified exam in which real learning is measured, not memorization system.
PISA implementation focuses on only one of the reading skills, mathematics and science literacy areas in each of the three-year periods. At the end of nine years, this cycle returns to the beginning (MEB, 2010). The reading skills based on the PISA application, which was carried out for the first time in Turkey in 2000, became mathematical literacy in 2003 and

science literacy in 2006. In 2009, reading skills became the main focus again. 27 In this cycle that started again, reading skills were revised and restructured. In the PISA 2015 application, the main weight was science literacy. Restructured reading skills in this direction include reading electronic texts, metacognitive and detailed reading contexts (OECD, 2009).

The PISA student population, which is applied on an international scale, consists of students who study at schools, regardless of school type, and who have completed at least six years of formal education, aged between 15 years 3 months and 16 years 2 months as of the date of the assessment. The use of the 15age group enables student achievement to be compared at the end of compulsory education in all countries or before the completion of compulsory education (MEB, 2010).
15-year-old age group, as compulsory education continues at least until the age of 15 in all countries
It was aimed to increase the reliability of the sample by selecting the sample.
The PISA Exam is held with the participation of OECD countries.
OECD: Organization for Economic Co-operation and Development (OECD) is an international organization that works to create better policies for better lives (OECD,2019).
The Finnish education system has consistently ranked in the top five in the exams.

2.GENERAL PROPERTIES OF METHOD

2010-2022 Pisa FINLAND TURKEY Education Success google academy article review By finding 8 articles. Since the abstracts of 3-4 articles are not opened as full text, their abstracts were read Document analysis meticulously and systematically analyzes the content of written documents. It is a qualitative research method used to analyze (Wach, 2013). In qualitative research Document analysis, like other methods used, is to make sense of the relevant subject. It requires examining and interpreting data to develop an understanding of and empirical knowledge (Corbin & Strauss, 2008). Comparing the Turkish education system with the Finnish education system. 2010-2022 Pisa FINLAND TURKEY Education Success google academy national document analysis was done by finding 8 articles. Abstracts of 3-4 articles are read as they are not fully reviewed.

3.APPLICATIONS

During compulsory basic education, there is no national exam or end-of-year exam for evaluation, and students are evaluated with questions prepared by the teacher (Sahlberg, 2007). Therefore, the focus of teaching is purely learning rather than preparing students for test exams (Berry & Sahlberg, 2006).
After secondary school, students move on to high schools based on skills and teacher evaluation. High school and university assessments are evaluated within the scope of the individual's skills and abilities, and the career development process continues. There is no work other than job anxiety and the department they are studying.

The most important feature of Finnish teacher training programs is to keep the quality of teacher education high by accepting highly motivated and talented students at the beginning (Malaty, 2006).
Teaching in Finland is one of the programs preferred by the most successful high school graduates. High school graduates who decide to become a teacher must first pass the Marticulation Examination exam, which is similar to the LYS (Undergraduate Placement Exam) applied in Turkey, and then the three-stage acceptance test in order to participate in this program. According to Malaty (2006), the acceptance test consists of a book exam, interview, and sample lectures or conducting a group discussion
Pre-service teachers are provided with the opportunity to do internships in practice schools for four weeks in the first three years of the program and five weeks in the last year. It is not enough to complete a degree program to become a teacher. After that, prospective classroom and branch teachers must have a master's degree with a thesis related to their field (Sahlberg, 2007; Simola, 2005). In Finland, giving practice and theory courses as a whole in pre-service education helps candidates to develop themselves in effective teaching techniques (Jussila & Saari, 2000). The phonetic character of Finnish language makes decoding easy, and beyond the lower grades, dictation is common only in foreign language classes. As it is, after children learn to decode the language which 'is spelled as it is pronounced', they soon learn to be ever more fl uent readers due to the subtitling of all foreign language TV-programmes and films (Kupainen et al.,2009). Combined with the long-standing tradition of newspapers and magazines subscribed for home delivery, a well-functioning network of free libraries, and zero illiteracy among native adults, Finnish children are truly embedded in written language from birth on. (Kupainen et al.,2009). Finland has not adopted the strong version of consequential accountability with national testing, and our standards are relatively open to local flexibility and diversity with a strong emphasis on basic literacy and numeracy concurrent with a wide-range education for all (Kupainen et al.,2009).
One of the key features of Finnish teacher education is a research-based its approach. This high level of education gives teachers a lot of freedom and allows them to be responsible. Freedom and responsibility are teachers' own Curriculum improvements for courses, teaching and assessment based on national principles This means determining their methods and choosing learning materials. This In line with this, Finnish teachers are trained to become autonomous and reflective experts (Ahte et al., 2007, p. 39).
Teacher candidates who graduate from education faculties with their diplomas do not take any national exams. It is sufficient to apply personally to work in the schools determined by the local administration of the region in which they want to work. The teacher, who is interviewed by a committee including the school administrator, teacher and parent representative, starts his/her job if he/she is successful (Yonca,2018).
The contribution of in-service training, which is continued after becoming a teacher, is as great as the teacher training program in Finland. Thanks to in-service training, teachers have the opportunity to renew and improve themselves in the subjects they need. These courses are mostly free or financed by the school they work for (Yonca,2018). There will be events, not the subject, and not only a single course, but also other elements of the different courses that the event contains are transferred to the students. For example, while a historical event is being

processed, it will be examined both historically, geographically and mathematically, and the data obtained are given together.
Schools are covered with carpets so that students feel free and comfortable as they are at home. Students enter the school with socks or slippers
Finns, who give their children a sense of freedom and independence from a young age, go to school alone and by bicycle. While children are using a bicycle, their mental psychomotor skills are active and they do their daily sports. The concept that the lesson is learned in the lesson is dominant. Applications are made in workshops within the school. There are workshops such as music, painting, wood, sewing and an indoor gym.

Only milk, water, juice, etc. in the school canteen. There are food products and the calories and food value of each meal are calculated and given to the students at meals. Thus, unnecessary energy is not loaded on the children and children do not need to be kept under control during the lesson, and the lesson hours are carried out efficiently. Active clubs are available for the development of children's imagination and creativity. The teacher should involve the student in the lesson and give active roles. There is an understanding that the teacher should be a guide with workshops and practices.
Constructivistspiral training model. Throughout the education, students study the same units. The subjects learned over the years are presented to the student by deepening. This situation causes the misconceptions to increase by spreading the learning over a long period of time
Students can consume plenty of sugary foods and beverages in the canteens. Most schools do not have a cafeteria
Since the education model is based on the examination system, students are constantly exposed to stress and competition. Stress naturally affects learning negatively
If you happen to go to a school by chance, you will likely encounter a few paid teachers. Individuals who do not graduate from the faculty of education can provide education for a very low price, which causes wrong or incomplete learning in children.
Selection for teacher training programs in Turkey is made with general talent, general culture and school exams, YGS/LYS exams. An excellent training in education in Turkey for the upcoming season. related student candidates are in a position to achieve the theoretical gains in accordance with the practical gains and in a good way. Selection of teacher candidates to be elected every year in the selection of employment (according to the Public Personnel Selection Examination). KPSS exam is an elective exam for general culture, general and pedagogical knowledge (Yonca,2018).
While students are selected for the teaching program in Turkey, surplus students are accepted at the beginning and at the end of the academic education, a selection is made from among the graduate candidates. Since more than enough teacher candidates are recruited into teaching programs, the quality of pre-service education, especially the practice courses carried out in cooperation with schools, decreases, and even it is difficult to find internship schools for students. Accordingly, some of the graduates cannot be appointed due to the surplus students, and the prestige of the profession and the success profile of the students who turn to the teaching program decrease (Yonca,2018).

When choosing the course content and methods, teachers cannot go beyond the framework drawn by the curriculum and textbooks. This situation is supervised by school management and inspectors (Öztürk, 2009; Yıldırım, 2003).

He has been a candidate for 2005-2013-2018 education. 2005 Science and Technology Curriculum and 2013 Science and Technology Curriculum were emphasized (Saban, Aydoğdu and Elmas 2014). 2005 science curriculum adopted the constructivist approach, while the inquiry-based learning strategy was included in the 2013 and 2018 curriculum (MEB, 2005; MEB, 2013; MEB, 2018).

2018 Science, Engineering and Science Applications addon unlike previous programs. A program about its emergence in this design is introduced as the emerging term. Universal, national and young children included in the programs for 2018 use are programs that are not accepted from the program of ethical issues (Özcan, 2018).

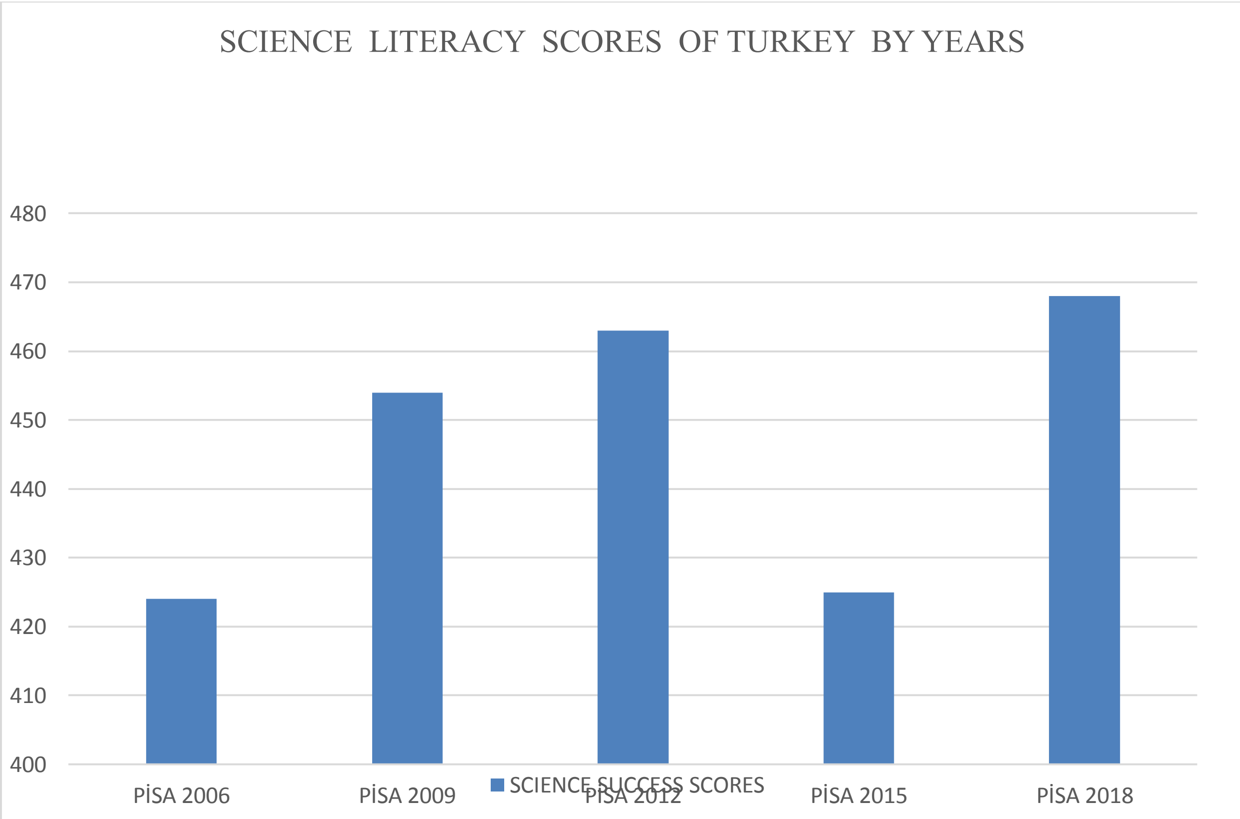

Figure 1

Article number	Year of study	written language
1	2017	Turkısh
2	2018	Turkısh
3	2019	The English
4	2017	Turkısh
5	2020	Turkısh
6	2014	Turkısh
7	2021	The English
8	2021	Turkısh

Figure 2

Figure 3

Article number	study name	Year of study	study purpose	Types of research	Results
1	Comparison of Preschool Education and Teacher Training and Appointment Policies	2017	to examine them comparatively in the context of the distribution of education investments	Qualitative research document analysis/ literature review	In order to improve the Turkish education system, the budget allocated to education should be expanded by implementing a higher quality teacher training policy
2	Investments in Education and PISA 2015 Results: A Comparative Review	2018	To compare the results of the most successful countries in the PISA 2015 program and Turkey in the context of the distribution of education investments	Qualitative research document analysis/ literature review	It was concluded that the success after Pisa Turkey 2015 is related to the budget allocated to education, and it was mentioned that the budget should be increased for success.

3	COMPARISON OF HIGHER EDUCATION SYSTEMS OF FINLAND	Higher education comparison between Turkey and Finland	Qualitative research document analysis/ literature review	The most important difference between the two countries is the examination system, while in the Turkish system there is a selection based on assessment and evaluation, while in the Finnish system, talent and skill assessment is at the forefront.
4	Examination of Turkish teachers' views on the factors that ensure the success of Shanghai's (China) PISA	Chinese and Finnish education system comparison	mixed method	The most important difference between the two countries is that the finnish model has created a flexible and diverse curriculum model, while the china has implemented a standardized strict curriculum like the western model

5	Identifying key science concepts and examining science curricula and national textbooks in the context of these concepts.	It is aimed to identify key science concepts, which are one of the dimensions of science and technology literacy.	mixed method	It has also been determined that the densities of concepts in the textbooks written for the same grade level are very different from each other.
6	CRITICAL REVIEWS ON CHANGES IN EDUCATION	Studies for education reform were examined and comments were made.	Qualitative research	It was emphasized that it should not become a classic in education by emphasizing wide and diverse knowledge.

7	MODELS AND MODELING IN SCIENCE EDUCATION IN TURKEY: A LITERATURE REVIEW	2021	The effects of model studies in science education were examined and determinations were made.	Qualitative research	Teaching abstract subjects by embodying them increases permanence in learning.
8	Professional Capital of School Heads and Teachers: A Literature Review	2021	to examine the education method and educational capitals	Qualitative research	A significant positive relationship was found between the amount of capital and educational success

Figure 4

Changes Turkey Made To Increase Pisa Success

The FATIH (Opportunities Research and Technology Improvement Movement) project, which was launched in 2010, is described as a project that intertwines the concepts of information and communication and thus aims to make radical changes (Ekici and Yılmaz, 2013).
In addition, in order to increase the success and quality in education, the number of people per classroom has been significantly reduced, the difficulties of bussed education have been tried to be reduced, compulsory education has been extended to 12 years as 4+4+4, textbooks have been started to be distributed free of charge, studies on improving the physical environment conditions have been made. In addition, in-service training was emphasized for the quality of educators, which is mentioned in the five-year development plans (Yaşar, Şahan, & Tural, 2017).

4.CONCLUSIONS

Turkey has aimed to reach innovations and success by changing its education policy, in this context, it has changed the curriculum in 2005-2013-2018. With this change, Pisa science literacy scores increased, but in 2015 the science score regressed to the 2006 score. However, the decrease was observed not only in Turkey but also in all countries. A reading in Greece, Hatzinikita, Dimopoulos, and Christidou (2008) compared the characteristics of science textbooks with the texts in PISA, and found that the textual presentation in the textbook and PISA was also incomplete. This situation was also reported as an unapproved reason for PISA (Kömürcü, 2021). With the 2018 curriculum, the integration of science, technology, mathematics and engineering based on research and inquiry has been emphasized, and through engineering applications, a model has been started in which theoretical knowledge is transformed into practice, that is, scientific knowledge is transformed into a product. Thus, the Pisa science literacy score has been increased. Turkey was the country that increased the average science score the most in PISA 2018 compared to PISA 2015 (MEB, 2018).

Applicable suggestions to increase our success in Pisa exams:
1) We need to focus on education and training by reducing stress.
2) We need to train quality teachers by reducing quantity.
3) It should be ensured that the practices of teachers are improved by starting the practices in education faculties and internships from the first grade.
4) It is necessary to leave the profession only to teachers, giving due importance to teachers' salaries.
5) A holistic education should be started by leaving the education spread over the spiral years, so that misconceptions in children should be eliminated.
6) Security can be designed to be improved.
7) Models that give confidence to education should be developed, and job opportunities should be created after education.
8) Exercises will be applied for the use of classes by reducing their availability.
9) Dining halls should be built in schools and junk food should be limited or removed

REFERENCES

1. Milli Eğitim Bakanlığı, (2016). PISA 2015 Türkiye Ulusal Nihai Raporu. Millî Eğitim Bakanlığı, Ankara. Erişim Tarihi: 12. 08. 2019, http://odsgm.meb.gov.tr/test/analizler/docs/PISA/PISA2015_Ulusal_Rapor.pdf.
2. Organization for Economic Co-operation and Development. (2008). Education at a glance 2008: OECD Indicators. Paris, France: OECD Erişim Tarihi : 27.08.2019 http://www.oecd.org/dataoecd/23/46/41284038.pdf
3. Wach, E. (2013). Learning about qualitative document analysis.
4. Corbin, J. & Strauss, A. (2008). Basics of qualitative research: Techniques and procedures for developing grounded theory. Thousand Oaks: Sage
5. Benzer, A. (2019). Türkçe ders kitaplarının PISA okuma yeterlik düzeyleri ile imtihanı. *Okuma Yazma Eğitimi Araştırmaları*, *7*(2), 96-109
6. Çalışkan Maya İlknur, "AB Sürecinde Türkiye ile AB Ülkeleri Eğitim İstatistiklerinin Karşılaştırması", Türk Eğitim Bilimleri Dergisi, S:4 (2006), s.375-394
7. Özcan, C., & Kaptan, F. (2018). 2018 Fen Bilimleri Öğretim Programının Fen Bilimleri için Uyarlanmış Bloom Taksonomisine Göre İncelenmesi. *Gaziantep Üniversitesi Eğitim Bilimleri Dergisi*, *3*(2), 78-90.
8. Gürlen, E., Demirkaya, A. S., & Doğan, N. (2019). Uzmanların Pisa ve Timms sınavlarının eğitim politika ve programlarına etkisine ilişkin görüşleri. *Mehmet Akif Ersoy Üniversitesi Eğitim Fakültesi Dergisi*, (52), 287-319.
9. Özdemir, A. (2017). Bütün öğrencilerin okulu Finlandiya okulları. *İnformal Ortamlarda Araştırmalar Dergisi*, *2*(1), 59-91.
10. Kupiainen, S., Hautamäki, J., & Karjalainen, T. (2009). *The Finnish education system and PISA*. opetus-ja kulttuuriministeriö
11. Kömürcü, A. S. (2021). *Pisa fen okuryazarlığı yeterlik düzeylerine göre 5-8. sınıf fen bilimleri ders kitaplarındaki soruların incelenmesi* (Master's thesis, Alanya Alaaddin Keykubat Üniversitesi/Lisansüstü Eğitim Enstitüsü/Matematik ve Fen Bilimleri Eğitimi Ana Bilim Dalı).
12. Yonca, Z. D. (2018). Finlandiya'nin Pisa Başarisina Etki Eden Faktörler Ve Türkiye Açisindan Karşilaştirilmasi. *Uluslararası Eğitim Bilimleri Dergisi*, (14), 136-146.
13. Yüksel, M. (2019). *PISA 2015 Türkiye ve FInlandiya verilerine göre okul özellikleri ile öğrencilerin okuma becerileri arasındaki ilişkinin incelenmesi* (Master's thesis, Trakya Üniversitesi, Sosyal Bilimler Enstitüsü).

RECTANGULAR MICROSTRIP ANTENNA DESIGN FOR WIRELESS TECHNOLOGIES

Mustafa Mutlu[1] and Çetin Kurnaz[2]

[1]Vocational School of Technical Sciences

Ordu University, Ordu, Turkey

mustafamutlu@odu.edu.tr

[2]Department of Electrical and Electronics Engineering

Ondokuz Mayıs University, Samsun, Turkey

ckurnaz@omu.edu.tr

Abstract

A rectangular microstrip antenna operating for wireless technologies (Wi-Fi, Bluetooth and ISM) is designed which is made of PF-4 having dielectric constant of 1.06, loss tangent of 0.0001 and antenna patch and ground part consist of copper band whose one side is sticky. Operating frequency is 2.45 GHz. Its operating band is between 2.4136 GHz and 2.4791 GHz. Its gain at the critical frequency is 5.109 dB.

Keywords: Wifi; Bluetooth; ISM; Microstrip Antenna.

1. INTRODUCTION

The rapid development of technology in the world causes the expansion of the spectrum in the communication system. Bluetooth, which was developed by Ericsson in 1994 for mobile phones and other mobile devices to communicate wirelessly with each other, made wireless communication widespread. In this way, even within a short area (10m-100m), the devices were able to transmit and receive voice and data wirelessly. After the work in this area, wifi emerged. Thanks to this technology, devices such as personal computers, video game consoles, digital audio players and smartphones communicated wirelessly. It has provided people with free access to the internet not only in homes and offices, but also in public areas such as bus, airport, garage, restaurant, etc. Wireless communication, which was effective initially in a very small area with Bluetooth, has expanded its scope a little more with wifi. However, with wimax, this coverage area has expanded to 50 km. The evolution of wireless communication has not only expanded the coverage area, but also increased the communication speed. Table 1 shows the standard and frequency of wireless technologies [1].

Table 1. Comparison of wireless Technology

	Bluetooth	Wifi (b)	Wifi (g)	Wimax	ISM
Standard	802.15	802.11b	802.11g	802.16	802.11
Frequency (GHz)	2.402-2.480	2.4-2.497	2.4-2.497	2-66	2.400-2.483

Today, where everything is built over mobile phones, one of the biggest investments in technology are made in the field of wireless communication and it is predicted that this will continue in the future. Many studies in this field have been made in the literature.

A wearable rectangular patched antenna operating at dual band (2.44 GHz (Wireless Fidelity, Wi-Fi) and 3.54 GHz (Worldwide Interoperability for Microwave Access, Wi-MAX) using a 1 mm thick denim base is designed [2]. A circular microstrip antenna at a frequency of 2.45 GHz to destroy cancerous tissues using microwave energy is implemented [3]. An elliptical microstrip antenna operating at 2.4 GHz frequency is designed and fabricated [4]. An implant antenna operating in two bands ((Medical Implant Communication Service, MICS) and (Industrial Scientific Medical, ISM)) is realized [5]. An antenna implantable to the human body with wireless transmission operating at 2.4 GHz frequency is designed in the (High Frequency Structure Simulator, HFSS) environment [6]. Three rectangular microstrip antennas with 2.44 GHz coaxial feed [7] are implemented. A rectangular patch microstrip antenna used for biomedical applications at 2.45 GHz (2.52-2.38 GHz) is studied [8]. Two slotted ring microstrip implant antennas operating in the MICS and ISM bands are designed in the CST environment [9]. A rectangular microstrip antenna consisting of a conductive cloth copper with a patch and ground part and an insulating part made of denim is designed and manufactured to operate at 2.45 GHz for various applications [10]. A circular polarization antenna consisting of textile, which can operate at four resonant frequencies (2.4, 3.5, 5.8 and 5.9) GHz (Wi-Fi, Wi-MAX, ISM, (Wireless Local Area Network, W-LAN)) is designed and fabricated [11]. A circular polarized dual band dual slot antenna is designed and analyzed to work in WLAN, Wi-MAX and Wi-Fi applications [12]. U and inverted U shaped compact rectangular microstrip antennas operating in dual band (Wi-Max and WLAN) are designed [13]. A microstrip antenna operating in 3G, Wi-Fi, WLAN and WiMAX bands [14] is realized. A four/eight element (Multiple-In Multiple-Out, MIMO) antenna that can operate in Wi-MAX (IEEE 802.16d) and 5G band is designed and fabricated [15]. A circularly-polarized elliptical antenna working in WiFi/WiMAX applications is studied [16]. An antenna that works in WLAN, Wi-Max and C-band applications is worked [17]. A circularly-polarized microstrip antenna that can operate in Long Term Evolution (LTE), Wi-Fi/WLAN, Bluetooth and Wi-MAX applications is designed and fabricated [18]. A pentagonal patched microstrip antenna that can operate in Wimax, Wi-Fi, 802.119 and C-band is designed [19]. A rectangular patch microstrip antenna that can operate at 2.4 GHz, 5.5 GHz and 7.5 GHz frequencies is designed and fabricated [20]. WiMAX, Wi-Fi, (Global System for Mobile Communications, GSM (1.9 GHz), Bluetooth, ISM band (2.4–2.5 GHz), 3 G (2.1 GHz), 4 G LTE (2.1–2.5 GHz), 3G (Wideband A circular patch microstrip antenna that can operate in applications such as Code Division Multiple Access, WCDMA) (1.9, 2.1 GHz) is designed [21]. A monopole microstrip antenna that can operate at 1.85 GHz (GSM 1900 MHz), 2.42 GHz Bluetooth/IMTE, 3.4 GHz (Wi-MAX) and 5.3 GHz (Local Area Network, LAN) (WLAN) [22] is studied. A dual-band microstrip antenna is designed for wireless LAN applications [23]. In a study, a dual-band implantable antenna (MICS, 402–405 MHz and ISM, 2400–2480 MHz) for medical telemetry is designed [24]. A microstrip antenna to communicate with implants in the MICS band [25] is studied. A microstrip antenna for wireless communication [(WiMAX), mobile WiMAX and wireless local area network [26] is designed. A microstrip antenna to be used for Bluetooth, WLAN, WiMAX (IEEE 802.16 and 802.20 standards. (Radio Local Area Network, RLAN), (Fixed Wireless Access, FWA) and (Non-line of sight, NLOS) applications [27] is studied. The studies that we have cited in the literature as a source have been compared according to insulator material, operating frequency and bandwidth in Table 2 of this study we have done. Although antenna arrays are used in many parts of the studies, it is seen that both bandwidth and gain or directivity are well below the results obtained in our study. In addition, the narrow coverage area of the antenna and the low side lobe directivity values make our antenna more important in terms of showing that the power is sent only to a narrow area, and that the signal sent from the antenna can reach farther.

Table 2: Comparison of our study and the studies in the literature

Reference article	Substrate/h (substrate thickness)/ tanδ (loss tangent)/Patch type	ε_r Dielectric constant	f_r (GHz) Critical frequency	Bandwidth B_w (GHz)	Gain/Directivity (dB/dB)
2	Denim Jeans, h=1 mm tanδ=0.0001 rectangular patch antenna designed	1.7	2.44, 3.54	MHz (50, 40)	5.73dB 9.17 dB
3	Rogers RO4003, tanδ=0.0027, h=0.508 mm Taconics TLY 5 0620 CH-CH, tanδ=0.0009, h=1.57 mm, circular patch antenna designed	3.55, 2.2	2.41 2.46	MHZ (33.55, 66.4)	D(6.93,2.01) dBi
4	FR4 Spoon-shaped patch antenna fabricated	3.95	2.4	0.4 GHz	*G: 5.84 dB, D: 6.25 dBi,*
5	Rogers 3210, h=0.64 mm, tanδ=0.003	10.2	403 MHz, 2.45 GHz	0.3 GHz 0.35 GHz	P: 8.8 mW
6	FR4-ADK, h_1=37.26 mm, h_2=28.83 mm. rectangular patch antenna designed		2.4GHz	0.01 GHz	6.63 dB

7	FR-4, h=1.6 mm, tanδ= 0.02, rectangular patch antenna designed	4.4	2.44 GHz	60 MHz	Peak gain 1.3,peak directivity 2.8, radiation effcy %45
8	FR-4, h=1.6 mm, rectangular patch antenna designed	10.2	2.45 GHz	0.14 GHz	
9	(Rogers RO3210, tanδ=0.0027) h=1.27 mm double-layer dielectric, nested rectangular patch antenna is designed	10.2	403 MHz, 2.44 GHz	3 MHz, 0.08 GHz	*D2.1 dBi ve D4.52 dBi*
10	jeans, h=3.5 mm rectangular patch antenna designed	1.6	2.45 GHz	0.099 GHz	7.2 dB
11			(2.4, 3.5, 5.8, 5.9) GHz		a peak gain of 4.93, 5.67, 8.86, and10.07 dBi
14	FR4, h=1.6 mm tanδ=0.02, an inverted chair-shaped patch antenna is fabricated	4.4	(2.45, 5.2) GHz	0.99GHz, 0.59 GHz	2.7 and 4.6 dB,
16	A koch fractal antenna, h=3.2 mm, antenna designed and fabricated	2.2	2.4 GHz, 3.4 GHz.	58 MHz and 120 MHz	6.8 dBi,4.9 dBi
18	FR-4, tanδ=0.02 and h=1.6 mm) 2x2 array Elliptical+rectangular patch antenna fabricated	4.4	2.4 GHz, 5.5 GHz	2.08 GHz 1.83GHz	2.75–4.19 dBi
20	FR4, h=1.6 mm rectangular single antenna fabricated	4.4	(2.4, 5.5, 7.5)GHz	(0.08, 0.22, 0.25) GHz	8.76 dBi
21	FR-4, Epoxy, h=1.6 mm, fan shaped antenna fabricated	4.4	1.9 GHz	1.19 GHz	Directivity 4.292 dBi Realized Gain 3.95 dBi Radiation Efficiency (ηrad) 92.85% Radiated Power (Prad.) 0.920973
22	FR-4 glass epoxy h=1 mm, 5 similar semicircular antennas fabricated		1.85 GHz 2.42 GHz, 3.4 GHz 5.3 GHz	0.21GHz, 0.2 GHz, 0.4 GHz, 0.5GHz	simulated gains 1.8, 3.45, 4.91, 0.86 dBi, measured gains 2.3, 2.7, 2.82, 2.6 dBi
23	FR4 Epoxy h=1.6 mm, An antenna with a smiley face patch fabricated	4.4	2.45GHz and 5.25 GHz	0.01GHz, 0.01 GHz	
24	Rogers RO3210, hsub=hsup=0.635 mm Rogers RO3210, hg=0.08 mm. Circular patch antenna fabricated	10.2 4.5	403 MHz, 2.45 GHz	30MHz and 151 MHz,	
27	h=3.2 mm human shaped microstrip patch antenna designed	1.0006	2.4 GHz and 5.4 GHz	0.01GHz, 0.3GHz	VSWR1.1,1.13, R_L -26.55 dB -38.58 dB
Mutlu-Kurnaz, 2022	PF-4, h=2mm, tan δ=0.0001 rectangular patch antenna designed	1.06	2.45 GHz	0.0655 GHz	5.92 dB D:6.62 dBi

2. MATERIAL AND METHOD

2.1 Design of the Elliptical Antenna

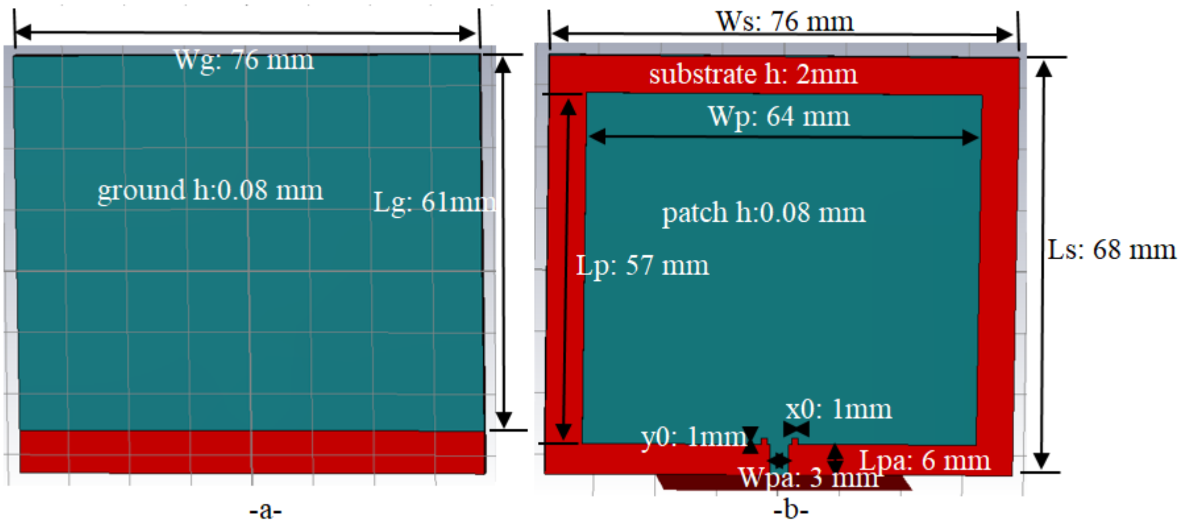

Figure 1. -A- rear, -b- front view of the designed antenna

The design procedure of the rectangular microstrip antenna shown in Figure 1 is carried out assuming that the dielectric constant of the substrate, the resonance frequency and the thickness of the substrate are known. By substituting these three data in the equation, the patch length and width are determined. The design consists of the following stages [28]:

I. Patch width (mm):

$$W = \frac{1}{2\times f_r \times \sqrt{\mu_0 \times \varepsilon_0}} \sqrt{\frac{2}{\varepsilon_r + 1}} \tag{1}$$

II. We can calculate the effective relative dielectric constant from Eq. (2) ($W/h > 1$).

$$\varepsilon_{reff} = \frac{\varepsilon_r + 1}{2} + \frac{\varepsilon_r - 1}{2}\left[1 + \frac{12\times h}{W}\right]^{-1/2} \tag{2}$$

III. By using the effective dielectric constant calculated from Eq. (2) and the patch width found from Eq. (1), the length increase from Eq. (3) (ΔL) can be calculated.

$$\frac{\Delta_L}{h} = \frac{0.412\,(\varepsilon_{reff} + 0.3)\left[\frac{W}{h} + 0.264\right]}{(\varepsilon_{reff} - 0.258)\left[\frac{W}{h} + 0.8\right]} \tag{3}$$

IV. The patch length can be calculated by using Eq. (4):

$$L = \frac{c}{2\times f_r}(\varepsilon_{reff})^{-1/2} - 2\times \Delta_L \tag{4}$$

V. Dimensions of ground and dielectric outside the patch portion of the microstrip antenna; W W_g and L_g are obtained by the equations of (1) and (4) as

$$W_g = W + 6 \times h \tag{5}$$

$$L_g = L + 6 \times h \tag{6}$$

where,

h: thickness of insulator (mm)

W_p: width of patch

W_{pa}: width of patch_arm

W_g: The width of the ground

W_s: The width of the substrate

L_p: Length of patch

L_{pa}: Length of Patcharm

L_g: Length of Ground

L_s: Length of Substrate

2.2 Determination of Isolating Material for Antenna

As an insulator, PF-4 was preferred because it is a single piece and has a low loss tangent indicating the loss of the insulating part. PF-4 with a small loss tangent, which is a single piece, is used as an insulator [29].

Table 3. Shows all the properties of PF-4.

Type of dielectric material (Substrate)	Dielectric constant (ε_r)	Loss tangent ($\tan_\delta$)	Substrate thickness h (mm)
PF-4	1.06	0.0001	2

2.3 Determination of Conductive Material for Antenna

For the conductive (patch and ground) part of the antenna, one side of the adhesive copper tape is chosen to be adhered to the insulating material, thus facilitating the production of the antenna. The electrical properties of the material used for the conductive patch and ground part of the antenna are given in Table 4.

Table 4. Properties of one side adhesive copper tape used for patch and ground part

Conductor (Patch and ground part)	Electrical conductivity σ (MS/m)	Thickness of the conductor t (mm)
One side ticky copper tape	58	0.08

3. APPLICATIONS

Simulation results contain clues about how well the antenna is designed or not. Since the electromagnetic wave sent from the antenna is multiplied by the gain of the antenna which is an important factor for it to radiate adequately. Looking at the gain-frequency curve of the antenna in Figure 2, it can be seen that the realized gain (Realized gain) of the antenna at the operating frequency (2.45 GHz) is as high as 5.92 dBi.

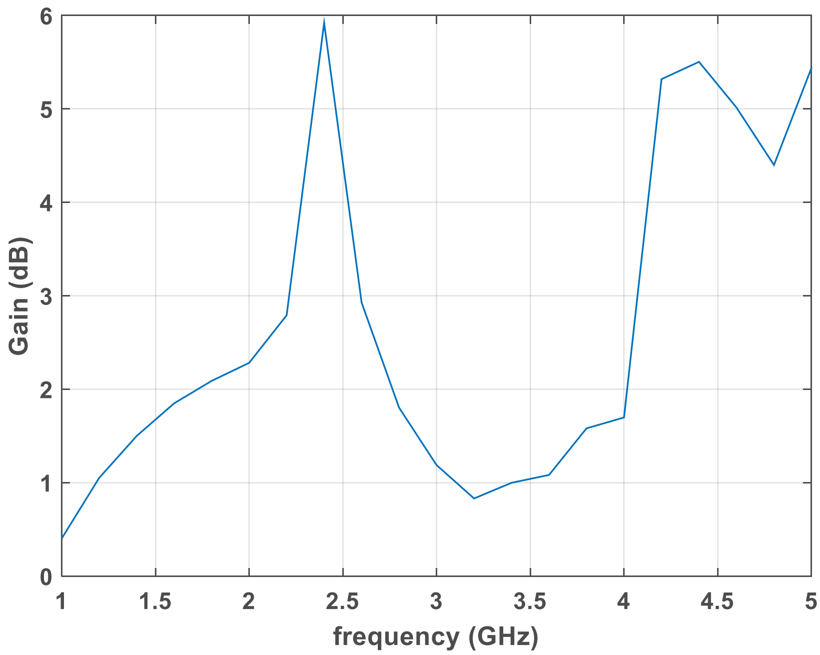

Figure 2. Variation of gain with frequency

The range of VSWR in a system, which satisfies 1≤VSWR<2 is considered as the operating band. Ideally this ratio is 1. Looking at Figure 3, it is possible to see that the antenna will work efficiently in regions that meet the above criterion. Figure 3 shows that the VSWR is 1.079 in the operating band (2.4136 GHz-2.4791 GHz), the critical frequency of 2.45 GHz.

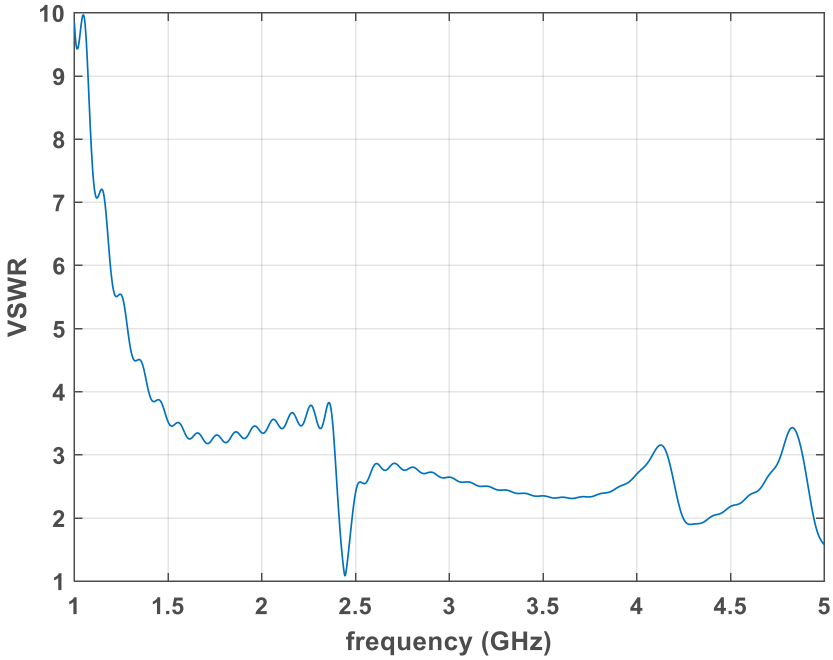

Figure 3. Variation of VSWR with frequency

The reflection coefficient, which shows the ratio of the reflected wave to the incident wave in a transmission line, is also an indicator of whether the impedance match is achieved.

$$|\Gamma| = \frac{V_0^-}{V_0^+} = \frac{Z_L - Z_0}{Z_L + Z_0} = \frac{1 - VSWR}{1 + VSWR} = \frac{1 - 1.079}{1 + 1.079} = 0.0379 \tag{7}$$

The reflection coefficient is ideally zero. S_{11} shows how much of the signal coming to the antenna is sent from the antenna, and how much is not emitted from the antenna but reflected back as shown in Figure 4. The parts where S_{11} is below -10 dB and -10 dB are taken as the operating band of the antenna. The ideal value of S_{11} is zero. However, the lower the logarithmic value of S_{11} is below -10 dB, the better the antenna will work in that region. The frequencies at which S_{11} is smallest in its operating region are the operating (critical) frequencies of the antenna.

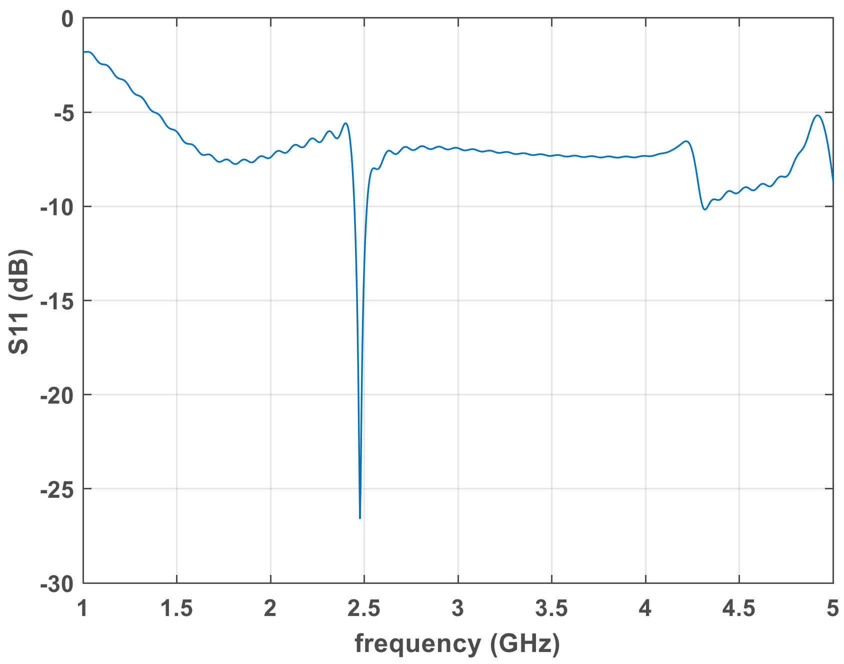

Figure 4. Variation of S_{11} with frequency

The one-dimensional variation of the antenna's directivity includes the 3 dB aperture of the far field, between which angles (antenna coverage) radiation is made, and in which region the target or receiving antenna should be located (Figure 5).

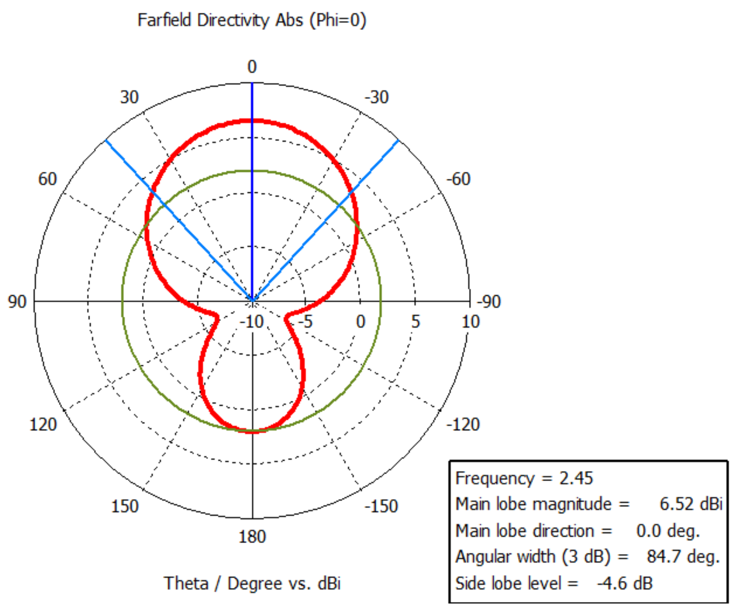

Figure 5. Variation of directionality (phi=0) at critical frequency depending on theta angle

Considering the S_{11} value of the antenna in Table 5; The frequency values where this value drops below -10 dB, the smallest S_{11} values in the operating range, the critical frequencies of the antenna and the change in the gain of these working bands are seen. The fact that S_{11} (-28.282 dB) in the 2.4136-2.4791 GHz range at the operating frequency (2.45 GHz) is the minimum of S_{11} in the entire operating range from the table shows that the selected operating frequency is chosen correctly.

Table 5. Antenna's working band, S_{11} value in this band, bandwidth and gain

Frequency band	S_{11} (dB)	Bandwidth (GHz)	gain(dB)
2.4136-2.4791	-28.282	0.0655	5.92

Figure 6 shows the top view of the distribution of the magnetic field on the antenna at 2.45 GHz operating frequency. This figure will help us in the correct positioning of the determined target if the antenna is to be used as a transmitter, in order to show in which regions the magnetic field is more intense on the antenna. Even if the antenna will be used as a receiver, it will provide important information in determining the most suitable position of the receiving antenna.

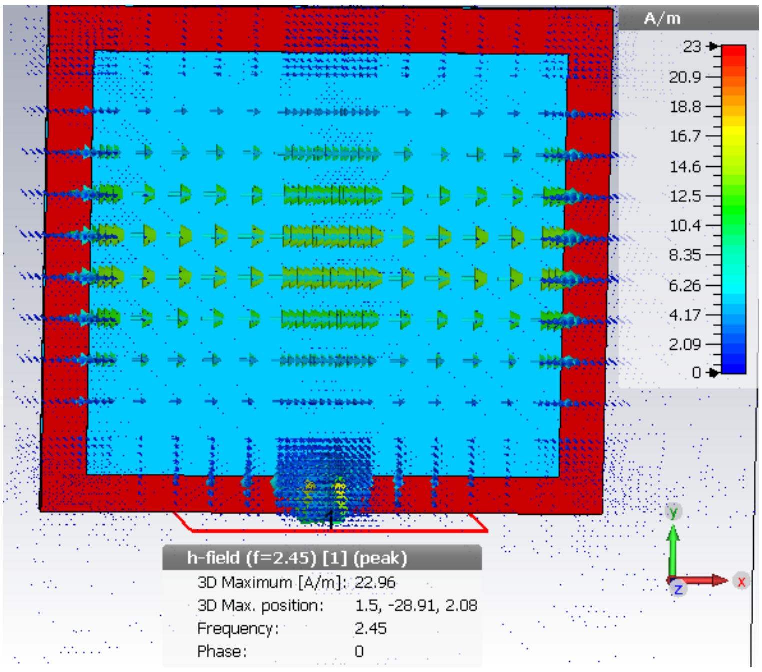

Figure 6. View of the magnetic field on the antenna (top view)

Figure 7 shows the variation of the surface current distribution on the antenna and the top view of the region where it is concentrated.

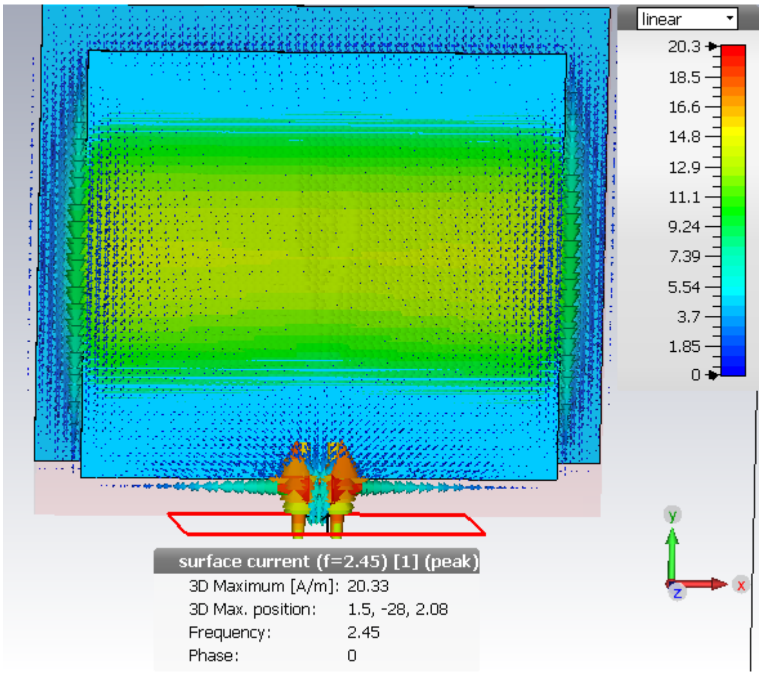

Figure 7. View of the surface current on the antenna (top view) at the critical frequency

Figure 8 shows the variation of the surface current density distribution on the antenna and the top view of the region where it is concentrated.

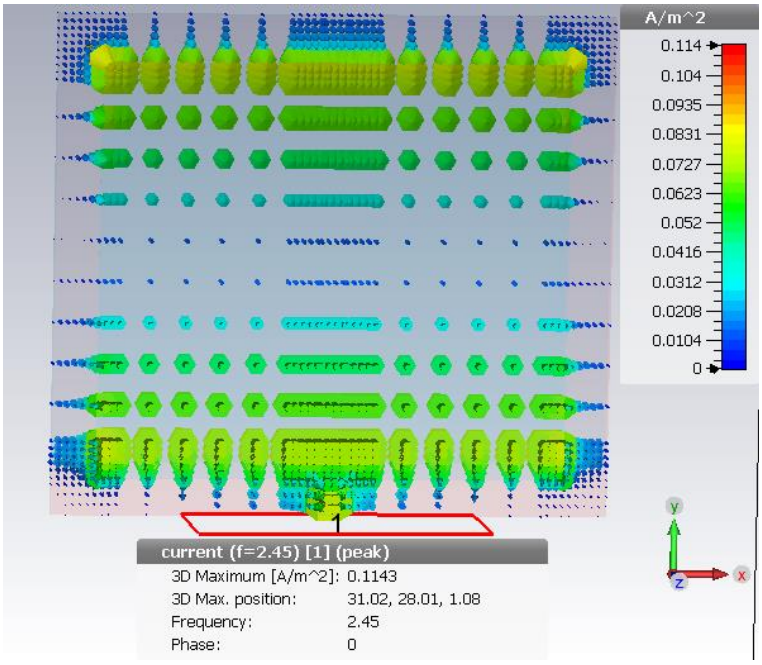

Figure 8. View of the current on the antenna (top view) at the critical frequency

Figure 9 shows the top view of the change in volumetric energy density on the antenna.

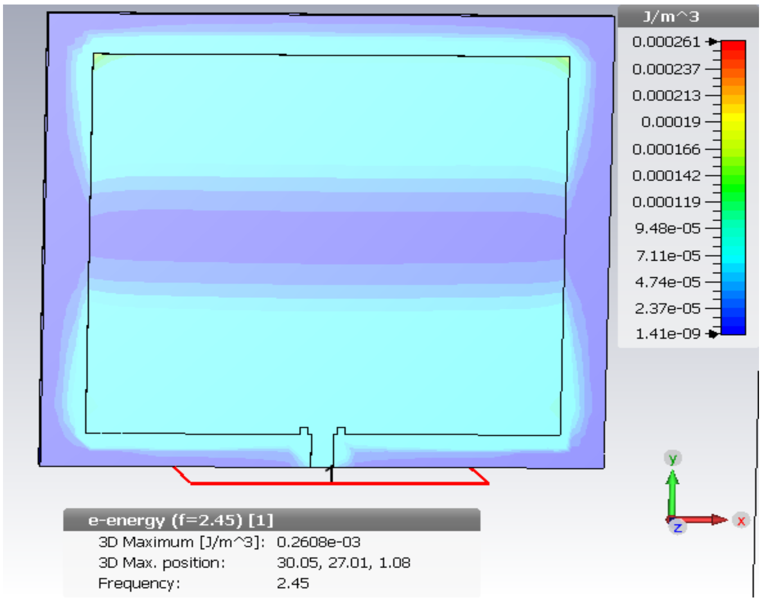

Figure 9. View of the volumetric energy density (top view) on the antenna at the critical frequency

Figure 10 shows the three-dimensional variation of the antenna's directivity depending on theta and phi. It can be seen from the figure that the directivity is maximum in the direction of propagation where power is important. It is the most important factor that determines the distance that the transmitter will reach. 3-dB aperture indicates that the power is directed maximally in the direction of the broadcast.

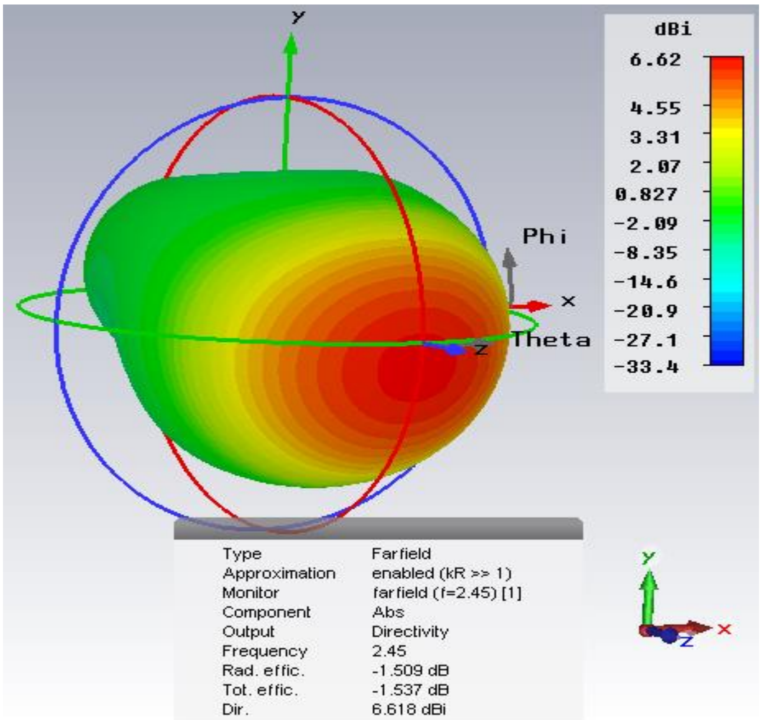

Figure 10. Variation of directionality at critical frequency depending on phi and theta angles

4. CONCLUSIONS

Today, when wireless communication is very important, a rectangular microstrip antenna whose infrastructure consists of PF-4 patch and ground part of adhesive copper tape on one side is designed and examined to be used in multiple standards for this communication. The fact that the antenna can be used in multiple standards (Bluetooth, wifib, wifig, wimax ISM) and its high directivity make the antenna different and special from other antennas made up to this time.

REFERENCES

1. Taiji Kondo, Hiroshi Fujita, Makoto Yoshida and Tamio Saito, Technology for WiFi/Bluetooth and WiMAX coexistence, 2010.
2. Khan, M.F. Shah, S. A. A. and Ullah, S., Dual-Band Frequency Reconfigurable Microstrip Patch Antenna on Wearable Substrate for Wi-Fi and Wi-MAX Applications, Technical Journal, University of Engineering and Technology (UET) Taxila, Pakistan Vol. 22 No. II, 2017.
3. Görgün, A.R. Çömlekçi, S. ve KAYA, A, Mikrodalga Tümör Ablasyonu için Hüzme Yönlülüğü Yüksek Kompakt Anten ve Kompakt çok Bandlı Düzlemsel Anten Tasarımı ve Analizi, Mühendislik Bilimleri ve Tasarım Dergisi 7(3), 662 – 670, e-ISSN: 1308-6693 Araştırma Makalesi, 2019.
4. Ferdous, N. Chin Hock, G. and Hamidah, S., Design of an Elliptical Patch Antenna for RF Energy Harvesting Application in 2.4 GHz Frequency band, International Journal of Engineering and Advanced Technology (IJEAT) ISSN: 2249 – 8958, Volume-9, Issue-2, December, 2019.
5. Palandöken, M. ve Kaya, A., Biyotelemetri Uygulamaları için Kompakt Implant Anten Tasarımı, 1. Ulusal Biyomedikal Cihaz Tasarımı-Üretimi Sempozyumu (UBİCTUS 2016), sayfa. 16-19, İstanbul, 2016.
6. Pragatheeswaran, P. and VinothKannan, A., Design and Analysis of MPAT for Biomedical Applications, Asian Journal of Applied Science and Technology (AJAST) Volume 1, Issue 3, Pages 238-242, April, 2017.
7. Mahale, A. Darwada, V. Deosarkar, S.B. and Kale, G.M., Analysis of Microstrip Patch Antenna Using Various Feeding Techniques for Bluetooth Applications, International Journal of New Technology and Research (IJNTR) ISSN:2454-4116, Volume-5, Issue-4, April, Pages 22-25, 2019.

8. Manna, S., Rectangular Microstrip Patch Antenna Operating in ISM band for Medical Applications, International Journal of Advanced Research in Electrical, Electronics and Instrumentation Engineering, Vol. 6, Issue 1, pp:179-181, 2017.
9. Sondaş, A. Uçar, M.H.B. ve Uras, E., Çift-Bantlı Mikroşerit İmplant Anten Tasarımı, 2014 IEEE 22nd Signal Processing and Communications Applications Conference (SIU 2014), sayfa. 1830-1832, 2014.
10. Purohit, S. and Raval, F., Wearable -Textile Patch Antenna using Jeans as Substrate at 2.45 GHz, International Journal of Engineering Research & Technology (IJERT) IJERTIJERT ISSN: 2278-0181, Vol. 3 Issue 5, May, 2014.
11. Ram Sandeep, D. Prabakaran, N. Madhav, B.T.P. Narayana, K.L. and Pratapa Reddy, Y., Semicircular shape hybrid reconfigurable antenna on Jute textile for ISM, Wi-Fi, Wi-MAX, and W-LAN applications, RF and Microwave Computer-Aided Engineering, Volume30, Issue11, https://doi.org/10.1002/mmce.22401, 2020.
12. Sura, P.R. and Sekhar, M., Circularly Polarized Dual Band Dual Slot Antenna for WLAN, Wi-MAX and Wi-Fi Applications, IETE Journal of Research, https://doi.org/10.1080/03772063.2020.1871423, 2021.
13. Singh, C. and Kumawat, G., A Compact Rectangular Ultra-Wideband Microstrip Patch Antenna with Double Band Notch Feature at Wi-Max and WLAN, Wireless Personal Communications 114:2063–2077, https://doi.org/10.1007/s11277-020-07465-1, 2020.
14. Sura, P.R. and Reddy, S.N., Dual-band Bisected Psi Antenna for 3G, Wi-Fi, WLAN and Wi-MAX Applications, Journal of Telecommunications and Information Technology,|nr 1| 56-61, 2020.
15. Lakshmi Narayana, D. Aruna, S. Roy, S. and Srinivasa Naik, K., Eight Element Low-Cost Microstrip MIMO Antenna for Wi-MAX and 5G Applications, Wireless Personal Communications, 2021.
16. Reddy, V.V. Harshith, S. Sravanthi, A. Saivarshith, P. and Susmita, R., Dual Band Koch Antenna for WiFi/WiMAX, 2021 6th International Conference on Communication and Electronics Systems (ICCES), DOI:10.1109/ICCES51350.2021.9489088, 2021.
17. Singh,P.P. Goswami, P.K. Sharma, S.K.and Goswami, G., Frequency Reconfigurable Multiband Antenna for IoT Applications in WLAN, Wi-Max, and C-Band, Progress In Electromagnetics Research C, Vol. 102, pp.149–162, 2020.
18. Tiwari, R.N. Singh, P. Kanaujia, B.K. Kumar, S. and Gupta, S.K., A low Profile Dual Band MIMO Antenna for LTE/Bluetooth/Wi-Fi/WLAN Applications, Journal of

Electromagnetic Waves and Applications, Volume 34, 2020 -Issue 9. https://doi.org/10.1080/09205071.2020.1716859, 2020.

19. Manohar, K. Bolisetti, V. and Kumar, S., An Investigation of Different Methodology Used for Achieving Compact Multiband Microstrip Antenna for Wireless Application, Next Generation Information Processing System, pp 151-160, Proceedings of ICCET 2020, Volume 2, https://doi.org/10.1007/978-981-15-4851-2-16, 2020.
20. Hossain, B. and Hossain, F., Design of a Triple Band Rectangular Slot Microstrip Patch Antenna for Wireless Applications, 2020 IEEE Region 10 Symposium (TENSYMP), DOI:10.1109/TENSYMP50017.2020.9230997, 2020.
21. Varshney, A. Cholake, N. and Sharma, V., Low-cost ELC-UWB fan-shaped antenna using parasitic SRR triplet for ISM band and PCS applications, International Journal of Electronics Letters, https://doi.org/10.1080/21681724.2021.1966655.
22. Sreelakshmi, K. and Rao, G.S., Reconfigurable Quad-Band Antenna for Wireless Communication, Journal of Electrical Engineering & Technology Volume.15, pp. 2239–2249, 2020.
23. Yan, B.S. Wang, L. Luo, Z.Q. Deng, D.M. and Feng, L.Y. and Zheng, H.X., “Dual-band Microstrip Antenna Fed by Coaxial Probe”,11th International Symposium on Antennas, Propagation and EM Theory, Oct, 2016.
24. Kiourti, A. Konstantinos, A. Psathas, J. R. Costa, C. A. and Konstantina, S. N., “Dual-Band Implantable Antennas for Medical Telemetry: A Fast Design Methodology and Validation for Intra-Cranial Pressure Monitoring”, Progress In Electromagnetics Research, 141, 161-183, 2013.
25. Soontornpipit, P. Furse, C.M. and Chung, Y.C., “Design of Implantable Microstrip Antenna for Communication with Medical Implants”, IEEE Trans. Microw. Theory Tech., 52(8), 1944-1951, 2004.
26. Romputtal, A. and Phongcharoenpanich, C. Frequency Reconfigurable Multiband Antenna with an Embedded Biasing Network. IET Microw Antennas Propag 11(10):1369–1378. https://doi.org/10.1049/iet-map.2016.0648, 2017.
27. Prasanna Lakshmi, Y.M. Umamaheswara Rao, B. and Babu, S, “A Dual band Human Shaped Microstrip Patch Antenna for 2.4 GHz and 5.4 GHz Applications,” International Journal Of Innovative Research In Electrical, Electronics, Instrumentation And Control Engineering Vol. 3, Issue 3, March 2015. March 2015 IJIREEICE DOI:10.17148/IJIREEICE.2015.3341.

28. Constantine A. Balanis, “Antenna Theory Analysis and Design,” Third Edition, John Wiley & Sons, Inc., Publication Published by John Wiley & Sons, Inc., Hoboken, New Jersey. Published Simultaneously in Canada, 2005.
29. Phani Srinivas, K. RamKiran, D.S. Bidichandani, S.C. Guntupalli, S.R. and Kishore, K.N.V.S., Improving the Bandwidth in the Design of Phased Array Antenna. International Journal of Recent Scientific Research, Vol. 4, Issue, 3, pp.304 -307, March, ISSN: 0976-3031, 2013.

Scattered Geometrical Optics Field by a Perfectly Conducting Half Plane Between Two Isorefractive Media

Mustafa Kara [1]

[1] Department of Electronics and Automation, Ordu University University TBMYO, Ordu, Türkiye

mustafa.kara@odu.edu.tr,

Abstract

Scattered geometrical optics field of plane electromagnetic waves by a perfectly conducting half plane between two isorefractive media is derived by means of the method of transition boundary. The interface between the two media is considered as a resistive surface and affects the reflection and transmission coefficients of the half plane, and it has both reflection and transmission coefficients. Initial field is determined first by excluding the half plane causing diffraction from the geometry. Secondly total geometrical optics field is determined. Finally, scattered geometrical optics field is obtained by subtracting the initial field from the total geometrical optics field.

Keywords: Scattered geometrical optics; Conducting half plane; isorefractive media

1. INTRODUCTION

Scattering of waves by some scatterers considered between isorefractive media has been investigated. Isorefractive media have diffrerent permeabilities and permittivities from each other, but the wavenumber of the wave traveling through each of them is the same. Isorefractivity feature of a medium is obtained by means of metamaterials. Tyo studied on such a medium isorefractive with free space [1]. Also, he suggested the use of isorefractive media to improve prompt aperture efficiency of a lens [2]. Uslenghi investigated scattering by a half plane at the interface between isorefractive media [3]. He also examined radiation of a line source over a half plane located at the interface between isorefractive media [4]. Umul studied on scattering by a conductive half screen between isorefractive media [5]. He examined scattering of waves by a soft-hard half plane between isorefractive media as well [6]. Also, he worked on the diffraction of a line source field by a resistive half plane for the same problem [7]. For the isorefractive media problem, Basdemir investigated scattering of waves by a perfectly conducting wedge [8], and scattering of evanescent plane waves by a black wedge [9]. Asymptotic diffraction of a PEC cylinder located at a plane interface between isorefractive media is studied by Zhang [10]. Umul examined scattering process of plane electromagnetic waves by a perfectly conducting half-plane, residing between isorefractive media [11]. We investigated diffraction of a plane wave by an aperture composed of two different resistive half planes between isorefractive media [12]. In this study, we will derive an equation for the scattered geometrical optics field by a perfectly conducting half plane between two isorefractive media by following the steps given in [13].

2. GENERAL PROPERTIES OF METHOD

Location of the half plane is at $x \in [0, \infty), y = 0$ and $z \in (-\infty, \infty)$ as shown in Fig.1.

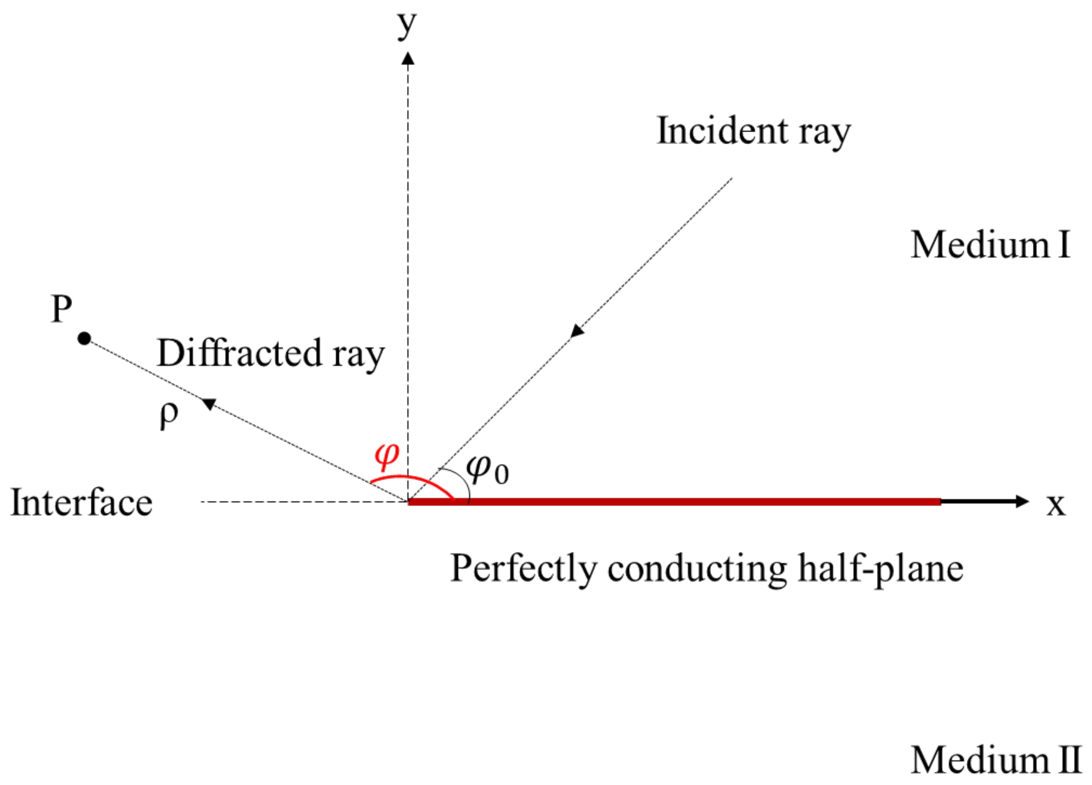

Figure 1. Geometry of the problem

Incident field is expressed as

$$\vec{E}_i = E_0 e^{jk\rho cos(\varphi-\varphi_0)}\vec{e}_z \tag{1}$$

where E_0 is the amplitude of the electric field. The cylindrical coordinates are expressed by (ρ, φ, z).

Reflected and transmitted fields are respectively expressed as

$$\vec{E}_r = E_r e^{jk\rho cos(\varphi+\varphi_0)} \vec{e}_z \tag{2}$$

and

$$\vec{E}_t = E_t e^{jk\rho cos(\varphi-\varphi_0)} \vec{e}_z \tag{3}$$

where E_r and E_t are the amplitudes of reflected and transmitted fields. Reflection and transmission coefficients are respectively given as

$$R = -\frac{\beta}{\beta+sin\varphi_0} \tag{4}$$

and

$$T = \frac{sin\varphi_0}{\beta+sin\varphi_0} \tag{5}$$

where

$$\beta = -\frac{1}{2}(sin\varphi_0 - sin\theta) \tag{6}$$

$$sin\theta = \frac{Z_1}{Z_2} sin\varphi_0 \tag{7}$$

Z_1 and Z_2 are the impedances of the first and second media.

From the Fig.1 the initial field is written as

$$\vec{E}_{in} = \left(\vec{E}_i + R\vec{E}_r\right)u(\pi-\varphi) + T\vec{E}_t u(\varphi-\pi) \tag{8}$$

where $u(t)$ is the unit step function which is equal to one for $t > 0$, and zero elsewhere. Again, from Fig.1, total geometrical field given in [11]is expressed as

$$\vec{E}_{TGO} = \left[\vec{E}_i - \vec{E}_r u(-\delta_+) + R\vec{E}_r u(\delta_+)\right]u(\pi-\varphi) + T\vec{E}_t u(-\delta_-)u(\varphi-\pi) \tag{9}$$

where

$$\delta_\pm = -\sqrt{2k\rho} cos\left(\frac{\varphi\pm\varphi_0}{2}\right) \tag{10}$$

Scattered geometrical optics field is obtained by the relation of

$$\vec{E}_{SGO} = \vec{E}_{TGO} - \vec{E}_{in} \tag{11}$$

Substituting the Eq. 8 and Eq.9 into Eq.11 we write

$$\vec{E}_{SGO} = \left[\vec{E}_i - \vec{E}_r u(-\delta_+) + R\vec{E}_r u(\delta_+)\right]u(\pi - \varphi) +$$

$$T\vec{E}_t u(-\delta_-)u(\varphi - \pi) - \left(\vec{E}_i + R\vec{E}_r\right)u(\pi - \varphi) + T\vec{E}_t u(\varphi - \pi) \qquad (12)$$

and

$$\vec{E}_{SGO} = \vec{E}_r u(\pi - \varphi)[Ru(\delta_+) - u(-\delta_+) - R] + T\vec{E}_t u(\varphi - \pi)[u(-\delta_- - 1)] \qquad (13)$$

By using the relation of

$$u(\delta_-) + u(-\delta_-) = 1 \qquad (14)$$

Eq.(13) can be rewritten as

$$\begin{aligned}\vec{E}_{SGO} = {} & \vec{E}_r u(\pi - \varphi)[R(u(\delta_+) - 1) - u(-\delta_+)] \\ & + T\vec{E}_t u(\varphi - \pi)\left[u(-\delta_-) - \left(u(\delta_-) + u(-\delta_-)\right)\right]\end{aligned}$$

$$(15)$$

$$\vec{E}_{SGO} = \vec{E}_r u(\pi - \varphi)\left[R\left(u(\delta_+) - u(\delta_+) - u(-\delta_+)\right) - u(-\delta_+)\right] + T\vec{E}_t u(\varphi - \pi)\left(-u(-\delta_-)\right)$$

$$(16)$$

$$\vec{E}_{SGO} = \vec{E}_r u(\pi - \varphi)[Ru(-\delta_+) - u(-\delta_+)] - T\vec{E}_t u(\varphi - \pi)u(\delta_-) \qquad (17)$$

$$\vec{E}_{SGO} = -\vec{E}_r u(\pi - \varphi)(R + 1)u(-\delta_+) - T\vec{E}_t u(\varphi - \pi)u(\delta_-) \qquad (18)$$

$$\vec{E}_{SGO} = -(R + 1)\vec{E}_r u(\pi - \varphi)u(-\delta_+) - T\vec{E}_t u(\varphi - \pi)u(\delta_-) \qquad (19)$$

where $R + 1 = T$

$$\vec{E}_{SGO} = -T\vec{E}_r u(\pi - \varphi)u(-\delta_+) - T\vec{E}_t u(\varphi - \pi)u(\delta_-) \qquad (20)$$

Finally, scattered geometrical optics field which is used for the evaluation of the diffracted field,

$$\vec{E}_{SGO} = -T\vec{E}_r u(-\delta_+) - T\vec{E}_t u(\delta_-) \qquad (21)$$

is obtained.

Fig.2 shows the scattered geometrical optics field variations. For the figure it is assumed that β=3, λ=0.1, and ρ=3λ. It is observed from Fig.2 that scattered geometrical optics field does not exist in the interval of $\varphi \in [\pi - \varphi_0, \; \pi + \varphi_0]$.

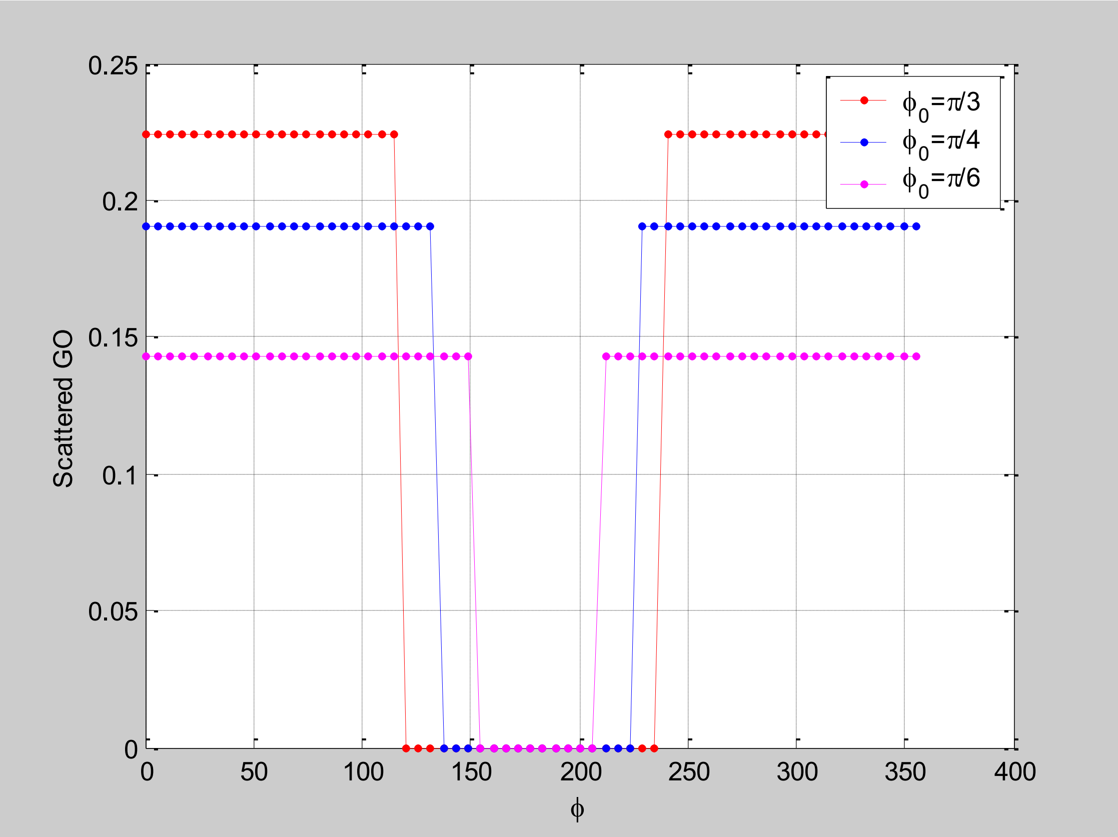

Figure 2. Scattered geometrical optics field for some φ_0 values

3. APPLICATIONS

The Method of Transition Boundary (MTB) employed here to obtain the scattered geometrical optics field is used for the evaluation of the exact solutions of some diffraction problems including the canonical structures that are constructed by metastructures. For instance, scattering by a half screen or conductive half screen between isorefractive media can be evaluated by means of this method. By using the MTB one can obtain the exact diffracted fields in real space where the scatterer and incident field are present.

4. CONCLUSIONS

In this study, the Method of Transition Boundary procedure is employed to find the scattered geometrical optics field created by a perfectly conducting half plane which is located between two isorefractive media. Firstly, initial field is determined. For the determination of the initial field the scatterer object which is the half plane in our problem, is assumed that it does not exist in the geometry. In that case the incident wave illuminated the planar interface between medium I and medium II. After this step, reflected and transmitted fields are expressed, and the initial field is expressed in terms of the reflected and transmitted fields. Next, the total geometrical optics field is expressed in terms of the incident, reflected and transmitted fields. Finally, the scattered geometrical optics field is obtained by subtracting the initial field from the total geometrical field.

REFERENCES

1. J.S. Tyo, A Class of Artificial Materials Isorefractive With Free Space, IEEE Trans. Antennas Propag., Vol:51, No:5, 1093–1099, 2003.
2. J.S. Tyo, C.J. Buchenauer, J.S.H. Schoenberg, Use of Isorefractive Media to Improve Prompt Aperture Efficiency in a Lens IRA, IEEE Trans. AntennasPropag., Vol:46, No:7, 1114–1115, 1998.
3. P.L.E. Uslenghi, Scattering by a Half-Plane at the Interface Between Isorefractive Media, IEEE Antennas Wirel. Propag. Lett., Vol:12, 1662–1664, 2013.
4. P.L.E. Uslenghi, Radiation of a Line Source Over a Half-Plane Located at the Interface Between Isorefractive Media, IEEE Antennas Wirel. Propag. Lett., Vol:15, 356–357, 2016.
5. Y.Z. Umul, Scattering by a conductive half-screen between isorefractive media, Appl. Opt., Vol:54, 10309–10313, 2015.
6. Y.Z. Umul, Scattering of waves by a soft-hard half-plane between isorefractive medium, J. Mod. Opt., Vol:64, No:4, 329–333, 2016.
7. Y.Z. Umul, Diffraction of line source field by a resistive half-plane between isorefractive media, Opt. Quant. Electron., Vol:49, No:1, 23, 2017.
8. H.D. Basdemir, Scattering of waves by a perfectly conducting wedge residing at the interface between two isorefractive media, IEEE Antennas Wirel.Propag. Lett., Vol:15, 1361–1364, 2016.
9. H.D. Basdemir, Scattering of evanescent plane waves by a black wedge at the interface between two isorefractive media, IEEE Trans. AntennasPropag., Vol:64, No:8, 3661–36642016.
10. J. Zhang, X. He, Asymptotic diffraction of a PEC cylinder located at a plane interface between isorefractive media, IEEE Trans. Antennas Propag., Vol:65, No:6, 3282–3287, 2017.

11. Y.Z. Umul, Scattering of waves by a half-screen between isorefractive media, Optik, Vol:156, 803-810, 2018
12. M. Kara, Diffraction of a plane wave by an aperture composed of two different resistive half planes between isorefractive media, Optical and Quantum Electronics, Vol:53, No:7, Article: 392, 2021.
13. Y.Z. Umul, The method of transition boundary for the solution of diffraction problems, Optical and Quantum Electronics, Vol: 51, 181, 2019.

KANTOROVICH TYPE (p,q)- GENERALIZATION OF BERNSTEIN OPERATORS

Hayatem Hamal[1] **Pembe Sabancıgil**[2]

[1] Department of Mathematics, Tripoli University, Libya

hafraj@yahoo.com

[2] Department of Mathematics, Eastern Mediterranean University, Gazimagusa, North Cyprus

pembe.sabancigil@emu.edu.tr

Abstract

In this paper, we introduce a new generalization of Kantorovich type Bernstein operators by means of (p,q)- calculus for $0<q<p\leq 1$ and we derive a recurrence formula for these newly defined operators to give explicit formulas for the m-th order moments which play an important role in approximation theory.

Keywords: (p,q)- calculus; Moments; Bernstein polynomials.

1.INTRODUCTION

The Kantorovich modifications of sequences of linear positive operators are a method to approximate the Lebesgue integrable functions. The idea behind Kantorovich modifications mainly depends on the replacing of the sample values $f\left(\frac{k}{n}\right)$ by the mean values of f in the intervals $\left[\frac{k}{n+1},\frac{k+1}{n+1}\right]$.

The classical Kantorovich operator K_n, $n=1,2,...$ is introduced as follows:

$$K_n\left(f;x\right)=(n+1)\sum_{k=0}^{n}\binom{n}{k}x^k(1-x)^{n-k}\int_{k/n+1}^{k+1/n+1}f(t)dt$$

$$=\sum_{k=0}^{n}\binom{n}{k}x^k(1-x)^{n-k}\int_0^1 f\left(\frac{k+t}{n+1}\right)dt,\ \ f:[0,1]\to\mathbb{R}.$$

Kantorovich type q-Bernstein operators are defined by Mahmudov and Sabancıgil in [1] as follows:

$$B_{n,q}^{*}\left(f,x\right)=\sum_{k=0}^{n}p_{n,k}\left(q,x\right)\int_{0}^{1}f\left(\frac{\left(\left[k\right]_{q}+q^{k}t\right)}{\left[n+1\right]_{q}}\right)d_{q}t,\ \ x\in\left[0,1\right],\ n\in\mathbb{N},\ 0<q<1. \tag{1}$$

where $p_{n,k}\left(q,x\right)=\begin{bmatrix} n \\ k \end{bmatrix}_{q} x^{k}\left(1-x\right)_{q}^{n-k},\ \ (1-x)_{q}^{n}=\prod_{s=0}^{n-1}(1-q^{s}x).$

If $q\rightarrow 1^{-}$ these operators becomes the classical Bernstein-Kantorovich operator.

In this paper, inspired by definition (1), we introduce a $\left(p,q\right)$- generalization of Kantorovich type Bernstein operators by means of $\left(p,q\right)$- calculus for $0<q<p\leq 1$. We find a recurrence formula for these newly defined operators to present the explicit formulas for the m-th order moments which play an important role in the approximation theory.

Firstly, we give some notations and definitions of $\left(p,q\right)$- calculus.

For any $p>0,\ q>0,$ non-negative integer n, the $\left(p,q\right)$- integer of the number n is defined as:

$$\left[n\right]_{p,q}=p^{n-1}+p^{n-2}q+p^{n-3}q^{2}+\cdots+pq^{n-2}+q^{n-1}=\begin{cases} \dfrac{p^{n}-q^{n}}{p-q} & if\ p\neq q\neq 1 \\ np^{n-1} & if\ p=q\neq 1 \\ \left[n\right]_{q} & if\ p=1 \\ n & if\ p=q=1 \end{cases}.$$

Note that, $\left[n\right]_{p,q}=p^{n(n-1)/2}\left[n\right]_{\frac{q}{p}}.$

$\left(p,q\right)$- factorial is defined by

$$\left[n\right]_{p,q}!=\prod_{k=1}^{n}\left[k\right]_{p,q},\ \ n\geq 1\ \text{ and }\ \left[0\right]_{p,q}!=1.$$

$\left(p,q\right)$- binomial coefficient is defined by

$$\begin{bmatrix} n \\ k \end{bmatrix}_{p,q}=\frac{\left[n\right]_{p,q}!}{\left[k\right]_{p,q}!\left[n-k\right]_{p,q}!},\ \ \ 0\leq k\leq n,$$

the formula of $\left(p,q\right)$- binomial expansion is

$$(ax+by)_{p,q}^{n}=\sum_{k=0}^{n} p^{\frac{(n-k)(n-k-1)}{2}} q^{\frac{k(k-1)}{2}} a^{n-k}b^{k}x^{n-k}y^{k}$$
$$=(ax+by)(pax+qby)(p^{2}ax+q^{2}by)...(p^{n-1}ax+q^{n-1}by),$$

and

$$(x-y)_{p,q}^{n}=(x-y)(px-qy)(p^{2}x-q^{2}y)(p^{3}x-q^{3}y)...(p^{n-1}x-q^{n-1}y).$$

From (p,q)- binomial expansion, we can see that

$$\sum_{k=0}^{n} p^{k(k-1)/2}\begin{bmatrix} n \\ k \end{bmatrix}_{p,q} x^{k}(1-x)_{p,q}^{n-k}=p^{n(n-1)/2} \quad , \ x\in[0,1].$$

Let $f:C[0,a]\to\mathbb{R}$, the (p,q)-integral of f is defined by:

$$\int_{0}^{a} f(t)d_{p,q}t=(p-q)a\sum_{k=0}^{\infty} f\left(\frac{q^{k}}{p^{k+1}}a\right)\frac{q^{k}}{p^{k+1}} \text{ if } \left|\frac{p}{q}\right|>1,$$

In [2], Mursaleenetal, introduced (p,q)-analogue of Bernstein operators as follows:

$$B_{n,p,q}(f,x)=\frac{1}{p^{\frac{n(n-1)}{2}}}\sum_{k=0}^{n}\begin{bmatrix} n \\ k \end{bmatrix} p^{\frac{k(k-1)}{2}} x^{k}\prod_{s=0}^{n-k-1}(p^{s}-q^{s}x) f\left(p^{n-k}\frac{[k]_{p,q}}{[n]_{p,q}}\right), \ x\in[0,1].$$

2. Construction of the Operators and Their Moments

Definition 1. Let $0<q<p\le 1$. Kantorovich type (p,q)-analogue of Bernstein operator is defined as follows:

$$B_{n,p,q}^{*}(f,x)=\sum_{k=0}^{n} b_{n,k}(p,q,x)\int_{0}^{1} f\left(\frac{p^{n-k}\left([k]_{p,q}+q^{k}t\right)}{[n+1]_{p,q}}\right) d_{p,q}t, \ \ x\in[0,1], \ n\in\mathbb{N}$$

where $b_{n,k}^{p,q}(x)=\frac{1}{p^{n(n-1)/2}}\begin{bmatrix} n \\ k \end{bmatrix}_{p,q} p^{k(k-1)/2}x^{k}(1-x)_{p,q}^{\ \ n-k}$.

Now we will construct the recurrence formula for $B_{n,p,q}^{*}(t^{m},x)$ and calculate the first three moments of $B_{n,p,q}^{*}(t^{m},x)$ for $m=0, \ 1, 2$.

Lemma 1. For all $n\in\mathbb{N}$, $x\in[0,1]$, $m\in\mathbb{Z}\cup\{0\}$ and $0<q<p\le 1$, we have

$$B^*_{n,p,q}\left(t^m,x\right)=\sum_{j=0}^{m}\binom{m}{j}\frac{[n]^j_{p,q}}{[n+1]^m_{p,q}}\frac{p^{nm}}{[m-j+1]_{p,q}}\sum_{i=0}^{m-j}\frac{1}{p^{n(i+j)}}\binom{m-j}{i}\left(q^n-p^n\right)^i B_{n,p,q}\left(t^{i+j},x\right),$$

where $B_{n,p,q}\left(f,x\right)=\sum_{k=0}^{n}b^{p,q}_{n,k}\left(x\right)f\left(p^{n-k}\frac{[k]_{p,q}}{[n]_{p,q}}\right).$

Proof. By direct calculations, the recurrence formula is obtained as follows:

$$B^*_{n,p,q}\left(t^m,x\right)=\sum_{k=0}^{n}b_{n,k}\left(p,q,x\right)\int_0^1 f\left(\frac{p^{n-k}\left([k]_{p,q}+q^k t\right)}{[n+1]_{p,q}}\right)^m d_{p,q}t,$$

by using the binomial expansion of $\left([k]_{p,q}+q^k t\right)^m$ and evaluating the $\left(p,q\right)$- integral we get

$$B^*_{n,p,q}\left(t^m,x\right)=\sum_{k=0}^{n}b_{n,k}\left(p,q,x\right)\sum_{j=0}^{m}\binom{m}{j}\frac{1}{[m-j+1]_{p,q}}\frac{p^{(n-k)m}}{[n+1]^m_{p,q}}[k]^j_{p,q}q^{k(m-j)}$$

$$=\sum_{j=0}^{m}\binom{m}{j}\frac{p^{nm}}{[m-j+1]_{p,q}[n+1]^m_{p,q}}\sum_{k=0}^{n}\sum_{i=0}^{m-j}\binom{m-j}{i}p^{-k(i+j)}\left(q^k-p^k\right)^i[k]^j_{p,q}b_{n,k}\left(p,q,x\right)$$

$$=\sum_{j=0}^{m}\binom{m}{j}\frac{p^{nm}}{[m-j+1]_{p,q}b^m_n}\sum_{i=0}^{m-j}\binom{m-j}{i}\left(q-p\right)^i\sum_{k=0}^{n}p^{-k(i+j)}[k]^{i+j}_{p,q}b_{n,k}\left(p,q,x\right)$$

$$=\sum_{j=0}^{m}\binom{m}{j}\frac{p^{n(m-j)}[n]^j_{p,q}}{[m-j+1]_{p,q}[n+1]^m_{p,q}}\sum_{i=0}^{m-j}\binom{m-j}{i}\left(\frac{a_n}{p^n}\right)^i\left(q^n-p^n\right)^i$$

$$\times\sum_{k=0}^{n}p^{(n-k)(i+j)}\frac{[k]^{i+j}_{p,q}}{[n]^{i+j}_{p,q}}b_{n,k}\left(p,q,x\right).$$

Now, in the last equality by using the definition of the operators $B_{n,p,q}\left(f,x\right)$ given by (3), we may write

$$B^*_{n,p,q}\left(t^m,x\right)=\sum_{j=0}^{m}\binom{m}{j}\frac{[n]^j_{p,q}}{[n+1]^m_{p,q}}\frac{p^{n(m-j)}}{[m-j+1]_{p,q}}\sum_{i=0}^{m-j}\frac{1}{p^{ni}}\binom{m-j}{i}\left(q^n-p^n\right)^i B_{n,p,q}\left(t^{i+j},x\right).$$

In the following lemma, we calculate $B_{n,p,q}\left(f,x\right)$ for the monomials $f(t^m)=t^m$, $m=0,1,2.$

Lemma 2. For $x\in[0,1]$, $0<q<p\le 1$ and $n\in\mathbb{N}$, we have

$$B^*_{n,p,q}(1,x)=1,$$

$$B^*_{n,p,q}(t,x)=\frac{p^n}{[2]_{p,q}}\frac{1}{[n+1]_{p,q}}+\frac{2q}{[2]_{p,q}}\frac{[n]_{p,q}}{[n+1]_{p,q}}x,$$

$$B^*_{n,p,q}(t^2,x)=\frac{p^{2n}}{[3]_{p,q}}\frac{1}{[n+1]^2_{p,q}}+\left\{\frac{4q^3p^{n-1}+5q^2p^n+3qp^{n+1}}{[2]_{p,q}[3]_{p,q}}\frac{[n]_{p,q}}{[n+1]^2_{p,q}}\right\}x$$

$$+\left\{\frac{4q^3+q^2+q}{[2]_{p,q}[3]_{p,q}}\frac{q[n]_{p,q}[n-1]_{p,q}}{[n+1]^2_{p,q}}\right\}x^2.$$

Proof.

$$B^*_{n,p,q}(1,x)=\frac{1}{p^{n(n-1)/2}}\sum_{k=0}^{n}\begin{bmatrix}n\\k\end{bmatrix}_{p,q}p^{k(k-1)/2}x^k(1-x)_{p,q}^{\;n-k}=1.$$

$$B^*_{n,p,q}(t,x)=\sum_{j=0}^{1}\binom{1}{j}\frac{[n]^j_{p,q}}{[n+1]_{p,q}}\frac{p^{n(1-j)}}{[2-j]_{p,q}}\sum_{i=0}^{1-j}\frac{1}{p^{ni}}\binom{1-j}{i}(q^n-p^n)^iB_{n,p,q}(t^{i+j},x)$$

$$=\frac{p^n}{[2]_{p,q}}\frac{1}{[n+1]_{p,q}}\left\{1+\frac{1}{p^n}(q^n-p^n)B_{n,p,q}(t,x)\right\}+\frac{[n]_{p,q}}{[n+1]_{p,q}}B_{n,p,q}(t,x)$$

$$=\frac{p^n}{[2]_{p,q}}\frac{1}{[n+1]_{p,q}}\left\{1+\frac{1}{p^n}(q^n-p^n)B_{n,p,q}(t,x)\right\}+\frac{[n]_{p,q}}{[n+1]_{p,q}}B_{n,p,q}(t,x).$$

Now, by using the formula for $B_{n,p,q}(t,x)$ which is given in [2], we get

$$B^*_{n,p,q}(t,x)=\frac{p^n}{[2]_{p,q}}\frac{1}{[n+1]_{p,q}}+\frac{2q}{[2]_{p,q}}\frac{[n]_{p,q}}{[n+1]_{p,q}}x.$$

Now to calculate $B^*_{n,p,q}(t^2,x)$, we write

$$B^*_{n,p,q}(t^2,x)=\sum_{j=0}^{2}\binom{2}{j}\frac{[n]^j_{p,q}}{[n+1]_{p,q}}\frac{p^{n(2-j)}}{[3-j]_{p,q}}\sum_{i=0}^{2-j}\frac{1}{p^{ni}}\binom{2-j}{i}(q^n-p^n)^iB_{n,p,q}(t^{i+j},x)$$

$$=\frac{p^{2n}}{[3]_{p,q}}\frac{1}{[n+1]^2_{p,q}}\left\{1+\frac{2}{p^n}(q^n-p^n)B_{n,p,q}(t,x)+\frac{1}{p^{2n}}(q^n-p^n)^2B_{n,p,q}(t^2,x)\right\}$$

$$=\frac{2p^{n}}{[2]_{p,q}}\frac{[n]_{p,q}}{[n+1]_{p,q}^{2}}\left\{B_{n,p,q}(t,x)+\frac{1}{p^{n}}(q^{n}-p^{n})B_{n,p,q}(t^{2},x)\right\}+\frac{[n]_{p,q}^{2}}{[n+1]_{p,q}^{2}}B_{n,p,q}(t^{2},x).$$

Again, by using the formulas of $B_{n,p,q}(t,x)$ and $B_{n,p,q}(t^{2},x)$ which are given in [2] and by simple calculations in the last equality, we get

$$B_{n,p,q}^{*}(t^{2},x)=\frac{p^{2n}}{[3]_{p,q}}\frac{1}{[n+1]_{p,q}^{2}}+\left\{\frac{4q^{3}p^{n-1}+5q^{2}p^{n}+3qp^{n+1}}{[2]_{p,q}[3]_{p,q}}\frac{[n]_{p,q}}{[n+1]_{p,q}^{2}}\right\}x$$

$$+\left\{\frac{4q^{3}+q^{2}+q}{[2]_{p,q}[3]_{p,q}}\frac{q[n]_{p,q}[n-1]_{p,q}}{[n+1]_{p,q}^{2}}\right\}x^{2}.$$

3.CONCLUSIONS

The Kantorovich modifications of sequences of linear positive operators are important in the sense to approximate the Lebesgue integrable functions. In this paper, we introduced a new (p,q)-generalization of Kantorovich type q-Bernstein operators given by (1) by means of (p,q)-calculus for $0<q<p\leq 1$. We derived a recurrence formula for these newly defined operators to give explicit formulas for the *m*-th order moments which are very important tools in approximation theory.

REFERENCES

1. Nazim Mahmudov, Pembe Sabancigil, Approximation Theorems for q-Bernstein-Kantorovich Operators, Filomat, vol: 27, No:4, 721-730, 2013.
2. Mohammad Mursaleen, Khursheed J. Ansari, Asif Khan, On (p,q)-analogue of Bernstein operators, Applied Mathematics and Computation, vol: 266, 874-882. Erratum: Applied Mathematics and Computation, vol: 278, 70-71, 2016.
3. Mohammad Mursaleen, Khursheed J Ansari, Asif Khan, Some approximation results by (p,q)-analogue of Bernstein–Stancu operators, Applied Mathematics and Computation, 264, 392-402, 2015.
4. Tuncer Acar, Ali Aral, SA Mohiuddine, On Kantorovich Modification of (p,q)-Bernstein Operators, Iranian Journal of Science and Technology, Transactions A: Science, vol: 42, 1459–1464, 2018.

5. S.A. Mohiuddine, Tuncer Acar, Abdullah Alotaibi, Construction of a new family of Bernstein-Kantorovich operators, Mathematical Methods in the Applied Sciences, vol: 40, 7749–7759, 2017.
6. Tuncer Acar, (p,q)- Generalization of Szász–Mirakyan operators, Mathematical Methods in the Applied Sciences, vol: 39, 2685–2695, 2016.
7. Yun-Shun Wu, Wen-Tao Cheng, Feng-Lin Chen, Yong-Hui Zhou, Approximation Theorem for New Modification of q- Bernstein Operators on $(0,1)$, Journal of Function Spaces, Article ID 6694032, 1-9, 2021.
8. Tuncer Acar, Ali Aral, SA Mohiuddine, Approximation by bivariate (p,q)- Bernstein – Kantorovich operators, Iranian Journal of Science and Technology, Transactions A: Science vol:42, 655–662, 2018.

A BRIEF SURVEY ON NUMERICAL SOLUTIONS OF SINGULARLY PERTURBED PROBLEMS

Ilhame Amirali[1] and **Ece Eroğlu**[2]

[1]Department of Mathematics, University of Duzce, Duzce, Turkey
[2]Department of Mathematics, University of Duzce, Duzce, Turkey
[1]ailhame@gmail.com

[2]eceeroglu90@gmail.com

August 8, 2022

Abstract

This work provides a brief overview of numerical solutions to singularly perturbed problems. The current survey in this paper does not aim to be a comprehensive bibliographical survey. A literature review was conducted between 2010-2021. A variety of articles of singularly perturbed differential and integro-differential equations are included in the list of references in this study.
Keywords: Singular perturbation, Ordinary differential equation, Integro-differential equation, Initial and boundary value problems, Uniform convergence, Boundary layer, Error estimate.

1 Introduction

Much scientific endeavour is aimed at the relation between causes and their effects. This becomes more intriguing whenever the cause is small and the effect large. The study of this relation in the field of the theory of perturbations in mathematical or physical systems has already a respectable history, which can be retraced to the time of Prandtl about a century ago. Despite this long history the subject is still in a state of vigorous development and it is known as the theory of singular perturbations, where the meaning of a "small" perturbation causing a "large" impact to be made explicitly clear.
In 1904 a little-known physicist Ludwig Prandtl revolutionized fluid dynamics with his notion that the effects of friction are experienced only very near an

object moving through a fluid. In his paper, "Fluid Flow in Very Little Friction", at the Third International Mathematics Congress in Heidelberg, he introduced the concept of boundary layer and its importance for grad and streamlining. Prandtl assumed the no-slip condition at the surface and that frictional effects were experienced only in a boundary layer, a thin region near the surface [15].

This boundary-layer theory became the foundation stone for modern fluid dynamics. The mathematical justification of boundary-layer theory provides us a more general theory to calculate asymptotic expansions of the solutions to the complete equations of the motion. The problem is reduced to a so-called singular perturbation problem, which is then solved by the method of matched asymptotic expansions. The term "singular perturbation" was first used by Friedrichs and Wasow in their paper [13], [21].

Definition

Consider the initial/boundary value problem that depends on a small parameter $\varepsilon > 0$. The problem obtained by setting $\varepsilon = 0$ in the equation and data is called the reduced problem. If the reduced problem is of the same type and order as the given one and both have unique solutions, then the given problem is called a regular perturbation problem; otherwise, it is called a singular perturbation problem. The parameter ε termed the perturbation parameter.

In singular perturbation case, if we let ε approach to 0, the order of differential equation reduces and some of the initial/boundary conditions will become superfluous [1-5]. The solution exhibits narrow regions of vary fast variation, so-called initial/boundary layers, while away from the layers the solution behaves regularly and varies slowly. More exactly, outside the layers the solution is mainly dominated by that of reduced problem.

But inside the layers the smoothness of the solution of singularly perturbed problems aggravates and the solution has derivatives which blow up for $\varepsilon \to 0$ [22-23].

That is why, the use of standard numerical methods for solving such problems may give rise to difficulties when the perturbation parameter ε is small. Often the root of these difficulties lies in the instability or in the convergence absence of the numerical process [10]. Classical difference methods for solving such problems, in general, do not converge uniformly with respect to the small parameter. Therefore these is a need to develop for such type of problems, special numerical methods, whose accuracy does not depend on the parameter value ε i. e. , methods that are convergence $\varepsilon-$ uniformly [24-25].

A variety of different numerical strategies have been proposed in an attempt to obtain reliable, accurate methods. These include fitted difference methods, finite element methods using special elements such as exponential elements and methods which use a priori refined or special non-uniform grids cendensing in a special manner in the boundary layer [26-27].

Further, it is also known that difference schemes on a uniform mesh are not suitable to nonlinear singularly perturbed problems as a special fine mesh is required in layer region and comparatively much coarser mesh elsewhere. Ideally, the mesh should be adapted to the features of the exact solution using an adaptive grid generation technique. This approach is now widely used for numerical solution of differential equations with step, continuous solutions.

Some examples of SPP's can be met very often in many areas of science, from fluid mechanics to biology and from control theory to quantum mechanics, for instance, the Navier-Stokes equations of fluid flow at high Reynold number, mathematical models of liquid crystal materials and others [17], [28].

Consider the example:

Example 1:

$$\begin{cases} u^{'} + \varepsilon u = 0, & \text{x>0}, \\ u(0) = 1. \end{cases}$$

The reduced problem is

$$\begin{cases} u^{'} = 0, \\ u(0) = 1. \end{cases}$$

That is has also order one. Thereby, the problem is regularly perturbed.
Consider the another example:

Example 2:

$$\begin{cases} \varepsilon u^{'} + u = 0, & \text{x>0}, \\ u(0) = 1. \end{cases}$$

The corresponding reduced problem has order zero with solution $u_0(x) = 0$ and initial condition is superfluous. Therefore, the problem is singularly perturbed.
The solution of first example is

$$u_\varepsilon(x) = e^{-\varepsilon x}$$

and this function, as well as it's derivatives uniformly bounded everywhere.
The solution of second example is

$$u_\varepsilon(x) = e^{-\frac{x}{\varepsilon}}.$$

$$|u^{(k)}(x)| = \frac{1}{\varepsilon^k} e^{-\frac{x}{\varepsilon}},$$

although $|u_\varepsilon(x)| \leq 1$, but $|u^{(k)}(x)|$, $k \geq 1$ is not uniformly bounded in ε everywhere.
Consider the following second-order linear self adjoint differential problem:

Example 3:

$$\begin{cases} \varepsilon u^{''} - u = 0, & 0 < x < 1, \\ u(0) = 1, & u(1) = -1, \end{cases}$$

where the exact solution is given by

$$u(x) = \frac{sinh(\frac{1-x}{\sqrt{\varepsilon}})}{sinh(\frac{1}{\sqrt{\varepsilon}})} - \frac{sinh(\frac{x}{\sqrt{\varepsilon}})}{sinh(\frac{1}{\sqrt{\varepsilon}})} = u_1(x) + u_2(x),$$

$$u_1(x) = \frac{sinh(\frac{1-x}{\sqrt{\varepsilon}})}{sinh(\frac{1}{\sqrt{\varepsilon}})},\ u_2(x) = -\frac{sinh(\frac{x}{\sqrt{\varepsilon}})}{sinh(\frac{1}{\sqrt{\varepsilon}})}.$$

$u_1(x)$ projects a left-hand side boundary layer behavior of solution and $u_2(x)$ is a right-hand side boundary layer behavior.

$$u_1^{'}(x) = \frac{-\frac{1}{\sqrt{\varepsilon}}cosh(\frac{1-x}{\sqrt{\varepsilon}})}{sinh(\frac{1}{\sqrt{\varepsilon}})} = -\frac{1}{\sqrt{\varepsilon}}\left(\frac{e^{-\frac{x}{\sqrt{\varepsilon}}} + e^{-\frac{2-x}{\sqrt{\varepsilon}}}}{1 - e^{-\frac{2}{\sqrt{\varepsilon}}}}\right),$$

$$u_2^{'}(x) = -\frac{\frac{1}{\sqrt{\varepsilon}}cosh(\frac{x}{\sqrt{\varepsilon}})}{sinh(\frac{1}{\sqrt{\varepsilon}})} = -\frac{e^{\frac{x-1}{\sqrt{\varepsilon}}}}{\sqrt{\varepsilon}}\left(\frac{1 + e^{-\frac{2x}{\sqrt{\varepsilon}}}}{1 - e^{-\frac{2}{\sqrt{\varepsilon}}}}\right).$$

$u_1^{'}(x) = O(\frac{1}{\sqrt{\varepsilon}})$ in boundary layer and outside the layer is uniformly bounded, for example

$$|u_1^{'}(1)| = \frac{1}{\sqrt{\varepsilon}}\left(\frac{2e^{-\frac{1}{\sqrt{\varepsilon}}}}{1 - e^{-\frac{2}{\sqrt{\varepsilon}}}}\right) \to 0, \text{ for } \varepsilon \to 0.$$

Analogous properties has the function $u_2(x)$ near $x = 1$. Thus, this example has two boundary layers, first at the neighbor of 0 and other at the neighbor of 1. Inside the layers the solution is bounded but the derivatives of solution blow up for $\varepsilon \to 0$.
Consider the non-self adjoint problem as

Example 4:

$$\begin{cases} \varepsilon u^{''} + u^{'} = 0, & 0 < x < 1, \\ u(0) = 1, & u(1) = 2. \end{cases}$$

The solution is given by

$$u(x) = 1 + \frac{1 - e^{-\frac{x}{\varepsilon}}}{1 - e^{-\frac{1}{\varepsilon}}}$$

and

$$u^{'}(x) = \frac{1}{\varepsilon}\left(\frac{e^{-\frac{x}{\varepsilon}}}{1 - e^{-\frac{1}{\varepsilon}}}\right)$$

and evidently that

$$u^{'}(x) \to \infty \text{ for } x = O(\varepsilon).$$

But, for example, if $x = \sqrt{\varepsilon}$ then $u^{'}(\sqrt{\varepsilon}) = \frac{1}{\varepsilon}\left(\frac{e^{-\frac{1}{\sqrt{\varepsilon}}}}{1-e^{-\frac{1}{\varepsilon}}}\right) \to 0.$

Explicit Euler Scheme

Consider the initial value problem:

$$\begin{cases} \varepsilon u^{'} + f(x,u) = 0, & 0 < x \leq l, \\ u(0) = A. \end{cases}$$

The appropriate explicit scheme will be

$$\begin{cases} \varepsilon \frac{y_{i+1} - y_i}{h} + f(x_i, y_i) = 0, & i = 0, 1, ..., N-1 \\ y_0 = A. \end{cases}$$

In interval $[0, l]$, $x_i = ih$ are mesh points, $i = 0, 1, 2, ..., N$, $h = \frac{l}{N}$, h is a step-size, n number of subintervals. y_i is an approximate solution at mesh point x_i. This scheme, in order to be convergent should be $|u^{''}(x)| \leq C$ in closed interval. But we know that even first derivative is not bounded, in general, in closed interval.
Consider the example:

Example 5:

$$\begin{cases} \varepsilon u^{'} + u = 0, & 0 < x \leq 1 \\ u(0) = 1. \end{cases}$$

The solution is

$$u(x) = e^{-\frac{x}{\varepsilon}}.$$

The appropriate explicit scheme will be

$$\begin{cases} \varepsilon \frac{y_{i+1} - y_i}{h} + y_i = 0, & i = 0, 1, ... \\ y_0 = 1. \end{cases}$$

Since

$$u(x_1) = e^{-\frac{h}{\varepsilon}},$$

$$y_1 = 1 - \frac{h}{\varepsilon},$$

then the error of approximate solution will be

$$|y_1 - u(x_1)| = \left|1 - \frac{h}{\varepsilon} - e^{-\frac{h}{\varepsilon}}\right|.$$

In a special case $h = \varepsilon$ we have $|y_1 - u(x_1)| = \left|1 - 1 - e^{-\frac{h}{\varepsilon}}\right| = \frac{1}{e}$, i.e., the uniform convergence is absent.

Implicit Euler Scheme
Consider the initial value problem again:

$$\begin{cases} \varepsilon u^{'} + f(x,u) = 0, & 0 < x \leq l, \\ u(0) = A. \end{cases}$$

The appropriate implicit scheme will be

$$\begin{cases} \varepsilon^{\frac{y_i - y_{i-1}}{h}} + f(x_i, y_i) = 0, \quad i = 1, 2, ..., N \\ y_0 = A. \end{cases}$$

This is a nonlinear scalar equation for each i and can be solved applying appropriate algorithm to nonlinear equations (fixed point iteration, Newton-Raphson, etc.), the uniform convergence in ε for such schemes generally is also absent. Consider again the example:

Example 5:

$$\begin{cases} \varepsilon u^{'} + u = 0, \quad 0 < x \leq 1 \\ u(0) = 1. \end{cases}$$

The solution is

$$u(x) = e^{-\frac{x}{\varepsilon}}.$$

The appropriate explicit scheme will be

$$\begin{cases} \varepsilon^{\frac{y_i - y_{i-1}}{h}} + y_i = 0, \quad i = 0, 1, ... \\ y_0 = 1. \end{cases}$$

Since

$$u(x_1) = e^{-\frac{h}{\varepsilon}},$$

$$y_1 = \frac{\varepsilon}{\varepsilon + h}$$

then the error of approximate solution will be

$$|y_1 - u(x_1)| = \left| \frac{\varepsilon}{\varepsilon + h} - e^{\frac{h}{\varepsilon}} \right|.$$

In a special case $h = \varepsilon$ we have $|y_1 - u(x_1)| = \frac{1}{2} - \frac{1}{e}$, i.e., the uniform convergence is absent.

Crank-Nicolson Scheme
If consider the above initial value problem

$$\begin{cases} \varepsilon u^{'} + f(x, u) = 0, \quad 0 < x \leq l, \\ u(0) = A, \end{cases}$$

the appropriate Crank-Nicolson scheme will be

$$\begin{cases} \varepsilon^{\frac{y_i - y_{i-1}}{h}} + \frac{1}{2}[f(x_i, y_i) + f(x_{i-1}, y_{i-1})] = 0, \quad i = 1, 2, ..., N \\ y_0 = A. \end{cases}$$

Consider the same example:

Example 5:

$$\begin{cases} \varepsilon u^{'} + u = 0, \quad 0 < x \leq 1 \\ u(0) = 1. \end{cases}$$

The solution is

$$u(x) = e^{-\frac{x}{\varepsilon}}.$$

The appropriate Crank-Nicolson scheme as

$$\begin{cases} \varepsilon \frac{y_i - y_{i-1}}{h} + \frac{1}{2}(y_i + y_{i-1}) = 0, \quad i = 0, 1, ... \\ y_0 = 1. \end{cases}$$

Since

$$u(x_1) = e^{-\frac{h}{\varepsilon}},$$

$$y_1 = \frac{2\varepsilon - h}{2\varepsilon + h},$$

then the error of approximate solution will be

$$|y_1 - u(x_1)| = \left|\frac{2\varepsilon - h}{2\varepsilon + h} - e^{-\frac{h}{\varepsilon}}\right|.$$

In a special case $h = \varepsilon$ we have

$$|y_1 - u(x_1)| = \left|\frac{1}{3} - \frac{1}{e}\right|,$$

i.e., the uniform convergence is absent.
The use of classical difference methods for solving such problem may give rise to difficulties when the singular perturbation parameter ε is small. It is important to develop suitable numerical methods to these problems. Here are being used two expansive approach:

Exponentially Fitted Schemes
They are generally used for the linear problems. Consider the initial value problem

$$\begin{cases} \varepsilon u^{'} + a(x)u = f(x), \quad 0 < x \leq l \\ u(0) = A. \end{cases}$$

The appropriate exponentially fitted scheme will be

$$\begin{cases} L_N y_i \equiv \varepsilon\theta_i \frac{y_i - y_{i-1}}{h} + a_i y_i = f_i \quad i = 1, 2, ..., N \\ y_0 = A, \\ \theta_i = \frac{\rho a_i}{1 - exp(-\rho a_i)} exp(-\rho a_i), \qquad \rho = \frac{h}{\varepsilon}. \end{cases}$$

7

The difference of this scheme that, it is uniform convergent in whole interval. This scheme contains exponential factor θ_i and the truncation error includes only $u(x)$. But we observed that the truncation error of classical difference schemes was included second derivative.

Non Uniform Meshes
The classical methods also can be used in special non uniform meshes. In such methods a special fine mesh is required in layer region and comparatively much coarser mesh elsewhere. Ideally, the mesh should be adapted to the features of the exact solution using an adaptive grid generation technique. One of the simplest ways to derive such methods consists of using a special piecewise uniform meshes. This approach is now widely used for numerical solution of differential equations with step, continuous solutions. Especially this type schemes are being used to nonlinear singular perturbation problems. A Shishkin mesh is a piecewise uniform mesh. What distinguishes a Shishkin mesh from any other piecewise uniform mesh, is the choice of the so-called transition parameter(s), which are the point(s) at which the mesh size changed abruptly. Piecewise-uniform meshes are the simplest kind of non-uniform mesh and they are constructed as follows.

The interval $(0, X]$ is divided into two pieces $(0, \sigma]$ and $(\sigma, X]$. N is chosen to be an even number and each piece is discretised by a uniform mesh with $\frac{N}{2}$ subintervals. If the point $\sigma = \frac{1}{2}$, it is clear that the complete mesh $\Omega_h^N = \{x_i\}_{i=0}^N$ on X is a uniform mesh, but if $\sigma \neq \frac{1}{2}$ say $\sigma < \frac{1}{2}$, then the mesh in $(0, \sigma]$ is finer than the mesh in $(\sigma, X]$ and the point σ is called the *transition point*.
Here $x_0 = 0, \quad x_{\frac{N}{2}=\sigma}, \quad x_N = X$. In the fine mesh the mesh spacing is
$x_i - x_{i-1} = \frac{2\sigma}{N}$, while in the coarse mesh it is $\frac{2(1-\sigma)}{N}$.

We derive our numerical methods using interpolating quadrature rules with weight and remainder terms in integral form and analyze finite difference schemes on special piecewise uniform meshes that are constructed a priori and are dependent on the parameter ε, the problem data and the number of corresponding mesh points. They have good convergence properties not just for small but also for moderate and large perturbation parameter values.

2 Numerical Techniques For Solving SPPs

In [6] various methods for solving SP boundary value problems are discussed.
In [7] considered an IVP for the nonlinear 2^{nd}-order SPDDE in the interval $\bar{l}[0, T]$:

$$Lu := \varepsilon u^{''}(t) + a(t)u^{'}(t) + f(t, u(t), u(t-r)) = 0,\ t \in l, \tag{1}$$

$$u(t) = \varphi(t),\ t \in l_0, \tag{2}$$

$$u^{'}(0) = A/\varepsilon, \tag{3}$$

where $l = (0,T] = \bigcup_{p=1}^{m},\ l_p = \{t : r_{p-1} < t \le r_p\},\ 1 \le p \le m$ and $r_s = sr$, for $0 \le s \le m$ and $l_0 = [-r, 0]$ (for simplicity supposed that T/r is integer; i.e., $T = mr$). $0 < \varepsilon << 1$ is the perturbation parameter, $a(t) \ge \alpha > 0, f(x,u,v)$ and $\varphi(t)$ are given sufficiently smooth functions satisfying certain regularity conditions in $\bar{l}, \bar{l} \times \mathbb{R}^2$ and l_0 respectively, to be specified, A is a constant and r is a constant delay, which is independent of ε. Moreover

$$\left|\frac{\partial f}{\partial u}\right| \le b^{*} and \left|\frac{\partial f}{\partial v}\right| \le c^{*}. \tag{4}$$

In this paper the authors present the completely exponentially fitted difference scheme on the uniform mesh for the (1)-(3).The difference scheme is constructed using the integral identities method, which employs exponentially basis functions and interpolating quadrature rules with integral weight and remainder terms. This approach of approximation has the advantage of being able to work even when the continuous problem is considered under specific restrictions. The authors estimate the errors and compute the experimental rates of convergence in their computed solution using the double mesh principle, i.e. they compare the computed solution to a solution on a mesh that is twice as fine.

Amiraliyev and Cimen [8] suggested the numerical method to solve the SP-BVP for a linear 2^{nd}-order DDE:

$$\varepsilon u^{''}(x) + a(x)u^{'}(x) + b(x)u(x-r) = f(x),\ x \in \Omega, \tag{5}$$

$$u(x) = \varphi(x),\ x \in \Omega_0;\ u(l) = B, \tag{6}$$

where $\Omega = \Omega_1 \cup \Omega_2,\ \Omega_1 = (0, r],\ \Omega_2 = (r, l),\ \overline{\Omega} = [0, l],\ \Omega_0 = [-r, 0]$ and $0 < \varepsilon \le 1$ is the perturbation parameter, $a(x) \ge \alpha > 0,\ b(x),\ f(x)$ and $\varphi(x)$ are given sufficiently smooth functions satisfying certain regularity conditions to be specified and r is a constant delay, which is independent of ε and B is a given constant. For small values of ε the function $u(x)$ has a boundary layer near $x = 0$. An exponentially fitted difference scheme on a uniform mesh is provided to solve this problem. 1^{st}-order convergence in the discrete maximum norm, independently of the perturbation parameter is obtained.

Cakır et al. [11] considered the SP quasilinear initial value problem

$$Lu := \varepsilon u^{''}(t) + a(t,u)u^{'}(t) + b(t)u(t) = f(t),\ 0 < t \le T, \tag{7}$$

$$u(0) = A, \tag{8}$$

$$u^{'}(0) = \frac{B}{\varepsilon}, \tag{9}$$

where $\varepsilon \in (0,1]$ is a small parameter, A and B are given constants, $a(t,u) \geq \alpha > 0$ and $b(t)$, $f(t)$ are assumed to be sufficiently continuously differentiable functions in $[0,T] \times \mathbb{R}$ and $[0,T]$, respectively and moreover $|\partial a/\partial u| \leq \overline{a}^{*}$. For this problem, the authors developed a numerical method, which generates ε-uniformly convergent numerical approximations to the solution and its derivatives. The approach comprises a non-uniform mesh that is fitted to the initial layer and built a priori in function of parameter ε sizes and the problem data. It is possible to attain 1^{st}-order convergence in the discrete maximum norm, regardless of the perturbation parameter. For various values of ε and N, the exact errors and rates of convergence are determined. 1^{st}-order convergence in the discrete maximum norm, independently of the perturbation parameter is obtained. The exact errors and the rates of convergence are computed for different values of ε and N. The numerical findings show that the theoretical results are fairly precise.

In [12], Kudu et al. presented the fitted numerical method for the SPVDIDE

$$Lu := \varepsilon u^{'}(t)a(t)u(t)+b(t)u(t-r)+\int_0^t \{K(t,s)u(s)+L(t,s)u(s-r)\}ds = f(t),\ t \in l, \tag{10}$$

$$u(t) = \psi(t),\ t \in l_0, \tag{11}$$

in the interval $\bar{l} = [0,T]$, where $l = (0,T] = \bigcup_{p=1}^{m} l_p,\ l_p = \{t : r_{p-1} < t \leq r_p\},\ 1 \leq p \leq m$ and $r_s = sr$, for $0 \leq s \leq m$ and $l_0 = [-r,0]$. $\varepsilon \in (0,1]$ is the ε and r is a constant delay, which is independent of ε. Assumed that $a(t) \geq \alpha > 0,\ b(t),\ f(t)\ (t \in \bar{l}),\ \psi(t)(t \in l_0),\ K(t,s)$ and $L(t,s)((t,s) \in \bar{l} \times \bar{l})$ are given sufficiently smooth functions satisfying certain regularity conditions to be specified. The IVP (11)-(12) has in general boundary layers on the right part of each points $t = r_s$ $(0 \leq s \leq m-1)$ for small values of ε. The solution to this problem is to use standard backward difference operators on a non-uniform mesh made up of special piecewise uniform meshes on each time subinterval. It is demonstrated that the approach converges uniformly with respect to the ε. Theoretical and numerical results were presented, and both were in agreement.

In 2017, Amiraliyev and Cimen [9] examined the numerical method for the non-linear 2^{nd}-order SPBVP for the DDE

$$Lu := \varepsilon u^{''}(x) + a(x)u^{'}(x) + f(x, u(x), u(x-r)) = 0,\ x \in \Omega, \tag{12}$$

subject to the interval and boundary conditions

$$u(x) = \varphi(x),\ x \in \Omega_0;\ u(l) = A, \tag{13}$$

where $\Omega = \Omega_1 \cup \Omega_2, \Omega_1 = (0,r],\ \Omega_2 = (r,l),\ \overline{\Omega} = [0,l],\ \Omega_0 = [-r,0]$ and $0 < \varepsilon \leq 1$ is the perturbation parameter, $a(x) \geq \alpha > 0, f(x,u,v)$ and $\varphi(x)$

are given sufficiently smooth functions satisfying certain regularity conditions in $\overline{\Omega}, \overline{\Omega} \times \mathbb{R}^2$ and Ω_0 respectively, to be specified and r is a constant delay, which is independent of ε and B is a given constant and furthermore

$$0 \leq \frac{\partial f}{\partial u} \leq b^* < \infty, \left|\frac{\partial f}{\partial v}\right| \leq c^*.$$

For small values of ε the function $u(x)$ has a boundary layer near $x = 0$.

The authors used an exponentially fitted difference scheme on a uniform mesh for the numerical solution of this problem, which was accomplished using the method of integral identities with the use of exponential basis functions and interpolating quadrature rules with weight and remainder term in integral form. In the discrete maximum norm, the approach is proved to be uniform convergent of 1^{st}-order. Numerical data is offered to back up the theory.

In [16], the authors considered a 2^{nd}-order BVP a SPFIDE and established a 2^{nd}-order uniformly convergent numerical method for the solution of problem. Authors used the exponentially fitted scheme on the Shishkin mesh.

[19] deals with the numerical study of a two parameter SPDPIBVP. To solve the problem, the authors have used a hybrid scheme combining the midpoint scheme, the upwind scheme and the 2^{nd}-order central difference scheme for the spatial derivatives. The proposed technique acquires almost 2^{nd}-order accuracy with respect to the discrete maximum norm. Further provided the numerical results to support the theoretical estimates

Panda et al. [18] considered a SPVIDE. On a Shishkin-type mesh, a fitted mesh finite difference method is applied using a composite trapezoidal rule for the integral part and a finite difference operator for the derivative part. To improve the accuracy of the solution, the Richardson extrapolation is used in the discrete maximum norm and almost 2^{nd}-order convergence is obtained.

[20] comprises a numerical solution of SPVIDEs using some finite difference techniques.Specific test problems have been performed to assess and test the performance of the numerical schemes and comparison is drawn.

3 Conclusion

This work presents a brief review of some numerical strategies for solving different types of SPPs. The numerical approaches used by the researchers included in this study are frequently classed as finite-difference methods, finite-element methods and finite-volume methods, however the survey has not been organized in this way. In general, the solution of SPPs exhibits layer behavior, the width of which is determined by the perturbation parameters, which may be taken as arbitrary small value. In the neighborhood of boundary and internal layers, the solutions of SPPs show a very complicated behavior. It is well known that standard numerical approaches for solving such problems are unstable and fail to produce accurate results for small values of ε. These include fitted finite difference methods, finite element methods using special elements such as exponential elements and methods which use a priori refined or special nonuniform grids condensing in a special manner in the boundary layers. One can add artificial diffusion using finite difference, finite element or finite volume methods. As a result, numerical grid generation has become an enormously significant tool for solving SPPs in a computationally effective way. The development of robust numerical methods for methods whose accuracy is independent on the local scales of singular components of the solution is a significant problem and an active subject in current research(s).

The authors believe that this survey report will assist researchers working in this field in constructing new numerical methods for solving SPPs.

References

1. Amiraliyev, G. M. and Duru, H., A Note on A Parameterized Singular Perturbation Problem, Journal of Computational and Applied Mathematics, Vol:182, No:1, 233–242, 2005.

2. Bawa, R. K. and Natesan, S., A Computational Method for Self-Adjoint Singular Perturbation Problems Using Quintic Spline, International Journal of Computers and Mathematics with Applications, Vol:50, No:8, 1371-1382, 2005.

3. Kumar, M. and Mishra, H. K., A Recent Survey on Computational Techniques for Solving Singularly Perturbed Boundary Value Problems, International Journal of Computer Mathematics, Vol:84, No:10, 1439 – 1463, 2007.

4. Kadalbajoo, M. K. and Gupta, V., A Brief Survey on Numerical Methods for Solving Singularly Perturbed Problems, Applied Mathematics and Computation, Vol:217, No:8, 3641–3716, 2010.

5. Kopteva, N. and O'Riordan, E., Shishkin Meshes in The Numerical Solution of Singularly Perturbed Differential Equations, International Journal of Numerical Analysis and Modeling, Vol:1, No:1, 1–18, 2009.

6. Mishra, H. K. and Saini, S., Various Numerical Methods for Singularly Perturbed Boundary Value Problems, American Journal of Applied Mathematics and Statistics, Vol:2, No:3, 129 – 142, 2014.

7. Amiraliyeva, I. G., Amiraliyev, G. M. and Erdogan, F., A Uniform Numerical Method for Dealing with A Singularly Perturbed Delay Initial-Value Problem, Applied Mathematics Letters, Vol:23, No:10, 1221 – 1225, 2010.

8. Amiraliyev, G. M. and Cimen, E., Numerical Method for A Singularly Perturbed Convection-Diffusion Problem with Delay, Applied Mathematics and Computation, Vol:216, No:8, 2351 – 2359, 2010.

9. Amiraliyev, G. M. and Cimen, E., Uniform Convergent Method for Singularly Perturbed Nonlinear Differential-Difference Equation, Journal of Informatics and Mathematical Sciences, Vol:9, No:1, 191 – 199, 2017.

10. Amiraliyev, G. M., Kudu, M. and Duru, H., Uniform Difference Method for A Parameterized Singular Perturbation Problem, Applied Mathematics and Computation, Vol:175, No:1, 89 – 100, 2006.

11. Cakir, M., Cimen, E., Amirali, I. and Amiraliyev, G. M., Numerical Treatment of A Quasilinear Initial Value Problem with Boundary Layer, International Journal of Computer Mathematics, Vol:93, No:11, 1845-1859, 2016.

12. Kudu, M., Amirali, I. and Amiraliyev, G. M., A Finite-Difference Method for A Singularly Perturbed Delay Integro-Differential Equation, Journal of Computational and Applied Mathematics, Vol:308, No:C, 379 – 390, 2016.

13. Friedrich, K. O. and Wasow, W., Singular Perturbations on Nonlinear Oscillations, Duke Math., 367 – 381, 1946.

14. Pearson, C. E., On Nonlinear Ordinary Differential Equations of Boundary Layer Type, J. Math. and Phys., Vol:47, 258–351, 1968.

15. Prandtl, L., Uber, Flussigkeits-Bewegung bei Kleiner Reibung, Verhandlungen, III Int. Math. Kongresses, Tuebner, Leipzig, Vol:308, 484 – 491, 1905.

16. Durmaz, M. E., Amiraliyev, G. M., A Robust Numerical Method for A Singularly Perturbed Fredholm Integro-Differential Equation, Mediterr. J. Math., Vol:18, No:24, https://doi.org/10.1007/s00009-020-01693-2, 2021.

17. Amiraliyev, G. M., Mamedov, Y. D., Difference Schemes on The Uniform Mesh for Singularly Perturbed Pseudo-Parabolic Equations, Turk. J. Math. Vol:19, 207–222, 1995.

18. Panda, A., Mohapatra, J., Amirali, I., A Second-Order Post-processing Technique for Singularly Perturbed Volterra Integro-differential Equations, Mediterranean Journal of Mathematics, Vol:18, No:231, 2021.

19. Sahu, S. R., Mohapatra, J., Numerical Investigation of Time Delay Parabolic Differential Equation Involving Two Small Parameters, Engineering Computations, Vol:38, No:6, 2882-2899, 2021.

20. Panda, A., Mohapatra, J., Reddy, N. R., A Comparative Study on the Numerical Solution for Singularly Perturbed Volterra Integro-Differential Equations, Computational Mathematics and Modeling, Vol:32, 364–375, 2021.

21 Linß, T., Analysis of a System of Singularly Perturbed Convection-Diffusion Equations with Strong Coupling, SINUM, Vol:47, No:3, 1847-1862, 2009.

22 Nayfeh, A. H., Introduction to Perturbation Techniques, Wiley, New York, 1993.

23 O'Malley, R. E., Singular Perturbations Methods for Ordinary Differential Equations, Springer, New York, 2013.

24 Farrell, P. A., Hegarty, A. F., Miller, J. J. H., O'Riordan, E. and Shishkin, G. I., Robust Computational Techniques for Boundary Layers, Chapman Hall/CRC, New York, 2000.

25 Miller, J. J. H., O'Riordan, E. and Shishkin, G. I., Fitted Numerical Methods for Singular Perturbation Problems: Error Estimates in the Maximum Norm for Linear Problems in One and Two Dimensions (Rev. Ed.), World Scientific, Singapore, 2012.

26 Samarskii, A. A., The Theory of Difference Schemes, Marcell Dekker, Inc. New York, 2001.

27 Roos, H. G., Stynes, M. and Tobiska, L., Robust Numerical Methods for Singularly Perturbed Differential Equations, Springer-Verlag, Berlin Heidelberg, 2008.

28 Thieme, H. R., A Model for The Spatial Spread of An Epidemic, J. Math. Biol., Vol:4, 337–351, 1977.

MODELING OF SPECIES DISTRIBUTIONS WITH DEEP LEARNING METHOD

Serkan ÖZDEMİR[1*], Ecir Uğur KÜÇÜKSİLLE[2], Serkan GÜLSOY[3], Özdemir ŞENTÜRK[4], Mehmet Güvenç NEGİZ[1], Halil SÜEL[1], Ahmet MERT[3], Kürşad ÖZKAN[3]

[1]Isparta University of Applied Sciences, Sutculer Prof. Dr. Hasan Gürbüz Vocational School, 32950, Isparta, Turkey

[2]Suleyman Demirel University, Faculty of Engineering, 32260, Isparta, Turkey

[3]Isparta University of Applied Sciences, Faculty of Forestry, 32260, Isparta, Turkey

[4]Burdur Mehmet Akif Ersoy University, Gölhisar Vocational School, 15400, Burdur, TurkeyTurkey

serkanozdemir@isparta.edu.tr,

Abstract

There are many methods used in species distribution modeling. In recent years, the deep learning method has started to be included in these methods due to its modeling performance. The fact that it offers successful results, especially with large amounts of data, has made this method stand out and be integrated into the field of ecology. In the present study, potential distribution modeling of Turkish red pine (*Pinus brutia* (Ten.)) was carried out using the deep learning method with Python. In addition to having distinctive site conditions within its wide distribution, the fact that it is an ecologically and economically important species is the main reason for the Turkish red pine being the target species in this study. Considering that they may be effective in the potential distribution of the Turkish red pine, the following independent variables for modeling were chosen: elevation, topographic position index, annual mean temperature, mean temperature of the wettest quarter, annual precipitation, precipitation of the driest month, distance from the sea, latitude and longitude. As a result of this deep learning application, it has been determined that the model is successful in terms of AUC values (AUC value for train data: 0.943, AUC value for test data: 0.930). According to the model map of the Turkish red pine, it was observed that the determined potential areas coincided with the results from the studies conducted on the ecology of the same taxon. The results from this study showed that the deep learning method can be an effective tool for species distribution modeling.

***Keywords*:** Deep learning, Neural network, Python, Species distribution modeling, Turkish red pine

1. INTRODUCTION

What is statistical ecology? According to Orlóci (2019), it is a set of powerful conceptual tools that can be used to test the expected and reveal the unexpected in natural complexity. We know that there are many complex relationships in natural ecosystems. Considering the evolutionary process of ecology, there are many approaches in ecology studies for revealing the mentioned complex relationships. In particular, the mixing of quantitative methods with ecology has caused a point break in the evolutionary process. With this break, the previously preferred descriptive methods have begun to be gradually replaced by quantitative methods. Many have described ecology as lucky because it has met the mentioned break earlier than many other branches of science (Kuhn 1982).

As ecology has internalized quantitative methods over time, new methods have been introduced in statistical ecology (Özdemir et al. 2020a). Especially with the triggering of parameters such as increasing population and climate change, the protection of species in nature has become important and methods have been rapidly integrated into the studies as biodiversity, community ecology, conservation ecology, climate change and others in the last few decades (Gomes et al. 2019; Schuwirth et al. 2019; Abdelaal et al. 2020; Zurell et al. 2020).

Various quantitative methods are proposed for the modeling and mapping of the potential distribution areas of the species. Among these methods, connection models are relatively more preferred. The methods in the connection models are expressed in two parts as profile techniques and group separation techniques. While profile techniques use only presence data for species, group separation techniques use either presence-absence data or continuous data (Özkan 2012; Mert et al. 2016, Özdemir 2018). According to the studies, the most preferred methods for group separation techniques are Generalized Additive Model (GAM), Random Forest (RF) and Classification and Regression Tree (CART) and the most preferred methods for profile techniques are MaxEnt, Genetic Algorithm for Rule Set Production (GARP) and Domain. However, it is noteworthy that the deep learning approach has also figured among species distribution models (SDM) in the past several years (Hastie and Tibshirani 1986; Phillips et al. 2004., Phillips et al. 2006; Tekin et al. 2018). Deep learning methods have gained in popularity since they have shown their ability to produce remarkably accurate models in various science disciplines such as image classification and speech recognition (Hinton et al. 2012; Krizhevsky et al. 2012; Christin et al. 2019). In the ongoing process, it has presented dramatic model results in disciplines such as classification, clustering and prediction (Olden et al. 2008; Christin et al. 2019). In conclusion, as expected, the deep learning method has gained a place in various fields such as video games, finance, medicine, bioinformatics and ecology (Heaton et al. 2016; Lample and Chaplot 2017; Min et al. 2017; Shen et al. 2017; Christin et al. 2019).

The present study aims to reveal the usability of the deep learning method for species distribution models. *Pinus brutia* (Ten.), the Turkish red pine, was preferred as the target species in the model. The potential distribution map was acquired by simulating the results obtained in the model, and the performance of the model was evaluated by comparing the results with the findings obtained in studies on the ecology of the species.

2. MATERIALS AND METHODS

2.1. Study area and data

In this study, we use the forest management data of the Turkey General Directorate of Forestry. Turkish red pine was selected as the target species and Turkey was chosen as the study area. The most productive areas (site index value: 1 in forest management planning) where red pine is distributed were used as the presence data. Randomly generated points for the areas where the species was not found were used as absence data. While generating the absence data, we ensured it was balanced with the presence data. Turkish red pine is a fire-sensitive species and has commercial importance. It has a wide distribution in the areas that have Mediterranean climate conditions from the east of the Mediterranean region to the Aegean and Marmara regions. In addition, the species has a local distribution in the central and western Black Sea Regions in Turkey (Figure 1). Determining it would be possible to model the distribution of this species in the specified variation, we decided to choose it as the target species in the study.

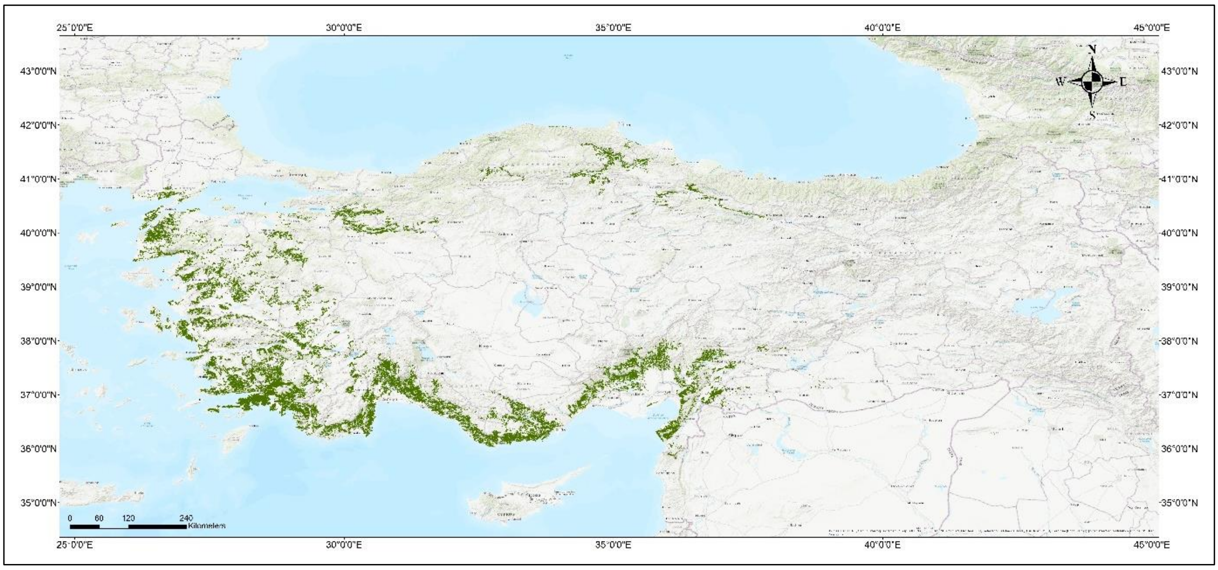

Figure 1. Location map of the study area and the current distribution areas of Turkish red pine (*Pinus brutia* (Ten.)) in Turkey

2.2. Variable selection and modeling

The parameters that were effective in the distribution of Turkish red pine in previous studies were chosen as variables in the present study. Accordingly, elevation (Elvtn), topographic position index (Tpi), annual mean temperature (Bio1), mean temperature of the wettest quarter (Bio8), annual precipitation (Bio12), precipitation in the driest month (Bio14), distance from the sea (SDist), latitude (x) and longitude (y) were selected as independent variables for the modeling of the potential distribution of Turkish red pine. Elvtn, Tpi, SDist, x and y were created in ArcMap 10.2, while the Bio1, Bio8, Bio12 and Bio14 variables were downloaded from the WorldClim (Version 2.1) database (WorldClim, 2020). After preparing all independent variables, the modeling process for Turkish red pine was performed using the deep learning method. The deep learning modeling was run via Python (using keras, numpy, pandas, sklearn, matplotlib, seaborn and VarImpVIANN).

Deep learning is defined as a class of machine learning. In deep learning, there is a structure based on learning more than one feature level or representation of data. This structure is referred to as multi-layered neural networks because, unlike artificial neural networks, the deep learning method has more than two hidden layers. Related-level features form a hierarchical representation derived from the previous level features. This representation creates multiple levels of representation that correspond to different levels of the structure. If an example is given for better understanding when it comes to representation in terms of species distribution modeling, it is possible to consider the presence-absence data of the species or species diversity values that vary according to the site factors of the sample plots. In addition, some of the mentioned factors present the presence of the species, or diversity of the sample plots, better than the other factors (Botella et al. 2018; Weinstein 2018; Christin et al. 2019).

The multi-layered structure mentioned above consists of three basic layers: input, hidden and output. Unlike single-layer structures, nonlinear classification can be made using this method. Multi-layer perceptron models run with feed-forward and backpropagation algorithms. In the first step of the backpropagation algorithm, variables are presented to the training network. By assigning a weight value for each neuron of each variable, after the values are multiplied by the weights and summed, the bias value is added to the neurons in the hidden layer by an activation function and sent to all neurons in the next layer. These values constitute the input values for the neurons in the output layer. After similar operations are performed in the output layer, an output value is obtained, the output and the actual value are compared and the error value is obtained (Botella et al. 2018; Tokmak and Küçüksille 2019).

Based on the above, the representation of the deep learning model built with the input, hidden and output layers used in the present study is shown in Figure 2.

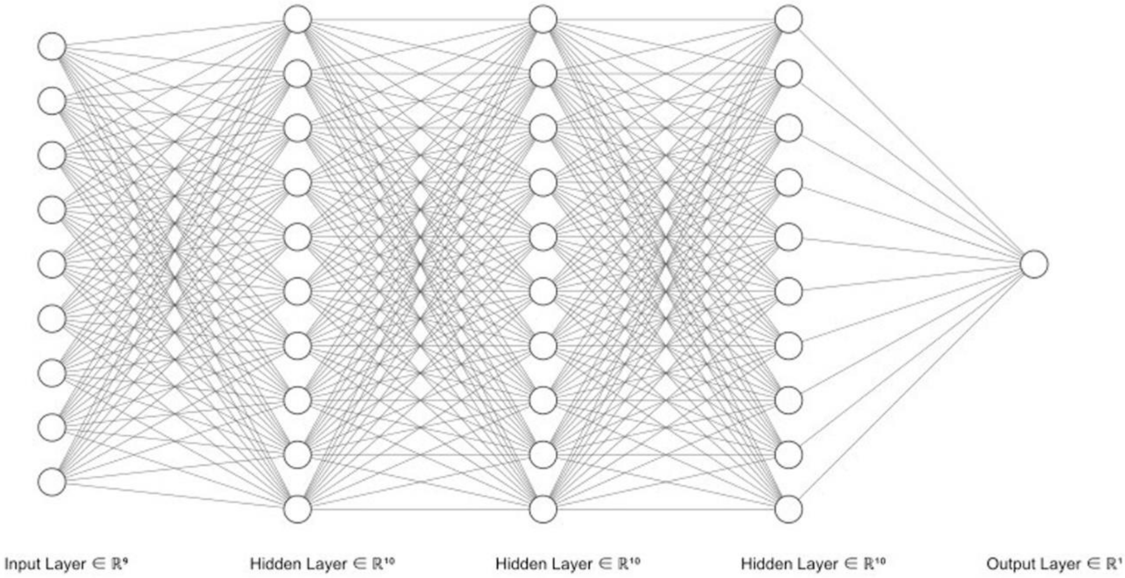

Figure 2. Representation of the deep learning model built in the study

3. RESULTS

In the study, the deep learning method has been used to determine the potential distribution areas of the Turkish red pine species. As a result, the variables that make up the model according to contribution rates are found to be Elvtn, x, Bio12, SDist, Bio1, Tpi, Bio8, Bio14 and y (Figure 3).

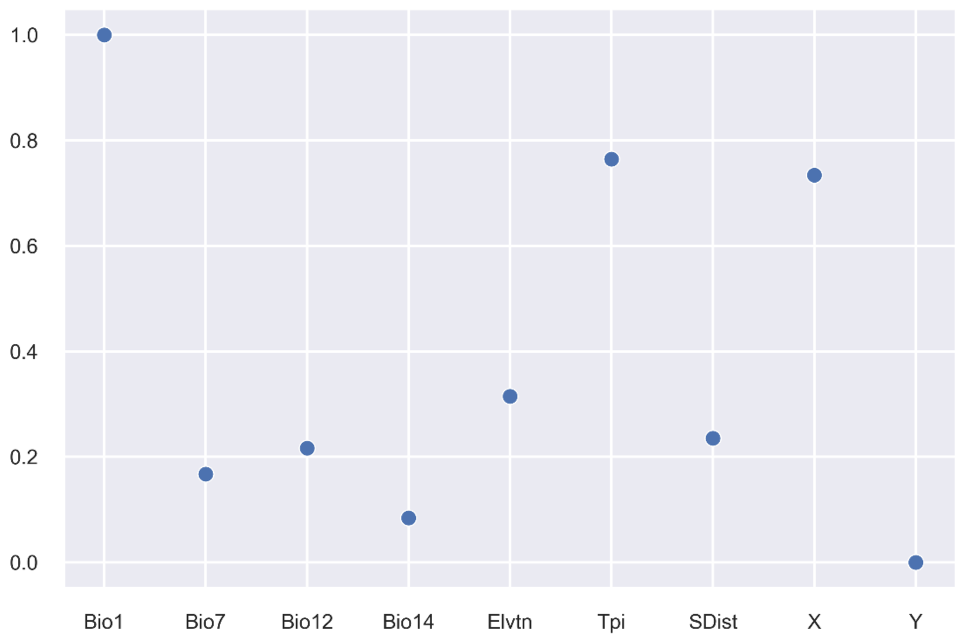

Figure 3. Contribution rates of variables to the deep learning model

Area under curve (AUC) values have been used to determine the validity of the model. The training data set AUC value and test data set AUC value of the model are determined as 0.943 and 0.930, respectively. The receiver operating characteristic (ROC) curve of the model is given in Figure 4.

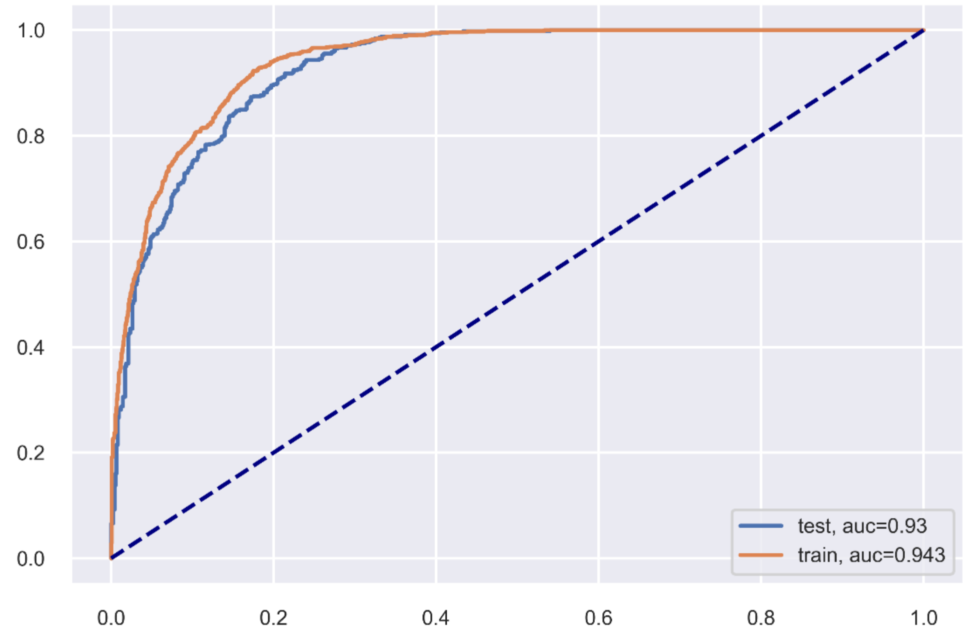

Figure 4. AUC values for train and test (0.10) datasets

The potential distribution of the species has been mapped across the study area by using the model obtained from the deep learning method (Figure 5). The areas with red color in the model map are determined to be suitable places for the potential distribution of the species.

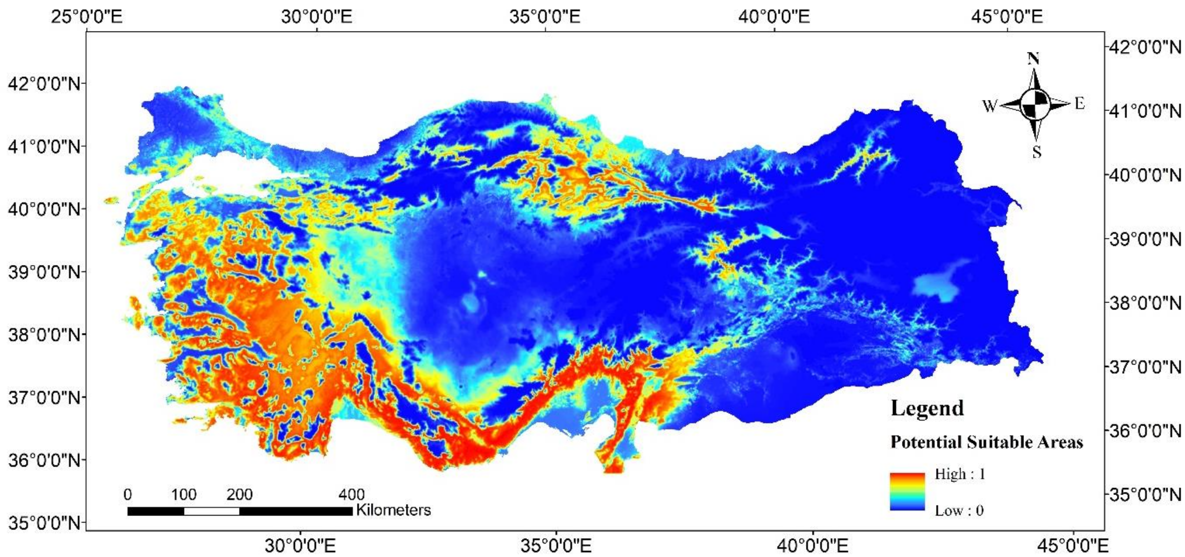

Figure 5. Potential distribution map of Turkish red pine

4. CONCLUSION

Studies modeling potential distribution areas of target species have increasingly come into prominence. The increasing degradation of natural ecosystems due to climate change and anthropogenic effects has been pointed out as the main reason for this popularity (Özdemir et al. 2020b). Researchers consider species distribution modeling as one of the most effective tools for protecting and maintaining the viability of species. This approach has caused many quantitative methods to take presence in the modeling processes over time. In recent years, deep learning especially has stood out among the mentioned methods. The fact that it has advantages including being able to present results with high accuracy in modeling and being adaptable to different problems has led to its intersection with ecology becoming inevitable. However, it is stated that the deep learning method can give better results with a large number of data (Benkendorf and Hawkins 2020). This is an advantage when considering the big data that can be obtained from databases (such as through gbif and management plans) or the studies that can be carried out in large areas.

In recent years, opportunities offered by open-source software applications such as Python and R have been preferably led to their use in modeling and statistic studies. These opportunities can be listed as combining and mapping different modeling methods, having rich libraries for data visualization, and developing methods by users. As a result of the increasing popularity of open-source software in data processing, many libraries have been created that can be used in this software system. In the present study, the deep learning method, which is a powerful machine learning technique, was performed for modeling with Python. The presence-absence data set of the Turkish red pine was modeled as the response variable in the study. The model obtained in the deep learning method yielded remarkably successful results in terms of AUC values in the train dataset (0.943) and the test dataset (0.930). When the contribution rates of the variables that shaped the model were evaluated, the results were quite consistent with the literature.

Turkish red pine is an important forest tree species that exists in many countries to the east of the Mediterranean reservoir. In Turkey, it can mainly be found in pure or mixed forests on slopes facing the sea in the Mediterranean, Aegean and Marmara regions and in local-scale areas in the Black Sea region which have Mediterranean climate conditions. In most of the studies conducted in the Mediterranean basin, it has been determined that elevation and climate in particular are more effective in the distribution of red pine compared to other descriptive variables (Şentürk et al. 2019; Keten and Gulsoy 2020). In a study conducted by Kaya (2020), elevation, temperature and dry period precipitation were found to be the most effective variables affecting the distribution and productivity of Turkish red pine. Another study performed by Biber and Lipschitz (1991) on Turkish red pine found that the distribution of the species is different from Pinus halepensis Miller (Aleppo pine), though both have similar habitat preferences. This study identified climate factors as the main reason for this difference. In addition, in terms of edaphic conditions where Turkish red pine distributes naturally, it has been stated that there are differences between the areas. It was observed that the information offered by Biber and Lipschitz (1991) for the distribution of Turkish red pine was remarkably similar to the results of the present study. Hence, in this study, it was proposed that the values of the temperature and precipitation parameters both throughout the year and in certain periods affected the distribution of Turkish red pine. In regard to edaphic conditions, while Turkish red pine can distribute up to an 1200m altitude in the Mediterranean Region of Turkey, it prefers lower altitudes in the Black Sea Region.

Although Turkish red pine is a widely distributed species, it is also a species with significant industrial use. Therefore, it is important to determine productive areas of the Turkish red pine together with the distribution areas. For this reason, in the present study, productive areas where the species are distributed were preferred as presence data. Keten and Gülsoy (2020) and Kaya (2020) used similar expressions for the importance of determining the productive areas of the Turkish red pine in their studies and identified similar variables in terms of those that affect the productive areas of Turkish red pine. Furthermore, the map obtained from this study coincides with the site conditions suitable for the distribution of the species. It is noteworthy that especially the potential areas in the Mediterranean, Aegean and Marmara regions coincide with the studies carried out, and the distribution of the species ends at the Melet River in the Black Sea and supports the distribution range in the literature (Terzioğlu et al. 2012).

Consequently, there are not many studies in the literature where potential distribution modeling with deep learning is performed and the model is simulated. On the other hand, there are not many studies performed for Turkish red pine on the scale of a country the size of Turkey. Hence, it is predicted that this study will set an example for the usability of the deep learning method in ecological studies such as species distribution modeling. In addition, it is thought that the deep learning method with high AUCs can be preferred as an alternative to the other methods used in species distribution models. Also, it was observed that the potential distribution areas predicted for Turkish red pine coincided with the results of the previous studies. However, to be able to reveal the potential distribution areas more accurately, other variables limiting the distribution of the species (e.g., bedrock, soil, etc.) should also be included in the modeling. Finally, the results to be revealed by using the presence-absence data obtained through field observations for the target species and making comparisons with different modeling techniques (e.g., GAM, MaxEnt, etc.) will be useful to see the pros and cons of the deep learning method on the potential distribution modeling.

REFERENCES

1. Abdelaal, M., Fois, m., Dakhil, m. A., Bacchetta, g., El-Sherbeny, G. A. Predicting the potential current and future distribution of the endangered endemic vascular plant Primula boveana decne. ex Duby in Egypt. Plants, 9(8), 957, 2020.
2. Benkendorf, D. J., Hawkins, C. P.. Effects of sample size and network depth on a deep learning approach to species distribution modeling. Ecological Informatics, 60, 101137, 2020.
3. Biger, G., Liphschitz, N. The recent distribution of Pinus brutia: A reassessment based on dendroarchaeological and dendrohistorical evidence from Israel. The Holocene, 1(2), 157–161, 1991.
4. Botella, C., Joly, A., Bonnet, P., Monestiez, P., Munoz, F. A deep learning approach to species distribution modelling, In Multimedia Tools and Applications for Environmental & Biodiversity Informatics. Springer, Cham, pp. 169–199, 2018.
5. Christin, S., Hervet, É., Lecomte, N. Applications for deep learning in ecology. Methods in Ecology and Evolution, 10(10), 1632–1644, 2019.
6. Gomes, V. H., Vieira, I. C., Salomão, R. P., Ter Steege, H. Amazonian tree species threatened by deforestation and climate change. Nature Climate Change, 9(7), 547–553, 2019.
7. Hastie, T., Tibshirani, R. Generalized additive models. Statistical Science, 1(3), 297–318, 1986.
8. Heaton, J. B., Witte, J. H., Polson, N. G. Deep learning for finance: Deep portfolios. Applied Stochastic Models in Business and Industry, 33(1), 3–12. https ://doi.org/10.1002/asmb.2209, 2016.
9. Hinton, G., Deng, L. I., Yu, D., Dahl, G., Mohamed, A.-R., Jaitly, N., Kingsbury, B. Deep neural networks for acoustic modeling in speech recognition: The shared views of four research groups. IEEE Signal Processing Magazine, 29(6), 82–97. https://doi.org/10.1109/ MSP.2012.2205597, 2012.
10. Kaya, C. Model based mapping of potential distribution and productivity for of Brutian pine (Pinus brutia (Ten.)) in the Gaziantep District. Isparta University of Applied Sciences, Institute of Graduate Education, Ph.D Thesis, p. 94, Isparta., 2020.
11. Keten İ., Gülsoy S. Research on site index in the red pine (Pinus brutia (Ten.)) forests. Bilge International Journal of Science and Technology Research, 4, 88–102, 2020.

12. Kiraç, A. (2021). Potential distribution of two lynx species in europe under paleoclimatological scenarios and anthropogenic climate change scenarios. CERNE.
13. Krizhevsky, A., Sutskever, I., Hinton, G. E. ImageNet classification with deep convolutional neural networks, in: Pereira, F., Burges, C. J. C., Bottou, L. & Weinberger, K. C. (Eds.), Advances in Neural Information Processing Systems. Curran Associates, Inc., New York, 25, pp. 1097–1105. http://papers.nips.cc/ paper/ 4824-image net-classification-with-deep-convolutional-neural-networks.pdf, 2012.
14. Kuhn, T. S. The Structure of Scientific Revolutions, University of Chicago Press, Chicago, 2012.
15. Lample, G., Chaplot, D. S. Playing FPS games with deep reinforcement learning, in: Thirty-First AAAI Conference on Artificial Intelligence. https://aaai.org/ocs/index.php/AAAI/ AAAI17/paper/view/14456, 2017.
16. Mert A., Özkan K., Şentürk Ö., Negiz M. G. Changing the potential distribution of turkey oak (Quercus cerris L) under climate change in Turkey. Polish Journal of Environmental Studies, 25, 1633–1638. doi:10.15244/pjoes/62230, 2016.
17. Min, S., Lee, B., Yoon, S. Deep learning in bioinformatics. Briefings in Bioinformatics, 18(5), 851–869. https ://doi.org/10.1093/bib/bbw068, 2017.
18. Olden, J. D., Lawler, J. J., Poff, N. L. Machine learning methods without tears: A primer for ecologists. The Quarterly Review of Biology, 83(2), 171–193. https ://doi.org/10.1086/587826, 2008.
19. Orlóci, L. Looking Back: A Life of Statistical Ecology, second ed. Scada Publishing, Canada, 2019.
20. Özdemir S. Potential distribution modeling and mapping using random forest method: An example of Yukarıgökdere District. Turkish Journal of Forestry, 1, 51–56. https://doi.org/10.18182/tjf.342504, 2018.
21. Özdemir S., Gülsoy S., Mert A. Predicting the effect of climate change on the potential distribution of Crimean Juniper. Kastamonu University Journal of Forestry Faculty, 20, 133–142, 2020a.
22. Özdemir S., Özkan K., Mert A. An ecological perspective on climate change scenarios. Biological Diversity and Conservation, 13, 361–371. doi.org/10.46309/biodicon.2020., 2020b.
23. Özkan, K. Modelling ecological data using classification and regression tree technique (CART). Turkish Journal of Forestry, 13, 1–4, 2012.

24. Phillips, S. J., Anderson, R. P., Schapire, R. E. Maximum entropy modeling of species geographic distributions. Ecological Modelling, 190(3–4), 231–259, 2006.
25. Phillips, S., Dudik, M., Schapire, R. A maximum entropy approach to species distribution modeling, in: Proceedings of the Twenty-First International Conference on Machine Learning (ICML '04). Association for Computing Machinery, New York, NY, USA, p. 83. DOI:10.1145/1015330.1015412, 2004.
26. Schuwirth, N., Borgwardt, F., Domisch, S., Friedrichs, M., Kattwinkel, M., Kneis, D., Kuemmerlena, M., Langhanscgh S.D., Martínez-López, J., Vermeiren, P. How to make ecological models useful for environmental management. Ecological Modelling, 411, 108784, 2019.
27. Şentürk, Ö., Negiz, M. G., Gülsoy, S. Alpha species diversity and ecological site factor relations in Brutian pine forests: A case study from Gölhisar District., Bilge International Journal of Science and Technology Research, 3(2), 178–188, 2019.
28. Shen, D., Wu, G., Suk, H.-I. Deep learning in medical image analysis. Annual Review of Biomedical Engineering, 19(1), 221–248. https ://doi.org/10.1146/annur ev-bioeng-071516-044442, 2017.
29. Tekin, S., Yalçinkaya, B., Acarer, A., Mert, A. 2018. A research on usage possibilities of satellite data in wildlife: Modeling habitat suitability of Roe deer (Capreolus capreolus L.) with MaxEnt. Bilge International Journal of Science and Technology Research, 2 (2), 147–156. DOI: 10.30516/bilgesci.399017, 2018.
30. Terzioğlu S., Bilgili, E., Karaköse, M. Forests of Turkey. Republic of Turkey Ministry of Forestry and Water Affairs General Directorate of Forestry, ISBN 978-605-393-044-0, Ankara, 2012.
31. Weinstein, B. G. A computer vision for animal ecology. Journal of Animal Ecology, 87(3), 533–545, 2018.
32. Zurell, D., Franklin, J., König, C., Bouchet, P. J., Dormann, C. F., Elith, J., Fandos, G., Feng, X., Guillera-Arroita, G., Guisan, A., Lahoz-Monfort, J. J., Leitão, P. J., Park, D. S., Peterson, A. T., Rapacciuolo, G., Schmatz, D. R., Schröder, B., Serra-Diaz, J. M., Thuiller, W., Yates, K. L., Zimmermann, N. E., Merow, C. A standard protocol for reporting species distribution models. Ecography, 43: 1261–1277. DOI: 10.1111/ecog.04960, 2020.

DEVELOPMENT OF A NATIONAL SMART METER SYSTEM

Fatih Coşkun[1], Beytullah Topçu[1], M. Fatih Akay[2]

[1]Nar Sistem Teknolojileri, İstanbul, Turkey

[2]Department of Computer Engineering, Cukurova University, Adana, Turkey

fatih.coskun@nar.com.tr, beytullah.topcu@nar.com.tr, mfakay@cu.edu.tr

Abstract

The electricity distribution sector in Turkey, which has been privatized since the early 2000's, is divided into 21 regions. This distribution network includes consumer and producer subscribers as well as transformers and lighting. Although the number of meters that are still measured at its location is quite high, the rate of meters read by remote reading systems is increasing day by day. Since world standards such as The International Electrotechnical Commission (IEC) and Device Language Message Specification (DLMS) are used in communication with the meters, there is a much cleaner system, while there is no such standard in communication with gateway devices. For this reason, each gateway manufacturer can create its own protocols and some of them even keep these protocols secret. This situation causes many problems. National Smart Meter System (MASS) is a protocol developed to solve this problem. Thanks to this protocol, which is based on JSON type data and designed in accordance with the most modern communication technologies such as MQ Telemetry Transport (MQTT) and NarrowBand-Internet of Things (NB-IoT), a more efficient and reliable energy reading network will be established.

Keywords: Meter, Gateway, IEC, DLMS, MQTT, NB-IoT.

1. INTRODUCTION

With the concept of smart electricity grids, reducing losses, improving supply continuity, integrated load management, minimizing manual processes, enabling users to access consumption information in real time and participating in the market, dynamic tariff applications, real-time demand tracking, advanced demand-side management. Concepts beyond the current network operating structure have emerged [1]. OSOS (Automatic Meter ReadingAMR), which has applications in our country and in various countries of the world, is a name given to systems where communication is one-way and meter data is transmitted to the central system in short-term intervals (hourly or less) [2]. In Figure-1, OSOS architecture is shown in detail. The Osos smart meter system, on the other hand, is a two-way communication system that allows advanced technological applications by providing remote access to measurement systems as well as collecting meter data [3]. To OSOS electricity distribution companies; It provides many gains such as workforce gain, financial savings, data security, ease of access, fast index reading. Due to this need, electricity distribution companies add new ones to the pool of electricity meters that they can receive remote data from every year. Reading millions of meters means a huge data pool. This data pool continues to grow every day. For example; Nar system software company serves 14 Electricity distribution companies and processes an average of 40Gb of data per day [4]. OSOS studies form the basis of studies on smart grids in our country. Each of the 21 Electricity Distribution Companies operating in Turkey has included its subscribers above a certain consumption limit on an annual basis into the scope of OSOS. In the current situation, the stamp period of an electricity meter is considered to be 10 years, and at the end of this 10-year period, the process continues in the form of replacing the stamped meters with new ones or performing their calibrations. Smart meter transformation has been initiated with the common practice in our country, replacing the expired meters with smart meters [5,6].

The number of meters that communicate with each other day by day increases, and the data received grows, and accordingly, synchronization and communication compatibility problems arise. Currently, most of the 21 electricity distribution companies in Turkey have their own protocols. These protocols are designed according to the technology of the 2000s. In fact, some protocols used in the field are no longer being developed. However, modems working on this old protocol continue to be produced. Counter, modem and head end working incompatible with each other cause labor loss and time loss, unnecessary costs and inefficiency. For smart metering, the readings from the energy meter must be collected without human intervention and the collected data must be accessible at all times to both consumer and utilities [7].

As technology has changed over the past decade, so have needs and laws. R&D projects carried out within this scope have led to the detection of such problems, the determination of road maps and the taking of these steps. Considering the interoperability that will be created by the integration between IT(Information Technologies') and OT(Operational Technologies) systems used in Smart Grids, it has been concluded that the benefits will be for all electricity distribution companies [8]. Based on these determinations and the roadmap, a nationally usable common counter, modem and head end system is essential and will provide a great benefit to the system.

The aim of this study is to eliminate the negativities caused by the modem counter head end system working with the old protocol and to ensure that the systems work in harmony with each other with a newly created common protocol. Integration of different structures will be realized easily with the created protocol.

2. METHODOLOGY

MASS is designed according to MQTT network protocol based on Nb-Iot technology. MQTT is a lightweight publish/subscribe protocol designed around a central broker.[9] But it also supports TCP\IP protocol. While there is a headend on one end of the communication and a modem on the other, an "MQTT Broker" provides the communication between these two. The headend server and modem must send an ACK (acknowledgement) packet after each message they receive, because MASS is designed to work asynchronously when working with MQTT. New low-power wide-area (LPWA) wireless networking technologies have been proposed to support a large number of asynchronous, low-bandwidth devices[10]. Communication in the protocol will be provided in JSON data structure. However, in order to ensure that the communication units and communication center software receive the incoming packets correctly, there will be a length mark before JSON [11]. Describes the notation of Joda (Json On Demand Analytics), an approach to processing large amounts of JSON documents in a vertically scalable manner [12]. Modems will be able to divide the messages they send into small packets (Figure 1).

Figure 1. Message format

The MASS protocol is designed to rely on a minimal amount of modems to read meters. For this purpose, a structure called "directive" has been used. A directive is a micro-operation that represents the smallest job the modem has to do. Thanks to the directives, meter reading operations are directly managed by the headend. The types of these directives are specified in the protocol document, and all modems that will receive MASS conformity certificate are expected to support these directives.

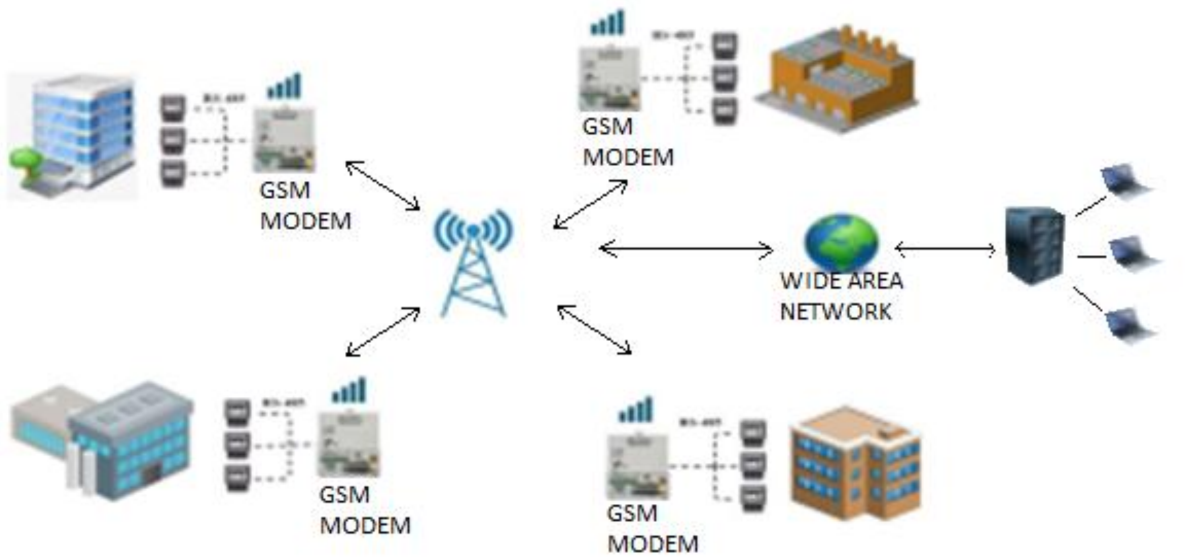

Figure 2. OSOS Architecture

In the MASS protocol, directives are called "directives". Each instruction consists of an indefinite number of steps. These 'steps' include an 'operation' and a 'parameter'. The task of the modem is to perform the 'operation' using the values in the 'parameter' at each step. The directive variables are: setBaud, setFraming, sendData, readData, wait, loop. Let's explain these directive types with an example: (Figure-3). The definitions of the instruction variables shown in the example are explained in the table in Table 1.


```
"id" : "ReadoutDirective",
"directive": [
  {
   "operation": "setBaud",
   "parameter": "300"
  },{
   "operation": "setFraming",
   "parameter": "7E1"
  },{
   "operation": "sendData",
   "parameter": [47, 63, 33, 13, 10]
  },{
   "operation": "wait",
   "parameter": "10"
  },{
   "operation": "readData",
   "parameter": "id"
  },
  {
   "operation": "sendData",
   "parameter": [6, 48, 53, 48, 13, 10]
  },{
   "operation": "setBaud",
   "parameter": "9600"
  },{
   "operation": "wait",
   "parameter": "600"
  },{
   "operation": "readData",
   "parameter": "rawData"
  }
]
```


Figure 3. Directive Example

id:	The instruction is saved to the modem under this name for later use.
setBaud:	It adjusts the communication of the modem with the counter according to the baud rate value in the parameter field.
setFraming	The modem starts to use the framing structure in the parameter field in its communication with the meter.
sendData:	sends the byte string in the modem parameter field to the counter
bekle:	the modem waits for the value in the parameter field until it moves to the next step
readData:	The modem listens for the data from the meter and saves it with the name in the parameter field.
döngü:	The modem repeats the next steps as many times as the number of parameters in the command.

Figure 4. Directive Variables Definitions

The created MASS Head-End software will be able to perform the following functions as a minimum.

-Remote meter reading,

-Remote counter on/off,

-Creating index values as a basis for invoicing,

-Remote error reporting (counter error and/or collector and other communication equipment errors, if any),

- Remote programming of meters

- Reading FF, GF alarm information coming from the meters to the center

-Reading routine defined packet data coming from the meters to the center

- Remote programming of modems

-Changing modem parameters and loading reading routines

-Modem firmware update processes

3. RESULTS AND DISCUSSION

Incompatibilities, labor losses, time losses, and unnecessary costs caused by old protocols used in the field and modems working with old protocols have been eliminated. With the use of the protocol, the counter, modem and head end have become compatible. Each electricity distribution company has been prevented from having its own protocol and a great labor gain has been achieved. Integration of different structures with a common protocol has become more feasible.

4. CONCLUSION

In this study; An application has been implemented that allows consumers to instantly monitor smart meter data. By providing access to an electricity meter with RS-485 communication, which is widely used in smart meter systems, electrical parameters are read and monitoring and consumption data are reported via the user interface developed with the MASS Head end program. In addition, a common protocol has been established that can be used by all electricity distribution companies. In this way, communication incompatibilities were eliminated and a modem head end system was created that works in full harmony.

REFERENCES

[1] Türkiye Akıllı Şebekeler 2023 Vizyon ve Strateji Belirleme Projesi, ELDER, EPDK., https://www.akillisebekelerturkiye.org/, (Haziran 2020).

[2] Muhammad Yousaf Ali Khan; Muhammad Ibrahim; Muhammad Ali; Hamayun Khan; Ehtasham Mustafa (2020) “ Cost Benefit Based Analytical Study of Automatic Meter Reading (AMR) and Blind Meter Reading (BMR) used by PESCO(WAPDA)”

[3] Deloitte, “Deloitte Türkiye Yayınları, Akıllı Sayaç Sistemleri: Avrupa uygulamaları analizi ve Türkiye uygulamaları üzerine düşünceler,”, https://www2.deloitte.com/content/dam/Deloitte/ tr/Documents/energy-resources/akıllı-sayacsistemleri.pdf., (Haziran 2020).

[4] Nar Sistem Teknoloji Günlük İşlenen Veri Oranı http://www.nar.com.tr/(May 2022).

[5] Öztemür, M., & Soysal, B. (2013). Akıllı Şebekeler Yolunda Akıllı Sayaçlar. Akıllı Şebekeler Sempozyumu.

[6] Dağıtım Şirketlerince Kurulacak Osos Kapsamına Dahil Edilecek Sayaçların, Haberleşme Donanımının ve İlave Teçhizat ve Altyapının Ortak Asgari Teknik Özellikleri, https://www.epdk.org.tr/, (Haziran 2020).

[7] R Sheeba; N Naufal; S Nadera Beevi; Ajith R Nair; S Amal; Anoop S Kumar; Anusree Mohan; Pm Arunjith; U Aswin (2021) “Real-time Monitoring of Energy Meters Using Cloud Storage”

[8] Türkiye Akıllı Şebekeler 2023 Vizyon ve Strateji Belirleme Projesi, ELDER, EPDK., https://www.akillisebekelerturkiye.org/, (May 2022).Dağıtım Şirketlerince Kurulacak Osos

[9] Edoardo Longo DEIB, Politecnico di Milano, Italy ; Alessandro E.C. Redondi; Matteo Cesana; Andrés Arcia-Moret; Pietro Manzoni (2020) “ MQTT-ST: a Spanning Tree Protocol for Distributed MQTT Brokers”

[10] Abhijeet Sahu; Ana Goulart (2019) “Implementation of a C-UNB Module for NS-3 and Validation for DLMS-COSEM Application Layer Protocol”

[11] Haberleşme_Protokolü_Protokolü_v_0-2.pdf https://www.mass.org.tr/wpcontent/uploads/2022/02/MASS_Haberlesme_Protokolu_v_0-2.pdf

[12] Nico Schäfer; Sebastian Michel (2020) “JODA: A Vertically Scalable, Lightweight JSON Processor for Big Data Transformations”

ANALYSIS OF THE SOLUTIONS OF A SPACE-TIME FRACTIONAL MATHEMATICAL MODEL WITH AN ANALYTICAL METHOD

Özlem Kırcı

Department of Mathematics, Faculty of Arts and Sciences, Kırklareli University, Turkey

ozlem.isik@klu.edu.tr

Abstract

In the present paper we have considered a nonlinear equation including the modified Riemann-Liouville (RL) fractional derivative of Jumarie, namely space-time fractional Calogero-Degasperis (CD) equation. The analytical solutions of CD equation which describes the (2+1)-dimensional interaction of a Riemann wave propagating along the y-axis with a long wave along the x-axis, are constructed by the modified exponential function method (MEFM). The proposed method is easy to implement and powerful. Consequently three types of exact solutions are obtained as hyperbolic function solutions, trigonometric function solutions and rational solutions. The appropriate graphical results are presented to the related cases.

Keywords: Modified exponential function method; Space-time fractional Calogero-Degasperis equation; Traveling wave solutions.

1. INTRODUCTION

The focus of the studies in the literature has changed towards the concept of the arbitrary order differential equations and qualified methods for the solutions of such equations. Fractional differential equations (FDEs) are more substantial in the modelling procedure than the integer order differential equations, due to its memory property. The order of the differential equation is referred as the memory indicator. The memory effect is related to the dependence of the system not only on the present state of the system but also on the past history of the system. FDEs have many applications in fluid mechanics, mathematical biology, electro-chemistry, physics, engineering, signal processing, systems identification, control theory, the finance, fractal dynamics and many other areas of science. For instance in [1] a fractional order model is suggested for earthquakes, [2] suggested a fractional order approach to model the behavior of the premotor neurons which control the movements of the eyes, the time evolution of the fractional electromagnetic waves are investigated in [3]. The use of FDEs in many applied fields can be substantial. Consequently, various methods are proposed for these equations such as functional variable method [4], $(G'/G, 1/G)$, modified (G'/G^2) and $(1/G')$-expansion methods [5], Generalized Kudryashov Method [6], improved fractional sub-equation method [7], Auxiliary equation method [8], the modified simple equation method [9], exp-function method [10], $(m + 1/G')$-expansion method [11] and so on.

In this study, the modified exponential function method is used. The space-time fractional CD equation (1.1) is chosen to demonstrate the verity of this method. The afore-mentioned space-time fractional equation can be written in the form:

$$D_t^\alpha D_x^\alpha u - 4D_x^\alpha u D_x^{2\alpha} u - 2D_y^\alpha u D_x^{2\alpha} u + D_y^\alpha D_x^{3\alpha} u = 0, \tag{1.1}$$

where $0 < \alpha \leq 1$ and $u = u(x, y, t), t > 0;\ x, y \in \mathbb{R}$ being time and space variables, respectively. This equation is important because it narrates various physical events in nonlinear science. Equation (1.1) describes the (2+1)-dimensional interfacing of a long wave along the x-axis with a Riemann wave propagating along the y-axis [12]. We have discovered new types of exact solutions to (1.1). It can be observed that our results are new when compared with the other results [12-15].

This Letter is investigated in three main sections to meet our goal. The mathematical preliminaries about the fractional order derivative and the description of the proposed method are given. Subsequently, numerical illustrations are presented and the conclusion section takes part at last.

2. GENERAL PROPERTIES OF METHOD

In this section the process for obtaining the analytical solutions of equation (1.1) is presented. The definition and the properties of the modified RL differentiation depicted by Jumarie are presented. Then the modified exponential function method is applied to obtain the exact solutions of space-time fractional CD equation associated with the mentioned derivative.

2.1. Jumarie's Modified RL Differentiation and Its Properties

The Jumarie's modified RL derivative of order α is defined by the expression [16]

$$D_t^\alpha f(t) = \frac{1}{\Gamma(1-\alpha)} \frac{d}{dt} \int_0^t (t-\xi)^{-\alpha} \left(f(\xi) - f(0) \right) d\xi;\ 0<\alpha<1. \tag{2.1}$$

Some significant properties of the modified RL derivative are listed as follows:

$$D_t^\alpha t^r = \frac{\Gamma(1+r)}{\Gamma(1+r-\alpha)} t^{r-\alpha},\ r > 0, \tag{2.2}$$

$$D_t^\alpha \left(f(t)g(t) \right) = g(t) D_t^\alpha f(t) + f(t) D_t^\alpha g(t), \tag{2.3}$$

$$D_t^\alpha f\left(g(t)\right) = f_g'\left(g(t)\right) D_t^\alpha g(t) = D_t^\alpha f\left(g(t)\right)\left(g'(t)\right)^\alpha, \tag{2.4}$$

$$D_t^\alpha \left\{ af(t) + bg(t) \right\} = aD_t^\alpha f(t) + bD_t^\alpha g(t), \tag{2.5}$$

$$D_t^\alpha c = 0, \tag{2.6}$$

where a, b and c are arbitrary constants. These properties are important in the way of obtaining the exact solutions of FDEs.

2.2. Algorithm

This section is related to the modified exponential function method which is an efficient method for analyzing the exact solutions of the nonlinear partial differential equations. The foremost steps of the proposed method can be concisely given as follows:

Step1: Suppose that a nonlinear FDE, say in 3 independent variables x, y and t, is given by

$$P\left(u, D_x^{\alpha}u, D_y^{\beta}u, D_t^{\delta}u, D_x^{\alpha}D_y^{\beta}u, D_t^{\delta}D_x^{\alpha}u, D_x^{2\alpha}u, \ldots\right) = 0, \tag{2.7}$$

where $0 < \alpha, \beta, \delta \leq 1$, $u = u(x, y, t)$ is the unknown function and P is a polynomial of u and its partial fractional derivatives in which the highest order derivatives and the nonlinear terms are involved. (2.7) is transformed into an integer order ordinary differential equation (ODE)

$$N\left(U, U', U'', \ldots\right) = 0, \tag{2.8}$$

by considering the fractional complex transformation

$$u(x, y, t) = U(\xi),\ \xi = \frac{k_1 x^{\alpha}}{\Gamma(1+\alpha)} + \frac{k_2 y^{\beta}}{\Gamma(1+\beta)} - \frac{k_3 t^{\delta}}{\Gamma(1+\delta)}, \tag{2.9}$$

where k_1, k_2, k_3 are constants which will be evaluated and the prime $'$ symbolizes the derivative with respect to ξ.

Step2: The solution to (2.8) is assumed to be expressed as,

$$U(\xi) = \frac{\sum_{i=0}^{n} A_i \left[\exp\left(-\Omega(\xi)\right)\right]^i}{\sum_{j=0}^{m} B_j \left[\exp\left(-\Omega(\xi)\right)\right]^j}, \tag{2.10}$$

where $A_i, B_j, (0 \leq i \leq n, 0 \leq j \leq m)$ are constants to be determined and $\Omega(\xi)$ is the solution of the following ODE,

$$\Omega'(\xi) = \exp\left(-\Omega(\xi)\right) + \mu \exp\left(\Omega(\xi)\right) + \lambda. \tag{2.11}$$

Balancing the highest order derivative and the highest order nonlinear term in (2.8) gives a relation between n and m. (2.10) is substituted into (2.8) by considering (2.11) and algebraic equations of powers of $e^{\Omega(\xi)}$ are obtained.

Step3: The system of algebraic equations which is established in step2, is solved by Mathematica. Consequently the coefficients $A_0, A_1, \ldots, A_N, B_0, B_1, \ldots, B_M, \mu, \lambda, k_1, k_2, k_3$ are evaluated. Together with these coefficients, $\Omega(\xi)$ families as stated in the following constitute the solution for (2.8).

Family1: When $\mu \neq 0, \lambda^2 - 4\mu > 0$,

$$\Omega(\xi) = \ln\left(\frac{-\sqrt{\lambda^2 - 4\mu}}{2\mu} \tanh\left(\frac{\sqrt{\lambda^2 - 4\mu}}{2}(\xi + E)\right) - \frac{\lambda}{2\mu}\right). \tag{2.12}$$

Family2: When $\mu \neq 0, \lambda^2 - 4\mu < 0$,

$$\Omega(\xi) = \ln\left(\frac{\sqrt{-\lambda^2 + 4\mu}}{2\mu} \tan\left(\frac{\sqrt{-\lambda^2 + 4\mu}}{2}(\xi + E)\right) - \frac{\lambda}{2\mu}\right). \tag{2.13}$$

Family3: When $\mu = 0,\ \lambda \neq 0$ and $\lambda^2 - 4\mu > 0$,

$$\Omega(\xi) = -\ln\left(\frac{\lambda}{\exp\left(\lambda(\xi + E)\right) - 1}\right). \tag{2.14}$$

Family4: When $\mu \neq 0,\ \lambda \neq 0$ and $\lambda^2 - 4\mu = 0$,

$$\Omega(\xi)=\ln\left(-\frac{2\lambda(\xi+E)+4}{\lambda^2(\xi+E)}\right). \tag{2.15}$$

Family5: When $\mu = 0,\ \lambda = 0$ and $\lambda^2 - 4\mu = 0$,

$$\Omega(\xi)=\ln(\xi+E), \tag{2.16}$$

where $A_0, A_1, \dots, A_n, B_0, B_1, \dots, B_m, E, \lambda, \mu$ are constants.

3. APPLICATION

In this section the modified exponential function method is applied to CD equation (1.1). The fractional complex transform (2.9) is applied to convert (1.1) into an ODE as stated in step1. The following ODE is obtained as a result of this transform,

$$-k_3U'-\left(2k_1^2+k_1k_2\right)\left(U'\right)^2+k_1^2k_2U'''=0. \tag{3.1}$$

The terms $(U')^2$ and U''' are used for balancing principle in (3.1) and the upper limits in (2.10) are determined as $n = 3, m = 1$. Then (2.10) becomes,

$$U(\xi)=\frac{A_0+A_1\exp(-\Omega(\xi))+A_2\exp(-2\Omega(\xi))+A_3\exp(-3\Omega(\xi))}{B_0+B_1\exp(-\Omega(\xi))}. \tag{3.2}$$

Substituting (3.2) into (3.1) and solving the generated system of algebraic equations by using Mathematica, result in the following outcomes:

Case-1:

$$A_0=\frac{\left(\lambda^2+2\mu\right)A_3B_0}{6B_1},\ A_1=\frac{A_3}{6}\left(\lambda^2+2\mu+\frac{6\lambda B_0}{B_1}\right),\ A_2=A_3\left(\lambda+\frac{B_0}{B_1}\right),$$

$$k_2=-\frac{2k_1A_3}{A_3-6k_1B_1},\ k_3=-\frac{2k_1^3\left(\lambda^2-4\mu\right)A_3}{-A_3+6k_1B_1}. \tag{3.3}$$

It is verified via Mathematica that equation (3.2) satisfies equation (3.1) together with these constants in (3.3). Considering the fractional complex transform $\xi = k_1x^\alpha/\Gamma(1+\alpha) + k_2y^\alpha/\Gamma(1+\alpha) - k_3t^\alpha/\Gamma(1+\alpha)$ some classes of solutions are obtained by employing the possible options for $\Omega(\xi)$ given through (2.12)-(2.16) as in the following;

Family-1:

$$u_{1,1}(x,y,t)=\frac{\omega_3^2\left(-3\lambda+\omega_1+2\mu(\xi+E)Cosh(\omega_2)-\frac{6\mu Sinh(\omega_2)}{\omega_3}\right)A_3}{6\left(\lambda^2-2\mu+2\mu Cosh(\omega_2)\right)B_1}, \tag{3.4}$$

where $\omega_1 = (\lambda^2 - 2\mu)(\mathrm{E} + \xi), \omega_2 = \sqrt{\lambda^2 - 4\mu}(\mathrm{E} + \xi), \omega_3 = \sqrt{\lambda^2 - 4\mu}$.

Family-2:

$$u_{1,2}(x,y,t)=\frac{\omega_3^2\left(-3\lambda+\omega_1+2\mu(\xi+E)Cos(\omega_4)-\frac{6\mu Sin(\omega_4)}{\omega_5}\right)A_3}{6\left(\lambda^2-2\mu+2\mu Cos(\omega_4)\right)B_1}, \tag{3.5}$$

where $\omega_4 = \sqrt{-\lambda^2 + 4\mu}(\mathrm{E} + \xi), \omega_5 = \sqrt{-\lambda^2 + 4\mu}$.

Family-3:

$$u_{1,3}(x,y,t) = \frac{\lambda\left(\lambda(\xi+E) - 3Coth\left(\frac{\lambda(\xi+E)}{2}\right)\right)A_3}{6B_1}. \tag{3.6}$$

Family-4:

$$u_{1,4}(x,y,t) = \frac{\left(-\frac{12\lambda}{2+\lambda(\xi+E)} - \frac{(\lambda^2-4\mu)\left(2+\lambda(\xi+E)\right)}{\lambda}\right)A_3}{12B_1}. \tag{3.7}$$

Family-5:

$$u_{1,5}(x,y,t) = -\frac{A_3}{(\xi+E)B_1}. \tag{3.8}$$

The graphs of the solutions through equations (3.4)-(3.8) are presented in Figure3.1-Figure3.5, respectively. The first row shows the 3D and 2D graphs and the second row exhibits the contour and the density plots from left to right.

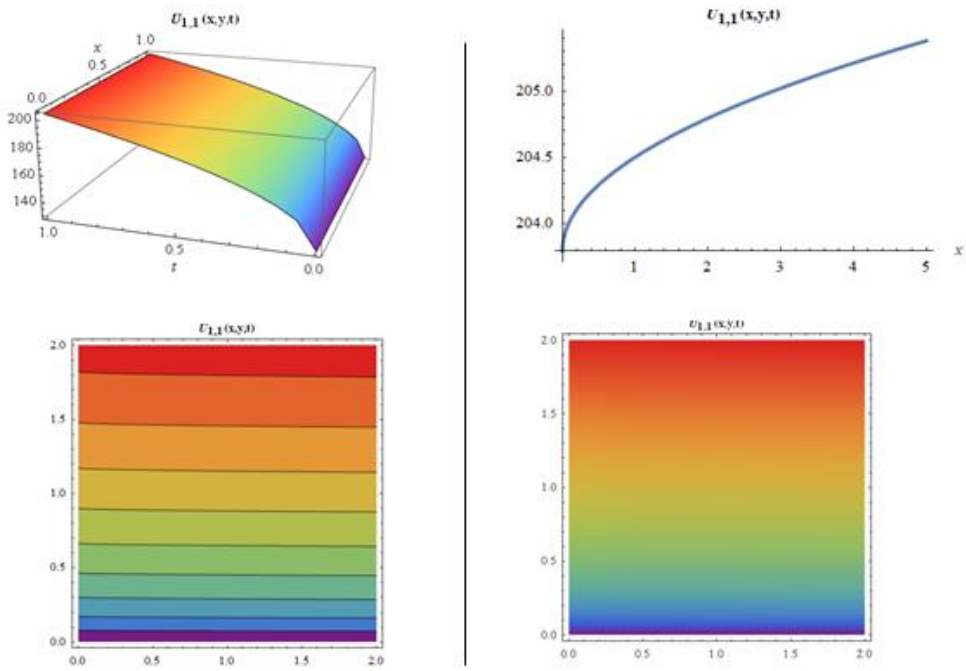

Figure3.1: The 3D, 2D, contour and density graphs of $u_{1,1}$ is illustrated for the values $\lambda = 4, \mu = 1, k_1 = 0.23, k_2 = 38.3333, k_3 = -24.334, B_0 = 0.66, B_1 = 1.1, A_3 = 1.5, A_0 = 2.7, A_1 = 8.1, A_2 = 6.9, \alpha = 0.5, y = 1.2, E = 0.75$

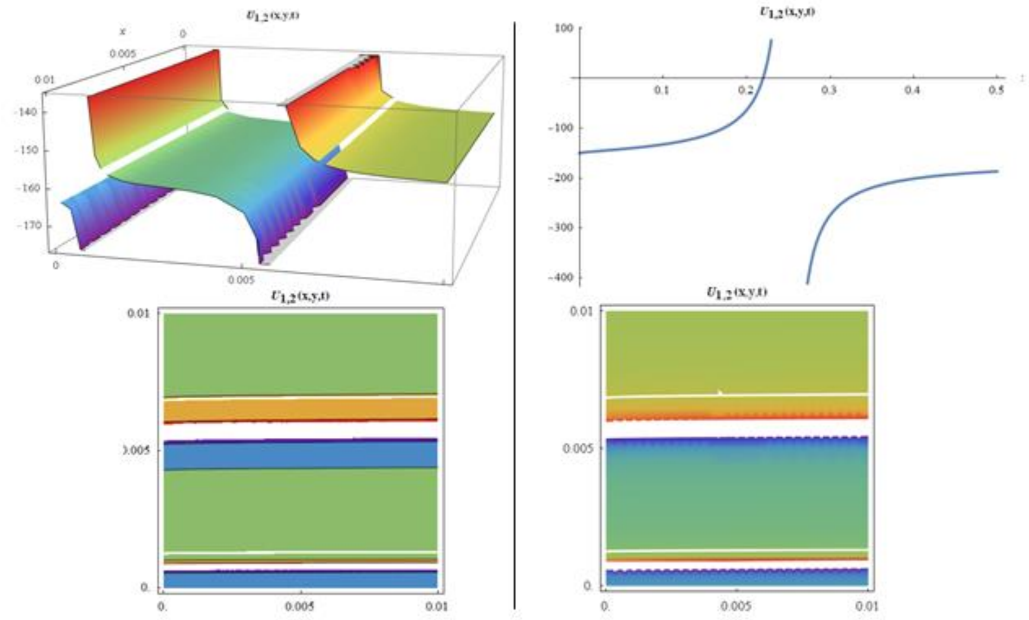

Figure3.2: The 3D, 2D, contour and density graphs of $u_{1,2}$ is illustrated for the values $\lambda = 1, \mu = 4, k_1 = 0.23, k_2 = 38.3333, k_3 = 30.4175, B_0 = 0.66, B_1 = 1.1, A_3 = 1.5, A_0 = 1.35, A_1 = 3.15, A_2 = 2.4, \alpha = 0.5, y = 1.2, E = 0.75$

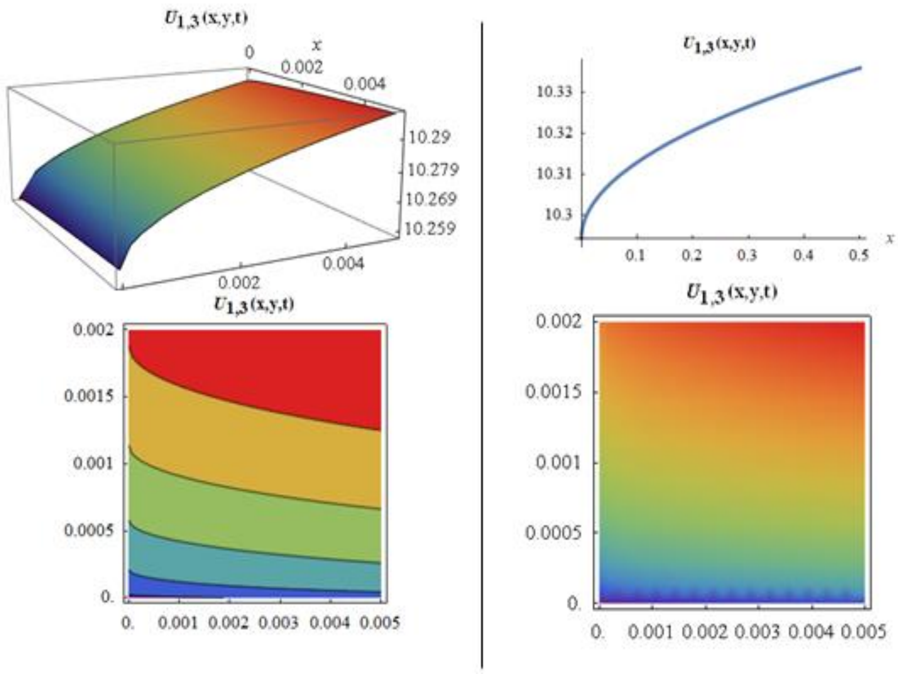

Figure3.3: The 3D, 2D, contour and density graphs of $u_{1,3}$ is illustrated for the values $\lambda = 1, \mu = 0, k_1 = 0.23, k_2 = 38.3333, k_3 = -2.02783, B_0 = 0.66, B_1 = 1.1, A_3 = 1.5, A_0 = 0.15, A_1 = 1.15, A_2 = 2.4, \alpha = 0.5, y = 1.2, E = 0.75$

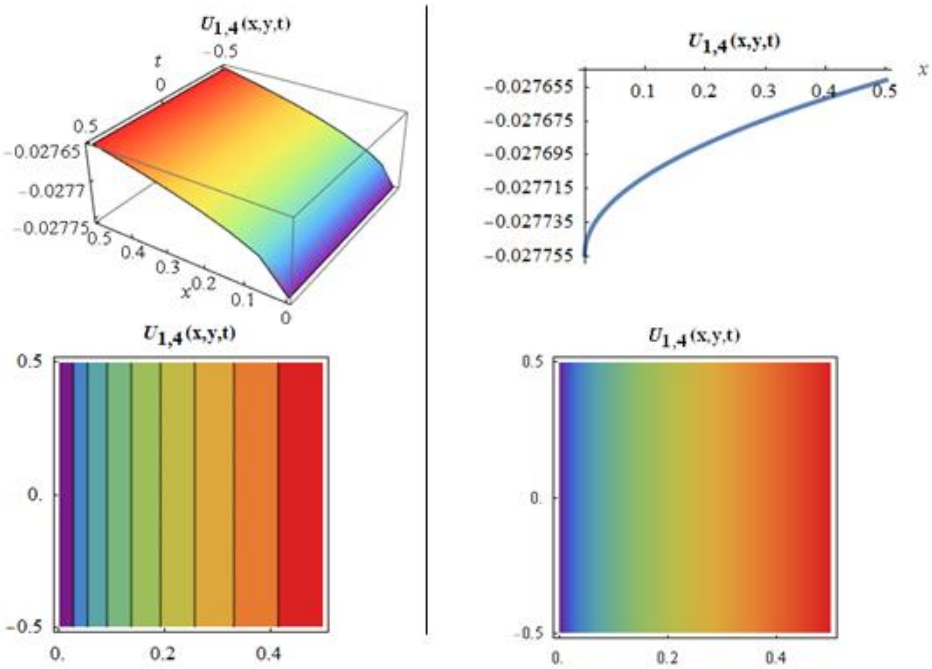

Figure3.4: The 3D, 2D, contour and density graphs of $u_{1,4}$ is illustrated for the values $\lambda = 2, \mu = 1, k_1 = 0.23, k_2 = 38.3333, k_3 = 0, B_0 = 0.66, B_1 = 1.1, A_3 = 1.5, A_0 = 0.9, A_1 = 3.3, A_2 = 3.9, \alpha = 0.5, y = 1.2, E = 0.75$

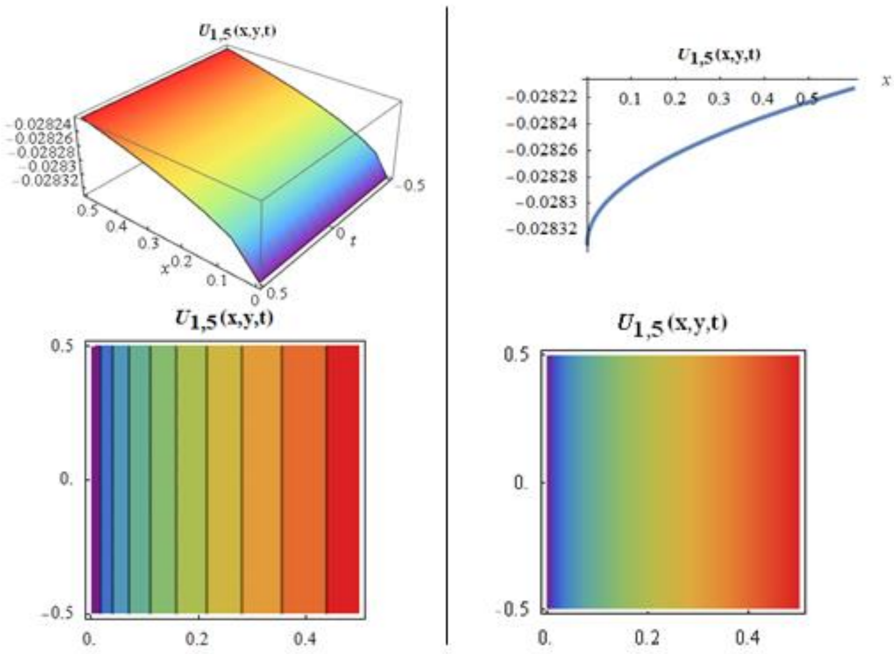

Figure3.5: The 3D, 2D, contour and density graphs of $u_{1,5}$ is illustrated for the values $\lambda = 0, \mu = 0, k_1 = 0.23, k_2 = 38.3333, k_3 = 0, B_0 = 0.66, B_1 = 1.1, A_3 = 1.5, A_0 = 0, A_1 = 0, A_2 = 0.9, \alpha = 0.5, y = 1.2, E = 0.75$

Case-2:

$$A_0=\frac{\left(k_3+3k_1^2k_2\lambda^2\right)B_0}{2k_1(2k_1+k_2)},\ A_1=\frac{1}{12}\left(\frac{k_3}{k_1^2k_2}+3\lambda^2\right)A_3+\frac{6k_1k_2\lambda B_0}{2k_1+k_2},\ A_2=\lambda A_3+\frac{6k_1k_2B_0}{2k_1+k_2},$$

$$B_1=\frac{\left(2k_1+k_2\right)A_3}{6k_1k_2},\ \mu=\frac{1}{4}\left(\frac{k_3}{k_1^2k_2}+\lambda^2\right). \tag{3.9}$$

Another solution class from the system of algebraic equation is given as case-2 in equation (3.9). The verification process is ensured by Mathematica again. Considering the fractional complex transform $\xi=k_1x^\alpha/\Gamma(1+\alpha)+k_2y^\alpha/\Gamma(1+\alpha)-k_3t^\alpha/\Gamma(1+\alpha)$ together with (2.12)-(2.16) the solutions for FDE (1.1) can be presented as follows:

Family-1:

$$u_{2,1}(x,y,t)=\frac{\omega_3\left(k_3\omega_1+3\upsilon(\omega_1-2\lambda)\right)+2\left(k_3+3\upsilon\right)\mu\omega_2Cosh(\omega_2)-12\upsilon\mu Sinh(\omega_2)}{2k_1\left(2k_1+k_2\right)\omega_3\left(\omega_1+2\mu Cosh(\omega_2)\right)}, \tag{3.10}$$

where $\upsilon=k_1^2k_2\omega_3^2$.

Family-2

$$u_{2,2}(x,y,t)=\frac{\omega_5\left(k_3\omega_1+3\sigma(\omega_1-2\lambda)\right)+2\left(k_3+\sigma\right)\mu\omega_4Cos(\omega_4)-12\sigma\mu Sin(\omega_4)}{2k_1\left(2k_1+k_2\right)\omega_5\left(\lambda^2-2\mu+2\mu Cos(\omega_4)\right)}, \tag{3.11}$$

where $\sigma=k_1^2k_2\omega_5^2$.

Family-3:

$$u_{2,3}(x,y,t)=\frac{k_3\xi+3k_1^2k_2\lambda\left(\dfrac{-4}{\exp\left(\lambda(\xi+E)\right)-1}+\lambda\xi\right)}{2k_1\left(2k_1+k_2\right)}. \tag{3.12}$$

Family-4:

$$u_{2,4}(x,y,t)=\frac{k_3\xi-\dfrac{12k_1^2k_2\lambda}{2+\lambda(\xi+E)}}{2k_1\left(2k_1+k_2\right)}. \tag{3.13}$$

Family-5:

$$u_{2,5}(x,y,t)=\frac{k_3\xi-\dfrac{12k_1^2k_2}{\xi+E}}{2k_1\left(2k_1+k_2\right)}. \tag{3.14}$$

The graphs of the solutions through equations (3.10)-(3.14) are presented in Figure3.6-Figure3.10, respectively. The first row shows the 3D and 2D graphs and the second row exhibits the contour and the density plots from left to right.

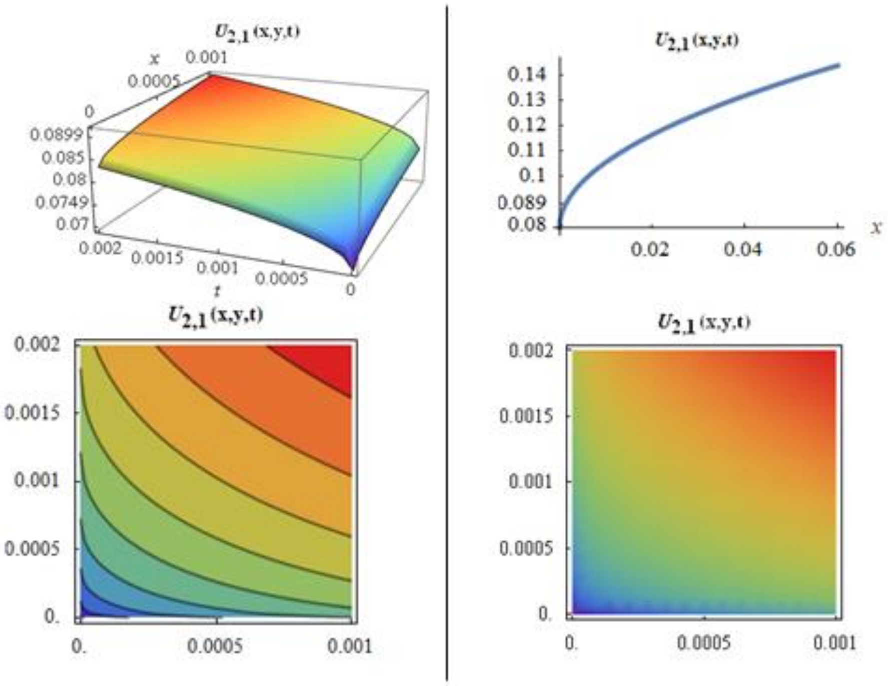

Figure3.6: The 3D, 2D, contour and density graphs of $u_{2,1}$ is illustrated for the values $\lambda = 3, \mu = 1.7954, k_1 = 0.5, k_2 = 1.32, k_3 = -0.6, B_0 = 0.66, B_1 = 0.1464, A_3 = 0.25, A_0 = 2.364, A_1 = 3.9042, A_2 = 1.8765, \alpha = 0.5, y = 1.2, E = 0.65$

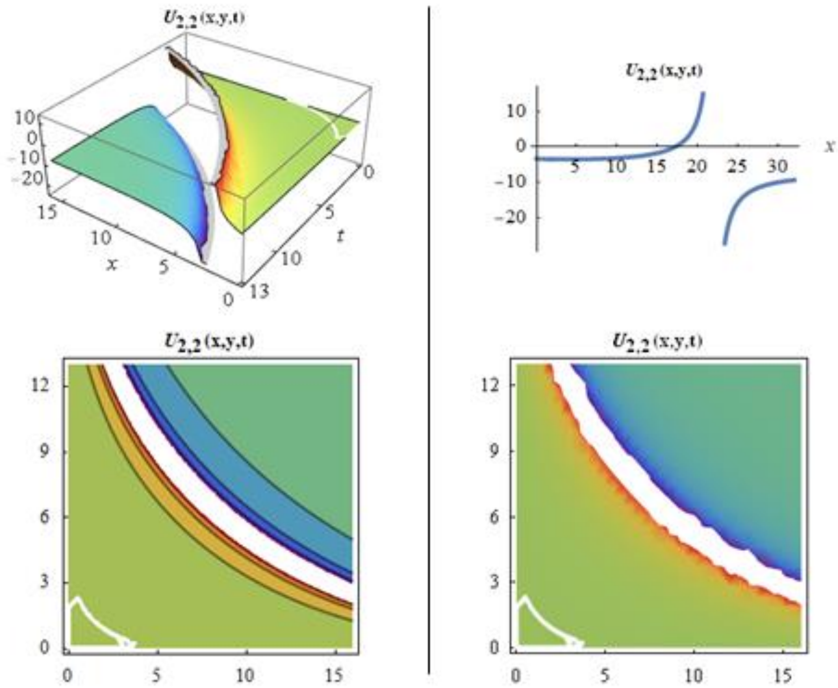

Figure3.7: The 3D, 2D, contour and density graphs of $u_{2,2}$ is illustrated for the values $\lambda = 1, \mu = 0.704545, k_1 = 0.5, k_2 = 1.32, k_3 = -0.6, B_0 = 0.66, B_1 = 0.1464, A_3 = 0.25, A_0 = 0.45232, A_1 = 1.22693, A_2 = 1.37655, \alpha = 0.5, y = 1.2, E = 0.65$

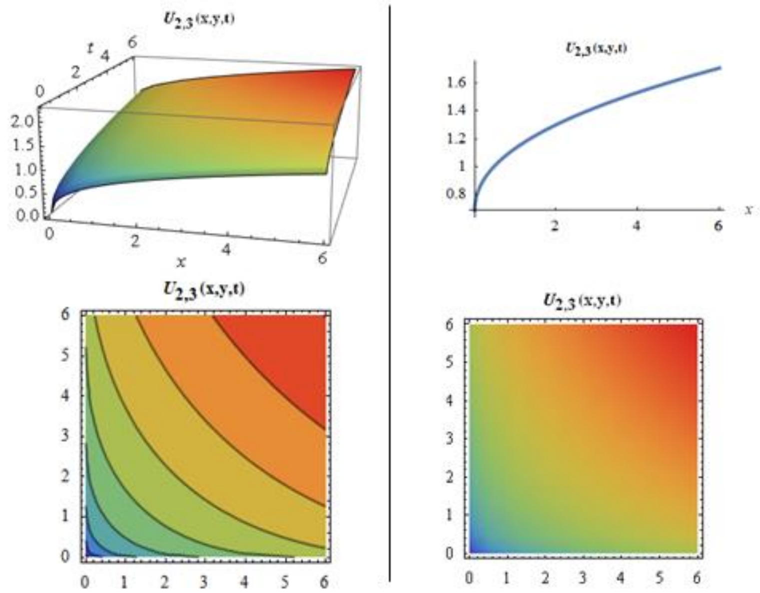

Figure3.8: The 3D, 2D, contour and density graphs of $u_{2,3}$ is illustrated for the values $\lambda = 1, \mu = 0, k_1 = 1, k_2 = 1, k_3 = -1, B_0 = 0.66, B_1 = 0.125, A_3 = 0.25, A_0 = 0.22, A_1 = 1.36167, A_2 = 1.57, \alpha = 0.5, y = 1.2, E = 0.65$

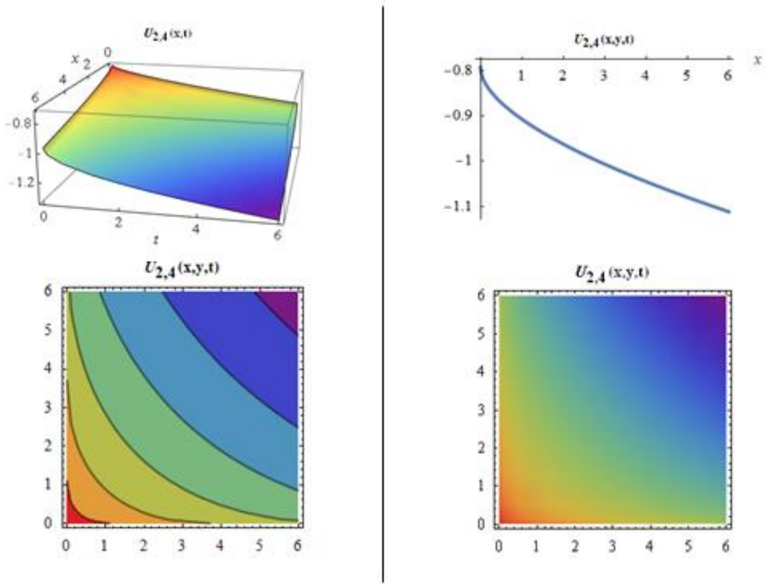

Figure3.9: The 3D, 2D, contour and density graphs of $u_{2,4}$ is illustrated for the values $\lambda = 1, \mu = 0.25, k_1 = 1, k_2 = 1, k_3 = -1, B_0 = 0.66, B_1 = 0.125, A_3 = 0.25, A_0 = 0.33, A_1 = 1.3825, A_2 = 1.57, \alpha = 0.5, y = 1.2, E = 0.65$

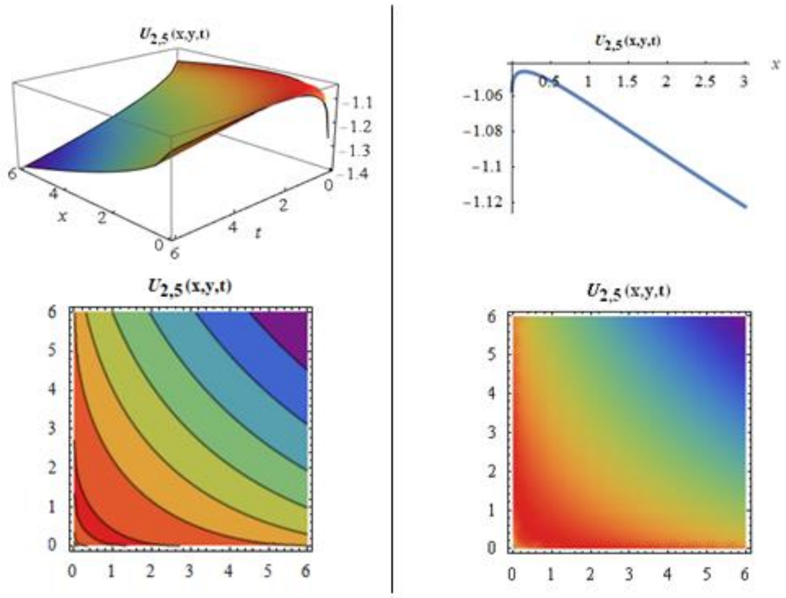

Figure3.10: The 3D, 2D, contour and density graphs of $u_{2,5}$ is illustrated for the values $\lambda = 0, \mu = 0, k_1 = 1, k_2 = 1, k_3 = -1, B_0 = 0.66, B_1 = 0.125, A_3 = 0.25, A_0 = 0, A_1 = 0, A_2 = 1.32, \alpha = 0.5, y = 1.2, E = 0.65$

4. CONCLUSION

In the present paper we have employed the MEFM to obtain the exact solutions of the space-time fractional CD equation along with the Jumarie's RL fractional derivative. Some of the exact solutions are presented and also depicted graphically to observe the behaviors of equations (3.4)-(3.8) and (3.10)-(3.14). The exact solutions achieved by MEFM are compared with the ones in [12-15] and it is concluded that they are new kind and they have not reported before.

In [13] it is stated that the ansatz method and the (G'/G)-expansion method give only one solution. Unlike this result the proposed method MEFM in the current study, has given different types of solution as hyperbolic, trigonometric and rational functions for space-time fractional CD equation.

The mentioned equation is used in coastal engineering to describe the propagation of shallow-water waves and to demonstrate the propagation of waves in dissipative and nonlinear media [14]. The results may be useful to interpret the phenomenon in this field. Because the studies in coastal engineering are on beach nourishment and seaport designing which require the knowledge of the wave features.

REFERENCES

1. El-Misiery, A.E.M., Ahmed, E., On a fractional model for earthquakes, Applied Mathematics and Computation, Vol:178, 207-211, 2006.
2. Podlubny, I., Fractional Differential Equations, Mathematics in Science and Engineering, Vol:198, Academic Press, 1999.
3. Nasrolahpour, H., A note on fractional electrodynamics, Communications in Nonlinear Science and Numerical Simulation, Vol:18, No:9, 2589-2593, 2013.

4. Liu, W., Chen, K., The functional variable method for finding exact solutions of some nonlinear time-fractional differential equations, Pramana-Journal of Physics, Vol:81, No:3, 377-384, 2013.
5. Siddique, I., Jaradat, M.M.M., Zafar, A., Mehdi, K.B., Osman, M.S., Exact traveling wave solutions for two prolific conformable M-Fractional differential equations via three diverse approaches, Results in Physics, Vol:28, 104557, 2021.
6. Demiray, S.T., Pandir, Y., Bulut, H., Generalized Kudryashov Method for Time-Fractional Differential Equations, Abstract and Applied Analysis, Vol: 2014, Article ID 901540, 13 pages, 2014. https://doi.org/10.1155/2014/901540.
7. Guo, S., Mei, L., Li, Y., Sun, Y., The improved fractional sub-equation method and its applications to the space–time fractional differential equations in fluid mechanics, Physics Letters A, Vol:376, No:4, 407-411, 2012.
8. Akbulut, A., Kaplan, M., Auxiliary equation method for time-fractional differential equations with conformable derivative, Computers & Mathematics with Applications, Vol:75, No:3, 876-882, 2018.
9. Kaplan, M., Bekir, A., The modified simple equation method for solving some fractional-order nonlinear equations, Pramana-Journal of Physics, Vol:87, No:15, 2016.
10. Guner, O., Atik, H., Soliton solution of fractional-order nonlinear differential equations based on the exp-function method, Optik, Vol:127, No:20, 10076-10083, 2016.
11. Bulut, H., Ismael, H.F., Exploring New Features for the Perturbed Chen-Lee-Liu Model via $(m+1/G')$-expansion Method, Proceedings of the Institute of Mathematics and Mechanics, National Academy of Sciences of Azerbaijan, Vol:48, No:1, 164–173, 2022.
12. Kaur, L., WazWaz, A.M., Dynamical Analysis Of Soliton Solutions For Space-Time Fractional Calogero-Degasperis And Sharma-Tasso-Olver Equations, Romanian Reports in Physics, 2022(in press).
13. Guner, O., Exact Travelling Wave Solutions To The Space-Time Fractional Calogero-Degasperis Equation Using Different Methods, Journal of Applied Analysis & Computation, Vol:9, No:2, 428-439, 2019.
14. Arefin, M.A., Saeed, Md. A., Akbar, M.A., Uddin, M.H., Analytical behavior of weakly dispersive surface and internal waves in the ocean, Journal of Ocean Engineering and Science, 2021, ISSN 2468-0133, https://doi.org/10.1016/j.joes.2021.08.012.
15. Mohyud-Din, S.T., Nawaz, T., Azhar, E., Akbar, M.A., Fractional sub-equation method to space–time fractional Calogero-Degasperis and potential Kadomtsev-Petviashvili equations, Journal of Taibah University for Science, Vol:11, No:2, 258-263, 2017.
16. Jumarie, G., Modified Riemann-Liouville derivative and fractional Taylor series of nondifferentiable functions further results, Computers & Mathematics with Applications, Vol:51, No:9–10, 1367-1376, 2006.

INVESTIGATION OF MECHANICAL AND MICROSCOPIC PROPERTIES OF RECYCLED CONCRETE BASED ON GEOPOLYMER POWDER CONTAINING LIME AND METAKAOLIN

Gökhan Kaplan[1], Oğuzhan Çelebi[1], Ali Öz[2], Haluk Görkem Alcan[3], Barış Bayrak[3], Abdulkadir Cüneyt Aydın[1]

[1] Department of Civil Engineering, University of Atatürk, Erzurum, Turkey

2Narman Vocational School, University of Atatürk, Erzurum, Turkey

[3]Department of Civil Engineering, University of Kafkas, Erzurum, Turkey

gkaplan@atauni.edu.tr,

Abstract

Mechanical and microanalyses were carried out on the recycled concrete samples obtained by preparing different mixtures of geopolymer powder, metakaolin, lime, quartz, and alkali activator sodium silicate and sodium hydroxide solution were formed by grinding the geopolymer concrete samples prepared with a certain temperature and low curing times. Recycled concrete samples with geopolymer powder, with a weight ratio of 36% in $1m^3$ volume, were prepared at 60℃ for 6-8-10 hours of curing. The test results showed that the highest compressive strength of the mixtures was 77.89 MPa with the increase of the lime ratio in the 8 hour curing period. It was determined that the highest compressive strength was 73 MPa in the samples in which metakaolin was never used and the lime ratio was maximum. The compressive strengths of the samples with 0.05% lime ratio of metakaolin and 0.025% lime ratio of metakaolin and 0.05% lime ratio of metakaolin were 74 and 77.89 MPa, respectively. In addition, capillary permeability tests were also carried out on the samples. Capillarity coefficients of geopolymer mixtures are below $0.377\ kg/m^2.min^{0.5}$. It has been suggested that concrete mixtures produced from recycled geopolymer powder can be used in the load-bearing elements of structures that need to remain at the level of use immediately under the effect of dynamic load.

Keywords: Geopolymer powder, Recycle concrete, Metakaolin, Lime. Sustainability

1. INTRODUCTION

Today, the consumption of natural resources due to increased energy demands causes some negative problems such as sudden climate changes and environmental pollution. There is a need to accelerate the construction of a low-carbon, efficient and sustainable energy system without depleting natural resources [1]. One of those limiting the possibility of sustainable energy is the construction sector. One of the causes of global problems such as climate change by spreading carbon dioxide emissions is the conventional cement sector [2-3]. In structural systems, traditional concrete, which wraps the reinforced concrete reinforcement, prevents the reinforcement from buckling, and increases the fire and compressive strength of the structural element, is generally composed of cement components. However, since cement-based concrete can cause many negative consequences such as environmental pollution and global warming by increasing CO_2 emissions, Geopolymers have become a potential alternative binder to ordinary Portland cement (OPC) in some applications due to sustainability criteria such as lower greenhouse gas emissions and low energy consumption [4]. Geopolymer concrete has five times lower energy consumption and carbon ratio than OPC due to its composition with fly ash (FA) and ground granulated blast furnace slag (GGBFS) [5]. The geopolymeric reaction occurs due to the chemical reaction between aluminosilicate oxides, sodium hydroxide and sodium silicate of powders such as FA and ground GGBFS [6]. Based on these characteristic features of geopolymerization, researchers have suggested that recycled concrete can be obtained by using wasted geopolymer powders. Considering the sustainable use of geopolymers resulting from the polymerization reaction with low energy consumption, its applicability in a wide range of engineering fields has been investigated [7-8].

In addition to creating a sustainable environment, for geopolymers to be an alternative to OPC, they must have appropriate compressive strength and stiffness that can be used in structural bearing systems. Many studies have been carried out in the literature to obtain these chemical and mechanical properties. Feng et al. (2012) determined the compressive strength of the geopolymer concrete, which was prepared by one-part mixing of albite, sodium hydroxide (NaOH) and sodium carbonate (Na_2CO_3) materials, was over 40 MPa after 28 days [9]. Nemetollahi et al. (2015) obtained a compressive strength of over 37 MPa 28 days after one-part mixing, which was prepared from low-calcium fly ash, slag, and sodium silicate (Na_2SiO_3) and sodium hydroxide (NaOH) and hydrated lime [10]. Yun-Ming et al. (2017) obtained geopolymer ceramics from one-part mixed geopolymer and sodium-based geopolymer powder. At the end of the study, it was determined that the compressive strength of one-piece mixed geopolymers was 10 MPa after 28 days and the flexural strength of the ceramics formed from geopolymer powder was 90 MPA at 1200 ℃ [11]. Xinjie et al. (2021), using metakaolin as the source material, created five different geopolymer mixtures containing 0%, 20%, 50%, 80% and 100% geopolymer powder. A mixture of sodium hydroxide (NaOH) and sodium silicate (Na_2SiO_3) was used as the alkali activator solution. In the study, the changes in compressive and flexural strengths were investigated depending on the change in the geopolymer powder ratio [12]. The results showed that the mixture with less than 50% geopolymer powder is sufficient to meet the heavy traffic loads, and the mix with more than 80% geopolymer powder is sufficient to meet the plaster-mortar requirement. Gharzouni et al. (2016). reported that the mechanical properties of the geopolymer concrete will change significantly if at least 20% of the mixture is composed of geopolymer powder [13]. Aydin et al. (2021), using NaOH and sodium silicate solutions as alkali activator solutions, applied flexural and compression experiments by keeping the geopolymer mixtures formed from GGBFS, silica fume (SF), fly ash (FA) wastes at 80 degrees for 4-6-8 hours. At the end of the study, it was determined that the compressive strength of the sample cured for 8 hours was over 140 MPa [14].

This study is related to the mechanical, physical and microscopic investigation of different mixtures formed from quartz, lime, metakaolin and geopolymer powders using sodium hydroxide (NaOH) and sodium silicate (Na_2SiO_3) solutions as alkali activators. The geopolymer powders used in the study were previously obtained by crushing the geopolymer concrete samples, which were formed due to the reaction of materials such as quartz sand, metakaolin, quartz powder, and alkali activators (NaOH and Na_2SiO_3). While the geopolymer powder ratios are constant in all mixtures, the metakaolin and lime ratios change in some mixtures. Compressive and flexural tests were performed on the geopolymer powder-based concrete samples, and microscopic examinations were also made.

2. GENERAL PROPERTIES OF METHOD

2.1. Materials

Metakaolin with aluminosilicate properties was used to form recycled geopolymer concrete samples. Besides metakaolin, 0-0.5 mm diameters and 1-3 mm diameters of quartz, lime and a mixture of sodium hydroxide (NaOH) and sodium silicate (Na_2SiO_3) as alkali activator were used. Sodium hydroxide contains 0.3% Na_2CO_3, <0.1% CI, <0.04% SO_4, <0.01% Fe and <0.01% Al. Sodium silicate with a specific gravity of 1.38 g/cm^3 contains 8.8% Na_2O, 28.2% SiO_2, 63% H_2O, <0.01% Fe and <0.10% heavy metals. The SiO_2 content of the quartz aggregate is 98.2% and the Mohs hardness is 7. Metakaolin, which contains SiO_2 and Al_2O_3, was preferred because it improves the mechanical properties of the concrete and increases its strength and does not have a negative impact on the environment [15-16]. The chemical and physical properties of metakaolin and lime are presented in Table 1. The physical and chemical properties of inorganic-based binder lime used in mixtures are given in Table 2.

Table 1. Chemical and physical properties of metakaolin

Components	CaO	SiO_2	Al_2O_3	Fe_2O_3	MgO	SO_3	Specific gravity	SSA (m^2/g)
Content %	<0.5	54.3	43.2	<0.8	<0.2	<0.1	2.60	20

* Specific surface area

Table 2. Chemical and physical properties of lime

Main component	İmpurity components	Specific gravity
$Ca(OH)_2$ (> 80%)	$CaCO_3$, $Mg(OH)_2$, SiO_2, Al_2O_3 (< 20%)	2,60

2.2. Mixture Design

This study prepared a recycled geopolymer concrete (RGC) mixture with a geopolymer powder dosage of 1000 kg/m^3. Quartz powder (0-0.5 mm) and quartz sand (1-3 mm) were used as additional structural materials with a content of 450 and 550 kg/m^3, respectively. Alkaline activator liquids were added to the mixture at the rate of 43% of the binder amount. The sodium silicate/sodium hydroxide ratio is 2.3 in all geopolymer mixtures. Three different mixtures were prepared to be used in the experiments. The amount of material contained in the mixtures is presented in Table 3.

Table 3. Amount of materials used in RGC samples with geopolymer powders (kg/m^3)

Raw material	K1 Mixture	K2 Mixture	K3 Mixture
Geopolymer powder	650	650	650
Metakaolin	100	50	0
Lime	50	100	150
Quartz powder (0-0.5 mm)	450	450	450
Quartz sand (1-3 mm)	550	550	550
Sodium silicate	160	160	160
Sodium hydroxide	400	400	400

As shown in Table 3, the results were analyzed according to the mixtures' varying lime and metakaolin weights. Three different 60 °C curing regimes (6-8-10 hours) were applied to the mixtures with geopolymer powder (Fig. 1). After the curing process, the mixtures were removed from their molds and their mechanical and physical properties were determined. RGC was tested one day after heat curing. The production process of RGCs is given in Figure 2.

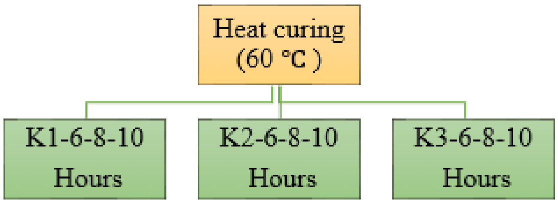

Figure 1. Curing hours for recycled concrete samples

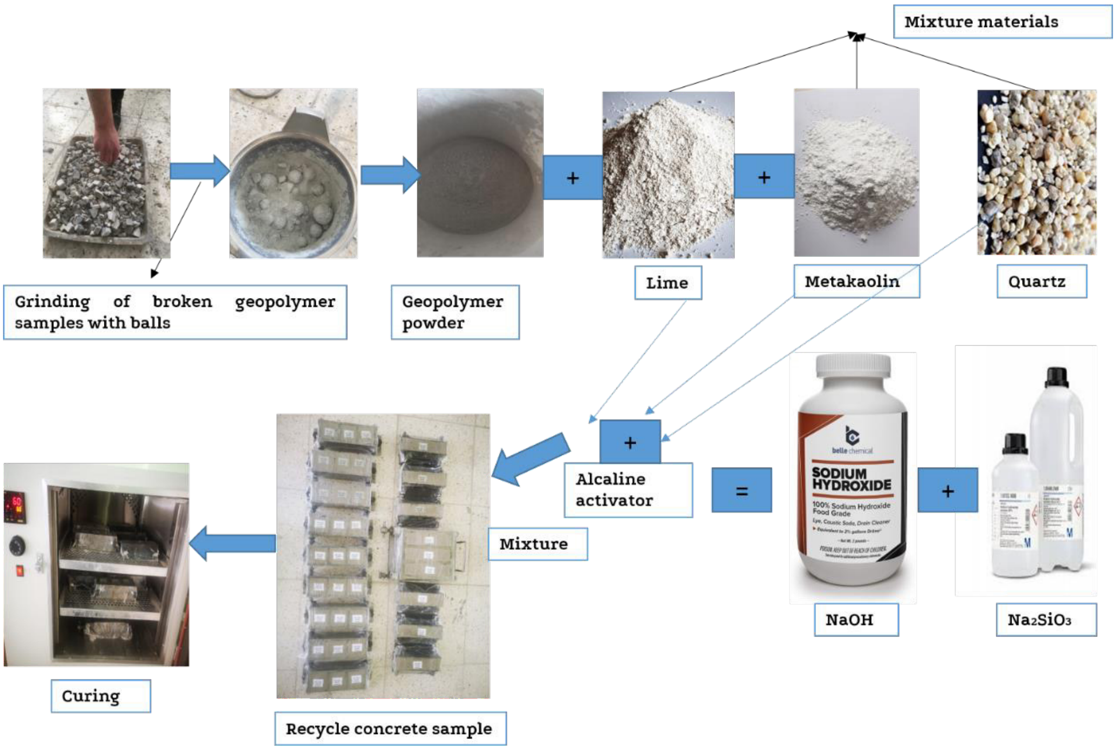

Figure 2. The production process of recycle concrete samples

2.3. Test Programs

For the fresh state properties of RGC mixtures, flow diameters were measured according to the ASTM C1437 [17]. In addition, unit weights of fresh RGC mixtures were also measured. Water absorption and dry unit weight physical properties of RGC mixtures were determined by ASTM C 642 standard [18]. Physical properties were determined in 50x50x50 mm cube samples. Compressive and flexural strengths of RGC mixtures were determined by ASTM C 348 [19] and ASTM C349 standards [20], respectively. The mechanical properties of the RGC mixtures were measured on 40x40x160 mm prism samples. Capillary water absorption of RGC mixtures was determined following EN 1015-18 standard [21]. With the determination of capillary water absorption, information about the transport properties of the RGC mixtures is obtained. Capillary water absorption of RGC mixtures was measured in 50x50x50 mm cube samples in the first 24 hours.

3. APPLICATIONS

3.1. Mechanical Properties

Compression and flexural tests were applied to the RGC samples with different mixing ratios shown in Table 3. The test results showed that after 10 hours of curing, the highest compressive and flexural strength were 77.89 and 9.36 MPa, respectively, in the K2 mixture. In the samples whose flexural and compressive strengths are shown in Figure 2, the increase in the lime ratio showed that both flexural and compressive strengths increased. In addition, it has been observed that the increase in the curing time provides an increase in the compressive and flexural strengths. Compared to the studies in the literature, the reaction of metakaolin and lime increased the compressive strength in this study. The lowest compressive strength was approximately 65 MPa in the K3 mixture after 6 hours at 60 degrees curing regimes. The fractured states of the sample with the highest compressive and flexural strength and the sample with the lowest strength are presented in Figure 3. It is shown that the samples with high strength are brittle, and the samples with low strength are slightly more ductile than the samples with high strength. In addition, it can be shown from the samples that the materials that make up the mixture form an adherence with each other. The reactions of the materials are explained more clearly with microscopic examinations.

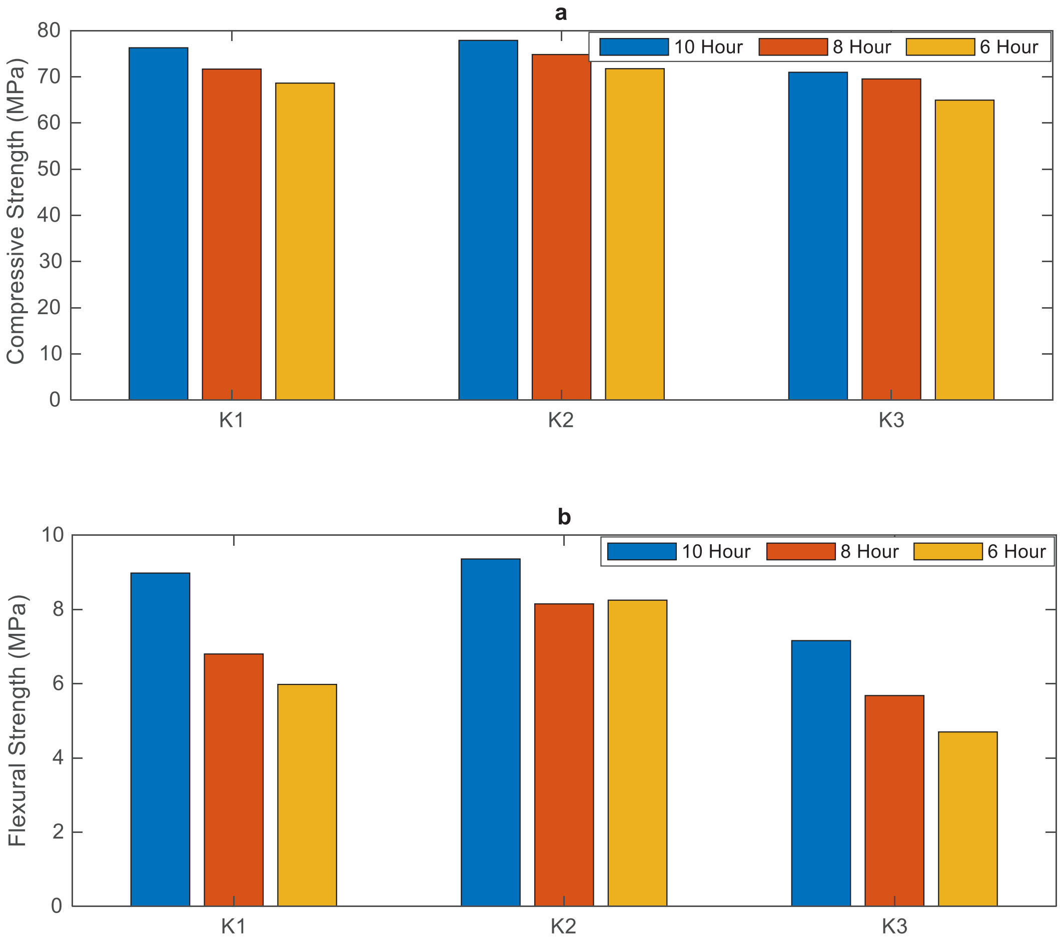

Figure 2. Compressive and flexural rest results a) compressive strength b) Flexural strength

a) b)

Figure 3. Mixtures with maximum and minimum strength a) cube samples b) prism samples

3.2. Physical Properties

As given in Figure 4, the dry unit weights of the RGC mixtures vary between 2142-2206 kg/m^3. According to the test results, the dry unit weights of the samples at different mixing ratios were close to each other. As the curing time decreases, the dry unit weights of the samples increase. Differences in dry unit weights between samples can be ignored. As a result of, the dry unit weights of RGC mixtures are above 2100 kg/m^3. In some studies, the decrease in the unit volume weights of the samples indicates that the geopolymer components react effectively. Kaplan et al. (2021) observed that as the curing time decreased, the unit volume weights increased and the geopolymerization improved [14,22].

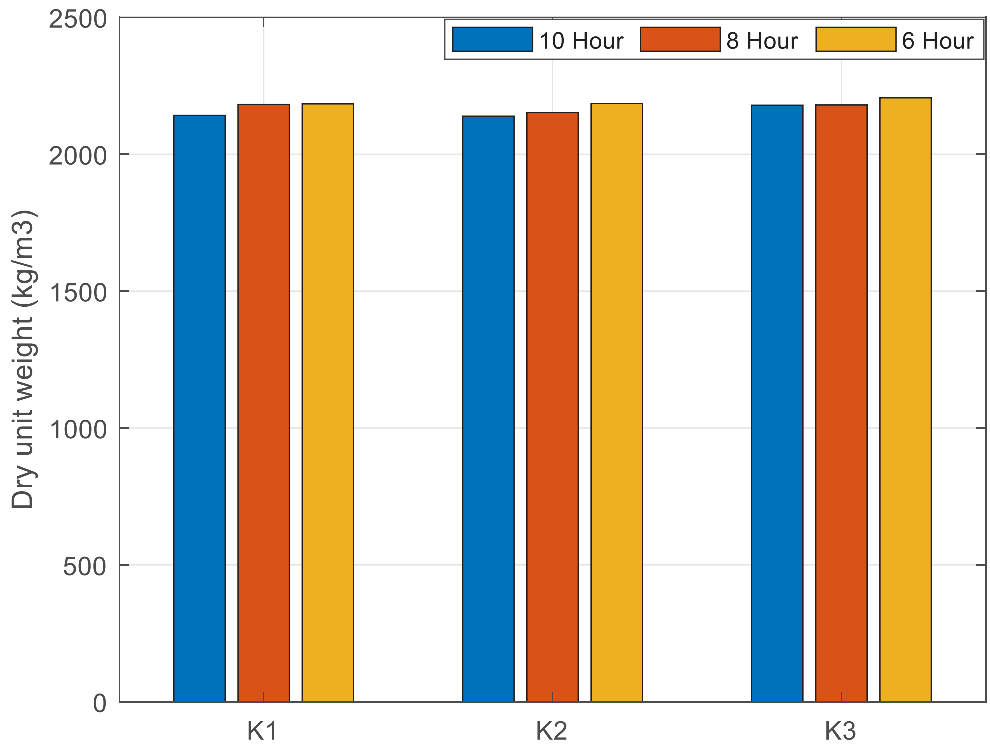

Figure 4. Dry unit weights of RCM mixtures

3.3. Transport Properties

In Figure 5, capillary water absorption according to the curing hours of RGC mixtures is given. At the end of 24 hours, the capillary water absorption of the mixtures is below 0.377 kg/m^2. The lowest capillary water absorption value was observed in the K1-60-10 mixture, with a value of 0.03 kg/m^2. It was determined that the capillary water absorption rates of the K1 mixture decreased by 83.24% and 68.15%, respectively, compared to the K3 mixture and the K2 mixture compared to the K3 mixture, in the 10-hour curing environment. Also, It was determined that the capillary water absorption rates of the K1 mixture decreased by 46.85% and 77.09%, respectively, compared to the K3 mixture and the K2 mixture compared to the K3 mixture, in the 8-hour curing environment. Finally, It was determined that the capillary water absorption rates of the K1 mixture decreased by 58.09% and 68.40%, respectively, compared to the K3 mixture and the K2 mixture compared to the K3 mixture, in the 8-hour curing environment. The results show that the increase in the compressive strength of the mixtures reduces the capillary water absorption rates. In addition, the results show that increasing the curing time at the same temperature decreases the capillary water absorption rates.

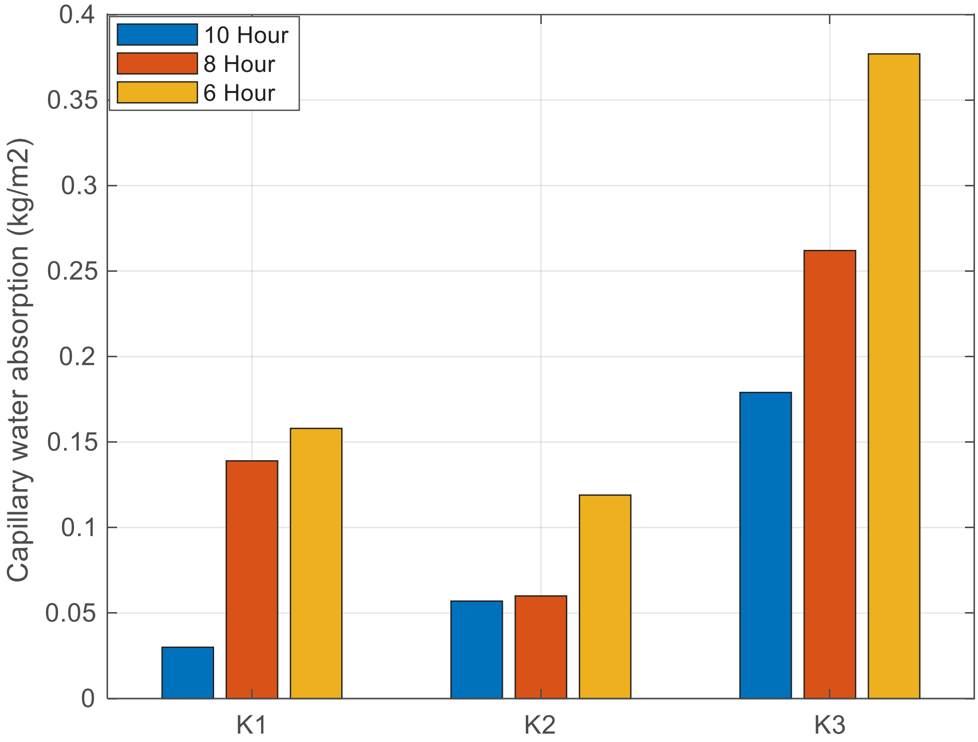

Figure 5. Capillary water absorption of RCM mixtures

3.4. Microstructures

SEM images of RGC mixtures are presented in Figure 6. Geopolymeric gel structure was observed in nanoscale SEM images. Heat curing applied to the mixtures resulted in the formation of alumina silicate gel in a zeolitic structure. It was determined that similar gel structures were formed in all three mixtures (K1, K2 and K3). Waste geopolymer powder contributed to the formation of geopolymeric gel. It was also observed that C-S-H gels were formed due to the lime used in the mixtures. C-S-H gels were formed due to the reaction of lime and metakaolin.

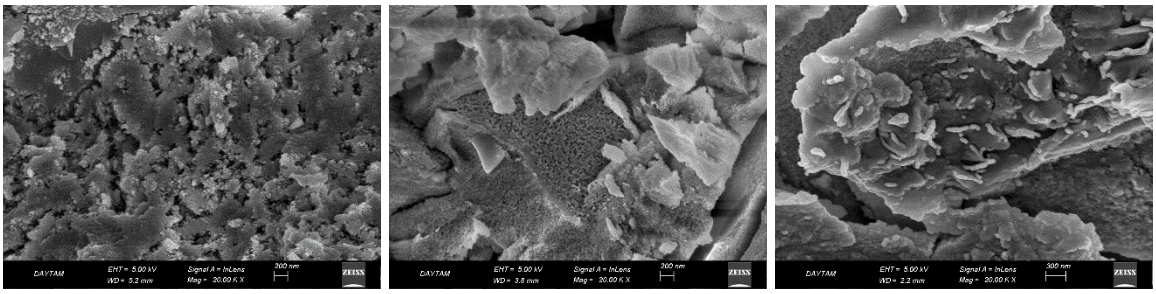

(a) K1 mixture (b) K2 mixture (c) K3 mixture

Figure 6. SEM images of RGC mixtures

4. CONCLUSIONS

In this study, geopolymer samples formed as a result of using materials such as quartz granule, quartz powder, aggregate, sand as aggregate, blast furnace slag as binder, and sodium hydroxide and sodium silicate as alkaline solution were ground with relevant balls and turned into powder. Recycle concrete samples were formed as a result of using the geopolymer powder as a binder, using metakaolin and lime as aggregate or sand, and using sodium hydroxide and sodium silicate as a solution. In addition to flexural and compressive, dry unit weight, capillary water absorption experiments, and microstructure analyzes were carried out on K1, K2 and K3 mixtures obtained at different mixing ratios. The test results showed that the flexural and compressive strength of the mixtures increased as the curing time increased at the same temperatures. In addition, it was determined that the highest compressive and flexural strength was 77.89 MPa and 8.98 MPa, respectively, due to the higher lime ratio in the mixtures than the metakaolin. In the mixture in which metakaolin was not used, the lowest compressive strength and flexural strength were determined as 64.96 MP and 3.07 MPa, respectively, in the 6-hour curing environment. The decrease in the curing time showed that the unit weight of the mixtures increased. The highest dry unit weight of 2206 kg/m^3 was determined in the K3 mixture, which was prepared in a 6-hour curing environment and where no metakaolin was used. The mixture with the lowest unit volume weight of 2139 kg/m^3, was determined as the mixture in which the lime ratio was higher than the metakalon ratio. Capillary water absorption experiments applied to the samples showed that increasing the curing time at the same temperature decreased the capillary water absorption rate. It was observed that the mixture with the lowest capillary water absorption rate was in the mixture where the metakaolin ratio was higher than the lime ratio, and the highest value was in the mixture without metakaolin. In SEM images, it was determined that a zeolitic geopolymeric gel was formed. C-S-H gels were also observed due to the presence of lime.

As a result, metakaolin and lime as a binder showed that recycled concrete with optimum compressive and flexural strength could be used from geopolymer powders. Using the mixtures obtained in structural applications predicts that the structure can remain in the elastic region, that is, at the level of immediate use, under dynamic loads such as earthquakes and winds.

REFERENCES

[1.] C.H. Wang , S. Wang , Q. Li , et al. , Fabrication and performance of a power gen- eration device based on stacked piezoelectric energy-harvesting units for pave- ments, Energy Convers. Manage. 163 (2018) 196–207 .

[2.] Huntzinger D N, Eatmon T D. A Life-cycle Assessment of Portland Cement Manufacturing: Comparing the Traditional Process with Alternative Technologies[J]. Journal of Cleaner Production, 2009, 17(7): 668-675.

[3.] Yun-Ming L, Cheng-Yong H, Al Bakri M M, et al. Structure and Properties of Clay-based Geopolymer Cements: A Review[J]. Progress in Materials Science, 2016, 83: 595-629.

[4.] P. Duxson et al., Geopolymer technology: the current state of the art, J. Mater. Sci. 42 (2007) 2917–2933.

[5.] A. Akbarnezhad, J.Z. Xiao, Estimation and minimization of embodied carbon of buildings: a review, Buildings 7 (1) (2017) 5, https://doi.org/10.3390/ buildings7010005.

[6.] G.F. Huseien, A.R.M. Sam, K.W. Shah, J. Mirza, M.M. Tahir, Evaluation of alkaliactivated mortars containing high volume waste ceramic powder and fly ash replacing GBFS, Constr. Build. Mater. 210 (2019) 78–92, https://doi.org/ 10.1016/j.conbuildmat.2019.03.194.

[7.] Parveen, Singhal D, Junaid M T, et al. Mechanical and Microstructural Properties of Fly Ash Based Geopolymer Concrete Incorporating Alccofine at Ambient Curing[J]. Construction and Building Materials, 2018, 180: 298-307.

[8.] Dadsetan S, Siad H, Lachemi M, et al. Construction and Demolition Waste in Geopolymer Concrete Technology: A Review[J]. Magazine of Concrete Research, 2019, 71(23): 1 232-1 252

[9.] D. Feng, J.L. Provis, J.S.J. Van Deventer, Thermal activation of albite for the synthesis of one-part mix geopolymers, J. Am. Ceram. Soc. 95 (2012) 565–572.

[10.] B. Nematollahi, J. Sanjayan, F.U.A. Shaikh, Synthesis of heat and ambient cured one-part geopolymer mixes with different grades of sodium silicate, Ceram. Int. 41 (4) (2015) 5596–5704.

[11.] Yun-Ming L, Cheng-Yong H, Li L.Y, Jaya N.A, Abdullah M.M.A.B, Jin T.S, Hussin K, (2017). Formation of one-part-mixing geopolymers and geopolymer ceramics from geopolymer powder. Construction and Building Materials, 156: 9-18.

[12.] Gharzouni A, Vidal L, Essaidi N, et al. Recycling of Geopolymer Waste: Influence on Geopolymer Formation and Mechanical Properties [J]. Materials & Design, 2016, 94: 221-229

[13.] Xinje W, Wei Y, Hui L, Pinghua Z, Ningwen Z, Jincai F, (2021). Strength and microstructural analysis of geopolymer prepared with recycled geopolymer powder. . Journal of Wuhan University of Technology-Mater. Sci. Ed. 439-445.

[14.] Aydın A.C, Kaplan G, Öz A, Bayrak B, Alcan H.G, Çelebi O, (2021). The Effect of Curing Temperature on the Early Age Properties of Granulated Furnace Slag Based Reactive Geopolymer Concrete. GEC-2021 First International Geopolymeric Composites Congress.

[15.] Siddique, R., Kalus, J., 2009, ”Influence of metakaolin on the properties of mortar and concrete: a review”, Applied Clay Science, 43, 392-400.

[16.] Khatib, J.M., Hibbert, J.J., 2005, “Selected engineering properties of concrete incorporating slag and metakaolin”, Construction and building materials, 19, 460-472.

[17.] ASTM, C1437 - Standard test method for flow of hydraulic cement mortar, 2013.

[18.] ASTM C642-13, Standard test method for density, absorption, and voids in hardened concrete, ASTM International, ASTM Int. (2013).

[19.] ASTM C348, Standard Test Method for Flexural Strength of Hydraulic-Cement Mortars, Annu. B. ASTM Stand. (1998).

[20.] ASTM C349, Standard test method for compressive strength of hydraulic-cement mortars (Using portions of prisms broken in flexure), ASTM Int. (2002).
[21.] BSI, BS EN 1015-18: Methods of Test for Mortar for Masonry - Determination of Water Absorption Coefficient Due to Capillary Action of Hardened Mortar, 2002.
[22.] T. Bakharev, Geopolymeric materials prepared using Class F fly ash and elevated temperature curing, Cem. Concr. Res. 35 (2005) 1224–1232

THE EFFECT OF POLYVINYL ALCOHOL FIBER ON THE MECHANICAL PROPERTIES OF HIGH STRENGTH GEOPOLYMER CONCRETES

Ali Öz[1], Oğuzhan Çelebi[2], Gökhan Kaplan[2], Barış Bayrak[3], Haluk Görkem Alcan[3], Abdulkadir Cüneyt Aydın[2]

[1] Narman Vocational School, University of Ataturk, Erzurum, Turkey

[2] Department of Civil Engineering, University of Ataturk, Erzurum, Turkey

[3] Department of Civil Engineering, University of Kafkas, Kars, Turkey

alioz@atauni.edu.tr

Abstract

Today, it is quite common to use ordinary Portland cement-based concrete in buildings. Geopolymer concrete has been proposed as an alternative to Portland cement concrete, due to the high greenhouse gas effect and the environmental pollution of energy consumption caused by cement consumption. In this study, metakaolin and ground blast furnace slag were preferred as binder materials in order to increase the early age strength of concrete and not to cause loss of strength due to possible porosity in later ages. In addition, due to the high probability of brittle fracture of geopolymer concrete after curing at high temperatures, it is aimed to cope with these negative properties by using polyvinyl alcohol fibers (PVAF) without reducing the flexural and compressive strengths of concrete. In this study, in order to examine the effect of PVAF on the mechanical properties of high strength geopolymer concrete, three mixtures were designed, 0.3%, 0.6 kg/m^3 fiber and did not contain any fibers which were kept in a curing environment at 80 ^{o}C for 10 hours. The amount of GGBFS and quartz powder varies, with the same weight percentage of metakaolin as binder in the mixtures. In addition, the aggregate (quartz) and alkali activator contents of the mixtures are the same. The test results showed that the mixture containing 0.6 kg/m^3 PVAF reached 137. 80 MPa by increasing the compressive strength by 18.77% compared to the fiberless mixture, and reaching 16.10 MPa by increasing the flexural strength by 63.41%. In addition, it has been determined that the use of PVAF as a reinforcing element prevents brittle fracture in geopolymer concrete samples. The results showed that PVAF can be used as a reinforcement element in order to prevent the negative properties of geopolymer concrete such as high energy consumption and brittle fracture without losing its mechanical properties such as high flexural and compressive strengths.

Keywords: Geopolymer, PVA Fiber, High Strength Concrete, Metakaolin, Sustainability

1. Introduction

Ordinary Portland cement (OPC) based concrete is the most widely used building material in structural bearing elements. OPC-based concretes, which are commonly produced globally, are important in meeting the axial compressive loads acting on the structural elements vertically and the tension cracks formed in the horizontal. The need for OPC has increased due to the rapid construction experienced today, and its production has exceeded 3 billion tons per year [1]. Although OPC-based concrete meets compressive strength and tension cracks in structural carrier systems, it causes environmental pollution and high energy consumption [2]. It also increases problems such as increasing carbon dioxide (CO_2) emissions [3]. Studies have been carried out to discover sustainable construction materials such as geopolymer and reactive powder concrete, which can show high mechanical properties without causing such negative effects [4-6]. The geopolymer, which is currently considered an alternative to OPC, was first described by Davidots in 1979 [7]. Geopolymer concretes are produced with various alkali activators and aluminosilicate binders [8]. Alkali activators consist of sodium hydroxide and sodium silicate, effective in the polymerization process [8]. These aluminosilicate binders contain dense silica (Si) and alumina (Al). In this context, ground blast furnace slag (GBFS) forming C-A-S-H gel and fly ash (FA) forming N-A-S-H gel are mostly used as binding materials in geopolymer concrete [9]. In addition, geopolymer concrete (GPC) can be used for blast furnace slag, metakaolin, silica fume, fly ash, etc. It is a product formed due to alkali activation of industrial wastes called pozzolan [10,11]. These pozzolan-activated materials improve the mechanical properties of geopolymer concrete and reduce energy consumption, environmental pollution, and consumption of natural resources [12-14]. Metakaolin can be used as a binder material to increase the early age strength of geopolymer concrete and to prevent the decrease in strength due to structural water loss in later ages [15].

Geopolymer concretes are generally used as repair and reinforcement materials in structural systems due to their high early-age strength [16]. However, geopolymer concretes have disadvantages such as brittle fracture and low deformation ability. Some studies have shown that GPC has more brittle surfaces than OPC-based concrete [17]. To prevent these disadvantages, fibers such as steel, glass, basalt, polypropylene, carbon and PVA can be added to geopolymer concretes as reinforcement [18,19]. Of these fibers, glass and steel fibers increase the structural integrity, mechanical properties, impact strength and ductility of concrete reducing the formation of micro cracks [20-22]. In addition, high modulus fibers improve the mechanical properties of concrete and low modulus fibers improve post cracking behavior [23]. Among these fibers, PVAF is preferred with concrete as it has properties such as modulus of elasticity suitable for concrete, thin diameter, acid and alkali resistance, abrasion resistance and good weather resistance [24,25]. In addition to its high modulus of elasticity, PVAF creates a strong bond between the fiber and the concrete matrix due to the hydroxyl group in its molecular chains [26,27].

Different studies have been carried out for high-strength geopolymer concrete in the literature. Many studies on geopolymer have shown that geopolymer concrete has high compressive strength, low friction, acid and fire resistance [28-31]. Ganesh et al. (2021) developed a high-performance, sustainable, optimized fiber-reinforced geopolymer concrete. In the study, extensive experimental studies were carried out to optimize the alkaline solution molarity, granule blast furnace slag and glass fiber in geopolymer concrete under different curing conditions. To understand the microstructure of the geopolymer matrix, further microstructure investigations have been carried out through scanning electron microscopic analysis (SEM) and energy distribution spectroscopy analysis [32]. Kaplan et al. (2022) investigated the effect of quartz powder on medium strength fly ash geopolymers at short curing time and low curing temperature. The physical, mechanical, capillary water permeability and microstructural properties were determined by keeping the geopolymer mixtures obtained in different quartz powder volumes in 40-60 and 80°C curing environments for 6, 8 and 10 hours. The results showed that fly ash geopolymers with a compressive strength of 60 MPa can be obtained in a short curing time of 10 hours using quartz powder [33]. Kaplan et al. (2021) investigated the effect of curing temperature on the early age properties of granule blast furnace slag-based reactive geopolymer concrete. Geopolymer concrete samples consisting of granule blast furnace slag (GBFS), river gravel, silica fume (SF), quartz and alkali activator (NaOH and Na2SO3) mixtures were kept in a curing environment at 40, 60 and 80°C for 8 hours. As a result of the study, compressive strength of over 140 MPa was obtained after 8 hours without high energy, such as autoclave curing [34]. Hasnaoui et al. (2019) conducted a study comparing the mechanical, porosity, rheological and stability properties of granule blast furnace slag (GBFS) and metakaolin (MK) geopolymer concrete with those of OPC-based concrete. As a result of the study, it has been reached that the increase in the GBFS/MK ratio gives optimum results [35]. In order to prevent brittle fracture by increasing the deformation capacity of OPC-based concretes, fiber-reinforced concrete studies were also carried out. In this study, studies on the use of PVAF as a reinforcement element in concrete due to the mechanical properties of PVAF compatible with concrete are presented in summary. Shen et al. (2021) investigated the effect of polyvinyl alcohol fiber (PVAF) on the cracking risk of high-strength concrete under uniaxial restrained conditions at an early age. The results showed that by incorporating PVAF into concrete, internal cracks were reduced by increasing the early compressive and tensile yield strength of HSC (High Strength Concrete) [36]. Kim et al. (2013) showed that PVAF has a better performance than other fibers in reducing cracks formed in concrete [37]. Ayub et al. (2014) conducted an experimental study of the mechanical properties of high-performance PVAF reinforced concrete. Experimental results showed that 3% PVAF was the optimum fiber volume to improve the mechanical properties of high-performance concrete [38].

Considering the literature studies, in this study, GBFS and MK-containing geopolymer concrete samples were designed in order to obtain early age high compressive and flexural strength, as well as to prevent the strength of the concrete from decreasing due to structural water losses in later ages. PVAF reinforcement was used in the mixtures in order to increase the deformation capacity by preventing brittle fracture in geopolymer concrete samples. Mechanical properties, and capillary water permeability of geopolymer concrete samples, formed with and without fibers, are determined and the results are discussed.

2. GENERAL PROPERTIES OF METHOD

The study used granule blast furnace slag (GBFS) with aluminosilicate properties and metakaolin (MK). In addition to the binder materials, quartz powder, 0-0.5 mm diameter quartz and 1-3 mm diameter quartz, and sodium hydroxide (NaOH) and sodium silicate (Na_2O_3) provide alkali activator formation as a solution, were used. To improve the mechanical and physical properties of geopolymer concrete at low curing times and low temperatures, quartz granule and powder containing 98.2% SiO_2 and a MOHS hardness of 7 were added to the mixture as aggregate [33]. Metakaolin and GBFS containing SiO_2 and Al_2O_3 were preferred because they improve the mechanical properties of concrete and do not have a negative impact on the environment [39,40]. Chemical and physical properties of GBFS and MK are given in Table 1.

Table 1. Chemical and physical properties of GBFS and MK

Oxide (%)	CaO	SiO_2	Al_2O3	Fe_2O_3	MgO	SO_3	Specific gravity	SSA* (cm^2/g)
GBFS	33.9	38.3	10.3	8.2	7.3	0.6	2.82	3200
MK	<0.5	54.3	43.2	<0.8	<0.2	<0.1	2.60	200000

* Specific surface area

In addition to improving the mechanical and physical properties of the geopolymer concrete samples, PVA fibers were added to the mixtures, which can increase the deformation properties and reduce the brittle fracture. The physical properties of PVA fibers are given in Table 2.

Table 2. Physical properties of PVA fibers

Length (mm)	Diameter (µm)	Density (g/cm^3)	Tensile strength (MPa)	Elongation (%)	Length/Diameter
6	40	1.3	1560	6.5	150

In the geopolymer mixtures designed in the study, metakaolin, quartz with 0-0.5 mm and 1-3 mm diameters, GBFS and quartz powder were prepared in variable amounts by keeping the amounts of NaOH and Na_2SiO_3 constant (Table 3). In the study, three different mixtures with varying weight/volume ratios of the materials were made. In these mixtures, nine different mixtures were designed by dividing them into 3 groups as fiber-free 0.3% and 0.6% PVA fiber content. Concrete samples were kept at 80 degrees for 10 hours in a caring environment.

Table 3. Geopolymer concrete mixing proportions (kg/m^3)

<table>
<tr><th colspan="2">Mixing</th><th>GBFS</th><th>Quartz powder</th><th>MK</th><th>0-0.5 mm quartz</th><th>1-3 mm quartz</th><th>NaOH</th><th>NaNa_2SiO_3</th><th>PVA</th></tr>
<tr><td rowspan="3">M1</td><td>0M1</td><td rowspan="3">700</td><td rowspan="3">50</td><td rowspan="9">100</td><td rowspan="9">500</td><td rowspan="9">450</td><td rowspan="9">140</td><td rowspan="9">350</td><td>-</td></tr>
<tr><td>3M1</td><td>0.30</td></tr>
<tr><td>6M1</td><td>0.60</td></tr>
<tr><td rowspan="3">M2</td><td>0M2</td><td rowspan="3">650</td><td rowspan="3">100</td><td>-</td></tr>
<tr><td>3M2</td><td>0.30</td></tr>
<tr><td>6M2</td><td>0.60</td></tr>
<tr><td rowspan="3">M3</td><td>0M3</td><td rowspan="3">600</td><td rowspan="3">150</td><td>-</td></tr>
<tr><td>3M3</td><td>0.30</td></tr>
<tr><td>6M3</td><td>0.60</td></tr>
</table>

In the study, TS EN 12390-2 Standard was taken into consideration to determine the consistency of geopolymer concrete mixtures [41]. The mechanical properties (flexural and compressive strength) of geopolymer concrete samples, which were formed by placing the relevant mixtures in 5x5x5 cm cube and 4x4x16 cm beam metal molds, were determined according to ASTM C 348 [42] and ASTM C349 [43] Standards, respectively. The capillary water permeability of the geopolymer concrete samples formed with different mixtures was calculated according to the EN 1015-18 Standard [44]. Capillary water permeability of fresh geopolymer concrete mixtures was measured in 5x5x5 cm cube samples in the first 24 hours.

3. APPLICATIONS

3.1. Mechanical Properties

Flexural and compression tests were applied to the fiber and non-fiber high strength concrete samples, kept for 10 hours in the 80-degree curing environment indicated in Table 3. Test results showed the highest compressive strength (137.8 MPa) and flexural strength (16.1MPa) in 6M3 mix with 6% fiber content. Figure 1 shows that increasing fiber content increases the mixtures' flexural and compressive strengths. In addition, it has been determined that the use of quartz powder as fine sand in the mixtures increases both the compressive and flexural strengths. It was observed that the lowest compressive and flexural strength was found in the 0M1 mixture, where the quartz powder was the least and the fiber content was absent. The fracture images of the samples with the highest and lowest compressive and flexural strengths are presented in Figure 2. It has been determined that the use of fiber increases the strength of the concrete samples and increases the ductile fracture.

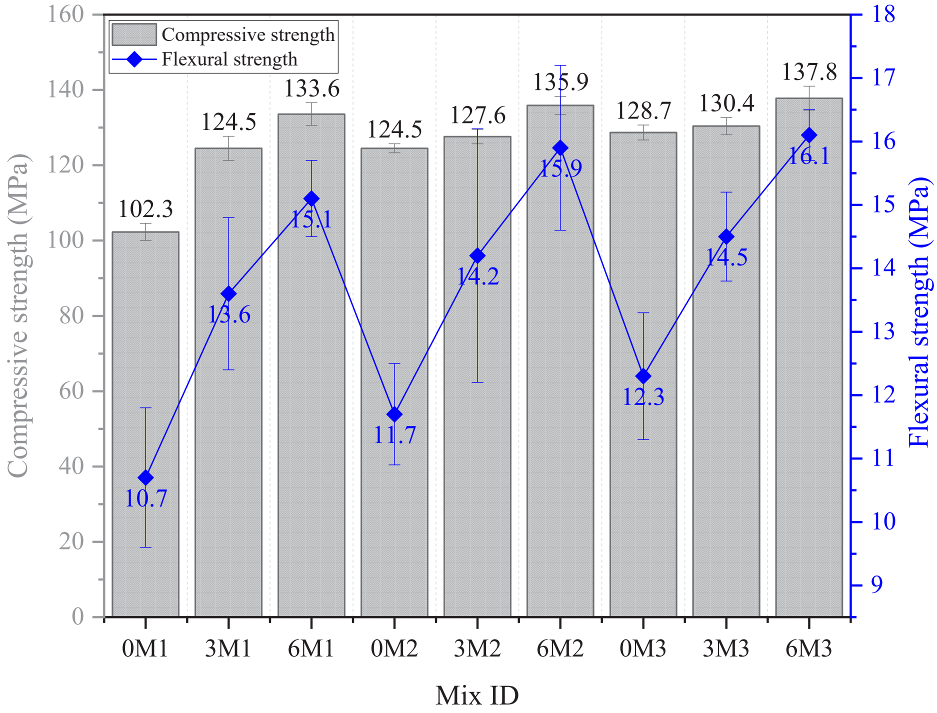

Figure 1. Flexural and compression test results

(a)

(b)

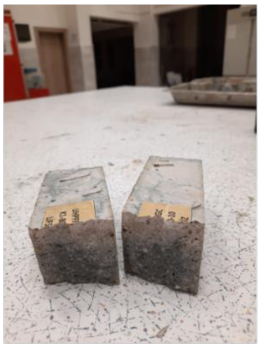

(c)

(d)

Figure 2. Broken samples figures a) cube sample for 0M1 mixture b) cube sample for 6M3 mixture c) prism sample for 0M1 mixture d) prism sample for 6M3 mixture

Figure 3 shows the relationship between flexural and compressive strengths of high concrete strength specimens. It is shown that the flexural strength of the samples increases as the compressive strength increases.

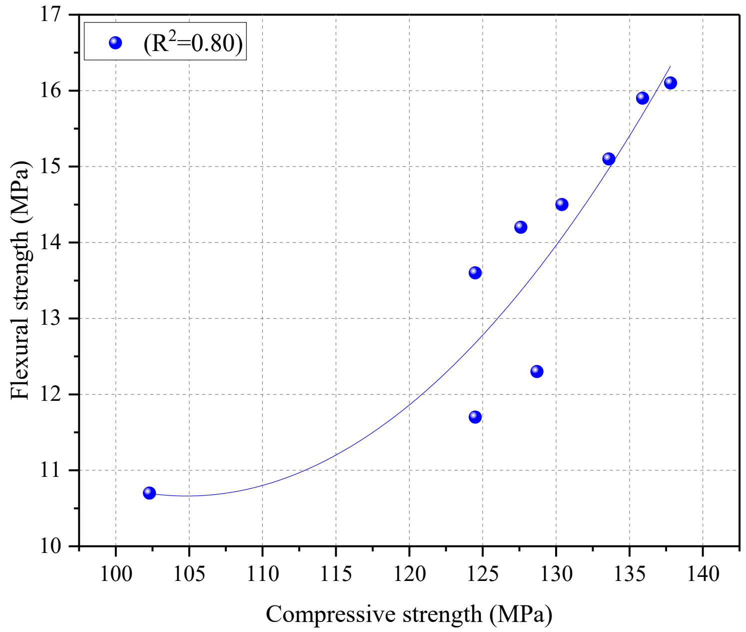

Figure 3. The relationship between flexural and compressive strengths

3.2. Transport Properties

As shown in Figure 4, the capillary water absorption of high-strength fiber concretes varies between 0.37 and 0.78 kg/m^2. The sample with the lowest capillary water absorption was determined to have a 6M3 mixture. It was determined that the capillary water absorption decreased as the amount of fiber in the mixtures increased. According to the test results, it was determined that the capillary water absorption of the M3 mixture decreased by 54.05% and 13.51 percent, respectively, compared to the M1 and M2 mixtures. It was observed that the use of 3% and 6% fiber in the mixture with the lowest quartz dust decreased the capillary water permeability by 21.79% and 26.92%, respectively.

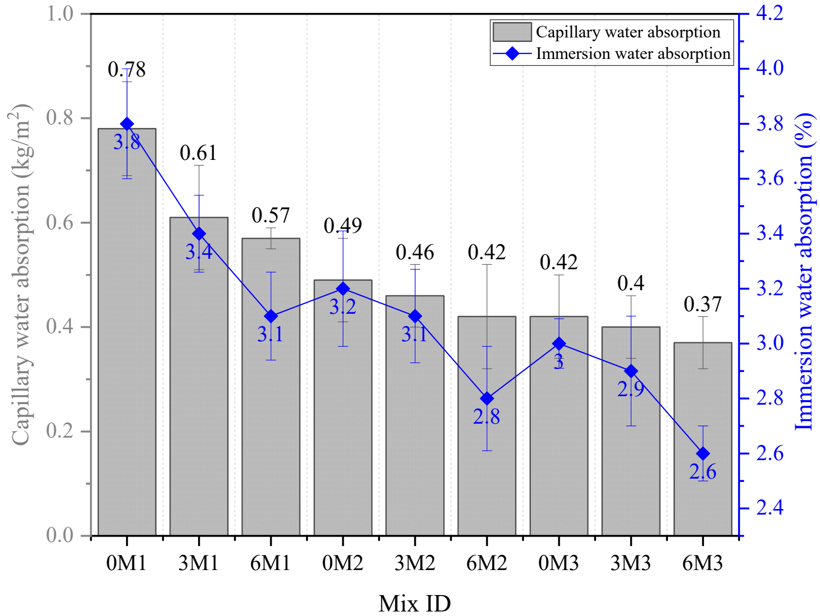

Figure 4. Capillary water absorption of high strength concrete mixtures

4. CONCLUSIONS

In this study, high-strength concrete samples were designed to show high strength without brittle collapse by using metakaolin and ground blast furnace slag as binder material to increase the early wet strength of the concrete and not cause loss of strength due to possible porosity in advanced ages. Concrete samples with different fiber content and binding material properties were subjected to compressive and flexural tests and mechanical properties were determined. In addition, capillary water absorption tests were applied on concrete samples based on the geopolymer concrete logic. The results showed that the flexural and compressive strengths of the samples increased by 18.77% and 63.41%, respectively, without brittle fracture with the increase in the amount of PVAF in the mixtures. In addition, increasing the fiber content showed that the capillary permeability of the concrete samples decreased by 26.92%. At the end of the study, it has been shown that the use of PVAF and geopolymer concrete can be used as a reinforcement element to prevent negative behaviors such as brittle fracture and positive behaviors such as high mechanical properties and less energy consumption to concrete.

REFERENCES

[1] I. Amer, M. Kohail, M.S. El-Feky, A. Rashad, M.A. Khalaf, A review on alkali-activated slag concrete, Ain Shams Eng. J. 12 (2021) 1475–1499. https://doi.org/10.1016/j.asej.2020.12.003.

[2]: G.F. Huseien, H.K. Hamzah, A.R. Mohd Sam, N.H.A. Khalid, K.W. Shah, D.P. Deogrescu, J. Mirza, Alkali-activated mortars blended with glass bottle waste nano powder: Environmental benefit and sustainability, J. Clean. Prod. 243 (2020). https://doi.org/10.1016/j.jclepro.2019.118636.

[3] J.B.M. Dassekpo, W. Feng, Y. Li, L. Miao, Z. Dong, J. Ye, Synthesis and characterization of alkali-activated loess and its application as protective coating, Constr. Build. Mater. 282 (2021). https://doi.org/10.1016/j.conbuildmat.2021.12263

[4] M. Sandanayake, C. Gunasekara, D. Law, G. Zhang, S. Setunge, D. Wanijuru, Sustainable criterion selection framework for green building materials – An optimisation based study of fly-ash Geopolymer concrete, Sustain. Mater. Technol. 25 (2020), https://doi.org/10.1016/j.susmat.2020.e00178.

[5] O. Youssf, M. Elchalakani, R. Hassanli, R. Roychand, Y. Zhuge, R.J. Gravina, J.E. Mills, Mechanical performance and durability of geopolymer lightweight rubber concrete, J. Build. Eng. 45 (2022), https://doi.org/10.1016/j.jobe.2021.103608.

[6] P. Chindaprasirt, B. Sriopas, P. Phosri, P. Yoddumrong, K. Anantakarn, W. Kroehong, Hybrid high calcium fly ash alkali-activated repair material for concrete exposed to sulfate environment, J. Build. Eng. 45 (2022), https://doi.org/10.1016/ j.jobe.2021.103590.

[7] A. Noushini, A. Castel, The effect of heat-curing on transport properties of lowcalcium fly ash-based geopolymer concrete, Constr. Build. Mater. 112 (2016) 464–477, https://doi.org/10.1016/j.conbuildmat.2016.02.210.

[8] M. Sadique, H. Al-Nageim, W. Atherton, L. Seton, N. Dempster, Mechano-chemical activation of high-Ca fly ash by cement free blending and gypsum aided grinding, Constr. Build. Mater. 43 (2013) 480–489. https://doi.org/10.1016/j.conbuildmat.2013.02.050.

[9] I. Amer, M. Kohail, M.S. El-Feky, A. Rashad, M.A. Khalaf, Characterization of alkali-activated hybrid slag/cement concrete, Ain Shams Eng. J. 12 (2021) 135–144. https://doi.org/10.1016/j.asej.2020.08.003.

[10] M. Kurt, T. Kotan, M.S. Gül, R. Gül, A.C. Aydin, The effect of blast furnace slag on the self-compactability of pumice aggregate lightweight concrete, Sadhana 41(2) (2016) 253-264.

[11] Tailby, K.J. MacKenzie, Structure and mechanical properties of aluminosilicate geopolymer composites with Portland cement and its constituent minerals, Cement and Concrete Research 40(5) (2010) 787-794.

[12] Hefni Y, Zaher YAE, Wahab MA. Influence of activation of fly ash on the mechanical properties of concrete. Constr Build Mater 2018;172:728–34. https://doi.org/10.1016/j.conbuildmat.2018.04.021.

[13] Pedro D, de Brito J, Evangelista L. Durability performance of high-performance concrete made with recycled aggregates, fly ash and densified silica fume. Cem Concr Compos 2018;93:63–74. https://doi.org/10.1016/j. cemconcomp.2018.07.002.

[14] Muduli R, Mukharjee BB. Effect of incorporation of metakaolin and recycled coarse aggregate on properties of concrete. J Clean Prod 2019;209:398–414. https://doi.org/10.1016/j.jclepro.2018.10.221.

[15] M.Z.N. Khan, F.U.A. Shaikh, Y. Hao, H. Hao, Effects of curing conditions and sand-to-binder ratios on compressive strength development of fly ash geopolymer, Journal of Materials in Civil Engineering 30(2) (2018) 04017267.

[16] P. Zhang, Z. Gao, J. Wang, K. Wang, Numerical modeling of rebar-matrix bond behaviors of nano-SiO2 and PVA fiber reinforced geopolymer composites, Ceram. Int. 47 (2021) 11727–11737. https://doi.org/10.1016/j.ceramint.2021.01.012.

[17] Sarker, P.K., Haque, R., Ramgolam, K.V., 2013. Fracture behaviour of heat cured fly ash based geopolymer concrete. Mater. Des. 44, 580e586

[18] P. Zhang, Y.N. Zhao, C.H. Liu, P. Wang, T.H. Zhang, Combined effect of nano-SiO2 particles and steel fibers on flexural properties of concrete composite containing fly ash, Sci. Eng. Compos. Mater. 21 (2014) 597–605. https://doi.org/10.1515/secm-2013-0179.

[19] P. Zhang, Q.F. Li, J. Wang, Y. Shi, Y.F. Ling, Effect of PVA fiber on durability of cementitious composite containing nano-SiO2, Nanotechnol. Rev. 8 (2019) 116–127. https://doi.org/10.1515/ntrev-2019-0011.

[20] Gornale, A., Quadri, S.I., Quadri, S.M., Ali, S.M.A., Hussaini, S.A., 2012. Strength aspects of glass fibre reinforced concrete. Int. J. Sci. Eng. Res. 3 (7), 1e5.

[21] X.Y. Zheng, T. Ji, S.M. Easa, B.B. Zhang, Z.L. Jiang, Tensile basic creep behavior of lightweight aggregate concrete reinforced with steel fiber, Constr. Build. Mater. 200 (2019) 356–367, https://doi.org/10.1016/j. conbuildmat.2018.12.138.

[22] A. Lau, M. Anson, Effect of high temperatures on high performance steel fibre reinforced concrete, Cem. Concr. Res. 36 (9) (2006) 1698–1707, https://doi.org/10.1016/j.cemconres.2006.03.024.

[23] Muthukannan, M., Ganesh, A., Mukilan, K., Examination on lightweight banana fibre (bunch) and polyester composite for industrial applications. Int. J. Recent Technol. Eng.. 8 (4S2), 45-48.

[24] L. Wang, T.S. He, Y.X. Zhou, S.W. Tang, J.J. Tan, Z.T. Liu, J.W. Su, The influence of fiber type and length on the cracking resistance, durability and pore structure of face slab concrete, Constr. Build. Mater. 282 (2021) 122706, https://doi.org/ 10.1016/j.conbuildmat.2021.122706.

[25] K.T. Xiao, J.Z. Li, H.Q. Yang, Study of crack resistance property of polyvinyl alcohol fiber reinforced concrete, Adv. Mater. Res. 287–290 (2011) 178–182, https://doi.org/10.4028/www.scientific.net/AMR.287-290.178.

[26] Z.N. Xu, T. Wang, W.L. Wang, Effect of PVA fiber content on creep property of fiber reinforced high-strength concrete columns, AIP Conf. Proc. 1955 (2018), 020026, https://doi.org/10.1063/1.5033598.

[27] A. Noushini, B. Samali, K. Vessalas, Effect of polyvinyl alcohol (PVA) fibre on dynamic and material properties of fibre reinforced concrete, Constr. Build. Mater. 49 (2013) 374–383, https://doi.org/10.1016/j.conbuildmat.2013.08.035.

[28] Ariffin, M.A.M., Bhutta, M.A.R., Hussin, M.W., Mohd Tahir, M., Aziah, N., 2013. Sulfuric acid resistance of blended ash geopolymer concrete. Construct. Build. Mater. 43, 80e86. https://doi.org/10.1016/j.conbuildmat.2013.01.018.

[29] Castel, A., Foster, S.J., Ng, T., Sanjayan, J.G., Gilbert, R.I., 2016. Creep and drying shrinkage of a blended slag and low calcium fly ash geopolymer Concrete. Mater. Struct. 49, 1619e1628.

[30] Duxson, P., Fern andez-Jim enez, A., Provis, J.L., Lukey, G.C., Palomo, A., Van Deventer, J.S.J., 2007. Geopolymer technology: the current state of the art. J. Mater. Sci. 42 (9), 2917e2933

[31] Mehta, A., Siddique, R., 2017. Sulfuric acid resistance of fly ash based geopolymer concrete. Construct. Build. Mater. 146, 136e143. https://doi.org/10.1016/ j.conbuildmat.2017.04.077.

[32] Ganesh, A.C., Rajeswaran, Muthukannan M., Shankar, T.U., Selvam, M., 2018. Comparative study on the behavior of geopolymer concrete using M-sand and conventional concrete exposed to elevated temperature. Int. J. Civ. Eng. Technol. 9 (11), 981e989.

[33] G. Kaplan, A. Öz, B. Bayrak, H.G. Alcan, O. Çelebi, A.C. Aydın, Effect of quartz powder on mid-strength fly ash geopolymers at short curing time and low curing temperature, Construction and Building Materials 329 (2022) 127153.

[34] Aydın A.C, Kaplan G, Öz A, Bayrak B, Alcan H.G, Çelebi O, (2021). The Effect of Curing Temperature on the Early Age Properties of Granulated Furnace Slag Based Reactive Geopolymer Concrete. GEC-2021 First International Geopolymeric Composites Congress

[35] A. Hasnaoui, E. Ghorbel, G. Wardeh, Optimization approach of granulated blast furnace slag and metakaolin based geopolymer mortars, Construction and Building Materials 198 (2019) 10-26.

[36] D. Shen, C. Liu, M. Wang, J. Kang, M. Li, Effect of polyvinyl alcohol fiber on the cracking risk of high strength concrete under uniaxial restrained condition at early age. Construction and Building Materials 300 (2021):

[37] Kim B, Doh J-H, Yi C-K, Lee J-Y. Effects of structural fibers on bonding mechanism changes in interface between GFRP bar and concrete. Compos Part B - Eng 2013;45 (1):768–79.

[38] Ayub T, Shafiq N, Nuruddin MF. Analytical prediction of the mechanical properties of high performance PVA fiber reinforced concrete. Appl Mech Mater 2014;567: 345–50. doi: 10.4028/www.scientific.net/AMM.567.345.

[39] Siddique, R., Kalus, J., 2009, ”Influence of metakaolin on the properties of mortar and concrete: a review”, Applied Clay Science, 43, 392-400.

[40] Khatib, J.M., Hibbert, J.J., 2005, “Selected engineering properties of concrete incorporating slag and metakaolin”, Construction and building materials, 19, 460-472

[41] EN 12390-2, E. (2009). Testing hardened concrete - Part 2: Making and curing specimens for strength tests. *BS En 12390-2:2009*, 1–12.

[42] ASTM C642. (1997). Standard Test Method for Density, Absorption, and Voids in Hardened Concrete, ASTM International, United States. *Annual Book of ASTM Standards*.

[43] ASTM C349. (2002). Standard test method for compressive strength of hydraulic-cement mortars (Using portions of prisms broken in flexure). *ASTM International*.

[44] EN 12350-2, E. (2009). Testing fresh concrete — Part 2: Slump test. *Bs En 12350-2*

AN EIGENVALUE PROBLEM WITH A SPECTRAL PARAMETER IN BOUNDARY CONDITIONS

Ayşe Kabataş [1]

[1] Department of Mathematics, Karadeniz Technical University, Trabzon, Turkey

akabatas@ktu.edu.tr

Abstract

In this paper, we improve asymptotic estimates of eigenfunctions for an eigenvalue problem considered by Kerimov and Mamedov (1999) with the spectral parameter in all boundary conditions when the potential function is continuous, also its differentiation exists and is integrable.

Keywords: Eigenvalue problem; Eigenfunctions; Asymptotics.

1.INTRODUCTION

Consider the eigenvalue problem

$$y'' + [\lambda + q(t)]y(t) = 0\,, 0 < t < 1, \tag{1}$$

$$[\alpha_0 + \alpha_1\lambda^{1/2} + \alpha_2\lambda]y(0) + y'(0) = 0, \tag{2}$$

$$[\beta_0 + \beta_1\lambda^{1/2} + \beta_2\lambda]y(0) + y'(0) = 0 \tag{3}$$

where λ is a real parameter; $q(t)$ is a real-valued function; $\alpha_i, \beta_i \in \mathbb{R}, i = 0,1,2$. Also, the following conditions will be imposed on the last constants [6]:

$$\alpha_0 < 0, \alpha_2 > 0, \beta_0 > 0, \beta_2 < 0, |\alpha_1| + |\alpha_2| \neq 0.$$

Our purpose is to investigate the asymptotic approximations of eigenfunctions of (1)-(3), when the potential function $q(t)$ is continuous, its differentiation exists and is integrable. The difference between (1)-(3) and Sturm-Liouville eigenvalue problem studied extensively in the literature is that the eigenvalue parameter λ appears in both boundary conditions.

We suppose without loss of generality that $q(t)$ has a mean value zero, i.e., $\int_0^1 q(t)dt = 0$.

2.GENERAL PROPERTIES OF METHOD

Let $y(t,\lambda)$ denote a solution of the equation (1) which is complex-valued in the sense that neither the real nor the imaginary part is identically zero. If $v(t,\lambda)=\frac{y\prime(t,\lambda)}{y(t,\lambda)}$ transform is applied to (1), we have the Riccati equation

$$v'=-\lambda+q-v^2. \tag{4}$$

We set

$$S(t,\lambda):=\mathrm{Re}\{v(t,\lambda)\}, T(t,\lambda):=\mathrm{Im}\{v(t,\lambda)\}$$

where $v(t,\lambda)$ is a complex-valued solution of (4).

It was shown in [2] that any nontrivial real-valued solution, z, of (1) can be expressed as

$$z(t,\lambda)=c_1\exp\left(\int_0^t S(x,\lambda)dx\right)\cos\left\{c_2+\int_0^t T(x,\lambda)dx\right\}, \tag{5}$$

with

$$z'(t,\lambda)=c_1 S(t,\lambda)\exp\left(\int_0^t S(x,\lambda)dx\right)\cos\left\{c_2+\int_0^t T(x,\lambda)dx\right\}$$

$$-c_1 T(t,\lambda)\exp\left(\int_0^t S(x,\lambda)dx\right)\sin\left\{c_2+\int_0^t T(x,\lambda)dx\right\}. \tag{6}$$

We seek approximate solution of (4) of the form

$$v(t,\lambda)=i\lambda^{1/2}+\sum_{n=1}^{\infty}v_n(t,\lambda) \tag{7}$$

where $\lim_{t\to\infty} v_n(t,\lambda)=0$ for $n=1,2,\ldots$ [2]. This implies that

$$S(t,\lambda)=\mathrm{Re}\sum_{n=1}^{\infty}v_n(t,\lambda),$$

$$T(t,\lambda)=\lambda^{1/2}+\mathrm{Im}\sum_{n=1}^{\infty}v_n(t,\lambda).$$

Substitution of (7) into (4) and rearrangement yield

$$v_1{}' + 2i\lambda^{1/2}v_1 + v_2{}' + 2i\lambda^{1/2}v_2 + \sum_{n=3}^{\infty}\left(v_n{}' + 2i\lambda^{1/2}v_n\right) =$$

$$= q - v_1^2 - \sum_{n=3}^{\infty}\left(v_{n-1}^2 + 2v_{n-1}\sum_{m=1}^{n-2} v_m\right).$$

If it is chosen as

$$v_1{}' + 2i\lambda^{1/2}v_1 = q,$$

$$v_2{}' + 2i\lambda^{1/2}v_2 = -v_1^2,$$

$$v_n{}' + 2i\lambda^{1/2}v_n = -\left(v_{n-1}^2 + 2v_{n-1}\sum_{m=1}^{n-2} v_m\right), \quad n \geq 3$$

then,

$$v_1(t,\lambda) = -e^{-2i\lambda^{1/2}t}\int_t^1 e^{2i\lambda^{1/2}x}q(x)dx,$$

$$v_2(t,\lambda) = e^{-2i\lambda^{1/2}t}\int_t^1 e^{2i\lambda^{1/2}x}v_1^2(x,\lambda)dx,$$

$$v_n(t,\lambda) = e^{-2i\lambda^{1/2}t}\int_t^1 e^{2i\lambda^{1/2}x}\left(v_{n-1}^2 + 2v_{n-1}\sum_{m=1}^{n-2} v_m\right)dx, \quad n \geq 3.$$

We suppose that there exist functions $A(t)$ and $\eta(\lambda)$ so that

$$\left|\int_t^1 e^{2i\lambda^{1/2}x}q'(x)dx\right| \leq A(t)\eta(\lambda)$$

where $A(t) := \int_t^1 |q'(x)|dx$ which is a decreasing function of t, $\lambda^{-1/2}\eta(\lambda) \to 0$ as $\lambda \to \infty$ and $A(t) \in L[0,1]$. For $q'(t) \in L[0,1]$ the existence of $A(t)$ and $\eta(\lambda)$ functions may be established for λ positive as follows. We note that, avoiding the trivial case $\int_t^1 |q'(x)|dx = 0$, so $\left|\int_t^1 e^{2i\lambda^{1/2}x}q'(x)dx\right| \leq \int_t^1 |q'(x)|dx < \infty$. If we define

$$F(t,\lambda):=\begin{cases}\left|\int_t^1 e^{2i\lambda^{1/2}x}q'(x)dx\right| / \int_t^1 |q'(x)|dx, \text{ if } \int_t^1 |q'(x)|dx \neq 0\\ 0, \qquad\qquad\qquad\qquad\qquad\qquad \text{if } \int_t^1 |q'(x)|dx = 0\end{cases} \tag{8}$$

then $0 \leq F(t,\lambda) \leq 1$ and we set $\eta(\lambda):=\sup_{0\leq t\leq 1}F(t,\lambda)$. $\eta(\lambda)$ is well-defined by (8) and $\lambda^{-1/2}\eta(\lambda) \to 0$ as $\lambda \to \infty$ [4].

As a result of these, the asymptotic forms of $S(t,\lambda)$ and $T(t,\lambda)$ are obtained in [4] as follows

$$S(t,\lambda) = -\frac{1}{2}\lambda^{-1/2}q(1)\sin 2\lambda^{1/2}(1-t) + \frac{1}{2}\lambda^{-1/2}\cos(2\lambda^{1/2}t+\xi_t)$$

$$+O(\lambda^{-1}\eta^2(\lambda)), \tag{9}$$

$$T(t,\lambda) = \lambda^{1/2} + \frac{1}{2}\lambda^{-1/2}q(1)\cos 2\lambda^{1/2}(1-t) - \frac{1}{2}\lambda^{-1/2}q(t) - \frac{1}{2}\lambda^{-1/2}\sin(2\lambda^{1/2}t+\xi_t)$$

$$+O(\lambda^{-1}\eta^2(\lambda)) \tag{10}$$

where

$$\sin\xi_t := \int_t^1 q'(x)\cos 2\lambda^{1/2}x dx, \cos\xi_t := \int_t^1 q'(x)\sin 2\lambda^{1/2}x dx. \tag{11}$$

Also,

$$\int_0^t S(x,\lambda)dx = \frac{1}{4}\lambda^{-1}\begin{Bmatrix} q(1)\left[\cos 2\lambda^{1/2} - \cos 2\lambda^{1/2}(1-t)\right] \\ +q(t) - q(0) + \sin(2\lambda^{1/2}t+\xi_t) - \sin\xi_0 \end{Bmatrix}$$

$$+O\left(\lambda^{-3/2}\eta^2(\lambda)\right), \tag{12}$$

$$\int_0^t T(x,\lambda)dx = \lambda^{1/2}t - \frac{1}{2}\lambda^{-1/2}\left[tq(t) - \int_0^t xq'(x)dx\right]$$

$$+\frac{1}{4}\lambda^{-1}\begin{Bmatrix}\sin 2\lambda^{1/2} - \sin 2\lambda^{1/2}(1-t) \\ +\cos(2\lambda^{1/2}t+\xi_t) - \cos\xi_0\end{Bmatrix} + O(\lambda^{-3/2}\eta^2(\lambda). \tag{13}$$

The last two equalities are obtained in [1].

3.EIGENFUNCTIONS

In this section, asymptotic approximations are obtained for the solutions of the eigenvalue problem (1)-(3). We define two solutions, $\psi(t,\lambda)$ and $\phi(t,\lambda)$ of (1)-(3) with the initial conditions

$$\psi(0,\lambda)=1,\psi'(0,\lambda)=-\alpha_0-\alpha_1\lambda^{1/2}-\alpha_2\lambda \tag{14}$$

and

$$\phi(1,\lambda)=1,\phi'(1,\lambda)=-\beta_0-\beta_1\lambda^{1/2}-\beta_2\lambda. \tag{15}$$

Theorem 3.1. Let $\psi(t,\lambda)$ and $\phi(t,\lambda)$ be the solutions of (1) satisfying (14) and (15), respectively. Then

(i)

$$\psi(t,\lambda)=\frac{1}{\cos\left\{\cot^{-1}\left[\frac{T(0,\lambda)}{\alpha_0+\alpha_1\lambda^{1/2}+\alpha_2\lambda+S(0,\lambda)}\right]\right\}}\exp\left(\int_0^t S(x,\lambda)dx\right)$$

$$\times\cos\left\{\cot^{-1}\left[\frac{T(0,\lambda)}{\alpha_0+\alpha_1\lambda^{1/2}+\alpha_2\lambda+S(0,\lambda)}\right]+\int_0^t T(x,\lambda)dx\right\}, \tag{16}$$

(ii)

$$\phi(t,\lambda)=\frac{1}{\cos\left\{\cot^{-1}\left[\frac{T(1,\lambda)}{\beta_0+\beta_1\lambda^{1/2}+\beta_2\lambda+S(1,\lambda)}\right]\right\}}\exp\left(-\int_t^1 S(x,\lambda)dx\right)$$

$$\times\cos\left\{\cot^{-1}\left[\frac{T(1,\lambda)}{\beta_0+\beta_1\lambda^{1/2}+\beta_2\lambda+S(1,\lambda)}\right]-\int_t^1 T(x,\lambda)dx\right\}. \tag{17}$$

Proof. Here the proof of (16) will be given. The proof of (17) is similar to that.

From (5), (6) and (14) it is obtained that

$$\psi(0,\lambda)=c_1\cos(c_2)=1, \tag{18}$$

$$\psi'(0,\lambda)=c_1S(0,\lambda)\cos(c_2)-c_1T(0,\lambda)\sin(c_2)=-\alpha_0-\alpha_1\lambda^{1/2}-\alpha_2\lambda. \tag{19}$$

From (18)

$$c_1 = \frac{1}{\cos(c_2)}. \tag{20}$$

Using this in (19), we have

$$c_2 = \cot^{-1}\left[\frac{T(0,\lambda)}{\alpha_0 + \alpha_1\lambda^{1/2} + \alpha_2\lambda + S(0,\lambda)}\right]. \tag{21}$$

Substituting the values of c_1 and c_2 into (5) proves the theorem.

Theorem 3.2. For the solutions of (1) with the initial conditions (14) and (15) respectively, we have, as $\lambda \to \infty$

(i)

$$\psi(t,\lambda) = -\alpha_2\lambda^{1/2}\sin(\lambda^{1/2}t) - \alpha_1\sin(\lambda^{1/2}t) + \left(1 + \frac{\alpha_2}{2}\int_0^t q(x)dx\right)$$

$$\times \cos(\lambda^{1/2}t) + O(\eta(\lambda)), \tag{22}$$

(ii)

$$\phi(t,\lambda) = \beta_2\lambda^{1/2}\sin\lambda^{1/2}(1-t) + \beta_1\sin\lambda^{1/2}(1-t) + \left(1 - \frac{\beta_2}{2}\int_t^1 q(x)dx\right)$$

$$\times \cos\lambda^{1/2}(1-t) + O(\eta(\lambda)). \tag{23}$$

Proof.

(i) The terms in (16) are evaluated as $\lambda \to \infty$. Firstly, using the values of $S(t,\lambda)$ and $T(t,\lambda)$ given by (9) and (10) together with the series expansion we find

$$\frac{T(0,\lambda)}{\alpha_0 + \alpha_1\lambda^{1/2} + \alpha_2\lambda + S(0,\lambda)} = \frac{\lambda^{1/2} + \frac{1}{2}\lambda^{-1/2}\left[q(1)\cos 2\lambda^{1/2} - q(0) - \sin\xi_0\right] + O(\lambda^{-1}\eta^2(\lambda))}{a_2\lambda\left[\begin{matrix} 1 + \frac{\alpha_1}{\alpha_2}\lambda^{-1/2} + \frac{\alpha_0}{\alpha_2}\lambda^{-1} \\ -\frac{1}{2\alpha_2}\lambda^{-3/2}q(1)\sin 2\lambda^{1/2} + O(\lambda^{-3/2}\eta(\lambda))\end{matrix}\right]}$$

$$= \left\{\frac{1}{\alpha_2}\lambda^{-1/2} + \frac{1}{2\alpha_2}\lambda^{-3/2}\left[q(1)\cos 2\lambda^{1/2} - q(0) - \sin\xi_0\right] + O(\lambda^{-2}\eta^2(\lambda))\right\}$$

$$\times \left\{1 - \frac{\alpha_1}{\alpha_2}\lambda^{-1/2} - \frac{\alpha_0}{\alpha_2}\lambda^{-1} + \frac{1}{2\alpha_2}\lambda^{-3/2}q(1)\sin 2\lambda^{1/2} + O(\lambda^{-3/2}\eta(\lambda))\right\}$$

$$= \frac{1}{\alpha_2}\lambda^{-1/2} - \frac{\alpha_1}{(\alpha_2)^2}\lambda^{-1} + \frac{1}{2\alpha_2}\lambda^{-3/2}\left[q(1)\cos 2\lambda^{1/2} - q(0) - \frac{2\alpha_0}{\alpha_2}\right] + O(\lambda^{-3/2}\eta(\lambda)).$$

By using the last equality it is obtained that

$$\cot^{-1}\left[\frac{T(0,\lambda)}{\alpha_0+\alpha_1\lambda^{1/2}+\alpha_2\lambda+S(0,\lambda)}\right]$$
$$=\frac{\pi}{2}-\frac{1}{\alpha_2}\lambda^{-1/2}+\frac{\alpha_1}{(\alpha_2)^2}\lambda^{-1}-\frac{1}{2\alpha_2}\lambda^{-3/2}\left[q(1)\cos 2\lambda^{1/2}-q(0)-\frac{2\alpha_0}{\alpha_2}\right]$$
$$+O(\lambda^{-3/2}\eta(\lambda))$$

and from that

$$\cos\left\{\cot^{-1}\left[\frac{T(0,\lambda)}{\alpha_0+\alpha_1\lambda^{1/2}+\alpha_2\lambda+S(0,\lambda)}\right]\right\}=\sin\{\frac{1}{\alpha_2}\lambda^{-1/2}-\frac{\alpha_1}{(\alpha_2)^2}\lambda^{-1}+\frac{1}{2\alpha_2}\lambda^{-3/2}$$
$$\times\left[q(1)\cos 2\lambda^{1/2}-q(0)-\frac{2\alpha_0}{\alpha_2}\right]+O(\lambda^{-3/2}\eta(\lambda))\}$$
$$=\frac{1}{\alpha_2}\lambda^{-1/2}-\frac{\alpha_1}{(\alpha_2)^2}\lambda^{-1}+\frac{1}{2\alpha_2}\lambda^{-3/2}\left[q(1)\cos 2\lambda^{1/2}-q(0)-\frac{2\alpha_0}{\alpha_2}\right]$$
$$+O(\lambda^{-3/2}\eta(\lambda)), \tag{24}$$

$$\sin\left\{\cot^{-1}\left[\frac{T(0,\lambda)}{\alpha_0+\alpha_1\lambda^{\frac{1}{2}}+\alpha_2\lambda+S(0,\lambda)}\right]\right\}=\cos\{\frac{1}{\alpha_2}\lambda^{-1/2}-\frac{\alpha_1}{(\alpha_2)^2}\lambda^{-1}+\frac{1}{2\alpha_2}\lambda^{-3/2}$$
$$\times\left[q(1)\cos 2\lambda^{1/2}-q(0)-\frac{2\alpha_0}{\alpha_2}\right]+O(\lambda^{-3/2}\eta(\lambda))\}$$
$$=1-\frac{1}{2(\alpha_2)^2}\lambda^{-1}+\frac{\alpha_1}{(\alpha_2)^3}\lambda^{-3/2}-\frac{1}{2(\alpha_2)^2}\lambda^{-2}$$
$$\times\left[q(1)\cos 2\lambda^{1/2}-q(0)-\frac{2\alpha_0}{\alpha_2}+\left(\frac{\alpha_1}{\alpha_2}\right)^2\right]+O(\lambda^{-2}\eta(\lambda)), \tag{25}$$

$$\frac{1}{\cos\left\{\cot^{-1}\left[\frac{T(0,\lambda)}{\alpha_0+\alpha_1\lambda^{1/2}+\alpha_2\lambda+S(0,\lambda)}\right]\right\}}=\alpha_2\lambda^{1/2}+\alpha_1-\frac{\alpha_2}{2}\lambda^{-1/2}\left[q(1)\cos 2\lambda^{1/2}-q(0)-\frac{2\alpha_0}{\alpha_2}\right]$$
$$+O(\lambda^{-1/2}\eta(\lambda)). \tag{26}$$

Using $\int_0^t S(x,\lambda)dx$ given by (12) we get

$$\exp\left(\int_0^t S(x,\lambda)dx\right)=1+\frac{1}{4}\lambda^{-1}\left\{\begin{matrix}q(1)\left[\cos 2\lambda^{1/2}-\cos 2\lambda^{1/2}(1-t)\right]\\+q(t)-q(0)+\sin(2\lambda^{1/2}t+\xi_t)-\sin\xi_0\end{matrix}\right\}$$

$$+O\left(\lambda^{-3/2}\eta^2(\lambda)\right) \tag{27}$$

and also, using $\int_0^t T(x,\lambda)dx$ given by (13)

$$\sin\left(\int_0^t T(x,\lambda)dx\right) = \sin\sigma + O(\lambda^{-1}\eta(\lambda)), \tag{28}$$

$$\cos\left(\int_0^t T(x,\lambda)dx\right) = \cos\sigma + O(\lambda^{-1}\eta(\lambda)) \tag{29}$$

where

$$\sigma := \lambda^{1/2}t - \frac{1}{2}\lambda^{-1/2}[tq(t) - \int_0^t xq'(x)dx] + \frac{1}{4}\lambda^{-1}q(1)[\sin 2\lambda^{1/2}$$

$$-\sin 2\lambda^{1/2}(1-t)].$$

Hence, from (24), (25), (28) and (29)

$$\cos\left\{\cot^{-1}\left[\frac{T(0,\lambda)}{\alpha_0 + \alpha_1\lambda^{1/2} + \alpha_2\lambda + S(0,\lambda)}\right] + \int_0^t T(x,\lambda)dx\right\} = -\sin\sigma + \frac{1}{\alpha_2}\lambda^{-1/2}\cos\sigma$$

$$-\frac{\alpha_1}{(\alpha_2)^2}\lambda^{-1}\cos\sigma - \frac{1}{2(\alpha_2)^2}\lambda^{-1}\sin\sigma + O(\lambda^{-1}\eta(\lambda)). \tag{30}$$

Substituting (26), (27) and (30) into (16) and using trigonometric expansions we complete the prove. For (ii), the proof is similar.

REFERENCES

1. Ayşe Kabataş, Asymptotic Solutions of Eigenfunctions and Green's Functions for Regular Sturm-Liouville Problems Having Eigenvalue Parameter in the Boundary Condition, PhD. Thesis, Karadeniz Technical University, The Graduate School of Natural and Applied Sciences Biology Graduate Program, Trabzon, 2015.
2. B. J. Harris, The Form of the Spectral Functions Associated with Sturm-Liouville Problems with Continuous Spectrum, Mathematika, Vol:44, 149-161, 1997.
3. Charles T. Fulton, Two-Point Boundary Value Problems with Eigenvalue Parameter Contained in the Boundary Conditions, Proceedings of the Royal Society of Edinburgh Section A: Mathematics, Vol:77, Issue:3-4, 293-308, 1977.

4. Elif Başkaya, Asymptotic of Eigenvalues for Sturm-Liouville Problem with Eigenparameter-Dependent Boundary Conditions, New Trends in Mathematical Sciences, Vol:6, No:2, 247-257, 2018.
5. Haskız Coşkun, Ayşe Kabataş, Asymptotic Approximations of Eigenfunctions for Regular Sturm-Liouville Problems with Eigenvalue Parameter in the Boundary Condition for Integrable Potential, Mathematica Scandinavica, Vol:113, No:1, 143-160, 2013.
6. N. B. Kerimov, Kh. R. Mamedov, On One Boundary Value Problem with A Spectral Parameter in the Boundary Conditions, Vol:40, No:2, 281-290, 1999.

A NEW CONSTRUCTION METHOD FOR TRIANGULAR NORMS AND TRIANGULAR CONORMS ON BOUNDED LATTICES

Gül Deniz Çaylı

Department of Mathematics, Faculty of Science, Karadeniz Technical University, 61080 Trabzon, Turkey

guldeniz.cayli@ktu.edu.tr

Abstract

In this paper, we demonstrate that it is possible to describe a construction method for triangular norms and triangular conorms on a bounded lattice L derived from triangular subnorms and triangular superconorms defined on the subinterval of L, respectively.

Keywords: T-norm; T-conorm; T-subnorm; T-superconorm.

1. INTRODUCTION

Menger [17] introduced triangular norms as an important generalization of the triangle inequality. Schweizer and Sklar [21] presented the modern definition of triangular norms on the unit interval. Triangular norms were then studied from several perspectives [1, 3, 9, 15]. These operators have also been demonstrated to be useful, as particular aggregation operators, in a variety of areas, such as fuzzy system modeling, fuzzy logic, neural networks, expert systems, and aggregation [8, 10, 13, 22]. Besides its practical usage, researchers prefer the unit interval because it allows them to investigate a number of important mathematical aspects. Due to the lack of some efficient features provided on the unit interval and the availability of some incomparable elements on bounded lattices, working on bounded lattices is more comprehensive than working on the unit interval. On the other hand, it is a more charming field of inquiry. In the literature, bounded lattices have also been the topic of some construction methods. In particular, Saminger [19] has discussed ordinal sums of t-norms acting on a bounded lattice, which is not necessarily an ordinal sum of lattices or a chain. Medina [16] has described some necessary and sufficient conditions for finding whether an ordinal sum of arbitrary triangular norms is a triangular norm on a bounded lattice. Ertuğrul et al. [12] have introduced a modified ordinal sum of triangular norms, being triangular norms on any bounded lattice. Çaylı [4] has proposed a new ordinal sum construction for getting triangular norms on an arbitrary bounded lattice. In the studies [5, 6, 7, 11, 20, 23], various construction methods for triangular norms on bounded lattices can be found.

The main aim of this study is to introduce a new construction method for triangular norms on a bounded lattice by use of triangular subnorms defined on the subinterval of the lattice. According to our best knowledge, no way develops a triangular subnorm on a subinterval of a lattice to a triangular norm on the bounded lattice. Our construction partially compensates for this gap in the literature. The following is the structure of the paper: In Section 2, we provide some additional details dealing with bounded lattices and triangular norms (triangular subnorms) on them. In Section 3, we present a method for developing the triangular subnorm on the subinterval of L to the bounded lattice L. Moreover, we give corresponding examples to demonstrate that our method is different from the proposed ways in [4, 5, 6, 12]. Finally, some concluding remarks are added.

2. PRELIMINARIES

In this section, we recall some basic concepts and notations for bounded lattices and some properties related to them, which will be used in the sequel.

A lattice [2] is a nonempty set L equipped with a partial order $\leq$ such that any two elements x and y have a greatest lower bound (called meet or infimum), denoted by $x \wedge y$, as well as a smallest upper bound (called join or supremum), denoted by $x \vee y$. For $a, b \in L$, the symbol $a < b$ means that $a \leq b$ and $a \neq b$. The elements a and b in L are comparable if $a \leq b$ or $b \leq a$. Otherwise, a and b are incomparable, in this case we use the notation $a \parallel b$. For the fixed element a in L, the set of all $x \in L$ with $x \parallel a$ is denoted by I_a; i.e., $I_a = \{x \in L : x \| a\}$. The transpose of a partial order $\leq$ of a lattice L, denoted by $\leq^d$; i.e., $x \leq^d y$ iff $y \leq x$, is also a partial order on L and the meet and the join with respect to $\leq^d$ are $\vee$ and $\wedge$, respectively. Namely, $(L, \leq^d, \vee, \wedge)$ is also a lattice, which is called the dual lattice to $(L, \leq, \wedge, \vee)$.

A lattice $(L, \leq, \wedge, \vee)$ is bounded if it has top and bottom elements, which are written as 1 and 0, respectively; that is, two elements $1, 0 \in L$ exist such that $0 \leq x \leq 1$ for all $x \in L$. Throughout this article, unless stated otherwise, L denotes a bounded lattice $(L, \leq, \wedge, \vee)$ with the top element 1 and the bottom element 0.

Let $(L, \leq, \wedge, \vee)$ be a lattice, $a, b \in L$ and $a \leq b$. The subinterval $[a, b]$ is defined as $[a, b] = \{x \in L : a \leq x \leq b\}$. Other subintervals such as $[a, b[$, $]a, b]$, and $]a, b[$ can be defined similarly. Obviously, $([a, b], \leq, \wedge, \vee)$ is a bounded lattice with the top element b and the bottom element a. The subinterval $[a, b]$ of $(L, \leq^d, \vee, \wedge)$ is exactly the subinterval $[b, a]$ of $(L, \leq, \wedge, \vee)$.

Definition 1 ([16, 19]). Let $[a, b]$ be a subinterval of L. A binary operation $T: [a, b]^2 \to [a, b]$ is called a triangular norm (or, shortly, t-norm) on $[a, b]$ if, for any $x, y, z \in [a, b]$, the following conditions are fulfilled:

(i) $T(x, y) = T(y, x)$ (commutativity);
(ii) If $x \leq y$, then $T(x, z) \leq T(y, z)$ (increasingness);
(iii) $T(x, T(y, z)) = T(T(x, y), z)$ (associativity);
(iv) $T(x, b) = x$ (neutrality).

Definition 2 ([16, 19]). Let $[a, b]$ be a subinterval of L. A binary operation $S: [a, b]^2 \to [a, b]$ is called a triangular conorm (or, shortly, t-conorm) on $[a, b]$ if it is commutative, associative, increasing and a is its neutral element; i.e., $S(x, a) = x$ for all $x \in [a, b]$.

T-norms and t-conorms are dual in the sense that S is a t-conorm on the subinterval $[a,b]$ of $(L,\leq,\wedge,\vee)$ if and only if it is a t-norm on the subinterval $[b,a]$ of $(L,\leq^d,\vee,\wedge)$.

Example 1. (i) The largest t-norm on $[a,b]$ is $T_\wedge$, defined by $T_\wedge(x,y)=x\wedge y$ for all $x,y\in[a,b]$, while the smallest t-norm on $[a,b]$ is T_D, which takes the value $x\wedge y$ if $b\in\{x,y\}$ and a otherwise. Hence, for any t-norm T on $[a,b]$, we have $T_D\leq T\leq T_\wedge$.

(ii) The smallest t-conorm on $[a,b]$ is $S_\vee$, defined by $S_\vee(x,y)=x\vee y$ for all $x,y\in[a,b]$, while the largest t-conorm on $[a,b]$ is S_D, which takes the value $x\vee y$ if $a\in\{x,y\}$ and b otherwise. Hence, for any t-conorm S on $[a,b]$, we have $S_\vee\leq S\leq S_D$.

Definition 3 ([14, 18]). Let $[a,b]$ be a subinterval of L. A binary operation $F:[a,b]^2\to[a,b]$ is called a triangular subnorm (or, shortly, t-subnorm) on $[a,b]$ if it is commutative, associative, increasing and satisfies $F(x,y)\leq x\wedge y$ for all $x,y\in[a,b]$.

Definition 4 ([14, 18]). Let $[a,b]$ be a subinterval of L. A binary operation $P:[a,b]^2\to[a,b]$ is called a triangular superconorm (or, shortly, t-superconorm) on $[a,b]$ if it is commutative, associative, increasing and satisfies $P(x,y)\geq x\vee y$ for all $x,y\in[a,b]$.

3. CONSTRUCTION METHODS FOR T-NORMS AND T-CONORMS

Saminger [19] introduced a method for constructing t-norms (and by duality, t-conorms) on a bounded lattice L. The additional conditions for ensuring that the method yields a t-norm on a bounded lattice L were investigated. Saminger's method can be summarized by the following theorems.

Theorem 1 ([19]). Let $a\in L\backslash\{0,1\}$ and $V:[a,1]^2\to[a,1]$ be a t-norm. Then the binary operation $T^{(1)}:L^2\to L$ given by the formula (1) is an ordinal sum of V.

$$T^{(1)}(x,y)=\begin{cases}V(x,y) & \text{if } (x,y)\in[a,1]^2\\ x\wedge y & \text{otherwise.}\end{cases}\qquad(1)$$

Theorem 2 ([19]). Let $a\in L\backslash\{0,1\}$ and $W:[0,a]^2\to[0,a]$ be a t-conorm. Then the binary operation $S^{(1)}:L^2\to L$ given by the formula (2) is an ordinal sum of W.

$$S^{(1)}(x,y)=\begin{cases}W(x,y) & \text{if } (x,y)\in[0,a]^2\\ x\vee y & \text{otherwise.}\end{cases}\qquad(2)$$

Obviously, the formulas (1) in Theorem 1 and (2) in Theorem 2 do not need to produce a t-norm and a t-conorm on an arbitrary bounded lattice L, respectively. Because they generally violate both the associativity property and the increasingness property (see Example 2). The following propositions present the additional conditions for the bounded lattice on which the ordinal sums defined by the formulas (1) in Theorem 1 and (2) in Theorem 2 yield a t-norm and a t-conorm on L, respectively.

Proposition 1 ([19]). Let $a\in L\backslash\{0,1\}$ and $V:[a,1]^2\to[a,1]$ be a t-norm. Then the following are equivalent:

(i) The ordinal sum $T^{(1)}: L^2 \to L$ given by the formula (1) in Theorem 1 is a t-norm for V.

(ii) For all $t \in L$, it holds that if t is incomparable to a, then it is incomparable with all elements of the subinterval $[a, 1[$ of L.

Proposition 2 ([19]). Let $a \in L \backslash \{0,1\}$ and $W: [0, a]^2 \to [0, a]$ be a t-conorm. Then the following are equivalent:

(i) The ordinal sum $S^{(1)}: L^2 \to L$ given by the formula (2) in Theorem 2 is a t-conorm for W.

(ii) For all $t \in L$, it holds that if t is incomparable to a, then it is incomparable with all elements of the subinterval $]0, a]$ of L.

It follows from Example 2 that the formula (1) does not need to procure a t-norm on a bounded lattice L. We can demonstrate, by duality, that the formula (2) does not always build a t-conorm on a bounded lattice L. In order to address these flaws, the authors [4-7, 11,12, 16, 20] described some modified versions of ordinal sums on bounded lattices of arbitrary t-norms (t-conorms) being, in fact, a t-norm (t-conorm). In the following, we provide two construction methods for t-norms and t-conorms on bounded lattices. In particular, we are interested in the problem: of whether any method for obtaining t-norms on a bounded lattice L, based on t-subnorms defined on the subintervals of L, constructs. Then, to show that it is possible, a construction method for t-norms on a bounded lattice L derived from a t-subnorm F defined on the subinterval $[a, 1]$ of L is introduced (see Theorem 3). In addition, using the t-superconorm P defined on the subinterval $[0, a]$ of L, a method for getting t-conorms on a bounded lattice L is provided (see Theorem 4).

Theorem 3. Let $a \in L \backslash \{0,1\}$. If $F: [a, 1]^2 \to [a, 1]$ is a t-subnorm, then the binary operation $T^{(2)}: L^2 \to L$ given by the formula (3) is a t-norm.

$$T^{(2)}(x, y) = \begin{cases} F(x, y) & \text{if } (x, y) \in [a, 1[^2 \\ x \wedge y \wedge a & \text{otherwise.} \end{cases} \tag{3}$$

Proof. It follows from the definition of $T^{(2)}$ that it satisfies the commutativity and neutrality properties.

(i) Monotonicity: We show that if $x \leq y$, then, for any $z \in L$, $T^{(2)}(x, z) \leq T^{(2)}(y, z)$. We have the following three different situations:

(1) $x = 1$ or $z = 1$: If $x = 1$, then also $y = 1$, and so, $T^{(2)}(x, z) = T^{(2)}(y, z) = z$; if $z = 1$, then $T^{(2)}(x, z) = x \leq y = T^{(2)}(y, z)$.

(2) $x, z \in [a, 1[$: Then, also $y \in [a, 1[$, and hence, $T^{(2)}(x, z) = F(x, z) \leq F(y, z) = T^{(2)}(y, z)$.

(3) In the remaining cases, $T^{(2)}(x, z) = x \wedge z \wedge a \leq y \wedge z \wedge a \leq T^{(2)}(y, z)$.

(ii) Associativity: We demonstrate that $T^{(2)}(x, T^{(2)}(y, z)) = T^{(2)}(T^{(2)}(x, y), z)$ for all $x, y, z \in L$. If at least one of $x, y, z \in L$ is 1, it is obvious. The proof is split into all remaining possible cases considering the relationships of the elements x, y, z, and a.

(1) Let $x \in [a, 1[$.

(1.1) $y \in [a, 1[$,

(1.1.1) $z \in [a, 1[$,

$$\begin{aligned} T^{(2)}(x, T^{(2)}(y,z)) &= T^{(2)}(x, F(y,z)) = F(x, F(y,z)) = F(F(x,y),z) \\ &= T^{(2)}(F(x,y),z) = T^{(2)}(T^{(2)}(x,y),z) \end{aligned}$$

(1.1.2) $z \in L \backslash [a, 1]$,

$$\begin{aligned} T^{(2)}(x, T^{(2)}(y,z)) &= T^{(2)}(x, y \wedge z \wedge a) = x \wedge y \wedge z \wedge a = z \wedge a \\ &= F(x,y) \wedge z \wedge a = T^{(2)}(F(x,y),z) = T^{(2)}(T^{(2)}(x,y),z) \end{aligned}$$

(1.2) $y \in L \backslash [a, 1]$ and $z \in L \backslash \{1\}$,

$$\begin{aligned} T^{(2)}(x, T^{(2)}(y,z)) &= T^{(2)}(x, y \wedge z \wedge a) = x \wedge y \wedge z \wedge a \\ &= T^{(2)}(x \wedge y \wedge a, z) = T^{(2)}(T^{(2)}(x,y),z) \end{aligned}$$

(2) Let $x \in L \backslash [a, 1]$.

(2.1) $y \in [a, 1[$,

(2.1.1) $z \in [a, 1[$,

$$\begin{aligned} T^{(2)}(x, T^{(2)}(y,z)) &= T^{(2)}\big(x, F(y,z)\big) = x \wedge F(y,z) \wedge a = x \wedge a \\ &= x \wedge y \wedge z \wedge a = T^{(2)}(x \wedge y \wedge a, z) = T^{(2)}(T^{(2)}(x,y),z) \end{aligned}$$

(2.1.2) $z \in L \backslash [a, 1]$,

$$\begin{aligned} T^{(2)}(x, T^{(2)}(y,z)) &= T^{(2)}(x, y \wedge z \wedge a) = x \wedge y \wedge z \wedge a \\ &= T^{(2)}(x \wedge y \wedge a, z) = T^{(2)}(T^{(2)}(x,y),z) \end{aligned}$$

(2.2) $y \in L \backslash [a, 1]$ and $z \in L \backslash \{1\}$,

$$\begin{aligned} T^{(2)}(x, T^{(2)}(y,z)) &= T^{(2)}(x, y \wedge z \wedge a) = x \wedge y \wedge z \wedge a \\ &= T^{(2)}(x \wedge y \wedge a, z) = T^{(2)}(T^{(2)}(x,y),z) \end{aligned}$$

Hence, $T^{(2)}$ is a t-norm on L.

Remark 1. Notice that the t-norm $T^{(2)}: L^2 \to L$ examined in Theorem 3 may also be represented as

$$T^{(2)}(x,y) = \begin{cases} F(x,y) & \text{if } (x,y) \in [a,1[^2, \\ x \wedge y \wedge a & \text{if } (x,y) \in I_a \times I_a \\ y \wedge a & \text{if } (x,y) \in [a,1[\times I_a, \\ x \wedge a & \text{if } (x,y) \in I_a \times [a,1[, \\ y & \text{if } (x,y) \in [a,1[\times [0,a], \\ x & \text{if } (x,y) \in [0,a] \times [a,1[, \\ x \wedge y & \text{otherwise.} \end{cases}$$

Remark 2. By Remark 1, the structure of the t-norm $T^{(2)}: L^2 \to L$ is visualized in Figure 1.

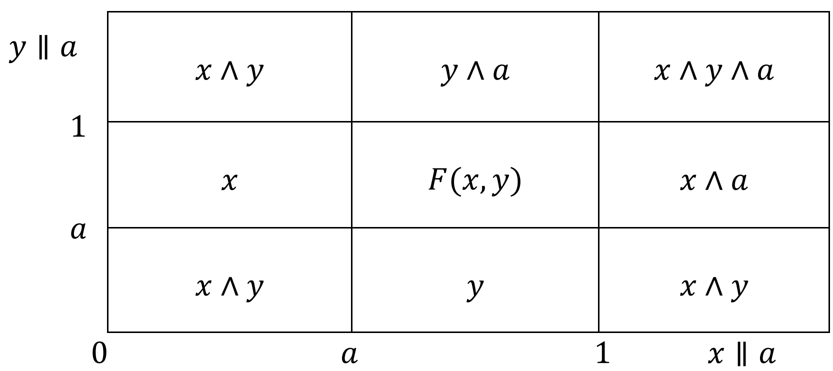

Figure 1: T-norm $T^{(2)}$ on L in Theorem 3

Example 2. Consider the lattice L_1 characterized by Hasse diagram shown in Figure 2.

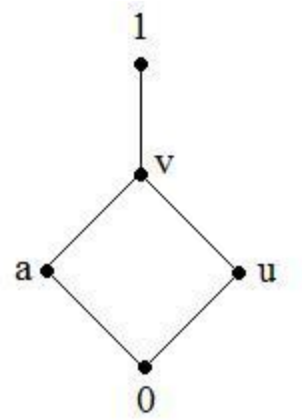

Figure 2: Lattice L_1

Notice that L_1 does not fulfill the condition in Proposition 1 (ii). The ordinal sum $T^{(1)}: {L_1}^2 \to L_1$ given by the formula (1) in Theorem 1 is not a t-norm for the t-norm $V_D: [a, 1]^2 \to [a, 1]$. Because we have $T^{(1)}\left(T^{(1)}(v, v), u\right) = T^{(1)}(V_D(v, v), u) = T^{(1)}(a, u) = a \wedge u = 0$ and $T^{(1)}\left(v, T^{(1)}(v, u)\right) = T^{(1)}(v, v \wedge u) = T^{(1)}(v, u) = v \wedge u = u$, which implies that the associativity of $T^{(1)}$ is violated. Moreover, the monotonicity of $T^{(1)}$ is violated since there holds $T^{(1)}(u, v) = u \wedge v = u \parallel a = V_D(v, v) = T^{(1)}(v, v)$ for $u \leq v$.

In the following, we demonstrate that the t-norm constructed by the formula (3) in Theorem 3 does not need to coincide with those in [4, 5, 6, 12].

Example 3. Consider the lattice L_2 characterized by Hasse diagram shown in Figure 3.

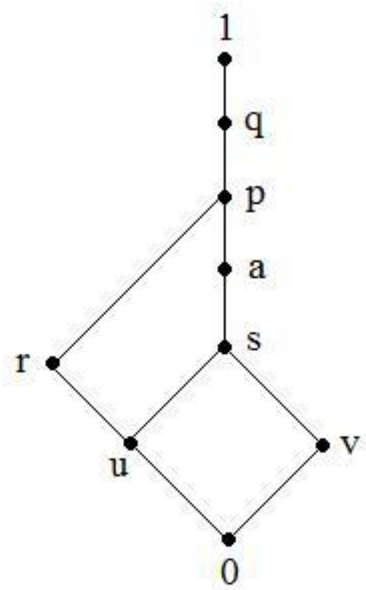

Figure 2: Lattice L_2

(i) The t-norm $T: {L_2}^2 \to L_2$, constructed by the methods in [4, 5], satisfies that $T(r, r) = 0$.

(ii) The t-norm $T: {L_2}^2 \to L_2$, constructed by the method in [6], satisfies that $T(q, q) = q$.

(iii) The t-norm $T: {L_2}^2 \to L_2$, constructed by the method in [12], satisfies that $T(p, p) = a$ for the t-norm $V_D: [a, 1]^2 \to [a, 1]$.

(iv) The t-norm $T^{(2)}: {L_2}^2 \to L_2$, constructed by the method in Theorem 3, is shown in Table 2, where the t-subnorm $F: [a, 1]^2 \to [a, 1]$ is given in Table 1. Obviously, it satisfies that $T^{(2)}(r, r) = u$, $T(p, p) = p$, and $T^{(2)}(q, q) = p$.

Hence, $T \neq T^{(2)}$.

F	a	p	q	1
a	a	a	a	a
p	a	p	p	p
q	a	p	p	p
1	a	p	p	p

Table 1: T-subnorm F on $[a, 1]$

$T^{(2)}$	0	u	v	s	r	a	p	q	1
0	0	0	0	0	0	0	0	0	0
u	0	u	0	u	u	u	u	u	u
v	0	0	v	v	0	v	v	v	v
s	0	u	v	s	u	s	s	s	s
r	0	u	0	u	u	u	u	u	r
a	0	u	v	s	u	a	a	a	a
p	0	u	v	s	u	a	p	p	p
q	0	u	v	s	u	a	p	p	q
1	0	u	v	s	r	a	p	q	1

Table 2: T-norm $T^{(2)}$ on L_2

Now, we present the following theorem to generate a t-conorm on a bounded lattice L derived from the t-superconorm P on the subintervals $[0, a]$ of L.

Theorem 4. Let $a \in L \backslash \{0,1\}$. If $P: [0, a]^2 \to [0, a]$ is a t-superconorm, then the binary operation $S^{(2)}: L^2 \to L$ given by the formula (4) is a t-conorm.

$$S^{(2)}(x, y) = \begin{cases} P(x, y) & \text{if } (x, y) \in]0, a]^2 \\ x \vee y \vee a & \text{otherwise.} \end{cases} \tag{4}$$

The result can be proved in a manner similar to the proof of Theorem 3, and thus, the proof is omitted.

Remark 3. Notice that the t-conorm $S^{(2)}: L^2 \to L$ examined in Theorem 4 may also be represented as

$$T^{(2)}(x,y)=\begin{cases} P(x,y) & \text{if } (x,y)\in\,]0,a]^2,\\ x\vee y\vee a & \text{if } (x,y)\in I_a\times I_a,\\ y\vee a & \text{if } (x,y)\in\,]0,a]\times I_a,\\ x\vee a & \text{if } (x,y)\in I_a\times\,]0,a],\\ y & \text{if } (x,y)\in\,]0,a]\times[a,1],\\ x & \text{if } (x,y)\in[a,1]\times\,]0,a],\\ x\vee y & \text{otherwise.}\end{cases}$$

Remark 4. From Remark 3, the structure of the t-conorm $S^{(2)}: L^2 \to L$ is visualized in Figure 4.

$y \parallel a$	$y \vee a$	$x \vee y$	$x \vee y \vee a$
1			
	y	$x \vee y$	$x \vee y$
a			
	$P(x,y)$	x	$x \vee a$
0	a	1	$x \parallel a$

Figure 4: T-conorm S on L in Theorem 4

4.CONCLUSIONS

In this paper, we first proposed a new construction method for t-norms on a bounded lattice L by means of the existence of t-subnorm F defined on the sublattice $[a,1]$ of L, for the indicated element $a \in L\backslash\{0,1\}$. Next, using the knowledge that a t-superconorm P on the sublattice [0,z] of L exists, we provided an approach to obtain t-conorms on a bounded lattice L. Furthertmore, we presented illustrative examples to show that our methods are different from the known ones.

REFERENCES

1. C. Alsina, M.J. Frank, B. Schweizer, Associative Functions: Triangular Norms and Copulas, World Scientific, Singapore, 2016.
2. G. Birkhoff, Lattice Theory, American Mathematical Society Colloquium Publishers, Providence, RI, 1967.
3. S. Bodjanova, M. Kalina, Uninorms on bounded lattices-recent development, in: J. Kacprzyk et al. (Eds.), IWIFSGN 2017, EUSFLAT 2017, AISC, vol. 641, Springer, Cham, 2018, pp. 224-234.
4. G. D. Çaylı, On a new class of t-norms and t-conorms on bounded lattices, Fuzzy Sets Syst. 332 (2018) 129-143.

5. G. D. Çaylı, Some methods to obtain t-norms and t-conorms on bounded lattices, Kybernetika 55 (2019) 273-294.

6. G. D. Çaylı, On generating of t-norms and t-conorms on bounded lattices, Int. J. Uncertain. Fuzz. 28 (2020) 807-835.

7. Y. Dan, B.Q. Hu, J. Qiao, New construction of t-norms and t-conorms on bounded lattices, Fuzzy Sets Syst. 395 (2020) 40-70.

8. B. De Baets, R. Mesiar, Triangular norms on product lattices, Fuzzy Sets Syst. 104 (1999) 61-75.

9. P. Drygaś and B. Pekala: Properties of decomposable operations on same etension of the fuzzy set theory. In: K. T. Atanassov et al. (Eds.), Advences in Fuzzy Sets, Intuitionistic Fuzzy Sets, Generalized Nets and Related Topics, Vol. I, Foundations, EXIT, Warszawa 2008, pp. 115-118

10. D. Dubios, H. Prade, A review of fuzzy set aggregation connectives, Inf. Sci. 3 (1995) 85-121.

11. A. Dvořák, M. Holčapek, New construction of an ordinal sum of t-norms and t-conorms on bounded lattices, Inf. Sci. 515 (2020) 116-131.

12. Ü. Ertuğrul, F. Karaçal, R. Mesiar, Modified ordinal sums of triangular norms and triangular conorms on bounded lattices, Int. J. Intell. Syst. 30 (2015) 807-817.

13. M. Grabisch, J.L. Marichal, R. Mesiar, E. Pap, Aggregation functions. Cambridge University Press Cambridge (2009).

14. W. Ji, Constructions of uninorms on bounded lattices by means of t-subnorms and t-subconorms, Fuzzy Sets Syst. 403 (2021) 38-55.

15. E.P. Klement, R. Mesiar, E. Pap, Triangular norms, Kluwer Acad. Publ., Dordrecht, 2000.

16. J. Medina, Characterizing when an ordinal sum of triangular norms is a triangular norm on bounded lattices, Fuzzy Sets Syst. 202 (2012) 75-88.

17. K. Menger, Statistical metrics, Proc. Natl. Acad. Sci. USA 8 (1942) 535-537.

18. E.S. Palmeira, B.C. Bedregal, Extension of fuzzy logic operators defined on bounded lattices via retractions, Comput. Math. Appl. 63 (2012) 1026-1038.

19. S. Saminger, On ordinal sums of triangular norms on bounded lattices, Fuzzy Sets Syst. 157 (10) (2006) 1403-1416.

20. S. Saminger-Platz, E. P. Klement, R. Mesiar, On extensions of triangular norms on bounded lattices, Indagationes Mathematicae 19 (1) (2008) 135-150.

21. B. Schweizer, A. Sklar, Statistical metric spaces, Pacific J. Math, 10 (1960) 313-334.

22. A. K. Tsadiras and R. G. Margaritis: The MYCIN certainty factor handling function as uninorm operator and its use as a threshold function in artificial neurons. Fuzzy Sets Syst. 93 (1998), 263-274.

23. D. Zhang, Triangular norms on bounded partially ordered sets, Fuzzy Sets Syst. 153 (2005) 195-209.

AN ALGORITHM FOR THE VERTICES ON THE PATHS OF MINIMAL LENGTH IN THE SUBORBITAL GRAPHS

Ümmügülsün AKBABA [1], Ali Hikmet DEĞER [1], Tolga BERBER[2]

[1] Department of Mathematics, University of Karadeniz Technical, Trabzon, Turkey

[2]Department of Statistics and Computer Sciences, University of Karadeniz Technical, Trabzon, Turkey

ummugulsun.akbaba@gmail.com,

ahikmetd@ktu.edu.tr,

tberber@ktu.edu.tr,

Abstract

The suborbital graphs are formed by the imprimitive action of the modular group Γ on the rational projective line $\widetilde{\mathbb{Q}} = \mathbb{Q} \cup \{\infty\}$. Jones, Singerman and Wicks extend the results of Farey graph $\mathbf{F}_{1,1}$ to suborbital graphs $\mathbf{F}_{u,N}$, where $(u, N) = 1$ and $N > 1$. Then, Değer defined the farthest vertices on the paths of minimal length on the suborbital graphs and investigated the related continued fractions.

In this paper, we present an algorithm which gives the values of the vertices on the paths of minimal length in the suborbital graphs $\mathbf{F}_{u,N}$. In addition, we present the program prepared using this algorithm to the attention of users.

Keywords: Suborbital graphs, Imprimitive action, Continued fractions

1.INTRODUCTION

$PSL(2,\mathbb{Z})$ is the set of all Mobius transformations of the form $\mathrm{T}: z \to \frac{az+b}{cz+d}$ where $a, b, c, d \in \mathbb{Z}$ and $ad - bc = 1$, that is group of automorphisms of upper half plane $\mathbb{H} := \{\mathrm{z} \in \ | \operatorname{Im}(\mathrm{z}) > 0\}$. So, the modular group the quotient of the unimodular group $SL(2,\mathbb{Z})$ by its center $\{\pm \mathrm{I}\}$. Thus, the elements of Γ are of the form as shown with pairs of matrices, that is:

$$\pm \begin{pmatrix} a & b \\ c & d \end{pmatrix} : \ a, b, c, d \in \mathbb{Z}, \quad ad - bc = 1$$

Here, we will omit the symbol $\pm$ and identify each matrix with its negative. Γ acts transitively on $\widehat{\mathbb{Q}}$ by the transformation

$$\begin{pmatrix} a & b \\ c & d \end{pmatrix} : \frac{x}{y} \to \frac{ax + by}{cx + dy}$$

where $\frac{x}{y} \in \widehat{\mathbb{Q}}$ is a reduced fraction, that is $(x, y) = 1$.

Here, if $\frac{x}{y}, \frac{r}{s} \in \widehat{\mathbb{Q}}$ there is a $T \in \Gamma$ where $\frac{r}{s} = T\left(\frac{x}{y}\right)$. So Γ modular group act on $\widehat{\mathbb{Q}}$ by transitively. Hence $(\Gamma, \widehat{\mathbb{Q}})$ generate a permutation group. An equivalence relation ≈ on Ω is called G_ invariant if, whenever $\alpha, \beta \in \Omega$ satisfy $\alpha \approx \beta$, then $g(\alpha) \approx g(\beta)$ for all $g \in G$; the equivalaence classes are called blocks. According to identity relation for $'\forall \alpha, \beta \in \widehat{\mathbb{Q}}\ ,\ \alpha = \beta \Leftrightarrow \alpha \approx \beta\,'$ and the universal relation for $'\forall \alpha, \beta \in \widehat{\mathbb{Q}}, \alpha \approx \beta'$ are Γ- equivalence invariant relations on $\widehat{\mathbb{Q}}$. We call $(\Gamma, \widehat{\mathbb{Q}})$ imprimitive if $\widehat{\mathbb{Q}}$ admits some Γ- equivalence invariant relation other than these relations; otherwise, we call $(\Gamma, \widehat{\mathbb{Q}})$ primitive.

Theorem 1.1. [2] Let (G, Ω) be transitive. Then (G, Ω) is primitive if and only if $G_\propto$, the stabilizer of a point $\propto \in \Omega$, is a maximal subgroup of G for each $\propto \in \Omega$. □

The stabilizer of ∞ on Γ modular group is $\Gamma_\infty = \left\langle \begin{pmatrix} 1 & 1 \\ 0 & 1 \end{pmatrix} \right\rangle$. If $\Gamma_0(N) = \left\{ \begin{pmatrix} a & b \\ c & d \end{pmatrix} \in \Gamma : c \equiv 0 (mod N) \right\}$ which is a subgroup of Γ, is taken, clearly we have that $\Gamma_\infty \lneqq \Gamma_0(N) \lneqq \Gamma$ where N>1. Here according to Theorem 1.1. $(\Gamma, \widehat{\mathbb{Q}})$ is imprimitive. In this situation there is a Γ- equivalence invariant relation on $\widehat{\mathbb{Q}}$. Because of the action of Γ on $\widehat{\mathbb{Q}}$ transitivily there is a $T \in \Gamma$, where $v = T(\infty)$. So on $\widehat{\mathbb{Q}}$ we have that $T(\infty) = v \approx w = S(\infty) \Leftrightarrow T^{-1}S \in \Gamma_0(N)$. Hence $\frac{r}{s} \approx \frac{x}{y} \Leftrightarrow ry - sx \equiv 0 (mod N)$ is written. The number of this equivalence relations classes is $\Psi(N) := |\Gamma : \Gamma_0(N)| = N \prod_{p|N}(1 + \frac{1}{p})$.

Theorem 1.2. [2] On $F_{u,N}$ suborbital graph there is $\frac{r}{s} \rightarrow \frac{x}{y}$ edge iff

$$x \equiv \pm ur\ (mod\ N)\ and\ ry - sx = N.$$

By our general discussion of imprimitivity upper, the subgraph of Γ leaving $F_{u,N}$ invariant is the congruance subgroup $\Gamma_0(N)$. Thus $\Gamma_0(N) \leq \mathrm{Aut}F_{u,N}$.

Theorem 1.3. **[2]** $\Gamma_0(N)$ permutes the vertices and edges of $F_{u,N}$ transitevely.

Corollary 1.4. [1] $F_{u,N}$ is self-paired graph $\Leftrightarrow u^2 \equiv -1\ (mod\ N)$.

Definition 1.5. [3]

a) Let $v_0, v_1, v_2, \dots, v_m$ be a sequence of different vertices of the graph $F_{u,N}$. If $m \geq 2$ then the configuration $v_0 \rightarrow v_1 \rightarrow \cdots \rightarrow v_m$ is called a directed circuit. If at least one arrow (not all) is reversed in this configuration, it is called an undirected (anti-directed) circuit. If $m = 2$ then the circuit, directed or not, is called a triangle. If $m = 1$ the configuration $v_0 \rightarrow v_1 \rightarrow v_0$ a self-paired edge.

b) The configurations $v_0 \rightarrow v_1 \rightarrow \cdots \rightarrow v_m$ and $v_0 \rightarrow v_1 \rightarrow \cdots$ called a path and an infinite path in $F_{u,N}$ respectively.

c) If $\frac{r}{s}\overset{<}{\rightarrow}\frac{x}{y}\in \boldsymbol{F}_{u,N}$ or $\frac{x}{y}\overset{<}{\leftarrow}\frac{r}{s}\in F_{u,N}$) the farthest vertex means that there is no vertex which has greater (or smaller) value than $\frac{x}{y}$ joined with the vertex $\frac{r}{s}$ in the suborbital graph $\boldsymbol{F}_{u,N}$ by the conditions from Theorem 1.2.

d) The path $v_0 \rightarrow v_1 \rightarrow \cdots \rightarrow v_m$ is called of minimal length iff $v_i \nleftrightarrow v_j$ where $i<j-1$, $i\in\{0,1,2,3,\ldots,m-2\}$, $j\in\{2,3,\ldots,m\}$ and v_{i+1} must be the farthest vertex which can be joined with the vertex v_i in $F_{u,N}$.

e) If $F_{u,N}$ does not contain any circuits, it is called a forest. If $F_{u,N}$ is a connected non-empty graph without circuits, it is called a tree.

1.1. Vertices of Paths of Minimal Length in the Suborbital Graphs

Theorem 1.1.1. [3] If $(u,N)=1$, there is a $k_i\in\mathbb{Z}, i=1,2$ which satisfies $u^2+(-1)^i k_i u+1\equiv 0\ mod(N)$ congruent equation. □

On $\boldsymbol{F}_{u,N}$ $\varphi_i=\begin{pmatrix}-u & \frac{u^2+(-1)^i k_i u+1}{N}\\ -N & u+(-1)^i k_i\end{pmatrix}\in\Gamma_0(N)$ is a transformation which joins the vertices to each other by respectively

$$\cdots\leftarrow\frac{u+\frac{1}{k_1-\frac{1}{k_1}}}{N}\leftarrow\frac{u+\frac{1}{k_1}}{N}\leftarrow\frac{u}{N}\leftarrow\infty=\frac{1}{0}\rightarrow\frac{u}{N}\rightarrow\frac{u-\frac{1}{k_2}}{N}\rightarrow\frac{u-\frac{1}{k_2-\frac{1}{k_2}}}{N}\rightarrow\frac{u-\frac{1}{k_2-\frac{1}{k_2-\frac{1}{k_2}}}}{N}\rightarrow\cdots$$

on the infinite minimal length path. So, this transformation forms the edges with a continued fractions construction for every edge.

Thus if $u+\frac{x}{y}$ is a vertex on the minimal length path of $F_{u,N}$, the farthest vertex which can be joined with this vertex is $\varphi\left(\frac{u+\frac{x}{y}}{N}\right)=\frac{u+\frac{y}{ky-x}}{N}$. If the initial vertex is taken $v_0=\frac{u}{N}$, for $\forall q\in\mathbb{Z}^+$ $v_q=\varphi^q(v_0)$ equality is handed.

Let continued fraction as $\mathrm{K}_{n=1}^{\infty}\left(\frac{-1}{-k_i}\right)$, where $a_n=-1$, $b_n=-k_i$ for all $n\geq 0, n\in\mathbf{N}$ and $i=1,2$. From recurrence relation, for this continued fraction, $B_n=-A_{n+1}$. Then, n^{th} vertex on the path of minimal length in the suborbital graph $\mathbf{F}_{u,N}$ can be given by

$$\overrightarrow{v_n}=\frac{u+T_n(0)}{N}=\frac{u+\frac{A_n}{B_n}}{N}=\frac{A_{n+1}u-A_n}{A_{n+1}N},$$

$$\overleftarrow{v_n}=\frac{u-T_n(0)}{N}=\frac{u-\frac{A_n}{B_n}}{N}=\frac{A_{n+1}u+A_n}{A_{n+1}N},$$

for right and left direction, respectively [5].

Also from matrix connections for continued fractions in [4], we get

$$\begin{pmatrix} A_{n-1} & A_n \\ -A_n & -A_{n+1} \end{pmatrix} = \begin{pmatrix} 0 & -1 \\ 1 & -k_i \end{pmatrix}^n, \; i = 1,2.$$

Thus, set of vertices of the path for both direction is

$$M_i := \bigcup_{n=0}^{\infty} \left\{ \frac{u+(-1)^i T_n(0)}{N} : T_n = t_0 t_1 t_2 \dots t_n,\; t_0(z) = z, t_n(z) := t(z) = \frac{-1}{-k_i+z},\; i = 1,2 \right\} \cup \{\infty\}.$$

From the set $M_i,\ i = 1,2$, if $k_i = 2$, then the Mobius transformation t is parabolic and if $k_i \geq 2$, then t is hyperbolic. Therefore, φ_i is an element of $\Gamma_0(N)$ and also if $k_i = 0$ and $k_i = 1$, then φ_i is an elliptic element of order 2 and 3, respectively. Moreover, if we solve the characteristic equation $A_n = -k_i A_{n-1} - A_{n-2},\ i = 1,2$, when $k_i = 2$, then $A_n = (-1)^n n$ and when $k_i > 2$, then $A_n = (-1)^n 2^{1-n} \sum_{t=1}^{n} (k_i + \sqrt{{k_i}^2 - 4})^{n-t} (k_i - \sqrt{{k_i}^2 - 4})^{t-1}$. Hence, if $k_i = 2,\ i = 1,2$, then for left and right direction, the n^{th} vertex on the path of minimal length starting with the vertex $\frac{u}{N}$ in the suborbital graph $\mathbf{F}_{u,N}$ are

$$\overleftarrow{v_n} = \frac{(n+1)u-n}{(n+1)N} \quad and \quad \overrightarrow{v_n} = \frac{(n+1)u+n}{(n+1)N},$$

respectively.

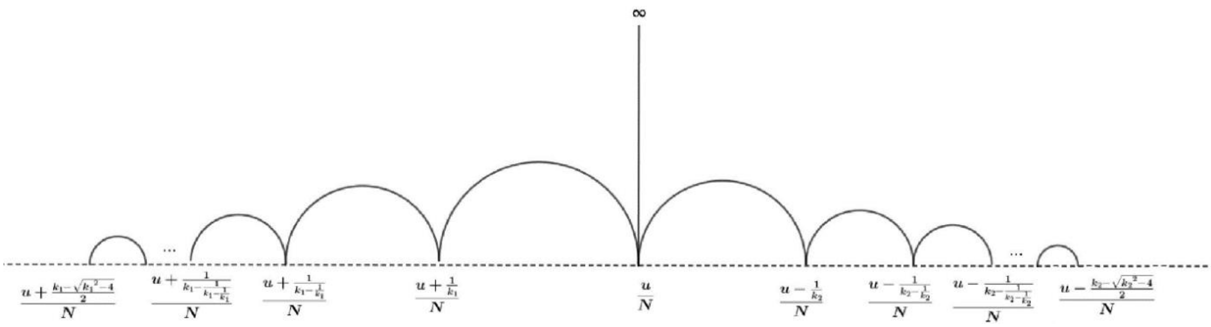

FIGURE 1.1.2. The vertices of the Suborbital Graphs on the Paths of Minimal Length

2. **PRESENTED THE ALGORITHM OF THE VERTICES OF THE PATHS OF MINIMAL LENGTH IN THE SUBORBITAL GRAPHS**

Algorithm 1: Vertices of the Suborbital Graphs on the Paths of Minimal Length

---

Input: $u, N, step \in \mathbb{N}$
if $(u, N) = 1$ **then**
  $k_1 \leftarrow 1;$
  $k_2 \leftarrow 1;$
  if $(u^2 + 1) \mod N = 0$ **then**
    $k_1 \leftarrow N;$
    $k_2 \leftarrow N;$
  else
    for $i \in [2, N]$ **do**
      if $\left((u^2 + 1) + i * u\right) \mod N = 0$ **then**
        $k_2 \leftarrow i;$
      end
      if $\left((u^2 + 1) - i * u\right) \mod N = 0$ **then**
        $k_1 \leftarrow i;$
      end
    end
  end
  $\overleftarrow{V} \leftarrow \{\frac{u}{N}\};$
  if $k_1 = 1$ **then**
    $\overleftarrow{V} \leftarrow \overleftarrow{V} \cup \{\frac{u-1}{N}\}$
  else
    for $n \in [1, step]$ **do**
      if $k_1 = 2$ **then**
        $\overleftarrow{V} \leftarrow \overleftarrow{V} \cup \left\{\frac{(n+1)u-n}{(n+1)N}\right\}$
      else
        $A_0 \leftarrow$
        $(-1)^n 2^{1-n} \sum_{t=1}^{n} \left(k_1 + \sqrt{k_1^2 - 4}\right)^{n-t} \left(k_1 - \sqrt{k_1^2 - 4}\right)^{t-1};$
        $A_1 \leftarrow$
        $(-1)^{n+1} 2^{-n} \sum_{t=1}^{n+1} \left(k_1 + \sqrt{k_1^2 - 4}\right)^{n+1-t} \left(k_1 - \sqrt{k_1^2 - 4}\right)^{t-1};$
        $\overleftarrow{V} \leftarrow \overleftarrow{V} \cup \left\{\frac{u}{N}\left(1 + \frac{A_0}{A_1 u}\right)\right\}$
      end
    end
  end
  $\overrightarrow{V} \leftarrow \{...\};$
  $\overleftarrow{V} \xrightarrow{n \to \infty} \frac{u - \frac{k_1 - \sqrt{k_1^2 - 4}}{2}}{N};$
  $\overrightarrow{V} \xrightarrow{n \to \infty} \frac{u + \frac{k_2 - \sqrt{k_2^2 - 4}}{2}}{N};$
end

Also, we present a link to users for downloading and using the program by setting up the algorithm.

https://www4.ktu.edu.tr/matematik-program

Now, we give example for the algorithm.

Example: For the suborbital graph $\boldsymbol{F}_{u,N}$, we take $u = 2, N = 4,$ according to the theorem, we can't write the vertices because of $(u, N) \neq 1$.

Example: On the suborbital graph $\boldsymbol{F}_{u,N}$, let's take $u = 1, N = 5,$ where $(u, N) = 1$. So, from the theorem we get $k_1 = 2,\ k_2$=3. Some vertices for left and right directions, as follows:

$$\overleftarrow{v}_1 = \frac{1}{10}, \ \overleftarrow{v}_2 = \frac{1}{15}, \ \overleftarrow{v}_3 = \frac{1}{10}, \ \overleftarrow{v}_4 = \frac{1}{20}, \dots$$

$$\overrightarrow{v}_1 = \frac{4}{15}, \ \overrightarrow{v}_2 = \frac{11}{40}, \ \overrightarrow{v}_3 = \frac{29}{105}, \ \overrightarrow{v}_4 = \frac{76}{275}, \dots .$$

REFERENCES

1. M. Akbas, On suborbital graphs for the modular group. Bulletin of the London Mathematical Society, 33, 647-152, 2001.
2. G.A. Jones, D. Singerman, K. Wicks, The modular group and generalized Farey graphs, London Math. Soc. Lecture Note Ser., 160, 316-338, 1991.
3. A.H. Deger, Vertices of paths of minimal lengths on suborbital graphs, Filomat, 31, 913-923, 2017.
4. A Cuyt, VB Petersen, B Verdonk, WB Jones, Handbook of Continued Fractions for Special Continued Fractions, New York: Springer, 2008.
5. Ü. Akbaba and A.H. Değer, Relation between matrices and the suborbital graphs by the special number sequences. Turkish Journal of Mathematics, 42, 753-767, 2022.
6. C.C Sims. Graphs and finite permutation groups. Mathematische Zeitschrift, 95, 76–86, 1967.

Fine Grinding of Marble Waste: Preliminary Test Results

Çimen Gül Kuluşaklı[1], Mustafa Birinci[2]*,

[1]Graduate School of Natural and Applied Sciences, İnönü University, Malatya, Turkey

[2]Department of Mining Engineering, İnönü University, Malatya, Turkey

mustafa.birinci@inonu.edu.tr, cimenaras@gmail.com

Abstract

The aim of this study was to investigate the production of ultrafine material from marble wastes. For this purpose, marble wastes were ground to fine sizes using planetary ball mill with porcelain milling media. The milling tests were performed at a constant mill speed of 150 rpm with three different ball to powder ratios (2.5, 5, and 10) and variable grinding times up to 240 min. The particle size analyses showed that the mean particle size (d_{50}) of the milled products was significantly reduced compared to the feed size. Finally, the preliminary test results from planetary milling indicated that marble wastes can be ground to the desired fine particle sizes for industrial utilization.

Keywords: Marble waste; Ultrafine grinding; Planetary ball mill.

1. Introduction

Marble is a composition formed by the recrystallization of limestone and dolomitic limestones as a result of metamorphism, and contains 90-98% $CaCO_3$ (i.e. calcite). Marble wastes, which include pieces of various sizes and shapes, are formed at almost every operation stage of the marble industry and create a growing environmental problem. A large part of these wastes are stored, and a very small part of them can be used for different purposes in the industry.

In recent years, marble wastes ground to very fine sizes have been used as a source of calcite in many industries such as paper and paint production. The production of submicron-size calcite is receiving greater attention due to the growing demand for paint and paper. Traditionally, such fine powders are produced in ball mills, stirred ball mills, roller mills, and vibration mills. However, these mills exhibit a limitation regarding product fineness: a size limit of one micron is often observed after several hours of grinding. This is due to the fact that particles are weakly confined in the breakage zone of these mills. Simply, the particles reside in the interstices of the ball mass and are confined only by the weight of the ball mass above, and in the dynamic environment, the particles easily escape from this zone [1].

For ultrafine particles (<10 μm), the use of mills delivering a huge amount of energy for particle breakage, such as vibratory, jet, and planetary mills, has been considered an alternative for mineral processing [2-4]. Planetary ball mill, a number of two or four bowls filled with the grinding balls are equidistantly installed on a supporting disk. The bowls and the disk are simultaneously and separately rotated at a high speed in opposite directions. The high speed of rotation of the bowls and the revolution speed of the supporting disk generate extremely high centrifugal forces acting on the balls. This results in, as an attrition effect, the grinding balls running along the inner wall of the bowl, and as an impact effect, the balls impacting strongly against the opposite wall of the bowl and against one another [5, 6]. Guzzo et al. (2014) studied particle size distribution and structural changes in limestone ground in planetary ball mill. They emphasized that grinding speed reduction occurs when the average particle size reaches 20 µm, and the mean particle size was reduced from 134 to 10 µm [7]. However, it is known that dry micronized calcite is reduced to much finer sizes (d_{50}= 3-5 µm) in industrial applications. There is no study in the literature that achieved the marble waste to a ultra fine size such as d_{50}= 3-5 µm by planetary mill.

The purpose of this study is to investigate the grindability of waste marble pieces to fine size using planetary mill, and to analyze the findings obtained from the preliminary experiments for the next study.

2. Material and Method

In this study, approximately 10 kg of marble pieces known as Uşak White (it is a kind of white marble quarried in Uşak, Turkey) were used. Sample preparation for planetary mill was carried out in two stages as shown in Figure 1(a). The marble pieces were crushed with two stage using jaw crusher until all particles being <10 mm. The crushed particles were ground in a porcelain ball mill in order to obtain particle size below 1 mm. The particle size distribution of the ground particles, which was used as a test material, is illustrated in Figure 1(b).

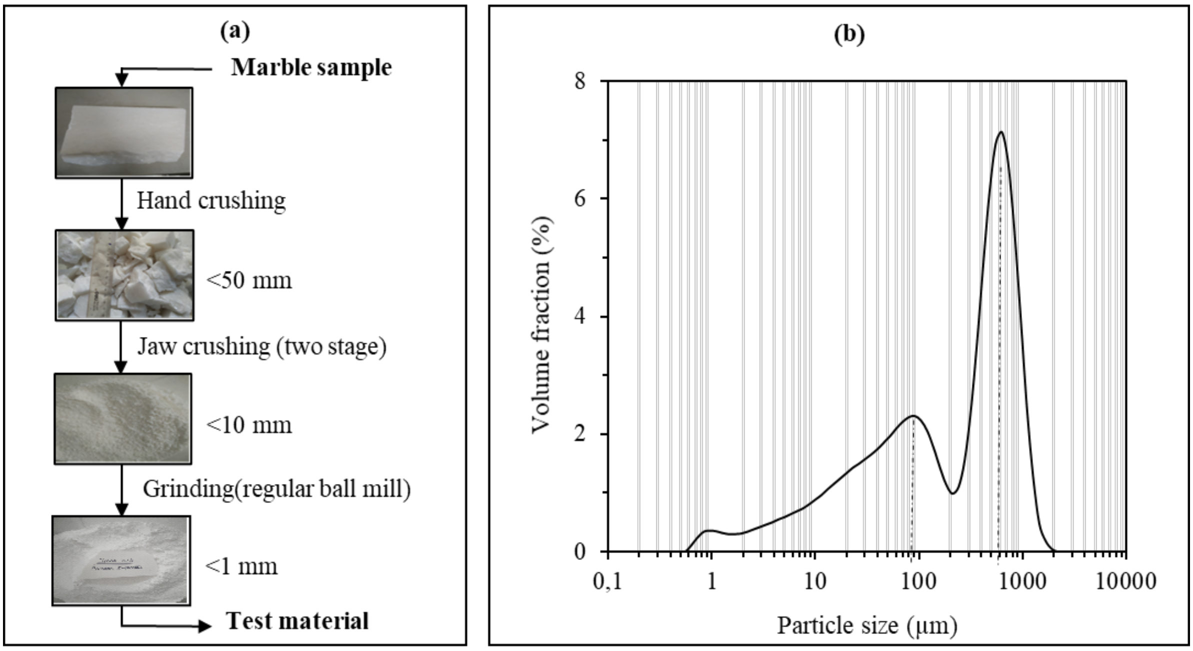

Figure 1. Test material: preparation (a) and particle size distribution (b)

Marble samples with particle size below 1 mm were ground to ultrafine sizes using planetary ball mill (Fritsch Pulverisette 6 Mono Mill) and agate grinding bowl with 70.6 mm inner diameter and 250 ml volume (Figure 2(a)). The grinding media was composed of 65 alumina/alubite balls with diameter equal to 10 mm. The milling experiments were carried out at 2.5 (330 g ball/132 g ore), 5 (330 g ball/66 g ore) and 10 (330 g ball/33 g ore) ball to powder ratio by weight (defined as B/P). In the present study, the revolution speed (RS) was chosen as 150 rpm and it was kept constant (other experiments not yet completed). The samples were dry milled for 7.5, 15, 30, 60, 120 and 240 min. For milling times greater than 60 minutes, a break of 5 min was adopted to prevent temperature rise in the mill after each 15 min of grinding. The milling tests were carried out in air atmosphere and at room temperature.

After milling, particle size distribution of the ground materials were measured by laser scattering using the Matersizer 2000 (Malvern Instruments Ltd., UK) with equipment (Figure 2(b)). The analysis is based upon laser diffraction technique, capable of Mie scattering, and covers a wide size range of 0.02 and 2000 µm. The device is capable of measuring the particle size of emulsions, suspensions and dry powders. In this study, a little sample (ca. 0.5 grams) was stirred with distilled water at 2500 rpm in a 1 liter cell integrated into the device and measurements were performed on particles in a fluid aqueous suspension. Before determination, marble particles were treated in 0.05 M sodium hexametaphosphate as a dispersing agent with ultrasound waves for 3 min. Particle size distribution data and d_{50} value were automatically obtained using Mastersizer 2000 software.

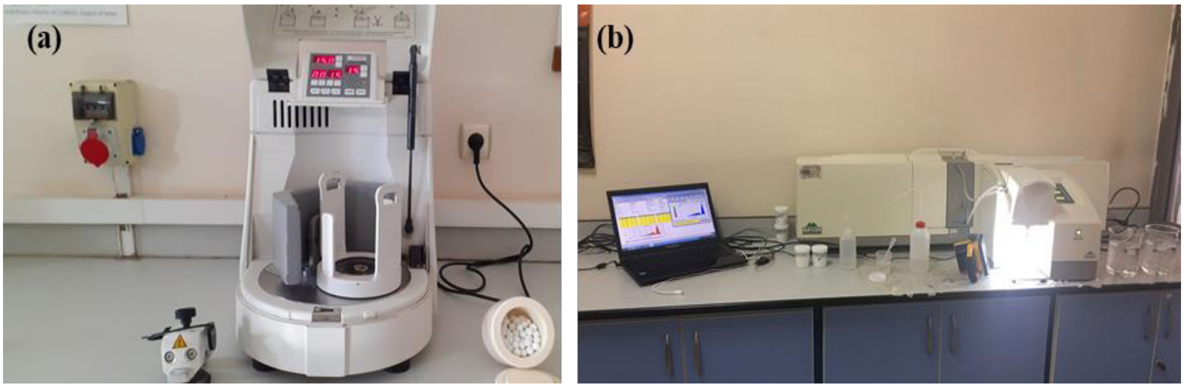

Figure 2. Planetary ball mill with grinding equipment (a) and laser particle size analyzer (b)

3. Experimental Results

3.1. Milling results for low ball to powder ratio (B/P=2.5)

In size reduction processes, the milling efficiency is generally controlled by particle size distribution. The milling process is also evaluated by measuring the main particle size (d_{50}) of the particles in the milled product. Particle size analysis was performed the planetary mill feed and milled product. Figure 3(a) shows the particle size distribution of the milled material at different times. As shown in Figure 3(a), the particle size distributions of samples milled in planetary ball mill shift gradually to finer size distributions as the milling time increases. The shift in the size distribution curves is slightly better pronounced at high milling time. Figure

3(b) illustrates changes of sample mean size (d_{50}) during comminution process at 150 rpm. As seen in Figure 3(b), the d_{50} value of the milled products shifted towards smaller sizes with the increase of the grinding time. It is clear that d_{50} decreases significantly with milling time up to 240 min but remained almost invariable for milling periods longer than 60 min. As a result of the experiments carried out at B/P=2.5 ratio, the d_{50} value decreased from 350 µm to 55 µm with 120 min grinding time.

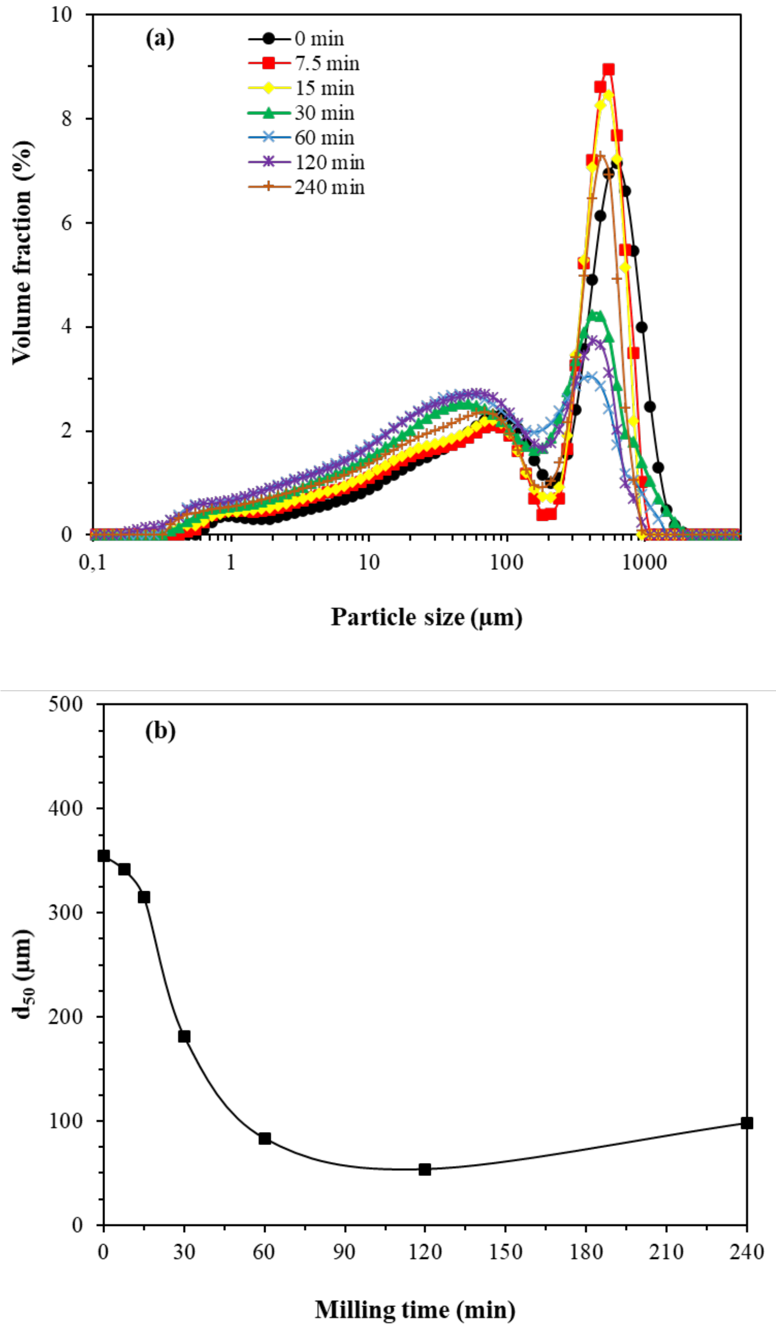

Figure 3. The variation of particle size distribution (a) and mean size diameter (d_{50}) (b) of marble samples milled at B/P=2.5 up to 240 minutes. (The zero time grinding indicates the feed size distribution.)

3.2. Milling results for medium ball to powder ratio (B/P=5)

For B/P=5, the particle size distribution of the marble powders produced by grinding in the planetary mill at different times is shown in Figure 4(a). It is clearly seen that the particle size distribution curves shift to the left as the grinding time increases. It indicates that as the grinding time increases, the material becomes finer. For example, the amount of 10 µm material increased from 1% to 2% at 120 min of grinding, emphasizing a significant reduction in particle size. The effect of grinding time on the mean particle size (d_{50}) of the marble sample ground at medium ball to powder ratio (B/P=5) is shown in Figure 4(b). It is observed that d_{50} values decreases sharply with grinding time up to 7.5 min but remained nearly constant for grinding periods longer than 60 min.

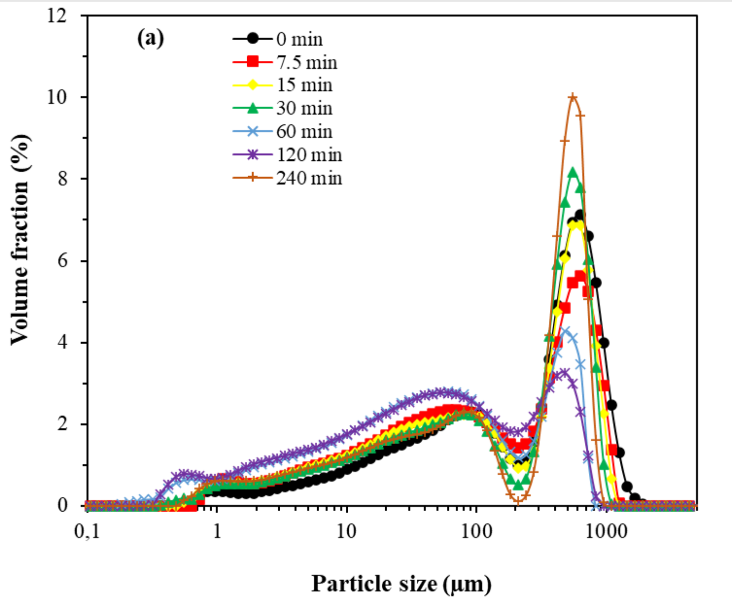

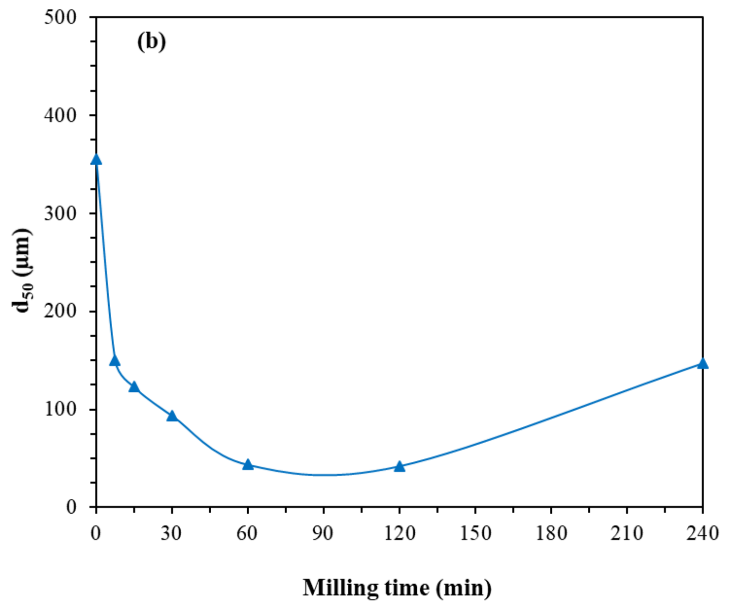

Figure 4. The variation of particle size distribution (a) and mean size diameter (d_{50}) (b) of marble samples milled at B/P=5 up to 240 minutes.

3.3. Milling results for high ball to powder ratio (B/P=10)

The size distributions of marble particles ground at different milling times are shown in Figure 5. As seen in Figure 5(a), before being ground using a planetary mill (grinding time of 0 min), the marble particles were mostly composed of a coarse particle fraction and a fine particle fraction. However, the fine size increased slightly with the increasing grinding time. There was also a significant difference in the average particle size of all products milled at different times. It was determined that d_{50} values generally decreases with increasing the milling time. The median particle size of ground samples decreased sharply during the initial stage (7.5 min) of grinding in comparison with starting materials, as shown in Figure 5(b). After 15 and 60 min of grinding, the median particle size showed a more stable decreasing trend.

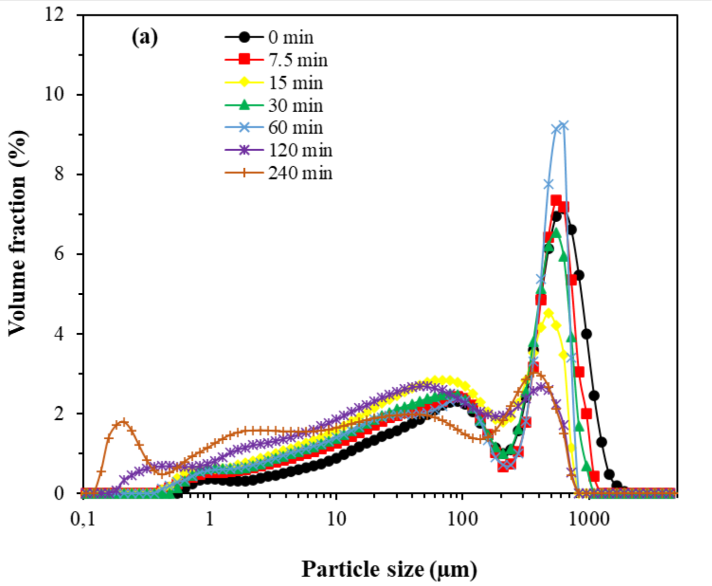

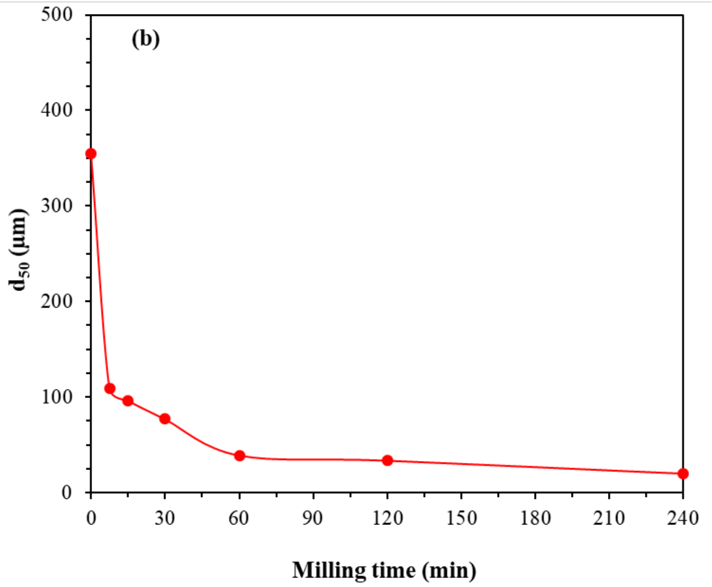

Figure 5. The variation of particle size distribution (a) and mean size diameter (d_{50}) (b) of marble samples milled at B/P=10 up to 240 minutes.

4. Conclusions

In all the figures, it is seen that the larger B/P ratio produces a finer product with a smaller d_{50} value. In other words, decreasing the powder filling has a pozitive effect on the mean size of the products. It is known that, as powder filling increases, the grinding energy per unit mass decreases and hence the corresponding decrease in all the effects. According to the grinding results, the smallest d_{50} value was found as about 25 μm for ball to powder ratio=10 as seen in Figure 5. It is clear that the finding is very promising result, compared to milling feed size with d_{50}=350 μm. Finally, ball to powder ratio is influential operating variable together with other grinding parameters such as revolution speed. It is clear that positive results will be obtained when the experiments are continued under different grinding conditions.

Acknowledgment

This work is financially supported by the İnönü University Scientific Research Projects Coordination Unit (Project Number: FYL-2021-2538)

References

[1] Milin, L. & Rajamani, R. K. (1997). Kinetics of Alumina Ultrafine Grinding in a Planetary Ball Mill, Materials and Manufacturing Processes, 12:2, 241-260.

[2] Osawaru, A., Orumwense, E.F.,(1992). Superfine and ultrafine grinding: a literature survey, Mineral Processing and Extractive Metallurgy Review, 11, 107-127.

[3] Wellenkamp, F.J., (1999). Moagens Fina e Ultrafina de Minerais Industriais: Uma Revisão. CETEM/MCT, Rio de Janeiro (55 pp. (in Portuguese)).

[4] He, M., Wang, Y., Forssberg, E. (2004). Slurry rheology in wet ultrafine grinding of industrial minerals: a review, Powder Technology, 147, 94-112.

[5] Mio, H., Kano, J., Saito, F., Kantaro, K. (2002). Effects of rotational direction and rotation-torevolution speed ratio in planetary ball mill. Scale-up method of planetary ball mill. Materials Science and Engineering: A, 332, 5909-5916.

[6] Pedro L.Guzzo, Filipe B. Marinho de Barrosa, Bruno R. Soares, Juliano B. Santos (2020). Evaluation of particle size reduction and agglomeration in dry grinding of natural quartz in a planetary ball mill, Powder Technology, 368, 149-159.

[7] Guzzo P. L., Santos, J. B., David, R. C. (2014). Particle size distribution and structural changes in limestone ground in planetary ball mill, International Journal of Mineral Processing, 126, 41-48.

ON THE SOLUTION PAVLOV EQUATION BY THE VARIATIONAL ITERATION METHOD

Derya DENİZ [1] **and Mücahit SAYDAM** [2]

[1,2]Department of Mathematics, University of Firat, Elazig, Turkey

deryadeniz485@yandex.com , mucahıtsydm@gmail.com

Abstract

In this work, the variational iteration method (VIM) that is a semi-analytical method is applied the (2 + 1)-dimensional Pavlov equation. The numerical results show that only a few terms are sufficient to obtain accurate solutions.

Keywords: Variational method; Pavlov equation;

1.INTRODUCTION

In recent years, because of the nonlinear structure appear in a wide variety of scientific applications, the research for solitary wave,periodic, rational and soliton solutions of nonlinear equations in mathematical physics has been an important subject in soliton theory and its applications.

The variational iteration method (VIM) was first proposed by He[9]. The variational iteration method (VIM) has been shown to solve effectively, easily and accurately a large class of nonlinear problems with approximations converging rapidly to accurate solutions. He applied his method to autonomous ordinary differential systems and nonlinear equations with convolution product nonlinearity.

The variational iteration method (VIM) the authors have worked; Inc and Cavlak to coupled MKdv [5] , Bulut and Baskonus a comparsion among homotopy perturbation method and the decomposition method with the variational iteration method (VIM) for disperse equation , Hussain and Khan to nonlinear Klein-Gordon equation [13] .

Pavlov equation has the following form:

$$u_{yy} = u_{tx} + u_y u_{xx} - u_x u_{xy} \ldots (1)$$

Where u(x, y,t) defines the amplitude of the respective wave which depends upon spatial variables x and y and temporal variable t. Equation (1) encloses both linear and nonlinear terms. This equation came into existence via symmetry reduction of second heavenly equation.

The nonlinearity of the Pavlov equation makes it difficult for us to Önd the closed form and exact solutions. The tanh-coth method provides a leading solution of the Pavlov equation [1] ,

$$u(x,y,t) = \alpha_1 \tanh\left(c_1 + \frac{c_3^2}{c_2}t + c_2x + c_3y\right) + \alpha_2 \tanh^3\left(c_1 + \frac{c_3^2}{c_2}t + c_2x + c_3y\right) + \alpha_3 \ldots (2)$$

From equation (3), we have initial condition

$$u(x,y,0) = \alpha_1 \tanh(c_1 + c_2x + c_3y) + \alpha_2 \tanh^3(c_1 + c_2x + c_3y) + \alpha_3 \ldots (3)$$

2.THE VARIATIONAL ITERATION METHOD

Consider the different equation

$$L_t u + Nu = g(t) \ldots (4)$$

Where L is a linear operator, N is a non-linear operator and g(t) is a known and Nonlinear analytical function.Ji Huvan He has modified the above method into an iteration method [9] in the following way:

$$u_{n+1} = u_n + \int_0^t \lambda(Lu_n(x) + Nu_n(x) - g(x))dx \ldots (5)$$

Where λ is a general Lagrange is multipler, which can be identified optimally via the variational theory, and $\tilde{u_n}$ is a restricted variational which means $\delta \tilde{u} = 0$.

It is obvious now that the main steps of He [9] is variational iteration method require first the determination of the Lagrangian multiplier λ that will be identified optimally. Having determined the Lagrangian multiplier, the successive approximations $u_{n+1}, n \geq 0$, of the solution

$$u = \lim u_n, \text{for } (n \to \infty) \ldots (6)$$

In other words, correction functional (5) will give several approximations, and therefore the exact solution is obtained at the limit of the resulting successive approximations.

To give a clear overview of the methodology, we consider several examples in the following section.

3.APPLICATIONS

For comparison purposes, we consider a Pavlov equation model problem in order to illustrate the technique discussed above. This problem is as follows;

$$u_{yy} = u_{tx} + u_y u_{xx} - u_x u_{xy} \ldots (1)$$

with in initial conditions

$$u(x,y,0) = \alpha_1 \tanh(c_1 + c_2 x + c_3 y) + \alpha_2 \tanh^3(c_1 + c_2 x + c_3 y) + \alpha_3 \ldots (3)$$

In order to solve Eq.(1) , using VIM ,we can construct a variational iteration method for this equation

The correction function to equation (1);

$$\delta u_{(n+1)}(x,y,t) = \delta u_n(x,y,t) + \delta \int_0^t \lambda_1 \{L(u_{nyy} - u_{n\xi x}) - N(u_{ny}u_{nxx} - u_{nx}u_{nxy})\} d\xi \ldots (4a)$$

$$\delta u_{(n+1)}(x,y,t) = \delta u_n(x,y,t) + \delta \int_0^t \lambda_2 \{L(u_{n\theta\theta} - u_{ntx}) - N(u_{n\theta}u_{nxx} - u_{nx}u_{nx\theta})\} d\theta \ldots (4b)$$

$$\delta u_{(n+1)}(x,y,t) = \delta u_n(x,y,t) + \delta \int_0^t \lambda_3 \{L(u_{nyy} - u_{nt\vartheta}) - N(u_{ny}u_{n\vartheta\vartheta} - u_{n\vartheta}u_{n\vartheta y})\} d\vartheta \ldots (4c)$$

Where λ is general Lagrange multiplier , which can be identified optimally via the variational theory and un is considered as a restricted variation , δu = 0 .

To find the λ Lagrange multiplier; In equation (4a), (4b) and (4c) is

$$\delta u_{(n+1)}(x,y,t) = \delta u_n(x,y,t) + \delta \int_0^t \lambda_1 \frac{\partial u_n}{u_\xi} d\xi \quad , (\lambda_1 = m, \lambda_1{}' d\xi = dm)$$

If partial integration is applied $\left(\frac{\partial u_n}{u_\xi} d\xi = dv \, , u_n = v\right)$

$$\delta u_{(n+1)}(x,y,t) = \delta u_n(x,y,t) + \delta \lambda_1 u_n|_{t=\xi} - \delta \int_0^t \lambda_1{}' \, u_n d\xi$$

$$= \delta u_n\left(1 + \lambda_1 u_n|_{t=\xi}\right) - \int_0^t \lambda_1{}' \, u_n d\xi$$

$$1 + \lambda_1 u_n|_{t=\xi} = 0 \; ve \; \lambda_1{}'(\xi) = 0 \; ise \; \lambda_1(\xi) = c_1$$

$\lambda_1 = \lambda_2 = \lambda_3 = -1$ lagrange factor is found.

Substituting the Lagrange multiplier in the equation (4) ;

n=0 ,

$$u_1(x,y,t) = u_0(x,y,t) - \int_0^t \left(u_{0yy} - u_{0\zeta x} - u_{0y}u_{0xx} + u_{0x}u_{0xy}\right) d\xi$$

n=1 ,

$$u_2(x,y,t) = u_1(x,y,t) - \int_0^t (u_{1yy} - u_{1\zeta x} - u_{1y}u_{1xx} + u_{1x}u_{1xy})\, d\xi$$

n=2 ,

$$u_3(x,y,t) = u_2(x,y,t) - \int_0^t (u_{2yy} - u_{2\zeta x} - u_{2y}u_{2xx} + u_{2x}u_{2xy})\, d\xi$$

.

.

.

we find in the form;

$$\mathrm{u(t)} = \lim_{n\to\infty} u_n(\mathrm{t}) = \Psi_{\mathrm{n}}$$

this equation is ;

$$u(x,y,t) = u_0(x,y,t) + u_1(x,y,t) + u_2(x,y,t) + \cdots$$

$$= 2\alpha_3 + 2\alpha_1 \tanh[c_1 + xc_2 + yc_3] + 2\alpha_2 \tanh[c_1 + xc_2 + yc_3]^3$$

$$-t(-2\mathrm{sech}\,[c_1 + xc_2 + yc_3]^2 c_3^2 \alpha_1 \tanh[c_1 + xc_2 + yc_3]$$

$$+6\mathrm{sech}[c_1 + xc_2 + yc_3]^4 c_3^2 \alpha_2 \tanh[c_1 + xc_2 + yc_3]$$

$$-6\mathrm{sech}[c_1 + xc_2 + yc_3]^2 c_3^2 \alpha_2 \tanh[c_1 + xc_2 + yc_3]^3$$

$$+(\mathrm{sech}[c_1 + xc_2 + yc_3]^2 c_2 \alpha_1$$

$$+3\mathrm{sech}[c_1 + xc_2 + yc_3]^2 c_2 \alpha_2 \tanh[c_1 + xc_2 + yc_3]^2)$$

$$(-2\mathrm{sech}[c_1 + xc_2 + yc_3]^2 c_2 c_3 \alpha_1 \tanh\,[c_1 + xc_2 + yc_3]$$

$$+6\mathrm{sech}[c_1 + xc_2 + yc_3]^4 c_2 c_3 \alpha_2 \tanh[c_1 + xc_2 + yc_3]$$

$$-6\mathrm{sech}[c_1 + xc_2 + yc_3]^2 c_2 c_3 \alpha_2 \tanh[c_1 + xc_2 + yc_3]^3)$$

$$-(\mathrm{sech}[c_1 + xc_2 + yc_3]^2 c_3 \alpha_1$$

$$+3\mathrm{sech}[c_1 + xc_2 + yc_3]^2 c_3 \alpha_2 \tanh[c_1 + xc_2 + yc_3]^2)$$

$$(\alpha_3 + \alpha_1 \tanh[c_1 + xc_2 + yc_3] + \alpha_2 \tanh[c_1 + xc_2 + yc_3]^3)$$

$$+x(\mathrm{sech}[c_1 + xc_2 + yc_3]^2 c_2 \alpha_1$$

$$+3\mathrm{sech}[c_1 + xc_2 + yc_3]^2 c_2 \alpha_2 \tanh[c_1 + xc_2 + yc_3]^2))) + \cdots$$

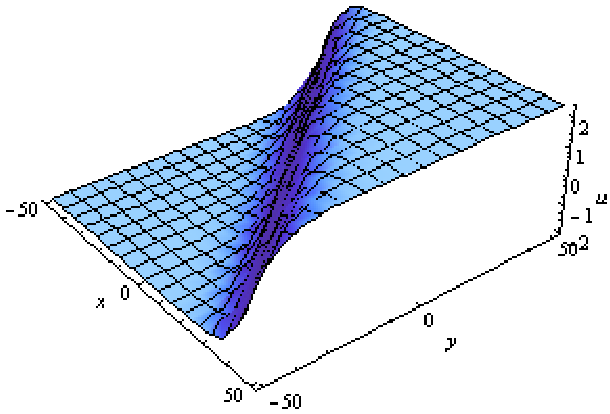

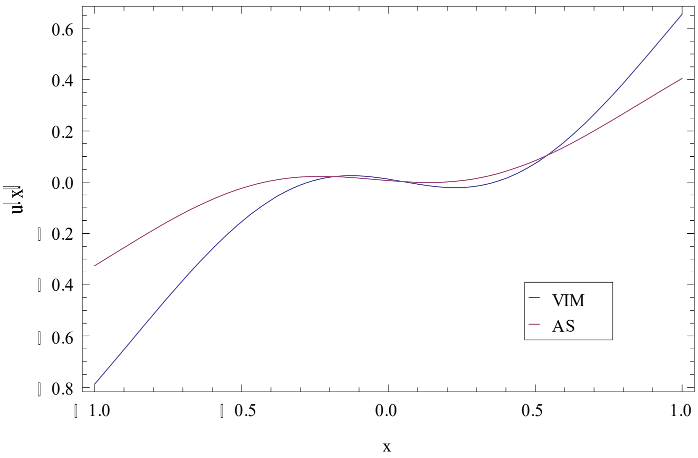

X	VIM	A.S	A.E
0.01	-1.94577×10^{-5}	-9.9658×10^{-6}	$\{9.49194\times10^{-6}\}$
0.02	-1.52127×10^{-5}	-7.78466×10^{-6}	$\{7.42805\times10^{-6}\}$
0.04	-1.09088×10^{-5}	-5.60228×10^{-6}	$\{5.30657\times10^{-6}\}$
0.06	-6.56239×10^{-6}	-3.42707×10^{-6}	$\{3.13533\times10^{-6}\}$
0.08	-2.18994×10^{-6}	-1.26732×10^{-6}	$\{9.2262\times10^{-7}\}$
0.1	2.19172×10^{-6}	8.68827×10^{-7}	$\{1.32289\times10^{-6}\}$
0.12	6.5657×10^{-6}	2.97347×10^{-6}	$\{3.59223\times10^{-6}\}$
0.14	1.09152×10^{-5}	5.03901×10^{-6}	$\{5.87619\times10^{-6}\}$
0.16	1.52236×10^{-5}	7.05819×10^{-6}	$\{8.16543\times10^{-6}\}$
0.18	1.94747×10^{-5}	9.02413×10^{-6}	$\{1.04505\times10^{-5}\}$
0.2	2.36525×10^{-5}	1.09304×10^{-5}	$\{1.27221\times10^{-5}\}$

4.CONCLUSIONS

As a result, nonlinear Pavlov equation have been investigated by the He’s variational iteration method.This variational iteration method solves the problem without any need for discretization of the varibles.The main goal is to show the usefulness of the VIM.The variational iteration method reduces the size of calculations and there is no need of expanding nonlinearities in terms of Adomian polynomials as we do in ADM. Nonlinear scientific models are arise frequently in engineering problems for expressing nonlinear phenomena. Heís variational iteration method provides an efficient method for handling this nonlinear behavior He’s VIM work much effectively , a few approximations can be used to achieved a high degree of accurarcy.

REFERENCES

1. Kumar, Sachin, Monika Niwas, and Abdul-Majid Wazwaz. "Lie symmetry analysis, exact analytical solutions and dynamics of solitons for (2+ 1)-dimensional NNV equations." *Physica Scripta* 95.9 (2020): 095204.
2. BULUT, Hasan. "A COMPARSION AMONG HOMOTOPY PERTURBATION METHOD AND THE DECOMPOSITION METHOD WITH THE VARIATIONAL ITERATION METHOD FOR HELMHOLTZ EQUATION." *Physical Sciences* 3.1: 93-106.
3. Bulut, Hasan. "Boussinesq denklem modeli problemi için sayısal yöntemlerin karşılaştırılması." *Kısmi Diferansiyel Denklemler için Sayısal Yöntemler* 25.4 (2009): 783-796.
4. Inc, Mustafa, and Ebru Cavlak. "On numerical solutions of a new coupled MKdV system by using the Adomian decomposition method and He's variational iteration method." *Physica Scripta* 78.4 (2008): 045008.
5. Alharbi, Abdulghani, and M. B. Almatrafi. "Numerical investigation of the dispersive long wave equation using an adaptive moving mesh method and its stability." *Results in Physics* 16 (2020): 102870.
6. Wang, Xuechuan, Qiuyi Xu ve Satya N. Atluri. "Doğrusal olmayan problemler için varyasyonel yineleme yöntemi ve sayısal algoritmaların kombinasyonu." *Uygulamalı Matematiksel Modelleme* 79 (2020): 243-259.
7. Mungkasi, Sudi. "Sürekli aşılama stratejisine sahip bir SIR salgın modeli için değişken yineleme ve ardışık yaklaşım yöntemleri." *Uygulamalı Matematiksel Modelleme* 90 (2021): 1-10.

8. ERDOĞAN, Hakan ve Safa Bozkurt COŞKUN. "Kısmen Elastik Zemin Üzerindeki Kiriş Titreşiminin Yarı Analitik ve Nümerik Yöntemler ile İncelenmesi." *Bilim ve Teknoloji Enstitüsü Dergisi* 10.4 (2020): 2679-2691.
9. He, Ji-Huan, and Habibolla Latifizadeh. "A general numerical algorithm for nonlinear differential equations by the variational iteration method." *International Journal of Numerical Methods for Heat & Fluid Flow* (2020).
10. Harir, A., et al. "Variational iteration method and differential transformation method for solving the SEIR epidemic model." *International Journal of Differential Equations* 2020 (2020).
11. GONZALEZ-GAXIOLA, O. , et al. Highly dispersive optical solitons with quadraticñcubic law of refractive index by the variational iteration method. Journal of Optics, 2022, 51.1: 29-36
12. DUNAJSKI, Maciej. A class of EinsteinñWeyl spaces associated to an integrable system of hydrodynamic type. Journal of Geometry and Physics, 2004, 51.1: 126-137.
13. HUSSAIN, M.; KHAN, Majid. A variational iterative method for solving the linear and nonlinear klein-gordon equations. Applied

ON P-SASAKIAN MANIFOLDS SATISFYING CERTAIN CURVATURE CONDITIONS

PAKIZE UYGUN

Abstract. The aim of this paper is to study the curvature tensors of P-Sasakian manifold satisfying the conditions $W_1 \cdot W_5 = 0$, $W_1 \cdot W_6 = 0$, $W_1 \cdot W_7 = 0$ and $W_1 \cdot W_8 = 0$. According these cases, P-Sasakian manifolds have been characterized such as η-Einstein and Einstein. Also, we study W_1-pseudo symmetry for a P-Sasakian manifold.

1. Introduction

In 1977, T. Adati and K. Matsumoto defined P-Sasakian and special P-Sasakian manifolds [2], which are special classes of an almost paracontact manifold introduced by I. Sato and K. Matsumoto [17]. Also they studied conformally symmetric P-Sasakian manifolds and they proved that an (2n+1)-dimensional conformally symmetric P-Sasakian manifold is conformally flat and special P-Sasakian.

A. Barman researched the relation of the curvature tensor between the Levi-Civita connection and the semi-symmetric metric connection of a P-Sasakian manifold. They introduced locally $\phi-$projectively symmetric P-Sasakian manifolds with respect to the semi-symmetric metric connection [6].

On the other hand, B. Prasad introduced a pseudo projective curvature tensor on a Riemannian manifold [15]. Since then several geometers studied curvature conditions and obtain various important properties [9, 10, 20]. Motivated by the work of many geometers using different manifolds and different curvature tensors, this paper deals with some curvature properties of the P-Sasakian manifold.

The aim of this paper is to study properties of the some certain curvature tensor in a P-Sasakian manifold we research $W_1 \cdot W_5 = 0$, $W_1 \cdot W_6 = 0$, $W_1 \cdot W_7 = 0$ and $W_1 \cdot W_8 = 0$, where W_1, W_5, W_6, W_7 and W_8 denote the curvature tensors of manifold, respectively. In addition, we research W_1-pseudo symmetry for a P-Sasakian manifold.

2. Preliminaries

An 2n+1-dimensional differentiable manifold M is said to admit an almost paracontact manifold Riemannian structure (ϕ, ξ, η), where ϕ is a $(1,1)-$tensor field, ξ is a vector field and η is a 1-form on M such that:

$$\phi^2(u_1) = u_1 - \eta(u_1)\xi, \tag{2.1}$$

for any vector field $u_1 \in \chi(M)$, where $\chi(M)$ the set of all differential vector fields on M,

$$\eta(\xi) = 1, \eta \circ \phi = 0, \ \phi\xi = 0. \tag{2.2}$$

1991 *Mathematics Subject Classification.* 53C15, 53C25.
Key words and phrases. P-Sasakian Manifold, η-Einstein manifold, W_1-curvature tensor.

Let g be a compatible Riemannian metric with (ϕ, ξ, η), that is,

$$g(\phi u_1, \phi u_2) = g(u_1, u_2) - \eta(u_1)\eta(u_2), \tag{2.3}$$

or equivalently,

$$g(u_1, \phi u_2) = g(\phi u_1, u_2) \quad \text{and} \quad g(u_1, \xi) = \eta(u_1) \;, \tag{2.4}$$

for all vector fields $u_1, u_2 \in \chi(M)$. Then, M becomes an almost paracontact Riemannian manifold equipped with an almost paracontact Riemannian structure (ϕ, ξ, η, g).

An almost paracontact Riemannian manifold is called a P-Sasakian manifold if it satisfies

$$(\widetilde{\nabla}_{u_1}\phi)u_2 = -g(u_1, u_2)\xi - \eta(u_2)u_1 + 2\eta(u_1)\eta(u_2)\xi, \tag{2.5}$$

for all $u_1, u_2 \in \chi(M)$, where $\widetilde{\nabla}$ denotes the Levi-Civita connection of g, then we have the following relation

$$d\eta = 0, \quad \widetilde{\nabla}_{u_1}\xi = \phi u_1, \tag{2.6}$$

$$(\widetilde{\nabla}_{u_1}\phi)u_2 = -g(u_1, u_2)\xi + \eta(u_2)u_1 \tag{2.7}$$

for any $u_1, u_2 \in \chi(M)$. In a P-Sasakian manifold the following relation hold:

$$R(u_1, u_2)\xi = \eta(u_1)u_2 - \eta(u_2)u_1, \tag{2.8}$$

$$R(\xi, u_1)u_2 = \eta(u_2)u_1 - g(u_1, u_2), \tag{2.9}$$

$$R(\xi, u_1)\xi = u_1 - \eta(u_1)\xi, \tag{2.10}$$

$$S(u_1, \xi) = -2n\eta(u_1), \tag{2.11}$$

$$S(\phi u_1, \phi u_2) = S(u_1, u_2) + 2n\eta(u_1)\eta(u_2), \tag{2.12}$$

$$Q\xi = -2n\xi, \tag{2.13}$$

$$\eta(R(u_1, u_2)u_3) = g(u_1, u_3)\eta(u_2) - g(u_2, u_3)\eta(u_1), \tag{2.14}$$

for all $u_1, u_2, u_3 \in \chi(M)$, where Q and S denotes the Ricci operator and Ricci tensor of (M^{2n+1}, g), respectively [4, 16, 17]

A P-Sasakian manifold M is said to be η-Einstein if its Ricci tensor S of type $(0, 2)$ is of the from $S(u_1, u_2) = ag(u_1, u_2) + b\eta(u_1)\eta(u_2)$,where a, b are smooth functions on M. If $b = 0$, then the manifold is also called Einstein [24].

The concept of W_1-curvature tensor was defined by G. Pokhariyal and R. S. Mishra [14]. W_5-curvature tensor, W_6-curvature tensor, W_7-curvature tensor and W_8-curvature tensor of a $2n+1$-dimensional Riemannian manifolds are, respectively, defined

$$W_1(u_1, u_2)u_3 = R(u_1, u_2)u_3 + \frac{1}{2n}[S(u_2, u_3)u_1 - S(u_1, u_3)u_2], \tag{2.15}$$

$$W_5(u_1, u_2)u_3 = R(u_1, u_2)u_3 - \frac{1}{2n}[S(u_1, u_3)u_2 - g(u_1, u_3)Qu_2], \tag{2.16}$$

$$W_6(u_1, u_2)u_3 = R(u_1, u_2)u_3 - \frac{1}{2n}[S(u_2, u_3)u_1 - g(u_1, u_2)Qu_3], \tag{2.17}$$

$$W_7(u_1, u_2)u_3 = R(u_1, u_2)u_3 - \frac{1}{2n}[S(u_2, u_3)u_1 - g(u_2, u_3)Qu_1] \tag{2.18}$$

and

$$W_8(u_1, u_2)u_3 = R(u_1, u_2)u_3 - \frac{1}{2n}[S(u_2, u_3)u_1 - S(u_1, u_2)u_3] \tag{2.19}$$

for all $u_1, u_2, u_3 \in \chi(M)$ [13, 14].

3. On P-Sasakian manifolds satisfying certain curvature conditions

In this section, we obtain necessary and sufficient conditions for P-Sasakian manifolds satisfying the derivation conditions $W_1 \cdot W_5 = 0$, $W_1 \cdot W_6 = 0$, $W_1 \cdot W_7 = 0$ and $W_1 \cdot W_8 = 0$.

Let M be $2n+1-$dimensional P-Sasakian manifold and we denote W_1-curvature tensor by W_1, then from (2.15), we have for later

$$W_1(\xi, u_2)u_3 = (\frac{3n-1}{2n})\eta(u_3)u_2 - g(u_2, u_3)\xi + \frac{1}{2n}S(u_2, u_3)\xi. \tag{3.1}$$

Putting $u_3 = \xi$, in (3.1)

$$W_1(\xi, u_2)\xi = (\frac{3n-1}{2n})(u_2 - \eta(u_2)\xi). \tag{3.2}$$

In (2.16), choosing $u_3 = \xi$ and using (2.8), we obtain

$$W_5(u_1, u_2)\xi = (\frac{3n-1}{2n})\eta(u_1)u_2 - \eta(u_2)u_1 + \frac{1}{2n}\eta(u_1)Qu_2. \tag{3.3}$$

In (3.3), it follows

$$W_5(\xi, u_2)\xi = (\frac{3n-1}{2n})u_2 - \eta(u_2)\xi + \frac{1}{2n}Qu_2. \tag{3.4}$$

In the same way, putting $u_3 = \xi$ in (2.17) and using (2.8), we have

$$W_6(u_1, u_2)\xi = \eta(u_1)u_2 - (\frac{n+1}{2n})\eta(u_2)u_1 - (\frac{n-1}{2n})g(u_1, u_2)\xi. \tag{3.5}$$

Using $u_1 = \xi$ in (3.5), we get

$$W_6(\xi, u_2)\xi = u_2 - \eta(u_2)\xi. \tag{3.6}$$

Again, if we choose $u_3 = \xi$, in equation (2.18), we have

$$W_7(u_1, u_2)\xi = \eta(u_1)u_2 - (\frac{n+1}{2n})\eta(u_2)u_1 + \frac{1}{2n}\eta(u_2)Qu_1. \tag{3.7}$$

Here,if we put $u_1 = \xi$, we obtain

$$W_7(\xi, u_2)\xi = u_2 - \eta(u_2)\xi. \tag{3.8}$$

Finally, if we choose $u_3 = \xi$ in equation (2.19), then it reduces the form

$$W_8(u_1, u_2)\xi = \eta(u_1)u_2 - (\frac{n+1}{2n})\eta(u_2)u_1 + \frac{1}{2n}S(u_1, u_2)\xi. \tag{3.9}$$

It follows in (3.9), we arrive

$$W_8(\xi, u_2)\xi = u_2 - \eta(u_2)\xi. \tag{3.10}$$

Theorem 3.1. *Let M be an 2n+1-dimensional P-Sasakian manifold. Then $W_1 \cdot W_5 = 0$ if and only if M is an $\eta-$Einstein manifold.*

Proof. Assume that $W_1 \cdot W_5 = 0$. This implies that

$$\begin{aligned}(W_1(u_1, u_2)W_5)(u_3, u_4)u_5 &= W_1(u_1, u_2)W_5(u_3, u_4)u_5 - W_5(W_1(u_1, u_2)u_3, u_4)u_5 \\ &\quad - W_5(u_3, W_1(u_1, u_2)u_4)u_5 \\ &\quad - W_5(u_3, u_4)W_1(u_1, u_2)u_5 = 0, \end{aligned} \tag{3.11}$$

for any $u_1, u_2, u_3, u_4, u_5 \in \chi(M)$. Taking $u_1 = u_5 = \xi$ in (3.11) and using (3.1), (3.2), (3.3), for $A = \frac{3n-1}{2n}$ and $B = \frac{1}{2n}$, we obtain

$$\begin{aligned}(W_1(\xi,u_2)W_5)(u_3,u_4)\xi &= W_1(\xi,u_2)(A\eta(u_3)u_4-\eta(u_4)u_3+B\eta(u_3)u_4)\\ &-W_5(A\eta(u_3)u_2-g(u_2,u_3)\xi+BS(u_2,u_3)\xi,u_4)\xi\\ &-W_5(u_3,A\eta(u_4)u_2-g(u_2,u_4)\xi+BS(u_2,u_4)\xi)\xi\\ &-W_5(u_3,u_4)(A(u_2-\eta(u_2)\xi))=0. \qquad (3.12)\end{aligned}$$

Again, taking into account that (3.1), (3.3), (3.4) in (3.12), we get

$$\begin{aligned}&AW_5(u_3,u_4)u_2+2nAB\eta(u_3)\eta(u_4)u_2+B\eta(u_3)S(u_2,u_4)\xi-B^2\eta(u_3)S(Qu_4,u_2)\xi\\ &+A\eta(u_3)g(u_2,u_4)\xi-AB\eta(u_3)S(u_2,u_4)\xi-Ag(u_2,u_3)u_4\\ &-Bg(u_2,u_3)Qu_4+ABS(u_2,u_3)u_4+B^2S(u_2,u_3)Qu_4+AB\eta(u_3)\eta(u_4)Qu_2\\ &+Ag(u_2,u_4)u_3-\eta(u_3)g(u_2,u_4)\xi+Bg(u_2,u_4)Qu_3-ABS(u_2,u_4)u_3\\ &+B\eta(u_3)S(u_2,u_4)\xi-B^2S(u_2,u_4)Qu_3=0. \qquad (3.13)\end{aligned}$$

Choosing $u_4=\xi$, inner product both sides of in (3.13) by $\xi\in\chi(M)$ and using (2.16), (2.11), we have

$$S(u_2,u_3)=2ng(u_2,u_3)+\left(\frac{9n^2-n+2}{n-1}\right)\eta(u_2)\eta(u_3).$$

So, M is an $\eta-$Einstein manifold. Conversely, let M^{2n+1} be an $\eta-$Einstein manifold, i.e. $S(u_2,u_3)=2ng(u_2,u_3)+\left(\frac{9n^2-n+2}{n-1}\right)\eta(u_2)\eta(u_3)$, then from equations (3.13), (3.12) and (3.11), we obtain $W_1\cdot W_5=0$. □

Theorem 3.2. *Let M be an $2n+1$-dimensional P-Sasakian manifold. Then $W_1\cdot W_6=0$ if and only if M is an $\eta-$Einstein manifold.*

Proof. Suppose that $W_1\cdot W_6=0$. This yields to

$$\begin{aligned}(W_1(u_1,u_2)W_6)(u_3,u_4)u_5 &= W_1(u_1,u_2)W_6(u_3,u_4)u_5-W_6(W_1(u_1,u_2)u_3,u_4)u_5\\ &-W_6(u_3,W_1(u_1,u_2)u_4)u_5\\ &-W_6(u_3,u_4)W_1(u_1,u_2)u_5=0, \qquad (3.14)\end{aligned}$$

for any $u_1,u_2,u_3,u_4,u_5\in\chi(M)$. Taking $u_1=u_5=\xi$ in (3.14) and using (3.1), (3.2), (3.5), for $A=-(\frac{n+1}{2n})$, $B=-(\frac{n-1}{2n})$, $C=(\frac{3n-1}{2n})$ and $D=\frac{1}{2n}$, we obtain

$$\begin{aligned}(W_1(\xi,u_2)W_6)(u_3,u_4)\xi &= W_1(\xi,u_2)(\eta(u_3)u_4+A\eta(u_4)u_3+Bg(u_3,u_4)\xi)\\ &-W_6(C\eta(u_3)u_2-g(u_2,u_3)\xi+DS(u_2,u_3)\xi,u_4)\xi\\ &-W_6(u_3,C\eta(u_4)u_2-g(u_2,u_4)\xi+DS(u_2,u_4)\xi)\xi\\ &-W_6(u_3,u_4)(C(u_2-\eta(u_2)\xi))=0. \qquad (3.15)\end{aligned}$$

Again, taking into account that (3.1), (3.5), (3.6) in (3.15), we get

$$\begin{aligned}&CW_6(u_3,u_4)u_2+A\eta(u_4)g(u_3,u_2)\xi-AD\eta(u_4)S(u_2,u_3)\xi-BCg(u_3,u_4)u_2\\ &+BC\eta(u_3)g(u_2,u_4)\xi-g(u_2,u_3)u_4+\eta(u_4)g(u_2,u_3)\xi+DS(u_2,u_3)u_4\\ &-D\eta(u_4)S(u_2,u_3)\xi+BC\eta(u_4)g(u_3,u_2)\xi+g(u_2,u_4)u_3-DS(u_4,u_2)u_3=0. \qquad (3.16)\end{aligned}$$

Taking $u_3=\xi$, using (2.17), (2.11) and inner product both sides of in (3.16) by $\xi\in\chi(M)$, we have

$$S(u_2,u_4)=\left(\frac{5n^2+6n-1}{5n-1}\right)g(u_2,u_4)-\left(\frac{4n^2+4n}{5n-1}\right)\eta(u_2)\eta(u_4).$$

Thus, M is an $\eta-$Einstein manifold. Conversely, let M^{2n+1} be an $\eta-$Einstein manifold, i.e. $S(u_2,u_4)=\left(\frac{5n^2+6n-1}{5n-1}\right)g(u_2,u_4)-\left(\frac{4n^2+4n}{5n-1}\right)\eta(u_2)\eta(u_4)$, then from equations (3.16), (3.15) and (3.14), we arrive $W_1\cdot W_6=0$. □

Theorem 3.3. *Let M be an $2n+1$-dimensional P-Sasakian manifold. Then $W_1\cdot W_7=0$ if and only if M is an $\eta-$Einstein manifold.*

Proof. Assume that $W_1\cdot W_7=0$. This implies that

$$\begin{aligned}(W_1(u_1,u_2)W_7)(u_3,u_4)u_5 &= W_1(u_1,u_2)W_7(u_3,u_4)u_5-W_7(W_1(u_1,u_2)u_3,u_4)u_5\\ &\quad -W_7(u_3,W_1(u_1,u_2)u_4)u_5\\ &\quad -W_7(u_3,u_4)W_1(u_1,u_2)u_5=0, \qquad (3.17)\end{aligned}$$

for any $u_1,u_2,u_3,u_4,u_5\in\chi(M)$. Setting $u_1=u_5=\xi$ in (3.17) and making use of (3.1), (3.2), (3.7), for $A=-(\frac{n+1}{2n})$, $B=\frac{1}{2n}$, $C=(\frac{3n-1}{2n})$ we obtain

$$\begin{aligned}(W_1(\xi,u_2)W_7)(u_3,u_4)\xi &= W_1(\xi,u_2)(\eta(u_3)u_4+A\eta(u_4)u_3+Bg(u_3,u_4)Qu_3)\\ &\quad -W_7(C\eta(u_3)u_2-g(u_2,u_3)\xi+BS(u_2,u_3)\xi,u_4)\xi\\ &\quad -W_7(u_3,C\eta(u_4)u_2-g(u_2,u_4)\xi+BS(u_2,u_4)\xi)\xi\\ &\quad -W_7(u_3,u_4)(C(u_2-\eta(u_2)\xi))=0. \qquad (3.18)\end{aligned}$$

Using of (3.18), (3.7), (3.8) and (3.3), we get

$$\begin{aligned}&CW_7(u_3,u_4)u_2+A\eta(u_4)g(u_3,u_2)\xi-AB\eta(u_4)S(u_2,u_3)\xi+2nBC\eta(u_3)\eta(u_4)u_2\\ &-B^2\eta(u_4)S(u_2,Qu_3)\xi+BC\eta(u_3)\eta(u_4)Qu_2-g(u_2,u_3)u_4+\eta(u_4)g(u_3,u_2)\xi\\ &+BS(u_2,u_3)u_4+g(u_4,u_2)u_3-BS(u_4,u_2)u_3=0. \qquad (3.19)\end{aligned}$$

Taking $u_3=\xi$ and inner product both sides of (3.19) by $\xi\in\chi(M)$ and using (2.18), we have

$$S(u_4,u_2)=\left(\frac{3n-1}{1-5n}\right)^2 g(u_4,u_2)+\left(\frac{6n^2+6n}{1-5n}\right)\eta(u_4)\eta(u_2).$$

This tell us, M is an $\eta-$Einstein manifold. Conversely, let M^{2n+1} be an $\eta-$Einstein manifold, i.e. $S(u_4,u_2)=\left(\frac{3n-1}{1-5n}\right)^2 g(u_4,u_2)+\left(\frac{6n^2+6n}{1-5n}\right)\eta(u_4)\eta(u_2)$, then from equations (3.19), (3.18) and (3.17), we get $W_1\cdot W_7=0$. □

Theorem 3.4. *Let M be an $2n+1$-dimensional P-Sasakian manifold. Then $W_1\cdot W_8=0$ if and only if M is an $\eta-$Einstein manifold.*

Proof. Suppose that $W_1\cdot W_8=0$. This means that

$$\begin{aligned}(W_1(u_1,u_2)W_8)(u_3,u_4)u_5 &= W_1(u_1,u_2)W_8(u_3,u_4)u_5-W_8(W_1(u_1,u_2)u_3,u_4)u_5\\ &\quad -W_8(u_3,W_1(u_1,u_2)u_4)u_5\\ &\quad -W_8(u_3,u_4)W_1(u_1,u_2)u_5=0, \qquad (3.20)\end{aligned}$$

for any $u_1,u_2,u_3,u_4,u_5\in\chi(M)$. Setting $u_1=u_5=\xi$ in (3.20) and making use of (3.1), (3.2), (3.9), for $A=-(\frac{n+1}{2n})$, $B=\frac{1}{2n}$, $C=(\frac{3n-1}{2n})$, we obtain

$$\begin{aligned}(W_1(\xi,u_2)W_8)(u_3,u_4)\xi &= W_1(\xi,u_2)(\eta(u_3)u_4+A\eta(u_4)u_3+BS(u_3,u_4)\xi)\\ &-W_8(C\eta(u_3)u_2-g(u_2,u_3)\xi+BS(u_2,u_3)\xi,u_4)\xi\\ &-W_8(u_3,C\eta(u_4)u_2-g(u_2,u_4)\xi+BS(u_2,u_4)\xi)\xi\\ &-W_8(u_3,u_4)(C(u_2-\eta(u_2)\xi))=0.\end{aligned} \tag{3.21}$$

Using of (3.21), (3.1) (3.9) and (3.10), we get

$$\begin{aligned}&CW_8(u_3,u_4)u_2+A\eta(u_4)g(u_3,u_2)\xi-AB\eta(u_4)S(u_2,u_3)\xi-BCS(u_3,u_4)u_2\\ &+BC\eta(u_3)S(u_2,u_4)\xi-g(u_2,u_3)u_4+\eta(u_4)g(u_3,u_2)\xi+BS(u_2,u_3)u_4\\ &-B\eta(u_4)S(u_2,u_3)\xi+BC\eta(u_4)S(u_2,u_3)\xi+g(u_4,u_2)u_3-BS(u_4,u_2)u_3=0.\end{aligned} \tag{3.22}$$

Taking $u_3=\xi$ and inner product both sides of (3.22) by $\xi\in\chi(M)$ and using (2.19), we have

$$S(u_4,u_2)=(1-n)g(u_4,u_2)+\left(\frac{3n^2+2n-1}{2n}\right)\eta(u_4)\eta(u_2).$$

Thus, M is an $\eta-$Einstein manifold. Conversely, let M^{2n+1} be an $\eta-$Einstein manifold, i.e. $S(u_4,u_2)=(1-n)g(u_4,u_2)+\left(\frac{3n^2+2n-1}{2n}\right)\eta(u_4)\eta(u_2)$, then from equations (3.22), (3.21) and (3.20),we obtain $W_1\cdot W_8=0$. □

Theorem 3.5. *Let M be an 2n+1-dimensional P-Sasakian manifold. Then W_1-pseudo symmetric if and only if M is an $\eta-$Einstein manifold.*

Proof. Lets assume that the manifold M is a W_1-pseudo symmetric manifold. Then, we can write

$$(R(u_1,u_2)W_1)(u_3,u_4,u_5)=\lambda_1 Q(g,W_1)(u_3,u_4,u_5;u_1,u_2) \tag{3.23}$$

for each $u_1,u_2,u_3,u_4,u_5\in\chi(M)$. In this case, we get

$$\begin{aligned}&R(u_1,u_2)W_1)(u_3,u_5)u_4-W_1(R(u_1,u_2)u_3,u_5)u_4\\ &-W_1(u_3,R(u_1,u_2)u_5)u_4-W_1(u_3,u_5)R(u_1,u_2)u_4\\ =\ &-\lambda_1\{W_1((u_1\wedge_g u_2)u_3,u_4,u_5)+W_1(u_3,(u_1\wedge_g u_2)u_5,u_4)\\ &+W_1(u_3,u_5,(u_1\wedge_g u_2)u_4)\}.\end{aligned} \tag{3.24}$$

for each $u_1,u_2,u_3,u_4,u_5\in\chi(M)$. In equation (3.24), if $u_1=u_3=\xi$ is written and (2.9), (3.1), (3.2) are used, we get

$$\begin{aligned}&-W_1(u_2,u_5)u_4+A\eta(u_4)\eta(u_5)u_2-g(u_4,u_5)u_2+BS(u_4,u_5)u_2\\ &-A\eta(u_4)g(u_5,u_2)\xi+\eta(u_2)g(u_5,u_4)\xi-A\eta(u_2)\eta(u_5)u_4-\eta(u_2)g(u_5,u_4)\xi\\ &-A\eta(u_4)\eta(u_5)u_2+\eta(u_5)g(u_2,u_4)\xi-B\eta(u_5)S(u_2,u_4)\xi-A\eta(u_4)\eta(u_2)u_5\\ &+\eta(u_4)g(u_2,u_5)\xi-B\eta(u_4)S(u_2,u_5)\xi+Ag(u_2,u_4)u_5-A\eta(u_5)g(u_2,u_4)\xi\\ =\ &-\lambda_1\{A\eta(u_2)\eta(u_4)u_5-\eta(u_2)g(u_5,u_4)\xi+B\eta(u_2)S(u_5,u_4)\xi-W_1(u_2,u_5)u_4\\ &-A\eta(u_4)g(u_5,u_2)\xi+\eta(u_4)g(u_5,u_2)\xi+2nB\eta(u_4)g(u_5,u_2)\xi-A\eta(u_5)\eta(u_4)u_2\\ &+\eta(u_5)g(u_2,u_4)\xi-B\eta(u_5)S(u_2,u_4)\xi+Ag(u_2,u_4)u_5-A\eta(u_5)g(u_2,u_4)\xi\\ &-A\eta(u_2)\eta(u_4)u_5+\eta(u_4)g(u_5,u_2)\xi-B\eta(u_4)S(u_2,u_5)\xi\}\end{aligned} \tag{3.25}$$

If we choose $u_4=\xi$ and taking inner product on both sides of the last equation by $\xi\in\chi(M)$, we arrive

$$S(u_2,u_5)=\left(\frac{1-n+4n\lambda_1}{\lambda_1+1}\right)g(u_2,u_5)-\left(\frac{(3n-1)(2+\lambda_1)}{\lambda_1+1}\right)\eta(u_2)\eta(u_5).$$

So, M is an $\eta-$Einstein manifold. Conversely, let M^{2n+1} be an $\eta-$Einstein manifold, i.e. $S(u_2,u_5)=\left(\frac{1-n+4n\lambda_1}{\lambda_1+1}\right)g(u_2,u_5)-\left(\frac{(3n-1)(2+\lambda_1)}{\lambda_1+1}\right)\eta(u_2)\eta(u_5)$, then from equations (3.25) and (3.24) and (3.23), we obtain W_1-pseudo symmetric. □

References

[1] A. Atçeken and P. Uygun, Characterizations for totally geodesic submanifolds of (k,μ)-paracontact metric manifolds, Korean J. Math. 28(2020), 555-571.

[2] T. Adati and K. Matsumoto, On conformally recurrent and conformally symmetric P-Sasakian manifolds, TRU Math., 13 (1997), 25-32.

[3] T. Adati and T. Miyazawa, Some properties of P-Sasakian manifolds, TRU Math. 13 (1977), 25-32.

[4] T. Adati and T. Miyazawa, On P-Sasakian manifolds satisfying certain conditions, Tensor (N.S.), 33 (1979), 173-178.

[5] A. Yıldız, M. Turan and B. E. Acet, On para-Sasakian manifolds, Dumlupınar Uni. Fen bilimleri Enstitüsü Dergisi, 24 (2011).

[6] A. Barman, On para-Sasakian manifolds admitting semi-symmetric metric connection, Publication De linstıtut mathematique, 95 (2014), 239-47.

[7] U.C. De and D. Tarafdar, On a type of P-Sasakian manifold, Math. Blkanica (N.S), 7 (1993), 211-215.

[8] D. Kowalezyk., On some subclass of semi-symmetric manifolds, Soochow J. Math., 27 (2001), 445-461.

[9] T. Mert, Characterization of some special curvature tensor on Almost $C(a)$-manifold, Asian Journal of Math. and Computer Research, 29 (1) (2022), 27-41.

[10] T. Mert and M. Atçeken, Almost $C(a)$-manifold on $W_0^{\star}-$curvature tensor, Applied Mathematical Sciences, 15 (15) (2021), 693-703.

[11] B. O. Neill, Semi-Riemannian Geometry with Applications to Relativity, Academic Press, New York, 1983.

[12] C. Özgür and M. M. Tripathi, On P-Sasakian manifolds satisfying certain conditions on the concircular curvature tensor, Turk J. Math., 31 (2007), 171-179.

[13] G. P. Pokhariyal, Relativistic significance of curvature tensors, Internat. J. Math. Sci., 5 (1) (1982), 133-139.

[14] G.P. Pokhariyal and R.S.Mishra, Curvature tensors and their relativistic significance II, Yokohama Math. J., 19 (2) (1971), 97-103.

[15] B. Prasad, A pseudo projective curvature tensor on a Riemannian manifold, Bull. Calcutta Math. Soc., 94 (3) (2002), 163-166.

[16] I. Sato., On a structure similar to the almost contact structure, 30 (1976), 219-224.

[17] I. Sato and K. Matsumoto., On P-Sasakian manifolds satisfying certain conditions, Tensor (N.S), 33 (1979), 173-178.

[18] Z.I. Szabo, Structure theorems on Riemannian spaces satisfying $R(X,Y)\cdot R=0$, I: The local version, J. Differential Geom., 17 (4) (1982), 531-582.

[19] M.M. Tripathi and P. Gupta, $T-$curvature tensor on a semi-Riemannian manifold, 4 (1) (2011), 117-129.

[20] P. Uygun and M. Atçeken, On (k,μ)-paracontact metric spaces satisfying some conditions on the $W_0^{\star}-$curvature tensor, NTMSCI, 9 (2) (2021) 26-37.

[21] P. Uygun, M. Atçeken and S. Dirik, Some curvature results on Kenmotsu metric spaces, Bull. Int. Math. Virtual Inst, 12 (2) (2022), 243-251.

[22] P. Uygun, M. Atçeken and S. Dirik, On Kenmotsu metric spaces satisfying some conditions on the W_1-curvature tensor, Filomat, (Kabul edildi).

[23] K. Yano and S. Bochner, Curvature and Betti numbers, Annals of Mathematics Studies, Princeton University Press, 32 (1953).

[24] K. Yano and M. Kon, Structures on manifolds, Series in Pure Math., World Sci., 3 (1984).

*Department of Mathematics, Faculty of Arts and Sciences, Tokat University, 60100, Tokat, Turkey

E-mail address: pakizeuygun@hotmail.com

INVESTIGATION OF THE EFFECTS OF AMBİENT VIBRATIONS FILTERED AT DIFFERENT FREQUENCY RANGE ON THE DYNAMIC BEHAVIOR OF THE BUILDING

Oğuzhan Çelebi[1], Barış Bayrak[2], Mahmut Kılıç[1], Abdulkadir Cüneyt Aydın[1]

[1]Department of Civil Engineering, University of Ataturk, Erzurum, Turkey

[2]Department of Civil Engineering, University of Kafkas, Kars, Turkey

celebioguzhan@atauni.edu.tr

Abstract

Ambient vibrations, which are constantly and intensely felt in buildings, significantly affect the dynamic properties of the building such as the natural dominant period, damping ratio, floor displacements and accelerations that change over time. Ambient vibrations caused by explosions, the passage of heavy vehicles and heavy human and vehicle traffic are recorded with sensors such as accelerometers and speedometers. Otherwise, considering the vibrations that are not related to the structure in the estimation of the dynamic behavior of the structure may lead to incorrect calculations. In this study, ambient vibrations taken from a structure using accelerometers with a measurement capacity of 3g acceleration and frequency ranges of 0.1-50 Hz were filtered in the frequency range of 0.1-10 Hz, 0.1-25 Hz and 0.1-50 Hz with bandpass filtering technique and used in structural analysis. In order to investigation the effect of filtered ambient vibrations in the study, a 9 m high steel state structure with 1 opening in the X direction and 7 spans in the Y direction with heavy traffic and noise flow was used. In order to represent the ambient vibrations in the structure, so-called acceleration-frequency curves were drawn and modal parameters were determined. By using the filtered ambient vibrations, the dynamic responses of the structure are calculated and the structural damping, structure acceleration and displacements are approximately calculated. The results of the study show that filtering in the 0.1-25 Hz frequency range is more appropriate in order to see the suitability of the structure in terms of dynamic behavior and the effects of modes such as bending, torsion and lateral torsional buckling. However, it is predicted that these frequency ranges may change in structures with different span distances and heights. The study showed that correct filtering and frequency ranges should be applied in order to determine the dynamic behavior of a structure under the influence of ambient vibrations.

Keywords: Ambient vibrations; Filtration; Frequency time domain; Structural dynamic behavior.

1. INTRODUCTION

Today, ambient vibrations that affect the dynamic behavior of structures are measured with devices such as accelerometers and speedometers. Using these test results, the modal parameters and dynamic behavior of the structure can be determined based on system diagnostic techniques [1]. In addition, ambient vibration tests can also determine the health of the structure, its evaluation and damage detection [2]. However, it is necessary to determine which data of the measured ambient vibrations belong to the structure itself. Otherwise, it would be possible to take into account many complex signals such as noise in determining the dynamic behavior of the structure. Filtering techniques are applied in order to obtain the effective frequency ranges of the measurements taken in the time domain and the parameters representing the dynamic behavior such as acceleration [3]. In addition, in order for the data measured as complex to be understood more clearly, Fourier transforms are taken and transferred to the frequency environment, and it is determined how much acceleration the structure produces at which frequency values. [4-6].

In the literature, there are many studies on the dynamic behavior of structures under the influence of ambient vibrations [7-9]. Kennedy (1947) was the first to propose modal analysis of the structure with ambient vibration recordings [10]. Beyen (2021) examined the damages in the Fatih Mosque in the frequency domain where it was subjected to ambient stress and free vibration [11]. Limongelli analyzed the dynamic behavior of the structure by defining the ambient vibration recording obtained by optimizing the position of the sensors at certain frequency ranges with the Kalman filter [12]. Ikeda et al (2022) studied the validation of multi-degrees-of-freedom building modeling for seismic response estimation based on microtremor measurement [13]. Akhlag et al (2022) evaluated the tower of a 90 m high building under ambient vibrations as structural [14].

In this study, the dynamic behavior of the steel-state structure taken from the 7-span steel-state structure was investigated. The modal frequencies of the structure were determined by converting the measurements taken in the time domain to the frequency domain with Fourier transforms. Vibrations were bandpass filtered in the range of 0.1-10 Hz, 0.1-25 Hz and 0.1-50 Hz in order to determine the structure response approximately accurately. The dynamic behavior of the steel state structure such as modal parameters, damping ratios and acceleration under the influence of filtered vibrations are shown in time steps.

2. GENERAL PROPERTIES OF METHOD

2.1. Definition of Steel Industrial Structure

The steel industrial structure used in the study has 7 spans, 6 m in the X direction, 20 m in the Y direction, with a single height of 9 m (Figure 1). S275 N/NL element material class specified in Turkish Steel Structures Regulation (TSSR), 8.8 material class as bolt and E480 material class as welding were preferred. The steel state structure is located within the borders of Erzurum Province, Turkey, at 40.5 latitude and 41.8 longitude. Earthquake parameters can be obtained according to the local soil class of the building by entering the latitude and longitude information of the building from the Turkey Hazardous Earthquake Ground Movement Map created by AFAD. According to the geotechnical studies, the local soil class of the structure was determined as ZD soil class (medium hard sand, gravel) according to TBEC [15]. The columns of the steel industrial structure are HEA450, the lateral stability beams are IPE240, the upper truss and lower truss beams are IPE360, the truss braces and uprights are IPE180, and the inter column braces are L150x15.

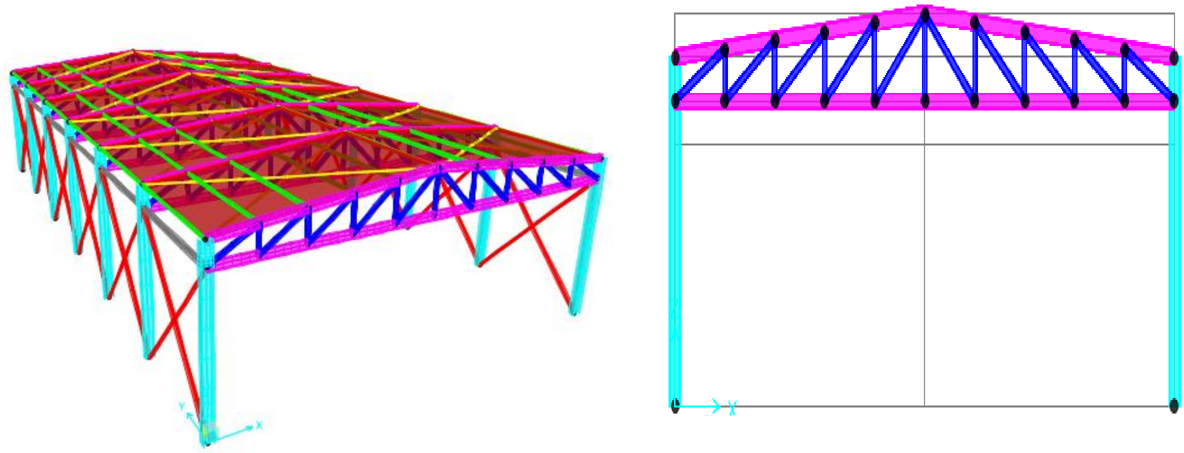

Figure 1. The structure of steel ındustrial

2.2. Signal Processing

On account of this structural simplicity and on-chip integration compatibility, it is of interest to develop high-performance bandpass filters with flat, low sidebands and narrow, high-efficiency passbands using analogous architectures. Previous related work has mostly focused on theoretical design and explanation of the underlying physics [16-19]. In the study, the data collected in the time history were filtered with the bandpass filtering technique in the frequency range of 0.1-10 Hz and 0.1-25 Hz.

The general dynamical equation is used to calculate the possible reactions of the accelerometer records in the time history. The general dynamical equation is solved using the Newmark Hill method. The acceleration and displacement spectra were obtained from the obtained solutions [4]. In Equation 1, f(t) is the filtered accelerations multiplied by the steel ındustrıal structure weight. Also, k represents the structural stiffness, c represents the structural turning and m represents the structural mass.

$$m\ddot{x} + c\dot{x} + kx = f(t) \tag{1}$$

Dynamic systems may have frequency properties that can change over time or have unusual interruptions or anomalies because of inelastic deformations at different times in their service life. Using the sinusoid type hyperbolic function as the basis, decomposing non-stationary behavior in finite length signal into sinusoids in usual Fourier Transformation (FT) may not capture and properly represent all components of the entire signal and frequency change in time. Fourier transform, F(w) of a time series f(t) and the inverse Fourier transform as seen in Eq. (2) can be obtained by combining the whole signal and this causes to get lost the local features changing with time and frequency. When F(w) is transformed back to time domain, the transformed signal that will repeat itself every time interval t shows no localization in time [11].

$$F(w) = \int_{-\infty}^{+\infty} f(t)e^{-iwt}dt \quad (1)$$

2.3. Calculating the Approximate Damping Ratio

The approximate damping ratio was calculated according to Figure 2 and Equation 3 defined in the Peak Picking Method, taking into account the acceleration frequency curve obtained by converting the acceleration data in the time history field resulting from ambient vibration in the structure to the frequency domain.

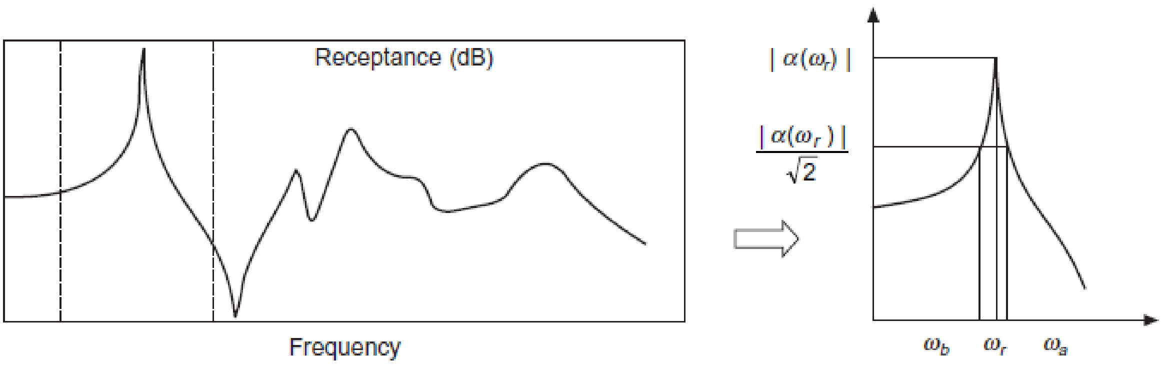

Figure 2. Peak Picking method [20]

$$\rho_r = \frac{w_b - w_a}{2w_r} \quad (3)$$

3. APPLİCATİONS

Figure 3 presents the environmental vibration recording taken in the time history. The environmental vibration recording was passed through a Bandpass filter between 0.1-10 Hz and 0.1-25 Hz, and the noise recordings were extracted as in Figure 4. The highest acceleration value in the unfiltered data of ambient vibration was determined as 3.5x10^{-8}g. The highest acceleration values of the filtered data in frequency ranges of 0.1-10 Hz, 0.1-25 Hz and 0.1-50 Hz were determined as 1.8x10^{-7}g, 2.2x10^{-6}g and 4.1x10^{-8}g, respectively.

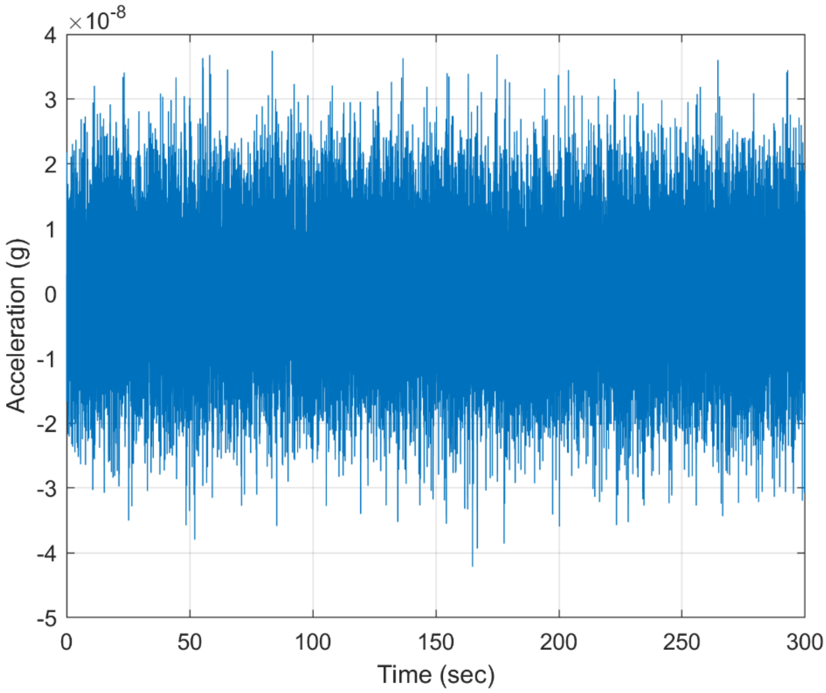

Figure 3. Ambient vibration data

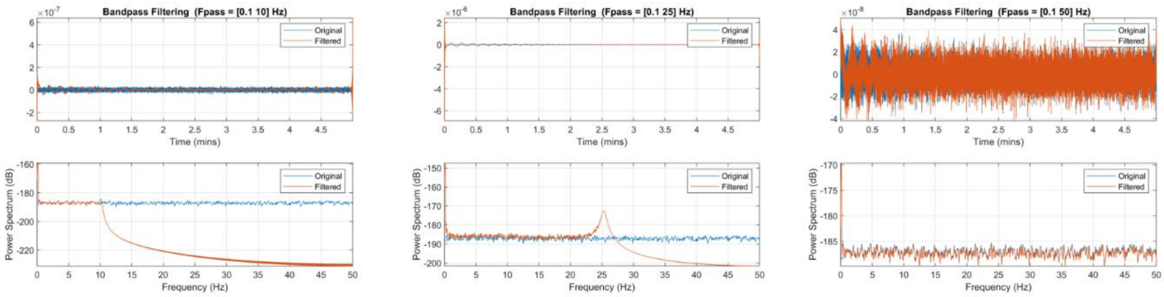

Figure 4. Filtered environmental vibration data

The spectrum curves of the filtered ive data obtained as a result of the solution of the general dynamical equation specified in Equation 1 with the Newmark method are presented in Figure 5 and the displacement spectrum curves are presented in Figure 6. In Figure 5, the spectral acceleration values of unfiltered environmental vibration, filtered acceleration data in the frequency range of 0.1-10 Hz, 0.1-25 Hz and 0.1-50 Hz were determined to be $5.8x10^{-6}$g, $2.5x10^{-5}$g, $1x10^{-4}$g and $6.0x10^{-6}$g. In Figure 6, the spectral displacement values of the unfiltered environmental vibration in the 0.1-10 Hz, 0.1-25 Hz and 0.1-50 Hz frequency ranges of the filtered acceleration data are $1.6x10^{-7}$m, $2.5x10^{-6}$m, $0.9x10^{-5}$m and $1.2x10^{-6}$m It was determined. The results show that filtered data in the 0.1-25 Hz frequency ranges produce lower acceleration and displacement spectrum values. It shows that the filtered data values between 0.1-50 Hz constitute the same value as the filtered data. Therefore, filtered data in the frequency ranges of 0.1-10 Hz and 0.1-25 Hz were used in the structural analysis.

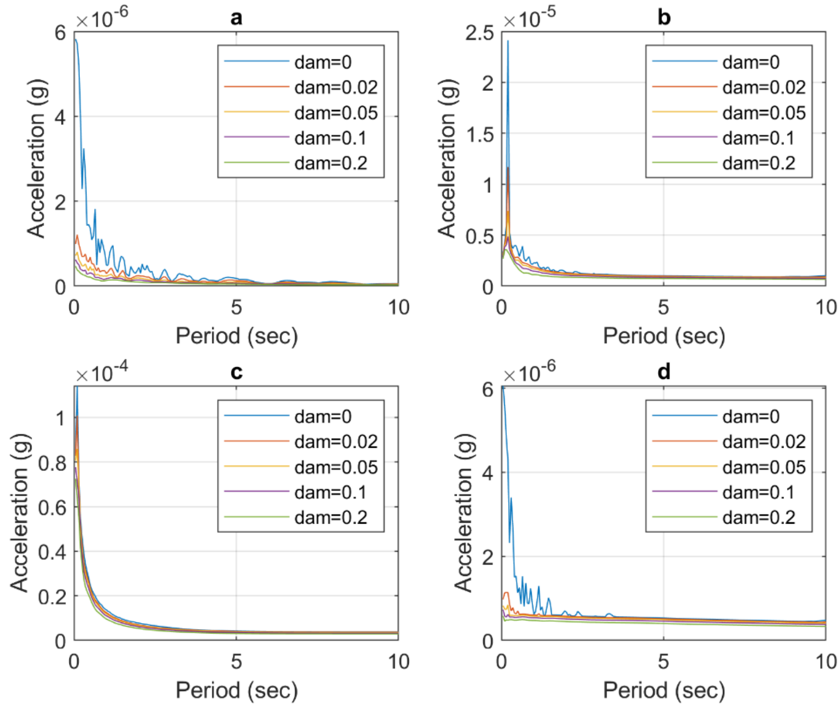

Figure 5. Pseudo accelerations spectrums for filtering data's

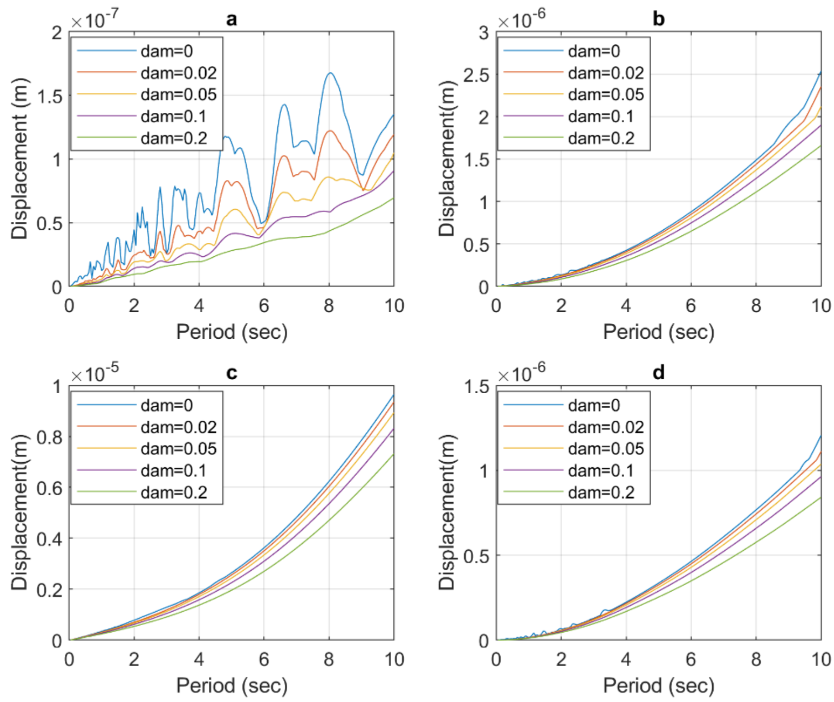

Figure 6. Pseudo displacement spectrums for filtering data's

Figure 7 and Figure 8 show the Fourier transforms of the structural responses filtered between 0.1-10 Hz and 0.1-25 Hz, respectively. In the dominant frequency ranges, the highest amplitudes of the filtered data in the range of 0.1-10 Hz and 0.1-25 Hz, respectively, were found to be 1.2x10^{-7}g and 0.65x10^{-5}g. Figure 8 shows 2 modes of filtered structural response in frequency ranges of 0.1-25 Hz and 1 mode of structural response in frequency ranges of 0.1-10 Hz.

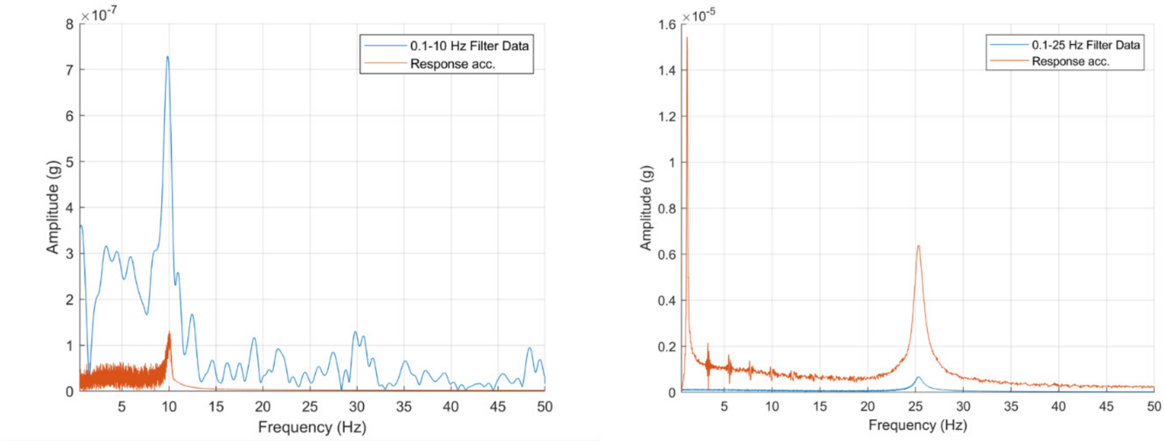

Figure 7. The response of the structure to the ambient vibrations affecting the structure in the frequency environment

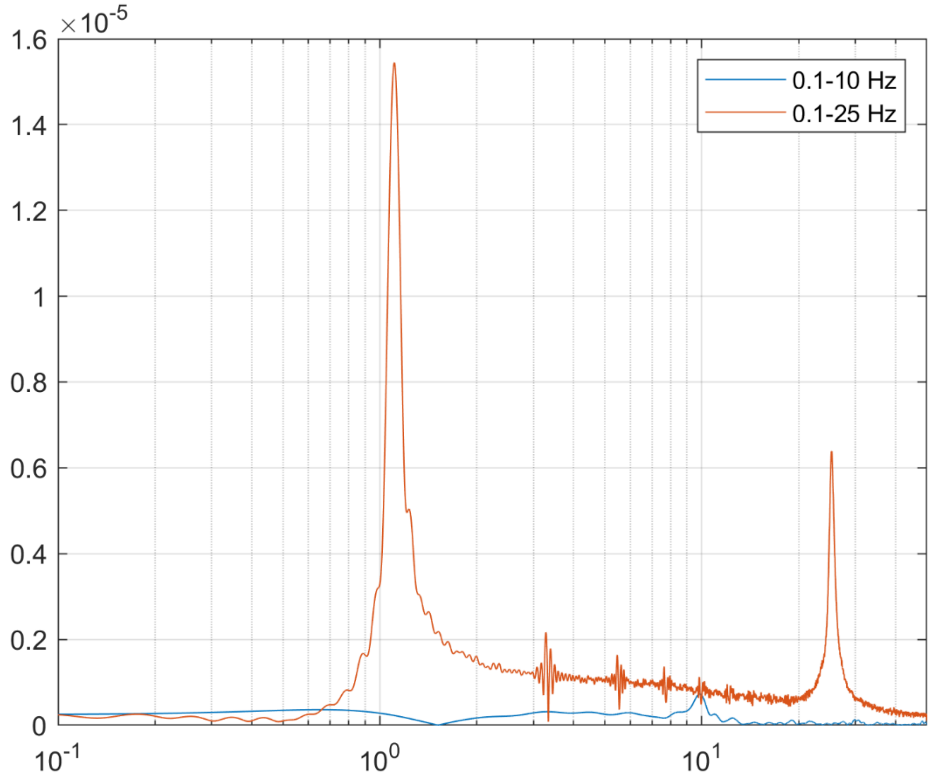

Figure 8. Fourier transforms of filtered structural response accelerations

Table 1 shows the modal parameters obtained as a result of the modal analysis of the structure and the ambient vibration analysis. The modal parameters obtained as a result of environmental vibration analysis in the building were calculated according to Equation 3. As a result of the modal analysis of the structure, the dominant frequency values obtained as a result of the ambient vibration analysis in the frequency ranges of 0.1-10 Hz and 0.1-25 Hz were determined as 6.59 Hz, 10.02 Hz and 27.3 Hz. In addition, the damping ratios were calculated as 0.025, 0.011 and 0.064, respectively.

Table 1. The modal parameters of the steel industrial structure under the influence of ambient vibration

Modal Parameters	Frequency (Hz)	Period (sec)	Damping Ratio
Modal Analysis	6.59	0.154	0.025
0.1-10 Hz Vibrations	10.02	0.099	0.011
0.1-25 Hz Vibrations	27.3	0.036	0.064

Figure 9 shows the time-varying acceleration values obtained as a result of the structural analysis in the time history. The filtered structural accelerations between 0.1-10 Hz and 0.1-25 Hz are shown to be $2x10^{-6}$g and $6x10^{-5}$g, respectively.

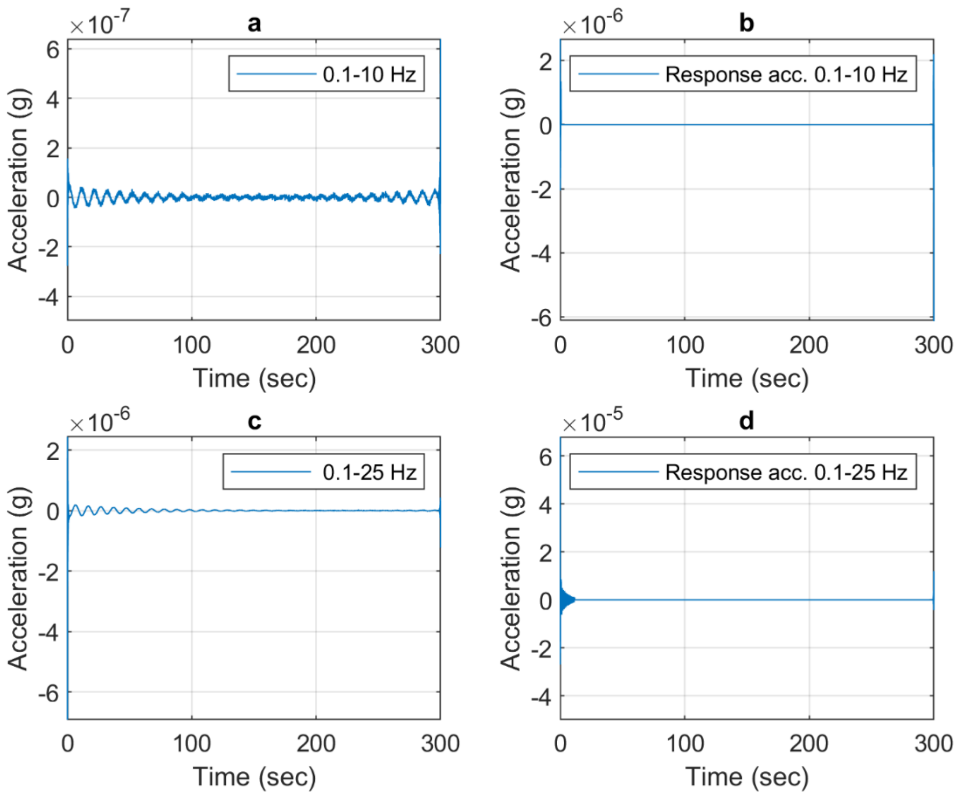

Figure 9. The structural response acceleration in the time domain a) filtered acceleration data between 0.1-10 Hz b) filtered structural response accelerations between 0.1-10 Hz c) filtered acceleration data between 0.1-25 Hz b) filtered structural response accelerations between 0.1-25 Hz

4. CONCLUSIONS

Ambient vibration analysis was carried out in the steel industrial structure with a 3g accelerometer and an accelerometer device that can measure in the frequency range of 0.1-50 Hz. The measurements taken were used in the study by passing them through the Bandpass filter in the frequency ranges of 0.1-10 Hz, 0.1-25 Hz and 0.1-50 Hz. The results of ambient vibration analysis applied in the study are summarized below.

- The results of the study show that filtering in the 0.1-25 Hz frequency range is more appropriate in order to see the suitability of the structure in terms of dynamic behavior and the effects of modes such as bending, torsion and lateral torsional buckling. The structure showed a damping of 0.064 against the filtered ambient vibrations between 0.1-25 Hz. It has also been observed that with the 2E5 structure response acceleration, it accelerates less than other vibrations. However, it is predicted that these frequency ranges may change in structures with different span distances and heights.
- The study showed that correct filtering and frequency ranges should be applied in order to determine the dynamic behavior of a structure under the influence of ambient vibrations.

REFERENCES

1. Ramos, L.F.; Marques, L.; Lourenço, P.B.; De Roeck, G.; Campos-Costa, A.; Roque, J. Monitoring historical masonry structures with operational modal analysis: Two case studies. Mech. Syst. Signal. Process. 2010, 24, 1291–1305.
2. Bayraktar, A.; Sevim, B.; Altunisik, A.C.; Türker, T. Analytical and operational modal analyses of Turkish style reinforced concrete minarets for structural identification. Exp. Tech. 2009, 33, 65–75.
3. L.F. Ramos, L. Marques, P.B. Lourenço, G. De Roeck, A. Campos-Costa, J. Roque, Monitoring historical masonry structures with operational modal analysis: two case studies, Mech. Syst. Signal Process. 24 (2010) 1291–1305.
4. Chopra, A. (1995). Dynamics of structures: theory and applications to earthquake engineering. Prentice Hall, Englewood Cliffs, NJ.
5. S. Rajasekaran, Structural dynamics of earthquake engineering, Boca Raton Boston New York Washington, DC, 2009.
6. Beyen, K., 2005, 'Fatih Camii Yapısal Davranışının Ve Dinamik Özelliklerinin Çevrel Ölçümler Işığında Tanımlanması', T.C. İstanbul Büyük Şehir Belediyesi İski Genel Müd., Mimtaş ile T.C. Boğaziçi Ü., T.C. Yıldız Teknik Ü. arasında İstanbul Fatih Camii ve Külliyesi Alt ve Üst Yapı Onarım – Restorasyon Projesi, İstanbul (in Turkish).
7. Diaferio, M.; Foti, D.; Giannoccaro, N.I. Non-destructive characterization and identification of the modal parameters of an old masonry tower. In Proceedings of the 2014 IEEEWorkshop on Environmental Energy and Structural Monitoring Systems (EESMS), Naples, Italy, 17–18 September 2014; IEEE: New York, NY, USA, 2014; pp. 1–6.

8. Yousefianmoghadam, S.; Behmanesh, I.; Stavridis, A.; Moaveni, B.; Nozari, A.; Sacco, A. System identification and modeling of a dynamically tested and gradually damaged 10-story reinforced concrete building. Earthq. Eng. Struct. Dyn. 2018, 47, 25–47.
9. He, X.; Moaveni, B.; Conte, J.P.; Elgamal, A.; Masri, S.F. System identification of alfred zampa memorial bridge using dynamic field test data. J. Struct. Eng. 2009, 135, 54–66.
10. Allemang, R.J. 1984: Experimental Modal Analysis Bibliography. Proceedings of the 2nd International Modal Analysis Conference, Orlando, Florida, 1085–1097.
11. K. Beyen, Damage ıdentification analyses of a historic masonry structure in T-F domain, Journal of Technical, 604 (2021): 10577-10610.
12. Limongelli MP. Optimal location of sensors for reconstruction of seismic responses through spline function interpolation. Earthquake Eng Struct Dyn. 2003;32(7):1055–1074.
13. Ikeda Y., Kurata M., Xie J., Verification ofmulti-degree-of-freedom building modelling for seismic response prediction based on microtremor measurement. Earthquake Engng Struct Dyn. 2022;51:1610–1635.
14. Akhlag H., Butt F., Alwetaishi M., Riaz M., Banjeddou O., Hussein E.E., Structural Identification of a 90 m High Minaret of a Landmark Structure under Ambient Vibrations. Buildings, 2022, 12, 252. https://doi.org/10.3390/ buildings12020252.
15. TBEC (2018), Turkish Building Earthquake Code, The Disaster and Emergency Management Presidency of Turkey, 18 18th of March of Official Gazette, Ankara, Turkey.
16. S. Tibuleac and R. Magnusson, IEEE Phot. Tech. Lett. 9, 464 (1997).
17. S. Tibuleac and R. Magnusson, Opt. Lett. 26, 584 (2001).
18. M. Shokooh-Saremi and R. Magnusson, Opt. Lett. 32, 894 (2007).
19. Y. Ding and R. Magnusson, Opt. Lett. 29, 1135 (2004).
20. He J., Fu Z.F., Modal Analysis. Oxford Auckland Boston Johannesburg Melbourne New Delhi, 2001.

ARDUINO BASED DIGITAL TACHOMETER WITH TRACKING PROGRAM

Furkan ŞİMŞEK[1], **Şükrü KİTİŞ**[1]

[1] Department of Electrical-Electronic Engineering, University of Dumlupınar, Kutahya, Turkey

furkansimsek2@outlook.com, sukrukitis@dpu.edu.tr

Abstract

Digital RPMmeter (tachometer), which is frequently and widely used today, plays an important role in control circuits and systems. In this project, a prototype of this equipment was created with Arduino technology. The biggest auxiliary in the calculation of the number of motor movements per minute is IR sensor. In the structure of IR sensors, there is an IR LED (light-emitting diode) transmitter and an IR photo-diode receiver. Generally, the light produced by e infrared LED from ground to be measured is reflected by generating emission, and a part of produced emission is reflected back to IR photo-diode receiver. The intensity of the response in this reflection event constitutes output of the sensor. This prototype created with Arduino, apart from standard ones, will be very popular because it can be programmed. C# was chosen as programming language. Due to high cost of existing tachometers, the prototype also provides benefits in this context.

Keywords: Arduino, RPM, tachometer, IR

1.INTRODUCTION

1.1 The Aim of the Project

Engines, which are used to alleviate and facilitate human workload, are used in many machines in different areas. Generally, motors used in industry are expected to operate at rated speed. Rated speed can be achieved with rated voltage and frequency. Voltage imbalances cause serious problems in most engines. Tachometer devices are used to monitor asynchronous event in engine speed caused by these faults.

Tachometers work with logic of calculating the intensity of reflection and return of infrared light, which is invisible to the human eye, without any contact with engine and gear. The amount of rotation per unit time is defined as RPM (revolution). The unit of measurement in tachometers is also called RPM.

Revolution meters, which are especially needed in industrial and vocational education institutions, can obtain different results based on the speed of controlled mechanism.

Today's standard tachometers are limited to showing only a single value. This problem presents a serious problem in instantaneous control and evaluation of data. There is a need for instant recording and visualization of the measured values. These problems are eliminated in the computer aided circuit made in this study.

2. GENERAL PROPERTIES OF METHOD

2.1 Items Used and Their Properties

2.1.1 Arduino

Arduino is open-source software-based and easy-to-use prototype hardware. This hardware, which has a micro-controller inside, can be operated according to its purpose with codes prepared in computer environment. Arduino IDE (Integrated Development Environment) is used to upload these codes. Data from sensors connected with Arduino can be read with Arduino IDE and electronic equipment can be controlled with these inputs.

It is a platform that has emerged as an alternative to micro-controllers such as PIC (Peripheral Interface Controller) and ARM (Advanced RISC Machine), which can be programmed more easily and enables complex operations with short codes thanks to its wider library support. Micro-controllers provide convenience in terms of use because they are easily programmable thanks to their own libraries. It has inputs that can process digital and analog data. It can receive data from other devices and produce data such as sound and light [1].

2.1.1.1 Arduino Nano

Arduino Nano (figure 1) is a classic style microcontroller board with the smallest dimensions among Arduino range. There are pin headers that provide easy connection for connections in circuits to be established in Arduino Nano, and a computer connection is provided with a Mini-B USB connector. The biggest difference and advantage of Arduino Nano from Arduino Uno model is that it has a more minimalist design in size and does not require an external power connection. ATmega328 CPU (Central Processing Unit), which is microcontroller on Arduino Nano, runs at 16 MHz and has 32 KB Flash memory [5,9].

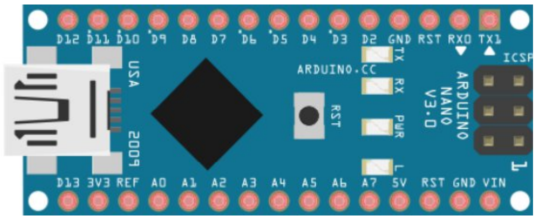

Figure 1. Arduino Nano V3.0 microcontroller board image

2.1.2 IR Receiver Module

IR LEDs, which have no difference with normal LEDs in terms of image, works in range of 3.9x10^14 -3x10^11 Hz, which is a frequency that human eye cannot perceive. Cellular structure of human eye sees up to red color. Colors beyond red are called infrared [8,9].

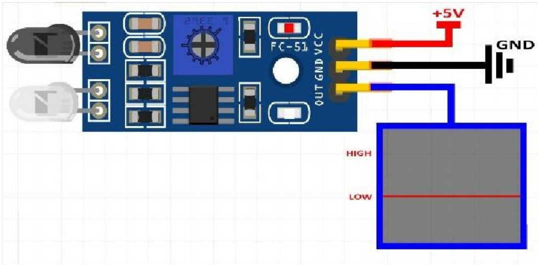

Figure 2. Image of No IR Transceiver Module Detection

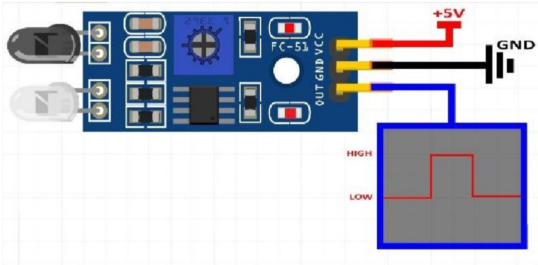

Figure 3. IR Transceiver Module Detection Status Image

As seen in Figure 2, no fluctuation is observed in the output due to idle operation of the IR Transceiver Module. The signal light on the module turns white because no object is detected.

As seen in Figure 3, a square wave is observed at the output due to detection of the IR Transceiver Module. The signal light on the module turns red because it detects an object.

2.1.3 16x2 LCD Screen

LCDs (Liquid Crystal Displays) can display fixed characters (as in digital watches), as well as there are color graphic LCDs in computers and mobile phones. This type of LCD (figure 4) usually has an SPI communication interface. Since micro-controller cards such as Arduino do not have enough memory to create advanced graphics, they can generally be used to draw simple graphics or to display photo and image files on media such as SD cards [3].

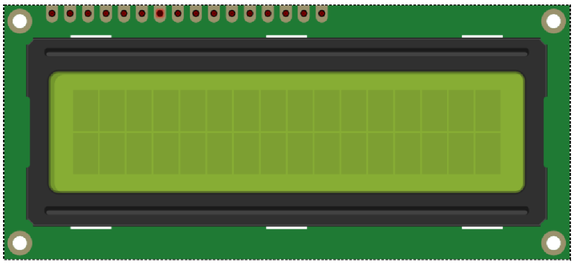

Figure 4. 16x2 LCD Screen Image

2.2 Project Device Architecture

As seen in Figure 5, established circuit was mounted in a plastic raw material lidded box obtained from a 3D (Three-Dimensional) printer. The box size was calculated as 10cm x 2cm. There are 2 slots for LEDs of the IR Transceiver Module and 1 slot for Usb socket of Arduino Nano on the outside of the box. A power button was added to the box so that the device can be turned on and off. Flex filament was used to minimize possible damage to the box. Arduino Nano and IR Transceiver Module were fixed to inside of the box with hot silicon. After necessary wiring was placed on relevant pins, it was soldered and strengthened. 16x2 LCD Screen was also fixed to the box with hot silicone.

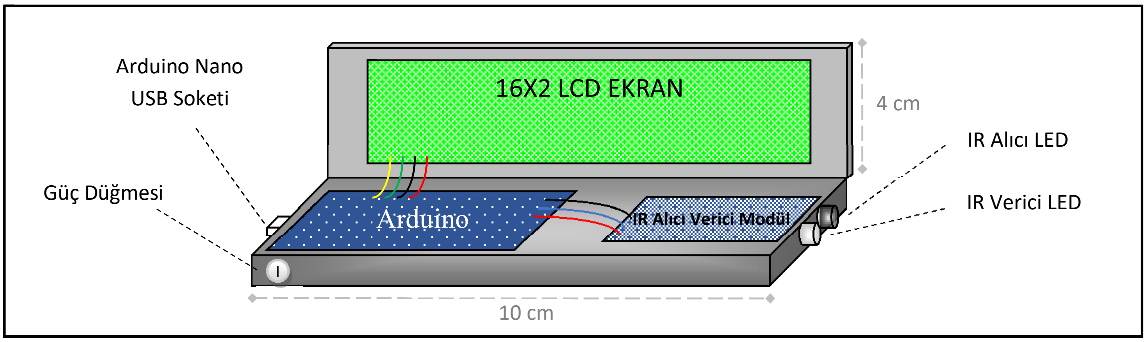

Figure 5. Schematic Drawing Image of Arduino Nano Based Digital Tachometer Device

2.3 System Architecture

As seen in Figure 6 and Figure 7 the main equipment of the system is Arduino Nano R3 in this project. Arduino Nano plays the role of compiler and organizer between IR sensor and the computer.

An IR transceiver sensor module was used for the transfer of mechanical part, a 16x2 LCD screen was used to display instant information, and an LCD I2C serial interface module, which facilitates connection of the LCD screen to Arduino nano, was used. A formulation was developed for analysis and calculation of values read from the IR sensor and added to the project in Arduino coding.

Information coming from the IR transceiver sensor module to the Arduino Nano R3 board is displayed in real time on the LCD screen and in software prepared in computer environment by passing through code filter. The value received in the software is listed instantaneously as a graphic and data set. It is aimed to reach desired result by limiting incoming data.

Some of the advantages of the system is to receive a string of errors from the system when the system goes beyond the desired by entering lowest speed and maximum speed values entered and instantaneous evaluation of the general situation in graphical environment. The system allows created graphic to be saved in picture format. In addition, it enables to record the data recorded in data set on a per-second basis in Microsoft Office Excel format.

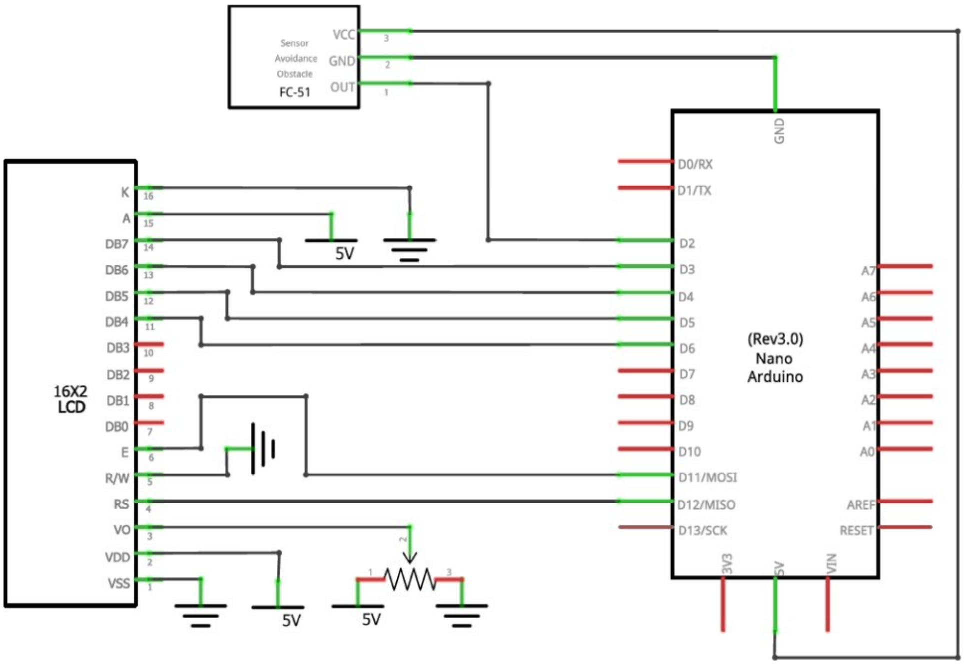

Figure 6. Schematic Drawing Image of Arduino Based Digital Tachometer Circuit

Figure 7: Prototype model

2.4 Calculation Formula

RPM has no equivalent in SL (Système International D'unités) System of Units. RPM is a cyclical concept. Simply, the number of revolutions per minute is counted as the equivalent of RPM expression. In order to measure RPM, some values of motor to be measured must be known [6,7].

In order to calculate RPM;

StartTime and endTime variables in the loop give a result from startTime-endTime formula at each pulse. This result allows the calculation of how many seconds for 1 full round is completed. Since the completion time of 1 full round is based on seconds, it must be converted to milliseconds.

$$\frac{2\pi}{60}\, rad/s = \frac{1}{60} Hz \ = 1\, rpm$$

Based on this formula;

$$time = \frac{startTime - endTime}{1000}$$

Time value is obtained by dividing the difference of startTime in milliseconds, which is the start time, and endTime in milliseconds, which is the end time, by 1000. The value of 1000 here is to express millisecond value in seconds.

$$rps(revs\ per\ second) = \frac{1}{time}$$

RPS value is needed to calculate RPM value. RPS value can be explained as the number of revolutions per second.

In order to find RPS value, it is necessary to reverse calculated time value.

$$rpm(revs\ per\ minutes) = rps * 60$$

RPM value is the number of revolutions per minute and is RPS multiplied by 60.

The developed formula is as follows;

$$RPM(Revs\ Per\ Minutes) = rps * 60 = \frac{1}{time} * 60$$

$$= \frac{1}{\left(\frac{startTime - endTime}{1000}\right)} * 60$$

$$= \frac{60000}{startTime - endTime}$$

rps: revs per second
rpm: revs per min
startTime: when the measurement mark on the rotary mechanism starts to be read
endTime: when the reading of the measurement mark on the rotary mechanism is complete

With this calculation formula, the number of revolutions per minute gives very close results with the correct value, although it is not precise. Depending on the hardware conditions, calculation formulation can be modified [10,11].

3.APPLICATIONS

3.1 Program Algorithm

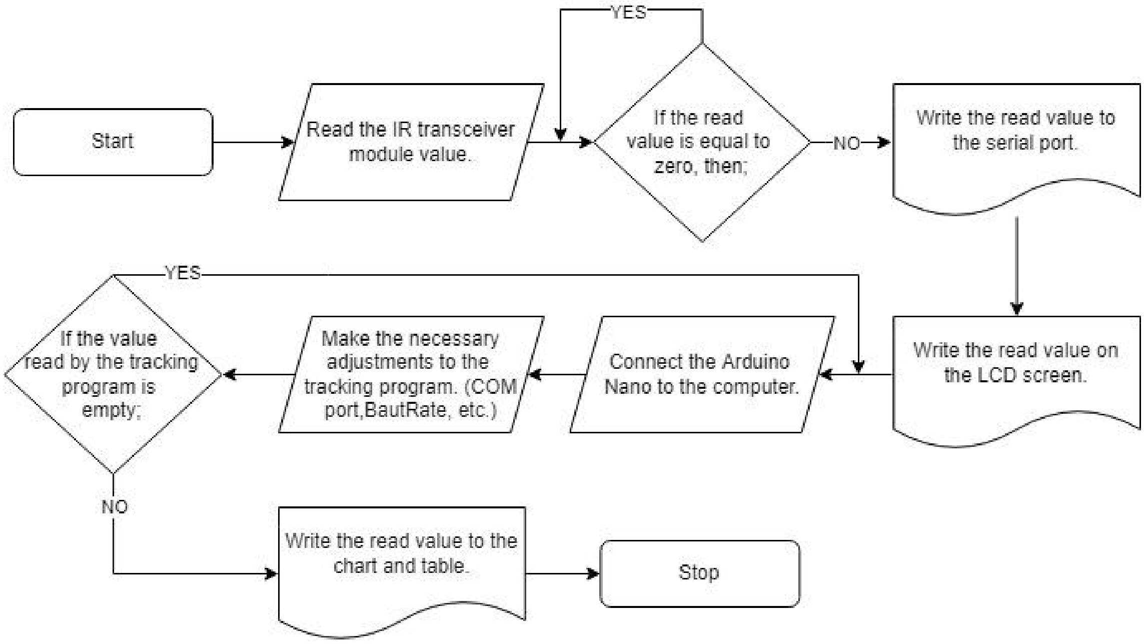

Figure 7. C# .Net Based RPM GRAPHIC Tracking Program Algorithm Image

In this Arduino-based project, the number of revolutions detected by the IR Transceiver Sensor is transferred to serial port. These values are transferred to computer with a USB cable. Monitoring program having C# .NET platform reads serial port values in computer environment. All values are tracked by recording values read here separately for each second. At the same time, the data is followed with cycle-time graph to make it easier to detect opposite situations. At the same time, it is possible to set upper and lower limits for incoming data thanks to this program. The tracking program will give a warning for every data outside the specified ranges. The created data graphic can be saved in PNG (Portable Network Graphics) format, and the data table can be saved in PDF or Excel format. At the same time, the data is transferred to the LCD screen on the device.

3.2 Program Architecture

The visual and explanation belongs to program are as in figure 8 and Table 1.

Figure 8. C# .Net Based RPM GRAPHIC Tracking Program Image

No:	**Section name:**		**Description:**
1	**Graphic Section**	:	This is the section where the read values are displayed on the time scale.
2	**DataSheet**	:	This is the section where the read values are listed on a per second basis.
3	**COM (Communications) Selection Setting**	:	It is the section where you can select which port Arduino is in so that the program can communicate with the Arduino.
4	**BautRate Selection Setting**	:	It is the data transfer rate selection section used for communication of the program with the Arduino.
5	**Minimum Value Setting**	:	It is input part of minimum restriction parameter of the read values.
6	**Maximum Value Setting**	:	It is input part of maximum restriction parameter of the read values.
7	**Connect Button**	:	After COM and Baud Rate values are entered, it is Arduino data reading and transfer start button.
8	**Graphic For PNG**	:	It is the button that provides opportunity to save instant graph created by the read value to computer storage as PNG.
9	**Data For PDF**	:	It is the button to save PDF format of the table of read values to computer storage.
10	**Data For Excel**	:	It is the button to save excel format of the table of read values to the computer storage.

Table 1. C# .Net Based RPM GRAPHIC Tracking Program Interface Description Table

4.CONCLUSIONS

4.1 Operating Conditions and Accuracy

In order for performed measurement to give the correct value;

1. The diameter of ground to be measured can show different values in each measurement. In order to prevent this, the device must be calibrated before each measurement.

2. It is necessary to remove objects that will prevent measurement between ground to be measured and the device or on ground.

3. The measurement must be at operating voltage levels of the Arduino Nano device, which is a microcontroller. Voltage imbalances can cause t measurement and caliber to deteriorate.

4. For measurements, the device should show zero before measurement starts and it should be fixed in such a way that it is not affected by environmental factors.

5. In long-term measurements, deviations can be observed due to memory shortage caused by Arduino Nano microcontroller. Different modifications must be made for the measurements.

4.2 Measurement values and evaluation

In this section, measurement values of revolutions per minute of an asynchronous motor and their differences from commonly used tachometers are evaluated.

First of all, an opposite separator sign was added to the ground in order to follow rotations of the IR Transceiver Module on the asynchronous motor. With this signal, the IR Transceiver Sensor counted a continuous mark on the rotary ground and appropriate formula will perform rpm calculation.

Date	Number	Value	Time
5 Ocak 2021 Sal	55	206	00:05:20
5 Ocak 2021 Sal	56	202	00:05:21
5 Ocak 2021 Sal	57	204	00:05:22
5 Ocak 2021 Sal	58	204	00:05:23
5 Ocak 2021 Sal	59	213	00:05:24
5 Ocak 2021 Sal	60	214	00:05:25
5 Ocak 2021 Sal	61	213	00:05:26

Table 2. Table Cross Section Image Created from RPM Graphic Program

As can be seen in Table 2, number of revolutions of an asynchronous motor in 6 seconds is listed. Along with the revolution numbers, measurement date, measurement number and measurement time are displayed. The induction motor, running at a nominal speed, performed a deviation of 7 points in 6 seconds. At the same time, there was a 4 point deflection in the time of 05:20 to 05:21. The main cause for these deflections is due to the low processor memory od the Arduino nano board.

4.3 Suggestions and Improvements

The main purpose of measuring revolutions of asynchronous motors is for rapid detection of faults in the motor, but in some complex cases, the fault may not manifest itself with revolution. For this, the system needs to be developed. The improvement aspects of the system are as follows;

1. Imbalances in the nominal voltage can be measured with ohm-meter module and monitored via monitoring program.
2. The vibrations in the motor due to stresses in asynchronous motor can be measured with SW-420 Vibration Sensor and monitored through monitoring program.
3. Since all faults in asynchronous motor will increase temperature of the motor as a result, the motor can be measured with Infrared Temperature Module and monitored via monitoring program.
4. In order to monitor harmonics occurring in the induction motor, a circuit board can be designed, and resulting harmonics values can be transferred to tracking program to follow them graphically.

REFERENCES

[1] Uysal B., 2019: Arduino ve Bluetooth Kullanılarak Uzaktan Kontrollü Robot Tasarım, Yazılım ve Uygulamasının Yapılması, Yüksek Lisans Tezi

[2] Anonim,2022: arduino.cc, Web Sitesi: https://docs.arduino.cc/hardware/nano, Erişim Tarihi: 15.05.2022

[3] İzgöl K., 2016: robotistan.com, Web Sitesi: https://maker.robotistan.com/lcd-nedir, Erişim Tarihi: 15.05.2022

[4] Raj A., 2015: circuitdigest.com, Web Sitesi: https://circuitdigest.com/article/16x2-lcd-display-module-pinout-datasheet, Erişim Tarihi:15.05.2022

[5] Atılgan D.S., Gürman Ü. 2020: Material Design in Music Education Using Arduino Platform, Journal of Qualitative Research in Education – JOQRE, 8(4),1377-1402

[6] Doğan Z., Gözüoğlu S.G. 2020: Durum İzleme ve İstatistiksel Süreç Kontrolü Kullanarak Şebeke Kalkışlı Daimi Mıknatıslı Senkron Motorda Rulman Arızası Tespiti. El-Cezerî Journal of Science and Engineering Vol: 7, No: 2, 2020 (781-794)

[7] Çakı E. 2013: Asenkron Motor Test Düzeneği. Yüksek Lisans Tezi. 2013.

[8] Özdemir A., Mengi O.Ö. 2020: Güvenlik Seviyesi Arttırılmış Akıllı Otopark Sistemi. Karadeniz Fen Bilimleri Dergisi, 10(1), 131-149, 2020. DOI: 10.31466/kfbd.732637.

[9] Yabanova İ., Yumurtacı M. 2021: Hareketli Ürünlerin Sayımı için Kızılötesi Tabanlı Sensör Dizaynı ve Yumurta Sayma Uygulaması. Journal of Materials and Mechatronics: A (JournalMM), 2(2), 141-149.

[10] Çolak İ., Bayındır R. 2005: PIC 16F877 İle DA Motor Hız Kontrolü. Journal of Engineering Sciences 2005 11 (2) 277-285

[11] Güven B., Uzun T. 2005: Mikrodenetleyici Temelli Sistem ile Devir Hızı Ölçümü. EMO. 11. Elektrik-Elektronik Bilgisayar Mühendisliği Ulusal Kongresi. İstanbul.22-25 Eylül 2005.

ANNEX 1. : Arduino codes

```
1. #include <LiquidCrystal_I2C_AvrI2C.h>
2. LiquidCrystal_I2C_AvrI2C lcd(0x27,16,2);
3. #include <TimerOne.h>
4. const int rs = 12, en = 11, d4 = 6, d5 = 5, d6 = 4, d7 = 3;
5. const int IRSensorPin = 2;
6. const int ledPin = 13;
7. int ledState = HIGH;
8. int inputState;
9. int lastInputState = LOW;
10. long lastDebounceTime = 0;
11. long debounceDelay = 5;
12. long time;
13. long endTime;
14. long startTime;
15. int RPM = 0;
16. int i;
17. void setup(void)
18. {
19. pinMode(IRSensorPin, INPUT);
20. pinMode(ledPin, OUTPUT);
21. digitalWrite(ledPin, ledState);
22. Serial.begin(9600);
23. lcd.begin();
24. lcd.clear();
25. lcd.print("IO-IR");
26. lcd.setCursor(0, 1);
27. lcd.print("RPM METER");
28. delay(2000);
29. endTime = 0;
30. Timer1.initialize(1000000);
31. Timer1.attachInterrupt(timerIsr);
32. }
33. void loop(void) {
34. i=digitalRead(2);
35. if(Serial.read()==1)
36. {
37. Serial.println(i);
38. delay(5);
39. }
40. time = millis();
41. int currentSwitchState = digitalRead(IRSensorPin);
42. if (currentSwitchState != lastInputState)
{
6
43. lastDebounceTime = millis();
44. }
45. if ((millis() - lastDebounceTime) > debounceDelay) {
46. if (currentSwitchState != inputState) {
47. inputState = currentSwitchState;
48. if (inputState == LOW) {
49. digitalWrite(ledPin, LOW);
50. calculateRPM();
51. ledState = !ledState;
52. }
53. else {
54. digitalWrite(ledPin, HIGH);
55. }
56. }
57. }
58. lastInputState = currentSwitchState;
59. }
60. void calculateRPM() {
61. startTime = lastDebounceTime;
62. lnTime = startTime - endTime;
63. RPM = 60000 / (startTime - endTime);
64. endTime = startTime;
65. }
66. void timerIsr()
67. {
68. Serial.println(RPM);
69. delay(300);
70. lcd.clear();
71. lcd.print("MEASURING...");
72. lcd.setCursor(0, 1);
73. lcd.print(RPM);
74. lcd.setCursor(6,1);
75. lcd.print("RPM");
76. delay(500);
77. RPM = 0;
78. }
```

ON THE SEMI-ANALYTICAL METHODS FOR THE FIFTH ORDER NONLINEAR KdV EQUATIONS

İnci Çilingir Süngü [1] **Emre Aydın** [2]

[1] Department of Mathematics Education, University of Ondokuz Mayis, Samsun, Turkey

incicilingir@gmail.com,

[2]Department of Mathematics, University of Ondokuz Mayis, Samsun, Turkey,
emr_aydn_55@outlook.com

Abstract

In this study, the Caudrey-Dodd-Gibbon (CDG), Sawada-Kotera (SK) and Caudrey-Dodd-Gibbon-Sawada-Kotera (CDGSK) equations being from the class of fifth-order nonlinear KdV equations are investigated. Adomian Decomposition Method (ADM) and modified Variational Iteration Method (mVIM) are proposed semi-analytical solutions for the CDG, SK and CDGSK equations. ADM and mVIM solutions of these equations are compared with both their exact solutions and each other by using tables and graphs. Also, it is visualized using curve and surface graphs. It is shown that the semi-analytical solutions are calculable, convenient and highly compatible with the analytical solutions.

Keywords: Caudrey-Dodd-Gibbon (CDG) equations; Sawada-Kotera (SK) equations; Caudrey-Dodd-Gibbon-Sawada-Kotera (CDGSK) equations; Adomian decomposition method (ADM); modified variational iteration method (mVIM).

1.INTRODUCTION

Almost every natural phenomenon mathematically is observed that arises in the form of nonlinear evolution equations (NLEEs). Problems arising in the various fields of science and engineering such as fluid mechanics, solid state physics, chemical physics, plasma physics, biology, chemical kinematics, nonlinear optics, geochemistry, hydrodynamic, population models are often expressed in terms of NLEEs. Thus, studies on NLEE, a special type of nonlinear partial differential equations, have recently become one of the most active and interested research areas. In our study, Adomian decomposition method (ADM) and modified variational iteration method (mVIM) for some special types of fifth-order nonlinear KdV equation, which is a class of NLEEs, are investigated. There are many studies on ADM and mVIM in various scientific studies. Some of them are; Bulut et al **[1-2]** used ADM to solve the nonlinear Benjamin-Bona-Mahony equation and partial fractional differential equation systems. In the studies in **[3-7]**, on some fractional differential equations and equation systems, Fornberg-Whitham equation and ADM for epidemic modeling were used. Inc et al **[8]**, used mVIM for straight fins with temperature dependent thermal conductivity. Sakar and Ergoren **[9]**, proposed an alternative variational iteration method for the time-fractional Fornberg-Whitham equation. At the studies in **[10-14]** used mVIM for solving nonlinear partial differential equation, coefficient variant Boussinesq equation and equation system, nonlinear homogeneous initial value problem. The well-known fifth-order nonlinear KdV equations can be represented as:

$$u_t + au^2u_{xx} + bu_xu_{xx} + cuu_{xxx} + du_{xxxxx} = 0 \tag{1}$$

here a, b, c and d are non-zeros and real coefficients, $u = u(x,t)$ is a sufficiently smooth function.

If $a = b = 30, c = 180, d = 1$ in equation (1), the equation turns into the Caudrey-Dodd-Gibbon (CDG) equation **[15]**.

$$u_t + 30u^2u_{xx} + 30u_xu_{xx} + 180uu_{xxx} + u_{xxxxx} = 0 \tag{2}$$

Karaagac **[16]** examined collocation method via quintic B-spline basis for CDG equation. Veeresha and Prakasha **[17]** used homotopy analysis methods for fractional CDG equation. At the studies in **[18-21]** were used traveling wave solution, periodic, kink, bell shape wave solution and various wave solutions for CDG equation.

If $a = b = 15, c = 45, d = 1$ in equation (1), the equation turns into the Sawada-Kotera (SK) equation **[22]**.

$$u_t + 15u^2u_{xx} + 15u_xu_{xx} + 45uu_{xxx} + u_{xxxxx} = 0 \tag{3}$$

Durur and Yokus **[23]** used hyperbolic traveling wave solution via $1/G'$-expansion method for Sawada-Kotera equation. In **[24-26]**, some semi-analytical studies on the SK equation were examined.

If $a = b = c = 5, d = 1$ in equation (1), the equation turns into the Caudrey-Dodd-Gibbon-Sawada-Kotera (CDGSK) equation **[27-28]**.

$$u_t + 5u^2u_{xx} + 5u_xu_{xx} + 5uu_{xxx} + u_{xxxxx} = 0 \tag{4}$$

In the literature, there are limited studies on the Caudrey-Dodd-Gibbon-Sawada-Kotera (CDGSK) equation. The studies in **[27-28]** are on the analytical solutions of the equation. In this study, semi-analytical solutions of the CDGSK equation, which have not been studied before, are included.

2.GENERAL PROPERTIES OF METHOD

In this section, we consider equation (1) in the following operator form to illustrate the basics of ADM and mVIM.

$$L_tu + R_xu + Nu = 0 \tag{5}$$

Here the notations $L_t = \frac{\partial}{\partial t}$, $R_x = d\frac{\partial^5}{\partial x^5}$ represent linear differential operators and the notation $Nu = au^2\frac{\partial^2 u}{\partial x^2} + b\frac{\partial u}{\partial x}\frac{\partial^2 u}{\partial x^2} + cu\frac{\partial^3}{\partial x^3}$ represents nonlinear differential operator. The inverse operator of L_t is defined by $L_t^{-1} = \int_0^t (.)ds$.

2.1. *Adomian decomposition method (ADM)*

By applying the inverse operator L_t^{-1} to (5), the following equation is obtained.

$$u(x,t) = \varphi + L_t^{-1}[-R_x u - Nu] \tag{6}$$

Here $\varphi = u(x,0)$. The ADM method is based on the assumption of infinite series solutions of the $u(x,t)$ function in the form of

$$u(x,t) = \sum_{n=0}^{\infty} u_n(x,t) \tag{7}$$

The nonlinear operator Nu is decomposed as

$$Nu = \sum_{n=0}^{\infty} A_n(u_0, u_1, \dots, u_n) \tag{8}$$

Where A_n is an appropriate Adomian's polynomial which constructed by Adomian **[29]** and can be calculated for all forms of nonlinearity. Adomian polynomials can be calculated using the following basic formula:

$$\sum_{n=0}^{\infty} A_n(u_0, u_1, \dots, u_n) = \frac{1}{n!}\left[\frac{d^n}{d\lambda^n} N\left(\sum_{k=0}^{\infty} \lambda^k u_k\right)\right]_{\lambda=0}, n = 0,1,2,\dots \tag{9}$$

As substituting the initial value φ into (6), identifying the zeroth component u_0 and making necessary simplifications, the subsequent components are obtained from the recurrence relation below:

$$u_0 = u(x,t)$$

$$u_{n+1} = L_t^{-1}[-R_x u_n - NA_n],\ n \geq 0 \tag{10}$$

Consequently, the components $u_0, u_1, u_2, u_3, \dots$ are identified and the series solutions are determined entirely. Let the expansion $\varphi_n = \sum_{k=0}^{n-1} u_k$ express the n-term approach to u. In this case, the exact solution is $u(x,t) = \lim_{n\to\infty} \varphi_n(x,t)$ with the necessary convergence conditions.

2.2. Modified variational iteration method (mVIM)

The correction functional for equation (5) is as follows:

$$u_{n+1}(x,t) = u_0(x,t) + \int_0^t \lambda[R_x u_n(x,s) + Nu_n(x,s)]\, ds \tag{11}$$

Where λ is a Lagrange multiplier. For $L_t = \frac{\partial^m}{\partial t^m}$, the Lagrange multiplier can be taken in the form **[30]:**

$$\lambda(x,t) = \frac{(-1)^m}{(m-1)!}(t-x)^{m-1}, m \geq 1. \tag{12}$$

Let the initial approximate function u_0, be taken as $u(x,0)$. To avoid computational overhead and unnecessary terms, equation (10) is rearranged in the form:

$$u_{n+1} = u_0 + \int_0^t \lambda[R_x u_{n-1} + G_{n-1}]\,ds \; + \int_0^t \lambda[R_x(u_n - u_{n-1}) + G_n - G_{n-1}]\,ds \tag{13}$$

$$u_{n+1} = u_n + \int_0^t \lambda[R_x(u_n - u_{n-1}) + G_n - G_{n-1}]\,ds \tag{14}$$

Here G_n can be obtained from the equality $Nu_n = G_n + o(t^{n+1})$. Equation (14) is called the modified correction functional. Since $L_t = \frac{\partial}{\partial t}$ in equation (1), by rearranging the equation (12), we get $\lambda(x,t) = -1$. The simplified modified correction functional for the fifth-order nonlinear KdV equation used in this study is:

$$u_{n+1} = u_n - \int_0^t [R_x(u_n - u_{n-1}) + G_n - G_{n-1}]\,ds \tag{15}$$

$$u_0 = u(x,0), \quad u_{-1} = 0, \quad G_{-1} = 0\,, \;\; \mathrm{n} \geq 1$$

Last of all, the components $u_0, u_1, u_2, u_3, \ldots$ are identified and the semi-analytical solutions are determined entirely. Thus, $\lim_{n\to\infty} u_n \to u(x,t)$ happens under essential convergence conditions.

3.APPLICATIONS

In this section, three different versions of the fifth-order nonlinear KdV equation are presented to demonstrate the effectiveness of mVIM and ADM.

3.1. Example 1. For $a = b = 30, c = 180, d = 1$ in equation (1), we consider the Caudrey-Dodd-Gibbon equation with initial value:

$$u(x,0) = \frac{e^x}{(1+e^x)^2} \tag{16}$$

As shown in **[16].** The exact solution of the Caudrey-Dodd-Gibbon equation given with the initial value problem is as follows:

$$u(x,t) = \frac{e^{x-t}}{(1+e^{x-t})^2} \tag{17}$$

For $0 < x < 1,\; 0 < t < 0.1$, ADM solutions obtained as a result of 7 iterations in equation (10), their comparison with the exact solution and error values are shown in Table 1.

	Caudrey-Dodd-Gibbon Equation		
	Exact	ADM	|Exact-ADM|
0	0.2493760402	0.2493760402	0
0.1	0.2500000000	0.2500000000	0
0.2	0.2493760402	0.2493760402	0
0.3	0.2475165727	0.2475165728	0.0000000001
0.4	0.2444583117	0.2444583118	0.0000000001
0.5	0.2402607457	0.2402607458	0.0000000001
0.6	0.2350037122	0.2350037123	0.0000000001
0.7	0.2287842405	0.2287842404	0.0000000001
0.8	0.2217128733	0.2217128733	0
0.9	0.2139096965	0.2139096965	0
1.0	0.2055003073	0.2055003074	0.0000000001

Table1. Comparison of ADM and exact solutions

For $0 < x < 1,\ \ 0 < t < 0.1$, mVIM solutions obtained as a result of 7 iterations in equation (15), their comparison with the exact solution and error values are shown in Table 2

	Caudrey-Dodd-Gibbon Equation		
	Exact	mVIM	|Exact-mVIM|
0	0.2493760402	0.2493760402	0
0.1	0.2500000000	0.2500000000	0
0.2	0.2493760402	0.2493760403	0.0000000001
0.3	0.2475165727	0.2475165722	0.0000000005
0.4	0.2444583117	0.2444583117	0
0.5	0.2402607457	0.2402607456	0.0000000001
0.6	0.2350037122	0.2350037124	0.0000000002
0.7	0.2287842405	0.2287842406	0.0000000001
0.8	0.2217128733	0.2217128735	0.0000000002
0.9	0.2139096965	0.2139096965	0
1.0	0.2055003073	0.2055003075	0.0000000002

Table2. Comparison of mVIM and exact solutions

Comparison of surfaces and graphs of ADM, mVIM and exact solutions are shown in Fig.1-5, respectively.

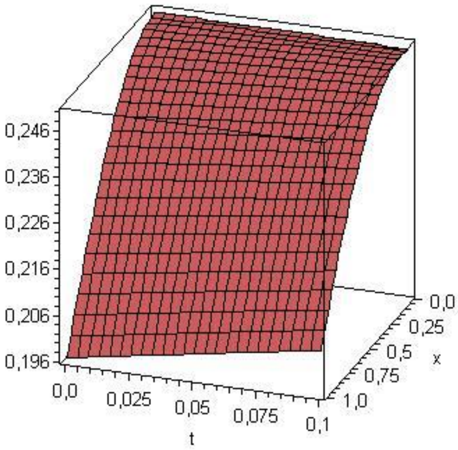

Figure1. Exact solution (3D)

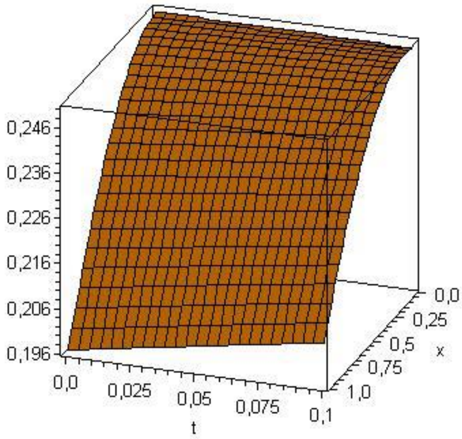

Figure2. ADM solution (3D)

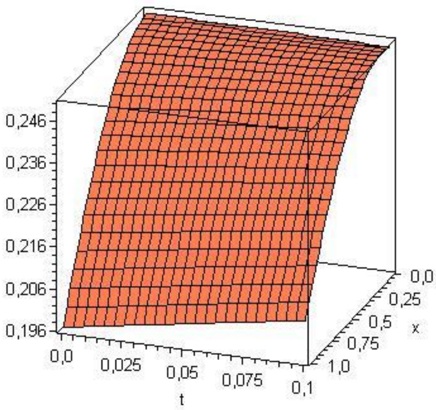

Figure3. mVIM solution (3D)

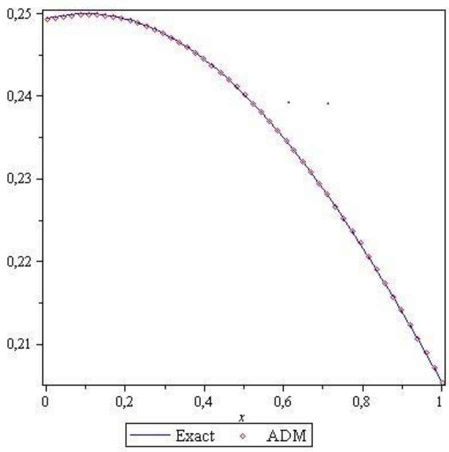

Figure4. Comparison of exact-ADM solutions (2D)

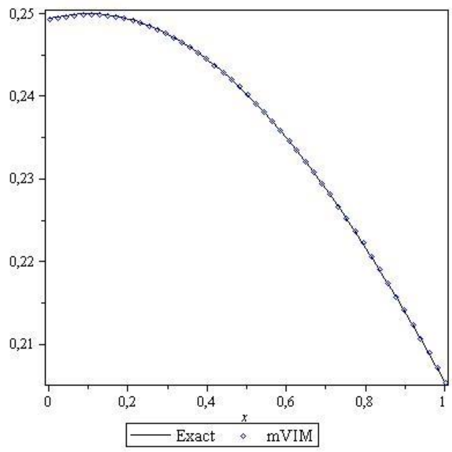

Figure5. Comparison of exact-mVIM solutions (2D)

3.2. Example 2. For $a = b = 15, c = 45, d = 1$ in equation (1), we consider the Sawada-Kotera equation with initial value:

$$u(x,0) = -\frac{2}{3} + \frac{1}{\sqrt{15}} - \frac{8}{(e^{2x+2}-1)} - \frac{8}{(e^{2x+2}-1)^2} \tag{18}$$

As shown in **[31].** The exact solution of the Sawada-Kotera equation given with the initial value problem is as follows:

$$u(x,t) = -\frac{2}{3} + \frac{1}{\sqrt{15}} - \frac{8}{(e^{2x+2t+2}-1)} - \frac{8}{(e^{2x+2t+2}-1)^2} \tag{19}$$

For $0 < x < 1,\ \ 0 < t < 0.1$, ADM solutions obtained as a result of 7 iterations in equation (10), their comparison with the exact solution and error values are shown in Table 3.

	Sawada-Kotera Equation		
	Exact	ADM	|Exact-ADM|
0	-1.5295728140	-1.5295742520	0.0000014380
0.1	-1.2862484170	-1.2862490320	0.0000006150
0.2	-1.1018281470	-1.1018284310	0.0000002840
0.3	-0.9599843603	-0.9599844998	0.0000001395
0.4	-0.8495958213	-0.8495958926	0.0000000713
0.5	-0.7628688923	-0.7628689309	0.0000000386
0.6	-0.6942078475	-0.6942078692	0.0000000217
0.7	-0.6395109840	-0.6395109965	0.0000000125
0.8	-0.5957181112	-0.5957181188	0.0000000076
0.9	-0.5605114367	-0.5605114414	0.0000000047
1.0	-0.5321128461	-0.5321128489	0.0000000028

Table3. Comparison of ADM and exact solutions

For $0 < x < 1,\ \ 0 < t < 0.1$, mVIM solutions obtained as a result of 7 iterations in equation (15), their comparison with the exact solution and error values are shown in Table 4.

	Sawada-Kotera Equation		
	Exact	mVIM	|Exact-mVIM|
0	-1.5295728140	-1.5295742520	0.0000014380
0.1	-1.2862484170	-1.2862490330	0.0000006160
0.2	-1.1018281470	-1.1018284310	0.0000002840
0.3	-0.9599843603	-0.9599844959	0.0000001356
0.4	-0.8495958213	-0.8495958930	0.0000000717
0.5	-0.7628688923	-0.7628689317	0.0000000394
0.6	-0.6942078475	-0.6942078682	0.0000000207
0.7	-0.6395109840	-0.6395109959	0.0000000119
0.8	-0.5957181112	-0.5957181191	0.0000000079
0.9	-0.5605114367	-0.5605114415	0.0000000048
1.0	-0.5321128461	-0.5321128493	0.0000000032

Table4. Comparison of mVIM and exact solutions

Comparison of surfaces and graphs of ADM, mVIM and exact solutions are shown in Fig.6-10, respectively.

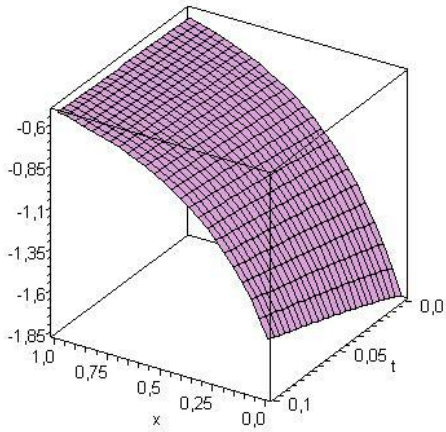

Figure6. Exact solution (3D)

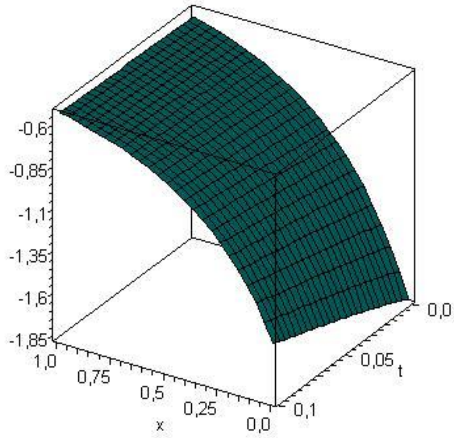

Figure7. ADM solution (3D)

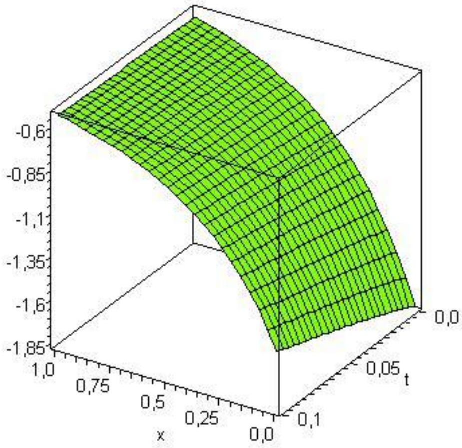

Figure8. mVIM solution (3D)

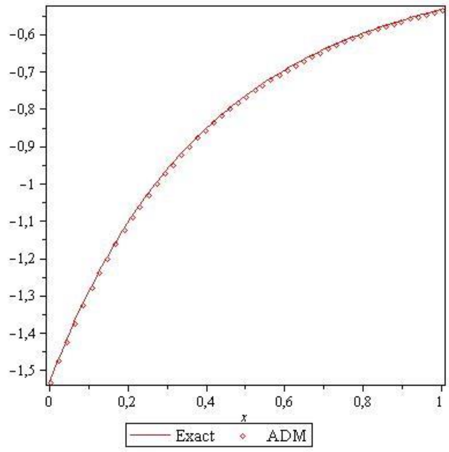

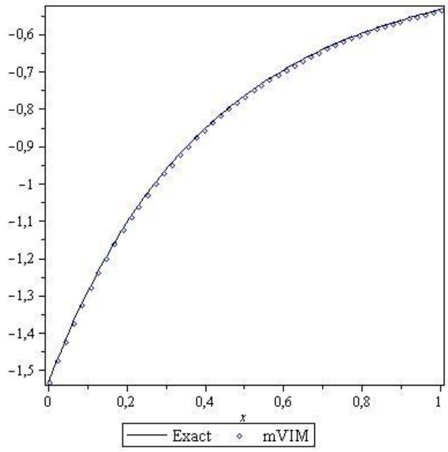

Figure9. Comparison of exact –ADM solutions (2D)   Figure10. Comparison of exact –mVIM solutions (2D)

3.3. Example 3. For $a = b = c = 5, d = 1$ in equation (1), we consider the Caudrey-Dodd-Gibbon-Sawada-Kotera equation with initial value:

$$u(x,0) = -1 - \frac{-\operatorname{sech}(\frac{x}{2})}{(\sinh\left(\frac{x}{2}\right) - 3\cosh\left(\frac{x}{2}\right))} - \frac{3}{2}\frac{-\operatorname{sech}^2(\frac{x}{2})}{(\sinh\left(\frac{x}{2}\right) - 3\cosh\left(\frac{x}{2}\right))^2} \tag{20}$$

As shown in **[27].** The exact solution of the Caudrey-Dodd-Gibbon-Sawada-Kotera equation given with the initial value problem is as follows:

$$u(x,t) = -1 - \frac{9\operatorname{sech}(\frac{x-t}{2})}{(\sinh\left(\frac{x-t}{2}\right) - 3\cosh\left(\frac{x-t}{2}\right))} - \frac{3}{2}\frac{-\operatorname{sech}^2(\frac{x-t}{2})}{(\sinh\left(\frac{x}{2}\right) - 3\cosh\left(\frac{x-t}{2}\right))^2} \tag{21}$$

For $0 < x < 1,\ \ 0 < t < 0.1$, ADM solutions obtained as a result of 7 iterations in equation (10), their comparison with the exact solution and error values are shown in Table 5.

	Caudrey-Dodd-Gibbon-Sawada-Kotera Equation		
	Exact	ADM	|Exact-ADM|
0	1.783047606	1.783047604	0.000000002
0.1	1.833333333	1.833333334	0.000000001
0.2	1.871689984	1.871689984	0
0.3	1.897474659	1.897474658	0.000000001
0.4	1.910249196	1.910249194	0.000000002
0.5	1.909794744	1.909794745	0.000000001
0.6	1.896119110	1.896119112	0.000000002
0.7	1.869456493	1.869456494	0.000000001
0.8	1.830259629	1.830259628	0.000000001
0.9	1.779184741	1.779184740	0.000000001
1.0	1.717070046	1.717070049	0.000000003

Table5. Comparison of ADM and exact solutions

For $0 < x < 1,\ \ 0 < t < 0.1$, mVIM solutions obtained as a result of 7 iterations in equation (15), their comparison with the exact solution and error values are shown in Table 6.

	Caudrey-Dodd-Gibbon-Sawada-Kotera Equation		
	Exact	mVIM	|Exact-mVIM|
0	1.783047606	1.783047610	0.000000004
0.1	1.833333333	1.833333328	0.000000005
0.2	1.871689984	1.871689987	0.000000003
0.3	1.897474659	1.897474646	0.000000013
0.4	1.910249196	1.910249189	0.000000007
0.5	1.909794744	1.909794744	0
0.6	1.896119110	1.896119134	0.000000024
0.7	1.869456493	1.869456495	0.000000002
0.8	1.830259629	1.830259637	0.000000008
0.9	1.779184741	1.779184742	0.000000001
1.0	1.717070046	1.717070053	0.000000007

Table6. Comparison of mVIM and exact solutions

Comparison of surfaces and graphs of ADM, mVIM and exact solutions are shown in Fig.11-15, respectively.

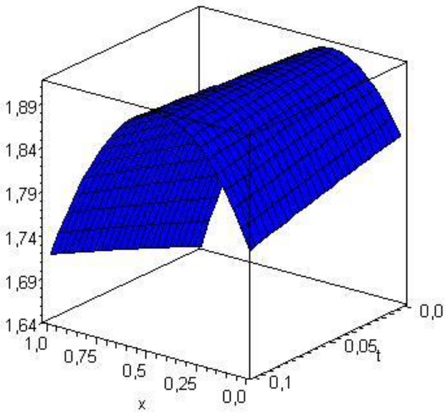

Figure11. Exact solution (3D)

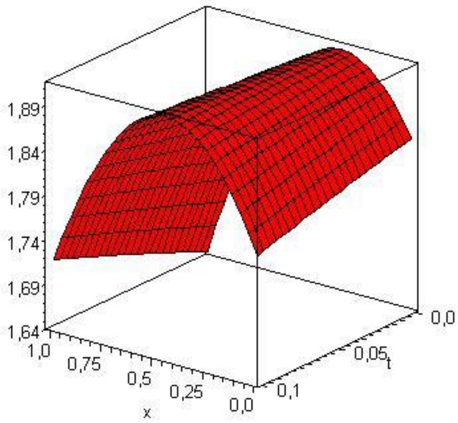

Figure12. ADM solution (3D)

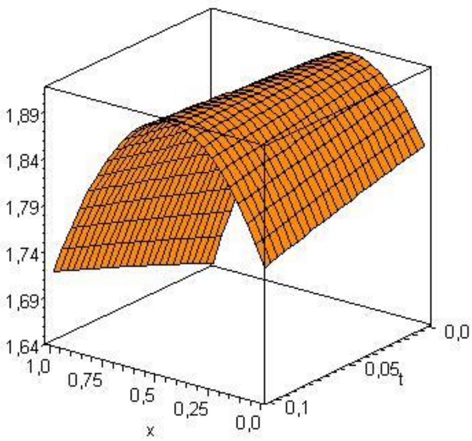

Figure13. mVIM solution (3D)

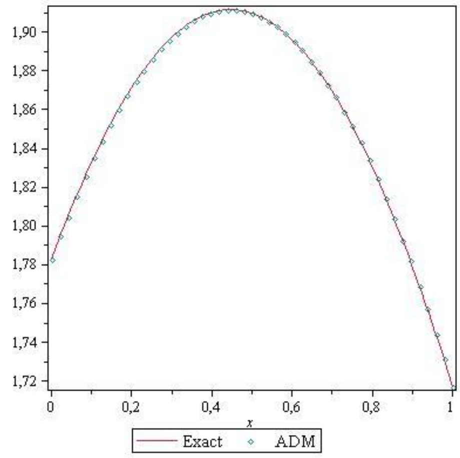

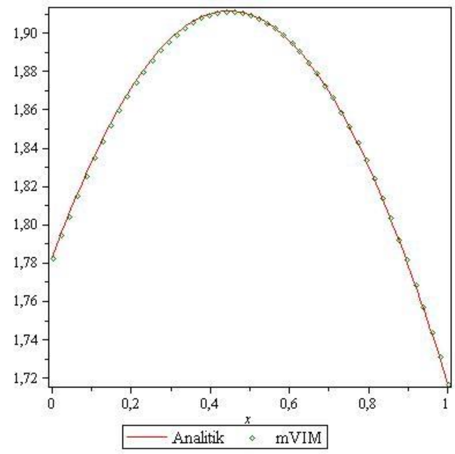

Figure14. Comparison of exact –ADM solutions (2D)

Figure15. Comparison of exact –mVIM solutions (2D)

4.CONCLUSIONS

In this study, the Caudrey-Dodd-Gibbon (CDG), Sawada-Kotera (SK) and Caudrey-Dodd-Gibbon-Sawada-Kotera (CDGSK) equations being from the class of fifth-order nonlinear KdV equations are investigated. Adomian decomposition method (ADM) and modified variational iteration method (mVIM) are proposed for semi-analytical solutions of the relevant to equations.

For semi-analytical solutions obtained by the ADM and mVIM method for the Caudrey-Dodd-Gibbon (CDG), errors around 10^{-10} are detected. For Sawada-Kotera (SK) equation, errors around 10^{-7} are detected. The error of the semi-analytical solutions obtained from the proposed ADM and mVIM methods for the Caudrey-Dodd-Gibbon-Sawada-Kotera (CDGSK) equations, whose semi-analytical solutions have not been investigated until now and examined our study is found around 10^{-9}. The ADM and the mVIM methods used for the related equations both gave results in a short time and produced semi-analytical solutions using less memory. It is visualized using curve and surface graphs that the semi-analytical solutions found are highly compatible with the analytical solutions. These methods are found to be highly effective and equivalent for the equations under consideration. Moreover, it can be said that these methods will be effective in other classes of fifth-order nonlinear KdV equations.

REFERENCES

1. Hasan Bulut, H. Mehmet Baskonus, Seyma Tuluce, Tolga Akturk, A Comparison Between HPM and ADM for the Nonlinear Benjamin-Bona-Mahony Equation, International Journal of Basic & Applied Sciences, Vol:11, No:3, 117-127, 2011.
2. Hasan Bulut, Belgacem, F. B. Muhammad, H. Mehmet Baskonus, Partial Differential Equation Systems Solutions by Using Adomian Decomposition Method Implementation, Proceedings of the Fourth International Conference on Mathematical and Computational Applications, 138-146, 2013.

3. Jun-Sheng Duon, Randolph Rach, Dumitru Baleanu, Abdul-Majid Wazwaz, A Review of the Adomian Decomposition Method and Its Applications to Fractional Differential Equations, Communications in Fractional Calculus, Vol: 3, No: 2, 73-99, 2012.
4. Hossein Jafari, Varsha Daftardar-Gejji, Solving a System of Nonlinear Fractional Differential Equations Using Adomian Decomposition, Journal of Computational and Applied Mathematics, Vol: 196, No: 2006, 644-651, 2006.
5. Faycal Abidi, Khaled Omrani, The Homotpy Analysis Method for Solving the Fornberg-Whitham Equation and Comparison with Adomian's Decomposition Method, Computers and Mathematics with Applications, Vol: 59, No: 2010, 2743-2750, 2010.
6. Jafar Biazer, Solution of the Epidemic Model by Adomian Decomposition Method, Applied Mathematics and Computation, Vol: 173, No: 2006, 1101-1106, 2006.
7. Jin-Fa Cheng, Yu-Ming Chu, Solution to the Linear Fractional Differential Equation Using Adomian Decomposition Method, Mathematical Problems in Engineering, Vol: 2011, article id: 587068, 14 pages, 2011.
8. Mustafa Inc, Hasib Khan, Dumitru Baleanu, Aziz Khan, Modified Variational Iteration Method for Straight Fins with Temperature Dependent Thermal Conductivity, Thermal Science, Vol: 22, No:1, 229-236, 2018.
9. Mehmet Giyas Sakar, Hilmi Ergoren, Alternative Variational Iteration Method for Solving the Time-Fractional Fornberg-Whitham Equation, Applied Mathematical Modelling, Vol: 39, No: 14, 3972-3979, 2015.
10. Tamer A. Abassy, Magdy A. El Tawil, H. El Zoheiry, Toward a Modified Variational Iteration Method, Journal of Computational and Applied Mathematics, Vol: 207, No: 1, 137-147, 2007.
11. Tamer A. Abassy, Magdy A. El Tawil, H. El Zoheiry, Solving Nonlinear Partial Differential Equations Using the Modified Variational Iteration Padé Technique, Journal of Computational and Applied Mathematics, Vol: 207, No: 1, 73-91, 2007.
12. Jun-Feng Lu, Modified Variational Iteration Method for Variant Boussinesq Equation, Thermal Science, Vol: 19, No: 4, 1195-1199, 2015.
13. Fadhil H. Easif, Saad A. Manaa, Ahmed J. Sabali, Modified Variational Iteration Method and Homotopy Analysis Method for Solving Variable Coefficient Variant Boussinesq System, General Letters in Mathematics, Vol: 8, No: 1, 26-32, 2020.
14. Tamer A. Abassy, Modified Variational Iteration Method (Nonlinear Homogeneous Initial Value Problem), Computers and Mathematics with Applications, Vol: 59, No: 2, 912-918, 2010.
15. P. J. Caudrey, R. K. Dodd, J.D. Gibbon, A New Hierarchy of Korteweg-De-Vries Equations, Proceeding of the Royal Saciety A, Vol: 351. No: 1666, 407-422, 1976.
16. Berat Karaagac, A Numerical Approach to Caudrey-Dodd-Gibbon Equation Via Collacation Method Using Quantic B-Spline Basis, Journal of Applied and Engineering Mathematics, Vol: 9, No: 1, 1-8, 2019.
17. P. Veeresha, D. G. Prakasha, A Reliable Analytical Technique for Fractional Caudrey-Dodd-Gibbon Equation with Mittag-Leffer Kernel, Nonlinear Engineering, Vol: 9, No: 1, 319-328, 2020.

18. M. Abdollahzadeh, M. Hosseini, M. Ghanbarpour, H. Shirvani, Exact Travelling Solutions for Fifth Order Caudrey-Dodd-Gibbon Equation, International Journal of Applied Mathematics and Computation, Vol: 2, No: 4, 81-90, 2010.
19. M. Khorsed Alam, Periodic, Kint and Bell Shape Wave Solutions to the Caudrey-Dodd-Gibbon (CDG) Equation and the Lax Equation, Advances in the Theory of Nonlinear Analysis and its Applications, Vol: 4, No: 4, 216-232, 2020.
20. Hasibun Naher, Farah Aini Abdullah, M. Ali Akbar, The (G'/G)- Expansion Method for Abundant Travelling Wave Solutions of Caudrey-Dodd-Gibbon Equation, Mathematical Problems in Engineering, Vol: 2011, article id: 218216, 11 pages, 2011.
21. Haifa Bin Jebreen, Yurilev Chalco-Cana, Application of the Multiple Exp-Function, Cross-Kink, Periodic-Kink, Solitary Wave Methods and Stability Analysis for the CDG Equation, Advance in Mathematical Physics, Vol: 2021, article id: 6643512, 12 pages, 2021.
22. Katuro Sawada, Takeyasu Kotera, A Method for Finding N-Soliton Solutions of the KdV Equation and KdV-like Equation, Progress of Theoretical Physics, Vol: 51, No:5, 1355-1367, 1974.
23. Hulya Durur, Asıf Yokus, Hyperbolic Travelling Wave Solutions for Sawada-Kotera Equation Using (1/G')-Expansion Method. Afton Kocatepe University Journal of Sciences and Engineering, Vol: 19, No: 2019, 615-619, 2019.
24. Hasibun Naher, Farah Aini Abdullah, M. Ali Akbar, Syed Tauseef Mohyud-Din, Some New Solutions of the Higher Order Sawada-Kotera Equations via the Exp-Function Method, Middle-East Journal of Scientific Research, Vol: 11, No:12, 1659-1667, 2012.
25. Hijaz Ahmed, Tufail A. Khan, Predrag S. Stanimirovic, Imtiaz Ahmed, Modified Variational Iteration Technique for the Numerical Solution of Fifth Order KdV-Type Equations, Journal of Applied and Computational Mechanics, Vol. 6 (SI), 1220-1227, 2020.
26. Huda O. Bakodah, Modified Adomian Decomposition Method for the Generalized Fifth Order KdV Equations, American Journal of Computational Mathematics, Vol:3, No: 1, 53-58, 2013.
27. Muhammad Shakeel, Syed Tauseef Mohyud-Din, Solution of Fifth Order Caudrey-Dodd-Gibbon- Sawada-Kotera Equations by the Alternative (G'/G)-Expansion Method with Generalized Riccati Equation, Walailak Journal of Science & Technology, Vol:12, No:10, 949-960, 2015.
28. Jin Hyuk Choi, Hyunsoo Kim, Exact Travelling Wave Solutions of the Stochastic Wick-Type Fractional Caudrey-Dodd-Gibbon-Sawada-Kotera Equation, AIMS Mathematics, Vol: 6, No: 4, 4053-4072, 2021.
29. George Adomian, A Rewiew of the Decomposition Method in Applied Mathematics, Journal of Mathematical Analysis and Applications, Vol:135, No:1, 501-544, 1988.
30. Saeid Abbasbandy, Elyas Shivanian, Application of the Variational Iteration Method for System of Nonlinear Volterra's Integro-Differential Equations. Mathematical and Computational Applications, Vol: 14, No:2, 147-158, 2009.

31. Yongyi Gu, Analytical Solutions to the Caudrey-Dodd-Gibbon-Sawada-Kotera Equation via Symbol Calculation Approach, Journal of Function Spaces, Vol:2020, article id: 5042724, 8 pages, 2020.

OPINIONS OF PRE-SERVICE SCIENCE TEACHERS ABOUT VIRTUAL TOURS TO SCIENCE CENTERS

Esma Kurban[1]

[1] Department of Mathematics and Science Education, Ordu University, Ordu, Turkey

esmakurban19@gmail.com,

Fatma Nur Büyükbayraktar [2]

[2] Department of Mathematics and Science Education, Ordu University, Ordu, Turkey

fnbuyukbayraktar@gmail.com,

Abstract

Science centers are defined as places that offer experimental and hands-on activities for individuals of different age levels, and that make science and technology understandable and accessible. Due to reasons such as the lack of science centers in every purposeful in Turkey and the cost of visits, science centers can be reached through virtual tours. In this study, it is aimed to examine the views of pre-service science teachers about their virtual tours to science centers. The sample of the research consists of 6 pre-service science teachers studying in the 3rd grade of the Science Teaching undergraduate program of the Faculty of Education of Ordu University. This research was carried out the case study method. In the research, semi-structured interview form and two worksheets were used as data collection tools. The findings obtained in this interview were interpreted through descriptive analysis. According to the results of the analysis of the findings obtained from the interview data, pre-service science teachers define science centers as the means that provide scientific information and technology. At the same time, they think of science centers as areas prepared to conduct experiments and reveal new ideas. Pre-service science teachers define virtual tour to science centers as reaching physical areas in virtual environment. In these virtual tours, besides visiting the areas, they expect to make discoveries by interacting with the areas. However, it has been revealed that pre-service science teachers do not have knowledge about science centers in their own countries. In our study, pre-service science teachers were provided to get to know Konya Science Center through virtual tours. During the virtual tour were made applications. In these applications, activities that pre-service science teachers can use in their professional lives are included. It is thought that virtual tours will contribute to the professional development of pre-service science teacher.

Keywords: Science centers; Virtual tour; Pre-service science teacher.

1.INTRODUCTION

The science center aims to bring individuals of different age levels together with science, to make technology accessible and understandable, to increase the importance of technology in the eyes of the society, to raise awareness by conducting experimental and applied activities and to encourage individuals to try and discover (TÜBİTAK, 2022). They are informal education institutions that contain exhibition facilities, where educational activities take place, and which have spread rapidly in Turkey in recent years. While emphasizing the importance of science, science centers are institutions that allow people of all ages and cultures to be free to question, think and explore (Sırtkaya & Ertaş, 2019). Science centers, which aim to bring generally accepted scientific principles and understanding skills to all ages, aim to raise well-educated, curious and asking questions by pushing the limits of individuals' creativity and imagination (Kırgız, 2018).

In 1888, the first science center was established in Berlin, the capital of Germany. This science center, Urania, was put into service between 1888 and 1928. The exhibitions on which interactive and applied exhibitions will be made are open to the public. The Pinellas Country Science Center is the first modern science center to meet the public in 1959 and opened in the United States. Since 1970, there has been a rapid increase in the number of science centers (Karadeniz, 2009). Feza Gürsey, the first science center in Turkey, was opened in Ankara on April 23, 1993. This science center is named after a world-renowned Physicist and Mathematician. After the opening of this science center, a rapid increase was observed in the establishment of science centers in Turkey and 17 science centers, including this science center, were put into service for the public (Öner & Öztürk, 2019). Due to the fact that science centers are not widespread in the world and there are few studies on this subject, students cannot fully benefit from science centers. In addition, these science center's cannot be visited by students due to many reasons such as the financial difficulties of the students going to the science center, the teachers' inability to spare time for trips to this science center to train their subjects at school, and the problems in obtaining permission. In this respect, it has enabled the science center to be visited via a virtual tour. In our country, we have two science centers that can be visited via virtual tours. These; Konya Science Center and Kayseri Science Center (Bozdoğan,2007; Yolcu & Karaosmanoğlu, 2021). Studies on science centers and virtual tours in the literature are presented below.

Erçetin & Görgülü (2018) examined the views of 6th grade students who visited the science center about the science course. As a result of these studies, it was observed that the majority of visitors to science centers had a positive view of the science course

Özcan, Demirel & Ergül (2019) examined the students' opinions about the Konya Science Center trip in their studies. As a result of the study, it was stated that the students stated that the science center was interesting and remerkable and useful for discovering new information.

Bozdoğan (2008) examined the effect of pre-service science teacher activities in science center on science teaching. At the end of the study, he stated that it would be beneficial for the professional development of pre-service science teachers, that they could gain science literacy to primary school students and that it could also affect their career choices.

Kubat (2018) examined the views of pre-service science teachers about out-of-school learning environments. As a result of this study, pre-service science teachers stated that out-of-school learning environments would make positive contributions to permanent learning.

In their study, Yolcu & Karaosmanoğlu (2021) examined the opinions of teachers about a virtual tour to Konya Science Center. As a result of this study, it has been determined that the teachers do not have enough knowledge about the science centers in Turkey. The teachers who participated in the study found the study useful; It was also stated that they considered it a good acquisition for themselves and their students.

In this study, it is aimed to examine the views of pre-service science teachers about their virtual tours to science centers. For this purpose, answers to the following research questions were sought.

1.What are the opinions of pre-service science teachers about the science center?

2.What are the opinions of pre-service science teachers about virtual tours to science centers?

Limitations

- The sample of the research, it is limited to prospective teachers studying in the 3rd year of the science teaching undergraduate program of the Faculty of Education of Ordu University.
- It is limited to the data collected within the scope of the study.

Assumptions

- It is assumed that the prospective science teachers participating in the research will answer the interview questions sincerely.
- It is assumed that they are not influenced by the interview environment and will naturally respond to their thoughts.
- It is assumed that the created worksheet will be filled in sincerely and accurately by the pre-service science teachers.

2.GENERAL PROPERTIES OF METHOD

Research Mode

In this study, which was carried out with the aim of examining the opinions of pre-service science teachers about virtual tours to science centers, the case study method, which is one of the qualitative research designs, was used. The case study method is a research method used to reveal the existing situation, which gives detailed information to the researcher even if the study group is small (Patton, 2014). A case study is also defined as a qualitative research in which a situation is revealed by examining the limited situations in a certain time selected from the current life situations in depth with various data collection tools. Creswell (2013).

Study group

The sample of the research consists of 3rd grade pre-service science teachers studying at the Faculty of Education of a state university in Turkey. The sample in this study was selected by purposeful sampling method. According to Patton (2014), purposeful sampling method is a research method that is useful in explaining and discovering many situations, events or phenomena that allows for in-depth study of situations that are thought to have rich information by creating a small sample in qualitative research, and the number of samples in the study was limited to 6 pre-service science teachers. Pre-service science teachers were coded as S1,S2,S3….S6 in the study. Before the application, the "Informed Voluntary Consent Form" was used for the voluntary participation of pre-service science teachers.

Data collection tool

The data of the study were collected in two stages.1. Stage: Before the virtual tour, three open-ended questions prepared by the researcher using the semi-structured interview method were directed to the pre-service science teachers and interviewed. In the semi-structured interview method, the interviewer has the freedom to both ask pre-prepared questions and ask additional questions in order to get more detailed information about these questions, by sticking to the subject or areas that he has prepared in advance, and this method is used as the most used data collection tool in qualitative research (Yıldırım & Şimşek , 2021, p.130).2. Stage: During the virtual tour, a worksheet containing 6 open-ended questions was distributed and secondary data were collected after the pre-service science teachers filled out this worksheet.

Analysis of Data

In this study, the data obtained from the views of science teacher candidates about the science center virtual trip were analyzed using descriptive analysis method. In this analysis method, data is clearly described and interpreted. This analysis method is used in research where the conceptual framework is clearly determined beforehand, and direct quotations are frequently used in order to reflect the views of the individuals interviewed or observed in a striking way. In this type of analysis, the aim is to present an organized and interpreted version of the findings to the reader (Çepni,2018).

Validity and Reliability

In order to ensure the validity and reliability of the research, the data collected from the participants were analyzed by a teacher who is an expert in the field, and a common conclusion was reached by reconsidering with the analysis of the researcher. In order to ensure the external validity of the research, every stage of the study was explained to the science teacher candidates in detail and all processes were explained.

3.APPLICATIONS

3.1. Findings Obtained from the Interview Questions

After the interview, the pre-service science teachers asked, “What does the concept of science center mean to you?” Their views on the question are given in Table 1.

Table 1.Science center for pre-service science teachers opinions on the concept

Data Source	f	Pre-service science teacher
Reaching Science	2	S_1 ve S_6
Reaching scientific technology	1	S_2
Presenting new ideas	2	S_4 ve S_5
do experiments	1	S_3

When Table 1 is examined, 4 different codes were created from the views of the pre-service science teachers participating in the research about the concept of science center. 2 of them are the concept of science center; accessing information, 1 as reaching scientific technology and doing experiments, and 2 as putting forth new ideas. Opinions of pre-service science teachers:

S1: "Science centers; They are centers where everyone can learn something about science.

S2: "Where scientific research or technologies are available".

S3: "Science centre; They are places where technology is advanced and experiments are made easier".

S4: "Where technology, inventions and ideas can emerge"

S5: "Science centre; the place where various researches related to the development of technology are carried out"

S6: "The place where technology takes the individual to knowledge and science"

After the interview, the pre-service science teachers asked, "Do you have any information about virtual tours to science centers?" Their views on the question are given in Table 2.

Table 2.Opinions of pre-service science teachers on virtual tours to the science center

Data Source	f	Pre-service science teacher
Visiting places with virtual methods	3	S_1, S_2, S_4
Virtual experimentation	1	S_3
Discovering information virtually	2	S_5 ve S_6

When Table 2 is examined, 3 different codes were created from the opinions of the science teacher candidates participating in the research about the virtual tours to the science centers. 3 of them took a virtual tour of the science center; They defined it as visiting places with virtual methods, 1 as experimenting virtually, and 2 as discovering information virtually. Opinions of pre-service science teachers:

S1: "People who are curious about the centers in the computer environment visit them"

S2: "Learning a scientific or anatomical subject by virtual tour"

S3: "Virtual tour or experiment"

S4: "The place where people are able to reach places where they cannot go and travel through virtual environments"

S5: "Research through various simulations in reality"

S6: "Accessing knowledge and science with virtual methods and discovering them"

In the last interview question, do you have any information about science centers in our country? When we asked the question, 6 pre-service science teachers said that they did not have any idea about this issue.

3.2. Findings from the Working Paper

In the worksheet prepared by the researcher, the pre-servive science teachers were asked, "Do you think the virtual tour to the science center is beneficial?" Their views on the question are given in Table 2.

Table 3.Pre-service science teachers thoughts on the usefulness of virtual tour

Data Source	**f**	**Pre-service science teacher**
Visuality	6	S_1, S_2, S_3 S_4 S_5,S_6
Permanence	3	S_1, S_4 ve S_5
Eliminating inequality of opportunity	1	S_3
Attracting attention to the course	2	S_2, S_3

When Table 3 is examined, 4 different codes were created from the opinions of the pre-service science teachers participating in the research about the usefulness of virtual trips to science centers. Our teacher candidates found this virtual tour to the science center useful in terms of being visually impressive and catchy, interesting and remarkable, and removing the inequality of opportunity. Opinions of pre-service science teachers:

S1: "I think. It is a tour that offers our students the opportunity to visualize the topics we have explained abstractly in their minds. The content described is also supported by visuals. It is very beneficial to offer this opportunity.

S2: "I think. I realized that it is one of the most important ways to make children love science. It was nice to see those models, even if the virtual tour didn't go into the tiniest details in the science center.

S3: "I think. Because children who do not have the opportunity to travel can change their perspectives on science and attract their attention thanks to such virtual tours.

S4: "I think. I think it will be useful because visually taught lessons are more permanent.

S5: "I think. By seeing the subjects that are difficult to understand, the child reinforces them better in his mind.

S6: "I think. They will add more visual memory to our students.

Table 4. Parts that attracted the attention of pre-service science teachers in the virtual tour to the science center

Data Source	**f**	**Pre-service science teachers**
Planetarium	6	S_2, S_5
Our Universe	3	S_2, S_3, S_4
DNA	1	S_6
Our body	2	S_1

Pre-service science teachers found it useful in the virtual trip to science centers in terms of providing effective learning, facilitating transportation, facilitating the visualization of abstract expressions, increasing retention, interest and attention in the teaching environment. At the same time, the pre-service teachers stated that they had knowledge thanks to this virtual trip, since they did not have any information about science centers.

Pre-service science teachers' suggestions for the science center virtual trip

- Science centers can be expanded in Turkey and virtual tours can be made in science classes. (S_1)
- The number of images and models can be increased for each subject. (S_1, S_4)
- In addition to visual, vehicles can be supported audibly or virtual trips can be made more effective with three-dimensional glasses (S_3)
- Materials related to all science subjects can be shared. (S_4)

- The number of science centers can be increased (S_1, S_4, S_5)
- Teachers can be trained on the use of virtual tours to science centers (S_6)

4.CONCLUSIONS

It was understood from the answers given during the interview that the pre-service science teachers did not have enough information about the science centers in Turkey. Similarly, Yolcu & Karaosmanoğlu (2021) emphasized that teachers do not have sufficient knowledge about science centers in Turkey while examining the opinions of teachers about a virtual tour to Konya Science Center. In order to solve this problem, as stated by the pre-service science teachers, teachers can be trained about the use of science centers and virtual tours to science centers.

Özcan, Demirel & Ergül (2019) examined the students' views on the Konya Science Center trip, they stated that the students' science center was interesting and intriguing and useful for discovering new information. In the present study, pre-service science teachers interpreted the science center virtual trip as visiting places, doing experiments and discovering knowledge using virtual methods. In this context, in order to increase the attention and interest of students in science centers, areas where students can experiment can be created in the science center or environments where simulation experiments will be carried out on virtual tours can be added to the system. Pre-service science teachers stated that virtual trips to the science center were beneficial in terms of being memorable. Kubat (2018) examined the views of pre-service science teachers about out-of-school learning environments and stated that out-of-school learning environments would make positive contributions to permanent learning. Studies in the literature have reported that visits to science center's positively affect students' interest in science lessons (Erçetin & Görgülü, 2018). In the present study, pre-service science teachers stated that virtual tours would be useful in attracting attention to the lesson. In this context, it can be said that science centers will increase their interest in science lessons, and virtual tours to these science centers will increase their interest in science lessons. By conducting research on this subject, the correlation between virtual tours and students' interest in the course can be examined.

Pre-service science teachers stated that they liked the virtual tour very much and found it useful. All the candidates stated that they would use this application in their teaching life. Bozdoğan (2008) stated in his study that science centers are beneficial for the professional development of teacher candidates. It is thought that the use of virtual tours will contribute to the professional development of teacher candidates when trips to science centers are not possible. It is recommended to include virtual tours of the science center in the lessons given to pre-service science teachers.

REFERENCES

1. Bozdoğan, A. E. (2008). The Assessment of The Science Centers of The Pre-Service Science Teachers in Terms of Science Education: The Case of Feza Gürsey Science Center. Uludağ University Journal of Education Faculty., 21(1), 19-41.

2. Bozdoğan, A. E. (2019). Role and Importance of Science and Technology in Education. Doctoral Dissertation Institute of Educational Science, 239 pages.
3. Creswell J. W. (2013). Qualitative Research Methods: Qualitative Research and Research Design According to Five Approachesi. (M. Bütün ve S. B. Demir, Çev.) Ankara: Siyasi Kitabevi
4. Çepni, S. (2018)., Introduction to Research and Project Studies, Third Edition, Üçyol Kültür Merkezi Yayıncılık, Trabzon.
5. Erçetin, Ş. Ş., & Görgülü, D. (2018). Examining the Opinions of 6th Grade Students Visiting Science Centers on Science Lesson: Example of Konya Science Center, Gazi University Turkish Journal of Educational Sciences, 16(2).
6. Karadeniz, C.(2009). Analysis of Children's Museums and Science, Technology and Discovery Centers around the World and Setting a Children's Museum Model for Turkey. Master Dissertation . Ankara University. Social Sciences Institute
7. Kırgız, M. (2018). Evaluation of Konya Science Center's Science Activities and İnvestigation of the Effects of This Activities on Attitudes and Behaviors Towards Science Lessons.
8. Kubat, U. (2018). Opinions of Pre-Service Science Teachers About Outdoor Educatıon. Mehmet Akif Ersoy University Journal of the Faculty of Education, (48), 111-135.
9. Öner G. & Öztürk, M. (2019). Science Centres as Outdoor Teaching Environments:Experience of Prospective Social Studies Teachers. Eskişehir Osmangazi University Journal of Social Sciences, 20, 1109-1135.
10. Özcan, H., Demirel, R. & Ergül, S. (2019. An Investigation of Middle School Students' Views About Konya Science Center. Balıkesir University Journal of Social Sciences Institute, 22(42), 141-158
11. Patton, M. Q. (2014). Qualitative Research and Evaluation Methods (S. B. Demir & M. Bütün, Ed.). Ankara: Pegem Akademi.
12. Sırtkaya, A.& Ertaş, Ş. (2019). Black Sea Summit 2. International Social Sciences Congress. 23-25 Ağustos RİZE
13. TÜBİTAK (Turkish Scientific and Technological Research Council), (2022). Science Center Establishment Support Program. www.tubitak.gov.tr. Son Erişim Tarihi: 01.03.2022.
14. Yolcu, H. & Karamustafaoğlu, O. (2021). Teachers' Opinions on the Scientific Effect of a Virtual Trip to Konya Science Center.Ahi Evran University Journal of Kirsehir Education Faculty, 22(3), 1925-1983
15. Yıldırım, A. & Şimşek, H. (2021).Qualitative Research Methods in Social Sciences. Seçkin Yayıncılık. Ankara.

SEGMENTATION OF ELECTRICITY SUBSCRIBERS BASED ON THE CONSUMPTION PATTERNS

Hicran Gümüşbaş[1], Ulas Vural[1, 2]

[1] Nar System Technology Inc., Istanbul, Turkey

[2] Kocaeli Health and Technology University, Kocaeli, Turkey

hicran.gumusbas@nar.com.tr, ulas.vural@kocaelisaglik.edu.tr

Abstract

Electricity is a strategic and expensive resource that must be carefully managed. Discovering and accurately modeling the temporal consumption patterns of the subscribers is crucial for offering a reliable energy supply. In addition, energy consumption models are also useful for determining anomalies in the consumption trends and forecasting high-load risks on power distribution nodes.

Feasible modeling of consumption data should be both efficient and accurate. This paper presents a method to cluster customers with similar consumption patterns to increase the overall model accuracy while keeping the number of generated models low. Hourly energy consumption data is collected from real commercial electricity subscribers by using automated meter reading systems. These time-series data are clustered by using the K-means algorithm.

The clustering algorithm is tested on a dataset that contains a 104-day record of hourly energy consumption of 376 commercial subscribers in Turkey. The experimental results are given for two different normalization schemes of daily and weekly usage. The optimal number of clusters for both experiments is determined as 6 by using the elbow heuristic. The inertia metric is calculated as 365.9 for weekly normalized and as 340.2 for the daily normalized data.

Keywords: Customer Segmentation; Electricity Consumption; Clustering; Time-series.

1.INTRODUCTION

Better recognition of customers' demands supports corporations improve customer satisfaction and optimally planning their productions. Today, companies have a very precious resource such as digitally stored information about customers' demographics and their completed transactions to identify the customers better. On these data, each customer may be identified independently. However, in this approach, it is needed to generate and maintain a huge number of standalone models and a considerable part of these models may suffer from a lack of data. One better approach to lessen these problems is to group similar customers and generate models for each group instead of the customers. Grouping of similar customers is called customer segmentation and because of its advantages, customer segmentation has become very popular in many different kinds of sectors such as e-commerce and retail to telco and energy corporations [1].

Energy resources are of critical importance for all countries. Especially; electrical energy, which is indispensable for both residences, businesses, and industries, should be managed effectively. It is technically hard and expensive to store large amounts of electricity, so its production must be planned to fully meet the needs. While over-production wastes resources, under-production causes the disruption of industrial production or the lack of energy in residential areas. Therefore, the power distribution and transmission companies have to recognize the consumers well and forecast their demands. A good way to achieve this is to segment customers with similar consumption patterns [2,3].

Electricity consumption is metered periodically and the amounts of usage are logged in the databases of the power transmission companies. Sequential recording of the measurements forms a time-series data and it adds valuable information on consumption trends [4]. Similar differentiation patterns in consumption are used to discover consistent customer segments [5,6].

There is a wide number of studies in the academic literature on the segmentation of electricity consumers [7]. Some of these studies prefer using statistical features of the data instead of using the time-series directly [8]. This approach makes those methods more efficient by reducing the dimension of the feature set. However, they ignore proximity in the temporal trends that are important for the identification of consumers with similar usage patterns. Gullo et. al proposes a time-series-based clustering method that uses Dynamic-Time Warping to achieve robustness against the temporal shifts [9]. To decrease the computational requirement of the time-series clustering, [10] suggests an iterative refinement clustering method for faster adaptation to the new cluster formations. Another study that aims to increase the efficiency of the time-series clustering, offers Principal Component Analysis to reduce the number of features and the non-uniform binary split algorithm as a low-complexity pre-clustering step [11]. Although all these methods work on the time-series data, they directly use raw measured data or normalization by the highest usage amount.

In this paper, we propose a customer segmentation method for electricity distribution companies. The method works on the time series of hourly collected smart-meter data that are normalized on daily and weekly bases. This normalization is used to suppress the effect of anomalies and in addition, it allows the trends on demand ratios to stand out. A time-series version of K-means algorithm is preferred to compute clusters and the optimal number of the clusters is estimated by using the elbow method. The proposed method was tested on the real data of an electricity distribution company in Turkey and its effectiveness is shown.

The rest of this paper is organized as follows: the details of the proposed method are described in Section 2 and the experimental results are given in Section 3. The paper concludes in Section 4 with a discussion of the results and the method.

2.GENERAL PROPERTIES OF METHOD

Description of The Method

The consumption profiles of each customer c in customer set C, form a time series data $t_c = (m_1, m_2, \ldots, m_n)$ where t_c is a vector of size n that holds metered usages m . All the t_c vectors in set C are of the same size and they are sorted in time using the timestamp values.

The k-means algorithm is adopted for clustering customers upon these time series. The basic flow of the algorithm is given as follows:

1. For a predetermined number of k clusters, the algorithm requires an input set of customers C and it outputs a vector $\mathrm{V} = \{v_1, v_2, \ldots, v_k\}$ of cluster centers where each element of V is also a vector of size t_c.
2. Each cluster center $v \in V$ is randomly initialized.
3. Distances of each $c \in C$ to each cluster centers of $v \in V$ are calculated by using Eq. 1.

$$Distance(c, v) = \sum(\|t_c - v\|)^2 \quad (1),$$

where $\|a - b\|$ is the Euclidean distance between two vectors of a and b.

4. Assign customer c to the cluster center v whose distance from the cluster center is minimum of all the cluster centers in V.
5. Recalculate the cluster centers of all $v \in V$ by using Eq. 2.

$$v = \frac{1}{s(v)} \sum\nolimits_{c \in v} t_c \quad (2),$$

where $s(v)$ is the number of customers assigned to the cluster v.

6. If there is not any customer c whose cluster assignment changed then finish the clustering, otherwise repeat from Step-3.

Description of The Dataset

In the dataset, there are records of 376 standalone commercial subscribers from Turkey. These records start from the first of January and there is a total of 104-day records for each subscriber. The data was collected on an hourly basis from the smart meters and the length of real-valued vectors t_c are 2,496 (24 measurements for 104 days).

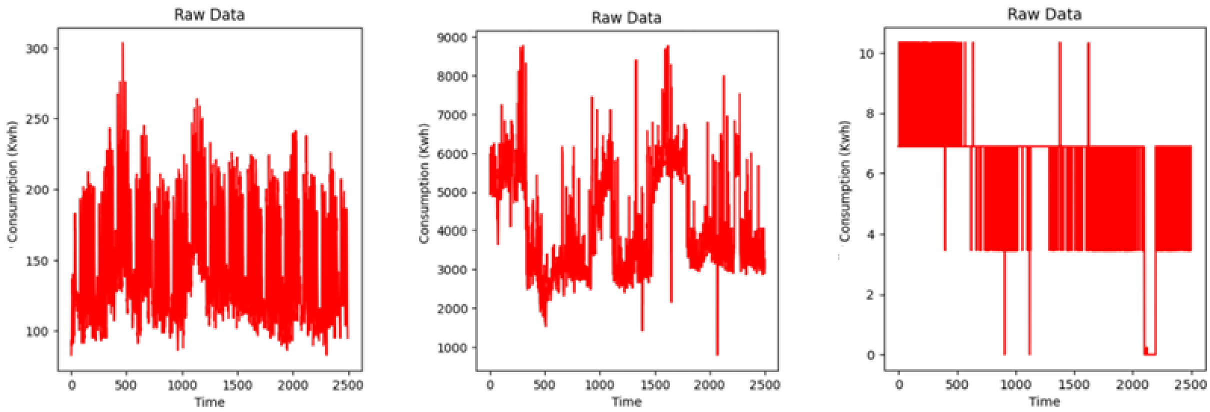

Figure 1. Load profiles of three different customers in the dataset.

In Fig. 1, one may see that there are high variations between subscribers' load profiles. For the subscriber that is in the middle of the figure, measured usage values vary between 1,000 kWh to 9,000 kWh while the subscriber on the right-hand side consumes a maximum of 10 kWh. Also, there are considerable variations in the own load profiles of the subscribers. This situation makes it harder to find out the consumption trends similarities. So, the data should be normalized for the fair calculation of Euclidean distances that are used to represent consumption trends.

Normalization

As the dynamic range of the raw consumption data is very large, the Euclidean distance will prioritize the similarity of consumption amounts instead of the trends. It is also known that data normalization is good to balance the weights of features. Therefore, in this study, the raw data is normalized in two different forms.

First, daily normalization is applied to obtain the percentage of electricity usage for that hourly period of time.

For doing this, each hourly measured amount is divided by the total amount of consumption on that day. We do this similarly for the weekly normalization. But this time each hourly measured amount is divided by the total amount of consumption on that week, instead of the day.

$$m_i = \frac{m_i}{\sum_j \begin{cases} m_j & if \left\lfloor \frac{j}{NS} \right\rfloor = \left\lfloor \frac{i}{NS} \right\rfloor \\ 0 & otherwise \end{cases}}, \forall m_i \in t_c$$

where NS is the number of samples in a normalization period and it is 24 for daily normalization and $168 = 24\ x\ 7$ for weekly normalization.

In Figure. 2, measured consumption amounts of a customer are shown. For this customer, the daily and weekly normalized time-series data are also given in the figure. The total values of normalized cases will be 100 and one can notice that the percentage values in the daily normalized case are nearly 7 times the weekly normalized one.

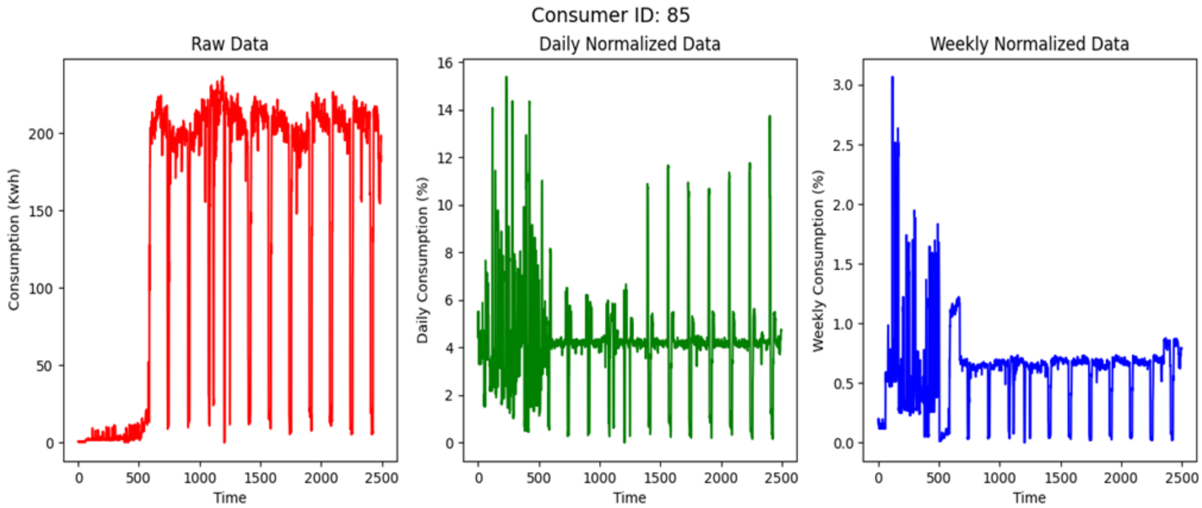

Figure 2. Graphics of raw consumption data of a consumer and its daily and weekly normalized cases.

3.APPLICATIONS

The application of the method needs a pre-calculation for the parameter k of the k-means algorithm. To find out the optimal k value, the time-series K-means algorithm is tested with a wide range of k values on daily normalized data and logged the inertia values. The inertia gives an indication of how coherent the different clusters are. It is simply based on the computation of the squared distance of each sample in a cluster to its cluster center. This process is done for each cluster and all samples within that data set. The resulting inertia is the sum of the inertia values of all clusters.

As the K-means has a nature of randomity, the inertia values of a specific k-value vary on different runs. So, we model these inertia values to suppress the randomity problem and the noisy data. We prefer to use a power curve for fitting. In Figures 3. and 4., the inertia values for given k values are given. The blue solid lines are representing the raw inertia values and the solid orange curves are for the modeled power curves. The modeled power curve for the daily normalized data is $y = 420.0818 * x^{-0.1057239}$ and is $y = 442.8546 * x^{-0.1062802}$ for the weekly normalized data. Red dashed lines are two fitted lines to the modeled data and it is assumed that the rounding values of their intersections are giving the optimal k values.

In Figure 5, the results of time-series clustering for the optimal k-value computed as six are shown. Red lines show the cluster models and the black lines are the overlapping load profiles of the cluster members.

The optimal number of clusters for both experiments is determined as 6 by using the elbow heuristic. The inertia metric is calculated as 365.9 for weekly normalized and as 340.2 for the daily normalized data for k=6.

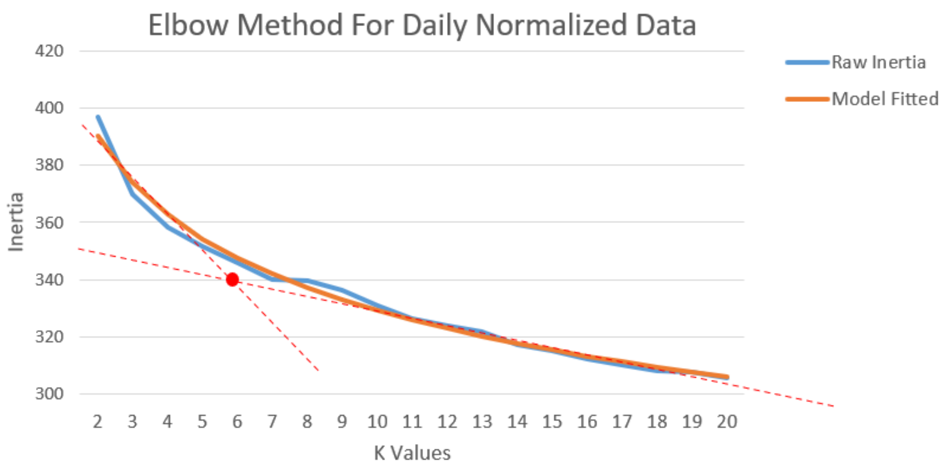

Figure 3. Elbow analysis to find out the optimal k value for the daily normalized data

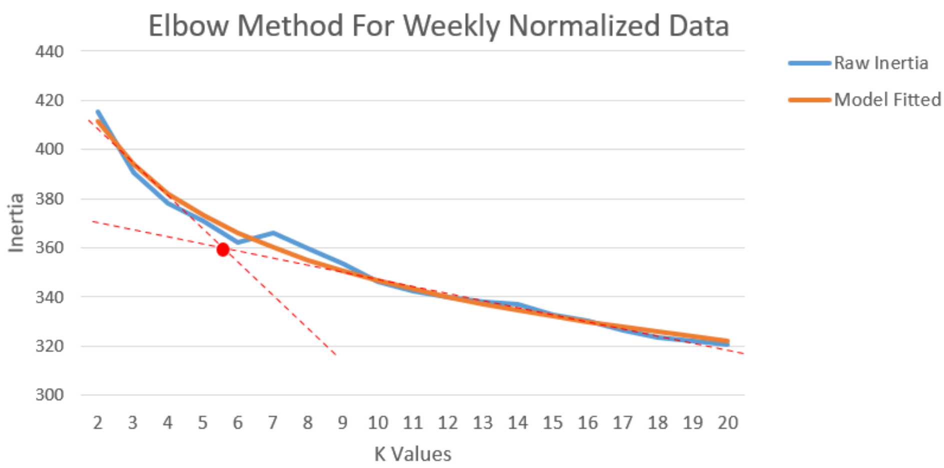

Figure 4. Elbow analysis to find out the optimal k value for the weekly normalized data

For the daily normalized data, Cluster-6 shows a good periodicity and it has more than 100 members. The other cluster models have some high-frequency patterns on the load profiles. In Cluster-3 there is a large variation based on the model and these customers need to be reconsidered to reduce the in-class variation.

For the weekly normalized cases, the models show obviously different periodicities but it may be seen that in Cluster-3 there is a large variance similar to the daily normalized data and this cluster should be reconsidered as well. In other clusters, the inner-class variance is acceptable. For Clusters-2, 4, and 6, weekly consumption patterns can obviously be seen on the graphs.

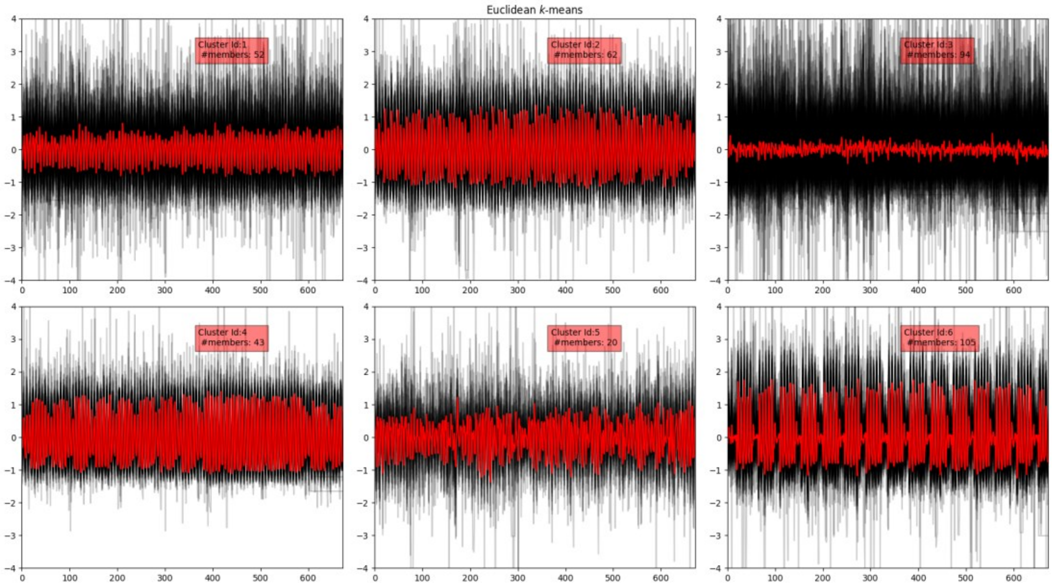

Figure 5. The clustering results for the daily normalized data

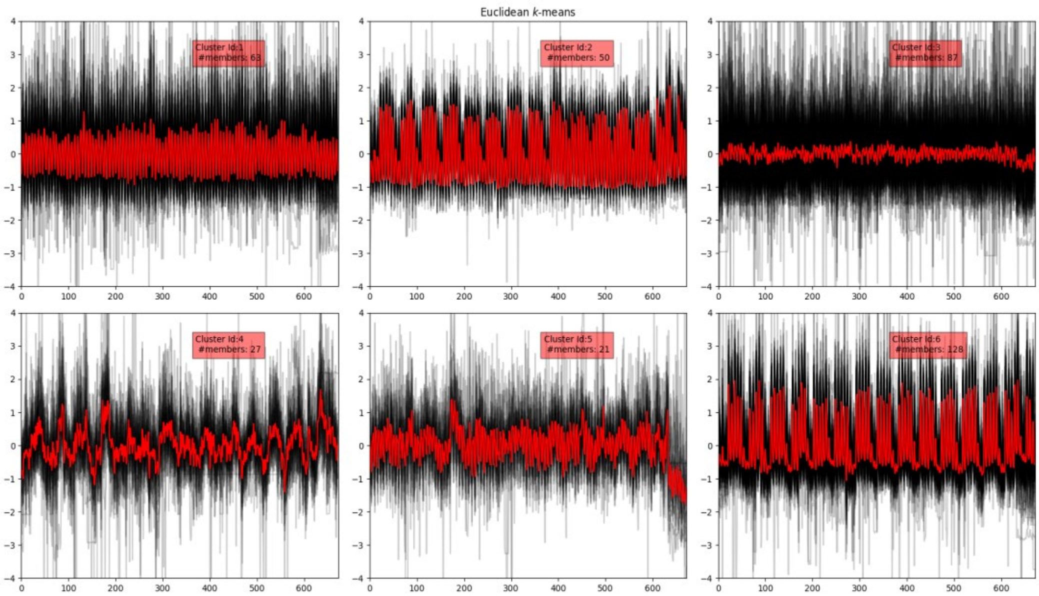

Figure 6. The clustering results for the weekly normalized data

4.CONCLUSIONS

Fast and consistent segmentation of electricity consumers keeps its academic and commercial importance. With the increased amount of data collected from smart meters and the developments in machine learning technologies, more advanced segmentation methods will appear. The common properties of these methods will be using the trend data on the load profiles. In this study, we showed the effectiveness of clustering algorithms working on daily and weekly normalized meter data. In the future, we plan to use customer segments to predict power demands and detect anomalies in the consumption patterns.

REFERENCES

1. Das S, Nayak J. Customer Segmentation via Data Mining Techniques: State-of-the-Art Review. Computational Intelligence in Data Mining. 2022:489-507.
2. Rajabi A, Eskandari M, Ghadi MJ, Li L, Zhang J, Siano P. A comparative study of clustering techniques for electrical load pattern segmentation. Ren. and Sust. Energy Reviews. 2020.
3. Pilo F, Pisano G, Ruggeri S, Troncia M. Data analytics for profiling low-voltage customers with smart meter readings. Applied Sciences. 2021.
4. Aghabozorgi S, Shirkhorshidi AS, Wah TY. Time-series clustering–a decade review. Information Systems. 2015 Oct 1;53:16-38.
5. Morales F, García-Torres M, Velázquez G, Daumas-Ladouce F, Gardel-Sotomayor PE, Gómez-Vela F, Divina F, Vázquez Noguera JL, Sauer Ayala C, Pinto-Roa DP, Mello-Román JC. Analysis of Electric Energy Consumption Profiles Using a Machine Learning Approach: A Paraguayan Case Study. Electronics. 2022.
6. Yilmaz S, Chambers J, Patel MK. Comparison of clustering approaches for domestic electricity load profile characterisation-Implications for demand side management. Energy. 2019 Aug 1;180:665-77.
7. Yildiz B, Bilbao JI, Dore J, Sproul AB. Recent advances in the analysis of residential electricity consumption and applications of smart meter data. Applied Energy. 2017 Dec 15;208:402-27.
8. Räsänen T, Kolehmainen M. Feature-based clustering for electricity use time series data. InInternational conference on adaptive and natural computing algorithms 2009 Apr 23 (pp. 401-412). Springer, Berlin, Heidelberg.
9. Gullo F, Ponti G, Tagarelli A, liritano S, Ruffolo M, Labate D. Low-voltage electricity customer profiling based on load data clustering. InProceedings of the 2009 International Database Engineering & Applications Symposium 2009 Sep 16 (pp. 330-333)
10. Batrinu F, Chicco G, Napoli R, Piglione F, Postolache P, Scutariu M, Toader C. Efficient iterative refinement clustering for electricity customer classification. In2005 IEEE Russia Power Tech 2005 Jun 27 (pp. 1-7). IEEE.
11. Du Toit J, Davimes R, Mohamed A, Patel K, Nye JM. Customer segmentation using unsupervised learning on daily energy load profiles. Journal of Advances in Information Technology Vol. 2016 May;7(2):69-75.

ENERGY BASED EVALUATION OF REINFORCED CONCRETE STRUCTURE AFFORDABLE BY FAR FIELD EARTHQUAKE

Oğuzhan Çelebi[1], Barış Bayrak[2], Mahmut Kılıç[1], Abdulkadir Cüneyt Aydın[1]

[1] Department of Civil Engineering, University of Ataturk, Erzurum, Turkey

[2]Department of Civil Engineering, University of Kafkas, Kars, Turkey

celebioguzhan@atauni.edu.tr

Abstract

In today's Standards, many methods are used for the structural evaluation of reinforced concrete buildings, such as non-linear analysis in the time integration, unimodal and multimodal static pushover analysis, and summing of modes. In the literature, the evaluation of energy-based structures is a subject that has not been studied much. In addition, the criteria for this method are not specified in any Standard. The energy-based evaluation method is compared with the capacity curve of the structure (base shear force-peak displacement curve) by calculating the input energies to be generated by the earthquake in the building. If the earthquake energy demands in the building remain below this capacity curve, the damage levels are not foreseen for the building, but if it stays above the capacity curves, it is based on the principle that damage to the structure is likely to occur. The input energy of the earthquake can be dissipated with the plastic deformations that the structures can make without collapse, the kinetic energy depending on the mass of the structure in the elastic region, and the energy dissipated by viscous damping. In this study, the energy capacity of a 4-storey reinforced concrete structure, which does not have the risk of soil amplification, at 39.9026 Latitude and 41.2498 Longitude coordinates, was calculated by obtaining the base shear force - peak displacement curve using the pushover analysis method. Then, the minimum and maximum earthquakes in 2020 and 2021 affecting the structure were given as input, and the demand energies created by the earthquakes in the structure were calculated. By showing how much of these earthquake energies the building can dissipate, damage ındex were determined and the damage levels of the building were determined. In the calculation of the demand energies of the earthquake, the analysis method in the time domain defined in the Turkish Building Earthquake Code 2018 was applied. At the end of the study, the amount of energy required to be stored in the structure is shown in order to distribute the energy of an earthquake without damaging the structure.

Keywords: Earthquake ınput energy; Reinforced structure; Energy- based structural assesment; Damage ındex

1. INTRODUCTION

Strength-based applications in earthquake resistant design of buildings and strain-based applications in evaluating performance are available in standards such as TBEC-2018, ATC-40, UBC 1997. Generally, earthquake resistant structure design is made by considering the equivalent earthquake lateral forces calculated by using the acceleration spectrum curves obtained with parameters such as the ground structure of the place where the structure is located, earthquake ground motion level, location information [1-3]. These traditional procedures take into account the maximum ground acceleration affecting the structure and ignore the effects such as the effect time of the earthquake on the structure, the hysterical behavior and the fault mechanism [4]. However, the earthquake energy affecting the structure is not only dependent on the PEAK ground acceleration [5,6]. According to the earthquake energy, the type of the earthquake's release at the source, the distance of the earthquake wave from the source to the earthquake source, the geological condition of the intermediate region where the earthquake wave emanating from the source passes until the consideration, the refraction and reflection of the earthquake wave on the faults or free surfaces in the intermediate region, and the condition of the ground in the affected region [7]. The use of energy-based method in earthquake resistant design of buildings is likely to yield more accurate results than methodologies based on strength and displacement, in terms of considering all aspects of earthquake energy affecting the structure and at the same time including strength and displacement properties of structures [8]. In the energy-based analysis of structures, it is based on the principles of distributing the earthquake energy that will occur in the structure with viscous damping in the elastic region of the structure and permanent deformation without collapse in the inelastic region, taking into account the geological and structural formations [9].

In the literature, many studies have been carried out on the analysis of energy-based structures. Akbas et al. (2001) used the energy approach for the performance analysis of moment-resisting steel frames [6]. Benavent-Climent and Mota-Paez (2017) evaluated the soft two-storey reinforced concrete structure reinforced by the use of hysteretic dampers as energy-based [10]. The energy-based design foundation shear forces were derived by Merter and Uçar (2017) based on the pre-selected failure mechanism and the target story drift ratio for multi-storey reinforced concrete frame structures [11]. Gulu et al. (2018) calculated the seismic energy demands of multi-degree-of-freedom (MDOF) systems with approximate methods and showed the distribution of hysteretic energy between building elements and between floors of structures [12]. Yang et al. (2017) investigated the energy absorption capacity of reinforced concrete frames reinforced with buckling-prevented steel braces [13]. Donaire-Avila et al. (2018) based the plastic energy dissipation capacity of a reinforced concrete structure at floor levels under the effect of an earthquake on a coefficient showing the ratio of the base shear force at the floor level at the time of flow to the seismic intensity [14]. Sang-Hoon Oh et al. (2021) studied the effects of torsion on seismic response using the energy-based approach [15].

In this study, a 4-storey reinforced concrete structure was designed according to TBEC-2018 (Turkish Building Earthquake Regulation) in Erzurum, Turkey. The possible energies of 5 different earthquakes in the region have been calculated approximately within the framework of different station records originating from far and near the area of the building. The possible input energies of earthquakes that will generate maximum and minimum energy in the selected earthquake records have been calculated with different methods defined in the literature. Finally, by drawing the capacity spectrum curve of the structure, the demand energies of the earthquakes in the building were compared with this capacity curve, and the energies distributed by the building were calculated.

2.GENERAL PROPERTIES OF METHOD

2.1. Seismicity of the Region

Earthquakes in Turkey are generally caused by the movement of the Arabian Plate. The speed of the Arabian plate blocked by the Eurasian plate decreased, resulting in the North Anatolian Fault (right slip) and the East Anatolian Fault (left slip), and the Anatolian plate was forced westward. In addition to these movements, the African Plate makes a subduction movement under the Eurasian Plate. As a result of these tectonic movements, compression, slipping, tearing as well as subduction and sinking occur along the faults separating the plates, and many earthquakes occur in the Aegean Depression region, which is compressed in between. In the Aegean Depression Region, there are many tectonic uplifts and depression-forming blocks of different sizes, which have a mixed appearance and whose edges are limited by small slip faults. The North Anatolian Fault is one of the most vital benefits of the world in terms of earthquake motion. Starting from Karlıova, its northern branch proceeds to the Soros Gulf through the Sea of Marmara, and its southern branch proceeds to the Aegean Sea. Starting from Karlıova, the East Anatolian Fault branches off at the Türkoğlu junction in the south-west. Its arms reach Cyprus in the north and the Dead Sea in the south. Faults change places at an annual rate of 5-70 mm/year. Hazardous earthquake location map including fault lines and ruptures in Turkey is shown in Figure 1 [7].

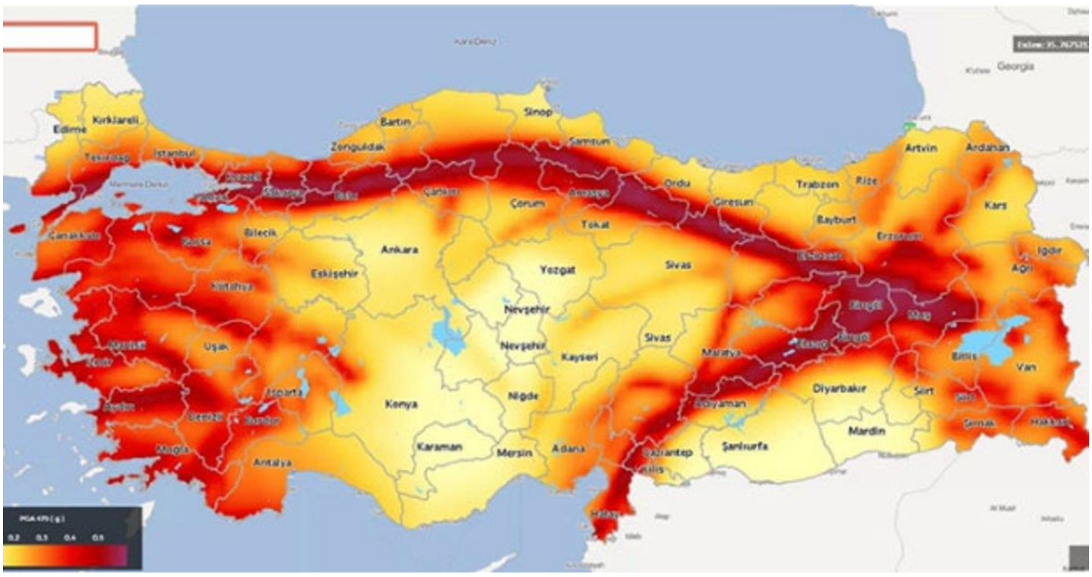

Figure 1. Fault lines and seismic zones in Turkey [16]

Since Turkey is located in the area where the convergence of the Arabian and Eurasian plates in the Eastern Anatolia Region takes place, it is located in the seismically active region [17]. In the Eastern Anatolia Region, an earthquake of more than 10 magnitudes occurred due to the Eastern Anatolian Fault Line and the North Anatolian Fault Line when looking at the historical periods [18]. Erzurum is a seismically active seismic region in Eastern Anatolia that reaches the highest ground accelerations (>0.5g) [16]. The Horasan-Şenkaya Fault Zone, located in the northwest of Erzurum, consists of faults that extend up to 10 km in length parallel to each other. Horasan-Şenkaya Fault Zone, which is a left-lateral strike-slip fault, produced an earthquake of Mw=6.6 on 30 October 1983 [17]. Examples of earthquakes with a moment magnitude of Mw>5.0 affecting the Erzurum surroundings from the 1900s to the present are given in Table 1. The earthquakes given in Table 1 are classified as earthquakes originating from nearby areas affecting Erzurum. In Table 2, some examples of earthquakes originating from remote areas affecting Erzurum and its surroundings are given. Earthquakes originating from the near field are seen in the records at a distance of 15-30 km. Such near-source ground motion is affected by the fracture mechanism and the permanent deformations that occur. Its distinctive feature is the presence of long-period and pulse-like oscillations in speed change. Another feature of near-source ground motion recording is that body waves are effective in motion. While Rayleigh and Love surface waves are effective in regions far from the source, the effect of body waves is not significant. On the other hand, P and S waves are significantly effective in near-source ground motion. While distant source ground motion creates horizontal displacements in the structure through surface waves, near source ground motion causes vertical oscillations [7].

Table 1. Some earthquakes affecting Erzurum and its surroundings (Mw>5.0) [16]

Location	Date	Type	Magnitude	Depth (km)	Heavy damage structure	Loss of live
Pasinler	13.09.1924	Ms	6.9	10	4300	310
Hınıs	25.10.1959	Ms	5.0	50	300	18
Şenkaya-Horasan	30.10.1983	Ms	6.8	16	3241	1155
Balkaya	18.09.1984	Ms	5.8	10	187	3
Aşkale	25.03.2004	Ms	5.1	3	1212	10
Köprüköy	19.10.2021	Mw	5.1	7	54	-

Table 2 Earthquakes originating from far field affecting Erzurum and its surroundings (Mw>5.0) [16]

Location	Date	Type	Magnitude	Depth (km)	Heavy damage structure	Loss of live
Erzincan Otlukbeli	13.03.1992	Mw	6.6	22.6	8057	653
Bingöl Merkez	01.05.2003	Mw	6.8	10	625	176
Elazığ Sivrice	24.01.2020	Mw	6.8	8	645	41

2.2. Earthquake Energy

Although the earthquake energy caused by the earthquakes originating from the nearby area increases in parallel with the magnitude, the magnitude of the earthquake energy entering the structure may differ. In some cases, the input energy of the earthquake, which acts as a far field, to the structure may be higher against the earthquake originating from the near field. Depending on the magnitude of the earthquake energy revealed by the ground motion vibration, the distance of the region where the earthquake energy is released at the source, the distance from the source where the earthquake energy is released, the geological condition of the intermediate region where the earthquake wave emanating from the source passes, the faults in the intermediate region or the free zone. It also differs according to the refraction and reflection of the earthquake wave on the surfaces and the condition of the ground in the area taken into account. In the event that an earthquake that occurs in a region affects another region from a distant area, more energy will be released if the ground state of that region is in different forms. For example, an earthquake at the epicenter with a medium-firm sandy ground is likely to have lower energy than the alluvial ground regions located far from the source. At the focal point, known as the origin of the earthquake, the energy of the earthquake is defined as in Equation 1, depending on the magnitude of the earthquake [9]. M_0 is the seismic moment, Δτ is the stress drop, and G is the shear modulus of the medium. The relationship between the magnitude of the earthquake and the energy released during the earthquake motion is given in Equation 2. It is explained by the energy reduction relations that an earthquake occurring at any focal point will create in any region due to the far field. The highest ground acceleration value that the earthquake will create in the epicenter regions and the highest ground acceleration value that it will create in the far-field sourced region differ. Therefore, it is predicted that the formulation specified in Equation 3 can be used to describe the effects of earthquakes originating from far-field sources. Energy calculation was made depending on the magnitude of the earthquake felt in the region, depending on the highest ground acceleration that an earthquake will create in any region [7].

$$Es=1/2G\ \Delta\tau M0 \tag{1}$$

$$logEs=1.5Ms+4.2 \tag{2}$$

$$M_s=\log A_{20}+1.66\log\Delta+2.0 \tag{3}$$

In Equation 3, Ms defines the earthquake's surface wave magnitude, A20 defines the 20 s period Rayleigh surface wave amplitude, and Δ (km) defines the intermediate distance from the epicenter. In this study, considering the campus located at 39.9026 Latitude and 41.2498 Longitude in Erzurum Yakutiye District, the total energies produced by earthquakes in this campus in 2020 and 2021 are given in Table 3 and Table 4, respectively.

Table 3. The energy generated by earthquakes in the campus referenced in 2020 [16]

Earthquake	Date	Magnitude (Mw)	Δ (km)	A20 (m/sn2)	Magnitude (Ms)	Es (J)
Elazığ Sivrice	24.1.2020	6,8	372	0,179	5,5	3,02E+12
Elazığ Sivrice	25.1.2020	5,1	372	0,0015	3,4	2,32E+09
Muş Merkez	9.2.2020	3,2	223	0,0037	3,5	2,51E+09
İran Khoy	23.2.2020	5,9	481	0,001	3,5	2,39E+09
İran Khoy	23.2.2020	5,9	481	0,0012	3,5	3,14E+09
Kars Sarıkamış	10.3.2020	4,0	174	0,0003	2,2	3,12E+07
Bingöl Karlıova	11.3.2020	3	136	0,0008	2,4	7,36E+07
Bingöl Karlıova	12.4.2020	4,3	136	0,00073	2,4	6,42E+07
Bingöl Karlıova	14.6.2020	5,7	136	0,0067	3,4	1,78E+09
Bingöl Karlıova	14.6.2020	4,6	136	0,00156	2,7	2,01E+08
Bingöl Karlıova	14.6.2020	4,7	136	0,00327	3,1	6,09E+08
Bingöl Karlıova	15.6.2020	5,6	136	0,0072	3,4	1,99E+09
Bingöl Karlıova	9.9.2020	3,5	136	0,0021	2,9	3,13E+08
Bingöl Karlıova	9.9.2020	4,1	136	0,0103	3,6	3,40E+09
Muş Korkut	16.9.2020	4,7	290	0,0006	2,9	3,15E+08
Muş Korkut	18.9.2020	4,2	290	0,0007	2,9	3,97E+08
Bingöl Merkez	25.10.2020	4,0	218	0,00018	2,1	2,54E+07
Bingöl Merkez	8.11.2020	4,2	218	0,0124	4,0	1,46E+10
Tunceli Pulümür	14.11.2020	4,1	195	0,0008	2,7	1,81E+08
Erzurum	28.11.2020	3,5	56	0,0185	3,2	8,99E+08

Pasinler	
Total	**3,05E+12**

Table 4. The energy generated by earthquakes in the campus referenced in 2020 [16]

Earthquake	**Date**	**Magnitude (Mw)**	Δ (km)	**A20 (m/sn2)**	**Magnitude Ms**	**Es (J)**
Bingöl Karlıova	7.1.2021	3,8	136	0,004	3,1	8,23E+08
Bingöl Karlıova	25.2.2021	4,1	136	0,0105	3,6	3,50E+09
Bingöl Merkez	9.3.2021	4,0	218	0,0053	3,6	4,07E+09
Muş Korkut	7.4.2021	4,2	290	0,0031	3,6	3,70E+09
Erzincan Otlukbeli	25.5.2021	4,2	176	0,0017	3,0	4,34E+08
Bingöl Kigi	25.6.2021	5,2	276	0,0058	3,8	8,38E+09
Bingöl Kigi	28.7.2021	4,3	276	0,0025	3,4	2,37E+09
Erzurum Aşkale	15.11.2021	3,5	74	0,0028	2,6	1,06E+08
Erzurum Köprüköy	19.11.2021	5,1	75	0,0235	3,5	2,66E+09
Erzurum Köprüköy	22.11.2021	4,7	75	0,0289	3,6	3,63E+09
Erzurum Tekman	27.12.2021	3,7	96	0,0144	3,4	2,36E+09
Total						**3,20E+10**

2.3. Structure Input Energy

Earthquakes create a vibrational energy by spreading freely on the earth. Earthquake energies can create many stresses (axial load, bending moment, shear force, torsion, etc.) on the structure. In order to meet all these demands, there must be an adaptation between stability, damping, sufficient stiffness, sufficient strength, lightness and carrier elements in the structure. In fact, such earthquake resistance basic principles are related to the energy that an earthquake will create in the structure. The earthquake creates an input energy in the structure by acting in the vertical and horizontal directions. This input energy generated in the structure can be dissipated by viscous damping in the elastic region of the structure and permanent deformation in the inelastic region without collapse. Depending on the general principle of dynamics (Equation 4), the right side of the equation shows the earthquake energy entering the structure, and the left side shows that this earthquake energy is dissipated by kinetic energy, damping energy and permanent deformation [9].

$$\int_0^u m\ddot{u}(t)du + \int_0^u c\,\dot{u}(t)du + \int_0^u f_s(u,\dot{u})du = -\int_0^u m\ddot{u}g(t)du \tag{4}$$

Where, $\int_0^u m\ddot{u}(t)du$ E_k kinetic energy, $\int_0^u c\,\dot{u}(t)du$ E_d damping energy, $\int_0^u f_s(u,\dot{u})du$ plastic strain (hysteretic energy) energy and $-\int_0^u m\ddot{u}g(t)du$ represents the earthquake energy entering the structure.

In the literature, earthquake input energy can be calculated with a number of approaches. Housner (1956) showed that some of the energy transferred to a structure during ground motion is dissipated by damping and nonlinear behavior of the structure, while the rest is stored as kinetic and elastic strain energy [19].

$$\frac{E_i}{m}=\frac{1}{2}(PSV)^2 \tag{5}$$

Considering three ground motion records, Akiyama (1985) stated that in Equation 5 it is acceptable in the inelastic condition, except for short-period structures, and that the equivalent velocity, Ve can be used instead of PSV in Equation 5 in the aforementioned study [20].

$$\frac{E_i}{m}=\frac{1}{2}(V_e)^2 \tag{6}$$

Ve, those given in Equation 7 are proposed for the equivalent velocity. In Equation 6, T represents the dominant period of the structure and Tg represents the dominant period of the earthquake.

$$\begin{aligned} V_e &= 2.5T \qquad T \leq T_g \\ V_e &= 2.5T_g \qquad T > T_g \end{aligned} \tag{7}$$

Kuwamura et al. (1994) showed that the equivalent input energy velocity spectrum in undamped elastic BSD systems is equal to the Fourier amplitude spectrum of the ground acceleration [21]:

$$V_e = FS(w) = \sqrt{\frac{2E_i}{m}} \tag{8}$$

It is also stated that in a multi-degree-of-freedom system, the spectral input energy can be obtained by directly summing the calculated input energies for all modes of the structure. Chai and Fajfar (2000) defined the equivalent input velocity as in Equation 9, based on the Fourier amplitude spectrum. Here, it is obtained according to Equation 10, with Ω being the amplification factor. PGV gives the highest velocity value of strong ground motion [22].

$$V_e = \Omega_v PGV \tag{9}$$

$$\Omega_v = {\Omega_v}^* \frac{T}{T_g} \rightarrow 0 \leq T \leq T_g \tag{10a}$$

$$\Omega_v = {\Omega_v}^* \frac{T}{T_g} \rightarrow T_g \leq T < \infty \tag{10b}$$

Here, ${\Omega_v}^*$ is calculated according to Equation 11 to define the largest amplification factor for the equivalent input velocity.

$${\Omega_v}^* = \frac{1}{Z}\frac{PGA}{PGV}\sqrt{t_d T_g}\sqrt{\frac{\lambda+1/2}{2\lambda}} \tag{11}$$

Here t_d is a multiplier showing the total duration of the earthquake obtained from the arias intensity curve, PGA the highest ground acceleration, Z the ratio of the highest ground acceleration to the square root of the mean of the squares of the ground acceleration. Manfrendi (2001) developed a method that allows obtaining a simplified expression for the cyclic and input energy spectra. The method is basically based on the evaluation of the equivalent number of cycles depending on the characteristics of the earthquake. Using the method, cyclic and input energy can be obtained depending on the ductility demand, the seismic index I_D and the maximum pseudo velocity. The seismic index I_D, which represents the earthquake characteristics, is calculated according to Equation 12 [23].

$$I_D = \frac{I_E}{PGA.PGV} \tag{12}$$

Here, I_E is calculated as in Equation 13 to show the acceleration record intensity of the earthquake. Manfrendi proposed Equation 14 to estimate the equivalent number of cycles for 5% damping.

$$I_E = \int_0^t \ddot{u}_g^2 \, dt \tag{13}$$

$$n_{eq} = 1 + 0.18(R_y - 1)^{3/5} I_D \tau^{-1/2} \qquad T > T_1 \rightarrow \tau = 1 \tag{14}$$

Here, Ry is the strength reduction coefficient, $\tau = T/T_1$ is the transition period from the middle period to the long period interval in the T_1 spectrum curve, and T is the elastic period of the system. Manfrendi formulated the spectral cyclic energy and the spectral input energy as in Equation 15 and Equation 16, respectively. Here, η_c is calculated as in Equation 17 to show the cyclic ductility coefficient. ΔXmax, specified in Equation 17, represents the largest amplitude of the plastic cycle and x_y represents the yield displacement.

$$\frac{E_h}{m} = (\eta_c - 1) n_{eq} (PSV)^2 \left(\frac{1}{R_y}\right)^2 \tag{15}$$

$$\frac{E_i}{m} = 1.4 \eta_c n_{eq} (PSV)^2 \left(\frac{1}{R_y}\right)^2 \tag{16}$$

$$\eta_c = 1 + \Delta X_{max}/x_y \geq 2.0 \tag{17}$$

In addition, the relationship between the strength reduction coefficient Ry and the ductility index μ is explained in Equation 18.

$$R_y = 1 + 0.5(\mu - 1)^{4/5} \tau^{3/4} \tag{18}$$

Based on all these suggestions for earthquake input energy calculations, Park et al. (1987) specified a damage index (DIPA) as in Equation 19 to evaluate structural damage on an energy basis.

$$DI_{PA} = \frac{u_m}{u} + \beta \frac{E_h}{F_y u_u} \tag{19}$$

Here, um is the nonlinear displacement obtained in the step-by-step structure analysis, u is the displacement at the time of yield, uu is the final displacement, Fy is the base shear force formed in the structure at the time of yield, Eh is the earthquake input energy, and β is the strength reduction parameter according to the section properties in Equation 20.

$$\beta = \left(-0.447 + 0.73\frac{L}{D} + 0.24\frac{P}{A_g f_c'} + 0.314\rho_1\right)0.7\rho_s \qquad (20)$$

Here, L/D ratio is aspect ratio, $\frac{P}{A_g f_c'}$ is dimensionless axial force, ρ_l is longitudinal reinforcement ratio and ρ_s is transverse reinforcement ratio.

By obtaining the capacity curve (base shear force-displacement curve) of the structure, the yield displacement, final displacement and base shear force values of the structure are obtained. The capacity curve of the structure is typically obtained by the single-mode or multi-mode static pushover analysis (pushover analysis) method as in Figure 2. Then, the earthquake data, scaled according to the relevant standards, are given to the building as input and the energy demands (Eh) of the earthquakes are calculated. Finally, the damage index of the building is calculated as in Equation 19, and the damage level of the structure is determined according to Table 5. In this case, the total energy dissipated by the building and the energy demanded by the earthquake are calculated.

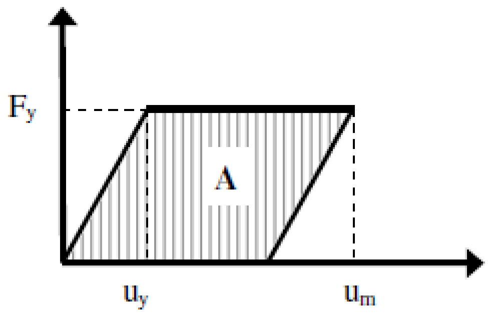

Figure 2. Idealized base shear force-displacement curve [8]

Table 5. Damage ındex [24]

DIPA<0.1	No-damage or local partial cracking
0.1<DIPA<0.25	Slight damage – slight cracking
0.25<DIPA<0.40	Middle damage – heavy cracking, local spill in concrete
0.40<DIPA<1.0	Heavy damage – crush in concrete, anchorage slip
DIPA≥1.0	Collapse

3.APPLICATIONS

3.1. Definition of Reinforced Concrete Structure

The reinforced concrete building, located at 39.9026 Latitude and 41.2498 Longitude locations, has 4 floors, a ground floor and three normal floors. The reinforced concrete building with a floor height of 3 meters on each floor has 3 openings in the X direction and 3 openings in the Y direction, and all floors have an area of 253 m^2 (Figure 4). The concrete class used in the bearing elements and floors of the reinforced concrete building is C35 and the reinforcement is S420a. The thickness of the outer walls used in the building is 20 cm, and the thickness of the inner walls is 10 cm. The central columns of the reinforced concrete building are 30x115 cm, the other columns are 30x50 cm, and the beams are 30x50 cm. The curtains on the ground floor are only 20 cm thick and the floors are 15 cm thick (Figure 3). The reinforcement details on the column, beam and shear of the reinforced concrete building are given in Table 6. Since the floors are formed with tile coating, in accordance with the TS500 Standard (Regulation on the calculation and design rules of reinforced concrete elements), the constant loads of the walls to the beams, with the live load (Q) 3.5 KN / m2 and the fixed load (G) 2.1 KN / m2 on the floors. given [25]. In accordance with Figure 3, Table 6 and related material-load information, the finite element model of the 4-storey reinforced concrete building was modeled as in Figure 4 using the SAP2000 program [26].

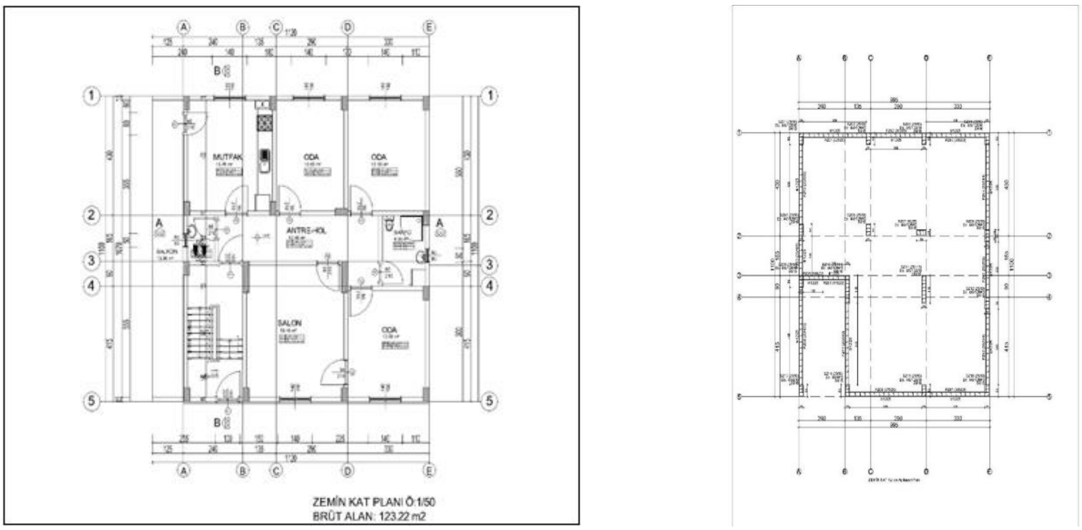

(a) (b)

Figure 3. The plan view of reinforced structure a) mold plan b) details of reinforcement

Figure 6. The details reinforcement of carrier members

Member	Longitudinal reinforcement	Transverse reinforcement	The class of reinforcement
S30x115 Column	16ϕ16	ϕ10/10/15	S420a
S30x50 Column	8ϕ16	ϕ10/10/15	S420a
K25x50 Beam	4ϕ14	ϕ10/10/15	S420a
P20 Shear wall	ϕ14/25	ϕ10	S420a

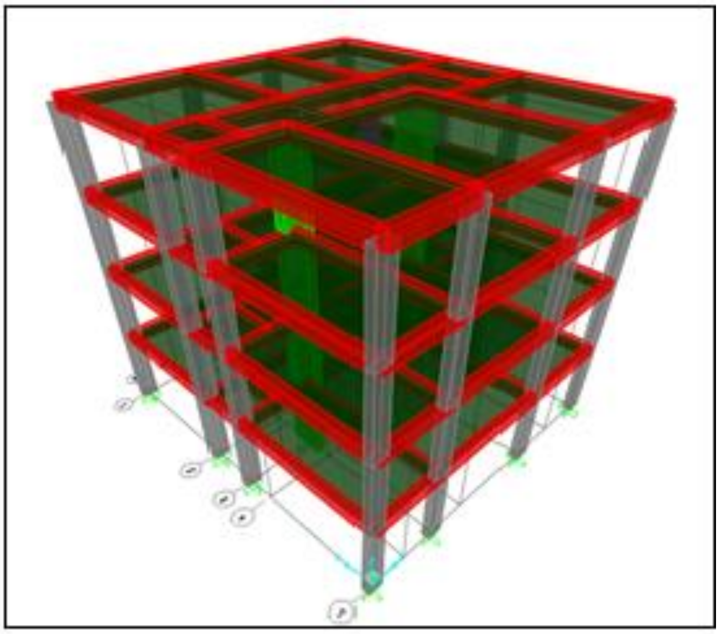

Figure 4. 3D modelling of reinforced structure

The reinforced concrete building has the Z_D floor class defined in TBDY 2018. Since it is an existing structure, earthquake ground motion level, DD-1, which has a 2% probability of being exceeded in 50 years (recurrence period of 2475 years) has been taken into account in the earthquake calculation and evaluation. Considering the Z_D ground class, DD-1 earthquake ground motion level and latitude-longitude location information, local earthquake parameters of the reinforced concrete structure were obtained from Turkey Hazardous Location Maps as in Table 7. In Table 7, SDS short period design spectral acceleration coefficient, S_{D1} map spectral acceleration coefficient for 1.0 second period, S_S short period map spectral acceleration coefficient, S_1 map spectral acceleration coefficient for 1.0 second period, PGA is the peak ground acceleration and PGV is the peak ground acceleration. is the ground speed.

Table 7. The local earthquake parameter of reinforced structure

DYD	S_{DS}	S_{D1}	S_S	S_1	PGA (g)	PGV (cm/sn)
DD-1	1.989	0.923	1.989	0.518	0.798	49.155
DD-2	1.13	0.567	1.048	0.277	0.440	26.664

Since it was designed for residential purposes, the building utilization class was taken as 3 (BKS=3) and the building importance coefficient 1 (I=1) according to TBDY 2018 Table 3.1. According to TBDY 2018 Table 3.2, earthquake design class was taken as 1 (DTS=1). According to TBDY 2018 Table 3.3, the building height class of the building was taken as 6 (BYS=6) due to the building height (HN= 12 m) and the earthquake design class (DTS=1). According to the local earthquake parameters obtained, the horizontal elastic acceleration and displacement spectrum of the reinforced concrete building is plotted in Figure 5, taking into account the TBDY 2018 Equations 2.2, 2.3 and 2.4.

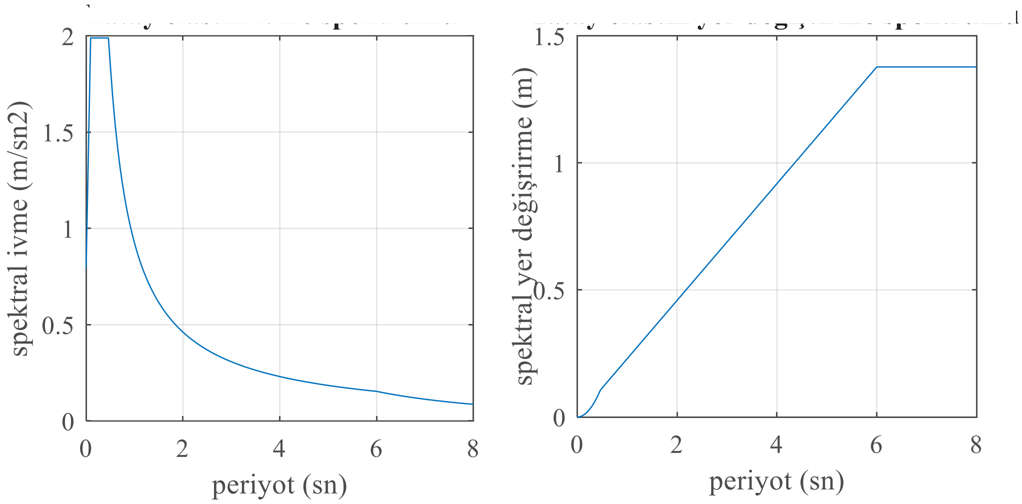

Figure 5. Horizontal elastic acceleration and displacement spectra

According to TBDY 2018, the live load participation coefficient of the buildings designed for residential purposes is considered as n=0.3. The weight (W) calculation of the building to be taken into account in the earthquake calculations is based on the G+nQ load combination. The modal parameters obtained as a result of the modal analysis of the structure are given in Table 8. Here T1 is the dominant period of the structure, T_2 is the 2nd mode period and T_3 is the 3rd mode period of the structure, Ux is the X-direction modal mass participation rate, Uy is the Y-direction modal mass participation rate, Uz is the Z-direction modal mass participation rate, and G+nQ is the kN-direction of the structure. gives its weight.

Table 8. The modal parameters of reinforced concrete structure

T_1	T_2	T_3	U_X	U_Y	U_Z	G+nQ
0.43 s	0.36 s	0.34 s	99.98	99.95	0.11	36644 kN

According to the results of the analysis, any of the irregularities in the vertical (weak story irregularity, soft story irregularity and discontinuity of the vertical elements of the carrier system) and plan (torsion irregularity, slab discontinuities and protrusions in the plan) explained in Table 3.6 of TBEC 2018 are not present in the reinforced concrete structure used in this study not detected. The reinforced concrete building meets the earthquake effects by the reinforced concrete frame and the gapless reinforced concrete shears on the ground floor. In this case, according to TBEC 2018 Table 4.1, while the structural system behavior coefficient of the reinforced concrete structure should be taken as R=4 and the excess strength coefficient as D=2.5, some calculations were made by taking the R and D values as 1 due to the evaluation of an existing structure.

3.2. Pushover Analysis

In the static pushover analysis, the displacement, plastic deformation (plastic rotation, elongation, plastic rotation, elongation, plastic rotation) occurring in the carrier system under the influence of the earthquake load increments applied step by step monotonically up to the earthquake displacement demand limit, proportional to the dominant vibration mode shape in the direction of the earthquake considered. etc) and internal force increments and their cumulative values are calculated. In the last step, the cumulative values corresponding to the earthquake demand are obtained as the base quantities for strain evaluation [1]. In order to apply the static thrust analysis method, the mass participation rate of the dominant mode should be at least 70% and the torsional irregularity coefficient should be less than 1.4. In this study, static thrust analysis was applied because the mass participation rate of the dominant mode is 99.98% and there is no torsional irregularity in the X-Y direction taken into account. The base shear force (V) and the peak displacement curve of the structure for which static thrust analysis was performed with horizontal load increments are plotted in Figure 6.

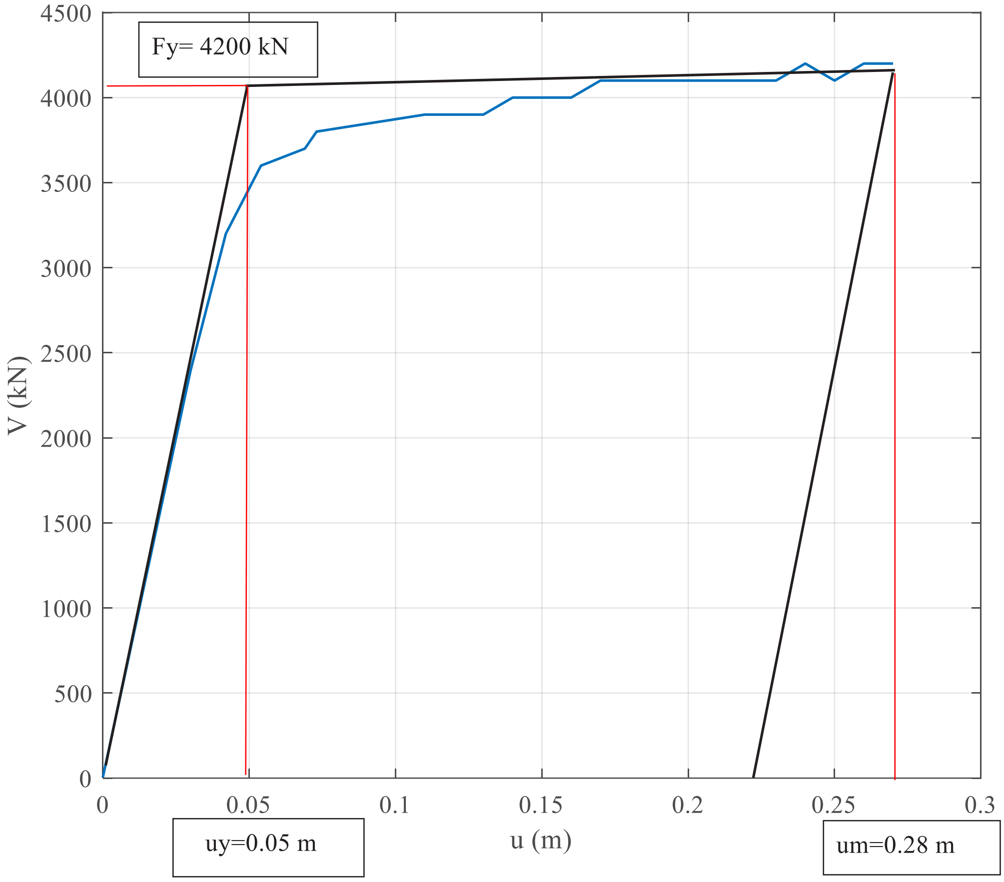

Figure 6. The shear force- roof displacement curve in the reinforced structure

According to Figure 6, the total energy capacity of the building, as the area under the curve, can be calculated in J (Joule) as follows.

E_k=4200x1000x0.05/2+4200x1000x(0.28-0.05)=1260000 J

3.3. The Analysis of Time Domain

For the analyzes in the time domain, the records of the 25.10.2020 dated Bingöl Central Earthquake and the 24.01.2020 Elazığ Sivrice Earthquake, which revealed minimum earthquake energy in the region, were used. Information on these earthquake records is given in Table 9. Here, I_D is the acceleration register intensity, PGA is the highest ground acceleration, PGV is the highest ground speed, M_W is the magnitude.

Table 9. The information for calculated of energy by using earthquake

Earthquake	Location	Station	PGA (cm/sn^2)	PGV (cm/sn)	M_W	Energy (J)	I_D
Elazığ Sivrice	38.359 E-39.063 B	2308 Sivrice	292.80	45.34	6.8	3.02E+12	106.29
Bingöl Merkez	38.966 E-40.444B	1201 Bingöl	13.66	0.84	4.0	2.54E+07	0.063

Acceleration time curves for earthquakes (Figure 7), velocity time curves (Figure 8), matching the earthquake spectra with the horizontal elastic acceleration spectrum of the reinforced concrete structure (Figure 9), and arias intensity curve (Figure 10) for calculating the effective time (td) is the maximum in any direction. plotted according to acceleration values.

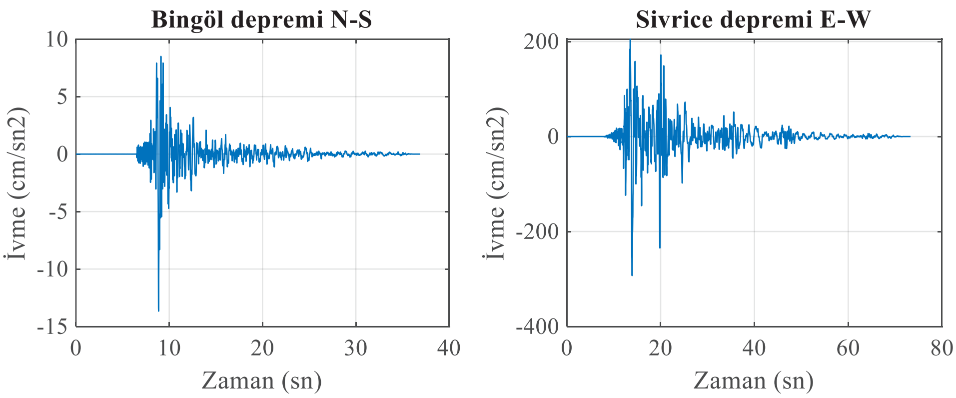

Figure 7. Acceleration-time history in the earthquake's

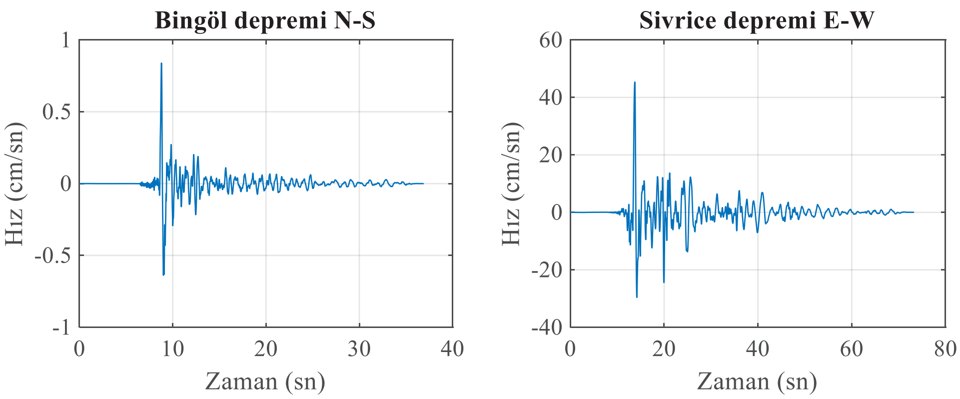

Figure 8. The velocity – time history in the earthquake's

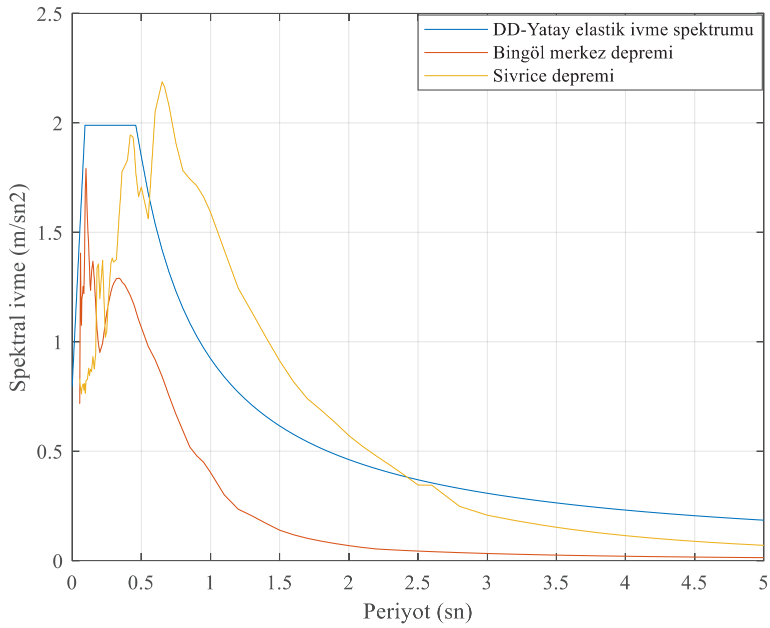

Figure 9. Matching the earthquake spectra with the horizontal elastic acceleration spectrum

In Figure 10, the earthquake records used from the study are scaled according to TBDY 2018 and matched with the horizontal elastic acceleration spectra. Here, it is seen that the earthquake spectrum values between 0.2 Tp and 1.5 Tp meet at least 90% of the horizontal elastic acceleration spectrum values in the same range [1].

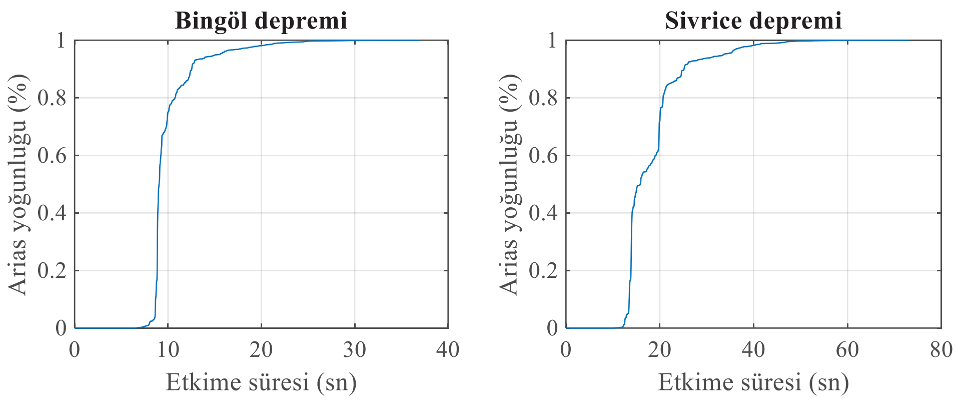

Figure 10. The arias intensity for earthquake's

According to the arias intensities, it was determined that the effect time (td) of the Bingöl earthquake was 8.5 seconds and the impact time of the Sivrice earthquake was 18.4 seconds.

Scaled earthquake records were applied to the structure in the SAP2000 program, as in Figure 11, and analyzes were made in the time history. PSA to spectrally describe the accelerations of earthquakes in the structure, PSV to define velocity values spectrally, and PSD to define displacement values spectrally were plotted in Figure 12 for the Sivrice earthquake and in Figure 13 for the Bingöl earthquake.

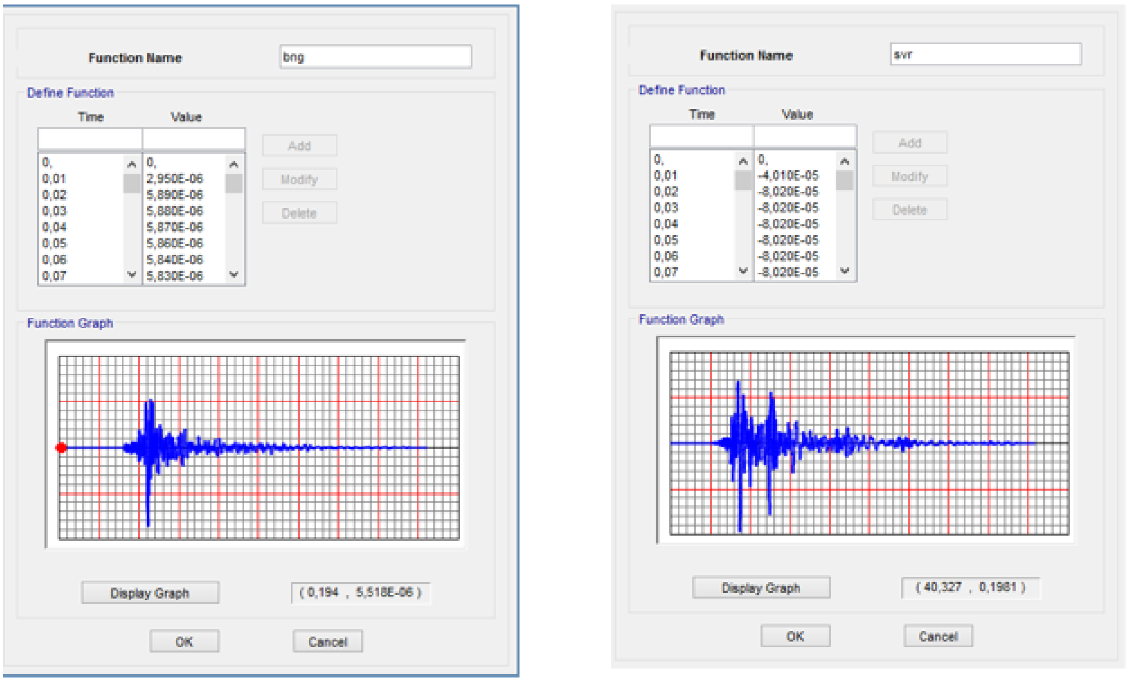

Figure 11. Defining earthquake data in the time history program [26]

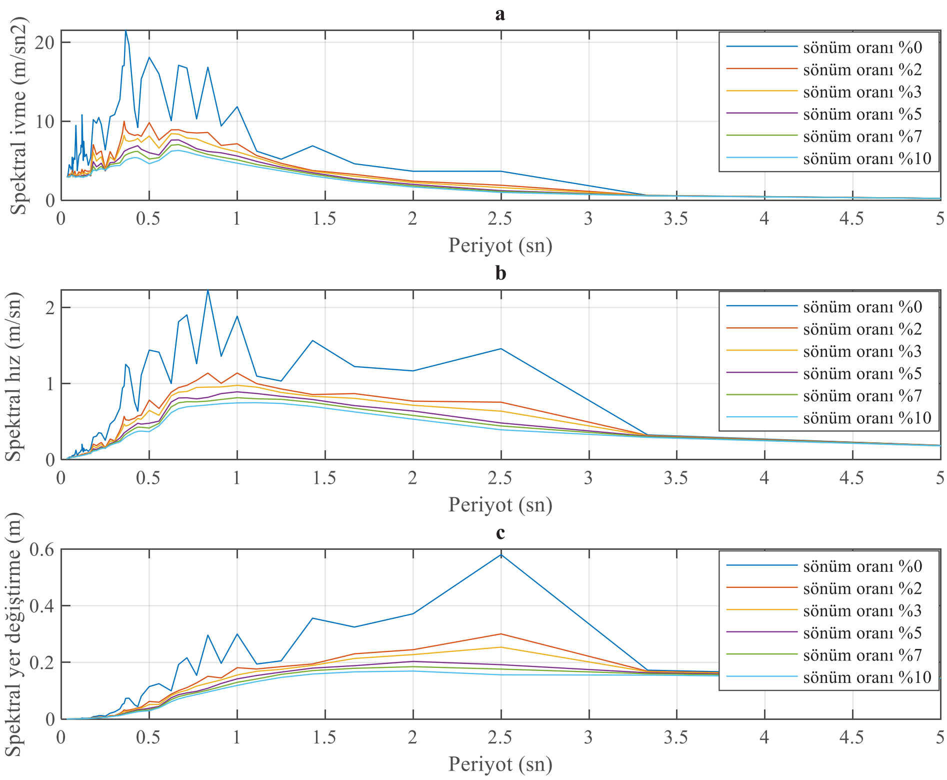

Figure 12. Response spectra of the structure against the Sivrice earthquake a) PSA b) PSV c) PSD

In Figure 12, the reinforced concrete building has a maximum damping rate of 0%, 2%, 3%, 5%, 7%, and 10% against Sivrice earthquake in the 0.36s earthquake period, at a maximum of 21, 10.5, 8.5, 7.7, 6.8 and 6.5 m/s2, respectively. It is seen that the earthquake produces spectral acceleration, while the earthquake has a spectral velocity of 2.26, 1.1, 1.02, 0.82, 0.76

and 0.73 m/sec, respectively, in the 0.826 s period step, while the earthquake has a spectral displacement of 0.58, 0.301, 0.254, 0.2, 0.183, 0.171 m in the 2.49 s period step. In this case, the short period value of the Sivrice earthquake was 0.36 s, the middle period value was 0.826 s, and the long period value was 2.49 s. In Figure 13, the reinforced concrete building is 0.95, 0.51, 0.35, 0.32, 0.28 and 0.25 m/s2 at the maximum damping rate of 0%, 2%, 3%, 5%, 7% and 10% against the Bingöl earthquake in the 0.25 s earthquake period. It produces spectral acceleration, while the earthquake produces a maximum velocity of 0.038, 0.022, 0.019, 0.017, 0.015 and 0.014 m/s in the 1.05 s period step of the earthquake, respectively, in 0.55 s period step, while 0.0035, 0.0023, 0.0021, 0.0019, 0.0017, 0.0014 m displacement. appears to have done. In this case, the short period of the Bingöl earthquake for the structure was 0.25 s, the middle period was 0.55 s, and the long period was 1.05 s.

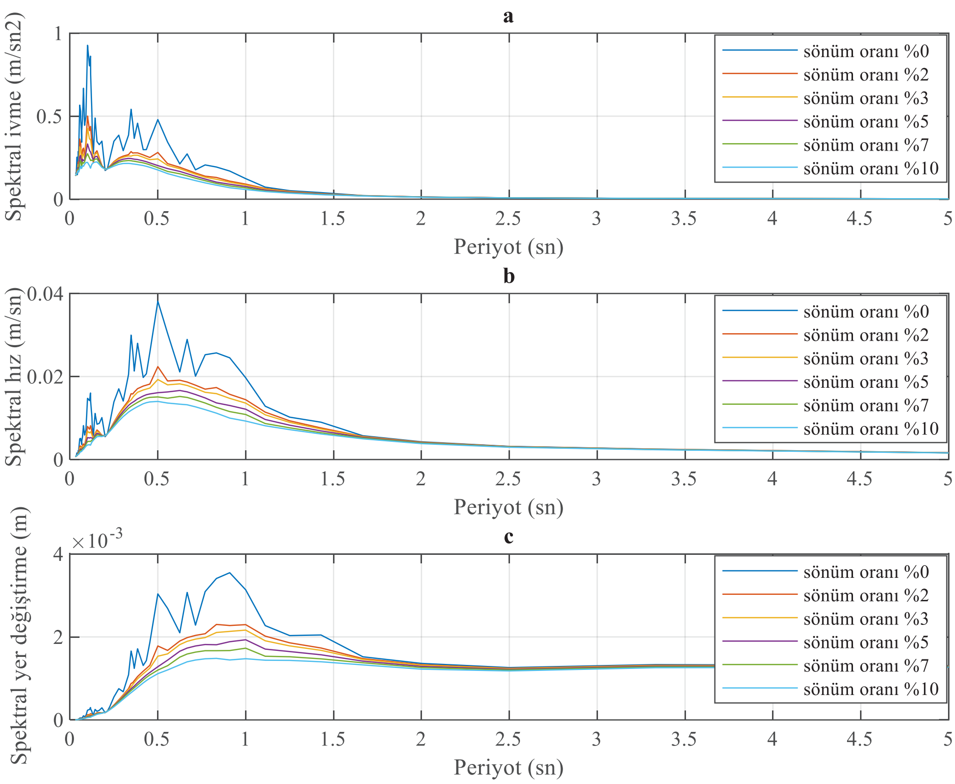

Figure 13. Response spectra of the structure against the Bingöl earthquake a) PSA b) PSV c) PSD

3.4. Calculation of Earthquake Input Energies

In this section, by using the earthquake input energy calculation methods suggested in Section 2.3, it has been calculated approximately how much of the Sivrice and Bingöl earthquakes are given to the structure as input energy. Calculations are made according to the approximately 5% damping rate for reinforced concrete buildings. According to the calculation approach proposed by Housner (1956), the structural input energy of the Sivrice earthquake was calculated as 1.23×10^7 J and the structure input energy of the Bingöl earthquake was calculated as 52.95 J.

$$\frac{E_i}{m} = \frac{1}{2}(\mathrm{PSV})^2 = 36644x0.5x(0.82)^2 = 1{,}23x10^7 J \rightarrow Sivrice\ depremi\ için$$

$\frac{E_i}{m} = \frac{1}{2}(PSV)^2 = 36644x0.5x(0.0017)^2 = 52.95\,J \rightarrow Sivrice\ depremi\ için$

According to the calculation approach proposed by Akiyama (1985) Housner (1956), the structural input energy of the Sivrice earthquake was calculated as 2.11x10^7 J and the structure input energy of the Bingöl earthquake was calculated as 0.7x10^7 J.

For Sivrice earthquake,

Since the dominant period of the structure is T=0.43 s and the effective period of the earthquake is Tg= 0.826 s, the equivalent velocity of the earthquake Ve=2.5xT=2.5x0.43=1.075 m/s

$\frac{E_i}{m} = \frac{1}{2}(Ve)^2 = 36644x0.5x(1.075)^2 = 2.11x10^7 J$

For Bingöl earthquake,

Since the dominant period of the structure is T=0.43 s and the effective period of the earthquake is Tg= 0.25 s for PSV values, the equivalent velocity of the earthquake Ve=2.5xTg=2.5x0.25=0.625 m/s

$\frac{E_i}{m} = \frac{1}{2}(Ve)^2 = 36644x0.5x(0.625)^2 = 0.7x10^7 J$

According to the calculation approach proposed by Chai and Fajfar (2000), the structural input energy of the Sivrice earthquake was calculated as 3.21x10^7 J and the structure input energy of the Bingöl earthquake was calculated as 7.44x10^3 J.

$\frac{E_i}{m} = 2.2t_d^{0.5}PGV^2 = 36644x18.4^{0.5}x0.453^2 = 3.21x10^7 J \rightarrow Sivrice\ için$

$\frac{E_i}{m} = 2.2t_d^{0.5}PGV^2 = 36644x8.3^{0.5}x0.0084^2 = 7.44x10^3 J \rightarrow Bingöl\ için$

According to the calculation approach proposed by Manfrendi (2001), the structural input energy of the Sivrice earthquake was calculated as 3.7x10^7 J and the structure input energy of the Bingöl earthquake was calculated as 0.7x10^3 J.

For Sivrice earthquake,

PSA= 0.77g

$w = \frac{2\pi}{T} = \frac{2\pi}{0.43} = 14.60\,hz$

Possible displacement prompt $u_{m,1}$,

$u_{m1} = SD(T) = 0.2\,m$

$Ry = \frac{PSA}{Sa} = \frac{0.77}{\frac{4000}{36644}} = 7.19 = \mu_1 = u_{m1}/Sdy$

$T = 0.43\,sn \rightarrow PSA = 0.77\ ve\ PSV = 0.82\frac{m}{sn^2}, \tau = \frac{T}{Te} = \frac{0.43}{0.826} = 0.520$

$$V_e = 1.45PSV^{0.86}R_y^{-0.1(T-0.55)}\tau^{-0.2} = 1.45x0.82^{0.86}x7.19^{-0.1x(0.43-0.55)}x0.520^{-0.2}$$

$V_e = 1.426\ m/sn$

$\frac{E_i}{m} = \frac{1}{2}(Ve)^2 = 36644x0.5x(1.426)^2 = 3{,}7x10^7 J$

For Bingöl earthquake,

PSA= 0.032g

$w = \frac{2\pi}{T} = \frac{2\pi}{0.43} = 14.60\ hz$

Possible displacement prompt $u_{m,1}$,

$u_{m1} = SD(T) = 0.0019\ m$

$Ry = \frac{PSA}{Sa} = \frac{0.032}{\frac{4000}{36644}} = 0.293 = \mu_1 = u_{m1}/Sdy$

$T = 0.43\ sn\ \rightarrow PSA = 0.032\ ve\ PSV = 0.0017\frac{m}{sn^2}, \tau = \frac{T}{Te} = \frac{0.43}{0.55} = 0.781$

$$V_e = 1.45PSV^{0.86}R_y^{-0.1(T-0.55)}\tau^{-0.2} = 1.45x0.0017^{0.86}x0.293^{-0.1x(0.43-0.55)}x0.78^{-0.2}$$

$V_e = 0.0062\ m/sn$

$\frac{E_i}{m} = \frac{1}{2}(Ve)^2 = 36644x0.5x(0.0062)^2 = 704{,}29\ J$

Considering the average of the energies calculated in all the proposed methods, the input energy of the building has the distribution shown in Figure 14.

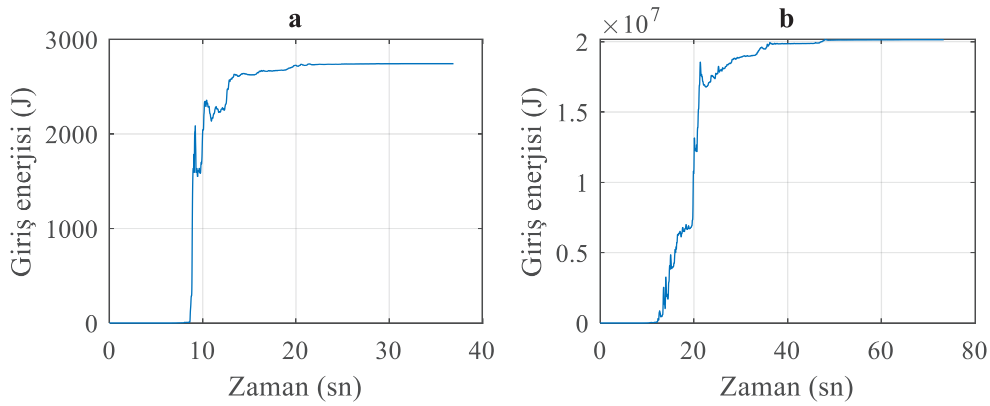

Figure 14. Input energies of earthquakes in reinforced concrete structures a) Bingöl earthquake b) Sivrice earthquake

The kinetic energy specified in Equation 4 and the energies obtained by permanent deformation are presented in Figure 6. In this case, the energy generated at the epicenter of the earthquake, the input energy to the structure and the energy dissipated by the structure are given in Table 10. It was determined that the structure distributed all of the Bingöl earthquake energy and 44% of the Sivrice earthquake.

Table 10. Percentage of dispersion of earthquake energies of reinforced concrete structure

Earthquake's	Earthquake energy (J)	Structure input energy (J)	The capacity energy of the structure (J)	The distribution energy by structure (%)
Bingöl earthquake	2.54×10^6	2730	1.2×10^7	%100
Sivrice earthquake	3.02×10^7	1.97×10^7	1.2×10^7	%44

As a result, it has been determined that the reinforced concrete building needs approximately 1.97×10^7 J of energy in order to disperse the Sivrice earthquake without any damage to the building.

4.CONCLUSIONS

In this study, a four-storey reinforced concrete building in Erzurum Region was evaluated as energy-based. The energies of earthquakes originating from far and near fields that occurred in the region in 2020 and 2021 were calculated with approximate methods. Bingöl Earthquake, which creates the minimum earthquake energy in the region, and Sivrice Earthquake, which creates the largest energy, were used in energy-based analyzes. Firstly, the base shear force-peak displacement curve, which shows the energy capacity of the structure, was obtained by static thrust analysis. Then, acceleration, velocity and displacement response spectra showing the effect of the time earthquake on the structure were obtained in order to calculate the building input energies. With the calculation methods suggested in the literature, the input energies created by the earthquakes in the building and how much of these energies are dissipated by the building without any damage are shown. The results showed that the structure dissipated all of the Bingol earthquake energy and 44% of the Sivrice earthquake. In order for the building to have this energy, it has been determined that it needs either a self-generating reinforcement system or a reinforcement system that provides its energy with the help of an external power source. At the end of the study, it has been suggested that reinforced concrete structures need an innovative earthquake energy absorbing system to withstand earthquakes of 7 Mw and above without being damaged.

REFERENCES

[1] TBEC (2018), Turkish Building Earthquake Code, The Disaster and Emergency Management Presidency of Turkey, 18 18th of March of Official Gazette, Ankara, Turkey.

[2] ATC (1996), Seismic Evaluation and Retrofit of Concrete Buildings,ATC-40: Applied Technology Council,Redwood City, CA, USA.

[3] UBC (1997), Uniform Building Code, International Conference of Building Officials,Whittier, California, USA.

[4] O. Merter, An investigation on the maximum earthquake input energy for elastic SDOF systems. Earthquakes and Structures Vol. 16, No. 4 (2019) 487-499

[5] Dindar, A.A., Yalcin, C., Yuksel, E., Ozkaynak, H. and Buyukozturk, O. (2015), "Development of earthquake energy demand spectra",Earthq. Spectra, 31(3), 1667-1689.

[6] Akbas, B., Shen, J. and Temiz, H. (2006), "Identifying the hysteretic energy demand and distribution in regular steel frames", Steel Compos. Struct., 6(6), 479-491.

[7] Celep, Z. (2018). Introduction to earthquake engineering and earthquake resistant structural design. Istanbul, Beta Press Release Distribution.

[8] Hancıoğlu, B. (2009), Energy-based analysis of earthquake behavior of structures, PhD Thesis, Istanbul Technical University, Istanbul, Turkey.

[9] Chopra, A. (1995). Dynamics of structures: theory and applications to earthquake engineering. Prentice Hall, Englewood Cliffs, NJ.

[10] A. Benavent-Climent, S. Mota-Páez, Earthquake retrofitting of R/C frames with soft first story using hysteretic dampers: Energy-based design method and evaluation. Engineering Structures 137 (2017) 19–32

[11] O. Merter, T. Ucar, Determination of earthquake safety of RC frame structures using an energybased approach. Computers and Concrete, Vol. 19, No. 6 (2017) 689-699

[12] Gullu, A., Yuksel, E. and Yalcin, C. (2018), "Seismic energy based design: numerical evaluation of diverse MDOF systems", Proceedings of the 16th European Conference on Earthquake Engineering, Thessaloniki.

[13] Yang, Y., Liu, R., Xue, Y. and Li, H. (2017), "Experimental study on seismic performance of reinforced concrete frames retrofitted with eccentric buckling-restrained braces (BRBs)", Earthq. Struct., 12(1), 79-89.

[14] Donaire-Avila, J., Lucchini, A., Benavent-Climent, A. and Mollaioli, F. (2018), "New approach for the optimal yield-force coefficient distribution in the seismic design of buildings", 16th European Conference on Earthquake Engineering, Thessaloniki, Greece, June.

[15] Sang-Hoon Oh, Seung-Hoon Shin, Bahador Bagheri, Effect of Torsion on Seismic Response of Single-Story Structures: an Energy-Based Design Approach (EBD). International Journal of Steel Structures (2021) 21(3):820–835

[16] AFAD, (2021)., T.C İçişleri Bakanlığı Afet ve Acil Durumu Yönetim Başkanlığı, Ankara, Türkiye.

[17] C. Ozer, M.E. Kocadagistan, S. Perk, Earthquake monitoring network of Erzurum: ATANET. International Journal of Scientific and Technological Research 5(8) (2019): 35-47.

[18] A. Şengör, N. Görür, F. Şaroğlu, Strike-slip faulting and related basin formation in zones of tectonic escape: Turkey as a case study. in: biddle k, christie-blick n (eds) strike-slip deformation, basin formation and sedimentation. Society of Economic Paleontologists and Mineralogists, Tulsa, OK, (1985): 227–264

[19] Housner, G.W., (1956)., Limit design of structures to resist earthquakes., Proceedings of the 1st World Conference on Earthquake Engineering, California, USA, 5, pp. 5-1 to 5-13.

[20] Akiyama, H., (1985), Earthquake-Resistant Limit-State Design for Buildings, the University of Tokyo Press, Tokyo, Japan.

[21] Kuwamura, H., Galambos, T.V., (1989), Earthquake Load For Structural Reliability, Journal of Structural Engineering, ASCE, Vol. 115, No. 6, pp. 1446-1462.

[22] Chai,, Y., H., Fajfar, P. (2000), A Procedure for Estimating Input Energy Spectra for Seismic Design, Journal of Earthquake Engineering, Vol. 4, No. 4, 539-561.

[23] Manfredi, G., Polese, M., Cosenza, E. (2003), Cumulative demand of the earthquake ground motions in the near source, Earthquake Engng Struct. Dyn.; 32:1853–1865.

[24] Park, Y.J., Ang, A.H.S., Wen, Y.K. (1987), Damage-limiting aseismic design of buildings Earthquake Spectra, Vol. 3, No. 1, pp. 1-26.

[25] TS 500, Requırements For Desıgn And Constructıon Of Reınforced Concrete Structures, Turkısh Standart Institute, 2000.

[26] SAP2000,. Structural Analysis Program, Computers and Structures Inc., Berkeley, California, 2021.

THE WIND LOAD CALCULATION OF A MASONRY MINARET BY USING DIN1056 STANDARD

Erdem TÜRKELİ [1]

[1] Vocational School of Technical Sciences, Construction Department, Ordu University, Ordu, Turkey

erdemturkeli@odu.edu.tr,

Abstract

Masonry minarets are the most special and specific structures for Islamic Culture that should be preserved to the next generations as they can carry the memories and the traces of the past generations. Even this is the case, there are so many outer factors that adversely affects the structural load carrying masonry system of these slender structures. The most dominant outer factors that adversely affect the load carrying system of masonry minarets are earthquakes and wind storms. Therefore, the effect of wind loads on these specific structures should be carefully investigated and determined. In this study, the wind loads for a masonry minaret is calculated by using DIN1056 standard and the details of procedure is provided explicitly.

Keywords: Wind load; Masonry; Minaret; DIN1056 standard

1.INTRODUCTION

Masonry structures are one of the most attractive and interesting structures from ancient times since they carry and reflect the traces of past generations to the future. Among these structures, masonry minarets can be categorized as the most slender and more vulnerable against wind storms since they have high height to width ratio. During wind storms, so many masonry minarets are heavily damaged or totally collapsed. Some of them are provided in Figure 1 [1].

Figure 1. Collapsed historical masonry minarets under severe wind storms [1]

In technical literature, some of the studies dealing with the wind response of masonry minarets are as follows. Türkeli dealt with the wind and earthquake behavior of the historical minaret of İskenderpaşa Mosque by using different wind loading standards, different design spectrums and the time histories of real ground motions [2]. Ural and Fırat studied about the collapse mechanism of the minarets that collapsed during the wind storm that hit Aksaray province in Turkey on the March 12, 2013 [3]. Ural et. al investigated the wind and earthquake response of a crooked minaret located in Aksaray province of Turkey [4]. Adam et. al studied about the masonry minaret (Al-Rifa'i minaret) representing a typical example of these kind of structure in Egypt [5]. Doğangün et. al discussed local stress concentrations and displacement behavior of masonry minarets [6]. Al-Zuhairi et. al described the behavior and response of a masonry historical minaret when subjected to wind pressure as a main external loading [7]. Hejazi et. al dealt with the wind effect on number of historical brick masonry minarets in Isfahan, built in the eleventh and twelfth centuries A.D [8].

2.GENERAL PROPERTIES OF METHOD

Due to the reason that there is no specific standard for the wind design of masonry minarets, existing standards for other tall and slender structures like chimneys can be utilized. Therefore, in this study, the procedures of the German Chimney standard DIN1056 was used [9]. Some of the assumptions in this standard are as follows: DIN 1056 German Chimney Standard accepts that wind load on structure used in the design is dominant in the direction of the wind and that the wind loads affect structures horizontally. The procedure of the standard can be summarized as follows.

The resultant wind load acting on chimney at section i, W_i, can be calculated from Eq.(1).

$$W_i = C_{fi} \cdot q_i \cdot A_i \cdot \varphi_B \tag{1}$$

In Eq.(1), C_{fi}, A_i, q_i and Φ_B are impending aerodynamic force parameter for section i, effective surface area, dynamic pressure at height z_i and instantaneous wind parameter, respectively. Also, dynamic pressure at ground level q_0 can be found from Eq.(2) where V is expressing wind speed.

$$q_0 = \frac{V^2}{1600} \quad \text{kN/m}^2 \tag{2}$$

Dynamic pressure (q_i) at height z_i is given in Eq.(3) and Eq.(4) which one is suitable for the given condition.

$$q_i = q_0 + 0{,}003 \cdot z_i \qquad 50\text{ m} < z_i < 300\text{ m} \tag{3}$$

$$q_i = q_0 + 0{,}9 \qquad z_i \geq 300m \tag{4}$$

In Eq.(3) and Eq.(4), z_i and q_0 are denoting any height on chimney and dynamic pressure at ground level, respectively.

In addition to Eq.(3) and Eq.(4), for chimneys whose heights are below 50 meters, the value of q_i can be calculated from Eq.(5) where h is denoting the chimney height from ground.

$$q_i = (0,75) \cdot \left(1 + \frac{h}{100}\right) \cdot q_0 \qquad h \leq 50m \tag{5}$$

From Figure 2, it is seen that d_i is expressing the width of i^{th} section and Δh_i is expressing the corresponding height of section.

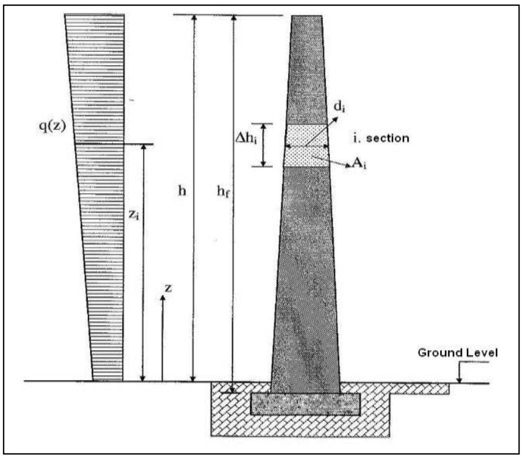

Figure 2. Symbols provided in DIN 1056 Standard [9]

Effective surface area, A_i is given in Eq.(6).

$$A_i = \Delta h_i \cdot d_i \tag{6}$$

Aerodynamic force parameter C_{fi} for section i can be calculated from Eq.(7).

$$C_{fi} = \psi \cdot C_{f0,i} \tag{7}$$

In Eq.(7), Ψ is expressing reduction factor and $C_{f0,i}$ is expressing aerodynamic force parameter depending on shape of section area for section i. The values of $C_{f0,i}$ parameter for different cross sections are given in Table 1.

Table 1. Aerodynamic force parameters depending on section shape [9].

Number of sides (n)	**$C_{f0,i}$**
For circle	0,95
16	1,00
14	1,05
12	1,10
10	1,25

Reduction factor ψ can be calculated from Eq.(8) or Eq.(9) which one is appropriate for the given condition.

$$\left(\frac{h}{d}\right) \leq 100 \quad \rightarrow \quad \psi = 0,65 + 0.0035 \cdot \left(\frac{h}{d}\right) \tag{8}$$

$$\left(\frac{h}{d}\right) > 100 \quad \rightarrow \quad \psi = 1,0 \tag{9}$$

In Eq.(8) and Eq.(9), h is denoting the height of chimney at height z_i and d is expressing the width of chimney wall at height z_i.

Instantaneous wind parameter φ_B is given in Eq.(10) where η and φ_{BO} are impending dimension parameter and basic instantaneous wind effect parameter, respectively.

$$\varphi_B = \varphi_{BO} \cdot \eta \tag{10}$$

Also, instantaneous wind effect parameter φ_B takes into account the changes in speed of wind which depend on spatial and time at structure vibration occurring in wind direction. η dimension parameter can be calculated from Eq.(11) or Eq.(12) which one is appropriate for the given condition where h is expressing the height of chimney at height z_i.

$$h \leq 50m \quad \rightarrow \quad \eta = 1 \tag{11}$$

$$h > 50m \quad \rightarrow \quad \eta = 1,05 - \left(\frac{h}{1000}\right) \tag{12}$$

Instantaneous wind effect parameter at ground level φ_{BO} can be calculated from Eq.(13);

$$\varphi_{BO} = 1 + (0,042 \cdot T - 0,0019 \cdot T^2) \cdot \delta^{-0,63} \tag{13}$$

In Eq.(13), T is expressing basic vibration period at 1st mod in seconds and δ is expressing logarithmic damping reduction taken as 0,1.

3.APPLICATIONS

In this part of the study, the historical minaret (Figure 3a) [11] of İskenderpaşa Mosque located in Trabzon district of Turkey is selected from technical literature whose dynamic characteristics are obtained and verified both analytically and experimentally by Altunişik [10]. Also, the FEM model of the cited minaret compared and verified by Türkeli [2] with the ones found in Altunişik [10] which is provided in Figure 3b.

(a) (b)

Figure 3. a) Minaret of İskenderpaşa Mosque [11] b) FEM Model of the minaret [2]

Firstly, the wind speed acting on the minaret is determined according to the logarithmic velocity profile by using basic wind speed as 45 m/s. This is provided in Table 2.

Table 2. Wind speed calculated according to the logarithmic velocity profile

Section No	Section Heights (m)	V_o	$Ln(H/z_o)$	$Ln(H_o/z_o)$	V(z)
0	0,0-3,0	45,00	0,000	5,298	0,000
1	3,0-5,0	45,00	4,094	5,298	34,774
2	5,0-16,5	45,00	4,605	5,298	39,113
3	16,5-19,5	45,00	5,799	5,298	49,253
4	19,5-20,5	45,00	5,966	5,298	50,672

Secondly, by using the wind speed provided in Table 2, the dynamic pressure at height z_i is calculated and given in Table 3.

Table 3. Dynamic pressure at height z_i

Section No	Section Heights (m)	V(z)	q_0	q_i
0	0,0-3,0	0,000	0,00	0,00
1	3,0-5,0	34,774	0,76	0,76
2	5,0-16,5	39,113	0,96	0,96
3	16,5-19,5	49,253	1,52	1,52
4	19,5-20,5	50,672	1,60	1,60

Then, the aerodynamic force parameter is calculated and provided in Table 4 by using the information given in Table 1 and Eq.(7).

Table 4. Aerodynamic Force Parameter

$C_{f0,i}$	Section Heights (m)	h/d	Ψ	C_{fi}
0,95	0,0-3,0	0,000	0,650	0,62
0,95	3,0-5,0	2,000	0,657	0,62
0,95	5,0-16,5	3,333	0,662	0,63
0,95	16,5-19,5	11,000	0,689	0,65
0,95	19,5-20,5	15,476	0,704	0,67

The other parameter that should be calculated is the basic instantaneous wind effect parameter which is provided in Table 5.

Table 5. Basic instantaneous wind effect parameter

Section Heights (m)	η	δ	φ_{BO}	φ_B
0,0-3,0	1,000	0,10	1,04	1,042
3,0-5,0	1,000	0,10	1,04	1,042
5,0-16,5	1,000	0,10	1,04	1,042
16,5-19,5	1,000	0,10	1,04	1,042
19,5-20,5	1,000	0,10	1,04	1,042

Lastly, by using the parameters calculated before, the resultant wind loads for the sections are provided in Table 6 and also in Figure 4.

Table 6. Resultant Wind Load (in kN)

$A_i(m^2)$	q_i	C_{fi}	φ_B	W_i(kN)
6,60	0,00	0,62	1,042	0,000
3,00	0,76	0,62	1,042	1,475
17,25	0,96	0,63	1,042	10,803
4,50	1,52	0,65	1,042	4,650
1,26	1,60	0,67	1,042	1,409

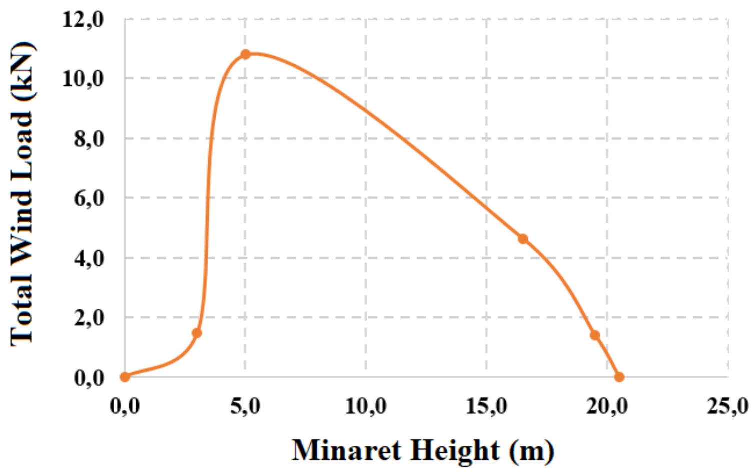

Figure 4. Total wind loads according to minaret heights

4.CONCLUSIONS

In this study, the total wind load on the historical masonry minaret of İskenderpaşa Mosque is calculated according to DIN 1056 German Chimney Standard. This historical masonry minaret is selected from the technical literature [10] due to the reason that the dynamic properties of the minaret is already verified which is the most important first step of dynamic structural analysis. Also, since there is no any specific standard or regulation for the wind response of masonry minarets, standards for tall and slender structures like chimneys or towers can be preferred and utilized in the wind analysis and design of these special structures. Although the results obtained from the wind load calculations seem as static, DIN 1056 takes into account the dynamic properties of the structure by using instantaneous wind effect parameter at ground level which includes the first mode period of the structure. Moreover, the details of the calculation procedure of the wind loads according to DIN 1056 is provided in tables explicitly which is believed to help the designers or academicians working on this specific subject. Another subject is that structural wind analyses are not performed in this study i.e. the wind loads calculated are not applied to the cited minaret. These analyses can be performed in the future studies. At the end, as is the case in this study, historical structures like minarets should be conserved for future generations. Therefore, so many structural wind analyses should be performed by using different wind loading standards for wind resistant design and conservation of historical masonry minarets.

REFERENCES

1. Günaydın, Murat, Tarihi Bir Yığma Minarenin Onarım Sonrasındaki Dinamik Karakteristiklerinin Deneysel Olarak Belirlenmesi, Gümüşhane Üniversitesi Fen Bilimleri Enstitüsü Dergisi, Vol:8, No:2, 381-395, 2018.

2. Türkeli, Erdem, Dynamic seismic and wind response of masonry minarets, Periodica Polytechnica Civil Engineering, Vol:64, No:2, 353-369, 2020.

3. Ural, Ali, Firat, Fatih K, Evaluation of masonry minarets collapsed by a strong wind under uncertainty, Natural Hazards, Vol:76, No:2, 999-1018, 2015.

4. Ural, Ali, Doğangün, Adem, Meraki, Şakir, Response evaluation of historical crooked minaret under wind and earthquake loadings, Wind and Structures, Vol:17, No:3, 345-359, 2013.

5. Adam, Maher A., El-Salakawy, Tarek S., Salama, Mohamed A., Mohamed Alaa A., Assessment of structural condition of a historic masonry minaret in Egypt, Case Studies in Construction Materials, Vol:13, e00409, 2020.

6. Doğangün, Adem, Acar, Ramazan, Livaoğlu, Ramazan, Tuluk, Ö. İskender, Performance of masonry minarets against earthquakes and winds in Turkey, In Proceedings of the 1st International Conference on Restoration of Heritage Masonry Structures, Vol:24, 27, April, 2006.

7. Al-Zuhairi, Alaa Hussein, Ahmed, Ammar R., Al-Zaidee, Salah R., Numerical Analysis of Historical Masonry Minaret Subjected to Wind Load, In Geotechnical Engineering and Sustainable Construction, 545-555, Springer, Singapore, 2022.

8. Hejazi, Mehrdad, Moayedian, Sayed Mohammad, Daei, Maryam, Structural Analysis of Persian Historical Brick Masonry Minarets under Wind Load, Journal of Solid and Fluid Mechanics, Vol:5, No:1, 165-176, 2015.

9. DIN (Deutsches Institut für Normung), DIN 1056, Freistehende Schornsteine in Massivbauart, Solid Construction, Freestanding Stacks; Calculation and Design, October 1984.

10. Altunışık, Ahmet Can, Dynamic response of masonry minarets strengthened with fiber reinforced polymer (FRP) composites, Natural Hazards and Earth System Sciences, Vol:11, No:7, 2011–2019, 2011.

11. Black Sea Cultural Inventory, İskenderpaşa Camii [online] Available at: https://karadeniz.gov.tr/iskenderpasa-camii/ [Accessed: 18 May 2022] (in Turkish).

DISTRIBUTION OF DISCRETE GEODESICS ON ALPHA COMPLEXES

Ömer Akgüller[1] **Mehmet Ali Balcı**[1]

[1] Department of Mathematics, Muğla Sıtkı Koçman University, Muğla, Turkey

oakguller@mu.edu.tr , mehmetalibalci@mu.edu.tr

Abstract

In this study, the shortest paths calculated on the graph structures expressed by alpha complex skeleton of the submanifold from which the point cloud is sampled will provide an approximation to the geodetic curves of the manifold. It should also be taken into account that this sampling will contain noise. Although the graph structures formed by the simplex complex skeleton are affected by this noise, the approaches to the geodesics of the submanifold are not affected much by the distributions of the geodesics. Thus, a kernel function to be defined by the Wasserstein similarity of the distributions of discrete geodesics in the skeletons of 3D point clouds will be an effective tool in the point cloud similarity measurement process.

Keywords: Discrete geodesics; Alpha Complex; Point cloud process.

1. INTRODUCTION

Point clouds are very important tools especially for geometric data set representation. Point clouds obtained by discrete sampling of a continuous geometry are finite geometry involving sets. This sampling process can be performed algorithmically, or it can be achieved with the work of laser scanners. Especially when a hardware such as a scanner is used, high noises are expected in the sampling. It is important to work with their direct representations for the processing of point clouds, which find more and more applications in different disciplines.

Graphs are often used for the direct representation of point clouds [1-3]. Graphs describe the structural relationships of data of all dimensions. A solution to the problem of measuring the similarity of different datasets of the same size is also performed by the inner product defined on the graph structures. Graph kernels are functions that resolve similarities between two graph structures, usually using subgraphs [4,5]. These functions determine the character of graphs in high-dimensional spaces and generally preserve the geometric properties of graphs.

In this study, a kernel function defined by discrete analogs on graphs of geodesy curves, which is one of the basic concepts of classical differential geometry, is discussed. This function selects the shortest path between two peaks in the graph as discrete geodesics and compares the distributions of these paths on a graph. This comparison is given with point cloud samples in the study. It should also be taken into account that this sampling may contain noise. Although the graph structures formed by the simplicial complex skeleton are affected by this noise, the approaches to the geodesics of the submanifold are not affected much by the distributions of the geodesics. Thus, a kernel function defined by the Wasserstein similarity of the distributions of discrete geodesics in the skeletons of 3D point clouds has been an effective tool in the point cloud similarity measurement process., the shortest paths calculated on the graph structures expressed by alpha complex skeleton of the submanifold from which the point cloud is sampled will provide an approximation to the geodesic curves of the manifold.

2. METHODOLOGY

Alpha complexes are parametrized triangulations formed over point clouds. They are widely used in different fields such as topological data analysis, computational geometry and computer graphics [6-10]. Mathematically, an alpha complex $\alpha_r(P)$ is d-dimensional simplicial complex having the faces of the Delaunay triangulation of a point cloud $P = \{p_i\}_{i=1}^{n} \subset \mathbb{R}^d$. It is well known that alpha complexes are homotopical equivalent to Cech complexes [11]. Different than the Cech complexes, an alpha complex contains only up to d-dimensional simplexes and there are at most $O(n^{\lceil d/2 \rceil})$ many of them [12]. Therefore, alpha complexes can be crucial for computing homology groups. In this study, we represent 3-dimensional point clouds with the 1-skelton of alpha complex constructed over them. Hence, the direct representation of geometric point clouds is obtained as the topological properties are preserved.

In Figure 1, we present the point cloud of a plant model and alpha shape with 0.1.

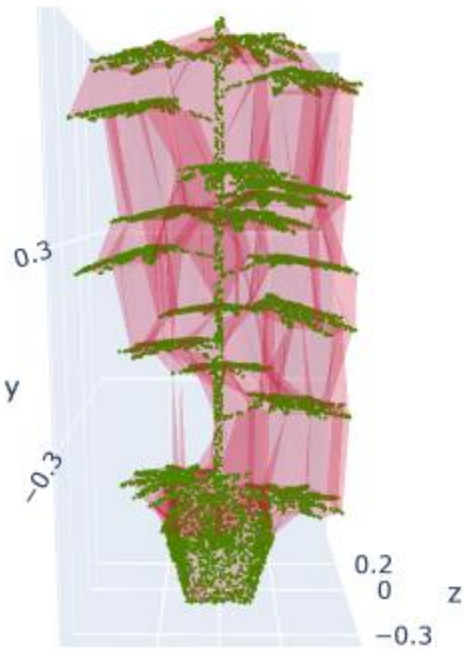

Figure 1. Point cloud with an alpha complex of a plant model.

One of the main problems of machine learning is modeling and computing similarity between objects. When it comes to graphs, graph kernels have received a lot of attention in recent years and have become the dominant approach for learning on graph-structured data. A graph kernel is a symmetric, positive semi-definite function defined in the space of graphs. This function can be expressed as an inner product in some Hilbert spaces. In particular, given a kernel κ, a $\varphi: G \to H$ maps a graph space G to a Hilbert H space such that for each $G_1, G_2 \in G$,

$$\kappa(G_1, G_2) = \langle \varphi(G_1), \varphi(G_2) \rangle.$$

In this study, the distributions of the shortest paths on the 1-skeletons of alpha complexes were examined and a kernel function was defined with these distributions. The shortest path in a graph is the one with the fewest edges and no loops between two vertices. Considering the centers and peripheral vertices of the graphs, the shortest paths through the peripheral vertices are orbital geodesics. Similarly, the shortest paths containing graph centers also become central geodesics. The probability densities of orbital and central geodesics can be measured by the Wasserstein-1 distance function, which is defined together with the Π coupling between these densities as

$$W(\rho_1, \rho_2) = \inf_{\pi \in \Pi(\rho_0, \rho_1)} \int_{\mathbb{R}^m \times \mathbb{R}^m} \|x - y\| \pi(dx, dy).$$

The kernel function then is defined by, with probability densities ρ_i^C and orbital probability densities ρ_i^O, of the central geodesics of the graph G_i,

$$\kappa(G_1, G_2) = \frac{W\left(\rho_1^C, \rho_2^C\right)}{W\left(\rho_1^O, \rho_2^O\right)}.$$

3. RESULTS

In order to show the efficiency of the kernel function we introduce in this study; we use 12 different plant models of Princeton ModelNet data set. The point clouds that we used in study are presented in Figure 2.

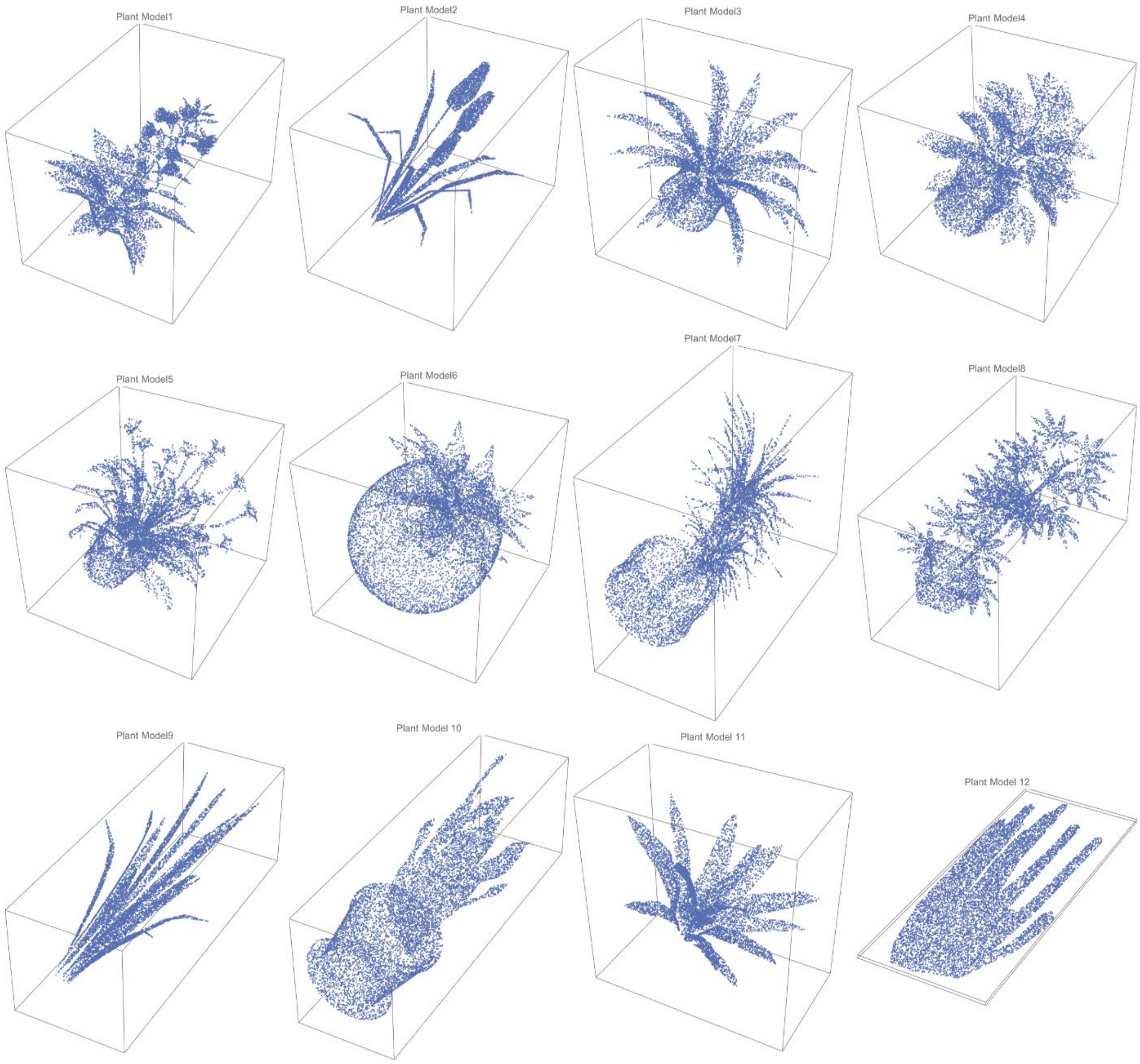

Figure 2. Point cloud models

The resulting matrix by using kernel function is presented in Figure 3.

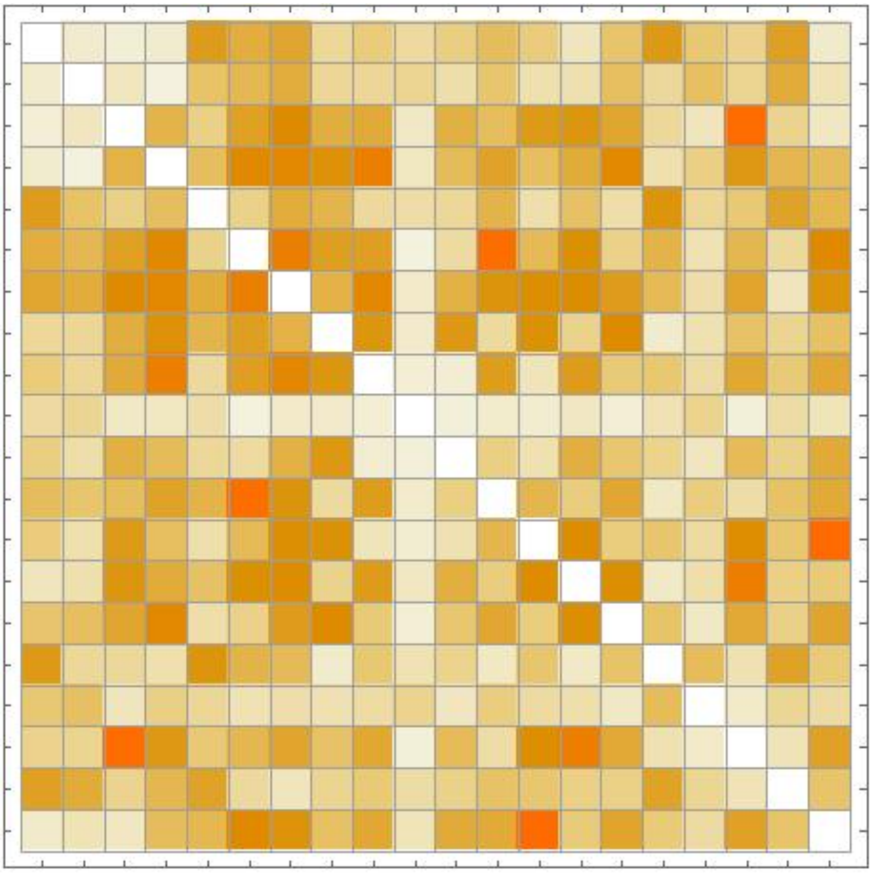

Figure 3. Kernel matrix with heat mapping

4. CONCLUSIONS

One of the increasingly popular approaches to measuring similarity between structured objects is to use kernel methods. In general, kernel methods measure the similarity between two objects with a kernel function corresponding to an inner product in reproducing kernel Hilbert space. The challenge for kernel methods is to find an appropriate kernel function that is computationally traceable while capturing the semantics of the structure. In this study, a kernel function defined by the distribution of discrete geodes on graphs is used as an approach to the point cloud comparison problem, which is one of the main problems of computer and vision. While defining this kernel function, an approach sensitive to isometries, topological transformations and noise levels is presented in the comparison process of point clouds.

The kernel function was run on point clouds of plant models with different topologies used in this study. According to the results obtained with this kernel function, it is observed that the defined function is sensitive to topologies. Thus, an effective kernel function is presented on graphs obtained with 1-skeletons of Alpha complexes.

ACKNOWLEDGMENT

This study is supported by The Scientific and Technological Research Council of Turkey (TUBİTAK) with project number 121E031 and title “Geodesic Distribution Based Graph Kernel and 3D Point Cloud Applications”.

REFERENCES

1. Natali, Mattia, Silvia Biasotti, Giuseppe Patanè, Bianca Falcidieno. Graph-based representations of point clouds. Graphical Models, Vol:73, No:5, 151-164, 2011
2. de Oliveira Rente, Paulo, Catarina Brites, Joao Ascenso, Fernando Pereira. Graph-based static 3D point clouds geometry coding. IEEE Transactions on Multimedia, Vol:21, No:2 284-299, 2018
3. Chen, Jintai, Biwen Lei, Qingyu Song, Haochao Ying, Danny Z. Chen, Jian Wu. A hierarchical graph network for 3d object detection on point clouds. In Proceedings of the IEEE/CVF conference on computer vision and pattern recognition, 392-401, 2020.
4. Vishwanathan, S. Vichy N., Nicol N. Schraudolph, Risi Kondor, Karsten M. Borgwardt. Graph kernels. Journal of Machine Learning Research, Vol:11, 1201-1242, 2010
5. Kriege, Nils M., Fredrik D. Johansson, Christopher Morris. A survey on graph kernels. Applied Network Science, Vol:5, No:1, 1-42, 2020
6. Michael Krone, Barbora Kozlíková, Norbert Lindow, Marc Baaden, Daniel Baum, Julius Parulek, H-C Hege, Ivan Viola. Visual analysis of biomolecular cavities: State of the art. Computer Graphics Forum, Vol:35, No:3, 527–551, 2016
7. Jie Liang, Herbert Edelsbrunner, Ping Fu, Pamidighantam V. Sudhakar, Shankar Subramaniam. Analytical shape computation of macromolecules: I. molecular area and volume through alpha shape. Proteins: Structure, Function, and Bioinformatics, Vol:33, No:1, 1–17, 1998
8. Jie Liang, Clare Woodward, Herbert Edelsbrunner. Anatomy of protein pockets and cavities: Measurement of binding site geometry and implications for ligand design. Protein Science, Vol:7, No:9, 1884–1897, 1998
9. Pratyush Pranav, Herbert Edelsbrunner, Rien van de Weygaert, Gert Vegter, Michael Kerber, Bernard J. T. Jones, Mathijs Wintraecken. The topology of the cosmic web in terms of persistent Betti numbers. Monthly Notices of the Royal Astronomical Society, Vol:465, No:4, 4281–4310, 2016
10. Herbert Edelsbrunner, John L. Harer. Computational topology: an introduction. AMS Bookstore, 2010

11. Jean-Daniel Boissonnat, Frédéric Chazal, Mariette Yvinec. Geometric and topological inference, Vol:57. Cambridge University Press, 2018
12. Raimund Seidel. The upper bound theorem for polytopes: an easy proof of its asymptotic version. Computational Geometry, Vol:5, No:2, 115–116, 1995

STRESS ANALYSIS OF MULTI-LAYERED SOIL MEDIUM BY USING FINITE AND INFINITE ELEMENTS

Yusuf Ziya Yüksel[1] , Şeref Doğuşcan Akbaş[2],

[1,]Department of Civil Engineering, University of Bursa Technical, Bursa, Turkey
yusuf.yuksel@btu.edu.tr

[2,]Department of Civil Engineering, University of Bursa Technical, Bursa, Turkey
seref.akbas@btu.edu.tr,

Abstract

In this study, stress analysis of two dimensional elastic, isotropic semi-infinite layered soil medium is investigated by using finite element method. The soil is modelled by using finite-infinite elements. In the literature, more realistic results are obtained when using the infinite elements for infinite media solutions compared to finite element solutions. For solving the problem, cubic finite elements with 16 nodes and infinite elements with 8 nodes are generated in this study. The shape functions of the infinite elements are calculated separately for each direction. The region close to the soil surface is used with finite elements, and the region far from the soil surface is used with infinite elements. The integration processes of Finite-infinite elements are solved by Gauss Legendre integration method with five nodes. The numerical results obtained with the Boussinesq theory are compared and verified. A parametric study is performed using different layer thicknesses and different material properties in a semi-infinite soil medium. The numerical results and graphs obtained with MATLAB. The obtained results are compared.

Keywords: Stress analysis; Finite – infinite element method; Multi-layered soil.

1.INTRODUCTION

Soil-structure modelling should be considered within realistic solutions. The most realistic solutions for semi-infinite soil problems are provided by the direct method, which considers the soil structure as a whole. A realistic model can be created by defining the region extending towards infinity with infinite elements. The ground generally consists of a layered structure. In the study, a layered soil structure is modeled.

In the literature, there are many studies infinite soil media static problems; Lynn and Hadid (1981), used a new infinite element with damping function in solving infinite media static problems. Zienkiewicz (1983), developed a new infinite element for unbounded media problems solve. Curnier (1983), produced infinite elements for solving static infinite media problems. Bettess and Bettess (1983), studied static problems in unbounded media by using an infinite element with a decay function. Pıssanetzky (1984), modelled unbounded media with anisotropic properties under static load. Kumar (1985), produced four different types of infinite elements with damping functions for the static analysis of the two-dimensional infinite soil media. Karpurapu and Bathurst (1988), examined the semi-infinite medium using finite and infinite elements. Selvadurai and Karpurapu (1989), solved infinite saturated soil medium problems by using Gauss Legendre integration method. Liu and Novak (1991), performed the static pile-soil interaction analysis of piles in an elastic or elastic-plastic soil media under monotonic loading. El-Esnawy (1995), studied static problems in two dimensional unbounded media by using infinite element. Yerli et. al. (1998), studied the time dependent stress and displacement behavior of the two-dimensional infinite soil media. Bettess (1992), developed infinite elements damped in infinite media for two and three dimensional infinite media problems. Xie (2013), examined dynamic compaction of railway foundation using finite-infinite element method. Demidem et. al. (2014), examined analysis of underground structures by using finite and infinite elements. Erkal (2014), analyzed static unbounded media under uniform distributed load and point load. Liu et. al. (2015), analyzed static in asphalt structures by using infinite elements. Wen et. al. (2018), proposed a meshless infinite element for the solution of unbounded media problems. Haji et. al. (2021), developed a infinite element used in the solutions of underground applications.

In this study, stress analysis of laminated semi-infinite soil under uniform load is performed. The region close to the ground surface is modeled with finite elements, and the far region is modeled with infinite elements. Numerical results are obtained using the finite element method. The finite region is modelled with 16-node finite elements, and the infinite region is modeled with 8-node infinite elements. Numerical integration is performed by using the Gauss Legendre integration method.

2.GENERAL PROPERTIES OF METHOD

The layered semi-infinite soil was modeled using the finite element method. The layered soil is shown in figure 1.

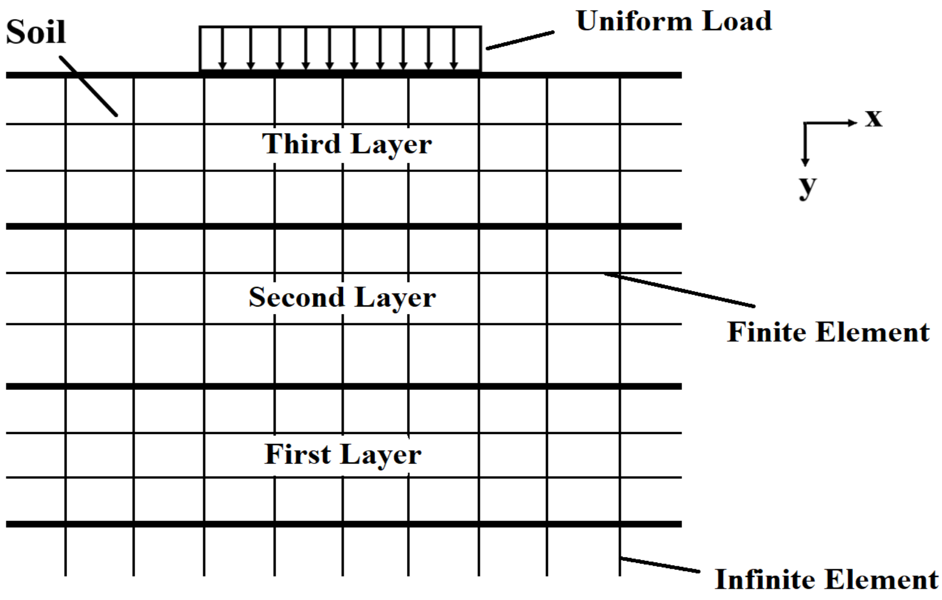

Figure 1. The layered semi-infinite soil under uniform load.

Equations of motion in 2D elasticity for a soil region are expressed as,

$$\frac{\partial \sigma_x}{\partial x} + \frac{\partial \tau_{xy}}{\partial y} + f_x = 0$$

$$\frac{\partial \tau_{xy}}{\partial x} + \frac{\partial \sigma_y}{\partial y} + f_y = 0 \tag{2.1}$$

where f_x and f_y are the volume forces in the x and y directions. σ_x and σ_y represent normal stresses, τ_{xy} represents shear stresses. The relations between strain and displacements are given;

$$\varepsilon_x = \frac{\partial u}{\partial x}$$

$$\varepsilon_y = \frac{\partial v}{\partial y}$$

$$\gamma_{xy} = \frac{\partial u}{\partial y} + \frac{\partial v}{\partial x} \tag{2.2}$$

Here u and v represent the displacements in the x, y directions. The material is assumed to be linear elastic, homogeneous and isotropic. The constitutive equations of the body are given.

$$\{\sigma\} = [D]\{\varepsilon\} \tag{2.3}$$

Stress $\{\sigma\}$ is expressed as material constants $[D]$ and strain $\{\varepsilon\}$.

$$\{\sigma\} = \begin{Bmatrix} \sigma_x \\ \sigma_y \\ \tau_{xy} \end{Bmatrix} \qquad \{\varepsilon\} = \begin{Bmatrix} \varepsilon_x \\ \varepsilon_y \\ \gamma_{xy} \end{Bmatrix} \qquad [D] = \begin{bmatrix} D_{11} & D_{12} & 0 \\ D_{21} & D_{22} & 0 \\ 0 & 0 & D_{33} \end{bmatrix} \tag{2.4}$$

$$D_{11} = D_{22} = \frac{E}{(1-\nu^2)}$$

$$D_{12} = D_{21} = \frac{\nu E}{(1-\nu^2)}$$

$$D_{33} = G = \frac{E}{2(1+\nu)} \tag{2.5}$$

Where, E and G are the modulus of elasticity and shear, and ν is the Poisson's ratio. The equations of motion in terms of displacements are given as follows;

$$\frac{\partial}{\partial x}\left(D_{11}\frac{\partial u}{\partial x} + D_{12}\frac{\partial v}{\partial y}\right) + \frac{\partial}{\partial y}\left(D_{33}\left(\frac{\partial u}{\partial y} + \frac{\partial v}{\partial x}\right)\right) = -f_x + \rho\frac{\partial^2 u}{\partial t^2}$$

$$\frac{\partial}{\partial y}\left(D_{12}\frac{\partial u}{\partial x} + D_{22}\frac{\partial v}{\partial y}\right) + \frac{\partial}{\partial x}\left(D_{33}\left(\frac{\partial u}{\partial y} + \frac{\partial v}{\partial x}\right)\right) = -f_y + \rho\frac{\partial^2 v}{\partial t^2} \tag{2.6}$$

Boundary conditions are given in terms of displacements as follows;

$$t_x = \left(D_{11}\frac{\partial u}{\partial x} + D_{12}\frac{\partial v}{\partial y}\right)n_x + D_{33}\left(\frac{\partial u}{\partial y} + \frac{\partial v}{\partial x}\right)$$

$$t_y = \left(D_{12}\frac{\partial u}{\partial x} + D_{22}\frac{\partial v}{\partial y}\right)n_y + D_{33}\left(\frac{\partial u}{\partial y} + \frac{\partial v}{\partial x}\right)n_x \tag{2.7}$$

Equations of motion converted to integral form with virtual work principle as follows;

$$\begin{bmatrix} \frac{\partial}{\partial x} & 0 & \frac{\partial}{\partial y} \\ 0 & \frac{\partial}{\partial y} & \frac{\partial}{\partial x} \end{bmatrix} \begin{Bmatrix} \sigma_x \\ \sigma_y \\ \tau_{xy} \end{Bmatrix} + \begin{Bmatrix} f_x \\ f_y \end{Bmatrix} = 0 \tag{2.8}$$

Displacements are given as follows;

$$\begin{Bmatrix} \varepsilon_x \\ \varepsilon_y \\ \gamma_{xy} \end{Bmatrix} = \begin{bmatrix} \frac{\partial}{\partial x} & 0 \\ 0 & \frac{\partial}{\partial x} \\ \frac{\partial}{\partial y} & \frac{\partial}{\partial x} \end{bmatrix} \begin{Bmatrix} u \\ v \end{Bmatrix} \tag{2.9}$$

The finite element formulation for plane elasticity problems is summarized. The interpolation shape functions are given;

$$u = \sum_{i=1}^{n} N_i u_i \qquad v = \sum_{i=1}^{n} N_i v_i \tag{2.10}$$

$$\begin{Bmatrix} u \\ v \end{Bmatrix} = \begin{bmatrix} N_1 & 0 & N_2 & 0 & \dots N_n & 0 \\ 0 & N_1 & 0 & N_2 & \dots 0 & \dots N_n \end{bmatrix} \begin{bmatrix} u_1 \\ v_1 \\ u_2 \\ v_2 \\ \vdots \\ u_n \\ v_n \end{bmatrix} \tag{2.11}$$

The variation of node displacements is expressed.

$$\{\delta u\} = [N]\{\delta u_d\} \tag{2.12}$$

Strain and stresses in terms of node displacements,

$$\{\varepsilon\} = [B]\{\Delta\}, \quad \{\sigma\} = [D][B]\{\Delta\} \tag{2.13}$$

Where $[B]$ is the strain matrix, $\{\Delta\}$ is the displacement.

$$[B] = [L]^T[N] \tag{2.14}$$

Here, the differential operators $[L]$ are given.

$$\begin{Bmatrix} \delta u \\ \delta v \end{Bmatrix} = [N]\{\delta\Delta\}, \qquad \{\delta\varepsilon\} = [B]\{\delta\Delta\} \tag{2.15}$$

$$h_e \int\int_{A_e} \{\delta\Delta\}^T([B]^T[D][B]\{\Delta\})dxdy - h_e \int\int_{A_e} \{\delta\Delta\}^T[N]^T \begin{Bmatrix} f_x \\ f_y \end{Bmatrix} dxdy = 0 \tag{2.16}$$

Element stiffness matrices and element load vectors were obtained, respectively.

$$[k] = h_e \int\int_{A_e} [B]^T[D][B]dxdy, \; [f] = h_e \int\int_{A_e} [N]^T \begin{Bmatrix} f_x \\ f_y \end{Bmatrix} dxdy \tag{2.17}$$

$$[k]\{\Delta\} = [f] \tag{2.18}$$

Equations obtained using interpolation shape functions are solved by the 5-point Gauss Legendre integration method.

$$I = \int_a^b f(x)dx = \sum_{i=1}^{n} w_i f_i(x) \tag{2.19}$$

3.APPLICATIONS

In order to verify the using formulations and modelling of this study, the numerical results of vertical displacements compared with the Boussinesq theoretical results (Goodier and Timoshenko, 1970) in figure 2. The three-dimensional problem of a point load (P=2) acting on an elastic half-space is analyzed. The material properties are $E = 1,\ \nu = 1$. The two dimensions elements used are 16-node finite elements and 8-node infinite elements. In the numerical solutions, $n_x = n_y = 20$ finite elements and 62 infinite elements are used. As seen from figure 2, the presented results of this study is close to the results of Boussinesq (Goodier and Timoshenko, 1970).

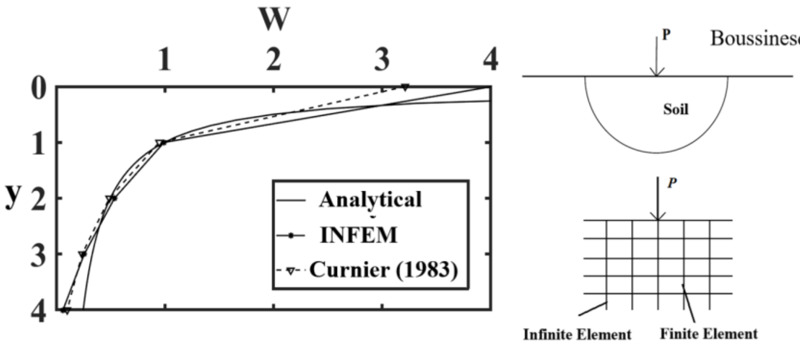

Figure 2. Point load acting on three-dimensional elastic half-space Boussinesq (Goodier and Timoshenko, 1970).

Table 1. The mechanical properties of semi-unbounded soil medium

		Model 1	Model 2	Model 3	Model 4
First Layer	$E_1\ (Pa)$	$200 * 10^8$	$100 * 10^8$	$400 * 10^8$	$100 * 10^8$
	ν_1	0	0	0	0
Second Layer	$E_2\ (Pa)$	$400 * 10^8$	$400 * 10^8$	$200 * 10^8$	$200 * 10^8$
	ν_2	0	0	0	0
Third Layer	$E_3\ (Pa)$	$100 * 10^8$	$200 * 10^8$	$100 * 10^8$	$400 * 10^8$
	ν_3	0	0	0	0

In the numerical results, normal stresses of three-layered soil medium are investigated for the different layer sequences with different material properties by using finite and infinite elements. The ground dimensions are taken as $L_x = L_y = 8\ m$ and $t = 1$ meters. In the uniform distributed load is selected a constant value as $q = 300\ N/m$ and 4 m. In this study, different soil layer sequences are used and their sequences are ordered as model-1, model-2, model-3, model-4. The mechanical properties of soil medium are shown Table 1. In the numerical results, $n_x = n_y = 20$ finite elements and 62 infinite elements are used. In the obtaining the numerical results and figures, MATLAB program is used.

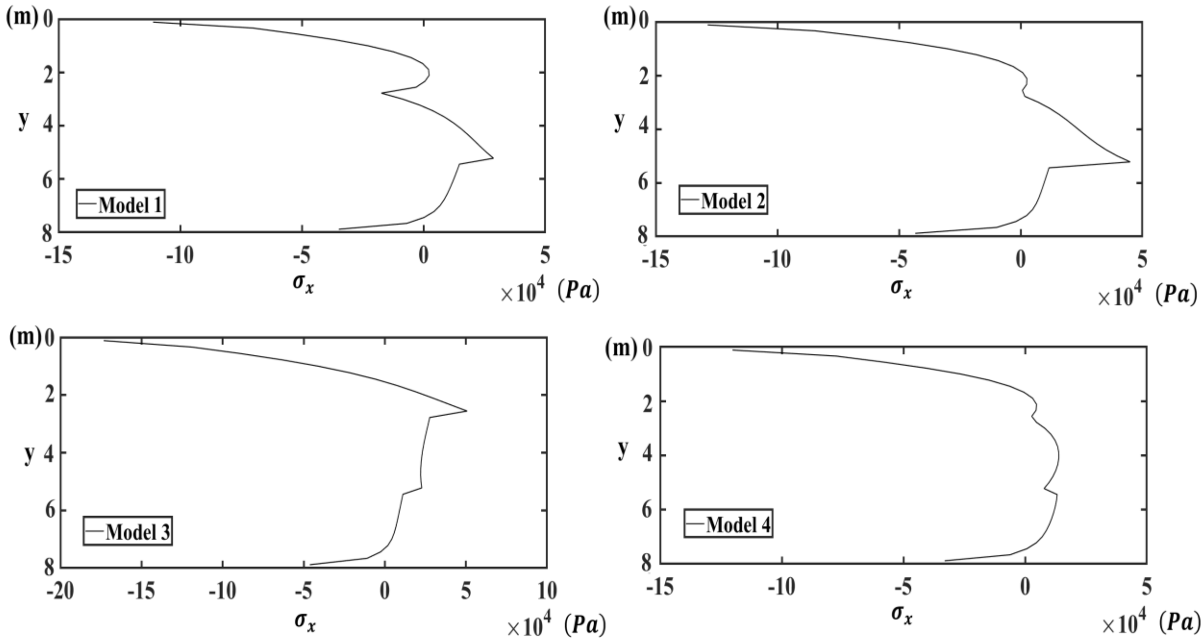

Figure 3. Stress analysis of layered semi-infinite soil under uniform load (σ_x).

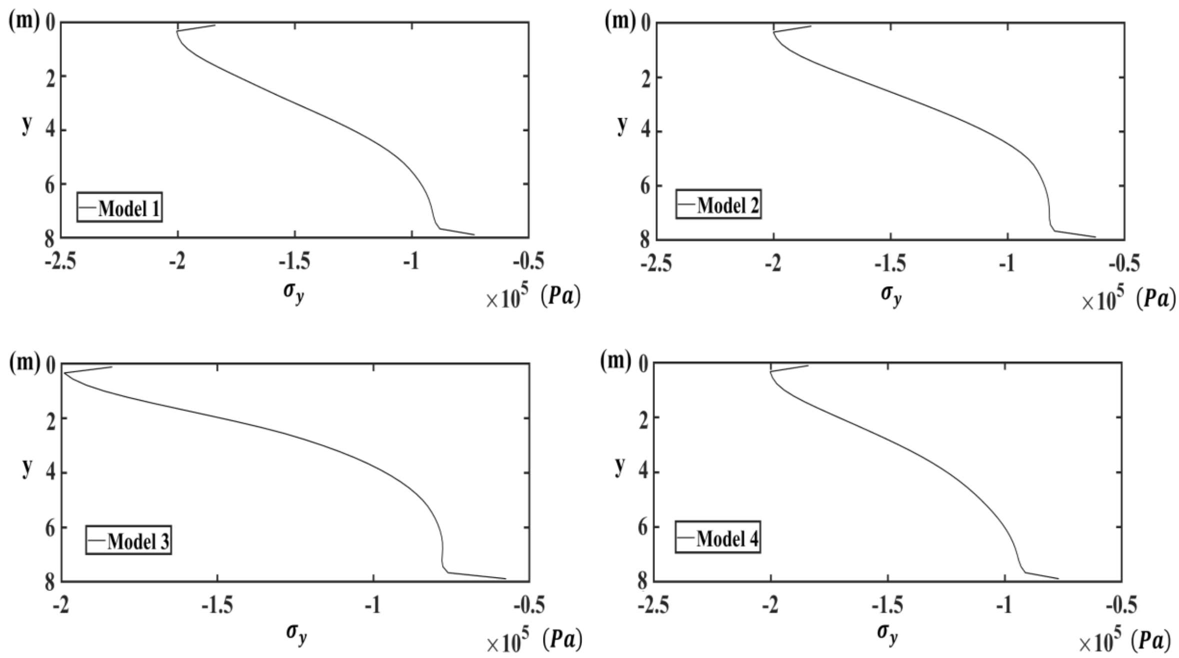

Figure 4. Stress analysis of layered semi-infinite soil under uniform load (σ_y).

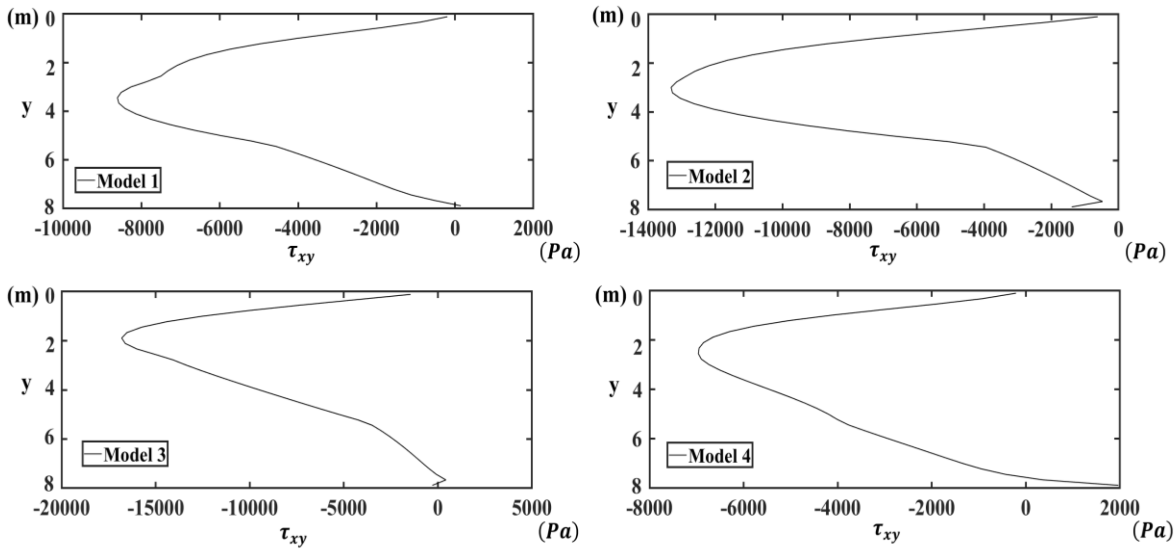

Figure 5. Stress analysis of layered semi-infinite soil under uniform load (τ_{xy}).

Figure 3 shows the normal stress in the x-direction in a layered soil under uniform load. Maximum stresses occurred on the ground surface. Different layer stiffnesses caused different stresses. In Figure 4, the normal stress in the y-direction in a layered soil under uniform load is shown. The layer stiffness changes did not change the normal stresses in the y direction much. In Figure 5, the shear stresses in a layered soil under uniform load are shown. The graphs are examined; the maximum shear stresses are towards the middle surface of the ground. In Model 3, due to the decrease in the stiffness of the upper surface of the soil, the shear stress has reached its maximum in the region closer to the surface.

4.CONCLUSIONS

In this study, normal stress analysis is performed on a 3-layer elastic, isotropic semi-infinite soil under uniform load. The finite infinite element model is coded in the MATLAB program. By using 1-dimensional 4-node finite elements, 2-dimensional 16-node finite elements are produced. By using a 1-dimensional 2-node infinite element, an 8-node infinite element is produced. The finite element model is solved by the 5-point Gauss Legendre Integration method. A comparison study was made with the Boussinesq theory. Normal stresses in the horizontal and vertical directions on the ground surface were high. As the load moved away from the impact area, the stresses towards the lower points of the ground decreased. Discontinuities have formed between layers with different mechanical properties. The low stiffness in the upper layers increased the stresses. It is shown from the result, the finite-infinite element models give more realistic results and better modelling of semi-infinite soils.

REFERENCES

1. Goodier, James Norman, and Stephen Timoshenko. Theory of Elasticity. McGraw-Hill, 1970.

2. Yerli, H. R., Temel, Beytullah and Kiral E., Transient Infinite Elements for 2D Soil-Structure Interaction Analysis, Journal of Geotechnical and Geoenvironmental Engineering Vol:124, No:10. 976-988, 1998.
3. Kumar, Prabhat, Static Infinite Element Formulation, Journal of Structural Engineering Vol:111, No:11, 2355-2372, 1985.
4. Liu Weiming, and Milos Novak, Soil–Pile–Cap Static Interaction Analysis By Finite and Infinite Elements, Canadian Geotechnical Journal, Vol:28, No:6, 771-783, 1991.
5. Karpurapu, Gopal R., and R. J. Bathurst, "Comparative Analysis of Some Geomechanics Problems Using Finite and Infinite Element Methods, Computers and Geotechnics, Vol:5, No:4, 269-284, 1988.
6. Haji, Twana Kamal, et al. Development of an Infinite Element Boundary to Model Gravity for Subsurface Civil Engineering Applications, International Journal for Numerical and Analytical Methods in Geomechanics, Vol:44, No:3, 418-431, 2020.
7. Lynn, Paul P., and Hassoun A. Hadid, Infinite Elements with 1/rn Type Decay, International Journal for Numerical Methods in Engineering, Vol:17, No:3, 347-355, 1981.
8. Bettess, Peter. Infinite Elements, International Journal for Numerical Methods in Engineering Vol:11, No:1, 53-64, 1977.
9. Wen, P. H., et al. Infinite Element in Meshless Approaches, European Journal of Mechanics-A/Solids No:72, 175-185, 2018.
10. Bettess, Peter, and Jacqueline A. Bettess. Infinite Elements for Static Problems, Engineering Computations, 1984.
11. Selvadurai, A. P. S., and Rajagopal Karpurapu. Composite Infinite Element for Modeling Unbounded Saturated-Soil Media, Journal of Geotechnical Engineering, Vol:115, No:11, 1633-1646, 1989.
12. Liu, Pengfei, Dawei Wang, and Markus Oeser, Application of Semi-Analytical Finite Element Method Coupled with Infinite Element for Analysis of Asphalt Pavement Structural Response, Journal of Traffic and Transportation Engineering (English Edition) Vol:2, No:1, 48-58, 2015.
13. Izra, Uporaba, and Unaz Neskon, Application of Infinite-Element Calculations for Consolidating a Railway Foundation of Blowıng Sand Reclamation, Materiali in Tehnologije Vol:47, No:5, 621-626, 2013.
14. Erkal, Aykut, Debra F. Laefer, and Semih Tezcan, Advantages of Infinite Elements over Prespecified Boundary Conditions in Unbounded Problems, Journal of Computing in Civil Engineering, Vol:29, No:6 04014085, 2015.

15. Curnier, Alain, A Static Infinite Element, International Journal for Numerical Methods in Engineering Vol:19, No:10, 1479-1488, 1983.
16. Pissanetzky, Sergio, A Simple Infinite Element, COMPEL-The International Journal for Computation and Mathematics in Electrical and Electronic Engineering, 1984.
17. Zienkiewicz, O. C., C. Emson, and P. Bettess, A Novel Boundary Infinite Element, International Journal for Numerical Methods in Engineering, Vol:19, No:3, 393-404, 1983.
18. El-Esnawy, N. A., A. Y. Akl, and A. S. Bazaraa, A New Parametric Infinite Domain Element." Finite Elements in Analysis and Design, Vol:19, No:1-2, 103-114, 1995.

AUTISM SPECTRUM DISORDER DETECTION USING MACHINE LEARNING ALGORITHMS

Afrah Said[1], Hanife Göker [1*]

[1] Department of Electrical Electronics Engineering, Kutahya, Turkey

afrah.said@ogr.dpu.edu.tr, hanife.goker@dpu.edu.tr

Abstract

Autism Spectrum Disorder is a neurological condition that affects brain development. It is characterized by how the person perceives things, learns, interacts, and socializes with others. It is also said that it is a "behavioral disease" because it affects their social communication such as having poor eye contact with others and repetitive behaviors such as repeating certain words or phrases. Detection of this disorder is associated with remarkable healthcare costs and is time-consuming. However, due to the advancement of Machine Learning algorithms in the diagnosis of many diseases, predicting this disorder using these methods could be beneficial as this could result in an early intervention treatment service that can improve a child's development and hence prevent this disorder to keep going on into adolescence and adulthood stage. Therefore, this paper aims to effective detection of autism spectrum disorder using machine learning algorithms. As the signs of this disorder could be seen at an early stage of a child's development, therefore, to carry out this study we used the autism screening data for toddler's dataset that is publicly available for researchers. This dataset consists of 1054 instances and 17 attributes. Feature selection was made on the dataset using InfoGain, SymmetricalUncert, OneR, CfsSubSetEval, and ChiSquared feature selection algorithms, and their performance are compared. According to their performances, the features that can be used in the differential diagnosis of the disorder and the predictive power of each feature are determined. Moreover, the performances of the Support Vector Machine, K-Nearest Neighbor, Naïve Bayes, Random Forest, and Sequential Minimal Optimization classification algorithms were compared.

Keywords: Autism spectrum disorder; Machine learning; Feature selection algorithms; Classification; Effective detection.

1.INTRODUCTION

Autism which is also known as an autism spectrum disorder (ASD) is a type of neurodevelopmental syndrome that is influenced by environmental and genetic factors (Oh et. al, 2021). Although symptoms of ASD are neurologically based, however, this neurological condition is manifested as behavioral characteristics such as affecting the physical impression of the face, thereby making them have a lack of eye contact. Despite that, several symptoms are associated with this disorder, most of which of them are behavioral symptoms that can be noticed early in childhood by their parents, schools, and teachers depending on their awareness of the disorder (Hyman et. al, 2020). Moreover, major symptoms usually appear in children between 6 and 17 years of age, besides that autism patients have decreased awareness of their surroundings which can make them have a high risk for injury such as making accidents on busy roads and this could be due to their wandering off (Sherkatghanad et. al, 2020; Hyman et. al, 2020).

Nowadays, due to the increased number of ASD cases, it is necessary to detect the disorder especially, in its early stage to enhance the patient's development and provide the required interventions before it is too late as this disorder starts in childhood and last forever if not treated (Oh et. al, 2021). As a consequence, core deficits can be detected in two domains, deficits in social communication and interaction, restricted and repetitive behaviors and interests (Hyman, 2020; Salgado-Cacho et. al, 2021). Additionally, children with autism encounter several problems in their daily life such as communication problems, difficulty in controlling their emotions, and sometimes too being aggressive (Oh et. al, 2021). Likewise, they also affect their family's daily life. Consequently, a research that was carried out in Croatia families of children with autism reported encountering fulfillment caring for their child on the autism spectrum and having a heightened risk of parenting stress which in succession affects their mental and physical wellbeing (Stošić et. al, 2020).

The major piling up of this disorder is the difficulty in obtaining a diagnosis, as this disorder is commonly diagnosed using clinical assessments such as screening tests to detect the symptoms (Oh et. al, 2021). However, doing parental educational workshops for parents increases the awareness of the syndrome and can help them diagnose their child by looking at the early symptoms of the disorder which can be noticed between 18 and 24 months of age (Stošić et. al, 2020; Alsaade & Alzahrani, 2022). As recognition of the diseases is the most significant point for the treatment of any certain disease, therefore, detection of this disorder is the first step to its treatment. Nowadays, disease prediction using modern model technologies such as machine learning algorithms has increased, this is because machine learning help in the prediction of the disease based on previous training data, for that reason we have used machine learning algorithms for the detection of ASD disorder thereby enabling the detection of the disorder without further interventions as machine learning models can learn without specifically programming them and make convenient predictions by learning from patterns in given training examples and hence enabling patients an effective detection of their disorder so that they can begin their required treatment and as a result enhancing their quality of life before it's too late (Ibrahim & Abdulazeez, 2021; Sherkatghanad et. al, 2020).

Several researchers have adopted machine learning techniques for the detection of autism. Sharif & Khan (2021); contributed to a machine learning model for the detection of autism using five different machine learning algorithms namely, Linear Discriminant Analysis (LDA), Support Vector Machine (SVM), Random Forest (RF), Multi-layer Perceptron (MLP) and K-nearest neighbor (KNN). They have used a feature selection algorithm to select the most important features that would facilitate the classification of ASD. The feature selection algorithms that they have used are InfoGain, Information Gain Ratio, Chi-Square, and Symmetrical Uncertainty feature selection algorithms. Moreover, using the machine learning algorithms to test their model, they have achieved an average accuracy of 55.93% for LDA, 52.20% for SVM, 54.79% for RF, 54.98% for MLP, and 51.00% for the KNN algorithm. Moreover, after comparing these algorithms, the LDA algorithm achieved the highest among them with an accuracy of 55.93%. Raj & Masood (2020); introduced a machine learning technique for the detection of ASD using three different datasets each of different categories of adults, children, and adolescents respectively to carry out their study. After preprocessing their datasets such as handling the missing values, they used several classifiers like Naïve Bayes (NB), SVM, KNN, Logistic Regression, neural network, and convolutional neural network algorithms. After checking the performance of these algorithms, the SVM showed the highest accuracy among the machine learning algorithms that they have used, achieving an accuracy of 96.88% for the adolescent dataset. Moon et al. (2019); also proposed a machine learning model for the detection of ASD by distinguishing individuals with ASD from control groups, however, using structural magnetic resonance imaging (sMRI) dataset with 1776 participants. As a result, they have achieved a sensitivity of 0.83, specificity of 0.84, and an accuracy value based on AUC/pAUC of 0.90/0.83. Küpper et al. (2020); developed a model for identifying the predictive features of ASD based on the behavioral diagnostic tools called the Autism Diagnostic Observation Schedule (ADOS) in adolescents and adults dataset using the SVM machine learning algorithm. However, they have tested their model using different features, like 5-feature models, 11-feature model (ADOS), 31-feature model (all ADOS items), and 12-feature model. Moreover, they have also compared the training set with the test set for all ages and both the adolescent and adult categories. After contrasting the performance of the algorithm of all ages, the 11-feature model showed the highest in both the training and the test set with 0.87 AUC, 0.75 Sensitivity, and 0.88 Specificity for the training set and 0.84 (0.85, 0.76) values of AUC (Sensitivity, Specificity) respectively for the test set. While the performance of the algorithm for the Adolescents and adults categories, the 5-feature model achieved the highest among the rest of the models for the test set with an AUC (Sensitivity, Specificity) of 0.90 (0.78, 0.88) for the adolescent's dataset and the12-feature-based model being the highest between the training set with 0.85 (0.70, 0.86) respectively, in addition to that, the adult's dataset using 11-feature based model (ADOS) showed the highest performance of AUC (Sensitivity, Specificity) with 0.87 (0.92, 0.84) for the test set and 0.88 (0.71, 0.89) respectively for the training set. Recently, machine learning based on disease detection is getting popular among researchers due to its ability to detect the disease without further interventions (Tawhid et. al, 2021). For that reason, we have used the machine learning method for the detection of autism disorder.

In this study, we proposed a machine learning model to detect children with ASD from control groups using classification algorithms namely SVM, KNN, NB, RF, and Sequential Minimal Optimization (SMO) classifier with several feature selection algorithms such as InfoGain, SymmetricalUncert, OneR, CfsSubSetEval, and ChiSquared feature selection algorithms. In addition, we have compared the performances of these algorithms for the detection of ASD to determine the best classification algorithm and after comparing them, the RF algorithm achieved the highest performance among the other algorithms that were used in the model. Moreover, the results performance of the RF algorithm showed 0.97% sensitivity, 0.98% specificity, 0.96% precision, 0.96% f1 score, 0.95% Matthews correlation coefficient (MCC) and, 98.10% accuracy.

2.GENERAL PROPERTIES OF METHOD

2.1. Proposed model

In the study, we proposed a machine learning model for the detection of autism disorder. The flow chart of the proposed model is given in Figure 1.

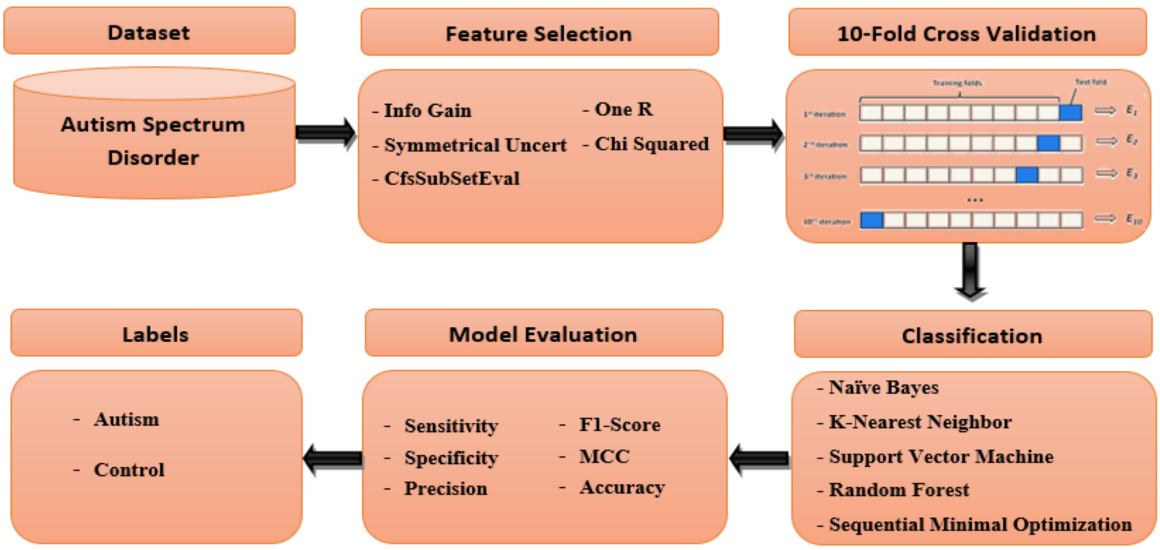

Figure 1. Flow diagram of the proposed methods

2.2. Dataset

To conduct this study, we have used the ASD dataset that is available on the Kaggle website (Thabtah, 2018). More information about the dataset is shown in Table 1.

Table 1. Characteristics of the dataset used.

Dataset	Number of Classes	Number of Attributes	Number of Samples
Autism Spectrum Disorder	2	17	1054

The ASD dataset contains clinical screening data of toddlers with several key indicators for the analysis of the disorder. It contains ten behavioral features named "A1 to A10" items and other individual characteristic features that enable the detection of the disorder from the control groups. Moreover, the features of A1 to A10 items are questions that are based on determining autistic traits and the answers to those questions could be "always, usually, sometimes, rarely, and never" for example, the A1 question states "Does your child look at you when you call his/her name?" and according to their answer they are assigned "1" or "0". Additionally, there is also a Qchat-10-Score attribute that counts the points for all the ten questions by adding them, therefore, if the toddler obtained 3 points or less then this means that they are normal otherwise there is a potential ASD trait if their points are 4 or above (Thabtah, 2018). Furthermore, the features of the dataset and their meaning is given in Table2.

Table 2. Clinical data for ASD dataset features.

No	Attribute	Description
1	Age_Mons	Toddlers (months)
2	Qchat-10-Score	1-10 (Less than or equal 3 no ASD traits; > 3 ASD traits
4	Sex	Male or Female
5	Ethnicity	List of common ethnicities in text format
6	Jaundice	Whether the case was born with jaundice
7	Family_mem_with_ASD	Whether any immediate family member has a PDD
8	Who completed the test	Parent, self, caregiver, medical staff, clinician ,etc.
9	Question 1 (A1)	Does your child look at you when you call his/her name?
10	Question 2 (A2)	How easy is it for you to get eye contact with your child?
11	Question 3 (A3)	Does your child point to indicate that s/he wants something? (e.g. a toy that is

		out of reach)
12	Question 4 (A4)	Does your child point to share interest with you? (e.g. pointing at an interesting sight)
13	Question 5 (A5)	Does your child pretend? (e.g. care for dolls, talk on a toy phone)
14	Question 6 (A6)	Does your child follow where you're looking?
15	Question 7 (A7)	If you or someone else in the family is visibly upset, does your child show signs of wanting to comfort them? (e.g. stroking hair, hugging them)
16	Question 8 (A8)	Would you describe your child's first words as:
17	Question 9 (A9)	Does your child use simple gestures? (e.g. wave goodbye)
18	Question 10 (A10)	Does your child stare at nothing with no apparent purpose?
19	Class	Autism, Control

2.3. Feature Selection

Feature selection which is also known as attribute selection is an important step in machine learning models, as feature selection algorithms help in the selection of the most useful features based on the correlation between a class variable and predictive features without capturing normal relationships between them, thereby reducing the dimensionality of the dataset and hence leading to have a more compact model (Solorio-Fernández et. al, 2020; Yu et. al, 2020).

Among the many features of the data, it may not be known which features determine the dataset, class, and value more. In these cases, a subset of the entire feature set is selected by feature selection. In the ASD dataset, 17 characteristics affect the autism disorder. At the feature selection stage, feature selection was performed to identify the factors affecting autism the most, reduce the complexity of the procedure, and generalize more accurately. In the feature selection step, 10 features were selected from 17 features using InfoGain, SymmetricalUncert, OneR, CfsSubSetEval, and ChiSquared algorithms.

2.4. Division of data into training and test sets

While the accuracy rates of the classification algorithms are compared, the data in the knowledge base is divided into two groups, training data and test data. K-fold Cross-Validation and Holdout methods are widely used in the process of verifying the performance of the system.

After making the data suitable for analysis using feature selection algorithms, the dataset was divided into training and testing sets using the k-fold cross-validation method. In this study, the 10-fold cross-validation method was used by reserving one subset of the dataset for evaluation and the remaining subsets for training. The dataset is divided into k- parts of equal size and thus the process is repeated k times, however, every time using a different part for evaluation by removing one of the subsets from the training set and then using it as the test set (Gholamiangonabadi et. al, 2020).

After dividing the dataset into training and test sets, the model was trained with the training dataset and the performance of the model was tested using classification algorithms such as SVM, NB, KNN, RF, and SMO Classifier.

2.5. Model evaluation

After training the dataset with the training set, the model is evaluated with the test set as model evaluation checks the efficiency of the model and gives the decision whether a model is adequate or not (Parker, 2020). Therefore, we have used several classification algorithms to evaluate the model and the best classification algorithm that is suitable for the data is chosen by demonstrating all the possible models and comparing them. Moreover, to evaluate the performance metrics of the model we used the confusion matrix. A confusion matrix is a term used in machine learning models in order to measure the accuracy of the model by making a comparison between the predicted values and the actual values that is the actual subjects with autism disorder or without them and the predicted subjects with the autism disorder or without them (Zeng, 2020). It consists of True Positive (TP), False Positive (FP), False

Negative (FN), and True Negative (TN). The TP and the TN are the number of positive and negative samples that are correctly classified, respectively, while the FP and FN are the number of positive and negative samples that were incorrectly classified (Gholamiangonabadi et. al, 2020).

After finding the TP, FP, FN and TN values, the results performance of the algorithms is compared and efficiency of the model is decided. The basic model performance criteria and the calculation of the metrics of sensitivity, specificity, precision, F1-score, MCC and the evaluation metrics of the model accuracy that involves the confusion matrix measures are given in below.

$$\text{Sensitivity} = \frac{\text{TP}}{(\text{TP} + \text{FN})} \tag{1}$$

$$\text{Specificity} = \frac{\text{TN}}{(\text{TN}+\text{FP})} \tag{2}$$

$$\text{Precision} = \frac{\text{TP}}{(\text{TP} + \text{FP})} \tag{3}$$

$$\text{F1- score} = \frac{2 \text{ x Recall x Precision}}{(\text{Recall} + \text{Precision})} \tag{4}$$

$$\text{MCC} = \frac{(\text{TN x TP} - \text{FP x FN})}{\sqrt{(TN+FN)\text{x}\,(FP+TP)\text{x}\,(TN+FP)\text{x}\,(FN+TP)}} \tag{5}$$

$$\text{Accuracy} = \frac{(\text{TP} + \text{TN})}{(\text{TP} + \text{FN} + \text{FP} + \text{TN})} \tag{6}$$

3. Applications

In the study, firstly, the feature selection process was carried out. In the feature selection process, the feature selection algorithms in the "Select attributes" section of the WEKA software were used. InfoGain, SymmetricalUncert, OneR, CfsSubSetEval, and ChiSquared algorithms are among the most used feature selection algorithms in the literature (Amasyalı, 2008). To check how well a model works, measuring its performance is the key to knowing it (Raj & Massod, 2020). Therefore, in order to check our model's effectiveness, we have done performance comparisons between our selected classification algorithms namely**,** NB, SVM, RF, KNN, and SMO machine learning algorithms. For that reason, to identify the features that contribute to the diagnosis of the disorder between the other features that are in the dataset, we used feature selection algorithms such as InfoGain, SymmetricalUncert, OneR, CfsSubSetEval, and ChiSquared, furthermore, we have compared between them using classification algorithms and their comparisons are given in Table 3.

Table 3. Comparison of feature selection algorithms on ASD dataset.

Classification Algorithms	**Feature Selection Algorithms**				
	InfoGain	**SymmetricalUncert**	**OneR**	**CfsSubSetEval**	**ChiSquared**
NB	96.96 %	96.96 %	96.77	96.48	96.96
SVM	97.34 %	97.34 %	94.68	95.06	97.34
KNN (3)	96.86 %	96.86 %	94.49	94.97	96.86
RF	98.10%	98.10 %	96.48	95.44	98.10
SMO	96.48%	96.48 %	94.68	97.24	96.48

By using feature selection algorithms, 10 features were selected among 17 features according to the power of representation of the dataset. When Table 2 is examined, it is seen that the classification performances made with the features selected by the InfoGain, SymmetricalUncert, and ChiSquared feature selection algorithms are higher (98.10%) in the RF algorithm. Any of the InfoGain, SymmetricalUncert, and ChiSquared attribute algorithms can be selected. Therefore, we have selected the InfoGain algorithm as it computes how much information with respect to the classification target the attribute gives (Badnjević et. al, 2019). For that reason, in this study the InfoGain algorithm has been used and 10 attributes that primarily affect Autism were selected from the17 attribute information. According to this algorithm, the qualities that primarily affect Autism are; A1, A2, A3, A4, A5, A6, A7, A8, A9, and Qchat-10-Score which are explained in Table 2. Moreover, the model performance of the classification algorithms using InfoGain feature selection algorithm is shown in Table 4.

Table 4. Comparison results of classification algorithms according to number of subjects.

Classification models	Confusion Matrix Parameters				Classified	
	TP	FP	FN	TN	Incorrectly	Correctly
NB	326	0	32	696	32	1022
SVM	319	7	21	707	28	1026
KNN (3)	315	11	22	706	33	1021
RF	315	11	9	719	20	1034
SMO	297	29	8	720	37	1017

After examining Table 4, it is noticed that the RF classification algorithm has the highest number of correctly classified samples with 1034 samples correctly classified, and with the least incorrectly classified samples which are 20 samples among the other algorithms. Moreover, after examining the confusion matrix TP, FP, FN, and TN values it is found that TP classified samples were 315, FP classified samples were 11, FN classified samples were 9 and the TN classified samples were 719.

Table 5. Statistic performance of accuracy metrics of the classification algorithms

Classification models	Model performance evaluation					
	Sensitivity	**Specificity**	**Precision**	**F1- score**	**MCC**	**Accuracy**
NB	0.91	1.00	1.00	0.95	0.93	96.96
SVM	0.93	0.99	0.97	0.95	0.93	97.34
KNN (3)	0.93	0.98	0.96	0.95	0.92	96.87
RF	0.97	0.98	0.96	0.96	0.95	98.10
SMO	0.97	0.96	0.91	0.94	0.91	96.49

When sensitivity, specificity, precision, F1- score, MCC, and accuracy values are examined it is shown that the RF algorithm has the highest value for all the model performance criteria among the other algorithms. For example, when the accuracies of the algorithms are examined the RF algorithm has the highest value with an accuracy of 98.10% and a precision of 96%, Furthermore, the model performance criteria of the classification algorithms are given in Table 5. Moreover, the comparison results of the classification algorithms according to the number of instances are shown in Table 4.

A comparative analysis was done between our proposed model and the existing models that were carried out for the detection of ASD, besides, the accuracies and the algorithms that were used in these studies were compared to reach a conclusion and this comparison is shown in Table 7.

Table 7. A comparative analysis with relevant literature studies

Researchers	Attributes	Algorithms	Dataset	Best Classifier	Accuracy
Thabtah & Peebles (2020)	ASD Child dataset	RIPPER, RIDOR, Nnge, Bagging, CART, PRISM, Rules-Machine Learning (RML), C4.5 and AdaBoost algorithms	151 Controls and 141 ASD patients	RML	91%
Guttenberg & Kanai (2018)	ASD dataset	KNN, RF, LSVC, XGBoost, SVC, CG and FTCG	515 Controls and 189 ASD patients	XGBoost	87.8%
Thabtah et al. (2019)	ASD adolescent dataset	Logistic Regression	122 Controls and 127 ASD patients	Logistic Regression	97.58
Omar et al. (2019)	ASD child dataset	Decision Tree-Classification and Regression Trees (CART), RF-CART	100 ASD, 150 Non-ASD	RF-CART +RF-ID3 classifier	92.26%
The Proposed Model (2022)	ASD toddler dataset	NB, SVM, RF, KNN and SMO	326 controls and 728 ASD patients	RF	98.10%

The above table shows the previous studies that were carried out for the detection of autism. Thabtah & Peebles (2020) proposed a machine learning model for the detection of autism. They have evaluated their dataset using Boosting, rule induction, Bagging, and decision trees algorithms namely; RIPPER, RIDOR, Nnge, Bagging, CART, PRISM, RML, C4.5, and AdaBoost algorithms, after evaluating the performance of their autism child dataset the RML classifier showed the highest among the algorithms used with an accuracy of 91%. Guttenberg & Kanai (2018) tested several algorithms such as SVM, RF, XGBoost, and KNN on a range of small datasets including the ASD dataset. The XGBoost algorithm achieved the highest with 87.8% for the ASD dataset. Thabtah et al. (2019) also presented a machine learning model for the detection of autism however using only logistic regression algorithm. They have tested the algorithm on two datasets adults and adolescents, giving the adolescent dataset an accuracy of 97.58%. Omar et al. (2019) proposed a new model by using two models to study their findings using two datasets (AQ-10 dataset and Real dataset) of three categories, child, adolescent, and adult. They have compared those two datasets by carrying out three models namely a model based on decision tree-CART, a model based on random RF-CART, and a combination of RF-CART and RF-ID3. After the comparison, the third model achieved the highest accuracy among them with an accuracy of 92.26 for the child category of the AQ-10 dataset. In our findings, we have used the toddler's dataset for the detection of autism in children using NB, SVM, RF, KNN, and SMO machine learning algorithms. We have compared these algorithms and the RF algorithm showed the highest among them with an accuracy of 98.10%.

4.CONCLUSIONS

In conclusion, we have developed a model that correctly classifies ASD cases from those without the disorder. This was done by first applying several feature selection algorithms to the dataset and comparing them to evaluate their effectiveness using classification algorithms. As a consequence, we have concluded that the InfoGain feature selection algorithm is the effective feature selection algorithm for our model. After selecting the feature selection algorithm that is suitable for the model, we have evaluated the performance of the classification algorithm with model performance metrics such as sensitivity, specificity, precision, F1- score, MCC, and accuracy. Evaluating those criteria showed that the RF algorithm works best for the detection of ASD cases with 0.97 sensitivity, 0.98 specificity, 0.96 precision, 0.96 f1 score, 0.95 MCC, and highest accuracy of 98.10%. Moreover, we have used 10-fold cross-validation method for the evaluation of the dataset. In our future works, we plan to work on several methods such as deep learning methods with machine learning methods to improve the performance.

REFERENCES

1. Alsaade, F. W., & Alzahrani, M. S. (2022). Classification and detection of autism spectrum disorder based on deep learning algorithms. *Computational Intelligence and Neuroscience*, 1-10.
2. Badnjević, A., Pokvić, L. G., Hasičić, M., Bandić, L., Mašetić, Z., Kovačević, Ž., Kevrić, J. & Pecchia, L. (2019). Evidence-based clinical engineering: machine learning algorithms for prediction of defibrillator performance. *Biomedical Signal Processing and Control, 54,*101629, 1-9.
3. Gholamiangonabadi, D., Kiselov, N., & Grolinger, K. (2020). Deep neural networks for human activity recognition with wearable sensors: Leave-one-subject-out cross-validation for model selection. *IEEE Access, 8*, 133982-133994.
4. Guttenberg, N., & Kanai, R. (2018). Learning to generate classifiers. ArXiv Preprint ArXiv:1803.11373.
5. Hyman, S. L., Levy, S. E., Myers, S. M., Kuo, D. Z., Apkon, S., Davidson, L. F., Ellerbeck, K. E., Foster, J. E. A., Noritz, G. H., Leppert, M. O., Saunders, B. S., Stille, C., Yin, L., Weitzman, C. C., Childers, D. O., Levine, J. M., Peralta-Carcelen, A. M., Poon, J. K., Smith, P. J., Blum, N. J., Takayama, J. I., Baum, R., Voigt, R.G., & Bridgemohan, C. (2020). Identification, evaluation, and management of children with autism spectrum disorder. *Pediatrics, 145*(1).1-69.
6. Ibrahim, I., & Abdulazeez, A. (2021). The role of machine learning algorithms for diagnosing diseases. Journal of Applied Science and Technology Trends, 2(01), 10-19.
7. Küpper, C., Stroth, S., Wolff, N., Hauck, F., Kliewer, N., Schad-Hansjosten, T., Kamp-Becker, I., Poustka, L., Roessner, V., Schultebraucks, K., & Roepke, S. (2020). Identifying predictive features of autism spectrum disorders in a clinical sample of adolescents and adults using machine learning. *Scientific Reports, 10*(1), 1-11.
8. Moon, S. J., Hwang, J., Kana, R., Torous, J., & Kim, J. W. (2019). Accuracy of machine learning algorithms for the diagnosis of autism spectrum disorder: Systematic review and meta-analysis of brain magnetic resonance imaging studies. JMIR mental health, 6(12), e14108.
9. Oh, S. L., Jahmunah, V., Arunkumar, N., Abdulhay, E. W., Gururajan, R., Adib, N., Ciaccio, E. J., Cheong, K. H., & Acharya, U. R. (2021). A novel automated autism spectrum disorder detection system. *Complex & Intelligent Systems, 7*(5), 2399-2413.
10. Omar, K. S., Mondal, P., Khan, N. S., Rizvi, M. R. K., & Islam, M. N. (2019, February). A machine learning approach to predict autism spectrum disorder. In 2019 International Conference on Electrical, Computer and Communication Engineering (ECCE) (pp. 1-6). IEEE.
11. Parker, W. S. (2020). Model evaluation: An adequacy-for-purpose view. *Philosophy of Science, 87*(3), 457-477.
12. Raj, S., & Masood, S. (2020). Analysis and detection of autism spectrum disorder using machine learning techniques. *Procedia Computer Science, 167*, 994-1004.

13. Salgado-Cacho, J. M., Moreno-Jiménez, M. D. P., & de Diego-Otero, Y. (2021). Detection of early warning signs in autism spectrum disorders: a systematic review. *Children, 8*(2), 164.
14. Sharif, H., & Khan, R. A. (2021). A novel machine learning based framework for detection of autism spectrum disorder (ASD). *Applied Artificial Intelligence*, 1-33.
15. Sherkatghanad, Z., Akhondzadeh, M., Salari, S., Zomorodi-Moghadam, M., Abdar, M., Acharya, U. R., Khosrowabadi, R., & Salari, V. (2020). Automated detection of autism spectrum disorder using a convolutional neural network. *Frontiers in Neuroscience, 13*, 1325.
16. Solorio-Fernández, S., Carrasco-Ochoa, J. A., & Martínez-Trinidad, J. F. (2020). A review of unsupervised feature selection methods. *Artificial Intelligence Review, 53*(2), 907-948.
17. Stošić, J., Frey Škrinjar, J., & Preece, D. (2020). Families of children on the autism spectrum: experience of daily life and impact of parent education. *Support for Learning, 35*(2), 205-221.
18. Tawhid, M. N. A., Siuly, S., Wang, H., Whittaker, F., Wang, K., & Zhang, Y. (2021). A spectrogram image based intelligent technique for automatic detection of autism spectrum disorder from EEG. *Plos One, 16*(6), e0253094.
19. Thabtah, F., Abdelhamid, N., & Peebles, D. (2019). A machine learning autism classification based on logistic regression analysis. *Health Information Science and Systems, 7*(1), 1-11.
20. Thabtah, F., & Peebles, D. (2020). A new machine learning model based on induction of rules for autism detection. *Health Informatics Journal, 26*(1), 264-286.
21. Thabtah, D. F. (2018). Autism screening data for toddlers. Retrieved from Kaggle: https://www.kaggle.com/datasets/fabdelja/autism-screening-for-toddlers?select=Toddler+Autism+dataset+July+2018.csv
22. Yu, K., Guo, X., Liu, L., Li, J., Wang, H., Ling, Z., & Wu, X. (2020). Causality-based feature selection: Methods and evaluations. *ACM Computing Surveys (CSUR), 53*(5), 1-36.
23. Zeng, G. (2020). On the confusion matrix in credit scoring and its analytical properties. *Communications in Statistics-Theory and Methods, 49*(9), 2080-2093.

STATIC RESPONSES OF A CAVITY IN A HALF-SPACE BY USING FINITE ELEMENT METHOD

Yusuf Ziya Yüksel[1], **Şeref Doğuşcan Akbaş**[2],

[1,2]Department of Civil Engineering, University of Bursa Technical, Bursa, Turkey

yusuf.yuksel@btu.edu.tr, seref.akbas@btu.edu.tr,

Abstract

In this work, static analysis of two dimensional, elastic, isotropic semi-infinite soil space with a cavity is investigated. The analysis is performed by using the finite element method. The region close to the ground is modelled with finite elements, and the region far from the ground is modelled with infinite elements extending to infinity. In the literature, infinite elements used instead of finite elements for infinite media solutions. Infinite element shape functions are generated according to the direction. By using one-dimensional two-node infinite elements and 8-node infinite elements are produced. A finite element with 16 nodes is used to solve the problem. The numerical results compared with the Boussinesq theoretical results. Numerical solutions of finite-infinite elements are obtained by Gauss Legendre integration method. A single load is given from the ground surface. Effects of cavity geometry, point location and material and geometry parameters of soil on the static displacements are investigated. By using finite and infinite model. The finite-infinite element model is coded with MATLAB. Static results are compared.

Keywords: Finite – infinite element; Soil medium; Cavity, Half-Space

1.INTRODUCTION

A cavity structures in the semi-infinite soil media can create various problems in the ground. In order to understand these problems well, the problem should be solved in the most correct way. In this work, semi-infinite ground modeled by using finite-infinite elements, which is a direct method. The region close to the ground surface is modeled with finite elements, and the far region is modeled with infinite elements.

In the literature, there are many studies infinite soil media static problems; Lynn and Hadid (1981), proposed an infinite element of type $1/r^n$ for solving static problems in an elastic semi-infinite medium. Bettess and Bettess (1983), developed an infinite element damped in an infinite medium for the solution of static problems. Zienkiewicz (1983), produced a simple and new infinite element to solve two and three dimensional static infinite media problems. Curnier (1983), developed static infinite element and compared the theoretical results with obtained the numerical results. Pıssanetzky (1984), developed a simple infinite element type with damping function to model infinite media. Kumar (1985), developed infinite elements for the use of infinite media static problems. Karpurapu and Bathurst (1988), performed the solutions of geomechanical problems in semi-infinite medium using finite and infinite elements. Selvadurai and Karpurapu (1989), modelled infinite saturated soil medium by using composite infinite element. Liu and Novak (1991), presented pile-soil static interaction in infinite media by finite-infinite element method. Liu and Novak (1991), presented pile-soil static interaction in infinite media by finite-infinite element method. Bettess (1992), developed the infinite element method for the solution of infinite media problems and produced infinite elements for use in problem solutions. El-Esnawy (1995), examined static displacements under single loading in a two-dimensional infinite soil media using the finite-infinite element method. Yerli et. al. (1998), performed two dimensional soil-structure interaction analysis with different wave type of infinite elements. Liu (2012), studied the behavior of cast iron infrastructure tunnels under the impact of explosion. . Xie (2013), investigated dynamic consolidation behavior of railway foundation by using finite-infinite element method. Demidem et. al. (2014), examined analysis of underground structures by using finite and infinite elements. Liu et. al. (2015), performed static analysis of asphalt pavement by using finite-infinite element method. Erkal (2014), developed a method that facilitates the production of one and two dimensional infinite elements used in infinite media applications. Wen et. al. (2018), proposed a meshless infinite element for the solution of unbounded media problems. Haji et. al. (2021), developed a three-dimensional infinite element used in the solutions of underground civil engineering applications.

In this study, static displacements of semi-infinite soil with cavity structure under point load are investigated. Numerical results are obtained using finite and infinite elements. In the finite element model, a finite element with 16 nodes and an infinite element with 8 nodes are used. Numerical integration is performed by Gauss Legendre integration method.

2.GENERAL PROPERTIES OF METHOD

Semi-infinite soil with a cavity under point load is modeled with finite-infinite elements (Figure 1).

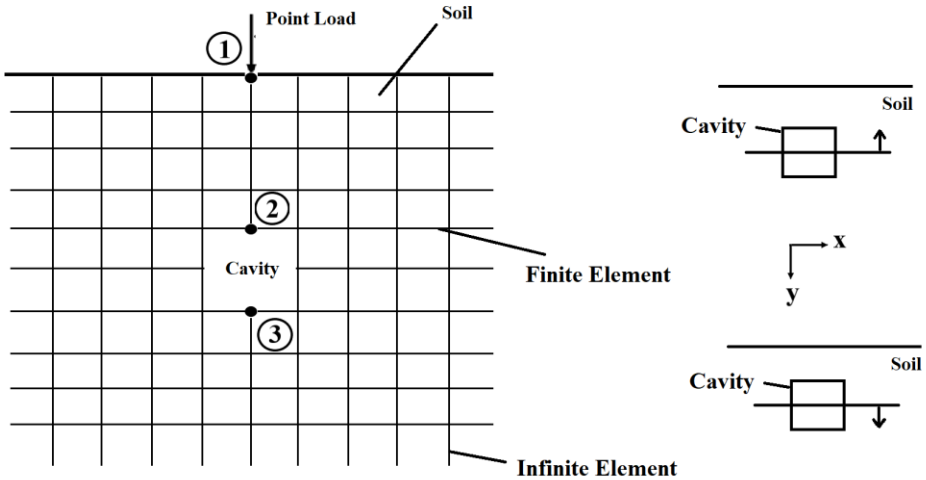

Figure 1. The semi-infinite ground with cavity under point load

Equations of motion in 2D elasticity are expressed as,

$$\frac{\partial \sigma_x}{\partial x} + \frac{\partial \tau_{xy}}{\partial y} + f_x = 0$$

$$\frac{\partial \tau_{xy}}{\partial x} + \frac{\partial \sigma_y}{\partial y} + f_y = 0 \tag{2.1}$$

where f_x and f_y are the volume forces in the x and y directions. σ_x and σ_y represent normal stresses, τ_{xy} represents shear stresses.

The relations between strain and displacements are given;

$$\varepsilon_x = \frac{\partial u}{\partial x}$$

$$\varepsilon_y = \frac{\partial v}{\partial y}$$

$$\gamma_{xy} = \frac{\partial u}{\partial y} + \frac{\partial v}{\partial x} \tag{2.2}$$

Here u and v represent the displacements in the x, y directions. The material is assumed to be linear elastic, homogeneous and isotropic. The constitutive equations of the body are given.

$$\{\sigma\} = [D]\{\varepsilon\} \tag{2.3}$$

Stress $\{\sigma\}$ is expressed as material constants $[D]$ and strain $\{\varepsilon\}$.

$$\{\sigma\} = \begin{Bmatrix} \sigma_x \\ \sigma_y \\ \tau_{xy} \end{Bmatrix} \qquad \{\varepsilon\} = \begin{Bmatrix} \varepsilon_x \\ \varepsilon_y \\ \gamma_{xy} \end{Bmatrix} \qquad [D] = \begin{bmatrix} D_{11} & D_{12} & 0 \\ D_{21} & D_{22} & 0 \\ 0 & 0 & D_{33} \end{bmatrix} \tag{2.4}$$

$$D_{11} = D_{22} = \frac{E}{(1-\nu^2)}$$

$$D_{12} = D_{21} = \frac{\nu E}{(1-\nu^2)}$$

$$D_{33} = G = \frac{E}{2(1+\nu)} \tag{2.5}$$

Where, E and G are the modulus of elasticity and shear, and ν is the Poisson's ratio.

The equations of motion in terms of displacements are given ass follows;

$$\frac{\partial}{\partial x}\left(D_{11}\frac{\partial u}{\partial x} + D_{12}\frac{\partial v}{\partial y}\right) + \frac{\partial}{\partial y}\left(D_{33}\left(\frac{\partial u}{\partial y} + \frac{\partial v}{\partial x}\right)\right) = -f_x + \rho\frac{\partial^2 u}{\partial t^2}$$

$$\frac{\partial}{\partial y}\left(D_{12}\frac{\partial u}{\partial x}+D_{22}\frac{\partial v}{\partial y}\right)+\frac{\partial}{\partial x}\left(D_{33}\left(\frac{\partial u}{\partial y}+\frac{\partial v}{\partial x}\right)\right)=-f_y+\rho\frac{\partial^2 v}{\partial t^2} \tag{2.6}$$

Boundary conditions are given in terms of displacements.

$$t_x=\left(D_{11}\frac{\partial u}{\partial x}+D_{12}\frac{\partial v}{\partial y}\right)n_x+D_{33}\left(\frac{\partial u}{\partial y}+\frac{\partial v}{\partial x}\right)$$

$$t_y=\left(D_{12}\frac{\partial u}{\partial x}+D_{22}\frac{\partial v}{\partial y}\right)n_y+D_{33}\left(\frac{\partial u}{\partial y}+\frac{\partial v}{\partial x}\right)n_x \tag{2.7}$$

Equations of motion converted to integral form with virtual work principle.

$$\begin{bmatrix}\frac{\partial}{\partial x} & 0 & \frac{\partial}{\partial y}\\ 0 & \frac{\partial}{\partial y} & \frac{\partial}{\partial x}\end{bmatrix}\begin{Bmatrix}\sigma_x\\ \sigma_y\\ \tau_{xy}\end{Bmatrix}+\begin{Bmatrix}f_x\\ f_y\end{Bmatrix}=0 \tag{2.8}$$

Displacements are given as follows;

$$\begin{Bmatrix}\varepsilon_x\\ \varepsilon_y\\ \gamma_{xy}\end{Bmatrix}=\begin{bmatrix}\frac{\partial}{\partial x} & 0\\ 0 & \frac{\partial}{\partial x}\\ \frac{\partial}{\partial y} & \frac{\partial}{\partial x}\end{bmatrix}\begin{Bmatrix}u\\ v\end{Bmatrix} \tag{2.9}$$

The finite element formulation for plane elasticity problems is summarized.

Interpolation shape functions are given;

$$u=\sum_{i=1}^{n}N_iu_i \qquad v=\sum_{i=1}^{n}N_iv_i \tag{2.10}$$

$$\begin{Bmatrix}u\\ v\end{Bmatrix}=\begin{bmatrix}N_1 & 0 & N_2 & 0 & \dots N_n & 0\\ 0 & N_1 & 0 & N_2 & \dots 0 & \dots N_n\end{bmatrix}\begin{bmatrix}u_1\\ v_1\\ u_2\\ v_2\\ \vdots\\ u_n\\ v_n\end{bmatrix} \tag{2.11}$$

The variation of node displacements is expressed.

$$\{\delta u\}=[N]\{\delta u_d\} \tag{2.12}$$

Strain and stresses in terms of node displacements,

$$\{\varepsilon\} = [B]\{\Delta\}, \quad \{\sigma\} = [D][B]\{\Delta\} \tag{2.13}$$

Where $[B]$ is the strain matrix.

$$[B] = [L]^T[N] \tag{2.14}$$

Here, the differential operators $[L]$ are given.

$$\begin{Bmatrix} \delta u \\ \delta v \end{Bmatrix} = [N]\{\delta\Delta\}, \quad \{\delta\varepsilon\} = [B]\{\delta\Delta\} \tag{2.15}$$

$$h_e \int\int_{A_e} \{\delta\Delta\}^T([B]^T[D][B]\{\Delta\})dxdy - h_e \int\int_{A_e} \{\delta\Delta\}^T[N]^T \begin{Bmatrix} f_x \\ f_y \end{Bmatrix} dxdy = 0 \tag{2.16}$$

Element stiffness matrices and element load vectors were obtained, respectively.

$$[k] = h_e \int\int_{A_e} [B]^T[D][B]dxdy$$

$$[f] = h_e \int\int_{A_e} [N]^T \begin{Bmatrix} f_x \\ f_y \end{Bmatrix} dxdy \tag{2.17}$$

$$[k]\{\Delta\} = [f] \tag{2.18}$$

Equations obtained using interpolation shape functions were solved by the 5-point Gauss Legendre integration method.

$$I = \int_a^b f(x)dx = \sum_{i=1}^{n} w_i f_i(x) \tag{2.19}$$

3.APPLICATIONS

In the comparison study, the numerical results of vertical displacements compared with the Boussinesq theoretical results (Goodier and Timoshenko, 1970). The three-dimensional problem of a point load (P=2) acting on an elastic half-space is analyzed. The material properties are $E = 1, \nu = 1$. The two dimensions elements used are 16-node finite elements and 8-node infinite elements. In the numerical solutions, $n_x = n_y = 20$ finite elements and 62 infinite elements are used.

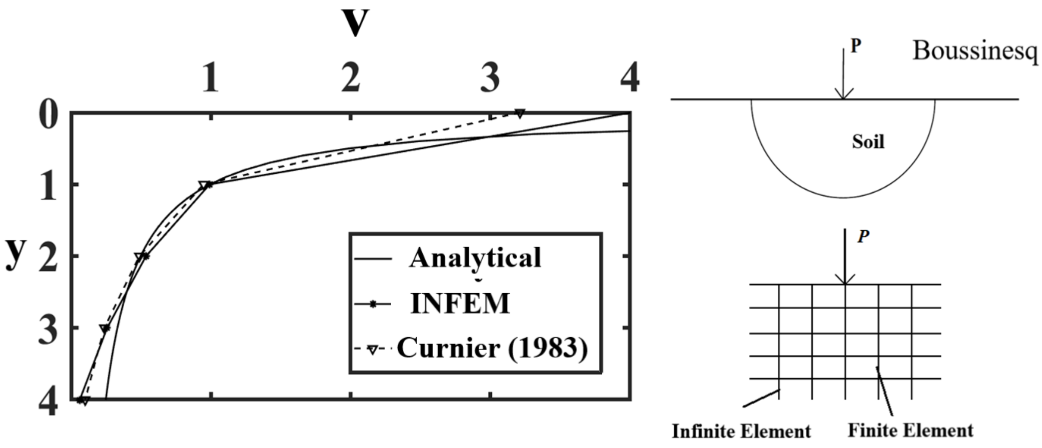

Figure 2. Point load acting on three-dimensional elastic half-space Boussinesq (Goodier and Timoshenko, 1970).

In the numerical results, static displacements of a cavity in unbounded soil media by using finite element method presented and discussed. In the problems, the static results of the top surface of the ground, the top surface of the cavity and the bottom surface of the cavity, respectively, as a result of the displacement of the cavity in the vertical direction are presented. The dimensions of the semi-infinite soil were considered as follows; $L_x = 8$, $L_y = 8$, $t = 1$ and cavity dimensions $l_x = l_y = 4$. The materials parameters are $E = 1, \nu = 0.1$ and point load $P = 1$. The two dimensions elements used are 16-node finite elements and 8-node infinite elements. In the numerical results, $n_x = n_y = 36$ finite elements and 110 infinite elements are used. In the obtaining the numerical results and figures, MATLAB program is used.

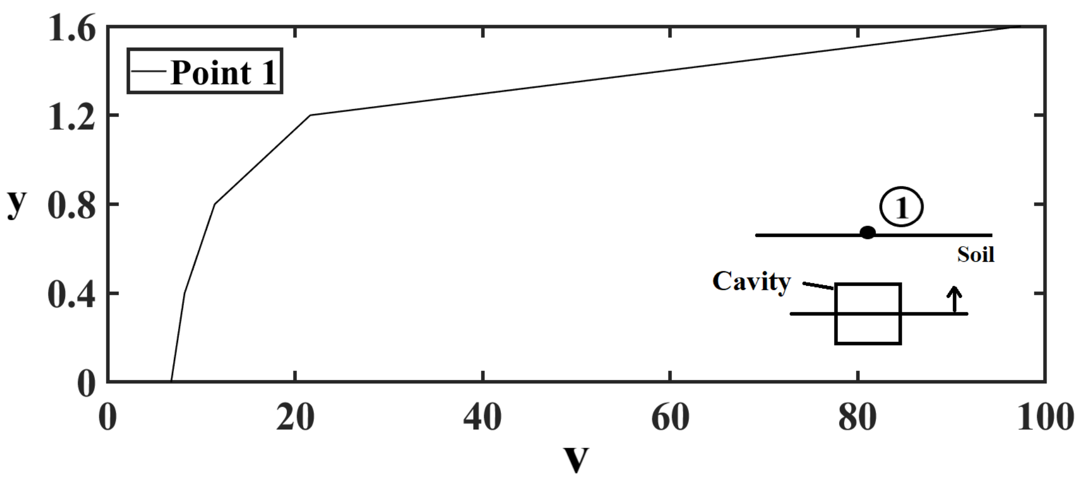

Figure 3. The displacement of the semi-infinite soil medium under the point load by the vertical upward movement of the cavity (Point 1).

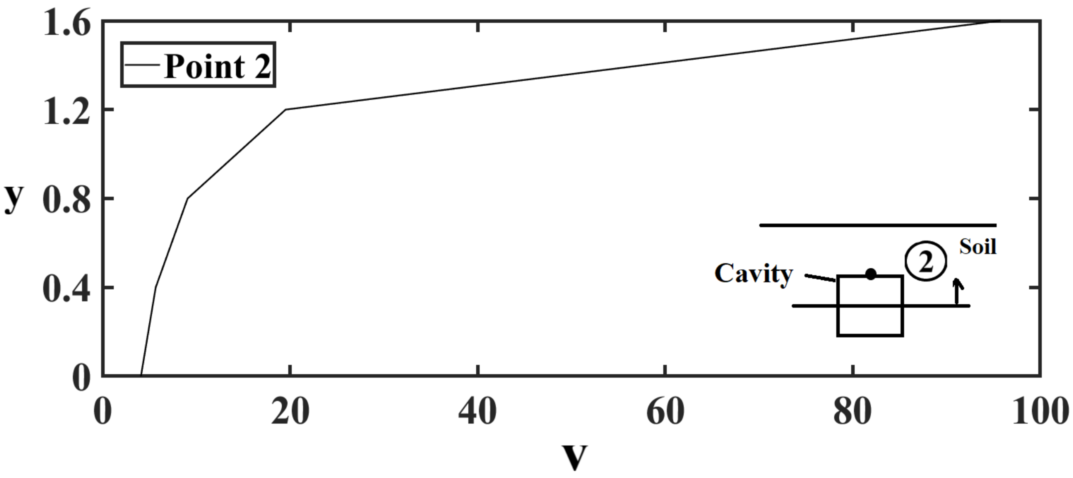

Figure 4. The displacement of the semi-infinite soil medium under the point load by the vertical upward movement of the cavity (Point 2).

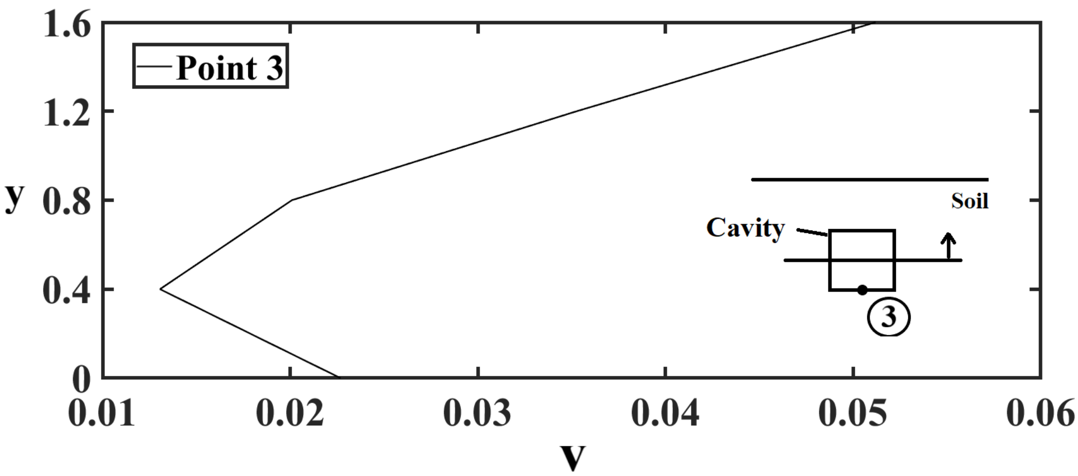

Figure 5. The displacement of the semi-infinite soil medium under the point load by the vertical upward movement of the cavity (Point 3).

Figures 3 and 4 are examined, the displacements at points 1 and 2 increase as the stiffness decreases as the cavity moves upwards from the middle of the ground. Larger displacements occur at points where the cavity is closer to the surface. In Figure 5, because of the lower point of the area with a cavity on the bottom surface of the ground, the displacement first decreased and then continued to increase.

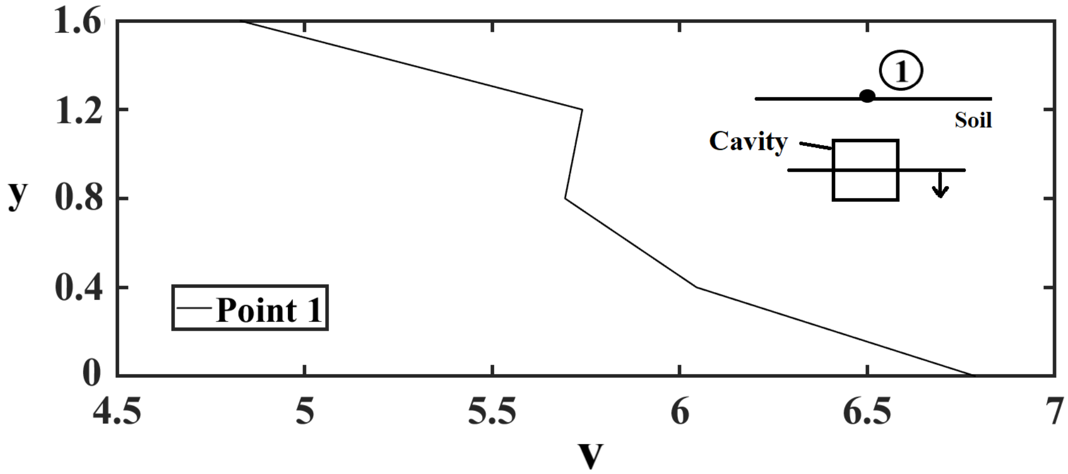

Figure 6. The displacement of the semi-infinite soil medium under a point load by the vertical downward movement of the cavity (Point1).

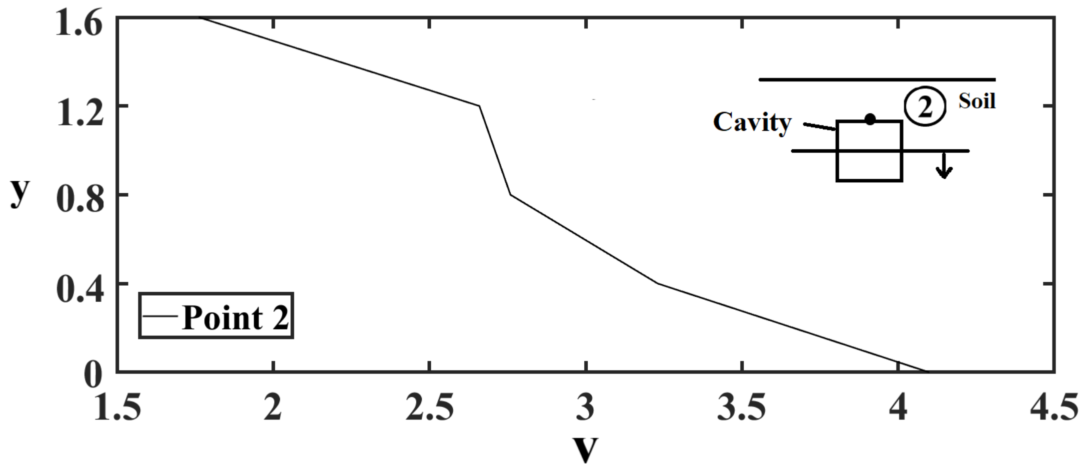

Figure 7. The displacement of the semi-infinite soil medium under a point load by the vertical downward movement of the cavity (Point2).

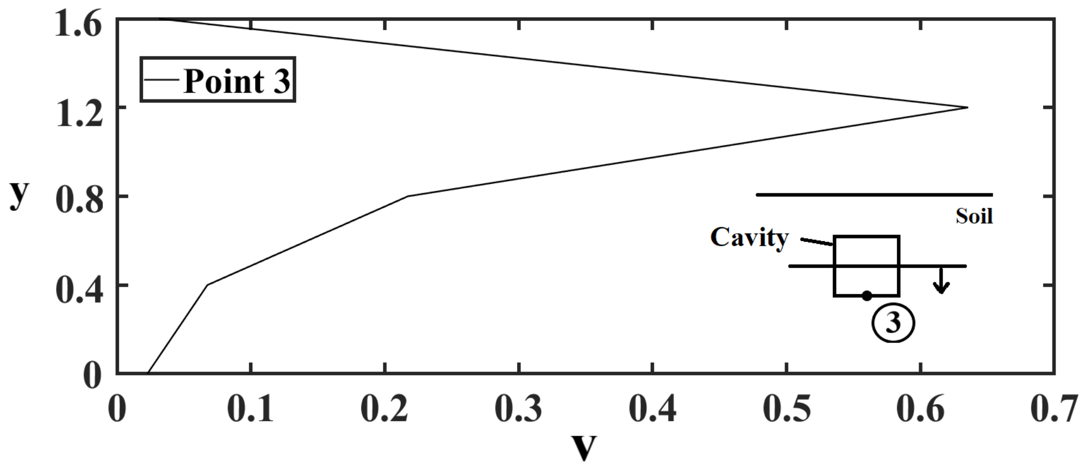

Figure 8. The displacement of the semi-infinite soil medium under a point load by the vertical downward movement of the cavity (Point3).

Figures 6 and 7 are examined, as the cavity moves downwards, the displacements decrease as it moves away from the impact area of the load. The displacements at point 1 are greater than the displacements at point 2. In point 3, the displacements increased as the cavity went down, and decreased after a certain point. The finite element model is coded in MATLAB.

4.CONCLUSIONS

In this work, the displacements of a semi-infinite soil with a cavity under a point load are investigated. In the static analysis, different situations created by the vertical movement of the void in the ground were investigated. The ground is modeled with finite and infinite elements. By using shape functions of 1-dimensional 4-node finite and 2-node infinite elements, 2-dimensional 16-node finite element and 8-node infinite element are produced. The numerical solutions of the finite-infinite element model were obtained by the 5-point Gauss Legendre integration method. The numerical results are compared with the Boussinesq theory results. Since the upward movement of the cavity reduces the stiffness, the displacements were increased. Since the downward movement of the cavity increases the rigidity, this situation causes a decrease in the displacements.

REFERENCES

1. Goodier, James Norman, and Stephen Timoshenko. Theory of Elasticity. McGraw-Hill, 1970.
2. Yerli, H. R., Temel, Beytullah and Kiral E., Transient Infinite Elements for 2D Soil-Structure Interaction Analysis, Journal of Geotechnical and Geoenvironmental Engineering Vol:124, No:10. 976-988, 1998.
3. Demidem, Mustapha, et al. Analysis of Structural and non-Structural Problems by Coupling of Finite and Infinite Elements, Applied Mechanics and Materials. Vol. 578. Trans Tech Publications Ltd, 2014.
4. Kumar, Prabhat, Static Infinite Element Formulation, Journal of Structural Engineering Vol:111, No:11, 2355-2372, 1985.
5. Liu, Huabei, Soil-Structure Interaction and Failure of Cast-İron Subway Tunnels Subjected to Medium Internal Blast Loading, Journal of Performance of Constructed Facilities, Vol:26, No:5, 691-701, 2012.
6. Liu Weiming, and Milos Novak, Soil–Pile–Cap Static Interaction Analysis By Finite and Infinite Elements, Canadian Geotechnical Journal, Vol:28, No:6, 771-783, 1991.
7. Karpurapu, Gopal R., and R. J. Bathurst, "Comparative Analysis of Some Geomechanics Problems Using Finite and Infinite Element Methods, Computers and Geotechnics, Vol:5, No:4, 269-284, 1988.

8. Haji, Twana Kamal, et al. Development of an Infinite Element Boundary to Model Gravity for Subsurface Civil Engineering Applications, International Journal for Numerical and Analytical Methods in Geomechanics, Vol:44, No:3, 418-431, 2020.
9. Lynn, Paul P., and Hassoun A. Hadid, Infinite Elements with 1/rn Type Decay, International Journal for Numerical Methods in Engineering, Vol:17, No:3, 347-355, 1981.
10. Bettess, Peter. Infinite Elements, International Journal for Numerical Methods in Engineering Vol:11, No:1, 53-64, 1977.
11. Wen, P. H., et al. Infinite Element in Meshless Approaches, European Journal of Mechanics-A/Solids No:72, 175-185, 2018.
12. Bettess, Peter, and Jacqueline A. Bettess. Infinite Elements for Static Problems, Engineering Computations, 1984.
13. Selvadurai, A. P. S., and Rajagopal Karpurapu. Composite Infinite Element for Modeling Unbounded Saturated-Soil Media, Journal of Geotechnical Engineering, Vol:115, No:11, 1633-1646, 1989.
14. Liu, Pengfei, Dawei Wang, and Markus Oeser, Application of Semi-Analytical Finite Element Method Coupled with Infinite Element for Analysis of Asphalt Pavement Structural Response, Journal of Traffic and Transportation Engineering (English Edition) Vol:2, No:1, 48-58, 2015.
15. Izra, Uporaba, and Unaz Neskon, Application of Infinite-Element Calculations for Consolidating a Railway Foundation of Blowıng Sand Reclamation, Materiali in Tehnologije Vol:47, No:5, 621-626, 2013.
16. Erkal, Aykut, Debra F. Laefer, and Semih Tezcan, Advantages of Infinite Elements over Prespecified Boundary Conditions in Unbounded Problems, Journal of Computing in Civil Engineering, Vol:29, No:6 04014085, 2015.
17. Curnier, Alain, A Static Infinite Element, International Journal for Numerical Methods in Engineering Vol:19, No:10, 1479-1488, 1983.
18. Pissanetzky, Sergio, A Simple Infinite Element, COMPEL-The International Journal for Computation and Mathematics in Electrical and Electronic Engineering, 1984.
19. Zienkiewicz, O. C., C. Emson, and P. Bettess, A Novel Boundary Infinite Element, International Journal for Numerical Methods in Engineering, Vol:19, No:3, 393-404, 1983.
20. El-Esnawy, N. A., A. Y. Akl, and A. S. Bazaraa, A New Parametric Infinite Domain Element." Finite Elements in Analysis and Design, Vol:19, No:1-2, 103-114, 1995.

COMPLEX TRANSFORM METHOD FOR SYSTEM OF FRACTIONAL DIFFERENTIAL EQUATIONS AND APPLICATIONS.

ELHAM SEFIDGAR[1], ERCAN CELIK[2], BABAK SHIRI[3]

Abstract. The complex transform method for solving system of the system of fractional differential equations introduced. We applied complex transform method for solving a system appeared in the dynamics of the drug therapy efficiently. Various examples shows that these methods are effective and efficient.

Keywords: Complex Transform method, Fractional calculus, System of fractional differential equations, Riemann-Liouville fractional derivative.

AMS Subject Classification: 65R20, 26A33, 34A08.

1. Introduction

Fractional differential equations arise in many engineering and scientific disciplines as the mathematical modeling of systems and processes in the fields of physics, chemistry, aerodynamics, electrodynamics of complex medium, polymer rheology, etc., [8, 10, 17, 22, 23, 24]. It has been discovered that in most cases fractional derivatives provide more accurate results to the physical problem under consideration as compared to the ordinary derivatives.

By developing the fractional differential equations, the system of these equations and their applications has been received more attention recently. For example the coupled system of these equations with differential equations can be found in [16, 23]. In this paper, we study system of fractional differential equations of the form Consider the SFDE of the form

$$D^{\alpha}y(t) = f(t, y(t)) \qquad t \in \mathcal{I} := [0, T], \quad T \in \mathcal{R} \tag{1}$$

$$y(0) = y_0 \tag{2}$$

where D is a alternative Riemann-Liouville fractional derivative of order $0 < \alpha \leq 1$, $y : \mathcal{R} \to \mathcal{R}^{\nu}$ is the unknown vector function, $y_0 \in \mathcal{R}^{\nu}$, $f : \mathcal{I} \to \mathcal{R}^{\nu}$ is a vector function, and ν is the dimension of this system. The existence of solutions and positive solutions of the system (1)-(2) have been studied in [2, 3, 4, 5, 7, 28]. These systems may be referred as the first kind multi- term fractional equations (FMTFE). Analytical solutions such as iterative, Adomian decompositions and homotopy analysis methods for solving system of FMTFE have been studied in [6, 11, 12]. Furthermore, the existence results for the solution of the boundary value problem of these systems have been studied in [25]. Khalil et. al. [16] proposed this system for the dynamics of the drug therapy.

Fractional complex transform method via the modified Riemann-Liouville derivative [14, 15, 26, 27] was first proposed in [18, 19] and was applied to model the heat conduction problem and differential equations [9, 20]. The fractional complex transform met some problems in applications when the modified Riemann-Liouville derivative [14, 15, 26, 27] was adopted due

[1]Ataturk University Faculty of Science, Department of Mathematics, Erzurum-Turkey,
e-mail: e sefidgar@yahoo.com,
[2] Department of Applied Mathematics and Informatics, Kyrgyz- Turkish Manas University, Bishkek, Kyrgyzstan,
e-mail: ercan.celik@manas.edu.kg
[3]Faculty of mathematical science, University of Tabriz, Tabriz – Iran,
e-mail: shiri@tabrizu.ac.ir

to the complex chain rule [9]. In this paper, we show that this method are efficient for solving system of the form (1)-(2).

The paper is organized as follow: In section 2, we give some preliminaries and notations that we use throughout the paper. In section 3, we introduce fractional complex transform method. Finally, in section 3, we apply fractional complex transform method for solving system of the form (1)-(2).

2. Preliminaries

We give some basic definitions [21, 22] and theorems which are used in this paper.

Definition 2.0.1. Let $f : [a,b] \mapsto R$, and $f \in L^1[a,b]$. The left-sided Rimann-Liouville fractional integral of f of order α is defined as

$$ {}_aI_x^\alpha = \frac{1}{\Gamma(\alpha)} \int_a^x \frac{f(t)}{(x-t)^{1-\alpha}} dt. \tag{3}$$

where $\alpha > 0$ and $a < x < b$.

Definition 2.0.2. The Left-sided Riemann-Liouville fractional derivative of a function $f : [a,b] \mapsto R$ to defined as

$$ {}_aD_x^\alpha f(x) = D_a I_x^{1-\alpha} f(x) \qquad 0 < \alpha < 1 \tag{4}$$

where $a < x < b$.

It is straightforward to show

$$ {}_aD_x^\alpha = \frac{1}{\Gamma(1-\alpha)} \frac{d}{dx} \int_a^x \frac{f(t)}{(x-t)^\alpha} dt. \tag{5}$$

Definition 2.0.3. Recently, Guy Jumarie has proposed [24, 13] a simple alternative definition to the Riemann-Liouville derivative as follow:

$$ {}_a^{al}D_x^\alpha f(x) = \frac{1}{\Gamma(1-\alpha)} \frac{d}{dx} \int_a^x \frac{f(t)-f(0)}{(x-t)^\alpha} dt. \tag{6}$$

Therefore, we can write

$$ {}_a^{al}D_x^\alpha f(x) = {}_a D_x^\alpha f(x) - {}_a D_x^\alpha f(0) \tag{7}$$

Now, we summarize some important properties of the Riemann-Liouville fractional derivative as follow:

$$ {}_aD_x^\alpha c = \frac{c}{\Gamma(1-\alpha)} t^{-\alpha} \neq 0, \tag{8}$$

Theorem 2.0.4. *The Riemann-Liouville fractional derivative of the power function satisfies*

$$ {}_aD_x^\alpha t^p = \frac{\Gamma(p+1)}{\Gamma(p+1-\alpha)} t^{p-\alpha}, \qquad n-1 < \alpha < n, \quad p > -1. \tag{9}$$

Proof. See Podlubny [10], p., 72. □

3. Complex Transform method

In recent times, one of the most important and useful methods for fractional calculus called fractional complex transform has appeared [14, 15, 18, 19, 26, 27]. Fractional complex transform is to renovate the fractional differential equation into ordinary differential equations, yielding a tremendously simple solution procedure. In this section, we illustrate some fractional complex transform using properties of the Srivastava-Owa fractional operator and its generalization. Analogous to wave transformation

$$ \eta = az + bw + cu + \cdots , $$

Where a, b and c are constant, the fractional complex transform is

$$\eta = az^{\alpha} + bw^{\beta} + cu^{\gamma} + \cdots,$$

For the fractional differential equation in the sense of the Srivastava-owa fractional operators. We impose the fractional complex transform

$$ {}_0D_z^{\alpha} f(z) = \frac{\partial f}{\partial Z}\, {}_0D_z^{\alpha} Z, \quad Z := z^{\alpha}. \tag{10}$$

If we denote $D_z^{\alpha} f(z) := \frac{\partial^{\alpha} f}{\partial z^{\alpha}}$ it yields

$$\begin{aligned} \frac{\partial^{\alpha} f}{\partial z^{\alpha}} &= \frac{\partial f}{\partial Z}\frac{\partial^{\alpha} Z}{\partial z^{\alpha}} \\ &:= \frac{\partial f}{\partial Z}\theta_{\alpha} \end{aligned}$$

Where θ_{α} is the fractal index, which is usually determined in terms of gamma functions.

Let $Z = z^{\alpha}$ and $f = Z^n$, $n \neq 0$ then in view of then in view of Theorem 2.0.4 similar to [], we obtain

$$\frac{\partial^{\alpha} f}{\partial z^{\alpha}} = \frac{\partial f}{\partial Z}\frac{\partial^{\alpha} Z}{\partial z^{\alpha}} = \frac{\Gamma(1+n\alpha) z^{n\alpha-\alpha}}{\Gamma(1+n\alpha-\alpha)} := \frac{\partial f}{\partial Z}\theta_{\alpha} = n\theta_{\alpha} z^{n\alpha-\alpha}$$

We hence can receive that

$$\theta_{\alpha} = \frac{\Gamma(1+n\alpha)}{n\Gamma(1+n\alpha-\alpha)}. \tag{11}$$

Here, we also need the two-parameter Mittag-leffler function which we use it in the examples section [1]. The Mittag-Leffler function with parameters α and β defined as follow:

$$E_{\alpha,\beta}(z) = \sum_{k=0}^{\infty} \frac{z^k}{\Gamma(\alpha k + \beta)}$$

4. Example

To illustrate the effectiveness of the proposed method in the present paper, three test examples are carried out in this section. First, we solve a simple one-dimensional fractional differential equation, then we solve a system of two-dimensional fractional differential equation and finally we solve a two-dimensional system which appears in a model for dynamics of the drug therapy [16].

Example 4.0.5. Consider the following system of fractional differential equations

$$\begin{cases} \frac{{}^{al}d^{\alpha} y(t)}{dt^{\alpha}} = y(t) \\ y(0) = 0 \end{cases} \tag{12}$$

with exact solution $E_{\alpha,1}(t^{\alpha})$. To apply the complex transform method, let

$$T = t^{\alpha}, \quad f(T) = T^m$$

and

$$y(t) = \sum_{m=0}^{\infty} \mu_m T^m, \tag{13}$$

where μ_m for $m = 0, \cdots, \infty$ are unknown constants. Therefore, we have

$$\frac{d^{\alpha} f}{dt^{\alpha}} = \frac{df}{dT}\frac{d^{\alpha} T}{dt^{\alpha}} = m\theta_{m,\alpha} t^{m\alpha-\alpha} = m\theta_{m,\alpha} T^{m-1}$$

and

$$\frac{d^{\alpha} y(0)}{dt^{\alpha}} = \frac{d^{\alpha} 1}{dt^{\alpha}} = \frac{t^{-\alpha}}{\Gamma(1-\alpha)} = \frac{T^{-1}}{\Gamma(1-\alpha)},$$

where

$$m\theta_{m,\alpha} = \frac{\Gamma(1+m\alpha)}{\Gamma(1+m\alpha-\alpha)}.$$

Consequently, we have

$$\frac{^{al}d^{\alpha}}{dt^{\alpha}}y(t) = \sum_{m=0}^{\infty} m\mu_m\theta_{m,\alpha}T^{m-1} - \frac{T^{-1}}{\Gamma(1-\alpha)}. \tag{14}$$

Substituting from (13) and (14) into (12) we obtain

$$\sum_{m=0}^{\infty} m\mu_m\theta_{m,\alpha}T^{m-1} - \frac{T^{-1}}{\Gamma(1-\alpha)} = \sum_{m=0}^{\infty} \mu_m T^m. \tag{15}$$

Equating the coefficient of T^{m-1} in two side of the equation (15), we obtain the recursion formula

$$\mu_m m\theta_{m,\alpha} = \mu_{m-1} \tag{16}$$

and hence

$$\mu_m = \frac{\mu_{m-1}}{m\theta_{m,\alpha}} = \frac{\Gamma(1+m\alpha-\alpha)}{\Gamma(1+m\alpha)}\mu_{m-1} \tag{17}$$

From initial value and equation (13), one can find

$$\mu_0 = 1.$$

Now, using the recursion formula (17), we obtain

$$\mu_m = \frac{1}{\Gamma(1+m\alpha)} \tag{18}$$

Finally, we substitute from (18) into (13) to obtain

$$y(t) = \sum_{m=0}^{\infty} \frac{1}{\Gamma(1+m\alpha)}T^m = \sum_{m=0}^{\infty} \frac{1}{\Gamma(1+m\alpha)}t^{\alpha m} = E_{\alpha,1}(t^{\alpha}). \tag{19}$$

Example 4.0.6. Consider the following system of fractional differential equations

$$\begin{aligned} \frac{^{al}d^{\frac{1}{2}}x(t)}{dt^{\alpha}} =& x(t) + y(t) - t^3 - t^{\frac{3}{2}} + \frac{6}{\Gamma(4-\alpha)}t^{\frac{5}{2}}, \\ \frac{^{al}d^{\frac{1}{2}}y(t)}{dt^{\alpha}} =& x(t) - y(t) - t^3 + t^{\frac{3}{2}} + \frac{\Gamma(\frac{5}{2})}{\Gamma(\frac{5}{2}+\alpha)}t^1, \end{aligned} \tag{20}$$

with initial conditions

$$\begin{aligned} x(0) =& 0, \\ y(0) =& 0. \end{aligned} \tag{21}$$

and exact solutions

$$\begin{aligned} x(t) =& t^3, \\ y(t) =& t^{\frac{3}{2}}. \end{aligned} \tag{22}$$

To apply the complex transform method, let

$$\begin{aligned} x(t) &= \sum_{m=0}^{\infty} \mu_m T^m, \\ y(t) &= \sum_{m=0}^{\infty} \gamma_m T^m, \end{aligned} \tag{23}$$

and

$$T = t^{\frac{1}{2}},\ t = T^2,$$

where μ_m and γ_m for $m = 0, \cdots, \infty$ are unknown constants. Therefore, we have

$$\begin{aligned}
{}_0^{al}D_x^{\alpha} x(t) &= {}_0D_x^{\alpha}(x(t)) - {}_0D_x^{\alpha}(x(0)) \\
&= {}_0D_x^{\alpha}(x(t)) - 0 \\
&= \sum_{m=0}^{\infty} \mu_m\ {}_0D_x^{\alpha} T^m \\
&= \sum_{m=0}^{\infty} \mu_m \theta_{m,\alpha} T^{m-1}
\end{aligned} \tag{24}$$

and

$$\begin{aligned}
{}_0^{al}D_x^{\alpha} y(t) &= {}_0D_x^{\alpha}(y(t)) - {}_0D_x^{\alpha}(y(0)) \\
&= {}_0D_x^{\alpha}(x(t)) - 0 \\
&= \sum_{m=0}^{\infty} \gamma_m\ {}_0D_x^{\alpha} T^m \\
&= \sum_{m=0}^{\infty} \gamma_m \theta_{m,\alpha} T^{m-1}
\end{aligned} \tag{25}$$

Substituting from (24) and (25) into (20) we obtain

$$\sum_{m=0}^{\infty} \mu_m \theta_{m,\alpha} T^{m-1} = \sum_{m=0}^{\infty} \mu_m T^m + \sum_{m=0}^{\infty} \gamma_m T^m \ - T^6 - T^3 + \frac{6}{\Gamma(4-\alpha)} T^5, \tag{26}$$

and

$$\sum_{m=0}^{\infty} \gamma_m \theta_{m,\alpha} T^{m-1} = \sum_{m=0}^{\infty} \mu_m T^m - \sum_{m=0}^{\infty} \gamma_m T^m \ - T^{\frac{3}{\alpha}} + T^{\frac{3}{2\alpha}} + \frac{\Gamma(\frac{5}{2})}{\Gamma(\frac{5}{2}-\alpha)} (T^{\frac{\frac{3}{2}-\alpha}{\alpha}}), \tag{27}$$

and therefore,

$$\sum_{m=0}^{\infty} \mu_m \theta_{m,\alpha} T^{m-1} = \sum_{m=0}^{\infty} \mu_m T^m \text{-} \sum_{m=0}^{\infty} \gamma_m T^m \ - T^6 - T^3 + \frac{6}{\Gamma(\frac{7}{2})} T^5, \tag{28}$$

and

$$\sum_{m=0}^{\infty} \gamma_m \theta_{m,\alpha} T^{m-1} = \sum_{m=0}^{\infty} \mu_m T^m \text{-} \sum_{m=0}^{\infty} \gamma_m T^m \ - T^6 + T^3 + \frac{(\frac{5}{2})}{\Gamma(2)} T^2. \tag{29}$$

Equating the coefficient of T^{m-1}, for $m = 0 \ldots \infty$, in two side of the system (28)-(29) and using initial values, we obtain the unknown parameters as follow:
for $m = 0$:

$$\begin{aligned}
\mu_0 &= 0 \\
\gamma_0 &= 0
\end{aligned} \tag{30}$$

for $m = 1$:

$$\begin{aligned}
\mu_1 \theta_{\alpha,1} &= \mu_0 + \gamma_0 = 0 \quad \Rightarrow \quad \mu_1 = 0 \\
\gamma_1 \theta_{\alpha,1} &= \mu_0 - \gamma_0 = 0 \quad \Rightarrow \quad \gamma_1 = 0
\end{aligned} \tag{31}$$

for $m = 2$:

$$\begin{aligned}
\mu_2 2\theta_{\alpha,2} &= \mu_1 + \gamma_1 = 0 \quad \Rightarrow \quad \mu_2 = 0 \\
\gamma_2 2\theta_{\alpha,2} &= \mu_1 - \gamma_1 = 0 \quad \Rightarrow \quad \gamma_2 = 0
\end{aligned} \tag{32}$$

for $m = 3$:

$$\begin{aligned}\mu_3 3\theta_{\alpha,3} &= \mu_2 + \gamma_2 = 0 \quad \Rightarrow \ \mu_3 = 0 \\ \gamma_3 3\theta_{\alpha,3} &= \mu_2 - \gamma_2 + \frac{\Gamma(\frac{5}{2})}{\Gamma(2)} = \frac{\Gamma(\frac{5}{2})}{\Gamma(2)} \quad \Rightarrow \ \gamma_3 = 1\end{aligned} \tag{33}$$

for $m = 4$:

$$\begin{aligned}\mu_4 4\theta_{\alpha,4} &= \mu_3 + \gamma_3 - 1 = 0 \quad \Rightarrow \ \mu_4 = 0 \\ \gamma_4 4\theta_{\alpha,4} &= \mu_3 - \gamma_3 + 1 = 0 \quad \Rightarrow \ \gamma_4 = 0\end{aligned} \tag{34}$$

for $m = 5$:

$$\begin{aligned}\mu_5 5\theta_{\alpha,5} &= \mu_4 + \gamma_4 = 0 \quad \Rightarrow \ \mu_5 = 0 \\ \gamma_5 5\theta_{\alpha,5} &= \mu_4 - \gamma_4 = 0 \quad \Rightarrow \ \gamma_5 = 0\end{aligned} \tag{35}$$

for $m = 6$:

$$\begin{aligned}\mu_6 6\theta_{\alpha,6} &= \mu_5 + \gamma_5 + \frac{6}{\Gamma(\frac{7}{2})} = \frac{6}{\Gamma(\frac{7}{2})} \quad \Rightarrow \ \mu_6 = 1 \\ \gamma_6 6\theta_{\alpha,6} &= \mu_5 - \gamma_5 = 0 \quad \Rightarrow \ \gamma_6 = 0\end{aligned} \tag{36}$$

for $m = 7$:

$$\begin{aligned}\mu_7 7\theta_{\alpha,7} &= \mu_6 + \gamma_6 - 1 = 0 \quad \Rightarrow \ \mu_7 = 0 \\ \gamma_7 7\theta_{\alpha,7} &= \mu_6 - \gamma_6 - 1 = 0 \quad \Rightarrow \ \gamma_7 = 0\end{aligned} \tag{37}$$

for $m > 7$:

$$\begin{aligned}\mu_m m\theta_{\alpha,m} &= \mu_{m-1} + \gamma_{m-1} = 0 \quad \Rightarrow \ \mu_m = 0 \\ \gamma_m m\theta_{\alpha,m} &= \mu_{m-1} - \gamma_{m-1} = 0 \quad \Rightarrow \ \gamma_m = 0\end{aligned} \tag{38}$$

Therefore, we have

$$\begin{aligned}x(t) &= \sum_{m=0}^{\infty} \mu_m T^m = \mu_6 T^6 = t^3, \\ y(t) &= \sum_{m=0}^{\infty} \gamma_m T^m = \gamma_3 T^3 = t^{1.5}.\end{aligned} \tag{39}$$

In the next example we solve a fractional system appeared in the dynamics of a drug therapy [16].

Example 4.0.7. The human malady of ventricular arrythmia or irregular heartbeat is treated clinically using the drug lidocaine. A differential equation model for the dynamics of the drug therapy uses

$$\begin{aligned}X(t) =&\text{amount of lidocaine in the bloodstream}, \\ Y(t) =&\text{amount of lidocaine in body tissue},\end{aligned}$$

$$\begin{aligned}{}_0^{al}D_x^{\alpha} X(t) =& -0.09x(t) + 0.038y(t), \\ {}_0^{al}D_x^{\alpha} y(t) =& 0.66x(t) - 0.038y(t),\end{aligned} \tag{40}$$

with initial conditions

$$\begin{aligned}x(0) =& 0, \\ y(0) =& y_0.\end{aligned} \tag{41}$$

Similar to the previous examples, we set

$$\begin{aligned} x(t) &= \sum_{m=0}^{\infty} \mu_m T^m \ = \mu_0 + \mu_1 T + \cdots , \\ y(t) &= \sum_{m=0}^{\infty} \gamma_m T^m \ = \gamma_0 + \gamma_1 T + \cdots , \end{aligned} \tag{42}$$

and

$$T = t^{\alpha}.$$

By fractional differentiating of order α, we obtain

$$\begin{aligned} {}_0^{al}D_x^{\alpha} x(t) &= \sum_{m=0}^{\infty} \mu_m m \theta_{m,\alpha} T^{m-1} - {}_0D_x^{\alpha} x(0) \\ &= \sum_{m=0}^{\infty} \mu_m m \theta_{m,\alpha} T^{m-1} \end{aligned} \tag{43}$$

and

$$\begin{aligned} {}_0^{al}D_x^{\alpha} y(t) &= \sum_{m=0}^{\infty} \gamma_m m \theta_{m,\alpha} T^{m-1} - {}_0D_x^{\alpha} y(0) \\ &= \sum_{m=0}^{\infty} \gamma_m m \theta_{m,\alpha} T^{m-1} - \frac{y_0 T^{-1}}{\Gamma(1-\alpha)} \end{aligned} \tag{44}$$

Substituting from (43) and (44) into (40) we obtain

$$\sum_{m=0}^{\infty} \mu_m m \theta_{m,\alpha} T^{m-1} = -0.099(\sum_{m=0}^{\infty} \mu_m T^m \ ) + 0.038(\sum_{m=0}^{\infty} \gamma_m T^m \ ), \tag{45}$$

and

$$\sum_{m=0}^{\infty} \gamma_m m \theta_{m,\alpha} T^{m-1} - \frac{y_0 T^{-1}}{\Gamma(1-\alpha)} = 0.66(\sum_{m=0}^{\infty} \mu_m T^m \ ) - 0.038(\sum_{m=0}^{\infty} \gamma_m T^m \ ). \tag{46}$$

Using initial conditions we have

$$x(0) = \sum_{m=0}^{\infty} \mu_m 0^m = \mu_0 + \mu_1 T + \cdots , \quad \Rightarrow \mu_0 = 0, \tag{47}$$

and

$$y(0) = \sum_{m=0}^{\infty} \gamma_m 0^m = \gamma_0 + \gamma_1 T + \cdots , \quad \Rightarrow \gamma_0 = y_0. \tag{48}$$

Equating the coefficient of T^{m-1}, for $m = 0 \ldots \infty$, in two side of the system (51)-(52), we obtain

$$\mu_m m \theta_{m,\alpha} = -0.09(\mu_{m-1}) + 0.038(\gamma_{m-1}), \tag{49}$$

and

$$\gamma_m m \theta_{m,\alpha} = 0.66(\mu_{m-1}) - 0.038(\gamma_{m-1}). \tag{50}$$

and therefore, we obtain the recursion formula

$$\mu_m = \frac{\Gamma(1 + m\alpha - \alpha)}{\Gamma(1 + m\alpha)}(-0.09(\mu_{m-1}) + 0.038(\gamma_{m-1})), \tag{51}$$

and

$$\gamma_m = \frac{\Gamma(1 + m\alpha - \alpha)}{\Gamma(1 + m\alpha)}(0.66(\mu_{m-1}) - 0.038(\gamma_{m-1})). \tag{52}$$

The system (51)-(52) can be written in the matrix form

$$\Upsilon_m = \frac{\Gamma(1+m\alpha-\alpha)}{\Gamma(1+m\alpha)} A\Upsilon_{m-1} \tag{53}$$

where

$$A = \begin{bmatrix} -0.09 & 0.038 \\ 0.66 & -0.038 \end{bmatrix}$$

and

$$\Upsilon_m = [\mu_m, \gamma_m]^T.$$

Hence, we can compute Υ_m by

$$\Upsilon_m = \frac{1}{\Gamma(1+m\alpha)} A^m \Upsilon_0$$

We can write A as

$$A = PDP^{-1}$$

where

$$P = \begin{bmatrix} -0.271909774618571 & -0.199664801640642 \\ 0.962322749635941 & -0.979864259469547 \end{bmatrix}$$

and D is a diagonal matrix

$$D := diag([\lambda_1, \lambda_2]) = \begin{bmatrix} \lambda_1 & 0 \\ 0 & \lambda_2 \end{bmatrix}$$

where

$$\lambda_1 = -.224486759578477$$

and

$$\lambda_2 = 0.096486759578477.$$

Since,

$$A^m = PD^mP^{-1} = P \begin{bmatrix} \lambda_1^m & 0 \\ 0 & \lambda_2^m \end{bmatrix} P^{-1},$$

we have

$$\Upsilon_m = \frac{1}{\Gamma(1+m\alpha)} PD^M P^{-1}\Upsilon_0 = \frac{1}{\Gamma(1+m\alpha)} \begin{pmatrix} -.1183898289 y_0 \lambda_1^m + 0.1183898288 y_0 \lambda_2^m \\ 0.4189964329 y_0 \lambda_1^m + 0.5810035671 y_0 \lambda_2^m \end{pmatrix}.$$

Therefore, the parameters of the exact solutions can be computed as

$$\mu_m = \frac{y_0}{\Gamma(1+m\alpha)} \left(-.1183898289\lambda_1^m + 0.1183898288\lambda_2^m\right) \tag{54}$$

and

$$\gamma_m = \frac{y_0}{\Gamma(1+m\alpha)} \left(0.4189964329 y_0 \lambda_1^m + 0.5810035671 y_0 \lambda_2^m\right). \tag{55}$$

and hence the exact solutions can be evaluated as

$$\begin{aligned} x(t) &= \sum_{m=0}^{\infty} \mu_m T^m = -.1183898289 y_0 E_{\alpha,1}(\lambda_1 T) + 0.1183898288 y_0 E_{\alpha,1}(\lambda_2 T) \\ y(t) &= \sum_{m=0}^{\infty} \gamma_m T^m = 0.4189964329 y_0 E_{\alpha,1}(\lambda_1 T) + 0.5810035671 y_0 E_{\alpha,1}(\lambda_2 T) \end{aligned} \tag{56}$$

5. Conclusion

In this paper, we applied differential transform method for system of the fractional differential equations. First, we applied them effectively, for the system of dimension 1, and 2, which their exact solution was known. Then, we applied them for solving a system appeared in the model of the dynamics of the drug therapy.

References

[1] Agrwal R. P. A propos d'une note de M. Pierre Humbert, *C. R. Se'ances Acad. Sci.,* v.236, n.21, 1953, pp. 2031-2033.

[2] Ahmad B., Nieto J.J. Existence results for a coupled system of nonlinear fractional differential equations with three-point boundary conditions, *Computers and Mathematics with Applications,* v.58, n.9, 2009, pp. 1838–1843.

[3] Bai Z, L H. Positive solutions for boundary value problem of nonlinear fractional differential equation, *Journal of Mathematical Analysis and Applications,* v.311, n.2, 2005, pp. 495–505.

[4] Daftardar-Gejji V. Babakhani A. Analysis of a system of fractional differential equations, *Journal of Mathematical Analysis and Applications,* v.293, n.2, 2004, pp. 511–522.

[5] Daftardar-Gejji V. Positive solutions of a system of non-autonomous fractional differential equations. *Journal of Mathematical Analysis and Applications,* v.302, n.1, 2005, pp. 56–64.

[6] Daftardar-Gejji V. and Jafari H. An iterative method for solving nonlinear functional equations. *Journal of Mathematical Analysis and Applications,* v.316, n.2, 2006, pp. 753-763.

[7] Debbouche A, Nieto, J. J. Sobolev type fractional abstract evolution equations with nonlocal conditions and optimal multi-controls, *Applied Mathematics and Computation,* v.245, 2014, pp. 74–85.

[8] Diethelm K. *The analysis of fractional differential equations: An application-oriented exposition using differential operators of Caputo type*. Springer, 2010.

[9] He, J.H., Elagan, S.K., Li, Z.B., . Geometrical explanation of the fractional complex transform and derivative chain rule for fractional calculus, *Physics Letters A,* v.376, n.4, 2012, pp. 257-259.

[10] Hilfer R, *Applications of fractional calculus in physics. World Scientific,* 2000 Mar 2.

[11] Jafari H, Daftardar-Gejji V. Solving a system of nonlinear fractional differential equations using Adomian decomposition, *Journal of Computational and Applied Mathematics,* v.196, n.2, 2006, pp. 644–51.

[12] Jafari H, and Seifi S. Solving a system of nonlinear fractional partial differential equations using homotopy analysis method, *Communications in Nonlinear Science and Numerical Simulation,* v.14, n.5, 2009, pp. 1962-1969.

[13] Jumarie G. On the representation of fractional Brownian motion as an integral with respect to, *Applied Mathematics Letters,* v.18, n.7, 2005, pp. 739-48.

[14] Jumarie G. Modified Riemann-Liouville derivative and fractional Taylor series of nondifferentiable functions further results, *Computers & Mathematics with Applications* n.51, v.9, 2006, pp. 1367-76.

[15] Jumarie G. The Minkowski's spacetime is consistent with differential geometry of fractional order, *Physics Letters A.,* v.63, n.1, 2007, pp. 5-11.

[16] Khalil H, Khan R. A. The use of Jacobi polynomials in the numerical solution of coupled system of fractional differential equations, *International Journal of Computer Mathematics,* v.92, n.7, 2015, pp. 1452-72.

[17] Kilbas A. A. A, Srivastava H. M, Trujillo J. J. *Theory and applications of fractional differential equations.* Elsevier Science Limited, 2006.

[18] Li Z. B., He J. H. Fractional complex transform for fractional differential equations, *Math. Comput. Appl,* v.15, n.5, 2010, pp. 970-3.

[19] Li ZB. An extended fractional complex transform, *International Journal of Nonlinear Sciences and Numerical Simulation,* v.11, 2010, pp. 335-8.

[20] Li, Z.B., Zhu, W.H., He, J.H. Exact solutions of time-fractional heat conduction equation by the fractional complex transform. *Thermal Science,* v.16, n.2, 2012, pp. 335-338.

[21] F. Mainardi, Mainardi F. Fractional calculus: some basic problems in continuum and statistical mechanics. *arXiv preprint arXiv*, v.1201, n.0863, 2012.

[22] Miller K. S., Ross B. *An Introduction to the Fractional Calculus and Fractional Differential Equations,* Wiley, New York, 1993.

[23] Podlubny I. *Fractional differential equations: an introduction to fractional derivatives, fractional differential equations, to methods of their solution and some of their applications*, 1999.

[24] Samko S. G, Kilbas A. A., Marichev O. I. Fractional integrals and derivatives. Theory and Applications, *Gordon and Breach, Yverdon.* 1993, 1993. Breach,Yverdon(1993). Translated from the 1987 Russian original.

[25] Su, X. Boundary value problem for a coupled system of nonlinear fractional differential equations, *Applied Mathematics Letters*, v.22, n.1, 2009, pp. 64-69.

[26] Yang X. J. *Local Fractional Functional Analysis and Its Applications,* 2011.

[27] Yang X. J. *Advanced local fractional calculus and its applications*, World Science, New York, NY, USA. 2012.

[28] Zhou Y. Existence and uniqueness of solutions for a system of fractional differential equations, *J. Frac. Calc. Appl. Anal,* v.12, 2009, pp. 195-204.

CoCo Antenna Design and Manufacturing

Sefa Yıldırım[1], Beyza Canbolat[3], M. Enes Güngör[4], Şahin Akdoğan[2], Lokman Kuzu[1,2]

[1] Electrical-Electronics Engineering, Karabuk University, Karabük, Türkiye

[2] TR Anten Elektronik A.Ş., Ankara, Türkiye

[3] Electrical-Electronic Engineering, Gazi University, Ankara, Türkiye

[4] Electrical-Elektronics Engineering, Abdullah Gül University, Kayseri, Türkiye

Abstract

In this article, a Coaxial Collinear (CoCo) antenna was designed and manufactured with students studying in Electrical and Electronics Engineering departments in Turkey during their interns. In some environments, high-gain and omnidirectional antennas are preferred to obtain good communication quality. CoCo antennas are preferred because they have the advantages of omnidirectional radiation, simple structure, and being easy to form an array. In this study, first theoretical and parametric studies were carried out, and then the antenna was verified with the CST Studio simulation program using half and quarter wavelength coaxial lengths. In order to meet the technical requirements, necessary parametric changes were made in the simulation and the final version of the design was manufactured. The VSWR, bandwidth and S parameters of the manufactured antenna were measured and the values obtained were compared with that of the antennas in the literature.

Keywords: Coaxial cable, antenna array, CoCo antenna, bandwidth.

1. INTRODUCTION

Antennas are such devices that collect electromagnetic waves in the air and transmit these waves to the transmission line or spread the signals from the transmission lines to the space as waves. When antennas are used as transmitters, they convert the electrical signal into electromagnetic waveform and radiate or direct this energy into space. When used as a receiver, it collects electromagnetic waves in space and converts them into electrical signals. Whether transmitting or receiving, an antenna is a passive equipment which does not offer any added power to the signal and more importantly if they are produced with simple materials, they are reciprocal devices. So they can be tested as either a receiver or a transmitter.

There are different types of antennas according to their application areas. Examples of antennas used in different areas can be given as microstrip, isotropic, monopole, dipole, whip, helix, yagi-uda, dish antenna and collinear antennas. [1][2][3].

Colinear antennas were first used by Charles Samuel Franklin in 1925. The coaxial collinear antenna, one of the coaxial antenna types, was first designed by Balsley and Ecklund in 1972. The coaxial collinear (CoCo) antenna is a type of array antenna. Because the CoCo antenna is a high-gain and omnidirectional antenna, better communication quality can be achieved. This type of antenna is used in the communication centers of the institutions responsible for public security. The gain of this antenna, which consists of half- and quarter-wave coaxial cables, can be increased with number of the parts used. According to Ampere's law, the currents in the center conductor and on the surface of the outer conductor must be equal and opposite. However, it is difficult to provide this principle exactly because both the dielectric and the live end and ground changes at the transitions. CoCo antenna has a simple structure and at the same time, be easy to form an antenna array [4][5].

While designing the CoCo antenna, the first thing to do is to calculate the half- and quarter-wavelength lengths of the coaxial cables to be used. The lengths are decreasing due to the speed factor of the coaxial cable used at the desired frequency. The aim of this study is to obtain a CoCo antenna with the desired bandwidth by using half- and quarter-wavelength coaxial cables. For this purpose, after some theoretical calculations, parametric study was carried out on the CST Studio program and the final version of the design was obtained. This design was realized and the simulation and measurement results were compared [6].

2. ANTENNA DESIGN AND MANUFACTURING

In this study, a CoCo antenna design with a center frequency of 400 MHz, a bandwidth of 10 MHz and a VSWR value of maximum 2 is made. The schematic drawing of the antenna is given in Fig. 1 below.

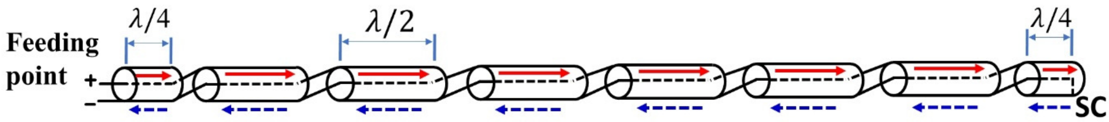

Figure 1. CoCo antenna schematic and connection diagram.

The feeding point can be made from the middle or from the end as in this example. The length of the coaxial cable pieces at the end points are chosen as quarter wavelengths. The coaxial cable at the right end is short-circuited. After the theoretical calculations were made, the results were modeled and simulated in the CST Studio. The antenna designed in the CST Studio program is shown in Fig. 2 below. In this design; RG58U coaxial cable with a relative dielectric constant (ε) of 2.3, a velocity factor of 0.66 and a characteristic impedance of 50 Ω is used. The cable has an internal diameter of 0.875 mm and a dielectric material diameter of 2.95 mm [7].

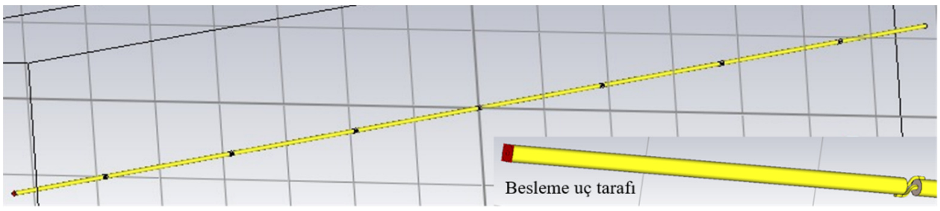

Figure 2. CoCo Antenna Design using CST Studio

The theoretical calculations are shown below:

$$\lambda = \frac{c}{f} = \frac{300\times10^6}{400\times10^6} = 75 \text{ cm (for free space)}$$

$$\lambda_{eff} = \frac{\lambda}{\sqrt{\varepsilon}} = \frac{\lambda}{\sqrt{2.3}} = 49.50 \text{ cm (for RG58U coaxial cable)}$$

The lengths of half and quarter wavelength coaxial cables are calculated as:

$$\lambda_{eff}/2 \; = 24.75 \text{ cm and } \; \lambda_{eff}/4 \; = 12.37 \text{ cm.}$$

Here, f denotes the frequency, c the speed of light in m/s, ε the relative permittivity of the dielectric, λ the wavelength and λ_{eff} the effective wavelength of the transmission line.

The CoCo antenna was manufactured by changing roles of the ground and live conductors at each half wavelength as in Fig. 3. Phase shift in the antenna is required to obtain a consistent single main beam that surrounds it at right angles to the axis of the wire. Therefore the live conductor soldered with the outer conductor at each gap between the parts. At the very end, it is terminated with $\lambda/4$ parts. If this polarity changing is not performed, almost no radiation will be received at or just above the ground line. Such an antenna cannot be used in communication systems, so collinear array antennas have been developed [8].

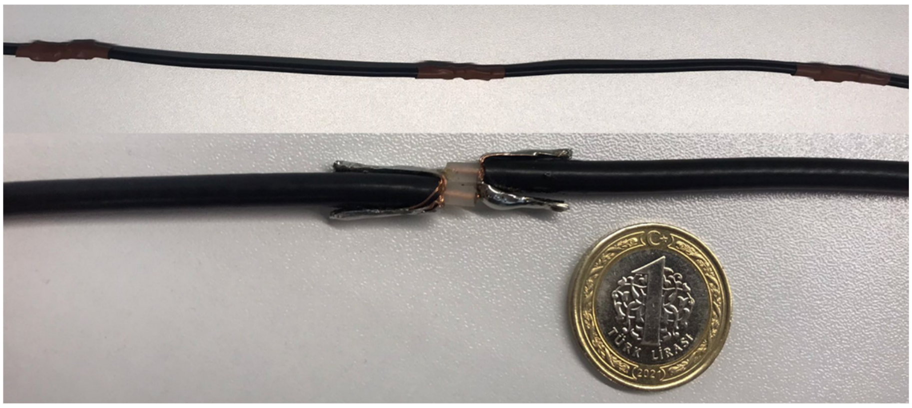

Figure 3. Manufactured Coaxial Collinear (CoCo) Antenna

3. RESULTS AND DISCUSSION

The aim of this study is to realize the CoCo antenna by investigating how the bandwidth, center frequency and VSWR parameters change with the wavelength of coaxial cable and finding a relationship between the parameters. After manufacturing of the CoCo antenna, the simulation and measurement results were compared. Return loss (S_{11}) and VSWR of the antenna are plotted in Fig. 4 and 5, respectively, for different half-wavelengths L_1 of the antenna. The shift of the center frequency can be seen for different half-wavelengths in these plots.

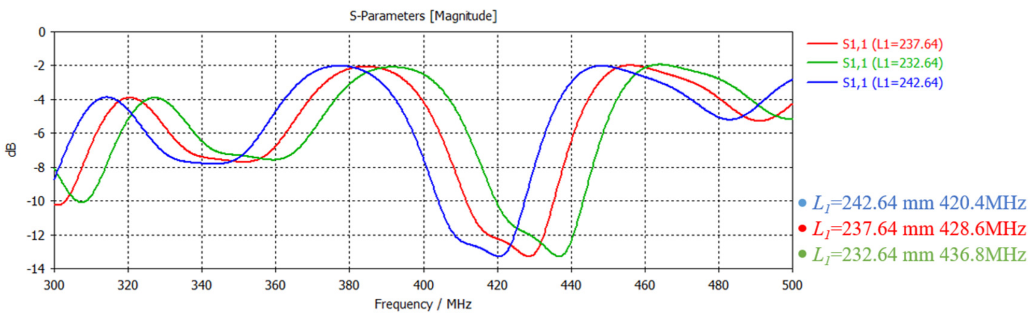

Figure 4. Return loss (S_{11}) of variable length half wavelength coaxial cable.

As observed in Fig. 4, changing each of the half wavelengths by 5 mm caused the center frequency to shift by 8.2 MHz. Center frequency becomes 420.4 MHz when L_1 value is 242.64 mm however it becomes 428.6 MHz when it is decreased to 237.64 mm. As seen in Fig. 4, only the center frequency was affected by this change, but there was no considerable change in the gain and bandwidth values.

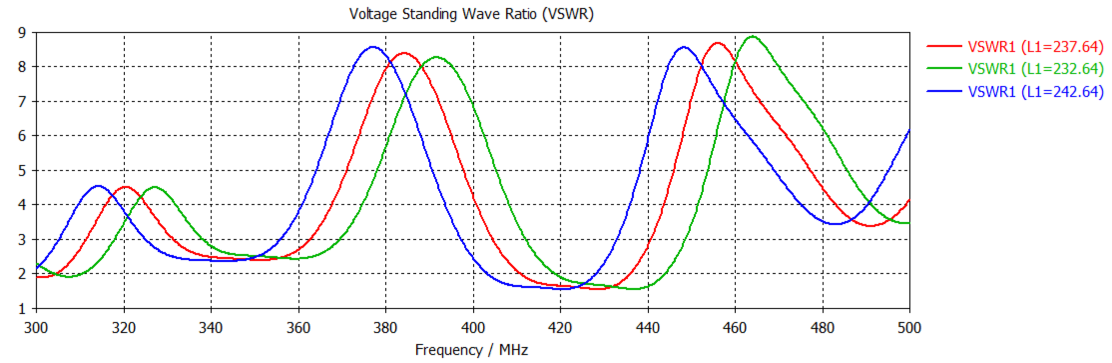

Figure 5. VSWR plot of half wavelength coaxial cable with variable lengths.

As observed in Fig. 5, changing the half wavelength value by 5 mm has no effect on the VSWR value.

The L_2 parameter represents the quarter wavelength value of the antenna, and the S_{11} and the VSWR values obtained based on the different quarter wavelength values are plotted in Fig. 6 and Fig. 7 respectively. As observed in Fig. 6 below, changing each quarter wavelength by 5 mm caused a frequency shift of 1.4 MHz and 0.9 MHz, respectively. In this case, no effect on bandwidth was observed. Center frequency becomes 419.1 MHz when L_2 value is 143.33 mm however center frequency increases to 421.4 MHz when it is decreased to 133.33mm. As a result, the effect of quarter wavelength on center frequency is less than that of half wavelength. On the other hand, it has an effect of about 1 dB on the antenna gain.

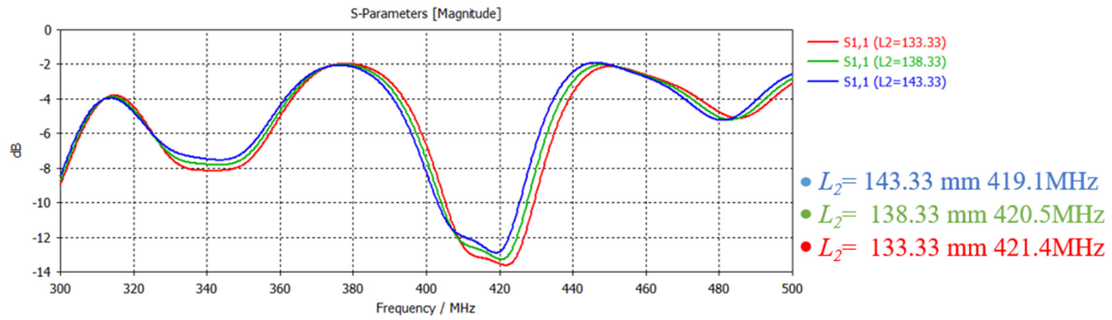

Figure 6. Return loss (S_{11}) of variable length quarter wavelength coaxial cable.

As observed in Fig. 7, changing each of the quarter wavelengths by 5 mm had no effect on the VSWR value.

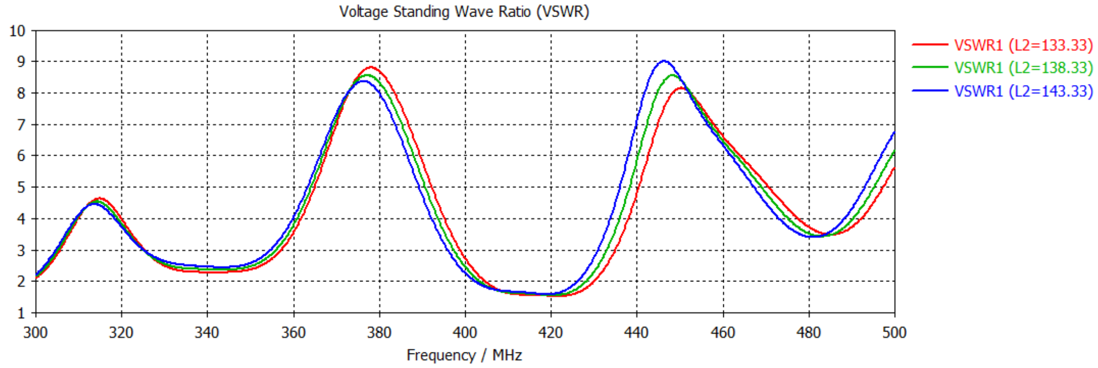

Figure 7. VSWR plot of quarter wavelength coaxial cable with variable lengths.

As seen in Fig. 8 below, the gain of the designed CoCo antenna is 6.25 dBi and half power beamwidth is (HPBW) is 16.5°.

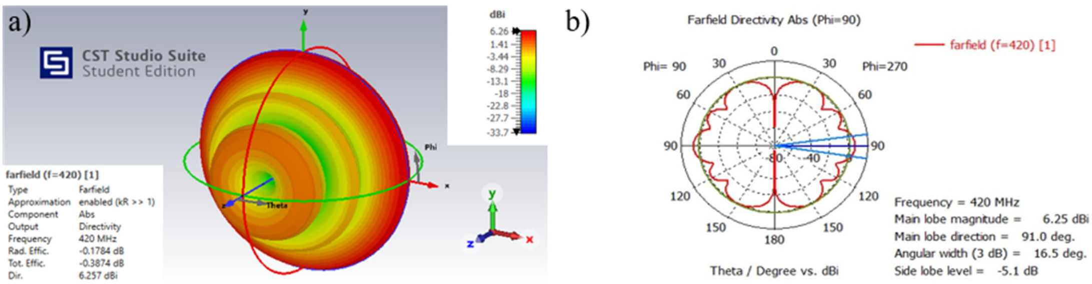

Figure 8. Far field radiation pattern a) 3D view, b) Polar view

There are differences between the simulation and measurement results. These are mainly due to the incomplete modelling of coaxial array antenna on the CST Studio and the environmental conditions in the measurement setup. One of these differences is that the antenna designed on CST Studio has a phase shift due to the gaps formed between the coaxial array elements. For this purpose, changes were made in half- and quarter-wavelength parts to obtain the desired bandwidth. As a result of these changes, half wavelength coaxial cable lengths were found according to the frequency of 408 MHz to obtain an average bandwidth of 8 MHz. Then, in order to find the quarter wavelengths, first the total length of the 6-element 400 MHz CoCo antenna was found and its length is subtracted from the 6 half wavelengths found when the center frequency is 408 MHz. As a result of this calculation; half wavelength was obtained as 24.26 cm and quarter wavelength as 13.84 cm. The VSWR, bandwidth and S_{11} values in the proposed antenna are 1.6, 25 MHz and −13.65 dB, respectively. The comparison of these values with the literature is shown in Table I. The difference is considered to come from the coaxial cable quality and the number of parts used.

Table I. Comparison of the proposed antenna and the literature

Parameter	**Proposed Antenna**	**Literature**
VSWR	1.6	1.9 [1]
Bandwidth	25 MHz	50 MHz [1]
S_{11}	$-13.65\ dB$	$-14\ dB$ [8]

4. CONCLUSION

In this study, a CoCo antenna was designed and manufactured using RG58U coaxial cable with an inner conductor diameter of 0.875 mm and a dielectric diameter of 2.95 mm. In the CST Studio, half- and quarter-wavelengths at 400 MHz center frequency were computed and the technical requirements were tried to be met by changing the transmission line lengths parametrically. As half-wavelength the following values, 232.64 mm, 237.64 mm and 242.64 mm lengths were tried. As for the quarter wavelengths, 133.33 mm, 138.33 mm and 143.33 mm values were taken. Thus, the effects of different lengths on antenna performances such as bandwidth, VSWR and gain of the CoCo antenna were investigated.

The computed center frequency of the antenna and the CST Studio results agree 98%. The biggest difference among the measured parameters occurred in the bandwidth. While the bandwidth of the CST Studio program was 25 MHz, the bandwidth of the manufactured antenna was only 9 MHz. It is considered that this is due to the difference between the antenna modeled in the CST Studio program and the antenna manufactured. As a result, the best result compatible with the theoretical calculations of the RG58U coaxial cable used in the CoCo antenna was obtained for the half-wavelength 242.64 mm. In such an antenna, the gain was measured as 6,25 dBi. The center frequency and bandwidth became 420 MHz, 9 MHz, respectively.

REFERENCES

[1] Y. Zhou, P. Lee, F. Jia, and B. Xu, "A Technique for Improving Bandwidth of COCO Antenna Array," in *2008 4th International Conference on Wireless Communications, Networking and Mobile Computing*, Oct. 2008, pp. 1–2. doi: 10.1109/WiCom.2008.545.

[2] P. V. Nikitin and K. V. S. Rao, "Reply to 'comments on 'antenna design for UHF RFID tags: A review and a practical application'’," *IEEE Trans. Antennas Propag.*, vol. 54, no. 6, pp. 1906–1907, 2006, doi: 10.1109/TAP.2006.875934.

[3] C. Rowell and E. Y. Lam, "Mobile-phone antenna design," *IEEE Antennas Propag. Mag.*, vol. 54, no. 4, pp. 14–34, 2012, doi: 10.1109/MAP.2012.6309152.

[4] B. Balsley and W. Ecklund, "A portable coaxial collinear antenna," *IEEE Trans. Antennas Propag.*, vol. 20, no. 4, pp. 513–516, Jul. 1972, doi: 10.1109/TAP.1972.1140233.

[5] P. H. Pathak, "High Frequency Techniques for Antenna Analysis," *Proc. IEEE*, vol. 80, no. 1, pp. 44–65, 1992, doi: 10.1109/5.119566.

[6] M. Rütschlin, T. Wittig, and Z. Iluz, "Phased antenna array design with CST STUDIO SUITE," *2016 10th Eur. Conf. Antennas Propagation, EuCAP 2016*, vol. 1, pp. 1–5, 2016, doi: 10.1109/EuCAP.2016.7481530.

[7] P. Bhartia and I. Bahl, "Frequency Agile Microstrip Antennas.," *Microw. J.*, vol. 25, no. 10, pp. 67–70, 1982, doi: 10.1109/aps.1982.1148900.

[8] B. M. Notaroš, M. Djordjević, and Z. Popović, "Generalized CoCo Antennas".

Compare K-Nearest Neighbor Method with Kernel Model in Nonparametric Functional Regression

Kurdistan M.Taher Omar[1], Shelan Saied Ismaeel[2]
[1,2]Department of Mathematics, Faculty of Science, University of Zakho, Kurdistan Region, Iraq
E-mail: kurdistan.taher@uoz.edu.krd
and Shelan.ismaeel@uoz.edu.krd

Guleshan Mohsin Hamid[3]
[3]Technical college of Administration, Duhok Polytechnic University.
E-mail: guleshan.hamid@dpu.edu.krd

***Abstract*--The point of this research is to compare K-Nearest Neighbor Model with Kernel Model in nonparametric functional data with conditional supposition in the case of response as a scalar variable while the function is covariates. We utilize the form of the Nadaraya-Watson estimator method for prediction with two kinds of semi-metrics: semi-metric built on the second derivatives and the second based on Functional Principle Component Analysis. The results get from K-Nearest Neighbor method is more accurate than the outcomes get from kernel model. The achievement of this research is then assessed by computing mean square errors. The method is illustrated by some applications.**

Keywords-- Nonparametric regression; Functional data; Kernel function; Functional covariates; KNN estimator; Semi-metrics

I. Introduction

The proposed article deals with the functional nonparametric regression model

$$\mathcal{Y} = m(x) + e,$$

where $\mathcal{Y}$ is a scalar responses, x is a function. Recently, functional data analysis has been developed sharply because of rising numeral of states coming from different fields of applied science (biometric, chemometric, medicine, environmetrics, etc.), where data are collected as curves. Measuring devices are now more stronger and the quality of collected data are more precise. Therefore, collecting data in a short time that let us to deal with a great data set of variables lead to expand the finite dimensional statistical structures to an infinite dimensional data technique. Therefore, this type of data needs special statistical structures or procedures. Ramsay and Silverman (1997) pointed to statistics of functional data, after that this field of statistics is becoming more popular because there are a number of applications in nonparametric regression of functional data analysis using curves and images as data. So, several different issues include functional data analysis (for instance, prediction, and classification).

Ramsay and Silverman (2005) and Cao et al. (2020) also define the functional data in details as well as mention several different instances and utilize linear regression model and multiple regression method (parametric model) for predicting scalar response from the functional covariate. Cardot et al. (2003) discussed also the linear method for regression with functional data analysis. While consecrating status projects and applied studies decreasing from collaborative study to explicate how functional data plans work out in application are discussed by Ramsay and Silverman (2002).

In 1960's, free-modelling was the idea of Mahalandobis (1961), who studied a regression analysis. Then, nonparametric regression statistics have been expanded in multivariate model and functional data methods. Therefore, initially statistical study, nonparametric functional prediction issues have been studied both in real data and multivariate data. The work of Nadaraya (1964) and Watson (1964) fixed these ideas.

There are a lot of a good manner about nonparametric statistics, so that Härdle (1990) studies the applied nonparametric regression. However, only classical framework, real and multivariate, is of concern. The local weighting models in the finite dimensional data are extremely popular in the society of non-parameterizations, particularly the kernel, particularly the kernel. Ferraty and Vieu (2006), Omar and Wang (2019) and Midi et al. (2021) mention some fundamental statistical concepts on local weighting techniques and expansion to the functional data analysis as well kernel weighting is special regard. There are different types of kernel methods with a lot automatic choices of bandwidth (smoothing parameter).

So, It is well known that the bandwidth chosen is a decisive point in nonparametric prediction kernel regression function according to (Ferraty and Vieu (2003, 2006), Ferraty et al. (2007), and Rachdi and Vieu (2007)), who propose an automatic data driven operation for selecting this parameter as well as the provision of theoretical support to the Functional Cross-Validation study of bandwidth chosen.

According to Ferraty and Vieu (2006) and Doori (2019), the functional characteristic of free-parameter comes from the nature of the subject to be predicted (for example functional density, and functional regression), which is not supposed to be parametrizable by a finite number of real qualities.

Consequently, Ramsay and Silverman (2005) have performed studies in functional data analysis that extend to nonparametric functional data analysis, one of that study is when the output is real value and the explanatory is function by (Ferraty and Vieu (2003, 2004, 2006), Ferraty et al. (2007), Burba et al. (2009), and Midi and Ismaeel (2018)). Nevertheless, the study of prediction function and scalar response developed by Baíllo and Grané (2009) introduced a new nonparametric regression method in the context of functional data, proposing a local linear regression estimator that can be compared with a Nadaraya-Watson type Kernel Regression by Monto Carlo study.

The main purpose of this article is to compare two methods Kernel function and K-Nearest Neighbor Method in nonparametric functional data and using two types of semi-metrics for both of them the first build on the second derivatives and the second type on the functional principle component analysis. Then, Spectrometric data and Canadian Weather Station are two examples for applying models and then for comparing results.

The rest of the article is an arranged as follows. Section 2 points the nonparametric functional regression (Kernel method and K-Nearest Neighbor Model). Two instances of real data are presented in Section 3. Section 4, includes conclusion.

II. METHODOLOGY

The general shape of the nonparametric functional regression is:

$$\mathcal{Y} = m(x_i) + \varepsilon_i, \quad i = 1, \ldots, n,$$

where $\mathcal{Y}$ is a response variables, x is a covariate function and ε_i is independent random error.

This paper considerate on two models to predict the different regression factors: the first one is built on the kernel model and is called *funopare.kernel.cv,* and the second one utilizes the KNN model and is called *funopare.knn.gcv*. The first one utilizes an automatic bandwidth selection by Cross-Validation structure. The main purpose is to compute the formula:

$$m_{CV}^{kernel} = \frac{\sum_{i=1}^{n} y_i\, K(d_q(\mathbf{x}_i, \mathbf{x})/h_{opt})}{\sum_{i=1}^{n} K\, (d_q(\mathbf{x}_i, \mathbf{x})/h_{opt})},$$

where k is the functional kernel and h_{opt} is a bandwidth of the kernel method is gotten by a Cross-Validation structure:

$$h_{opt} = \underset{h}{argmin} CV(h),$$

where

$$CV(h) = \sum_{i=1}^{n} \left(y_i - m_{(-i)}^{kernel}(\mathbf{x}_i)\right)^2,$$

with

$$m_{(-i)}^{kernel}(\mathbf{x}) = \frac{\sum_{j=1, j\neq i}^{n} y_j\, K\left(d_q(\mathbf{x}_j, \mathbf{x})/h\right)}{\sum_{j=1, j\neq i}^{n} K\, (d_q(\mathbf{x}_j, \mathbf{x})/h}).$$

The semi-metric $d_q(.,.)$ and the functional kernel $K(.)$ have been fixed by the partitioner by (Ferraty and Vieu (2004, 2006), and Burba et al. (2009)).

The KNN model uses a global smoothing parameter, and the main aim is to calculate the quantity:

$$m_{GCV}^{KNN}(\mathbf{x}) = \frac{\sum_{i=1}^{n} y_i\, K\left(\mathbf{d}_q(\mathbf{x}_i, \mathbf{x})/h_{kopt}(x)\right)}{\sum_{i=1}^{n} K\left(\mathbf{d}_q(\mathbf{x}_i, \mathbf{x})/h_{kopt}(x)\right)},$$

Where $h_{kopt}(x)$ is the bandwidth corresponding to the optimal number of neighbours get by a Cross-Validation method:

$$h_{kopt} = \underset{h}{argmin} GCV(k),$$

where

$$GCV(k) = \sum_{i=1}^{n} \left(y_i - m_{-i}^{KNN}(\mathbf{x}_i)\right)^2$$

with

$$m_{-i}^{KNN}(\mathbf{x}) = \frac{\sum_{j=1, j\neq i}^{n} y_i\, K\left(\mathbf{d}_q(\mathbf{x}_j, \mathbf{x})/h_k(x)\right)}{\sum_{j=1, j\neq i}^{n} K\left(\mathbf{d}_q(\mathbf{x}_j, \mathbf{x})/h_k(x)\right)}.$$

The same number of neighbors used at any curves supplies a global select. setting the semi-metric ($\mathbf{d}_q(.,.)$) and the functional kernel $K(.)$ (see for example, Ferrety and Vieu (2004, 2006), and Burba et al. (2009)).

III. APPLICATIONS

This section is devoted to the applications of the nonparametric functional prediction model based on regression. The section contains two different examples of prediction scalar response values from functional covariates. The first is the pre diction of percentage of fat content in the pieces of meat from the spectrometric curves. The second is the prediction of precipitation over one year from the mean monthly temperatures for 35 Canadian Weather Stations.

EXAMPLE1

Spectrometric Data: Predicting Fat Content from Spectrometric data by Two Different Methods (KNN-Model and Kernel Model):

This instance is practical among the nonparametricians's community because Tecator data was a starting point for improving the nonparametric functional data, and then a number of implementation have been done on this kind of data by different methods (see for example, Ferraty and Vieu (2003, 2006), Ferraty et al. (2007), and Burba et al. (2009)). A brief characterization of Tecator data gets from the quality control issue and can be found at http://lib.stat.cmu.edu/datasets/ tecator.

For every meat sample, the data contain of a 100 channel Spectrum of absorbance, where the absorbance is the −log10 of the transmittance measured by the spectrometer and the plot is the absorbance versus wavelength. The wave- length ranges between 850-1050 nm, and more detail about this shape of data can be found in the book published by Ferraty and Vieu (2006).

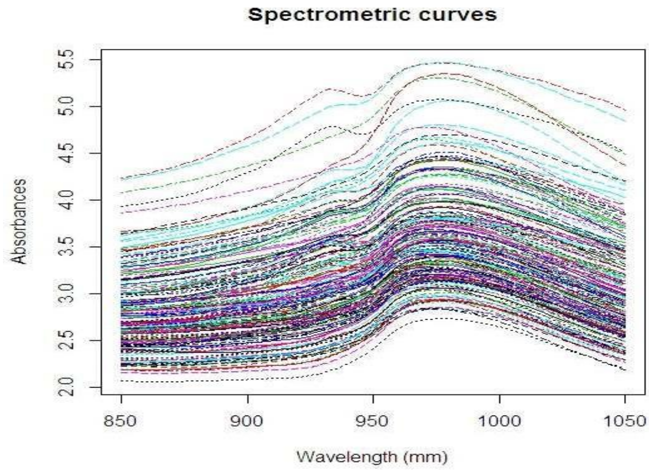

Fig. 1 The Spectrometric curves.

Figure 1 also shows that each unit show clearly as a discretized curve, which can see each unit as a persistent curve.

The goals of Tecator data is to allow for the find of the ratio of specific chemical tenor because chemistry method analysis would take more time and it will be more costly. For that reason, a regression functional problem with a response is a good way for this type for example Y is the rate of fat variable in the part of meat (the response variable), and utilize the spectrometric curves (functional covariate) to estimate y. This instance is also fixed (see for instance, Ferraty and Vieu (2006) and Shang (2014)), so we can use the same case study but different methods to address this problem.

The descriptive of the data in this way, since for each curve i among 215 pieces of meat, which notice one spectrometric discretized object (x_i), which correlate with to the absorbance measured on a grid of 100 wavelengths. Let y_i be represent fat part for each unit i.

The goal of this study is to estimate fat purport y^ from a new curve x.

Then, the rendering of nonparametric functional regression, splitting the data in to two groups. The first sample is learning which contains the 160 curves (x_i, y_i), i=1,2,...,160, for these sample utilize both the covariates function and the responding output variables, that allows us to structure the functional kernel estimators with optimal bandwidth. The rest group is called the testing sample includes the last 55 objects, which is useful for obtaining predictions of the model and computing their achievement.

Ferraty and Vieu(2003, 2006), Burba et al.(2009), and Han Lin (2014) prove that the functional prediction regression model measures the performance as :

i) Calculate the Square Errors: $S_{ei} = (y_i - \hat{y}_i)^2$, i = 161, ..., 215.

ii) Compute the Mean Square Errors: $MSE = \frac{1}{55}\sum_{i=161}^{215} Se_i$

Running the *funopare.kernel.cv* and *funopare.knn.gcv* in accordance with the prediction based on the conditional expectation model by R procedure (see website of Nonparametric Functional Data Analysis (NFDA)). In this analysis, utilizing the semi-metric build on the second derivatives because the curves are smooth, and the second derivative use for both kernel method and KNN method. Figure 2 displays the predicted responses get by these two models on the testing sample (responses of testing sample) when the semi-metric based on the second derivatives, so that the result by KNN method is more accurate than the kernel method because of the fineness of the grid of the curves.

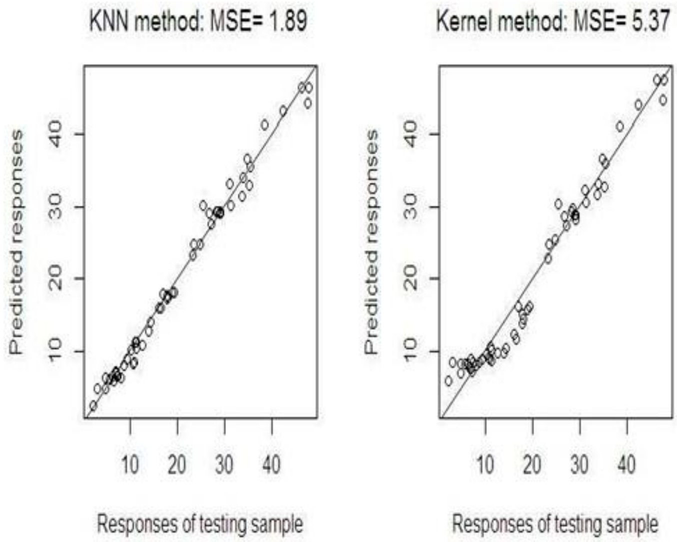

Fig. 2 The prediction of fat content from Spectrometric curves.

EXAMPLE2

Canadian Weather Stations: Prediction of Precipitation Over whole year from the Mean Monthly Temperatures for 35 Stations by Two Different Methods (KNN-Method and Kernel Method):

Data were got from Canadian Weather Stations, and set in the R package. In this instance, taking only 35 stations for each of the mean monthly precipitation and the mean monthly temperature.

Figure 3 displays 35 objects of the mean monthly temperature which contains of 12 observations, and clearly one station places as a discretized curve. Figure 4 shows the mean monthly precipitation of the 35 Stations, with each station representing the one curve. Then, for each station i among 35 curves has one discretized curve x_i which corresponds to the average monthly temperature measured at 12 time points. The prediction of each station i over the whole year contains y_i from Canadian Weather Stations.

The mean monthly temperatures represent to functional covariates, and the mean monthly precipitation correspond the output. The goal is to predict the mean monthly precipitation over the whole year $\hat{y}$, from a new mean monthly.

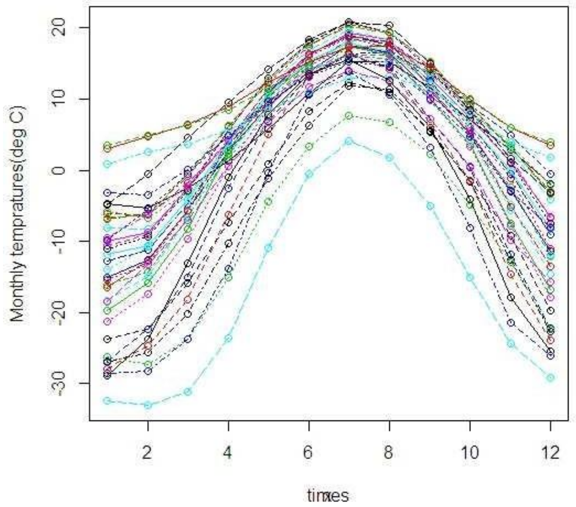

Fig. 3: The mean monthly temperature at thirty-five Canadian Weather Stations.

Then, the execution of nonparametric functional regression, using the cross-validation procedure which is split the sample in two subsample, the first 25 curves using as learning sample and the last 10 stations used as testing sample.

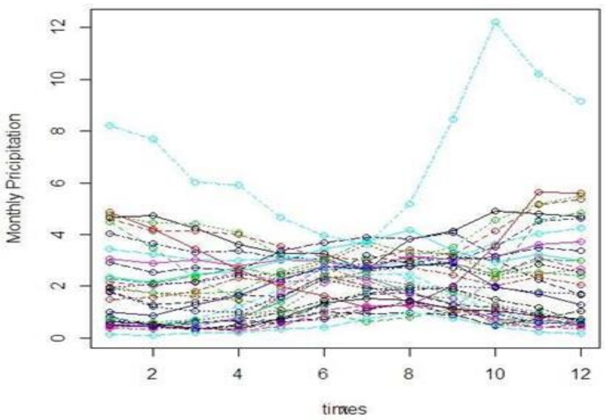

Fig. 4 The mean monthly precipitation at thirty-five Canadian Weather Stations. temperature station **x**,.

Ferraty and Vieu (2003, 2006), Burba et al. (2009), and Shang (2014) prove that the functional prediction regression model is measured by the performance as below:

i)Calculate the Square Errors: $Se_i = (y_i - \hat{y}_i)^2, i = 26,27,\ldots,35$.

ii) Compute the Mean Square Errors: $MSE = \frac{1}{10}\sum_{i=26}^{35} Se_i$.

We run the funopare.kernel.cv and funopare.knn.gcv corresponding to the pre- diction based on the conditional expectation (i.e. regression) model by R procedure (see the NFDA website). Also, in this analysis utilize the semi-metric build on second derivatives (q=2) because the curve is smooth, for both the kernel method and KNN method. Figure 5 shows the predicted response values versus the responses of testing the sample for both methods based on the second derivatives. As found that, both methods give poor prediction but the result produced by the KNN method is more accurate than the kernel method. The reason for that result leads to the collection of data from different stations in Canada. Thus, there is a distance between curves as well as a difference in weather (Atlantic, Continental, Pacific, and Arctic).

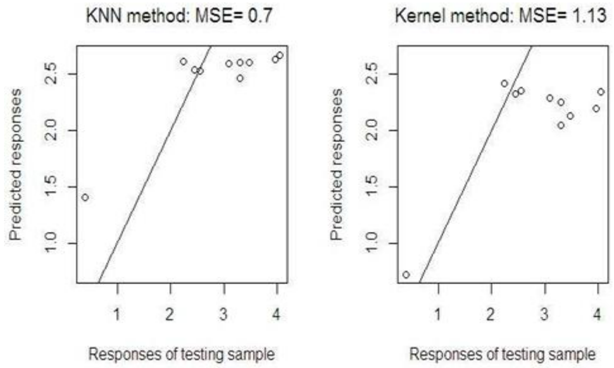

Fig. 5 Prediction of precipitation over one year from mean monthly temperature curves by KNN method and kernel method with a semi-metric setup on the second derivative

CONCLUSION

The main point of this article has presented a compare between two methods in functional nonparametric regression where the output is scalar value and the covariates are function. Under the presented model, notes that the K-Nearest Neighbor predictor supplies perfect estimation when compared with the results get from the kernel estimator model. Using the semi-metrics for the measure of closeness between the covariate function (semi-metric build on second derivatives and functional principle component analysis), as noted out by Ferraty and Vieu (2006). The using of the K-NN method and kernel model are clarified through some numerical examples. In future study, we will try to research functional nonparametric regression when the function is covariate and the response is multivariate response and then take the engagement between different components of the responses into consideration.

REFERENCES

[1] A. Ba´ıllo, A. Gran´e, Local linear regression for functional predictor and scalar response, Journal of Multivariate Analysis 100.1 (2009): 102-111.

[2] F. Burba, F. Ferraty, P. Vieu, k-Nearest Neighbor method in functional nonparametric regression, Journal of Nonparametric Statistics 21.4 (2009): 453-469.

[3] A. Doori, Hazard Rate Estimation Using Varying Kernel Function for Censored Data Type I, Baghdad Science Journal, 16(3 (Suppl.)) (2019): 0793-0793.

[4] G.Cao, S. Wang, L. Wang, Estimation and inference for functional linear regression models with partially varying regression coefficients, Stat, 9(1) (2020): p.e286Montgomery, A.A., T.J. Peters, and P. Little, Design, analysis and presentation of factorial randomised controlled trials. BMC medical research methodology, 2003. 3(1): p. 1-5.

[5] H. Cardot, F. Ferraty, P. Sarda, Spline estimators for the functional linear model, Statistica Sinica 13.3 (2003): 571-592.

[6] H. Midi, M. Sani, S.S. Ismaeel, J. Arasan, Fast Improvised Influential Distance for the Identification of Influential Observations in Multiple Linear Regression. Sains Malaysiana, 50(7)(2021) :2085-2094.

[7] H. Midi, S.S. Ismaeel, Fast improvised diagnostic robust measure for the identification of high leverage points in multiple linear regression. Journal of Statistics and Management Systems, 21(6) (2018): 1003-1019.

[8] F. Ferraty, A. Mas, P. Vieu, Nonparametric regression on functional data: inference and practical aspects, Australian and New Zealand Journal of Statistics, 49(3) (2007): 267-286.

[9] F. Ferraty, P. Vieu, Curves discrimination: a nonparametric functional approach, Computational Statistics and Data Analysis 44.1 (2003): 161-173.

[10] F. Ferraty, P. Vieu, Nonparametric models for functional data, with application in regression, time series prediction and curve discrimination, Nonparametric Statistics 16.1-2 (2004): 111-125.

[11] F. Ferraty, P. Vieu, Nonparametric functional data analysis: theory and practice, Springer Science, New York (2006).

[12] W. H¨ardle, Applied nonparametric regression, Cambridge university press, UK (1990).

[13] P.C. Mahalanobis, A method of fractile graphical analysis, Sankhy: The Indian Journal of Statistics, Series A 23.1 (1961): 41-64.

[14] E.A. Nadaraya, On estimating regression, Theory of Probability and Its Applications 9.1 (1964): 141-142.

[15] K.M.T. Omar, B. Wang, Nonparametric regression method with functional covariates and multivariate response, Communications in Statistics-Theory and Methods, 48(2) (2019): 368-380.

[16] M. Rachdi, P. Vieu, Nonparametric regression for functional data: automatic smoothing parameter selection, Journal of Statistical Planning and Inference 137.9 (2007): 2784-2801.

[17] J. Ramsay, B.W. Silverman, Applied Functional Data Analysis: Methods and case studies, Springer, New York (2002).

[18] J. Ramsay, B.W. Silverman, Functional Data Analysis, Springer, New York (1997).

[19] J. Ramsay, B.W. Silverman, Functional Data Analysis, Second ed., Springer, New York (2005).

[20] H.L. Shang, Bayesian bandwidth estimation for a nonparametric functional regression model with mixed types of regresses and unknown error density, arXiv preprint arXiv:1403.1913, 2014.

A MULTI CRITERIA DECISION MAKING APPROACH BASED ON ENTROPY AND MOORA METHOD FOR THE MASK SELECTION PROBLEM

Betül Turanoğlu Şirin[1]

[1] Department of Industrial Engineering, University of Ataturk, Erzurum, Turkey

b.turanoglu@atauni.edu.tr

Abstract

A new type of coronavirus disease (Covid-19) that was first reported in Wuhan province of China towards the end of 2019 and affected the world has suddenly changed the whole world's agenda due to its speed and way of spreading. All world countries and the World Health Organization have built a common consensus on the importance of wearing a mask within the scope of combating this epidemic disease. Therefore, the demand for masks has reached extreme figures and has become an important need. In this study, a decision-making problem faced by a company for the production of the most protective mask from 3 different mask types (surgical mask, respiratory mask and fabric mask) is discussed. 6 criteria (particle filtration, bacterial filtration efficiency, differential pressure, virus protection, fluid resistance and lifetime) were determined to solve this problem that is a multi-criteria decision-making problem. The criterion weights were calculated by Entropy method, and Moora method was used for ranking and selection process among the masks. According to the results obtained, the best alternative was found to be respiratory mask.

Keywords: Multi criteria decision making problems; Mask selection; Entropy; Moora.

1.INTRODUCTION

The Covid-19 pandemic has become a global health crisis that defines our era. The Covid-19 disease is a new viral respiratory disease characterized by high fever and shortness of breath. Now, it is rapidly spreading from person to person and to many countries outside China, and the number of patients and deaths has reached extreme figures. It is known that the disease is transmitted by droplets and contact. One of the measures that all world countries focus on is wearing masks within the scope of survival and combating epidemic disease. While the importance of masks has increased in combating the epidemic, the characteristics of the existing masks used have questioned by the society. The need for masks has reached such high figures throughout the world history and this has caused existing production systems to adopt a new discipline in order to meet this need. Moreover, it has become very important for them to meet the desired new criterion.

The World Health Organization has established certain criterion for the adequacy of existing masks to combat the epidemic, and manufacturers have been asked to meet these criteria. Manufacturers have conducted R&D studies in order to investigate that there are many mask types in the current system and which type of masks are how functional both in production and in combatting the epidemic. As a result of these studies, 3 types of masks offered to the use of the society were determined:

- Surgical mask: also known as a medical mask or simply a face mask. It is used by healthcare professionals to prevent bacteria transmitted by aerosol and liquid droplets in the user's mouth and nose during surgery and patient care.
- Respiratory mask: a type of protective mask approved by the European Union. It provides protection against particles such as dust particles.
- Fabric mask: a type of mask that can be washed and has a long lifetime. It is intended to prevent the spread of liquid droplets in the mouth and nose.

In this study, a multi-criteria decision-making approach is proposed for a company that is interested in which of these masks should be selected and produced. In the proposed approach, the criterion weights were calculated by Entropy method, and Moora method was used for the ranking among the masks.

2.GENERAL PROPERTIES OF METHOD

Multi-criteria decision-making (MCDM) was developed in the 1960s when methods to assist decision making were deemed necessary. MCDM is a method that helps to keep the decision-making mechanism under control and to obtain the decision result as quickly and easily as possible in cases where the number of criterion and alternatives is high. MCDM techniques are the techniques that try to find the best alternative in a collection of decision criteria and alternatives with different methods. These techniques do not aim to offer the most accurate one to decision makers, however they help to make evaluations in terms of benefit and risk among alternatives and numerical results. There is more than one MCDM method in the literature. The methods to be used in this study are Entropy and Moora methods. The criterion weights were determined by Entropy method, and Moora method was used in ranking among the alternatives.

1.1. Entropy Method

The concept of entropy was first defined in the literature by Rudolph Clausius (1865) as a measurement of disorder and uncertainty in a system (Zhang et al., 2011). The Entropy method is used to measure the amount of useful information provided by the existing data (Wu, 2011). The most important feature of the method is the possibility of application in various scales. The method is also one of the few objective evaluation methods that can be used in aesthetic evaluation (Bostancı and Ocakçı, 2009).

The steps of the Entropy method are as follows (Özaydın and Karakul, 2021):

Step 1- Creating decision matrix: The rows of the decision matrix include the alternatives to be decided, and the columns include the criterion data.

$$X=\begin{bmatrix} X_{11} & \cdots & X_{1n} \\ \vdots & \ddots & \vdots \\ X_{m1} & \cdots & X_{mm} \end{bmatrix} \tag{2.1}$$

Step 2- Standardization: After the decision matrix is created, the data obtained in the decision matrix is standardized in order to use different scale units together. There are two different calculations for this process to be carried out. While Equation (2.2) is used for benefit-based criteria, Equation (2.3) is applied for cost-based criteria.

$$r_{ij} = \frac{x_{ij}}{\max x_{ij}}, \text{ (i=1,2,…,m; j=1,2,…,n)} \tag{2.2}$$

$$r_{ij} = \frac{\min x_{ij}}{x_{ij}}, \min x_{ij} \neq 0, \text{ (i=1, 2,…,m; j=1,2,…,n)} \tag{2.3}$$

Step 3- Normalization: Normalization process is applied to the standardized values in Step 2 using Equation (2.4).

$$f_{ij}= \frac{r_{ij}}{\sum_{i=1}^{m} r_{ij}} \tag{2.4}$$

Step 3- Calculation of entropy: By using Equation (2.5), entropy value of each criterion is calculated by using the values obtained in Equation (2.4).

$$e_j = -k \sum_{i=1}^{m} f_{ij} \ln(f_{ij}) \tag{2.5}$$

k: Entropy coefficient = $\frac{1}{\ln m}$ (m= number of alternatives)

Step 4- Calculation of criteria weights: Weight values are calculated using Equation (2.6). The sum of the values w_j should be always 1.

$$w_j = \frac{1-e_j}{n-\sum_{j=1}^{n}(1-e_j)} \tag{2.6}$$

2.1. Moora Method

The Moora method was developed by Brauers and Zavadskas in 2006. There are different types of Moora that is a multi-purpose optimization method. These include Moora Ratio Method, Moora - Reference Point Approach, Moora - Significance Coefficient, Moora – Full Multiplication Form and Multi-Moora. In this study, Moora- Significance Coefficient method was used. The steps of the method are as follows (Özbek, 2015):

Step 1- Creating decision matrix: It is the determination of the objectives and bringing together the performance values of different alternatives according to different objectives in a matrix. In the matrix in Equation (2.7), alternatives are in the rows and criterion are in the columns. The elements of the matrix refer to the performance values of each alternative according to the criteria.

$$X=\begin{bmatrix} X_{11} & X_{12} & X_{1n} \\ X_{21} & X_{22} & X_{2n} \\ \vdots & \vdots & \vdots \\ X_{m1} & X_{m2} & X_{mn} \end{bmatrix} \tag{2.7}$$

Step 2- Normalization: It is the normalization of the matrix created in Step 1. Equation (2.8) is used for this process.

$$X_{ij}^{*}=\frac{X_{ij}}{\sqrt{\sum_{i=1}^{m} X_{ij}^{2}}} \tag{2.8}$$

Step 3- Calculation of the performance values of the alternatives: The performance values of the alternatives are calculated using Equation (2.9).

$$y_j^{*} =\sum_{i=1}^{g} w_i x_{ij}^{*} -\sum_{i=g+1}^{n} w_i x_{ij}^{*} \tag{2.9}$$

In Equation (2.9), w_i refers to the weight of criteria i, i=1,2,3…g is the criteria to be maximized, i=g+1,g+2…g+n, is the criteria to be minimized.

The calculated y_i^{*} values are ordered from largest to smallest, and the alternative with the highest value is selected as the best alternative.

3.APPLICATIONS

In this study; 6 criteria were determined as particle filtration, bacterial filtration efficiency, differential pressure, virus protection, fluid resistance and lifetime. The criteria weights were calculated by the Entropy method. For this, the decision matrix, which is the first step, was created (Table 1). Since there is no negative value in the data in the decision matrix, the positivity process was not required. Since all the criteria are beneficial, the data are standardized using Equation (2.2). The standardized decision matrix is given in Table 2. The standardized decision matrix was normalized using Equation (2.4) (Table 3). Entropy values were obtained with Equation (2.5). Finally, criteria weights were calculated with the help of Equation (2.6) (Table 4 and Table 5).

Table 1. The decision matrix

	Particle filtration	**Bacterial filtration efficiency (%)**	**Differential pressure**	**Virus protection (%)**	**Fluid resistance**	**Lifetime (min.)**
Surgical mask	98	0,98	40	0,95	160	240
Respiratoriy mask	98	0,95	40	0,95	120	420
Fabric Mask	95	0,9	60	0,001	80	180
Max.	98	0,98	60	0,95	160	420

Table 2. The standardized decision matrix

	Particle filtration	**Bacterial filtration efficiency (%)**	**Differential pressure**	**Virus protection (%)**	**Fluid resistance**	**Lifetime (min.)**
Surgical mask	1	1	0,666666667	1	1	0,571429
Respiratoriy mask	1	0,96938776	0,666666667	1	0,75	1
Fabric Mask	0,9693878	0,91836735	1	0,001053	0,5	0,428571
TOTAL	2,9693878	2,8877551	2,333333333	2,001053	2,25	2

Table 3. The normalized decision matrix

	Particle filtration	**Bacterial filtration efficiency (%)**	**Differential pressure**	**Virus protection (%)**	**Fluid resistance**	**Lifetime (min.)**
Surgical mask	0,3367698	0,34628975	0,285714286	0,499737	0,444444	0,285714
Respiratoriy mask	0,3367698	0,33568905	0,285714286	0,499737	0,333333	0,5

Fabric Mask	0,3264605	0,3180212	0,428571429	0,000526	0,222222	0,214286

Table 4. The entropy values

	Particle filtration	**Bacterial filtration efficiency (%)**	**Differential pressure**	**Virus protection (%)**	**Fluid resistance**	**Lifetime (min.)**	**TOTAL**
e_j	0,9999029	0,9994410	0,982141033	0,634692	0,965634	0,941735	5,523545

Table 5. The criteria weights

	Particle filtration	**Bacterial filtration efficiency (%)**	**Differential pressure**	**Virus protection (%)**	**Fluid resistance**	**Lifetime (min.)**	**TOTAL**
w_j	0,0002038	0,0011732	0,0374830	0,766721	0,0721	0,122289	1

After the criteria weights were determined by the entropy method, the selection process between the masks was made with the Moora method. At this stage, firstly, the decision matrix used in Entropy is discussed (Table 1). Then, by normalizing this matrix with Equation (2.8), the normalized Moora decision matrix in Table 6 was obtained. Finally, y_i^* values were calculated with the help of Equation (2.9) (Table 7). According to these values; the best alternative is the respiratory mask, and the worst alternative is the fabric mask.

Table 6. The normalized Moora decision matrix

	Particle filtration	**Bacterial filtration efficiency (%)**	**Differential pressure**	**Virus protection (%)**	**Fluid resistance**	**Lifetime (min.)**
Surgical mask	0,58324035	0,5994248	0,48507125	0,707107	0,74278	0,464991
Respiratoriy mask	0,58324035	0,5810751	0,48507125	0,707107	0,55709	0,813733
Fabric Mask	0,56538605	0,5504922	0,72760688	0,000744	0,37139	0,348743

Table 7. y_i^* values

	y_i^*	**Ranking**
Surgical Mask	0,671597	2
Respiratoriy Mask	0,700829	1
Fabric Mask	0,09804	3

4.CONCLUSIONS

The use of masks is at the forefront of the measures taken to protect from the Covid-19 epidemic, which has affected the world in recent years. The characteristics of the masks used play an important role in disease prevention. In this study, a decision-making problem about which type of mask a business should produce is discussed. Here, since both the number of alternatives (masks) and the number of criteria considered in the selection of masks are more than one, the problem considered is a multi-criteria decision-making problem. Two different methods, Entropy and Moora, were used to solve this problem. The criteria weights were determined with entropy, and the Moora method was used in mask selection. In the study, the best mask was found to be the respiratory mask according to the 6 criteria discussed.

REFERENCES

1. Bostancı, S.H. and Ocakçı, M., Kent Siluetlerine İlişkin Tasarım Niteliklerinin Entropi Yaklaşımı ile Değerlendirilmesi, İstanbul Teknik Üniversitesi Dergisi, Vol:8, No: 2, 27-36,2009.
2. Özaydın, G. and Karakul, A. K., Entropi tabanlı MAUT, SAW ve EDAS yöntemleri ile finansal performans değerlendirmesi, Süleyman Demirel Üniversitesi İktisadi ve İdari Bilimler Fakültesi Dergisi, Vol:26, No:1, 13-29, 2021.
3. Özbek, A., Akademik Birim Yöneticilerinin Moora Yöntemiyle Seçilmesi: Kırıkkale Üzerine Bir Uygulama, Sosyal Bilimler Enstitüsü Dergisi, Vol: 38, 1-18, 2015.
4. Zhang, H., Gu, C., Gu, L. and Zhang, Y., The Evaluation Of Tourism Destination Competitiveness By TOPSIS & Information Entropy - A Case In The Yangtze River Delta Of China, Tourism Management, Vol:32, 443-451, 2011.
5. Wu, J., Sun, J., Lıang, L. and Zha Y., Determination Of Weights For Ultimate Cross Efficiency Using Shannon Entropy, Expert Systems With Applications, Vol:38, No:5, 5162-5165, 2011.

Call Assistant Application for Call Centers

Mesut Tartuk[1], Furkan Taha Nurdağ[2], Vedat Acar[3], Mehmet Fatih Akay[4], Fatih Abut[5]

[1]*Comdata Teknoloji ve Müşteri Hizmetleri A.Ş., Turkey; mesut.tartuk@comdatagroup.com*

[2]*Comdata Teknoloji ve Müşteri Hizmetleri A.Ş., Turkey; furkan.nurdag@comdatagroup.com*

[3]*Comdata Teknoloji ve Müşteri Hizmetleri A.Ş., Turkey; vedat.acar@comdatagroup.com*

[4]*Çukurova Üniversitesi, Bilgisayar Mühendisliği Bölümü, Adana, TR; mfakay@cu.edu.tr*

[5]*Çukurova Üniversitesi, Bilgisayar Mühendisliği Bölümü, Adana, TR; fabut@cu.edu.tr*

Abstract

In this paper, we develop new tools to handle incoming calls into call centers when the centers are on holiday, non-working time or peak calls time. Previously, we were using a Voicemail server from Avaya by license. To reduce side effects like overloading and high currency cost, we made a definition between Interactive Voice Response (IVR) and Central. With this definition the load of the server is reduced significantly. Then, we developed an intermediate application that would forward the incoming calls from the exchange to the server for recording incoming calls on the IVR side. Incoming VoiceMail will be directed to the IVR according to the determined conditions, and the customer's speech will be translated into written text over IVR. Afterwards, these texts will be sent to the authorized people within the defined projects by email. This mail will contain the voice file and information of the person who sent this voice mail. Afterwards, the authorized person who receives this email will respond to this request within his own team.

Keywords: Voicemail; Callback requests; Abandon Calls; IVR.

1. INTRODUCTION

A Call center is a company that specializes in dealing with customers and can play a significant role in collecting customer information in a company [1]. Call centers are a layer between the customer and the company. Customer satisfaction in the business world is one of the most important things for the companies. To increase satisfaction, Call centers are developing useful applications for their clients. Most of the customers are becoming angry when they are not able to reach out to the call center. Some of those are significant calls and some of them not. For the companies each call is important. By caring for the important calls we developed the application to catch abandoned calls, callback requests and voicemails. Navigating through new voicemail messages to find messages of interest is a time-consuming task, particularly for high-volume users [2] and 60-80% of a call center budget is allocated on labor costs [3]. That's why decreasing the monotone processes by developing an application is significant for the Call Centers. For the call centers %77 of inbound calls were answered and remaining calls were directed to voicemail. 89% of all calls occurred between 9AM and 4PM, with slight variation each hour. Staffing Analysis revealed 91.3% availability rate equivalent to 5.48 agents available per day [4]. One of the goal of our research is to provide tools to overcome the inherent difficulties of speech access, by supporting visual scanning, search, and information extraction [5]. By doing this we will save huge amounts of time. Voicemails are paralleled to mass and interpersonal communication and implications make connections between information retention, temporality, and interpersonal memorialization [6]. There are several ways to extract data from the Voicemails such as using vector of lexical and prosodic features [7]. Even such basic information as the name of the caller/ sender or a phone number for returning calls is not represented explicitly and must be obtained from message transcripts or other sources [8]. For Voicemail there are different type of usage with integrated with speech analytics [9]. With all of these modules, Voicemail application might be offline media portal point that make up a contact center [10].

2. GENERAL PROPERTIES OF METHOD

Voice technologies are developing day by day. Regardless of the sector, every institution and call center develops new products and modules to improve their processes. Since it takes a lot of time to make sense of a large amount of data, the use of applications such as artificial intelligence technologies and speech analytics has increased considerably. Increasing amounts of public, corporate, and private speech data are now available on-line. These are limited in their usefulness, however, by the lack of tools to permit their browsing and search. The goal of our research is to provide tools to overcome the inherent difficulties of speech access, by supporting visual scanning, search, and information extraction [5]. Separating audio files containing such a large amount of data from information is essential for a successful call center. Voicemails are paralleled to mass and interpersonal communication and implications make connections between information retention, temporality, and interpersonal memorialization [6]. There are also some methods conducted by Konstantinos Koumpis and Steve Renals by using vector of lexical and prosodic features [7]. The proposed voicemail application will be stronger with increased amounts of data filled by the customer representatives. Making speech analytics to the incoming voicemail success percentage might be higher by getting an evaluation from the customer representatives. That's why we made an evaluation layer to increase this. Customer representatives will evaluate the speech and they will change if the success is not good to evaluate. By using this way actually the application will collect the amount of data like in snowball.

Indeed the application works with the help of Interactive voice response (IVR). IVR is taking the voice, converting it into text with an integration with our Speech analytics application and then sending the voicemail application with web service. After all, the Voice mail application is getting the information of the customer such as Phone number, VDN No, Text of speech. When the VoiceMail gets this information the layer which is developed for the evaluation will be started and the incoming data from IVR will be connected to each other by VDN No. With the loop of this process will be fed the 3rd phase of the project which is using deep learning ,machine learning and neural network to understand the status and the topic of the incoming voicemails. If a customer complains about a product and says something to the voicemail, the application will catch and will take an action by distributing the voicemail into customers CRM or any other system by creating a ticket. This system will be end to end inactive communication with the customer with high customer experience because the customer will be notified about each step of the ticket. That's why customers will be satisfied with the inactive communication.

3. APPLICATIONS

Voicemail is not like email. Even such basic information as the name of the caller/ sender or a phone number for returning calls is not represented explicitly and must be obtained from message transcripts or other sources[8]. By thinking this we build voicemail application with consisting of 9 pages. Each pages are restirectable from the admin page by using Navigation page. Admins are able to see "Users, Roles, Navigation,Menu, Project, Call Status" For Users, "Calls, Dashboard, Reports".

Dashboard

Figure 1 shows the dashboard screen. By using dashboard, operation managers and the agents can see the incoming Voicemails, Callbacks and abandoned calls. As a brief they also can see Unanswered calls, Completed calls and finished calls. Completed calls is not mean finished calls for call center. Because, even the customer representative communicates with the customer they might not finish the demand of the customer. The task is being completed right after the choosing completed status.

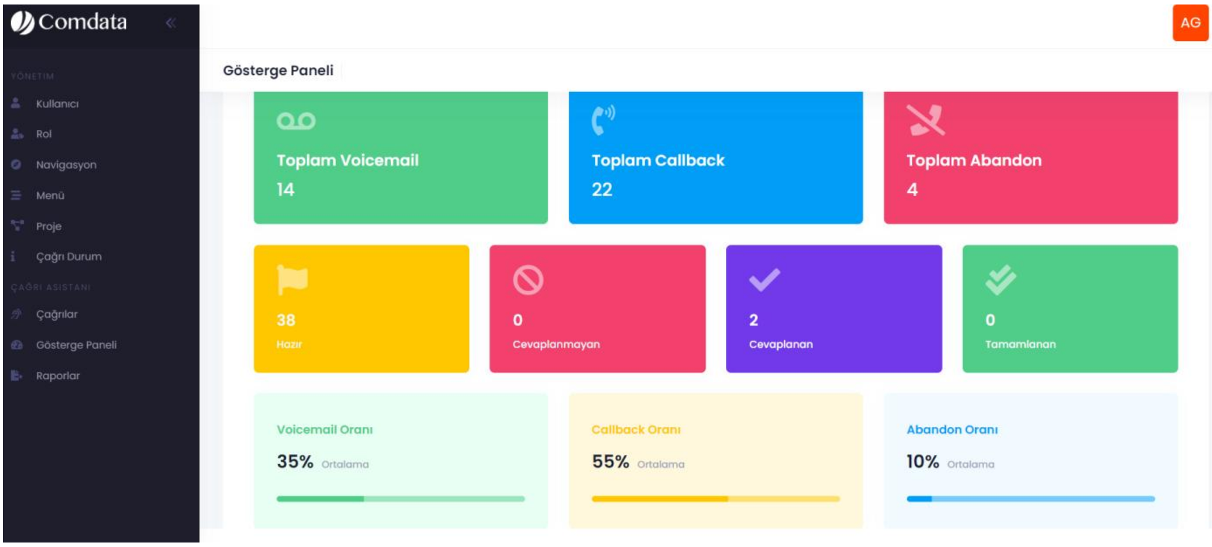

Figure 1 : Dashboard Screens

Calls Screen

In Figure 2, the operation members are able to see incoming calls with details. They can sort the type of call and they can start to take an action. By pressing yellow action button, they can see the text of incoming call by using speech analytics.

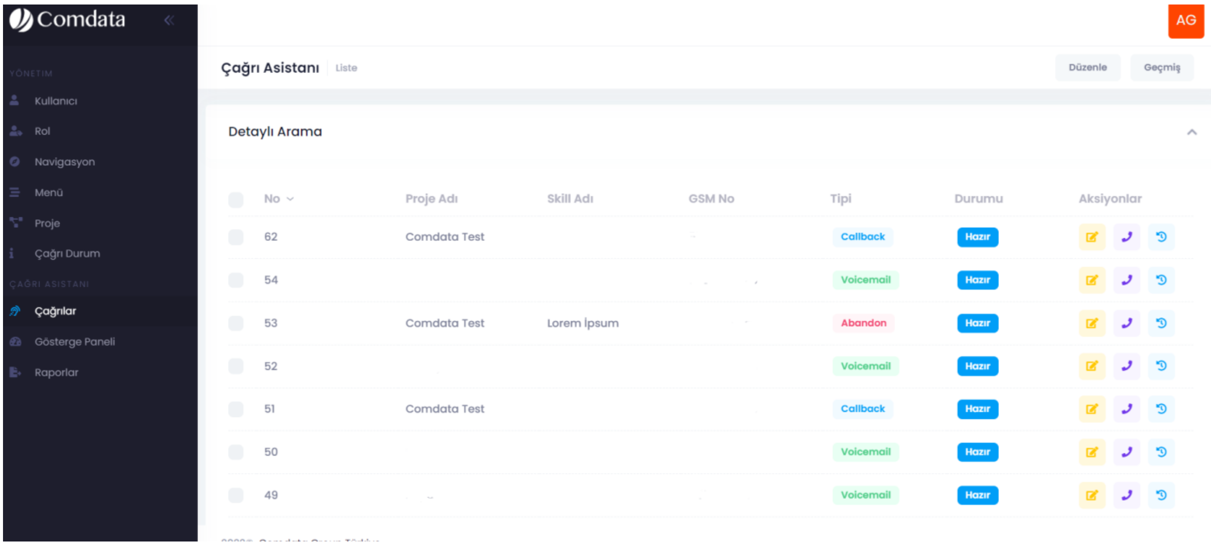

Figures 2 : Call Asistant Screen

Whenever the customer representative press the yellow button they are directed to the new page shown in Figure 3.

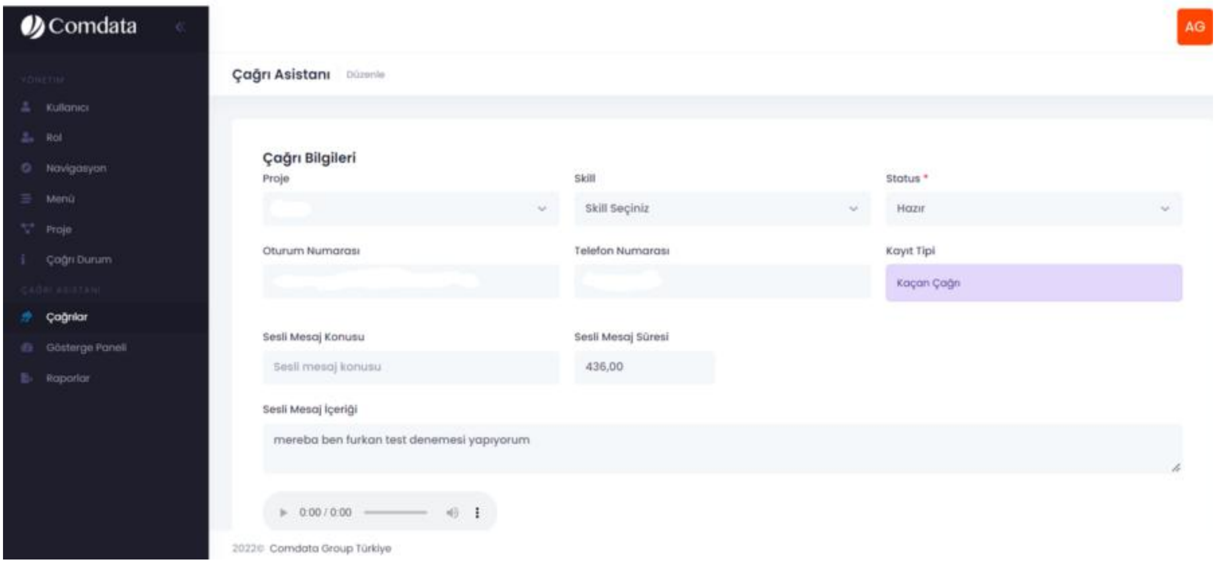

Figures 3 : Call Detail Screen

From the right top, they can change the status of the ticket and they can listen the incoming voicemail and edit to the message context.

Reports

Operation managers can get all important data from the application. They have to choose the project, Date and if they prefer for the spesicif user. When they fill the areas they can export

Voicemails, Callbacks and Abandoned calls. If they want to export all data by pressing "General Reports" they can export them all. It's shown in Figure 4.

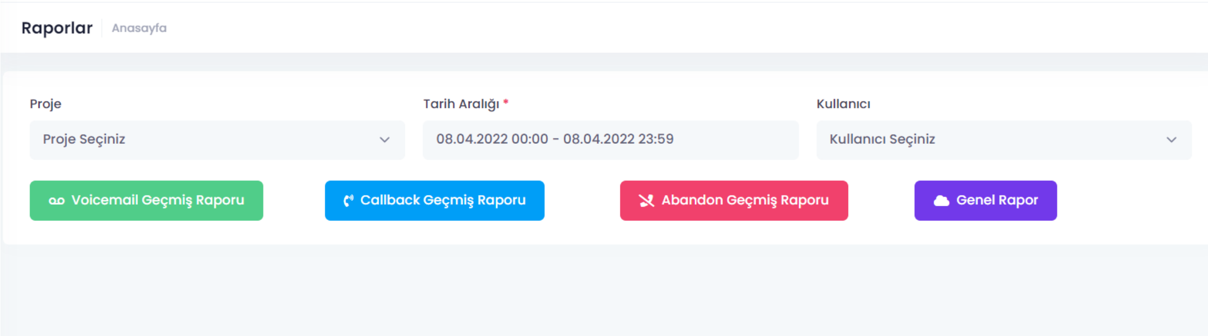

Figure 4 : Report Screen

Admin Pages

Admin pages are basic CRUD pages that can add users,roles,menus,project and call status.

User Page

Adding, Deleting and Updating user for Voicemail Application.

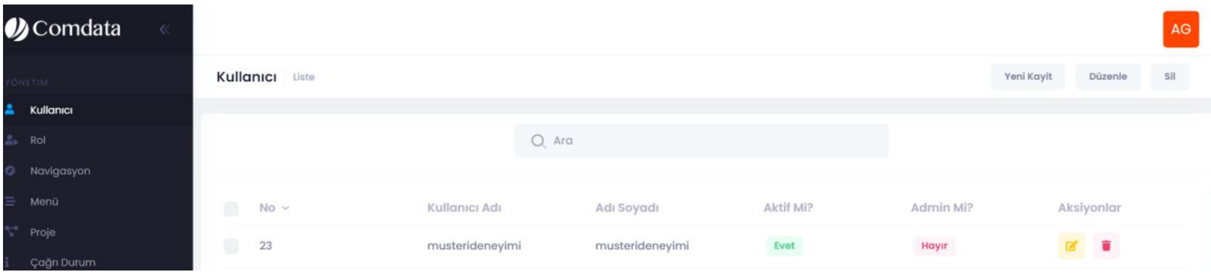

Figures 5 : Add User Page

Role Page

Adding, Deleting and Updating roles for Voicemail application.

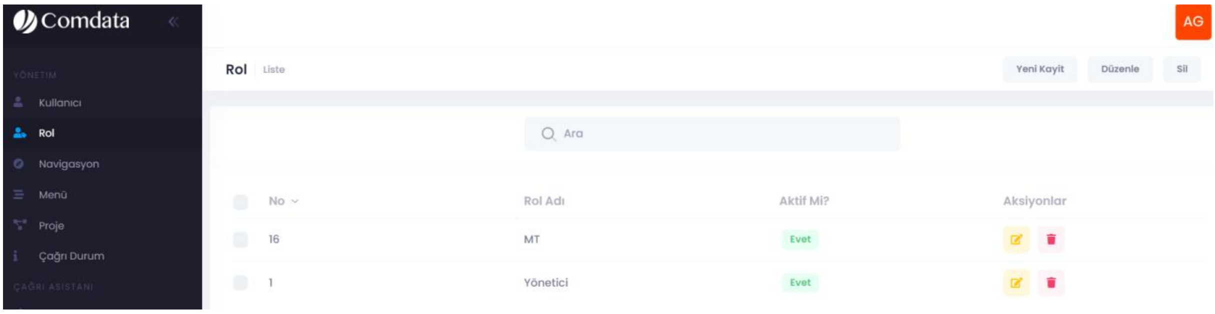

Figures 6 : Role Management Page

Navigation Page

To navigate users by their own roles, navigation page is helping to make this.

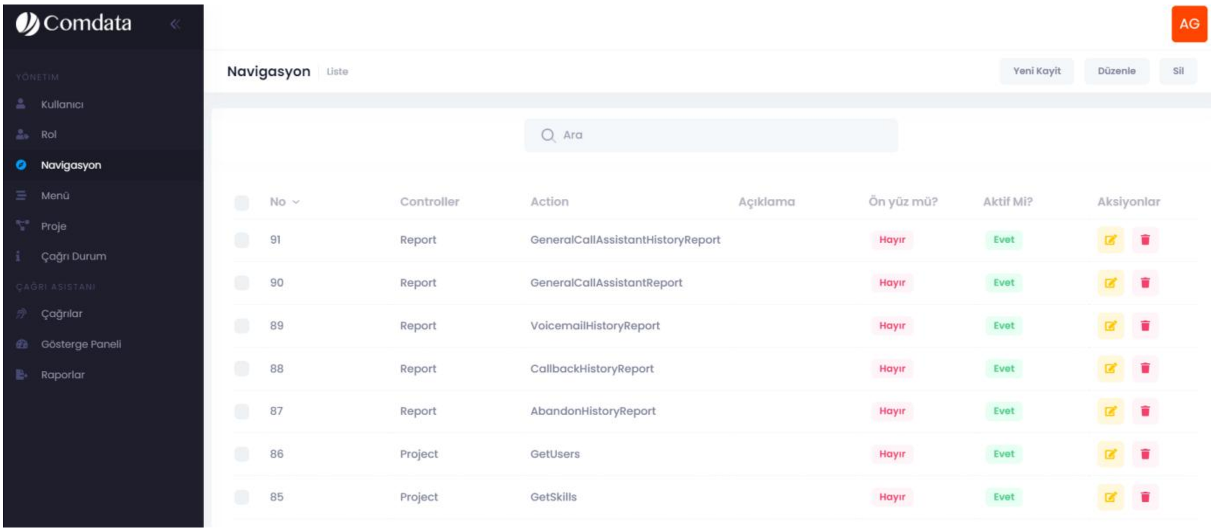

Figures 7: Navigation Pages

Project Page

To track a project, we have to add it from project page.

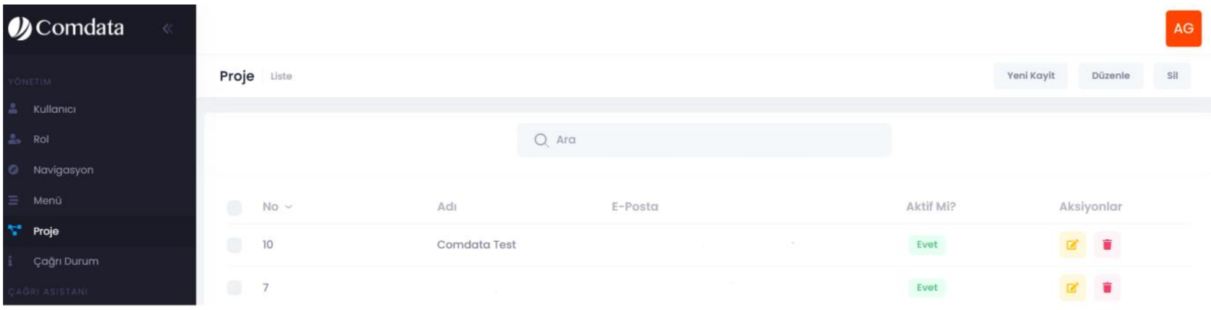

Figures 8 : Add Project Page

4. CONCLUSION

As a result, developing a voicemail application was welcomed and preferred by the operations and customers. Different types of customers have requested different modules and improvements to this product, making demands to increase the product's capabilities. After these improvements are made, the product will be more flexible and successful compared to the voicemail products in the industry. With the change requests on the switchboard side, the product will be able to identify the abandoned customers in seconds, and it will become a necessary application to provide the best customer experience to the customers who want to reach the end-to-end call center by sending information to these people. Listening and evaluating voice messages sent to call centers is a very challenging and time-consuming process for operations managers. Products such as Speech analytics shorten these processes considerably. For this reason, analyzing voice-related processes with speech analytics products and converting them into text positively affects voice processes and eliminates erroneous evaluations. In the future of the Call Assistant project we will make an interface to serve this application as a product to our customers in the call center. It will consist of a dynamic interface by getting feed from Call Management System and thanks to the C-Connect application will be able to make outbound calls to the incoming voicemails, abandon calls and call back requests to the end customer. For Voicemail there are different type of usage with integrated with speech analytics. With in this direction, this application has capability to use it as a service for these kind of applications. In the other hand, using voicemail webservices connecting with knowledge base applications would be usefull for the operations as well to provide a better uniform solution, call centers need to be supported by a knowledge asset which is owned by experience or other information sources.

REFERENCES

1. Kurt, M. (2019). Forecasting Call Center Arrivals: A Case Study in Telecommunication Sector

2. Ringel, M., & Hirschberg, J. (2002, April). Automated message prioritization: Making voicemail retrieval more efficient. In CHI'02 Extended Abstracts on Human Factors in Computing Systems (pp. 592-593).

3. Mehrotra, V., Ozlük, O., & Saltzman, R. (2010). Intelligent procedures for intra-day updating of call center agent schedules. Production and operations management, 19(3), 353-367.

4. Cummings, C. W., Comer, G., Bealer, N., Costantino, P., Davis, J., Heard, L., ... & Oh, K. (2019). Call center performance to drive patient access.

5. Whittaker, S., Hirschberg, J., Amento, B., Stark, L., Bacchiani, M., Isenhour, P., ... & Rosenberg, A. (2002, April). SCANMail: a voicemail interface that makes speech browsable, readable and searchable. In Proceedings of the SIGCHI conference on Human factors in computing systems (pp. 275-282).

6. LeFebvre, L. E., & Haggadone, B. A. (2019). Remembering the voice: Exploring information and sentiment in voicemail archival practices. Mobile Media & Communication, 7(2), 195-214.

7. Koumpis, K., & Renals, S. (2005). Automatic summarization of voicemail messages using lexical and prosodic features. ACM Transactions on Speech and Language Processing (TSLP), 2(1), 1-es.

8. Jansche, M., & Abney, S. (2002, July). Information extraction from voicemail transcripts. In Proceedings of the 2002 Conference on Empirical Methods in Natural Language Processing (EMNLP 2002) (pp. 320-327).

9. Padmanabhan, M., Eide, E., Ramabhadran, B., Ramaswamy, G., & Bahl, L. R. (1998, May). Speech recognition performance on a voicemail transcription task. In Proceedings of the 1998 IEEE International Conference on Acoustics, Speech and Signal Processing, ICASSP'98 (Cat. No. 98CH36181) (Vol. 2, pp. 913-916). IEEE.

10. Purwanto, Y., & WS, A. N. IMPLEMENTATION OF VOICE MAIL IN KNOWLEDGE BASED VOIP CALL CENTRE.

SIMULATION OF THERMOELECTRIC ENERGY CONVERSION FOR DIFFERENT THERMOELECTRIC DEVICE INSTALLATIONS IN A CHANNEL FLOW OPERATING WITH AIR AND HYBRID NANOFLUIDS

Damla Okulu[1], Fatih Selimefendigil[2], Hakan F. Öztop[3]*

[1,2]Department of Mechanical Engineering, Celal Bayar University, Manisa, Turkey

[3]Department of Mechanical Engineering, Technology Faculty, Fırat University, Elazığ, Turkey

hfoztop1@gmail.com

Abstract

In this study, three different TEG-installed channel system models are simulated by using air as hot fluid while water and water-based Ag/MgO hybrid nanofluid (volume fraction of 0.02) is used as cold fluid in opposite directions. The study is performed for five different Reynolds numbers between 300 and 1500. Three TEGs with equal distances between the channels is used in Model 1, two TEGs close to the entrance of hot and cold fluids into the channel is used in Model 2 while one TEG is considered in the mid of the channel in Model 3. When using water at Re=1500 in Model 1, TEG 1 (close to the hot fluid inlet) output power reached at a higher value of 15% and 25%, respectively, compared to TEG 2 (in the middle of the channels) and TEG 3 (near cold fluid inlet). When water-based Ag/MgO is used, TEG 1 output power is increased by 17.5% and 30%, respectively, compared to TEG 2 and TEG 3. In Model 2 with water-based Ag/MgO having the same Reynolds number, TEG 4 (close to the hot fluid inlet) produced 17.2% higher electrical potential and 37.5% higher output power compared to TEG 5 (close to the cold fluid inlet). The highest electrical potential and output power value is obtained with TEG 6 used in Model 3.

Keywords: Thermoelectric conversion; nanofluid; CFD

1.INTRODUCTION

The inadequacy of conventional fossil-based energy sources in the developing world has made the search for alternative energy sources important. In this context, researchers highlight renewable energy technologies that provide energy production by utilizing natural resources such as sun and wind. In addition, by emphasizing the damage caused by fossil fuels to the environment, societies that have become increasingly conscious about the use of clean energy have accelerated their work in this area. Thermoelectric generators (TEGs) which are among the technologies in which clean energy production is realized, have become interesting for researchers, especially in recent years. TEGs, which we can produce electrical energy from the temperature difference, have a very simple design and with these features they are separated from other renewable energy technologies. This device, which provides electricity generation in almost every condition where there is a temperature difference, can be designed in desired dimensions and included in other sustainable energy systems.

TEGs, which are currently used in various fields such as space studies, automotive sector, solar energy systems, are expanding their usage areas day by day. One of the most important reasons for this situation is the flexibility to benefit from different sources in the creation of temperature difference. Theoretical and experimental studies have developed different approaches to the creation of temperature difference in TEG systems. Among these approaches, it is offered as an option to form the required temperature difference for the electricity generation of the system by means of a fluid. Conventional fluids such as air and water are included in TEG systems as heat transfer fluids. However, in recent years, nanofluids, which have been applied in many different areas and have high performance as heat transfer fluids, have been integrated into TEG systems and outperformed conventional fluids. This type of fluid, which is obtained by dispersing the solid particles in micro dimensions into the base fluid, shows improved heat transfer properties, especially by reaching high thermal conductivity values.

There are various studies in the literature investigating the effects of nanofluids on TEG systems. For example, water-based CNT nanofluid was used in the TEG system, and when they evaluated the system under the same conditions, they achieved 14.2% improvement with water, while this situation was 31% with water-based CNT [1]. In another study, Karana et al. [2] compared MgO and ZnO nanofluid with EG-W (50/50) fluid and with both ZnO and MgO nanofluid obtained higher voltage than EG-W. MgO nanofluid exhibited the best performance, providing 20.33% higher voltage generation than EG-W. Ruan et al. [3] TEG system in which they integrated GNP (graphene nanoplatelet) nanofluid, obtained higher output power and TEG efficiency by 11.38% and 5.7%, respectively, compared to water.

In this study, air is used as the hot fluid while water and water-based Ag/MgO are used as the cold fluids. TEGs are placed between two channels. Flow field and thermo-electric energy conversion characteristics are analyzed.

2. NUMERICAL MODEL OF TEG SYSTEM

TEG is a device that enables us to produce electrical energy from heat energy. This energy conversion takes place with the help of thermoelectric effects and some thermodynamic processes. Thermoelectric effects, developed with the work of researchers named Seebeck, Peltier and Thomson, are phenomena that enable the expression of an energy conversion from heat energy to electrical energy or vice versa [4]. The Seebeck effect describes the generation of electricity in the presence of a temperature difference, which forms the basis of TEG. Although TEG has a working principle based on the Seebeck effect, other thermoelectric effects also show the existence of this device in the working processes. The Seebeck effect is the phenomenon that describes that voltage can be produced with the temperature gradient, and the voltage value produced by this principle is defined as the Seebeck electromotive force [5]. In the calculation of the Seebeck voltage (V_{oc}) in an open circuit, the Seebeck coefficient of the materials and the temperatures caused by the heat sink (T_c) and the heat source (T_h) are used (Eq. 1).

$$V_{oc} = \int_{T_c}^{T_h} (S_p - S_n) \; dT \tag{1}$$

where S_p and S_n are the p and n type Seebeck coefficients of the material, respectively. Amount of electrical potential produced is affected by the quality of the material used. The determination of this quality depends on the figure of merit values of the materials. For a good thermoelectric material, the figure of merit value should be high. The temperature-dependent figure of merit value (ZT) of a material is obtained with the following equation [6]:

$$ZT = \frac{S^2 \gamma}{k} T \tag{2}$$

ZT is directly proportional to Seebeck coefficient (S) and electrical conductivity (γ) and inversely proportional to thermal conductivity (k). Therefore, it is desired that the material has high Seebeck coefficient and electrical conductivity but low thermal conductivity. Considering this situation, semiconductor materials have become the preferred material class for TEG design. TEG be designed by bringing together thermoelectric modules (TEMs) consisting of thermoelectric legs, electrode and ceramic layers. The p and n type semiconductor legs, where energy conversion takes place, are thermally connected in parallel and electrically in series, the electrical connection between these legs is provided by electrodes (conductor), and this formation is placed between two ceramic layers exposed to heat sink (T_c) and heat source (T_h) [7,8]. By connecting the TEM to an external load resistance, current flow is provided, and accordingly can be produced electrical potential and power. Fig. 1 presents the TEM connected to an external load resistance.

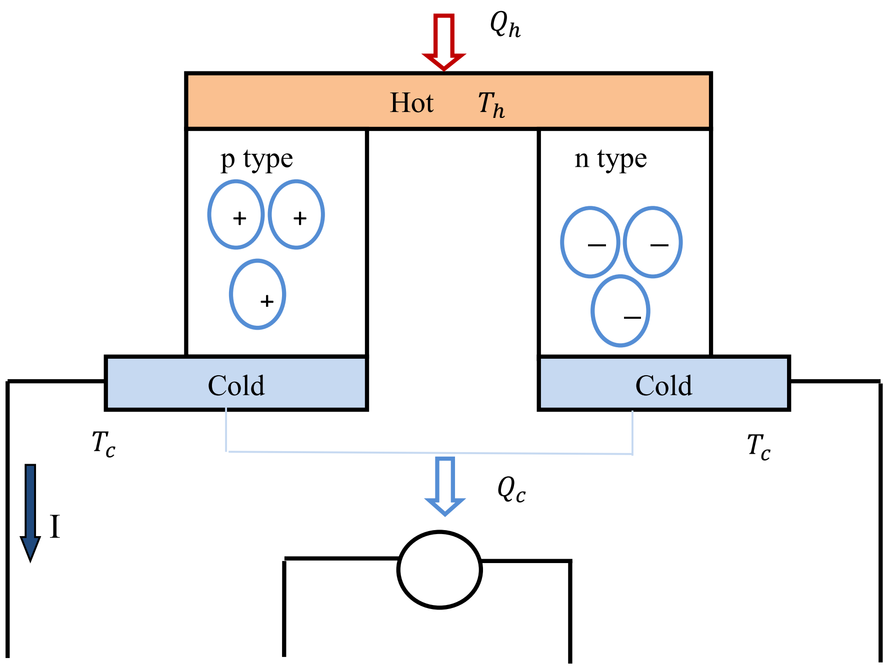

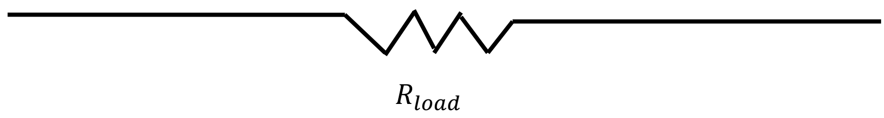

Fig. 1. Schematic representation of the TEM connected to the load resistance.

The following equations are used to determine TEG performance [9,10].

Electrical potential value produced in a TEG system created by using multiple TEMs shown in Fig. 1,

$$V = \left(\frac{V_{oc}\, R_{load}}{R_{load}+R_{int}}\right).\mathrm{M} \tag{3}$$

where R_{int} is internal resistance, R_{load} is load resistance and M is the number of TEMs. It is possible to calculate the current value when Eq. 3 is applied to Joule heating law ($V = I.\ R_{load}$).

$$I.\ R_{load} = \frac{V_{oc}\, R_{load}}{R_{load}+R_{int}} \tag{4}$$

The difference between the amount of heat absorbed on the hot side and the amount of heat output on the cold side is used to calculate the TEG output power (Eq. 5).

$$P_{\mathrm{out}} = Q_h - Q_c \tag{5}$$

Q_h is the amount of heat absorbed:

$$Q_h = k\,\Delta T + S\,T_h\,I - \frac{1}{2}\,I^2\,R_{int} \tag{6}$$

Q_c is the amount of heat released:

$$Q_c = k\,\Delta T + S\,T_c\,I + \frac{1}{2}\,I^2\,R_{int} \tag{7}$$

$$P_{out} = S.I\,(T_h - T_c\,) - I^2\,R_{int} \tag{8}$$

The TEG output power can be determined according to Joule heating law ($P_{out} = I^2.\ R_{load}$), and Eq. 9 is obtained when the previously calculated current value is substituted.

$$P_{out} = I^2.\ R_{load} = \left(\frac{S\,(\,T_h - T_c\,)}{R_{load}+\,R_{int}}\right)^2 R_{load} \tag{9}$$

The geometric structure of the thermoelectric legs that compose the TEM is an important factor in calculating the internal resistance value and in terms of the electrical potential produced. The dimensions of thermoelectric legs in the model we designed is shown in Fig. 2. TEG is created with a total of 48 TEMs with these dimensions.

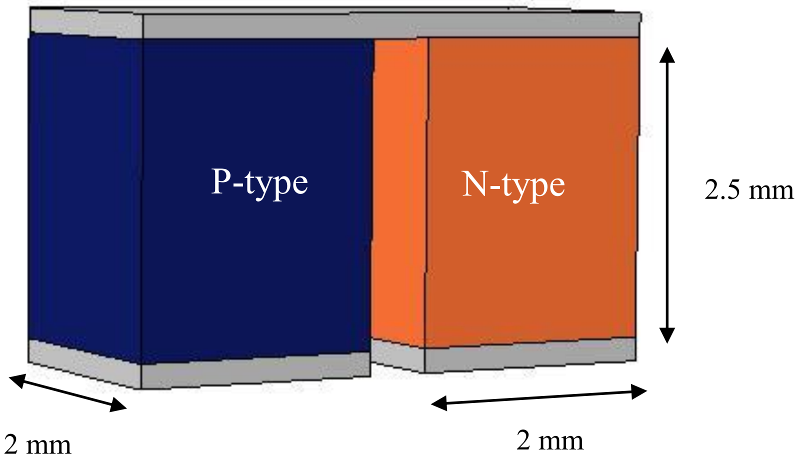

Fig. 2. Presentation of the dimensions of the thermoelectric legs at COMSOL Multiphysics.

Another important parameter in TEM design is material properties. Especially since the thermoelectric legs are effective in the realization of energy conversion, it is necessary to pay attention to the material used. Semiconductors are the material class that is frequently preferred in the design of thermoelectric devices because they cause better results in energy conversion than other material classes. In this model, bismuth telluride (Bi_2Te_3), which is used at not very high temperature values, was used for thermoelectric legs. In addition, copper (Cu) was chosen for the electrode and alumina (Al_2O_3) as the insulator material. The properties of these materials that compose the TEM is shown in Table 1.

Table 1. Properties of materials that compose TEM [11].

Material properties	Al_2O_3	Cu	Bi_2Te_3 (p-type)	Bi_2Te_3 (n-type)
C_p (J/kg.K)	900	385	154	154
k (W/K.m)	27	400	1.6	1.6
ρ (kg/m^3)	3900	8960	7700	7700
γ (S/m)	–	5.9×10^8	0.8×10^5	0.8×10^5
S (V/K)	–	6.5×10^{-6}	2.1×10^{-4}	-2.1×10^{-4}

In order to provide the temperature difference, the TEG is placed between two channels through which cold and hot fluid flows. Air flows as hot fluid, water and water-based Ag/MgO hybrid nanofluid (volume fraction of 0.02) flow as cold fluid. Three different TEG system models are designed. In Model 1, three TEGs of the same size are placed equidistantly between the channels. In Model 2, 2 TEGs of the same size were placed between the channels and lastly, only one TEG was used in Model 3. Channel dimensions are the same in each designed model. Fig. 3 shows the schematic view of the designed models and the TEG modeled in COMSOL Multiphysics.

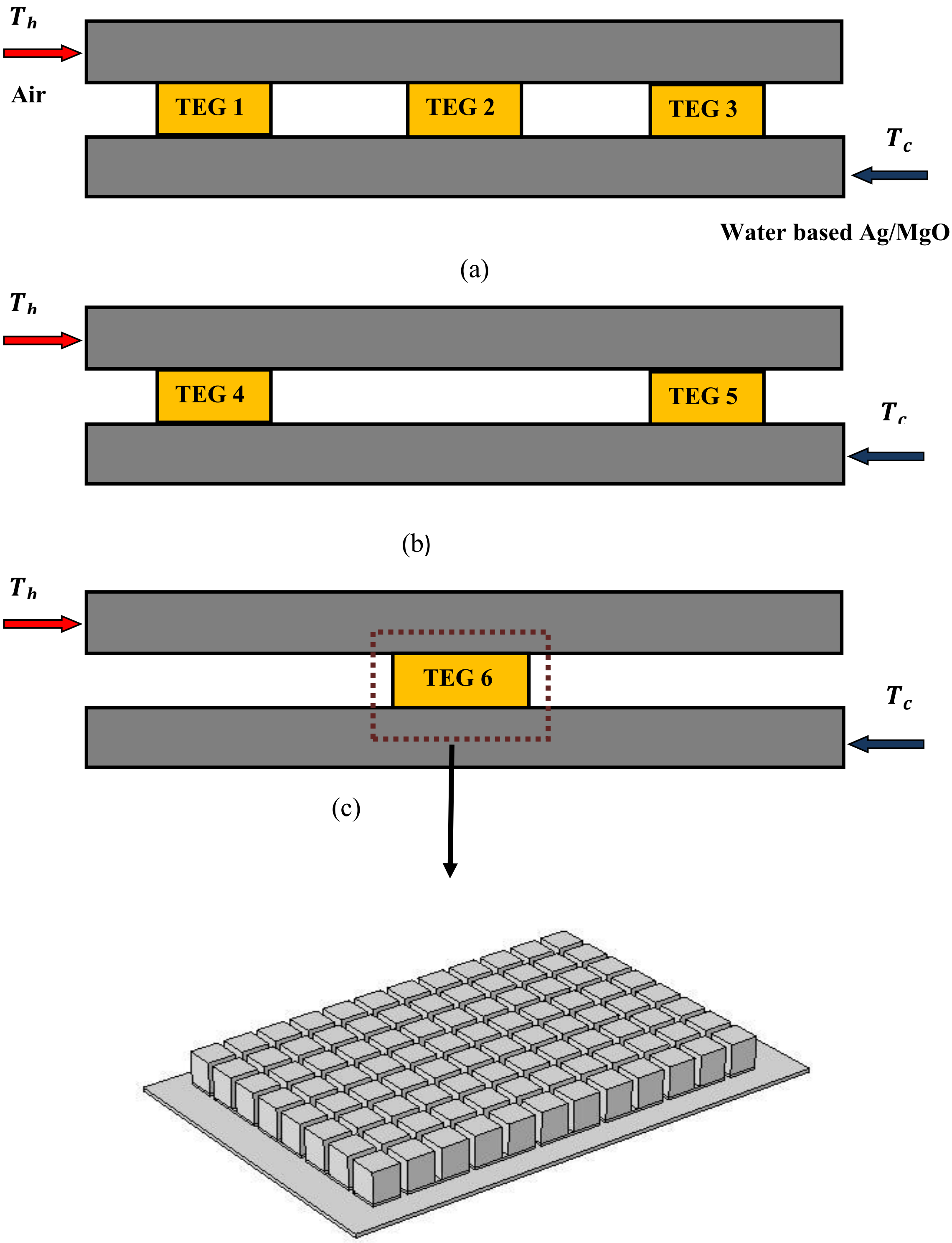

(d)

Fig. 3. Schematic representation of (a) Model 1, (b) Model 2, (c) Model 3 and (d) TEG modeled in COMSOL Multiphysics.

Nanofluid is a fluid class obtained by the suspension of solid particles with high thermophysical properties in the base fluid. By utilizing the high thermal properties of materials such as metals and metal oxides, nanofluids have been created and they have gained superiority over conventional fluids [12]. This new type of fluid, which is encountered in many fields, has allowed progress to be made especially on the performances of energy systems. With this situation, studies on their development have accelerated and their diversity have been increased with different particle-fluid combinations. Studies have taken a different approach to nanofluid by creating fluids, called hybrid nanofluids, that perform better with two or more different types of particles rather than a single solid particle. The thermal properties of the selected solid particles are an important factor in obtaining hybrid nanofluids. The hybrid nanofluid formed with silver (Ag) and MgO exhibited good heat transfer properties in previous studies, so it was used as a refrigerant in this study. The **Table 2** shows the material properties used to determine the thermophysical properties of the water-based Ag/MgO hybrid nanofluid.

Table 2. Thermophysical properties of the materials that compose the hybrid nanofluid [13].

Material properties	Ag	MgO	Water
ρ (kg/m^3)	3560	10.500	997.1
C_p (J/kg.K)	235	955	4179
k (W/K.m)	45	429	0.613
μ (kg/m.s)	–	–	8.98×10^{-4}

Using Table 2, the thermophysical properties of the water-based Ag/MgO hybrid nanofluid is obtained by the following equations [14,15].

The thermal conductivity of water-based Ag/MgO hybrid nanofluid,

$$k_{hnf} = \left(\frac{0.1747\times10^5+\varphi}{0.1747\times10^5-0.1498\times10^6\varphi+0.1117\times10^7\varphi^2+0.1997\times10^8\times\varphi^3}\right) k_{bf} \tag{10}$$

where k_{bf} is the thermal conductivity of water and φ is the total volume fraction. Ag and MgO has equal volume fraction. Dynamic viscosity value of hybrid nanofluid,

$$\mu_{hnf} = (1+ 32.795\varphi - 7214\varphi^2 + 714600\varphi^3 - 0.1941 \times 10^8 \varphi^4)\, \mu_{bf} \tag{11}$$

In calculating the heat capacity and density values of nanofluids, these properties of solid particles and water, along with particle volume fractions are used. φ_1 and φ_2 represent the volume fractions of Ag and MgO, and accordingly the density and heat capacity of the water-based hybrid nanofluid;

$$\rho_{hnf} = (1-\varphi)\rho_{bf} + (1-\varphi_1)\, \rho_{Ag} + (1-\varphi_2)\, \rho_{MgO} \tag{12}$$

$$(\rho C_p)_{hnf} = (1-\varphi)\, \rho_{bf}(C_p)_{bf} + (1-\varphi_1)\, \rho_{Ag} C_{P,Ag} + (1-\varphi_2)\, \rho_{MgO} C_{P,MgO} \quad (13)$$

In the process where TEG performs the conversion of heat to electrical energy, equations including thermoelectric effects are developed under steady-state conditions. Governing equations in the process of TEG's energy conversion [16,17]:

Conservation of energy for TEG,

$$\nabla\,(k.\nabla T) + \frac{C^2}{\gamma} - T.C.\,\nabla S = 0 \quad (14)$$

where C is the current density and continuity equation for a constant current,

$$\nabla.C = 0 \quad (15)$$

The electric field affected by the current flow,

$$E = \gamma.C + S.\nabla T \quad (16)$$

Heat flow can be affected by electrical field and temperature difference. The heat flux density obtained by the Thomson relationship,

$$q = P.C - k\nabla T \quad (17)$$

P is the Peltier coefficient,

$$P = S.T \quad (18)$$

$$C = \gamma\,(E - S.\nabla T) \quad (19)$$

The relationship between E and V in the absence of a magnetic field is;

$$E = -\nabla V \quad (20)$$

For fluids in the channel, the momentum conservation equation is [18]:

$$\rho\,(v.\,\nabla)\,v = \nabla\,[-P + \mu\,(\nabla v + (\nabla v)^T) - \frac{2}{3}\mu\,(\nabla.v)\,I\,] + F \quad (21)$$

Continuity equation;

$$\nabla.(\rho\, v) = 0 \quad (22)$$

Energy equation;

$$\rho\, C_p.\, v.\nabla\, T + \nabla.(-k.\,\nabla T) = Q \quad (23)$$

3. ANALYSIS OF THE TEG SYSTEM

The electrical potential and output power of three TEG system models placed between two channels and provided by the temperature difference fluid flow were analyzed. In Model 1, three TEGs are mounted equidistantly between the two channels. In Model 2, two TEGs were used and in Model 3, only one TEG was placed in the middle of the channels. Channel and TEG dimensions are the same in each designed model. Air flow occurs in the upper channel at a temperature of 363.15 K. Water and water-based Ag/MgO hybrid nanofluid at 293.15 K temperature were used separately in the lower channels and their effects on TEG were investigated. The hybrid nanofluid has a volume fraction of 0.02. In addition, hot and cold fluids are handled in five different Reynolds numbers as 300, 600, 900, 1200 and 1500. Hot and cold fluids entered from different sides of the channels. TEG 1 positioned on the side where the hot air inlet occurs, TEG 2 placed in the middle of the channel, and TEG 3 mounted at the point where the cold fluid inlet is located was investigated separately.

The heat transfer properties of fluids vary with different Reynolds numbers. Therefore, TEG 1, TEG 2 and TEG 3 is affected by this varying thermal performance. Fig. 4 is shown the temperature distribution on TEG 1, TEG 2, and TEG 3 with water-based Ag/MgO nanofluid when Reynolds numbers 900 and 1500.

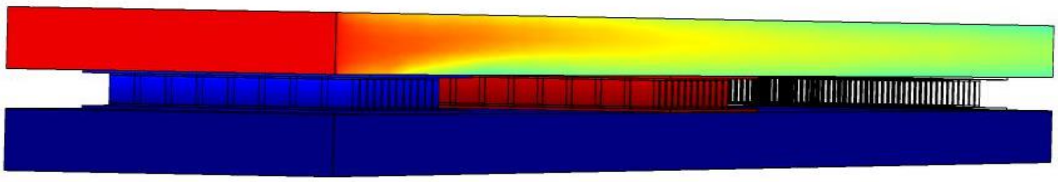

(a)

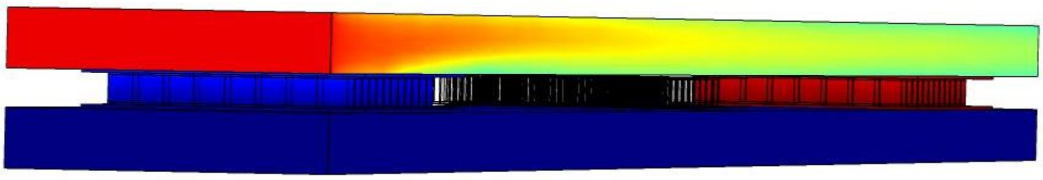

(b)

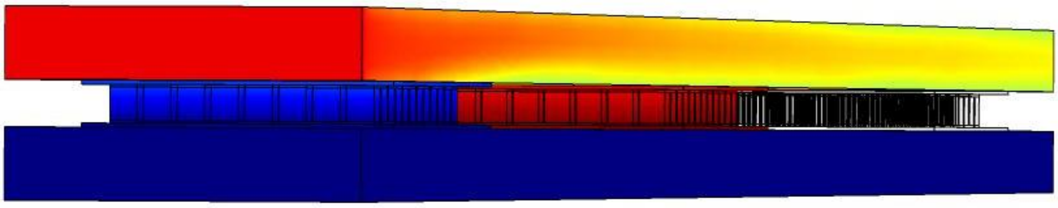

(c)

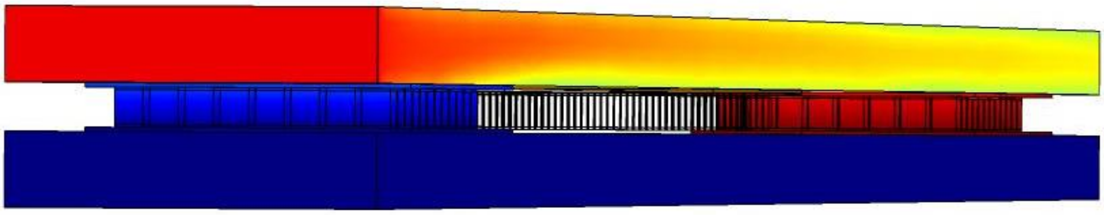

(d)

Fig. 4. Temperature distributions of TEG 1, TEG 2 and TEG 3 when Reynolds number is 900 (a)-(b), (c)-(d) 1500.

When water with Reynolds number of 1500 was used as the cold fluid, the electrical potential produced by TEG 1, TEG 2 and TEG 3 was found to be 0.217 V, 0.202 V and 0.193 V, respectively. The electrical potential generated by TEG 1 reached a higher value of 7.42% and 12.43%, respectively, compared to TEG 2 and TEG 3. The TEG 1 output power is calculated at a higher value of 15% and 25%, respectively, compared to TEG 2 and TEG 3. When the Reynolds number is taken as 1500, the electrical potential produced by TEG 1, TEG 2 and TEG 3 in the use of water is shown in Fig. 5.

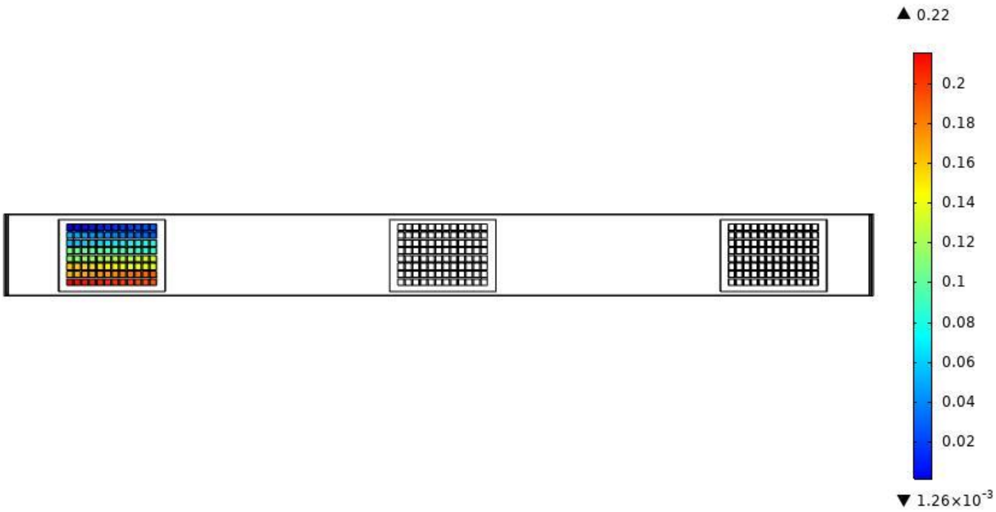
▲ 0.22
0.2
0.18
0.16
0.14
0.12
0.1
0.08
0.06
0.04
0.02
▼ 1.26×10⁻³

(a)

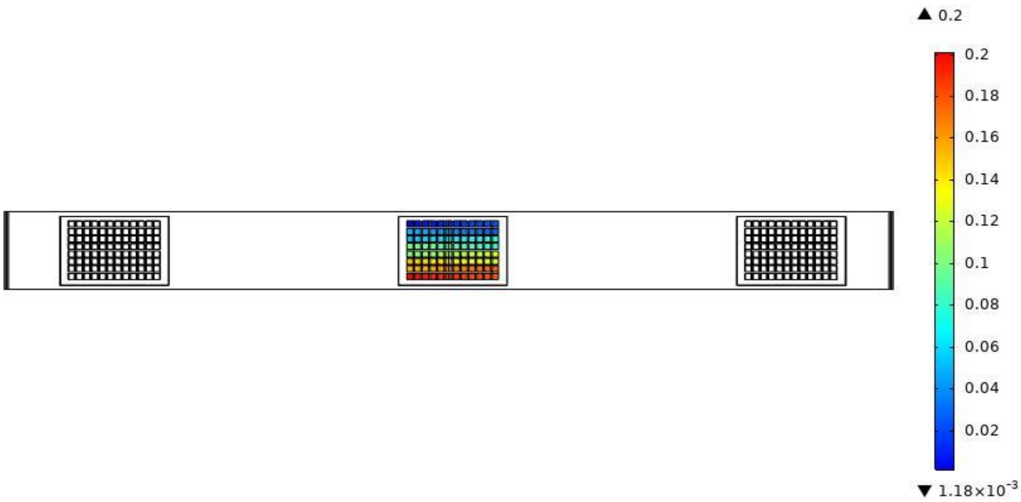
▲ 0.2
0.2
0.18
0.16
0.14
0.12
0.1
0.08
0.06
0.04
0.02
▼ 1.18×10⁻³

(b)

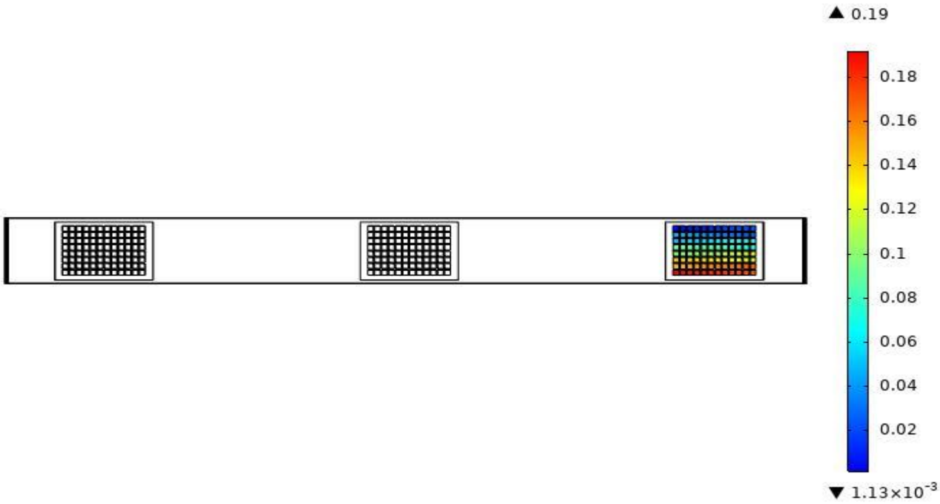

(c)

Fig. 5. Electrical potential generated by (a) TEG 1, (b) TEG 2 and (c) TEG 3 when water used at Reynolds number of 1500.

At the same Reynolds number, when water-based Ag/MgO hybrid nanofluid was used instead of water, the electrical potential produced by TEG 1, TEG 2 and TEG 3 were calculated as 0.22 V, 0.203 V and 0.193 V, respectively. The electrical potential generated by TEG 1 increased by 8.4% and 14% compared to TEG 2 and TEG 3, and the output power of TEG 1 increased by 17.5% and 30%, respectively, compared to TEG 2 and TEG 3. When the Reynolds number is taken as 1500, the electrical potential produced by TEG 1, TEG 2 and TEG 3 in the use of water-based Ag/MgO hybrid nanofluid is shown in Fig. 6.

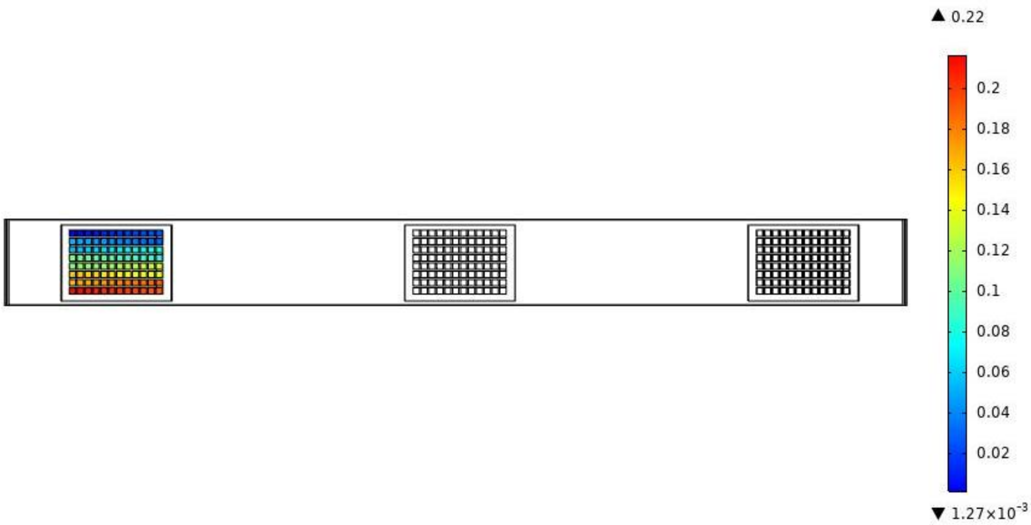

(a)

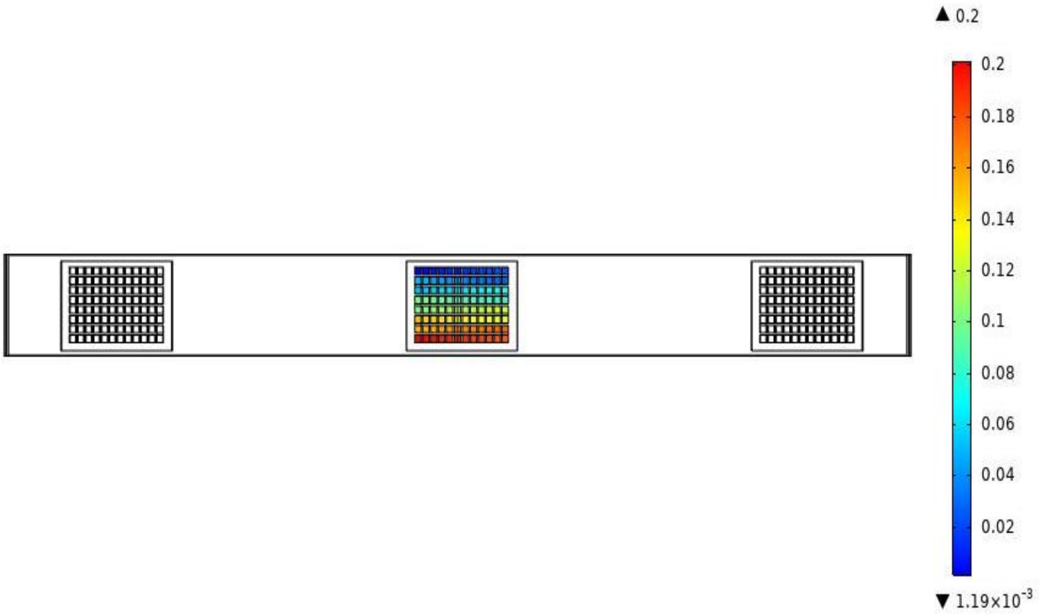

(b)

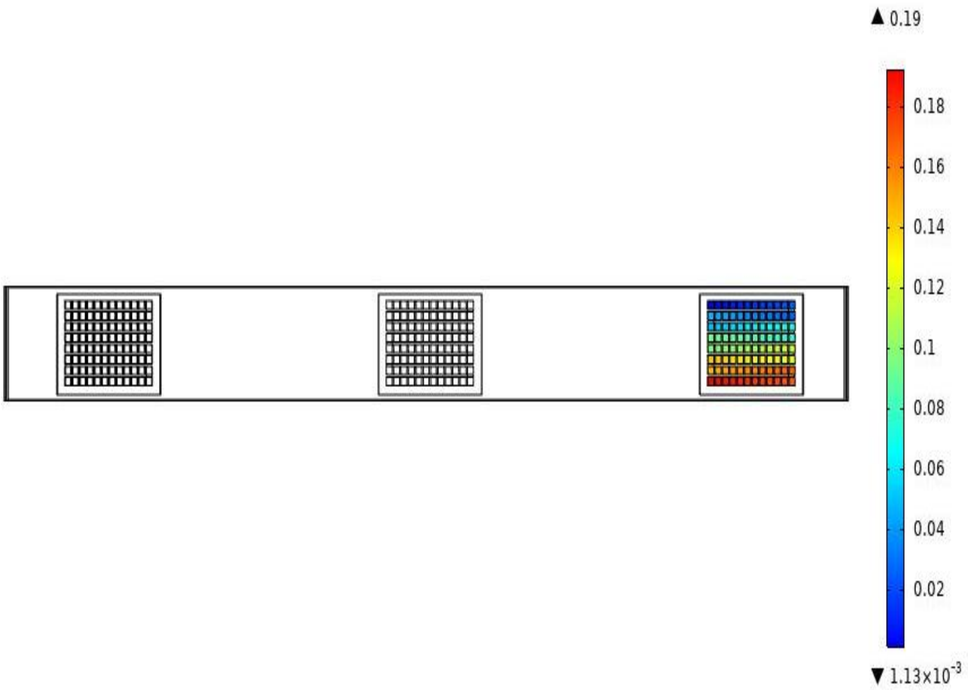

(c)

Fig. 6. Electrical potential generated by (a) TEG 1, (b) TEG 2 and (c) TEG 3 when water based Ag/MgO hybrid nanofluid used at Reynolds number of 1500.

For example, while the electrical potential produced by TEG 2 is 0.18 V in the model using Ag/MgO hybrid nanofluid with a Reynolds number of 1200, the electric potential is calculated as 0.122 V at the 600 Reynolds number. The output power of TEG 1, TEG 2 and TEG 3 was calculated for water and water-based Ag/MgO hybrid nanofluid at five different Reynolds number (300,600,900,1200,1500). Fig. 7 shows the TEG output powers obtained with water and Ag/MgO nanofluid depending on the Reynolds number.

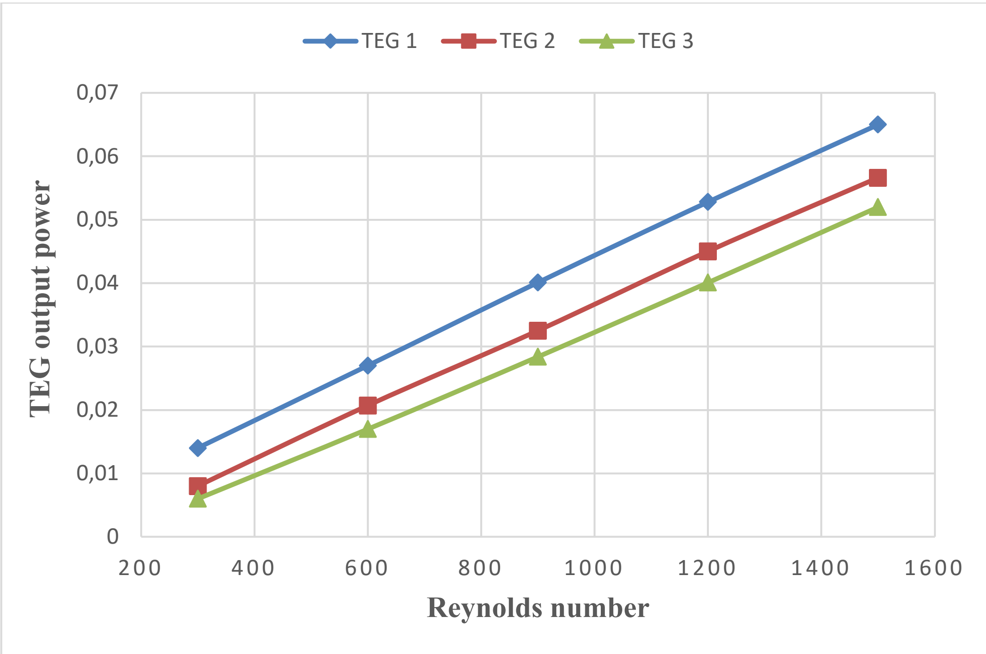

(a)

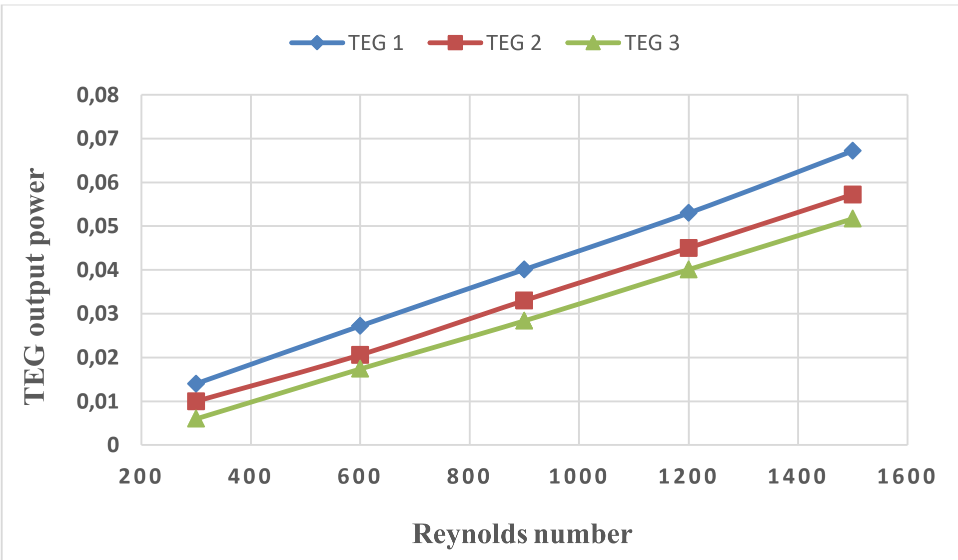

(b)

Fig. 7. TEG output powers obtained with water (a) and water-based Ag/MgO (b) at varying Reynolds number.

The two TEGs used in Model 2 were placed near the entrance of the fluids into the channel. The electrical potential and output power of TEG 4, which is mounted near the hot air inlet, and TEG 5, which is placed at the point where the cold fluid inlet takes place, were investigated. First, the temperature distribution of the model used Ag/MgO nanofluid with different Reynolds number was obtained to observe the effect of Reynolds number on heat transfer. Fig. 8 shows the temperature distribution on TEG 4 and TEG 5 in the use of Ag/MgO nanofluid, when taking Reynolds numbers 600 and 1200.

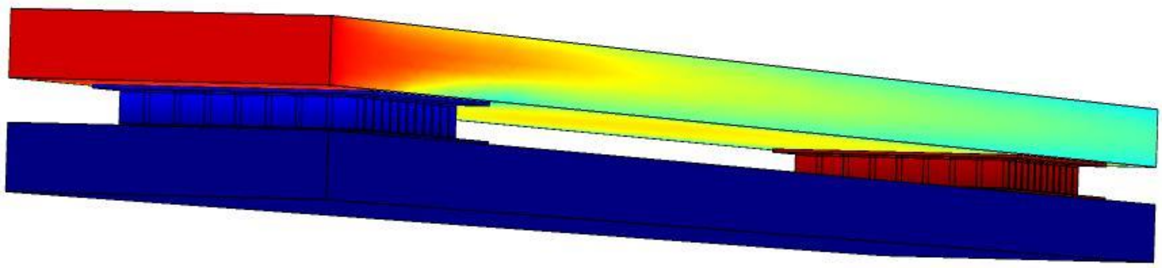

(a)

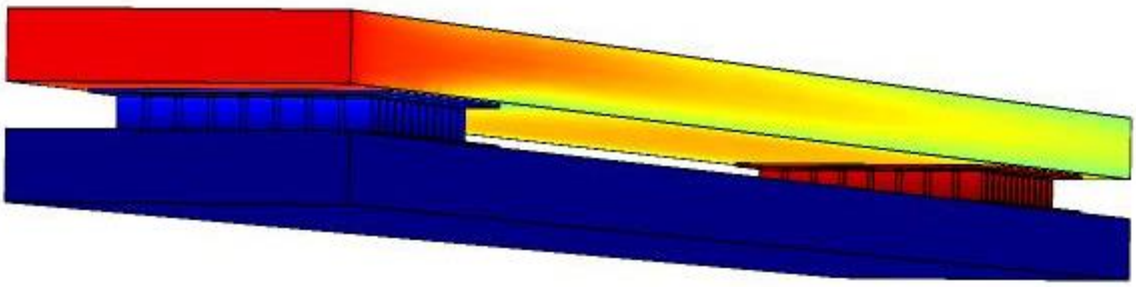

(b)

Fig. 8. Temperature distributions of TEG 4 and TEG 5 when Reynolds number is 600 (a), 1200 (b).

In this model, the use of water-based Ag/MgO hybrid nanofluid did not show any significant improvement on the system. Almost the same results were obtained with the use of water and nanofluid. Therefore, the model was analyzed only for the use of water-based Ag/MgO hybrid nanofluid. TEG 4 produced 17.2% higher electrical potential and 37.5% higher output power compared to TEG 5. Fig. 9 shows the electrical potential produced by TEG 4 and TEG 5 in use of nanofluid at Reynolds number 1500.

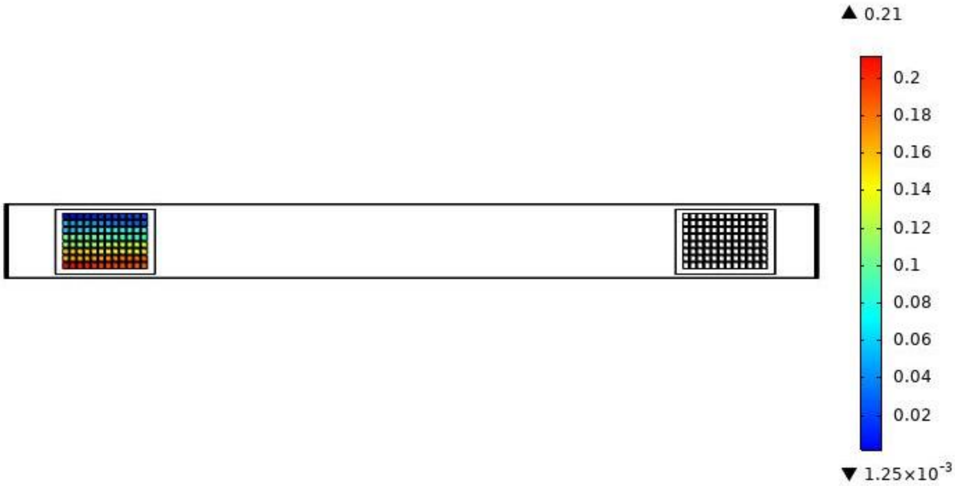

(a)

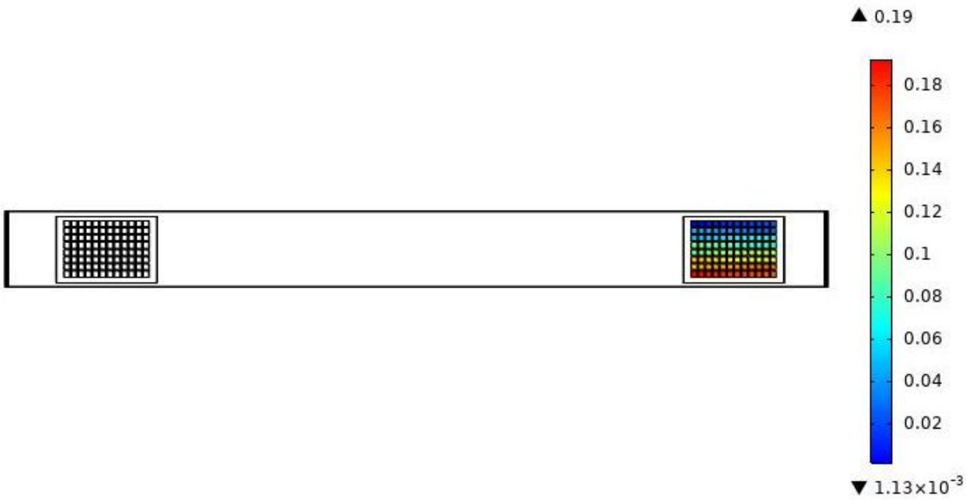

(b)

Fig. 9. Electrical potential produced by TEG 4 (a) and TEG 5 (b) in use of water based Ag/MgO hybrid nanofluid when Reynolds number 1500.

It is known that changing Reynolds number affects TEG output power. The Reynolds number affects the heat transfer of the fluids and causes changes on the TEG output power. Fig.

9 presents the output power of TEG 4 and TEG 5 depending on the Reynolds number. In such a system, an increase of approximately 4% in TEG output power was observed with the use of Ag/MgO nanofluid instead of water at 1500 Reynolds number.

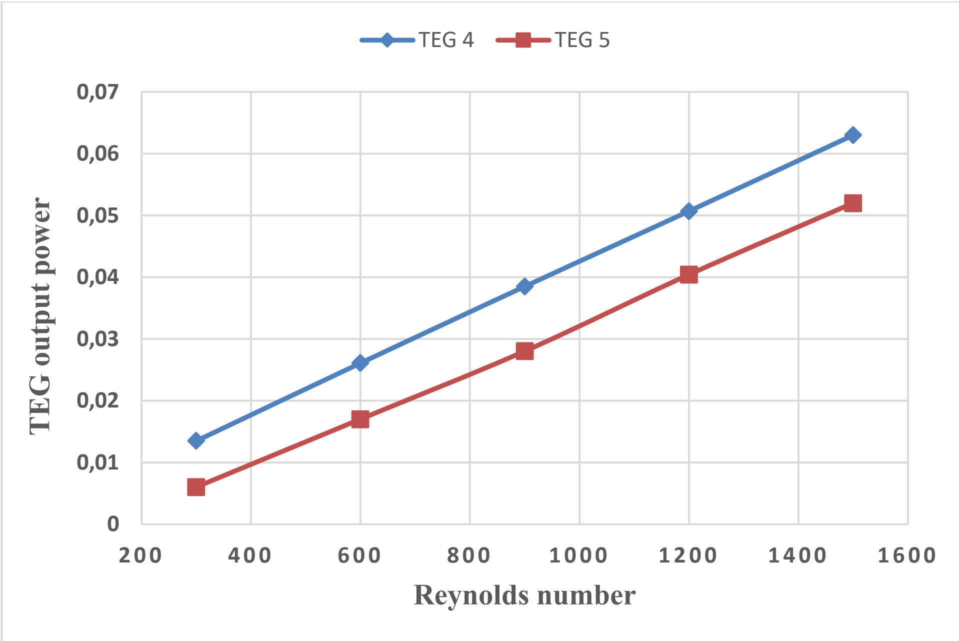

Fig. 10. TEG output power in Ag/MgO nanofluid model dependent on Reynolds number.

Finally, TEG 6 placed in the middle position of the channels is discussed. The highest electrical potential value was obtained in this model. However, like other models, the use of nanofluid did not lead to major changes in system performance. In the use of 1500 Reynolds number water, the electrical potential value produced by TEG 6 was 0.247 V, while it was calculated as 0.25 V with nanofluid. The Reynolds number affected the heat dissipation, but there were no significant differences between nanofluid and water usage. Fig. 11 shows the temperature distribution for TEG 6 when using a water-based Ag/MgO nanofluid with Reynolds numbers of 600 and 1500.

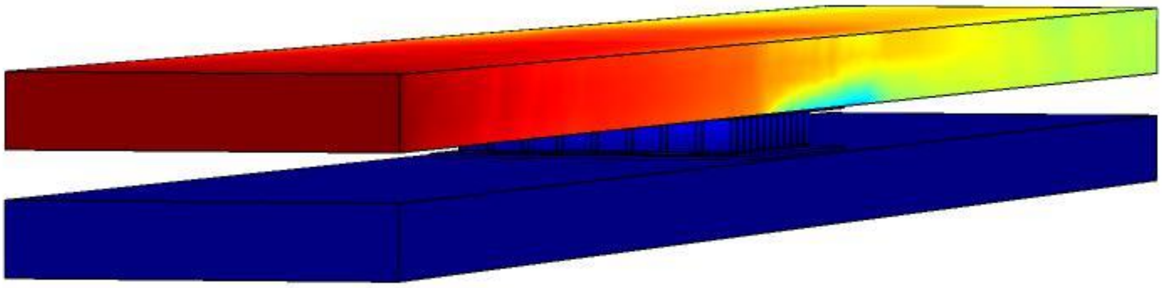

(a)

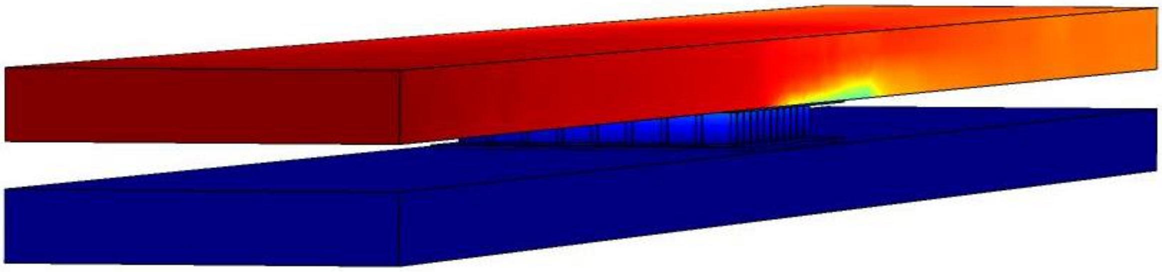

(b)

Fig 11. Temperature distributions TEG 6 when Reynolds number is 600 (a), 1500 (b).

Compared to TEG 2, which was previously located at the same coordinates, TEG 6 achieved a higher electric potential value. TEG 6 was able to reach higher electrical potential values when the heat transfers due to the fluid flow of TEG 1 and TEG 3 did not occur. This did not affect TEG 4 and TEG 5 in Model 2, which were located at the same coordinates as TEG 2 and TEG 3 in Model 1. When water is used in the TEG 6 system with a Reynolds number of 1200, the electrical potential value of 0.213 V, which is 18.3% higher, was calculated compared to the TEG 2 under the same conditions. When the nanofluid models under the same conditions are evaluated, TEG 6 has a higher electrical potential of approximately 19% (0.214 V) compared to TEG 2.The TEG 6 electrical potential obtained with a water-based Ag/MgO hybrid nanofluid at 1500 Reynolds number is shown in Fig. 12. TEG 6 output power obtained with water and water-based Ag/MgO hybrid nanofluid at 1500 Reynolds number was calculated as 0.085 W and 0.0868 W, respectively.

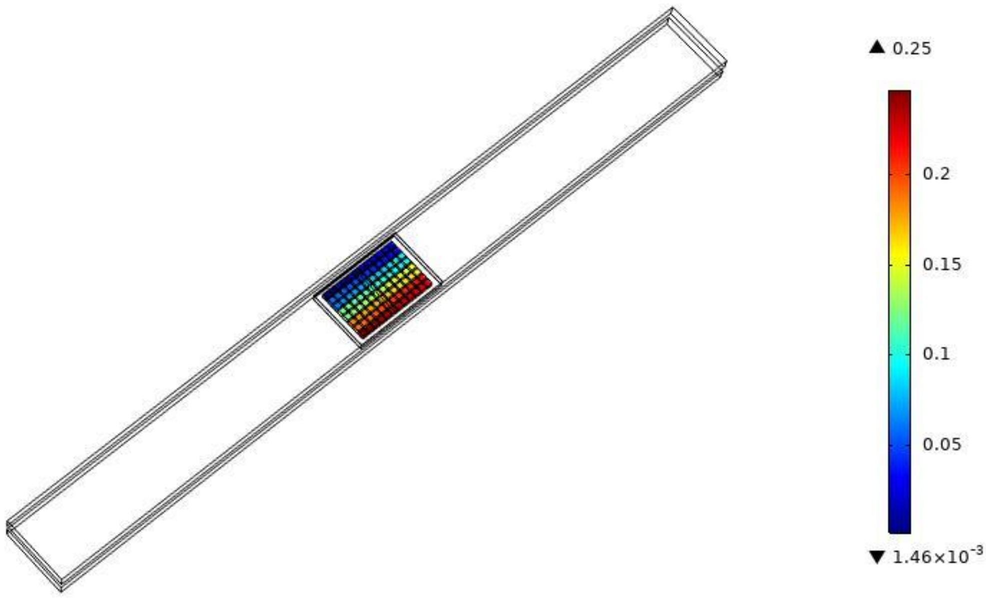

Fig. 16. TEG 6 electrical potential obtained with a 1500 Reynolds number water-based Ag/MgO hybrid nanofluid.

In previous studies, the use of water-based Ag/MgO instead of water allowed improvements on TEG performance.

4.CONCLUSIONS

In this study, when three different TEG system models (Model 1, Model 2 and Model 3) are examined while water and water-based Ag/MgO hybrid nanofluid (volume fraction of 0.02) are used as the coolant, and air is used as the hot fluid. Three TEGs with equal distances between the channels in Model 1, two TEGs close to the entrance of hot and cold fluids into the channel in Model 2, and one TEG in Model 3 are placed in the middle of the channels. TEG and channel sizes are the same. As a result of the analysis, the following conclusions are obtained:

- In Model 1, when water-based Ag/MgO hybrid nanofluid with Reynolds number of 1500, the electrical potential produced by TEG 1 (close to the hot fluid inlet), TEG 2 (in the middle of the channels) and TEG 3 (close cold fluid inlet was found to be 0.22 V, 0.203 V and 0.193 V, respectively.
- In Model 1, when using water with a Reynolds number of 1500, the TEG 1 output power is calculated to be 15% and 25% higher compared to TEG 2 and TEG 3, respectively. With the use of water-based Ag/MgO nanofluid under the same conditions, TEG 1

output power was calculated as 17.5% and 35% higher than TEG 2 and TEG 3, respectively.

- The increase in the Reynolds number also resulted in an increase in the electric potential produced by the TEG. For example, in Model 2, in the use of water-based Ag/MgO nanofluid, the TEG 4 (close to the hot fluid inlet), electrical potential was calculated as 0.1664 V when the Reynolds number was 900, and 0.191 V when the Reynolds number was taken as 1200.
- When using 1200 Reynolds number water-based Ag/MgO in Model 2, the output power of TEG 4 was calculated as 37.7% higher than TEG 5 (close to the hot fluid inlet).
- The highest electrical potential and output power value was achieved with TEG 6 used in Model 3. The electrical potential produced by the TEG with the nanofluid at 1500 Reynolds number is 0.25 V.
- The use of water-based Ag/MgO hybrid nanofluid instead of water did not show a significant increase over TEG systems.

REFERENCES

1. Selimefendigil, F., & Öztop, H. F. (2020). Identification of pulsating flow effects with CNT nanoparticles on the performance enhancements of thermoelectric generator (TEG) module in renewable energy applications. Renewable Energy.
2. Karana, D. R., & Sahoo, R. R. (2018). Effect on TEG performance for waste heat recovery of automobiles using MgO and ZnO nanofluid coolants. Case Studies in Thermal Engineering, 12, 358–364.
3. Ruan, H., Xie, H., Wang, J., Liao, J., Sun, L., Gao, M., Li, C. (2021). Numerical investigation and comparative analysis of nanofluid cooling enhancement for TEG and TEC systems. Case Studies in Thermal Engineering. 101331.
4. Su, N., Zhu, P., Pan, Y., Li, F., & Li, B. (2020). 3D-printing of shape-controllable thermoelectric devices with enhanced output performance. Energy, 116892.
5. Dunham, M. T., Hendricks, T. J., & Goodson, K. E. (2019). Thermoelectric generators: A case study in multi-scale thermal engineering design. Advances in Heat Transfer, 299–350.
6. Sajid, M., Hassan, I., & Rahman, A. (2017). An overview of cooling of thermoelectric devices. Renewable and Sustainable Energy Reviews, 78, 15–22.
7. Jang, E., Banerjee, P., Huang, J., & Madan, D. (2021). High performance scalable and cost-effective thermoelectric devices fabricated using energy efficient methods and naturally occuring materials. Applied Energy, 294, 117006.

8. Soleimani, Z., Zoras, S., Ceranic, B., Cui, Y., & Shahzad, S. (2021). A comprehensive review on the output voltage/power of wearable thermoelectric generators concerning their geometry and thermoelectric materials. Nano Energy, 89, 106325.
9. Abderezzak, B., & Randi, S. (2020). Experimental Investigation of Waste Heat Recovery Potential from Car Radiator with Thermoelectric Generator. Thermal Science and Engineering Progress, 100686.
10. Patil, D. S., Arakerimath, R. R., & Walke, P. V. (2018). Thermoelectric materials and heat exchangers for power generation – A review. Renewable and Sustainable Energy Reviews, 95, 1–22.
11. COMSOL, FEMLAB 3.2 User's Guide, Comsol AB, 2005.
12. Khatai, S., Kumar, R., Sahoo, A. K., Panda, A., & Das, D. (2020). Metal-oxide based nanofluid application in turning and grinding processes: A comprehensive review. Materials Today: Proceedings.
13. Y. Ma, R. Mohebbi, M.M Rashidi, Z. Yang. MHD convective heat transfer of Ag-MgO/water hybrid nanoluid in a channel with active heaters and coolers. International Journal of Heat and Mass Transfer. 2019, 13, 714-726.
14. Ghalambaz, M., Doostani, A., Izadpanahi, E., & Chamkha, A. J. (2019). Conjugate natural convection flow of Ag–MgO/water hybrid nanofluid in a square cavity. Journal of Thermal Analysis and Calorimetry, 139(3), 2321–2336.
15. Mehryan, S. A. M., Ghalambaz, M., Chamkha, A. J., & Izadi, M. (2020). Numerical study on natural convection of Ag–MgO hybrid/water nanofluid inside a porous enclosure: A local thermal non-equilibrium model. Powder Technology.
16. Zhu, W., Deng, Y., Gao, M., Wang, Y., Cui, J., & Gao, H. (2015). Thin-film solar thermoelectric generator with enhanced power output: Integrated optimization design to obtain directional heat flow. Energy, 89, 106–117.
17. Shittu, S., Li, G., Zhao, X., Ma, X., Akhlaghi, Y. G., & Ayodele, E. (2019). High performance and thermal stress analysis of a segmented annular thermoelectric generator. Energy Conversion and Management, 184, 180–193.
18. COMSOL 5.4, Heat Transfer Module User's Guide.

Time Optimal Trajectory Generation in Joint Space for 6R Industrial Serial Robots Using Cuckoo Search Algorithm

Oguzhan KARAHAN, Hasan KARCI, Ali TANGEL

Department of Electronics and Communications Engineering, Kocaeli University, Kocaeli, Turkey

E-mail: oguzhan.karahan@kocaeli.edu.tr, hsnkarci06@gmail.com, atangel@kocaeli.edu.tr

Abstract. In this paper, an optimal trajectory planning approach is proposed based on optimal time by utilizing the interpolation spline method. The method including a combination of cubic spline and 7th order polynomial is used for generating the trajectory in joint space for robot manipulators. Cuckoo Search (CS) optimization algorithm is chosen to optimize the joint trajectories based on objective, namely minimizing total travelling time along the whole trajectory. The spline method has been applied on PUMA robot for optimizing the joint trajectories with the CS algorithm based on objective. Moreover, results from the proposed algorithm have been compared with that of the algorithms suggested by earlier studies. With the trajectory planning method, the joint velocities, accelerations and jerks along the whole trajectory optimized by CS meet the requirements of the kinematic constraints in case of objective. Simulation results validated that the used trajectory planning method based on the proposed algorithm are very effective in comparison with the same methods based on the algorithms proposed by earlier authors.

Keywords: Trajectory planning, Interpolation spline methods, Industrial robots, CS.

1 Introduction

Use of industrial robots in production systems with the development of automation technology has grown tremendously over the past few decades. Especially, the robotic manipulators in industrial assembly lines and production systems are widely used todays due to their ability to achieve particular tasks with improved speed, reliability and quality. In these industrial activities, trajectory planning for industrial robots working in industrial environments is very important issue. Accordingly, the trajectory planning problem in industrial robotic applications has recently attracted great attention of many researchers.

The capability of trajectory planning algorithms is restricted by the time needed for carrying out the trajectory and also by physical limitations of the robot (Rubio, Llopis-Albert, Valero, & Suñer, 2016). Most of the trajectory planning algorithms has proposed an objective function consisting of execution time, actuator effort and absolute value of the jerk for performing certain criterion such as minimum execution time, minimum jerk and minimum kinetic energy consumed by the robot (Bobrow, 1988). The concept of minimum-time trajectory was firstly introduced (Bobrow, Dubowsky, & Gibson, 1985; Shin, & McKay, 1985; Chen, & Desrochers, 1989).

In order to enhance the manufacturing productivity and the movement stability, the trajectory planning with short execution time and smooth profile is required. Spline functions have a major role for improving smooth trajectory to ensure velocity continuity, acceleration continuity or jerk continuity in the motion of industrial robots. Lin, Chang and Luh (1983) constructed joint trajectories for industrial robots using cubic splines based on minimum time trajectory through polyhedron search method. Aribowo and Terashima (2014) proposed a combination of input shaping with cubic spline optimization for generating the minimum time trajectory of the robot arm. Sequential Quadratic Programming (SQP) was used for solving the constrained trajectory planning optimization problem outlined in that paper. Gasparetto and Zanotto (2008) suggested a technique based on B-spline for realizing the jerk continuity in the joint trajectory planning by minimizing of both time and jerk during optimization with the SQP. In (Gasparetto, & Zanotto, 2010), the same authors analyzed the results obtained from running the SQP algorithm based on an objective function comprising a weighted sum of time and jerk using cubic splines and fifth-order B-splines. Liu, Lai and Wu (2013) presented a smooth trajectory planning approach using a combination of the planning with multi-degree splines in Cartesian space and multi-degree B-splines in joint space for robot manipulators with kinematic constraints. In that paper, for solving the minimum execution time problem during optimal trajectory planning, the SQP method was used. Chen and Chen (2019) used the B-spline curve by fitting this curve through an approximation method and then in order to plan the motion trajectory, the intermediate points were interpolated by using S-Curve feed-rate profile for the trajectories of the tool tip and tool axis of a 6-DOF robot manipulator. On the other hand, for the 6-DOF robot manipulator, Perumaal and

Jawahar (2013) presented an automated trajectory planner in order to obtain a smooth and minimum-time trajectory based on the synchronized trigonometric S-Curve trajectory technique with jerk constraints. Moreover, in that paper, suitable examples and comparisons with the cubic spline-based trajectory were demonstrated. With fifth-order B-spline or quantic polynomial spline proposed in (Gasparetto, & Zanotto, 2007; Liu, Chen, Zhao, & Li, 2016), continuous motion in the position, velocity, acceleration and jerk is provided. But, for obtaining the smooth trajectory, the least six coefficients must be solved. Accordingly, computation complexity may arise. To overcome this problem, Boryga and Graboś (2009) designed a trajectory planning mode with high-degree polynomial for serial link manipulators. In that paper, the acceleration profile of the tool-tip was planned by means of the determination of only one polynomial coefficient using the property of the root multiplicity.

Recently, interpolation functions have been utilized for generating a trajectory under kinematical or dynamical constraints in joint space for industrial robots. In the literature on the trajectory planning problem, the optimal motion planning for robotic manipulators can be considered as an optimization problem applied to the nature inspired optimization algorithms using an objective function for minimizing execution (travelling) time. Several natures inspired optimization algorithms developed by researchers have been successfully applied to the trajectory optimization for industrial robots.

Machmudah et al. (2013) employed the GA and Particle Swarm Optimization (PSO) algorithms by minimizing the total travelling time and the torque under kinematic and dynamic limitations in order to find the feasible joint trajectory with the high degree polynomial curve for robotic arm in the obstacle environment. For a space robotic system composing of the 6-DOF space craft and the 7-DOF redundant manipulator, Wang et al. (2018) employed PSO to find the optimal solutions using the execution time criterion to construct fifth-order Bèzier curve in joint space under the velocity and acceleration boundaries. Kucuk (2018) developed a minimum time smooth motion trajectory in joint space by combining cubic spline with the 7th order polynomial for serial and parallel manipulators. Savsani et al. (2013) employed the TLBO and ABC algorithms by minimizing travelling time, travelling distance and total joint Cartesian lengths for planning point to point trajectory in joint space with high order polynomial spline for a 3-DOF robotic arm. In (Savsani et al., 2016), the same authors presented a comparative study of the proposed heuristic solution approaches for planning the trajectories in joint space based on high order polynomial spline by minimizing three different objective functions for a 3-DOF robotic arm. Wang et al. (2018) presented an optimal joint trajectory planning method using DE algorithm with specific objectives under kinematic limitations through Bèzier curve for a 7-DOF kinematically redundant manipulator. Bureeat et al. (2019) proposed the robot optimum trajectory planning in joint space via the five-order polynomial function for a 6-DOF robot. In that paper, for the robot optimum trajectory planning, the hybrid real code population based on incremental learning and DE was used based on the two objective functions as minimizing trajectory time and jerk under kinematic constraints of all joints.

Motivated by the above-mentioned studies, the central objective of this work is to present a comparative study of the S-curve profiles based on interpolation splines, i.e., the combination of cubic spline and 7th order polynomial model for point-to-point movements. For obtaining the optimal trajectory from initial to intermediate positions and from intermediate to final position in joint space under kinematic constraints, the CS based optimization algorithm is employed by minimizing the objective function, namely, travelling time objective function. Considering the concept of planning the trajectory optimization addressed in aforementioned works, the main contributions of this study are: (I) to provide independent comparison of the used interpolation methods for solving optimal joint trajectory planning problem, (II) to present the values of maximum joint velocities, accelerations, jerks generated by the used methods for each joint trajectory, (III) to demonstrate the maximal values of all kinematic variables of each joint along the path segments according to the combination of cubic spline and 7th order polynomial, (IV) to compare the obtained results with that of the other optimization algorithms proposed in the literature based on the same interpolation method for each joint along the path from initial to the final point.

The rest of the paper is organized as follows: Section 2 describes the problem statements, Section 3 introduces trajectory planning approaches, Section 4 explains the used optimization algorithms. In Section 5, implementation of methodology is presented. Some design examples for the proposed theory and simulation results are given in Section 6 and Section 7 comprises of the discussion and conclusion.

2 Problem Statements

Trajectory planning for industrial robots can be specified either in Cartesian space or joint space. The trajectory in Cartesian space can be constructed based on a set of consecutive intermediate points between the start and end points. In view of the kinematic and dynamic constraints imposed to the robot joints, complex modelling and heavy mathematical computations appear in Cartesian space, but trajectory planning in joint space is not the case. Therefore, planning a trajectory in joint space is preferred rather than trajectory planning in Cartesian space. By solving the inverse kinematic problem related to via-points determined in the Cartesian space, the corresponding counterparts in joint space can be found. Thus, a suitable trajectory is generated between two consecutive points under kinematic constraints such as displacement, velocity, acceleration and jerk.

In joint trajectory planning between the start position and the final position, the motion constraints specified in datasheet of the robot manipulator must be considered for each joint. Kinematic constraints for each joint in trajectory planning are defined as:

$$\begin{cases} |\theta_j(t)| \le \theta_j^{max}, j = 1, \dots, N \\ |\dot{\theta}_j(t)| \le \dot{\theta}_j^{max}, j = 1, \dots, N \\ |\ddot{\theta}_j(t)| \le \ddot{\theta}_j^{max}, j = 1, \dots, N \\ |\dddot{\theta}_j(t)| \le \dddot{\theta}_j^{max}, j = 1, \dots, N \end{cases} \tag{1}$$

In the trajectory planning, it is expected that smooth motion trajectory is generated by minimizing mechanical vibration and travelling time for achieving greater productivity with applying simultaneously kinematic limitations. The optimization problem is solved under kinematic constraints given above by minimizing the equation defined as follows:

$$f = \sum_{i=1}^{n} h_i \tag{2}$$

As can be observed from the objective function given above, the total duration of the trajectory is aimed to be minimized by function f. The symbol explanations aforementioned equations above are presented in Table 1.

In this work, the trajectory planning is applied between any pair of consecutive intermediate points based on minimization of objective function given above. Also, in order to apply the optimization algorithm, spline functions such as cubic spline, high order polynomial spline for the interpolation are chosen.

Table 1. Meaning of symbols in the optimization formulations.

Symbol	Meaning	Symbol	Meaning
N	Number of robot joints	$\dot{\theta}_j(t)$	Velocity of the j^{th} joint
n	Number of segments	$\ddot{\theta}_j(t)$	Acceleration of the j^{th} joint
h_i	Time interval between the i^{th} via-point and $(i+1)^{th}$ via-point	$\dddot{\theta}_j(t)$	Jerk of the j^{th} joint
t_f	Total travelling time of the trajectory	θ_j^{max}	Displacement constraint for the j^{th} joint
K_t	Weight of the term proportional to the travelling time	$\dot{\theta}_j^{max}$	Velocity constraint for the j^{th} joint
K_j	Weight of the term proportional to the jerk	$\ddot{\theta}_j^{max}$	Acceleration constraint for the j^{th} joint
$\theta_j(t)$	Displacement of the j^{th} joint	$\dddot{\theta}_j^{max}$	Jerk constraint for the j^{th} joint

3 Trajectory Planning Approach

The trajectory planning of the robot manipulator is usually based on the movement of the end effector in Cartesian space. Accordingly, from the points specified in Cartesian space, the displacements in Joint space can be calculated by using the inverse kinematics. Consequently, the joint displacement calculated by the inverse kinematics constitutes the trajectory of the motion between given points within the determined time. For obtaining smooth and continuous movements between these via points in Joint space of the robot manipulator, the appropriate interpolation splines are used. For this study, the spline functions widely used in trajectory planning are outlined in the following sections.

3.1 Cubic splines

For trajectory interpolation, the cubic spline is frequently used in the trajectory planning methods due to its easy and fast mathematical calculation. Also, it can produce continuous velocity and acceleration at every via-point (Kolter, & Andrew, 2009). In Cartesian space, intermediate points are kinematically defined between start and end points. By means of inverse kinematics, these nodes defined in Cartesian space are converted into Joint space. In Figure 1, the motion trajectory consisting of multiple segments is planned with the cubic spline for each joint. The trajectory in Joint space with n cubic segments has $n+1$ prespecified joint angles (Kucuk, 2016). In Figure 1, the generic component θ_j^i represents the angle value of the j^{th} joint at the i^{th} via-point and h_i denotes the length of time interval $t_{i+1} - t_i$.

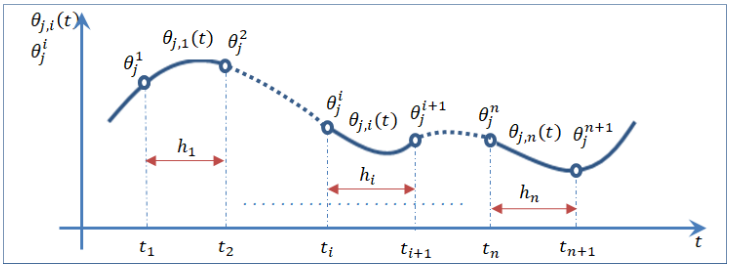

Figure 1. Cubic spline interpolation of the via-points in the joint trajectory.

The cubic spline piecewise polynomials can be given as follows:

$$\theta_{j,i}(t) = a_{j,i}(t - t_i)^3 + b_{j,i}(t - t_i)^2 + c_{j,i}(t - t_i) + d_{j,i} \qquad j = 1,2, \ldots, N \text{ and } i = 1,2, \ldots, n+1 \tag{3}$$

where the i^{th} cubic polynomial function for the j^{th} joint is shown by $\theta_{j,i}(t)$ with the time interval h_i. The coefficients of the cubic polynomial function are a_i, b_i, c_i and d_i. By taking the first and the second derivatives of the cubic polynomial function, the velocity and acceleration of the joint j^{th} at each via-point can be obtained.

3.2 Higher order polynomial splines

In trajectory planning, it is possible to generate the smooth path and to improve the movement stability interpolating the trajectory by means of a reasonable order polynomial function. The smooth trajectory can be achieved by obtaining the continuity of acceleration and jerk. At the beginning and ending points, cubic polynomial curve provides continuous displacement, velocity and acceleration; but this curve does not support the continuity of the jerk. Hence, this case may cause vibrations especially at the initial and the rest points. Accordingly, accurate trajectory may be reduced by this discontinuous jerk. At the beginning and ending of the trajectory, zero velocity, acceleration and jerk are desired especially by the robot designers for obtaining the faster and more accurately trajectory. It is possible to specify zero jerk at the start and end points of the trajectory by using 5th, 7th and 9th order polynomials. As examined the study in (Boryga, & Graboś, 2009), among these polynomials, minimum jerk trajectory in terms of linear and angular motion are provided with the 7th order polynomial.

The 7th order polynomial used to describe the joint displacement profile can be written as

$$\theta(t) = a_7(t - t_0)^7 + a_6(t - t_0)^6 + a_5(t - t_0)^5 + a_4(t - t_0)^4 + a_3(t - t_0)^3 + a_2(t - t_0)^2 + a_1(t - t_0) + a_0 \tag{4}$$

The profiles of velocity, acceleration and jerk of the robot joints are obtained by means of the first, second and third derivative of the above equation, respectively with eight limits specified as $\theta(t_0) = \theta_0$, $\theta(t_f) = \theta_f$, $\dot{\theta}(t_0) = \dot{\theta}_0$, $\dot{\theta}(t_f) = \dot{\theta}_f$, $\ddot{\theta}(t_0) = \ddot{\theta}_0$, $\ddot{\theta}(t_f) = \ddot{\theta}_f$, $\dddot{\theta}(t_0) = \dddot{\theta}_0$, $\dddot{\theta}(t_f) = \dddot{\theta}_f$. The initial time, position, velocity, acceleration and jerk are denoted by t_0, θ_0, $\dot{\theta}_0$, $\ddot{\theta}_0$ and $\dddot{\theta}_0$ while t_f, θ_f, $\dot{\theta}_f$, $\ddot{\theta}_f$and $\dddot{\theta}_f$ illustrate the final time, position, velocity, acceleration and jerk, respectively. By combining these profiles of the joints with the eight constraints, eight equations can be yielded with eight unknown coefficients.

4 Cuckoo Search Algorithm

Yang and Deb (2009) improved a new population-based metaheuristic optimization technique known as cuckoo search algorithm which is inspired by the brood parasitic breeding strategy of certain species of cuckoos by laying their eggs in the nests of other host birds.

In the CS optimization algorithm, each nest is considered a suitable solution candidate and the optimum nest is selected as the best nest. There are three important rules of this newly developed algorithm. These can be stated as follows (Yang, & Deb, 2010).

- Each cuckoo randomly selects one of the nests in its environment and lays one egg there.
- The best nests with high-quality eggs will be carried over to the next generation.
- The number of host nests in the selected environment is fixed and the eggs released by the cuckoo may be recognized by the host, probability (p_a) between 0 and 1. In such a case, the host bird may throw the foreign eggs out of the nest or leave the existing nest to establish a new nest.

The cuckoo finds the new nest with a general random walk using the Lévy flight law (Soneji, & Sanghvi, 2012). The Lévy flight process is basically a random walk which is derived from the Lévy distribution with infinite variance and infinite mean (Yang, & Deb, 2010). According to the Lévy flight, let x_k^{n-1} be the current solution for kth cuckoo, then new solution x_k^n is presented as given

$$\begin{cases} x_k^n = x_k^{n-1} + \propto \otimes \, levy(\lambda), & k = 1,2,\dots,n \\ levy(\lambda) = t^{-\lambda}, & (1 < \lambda \leq 3) \end{cases} \tag{5}$$

where $\alpha > 0$ is the step size for the scale of the problem, t presents the current iteration. The Lévy flight, one of the most outstanding features of cuckoo search, produces a new candidate solution by a random walk. The Lévy flight represented by $levy(\lambda)$ is the main parameter of the CS algorithm and is used for both local search and global search.

Summarizing the CS algorithm, the initial population is generated using random numbers. The error involved in each population is then specified. Some quality solutions obtained at each iteration are stored for further processing. Then, by using Lévy's flight, the rest is updated.

5 Implementation of Methodology

In this section, optimal trajectory planning for a 6-DOF industrial robot is performed by using the aforementioned trajectory planning method through the implementation of the CS optimization algorithm. The optimization algorithm and the planning method have been simulated in MATLAB R2018b executing on an Intel Core i5 laptop with 8250U at 3.40 GHz.

The path to be followed by the end-effector of the robot in Cartesian Space is shown in Figure 2. The flow chart of the optimal trajectory planning is shown in Figure 3. In this chart, the optimal trajectory planning consists of three basic sections: the input section for robot where initial and final configuration are obtained using inverse kinematics, optimization section where the optimization algorithm and spline method are applied using the objective function, and the last section where the position, velocity, acceleration and jerk profiles are calculated for each joint.

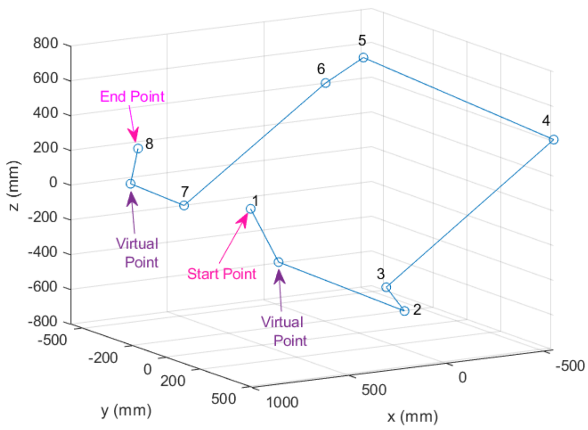

Figure 2. Path to be followed by end-effector of the robot in Cartesian Space.

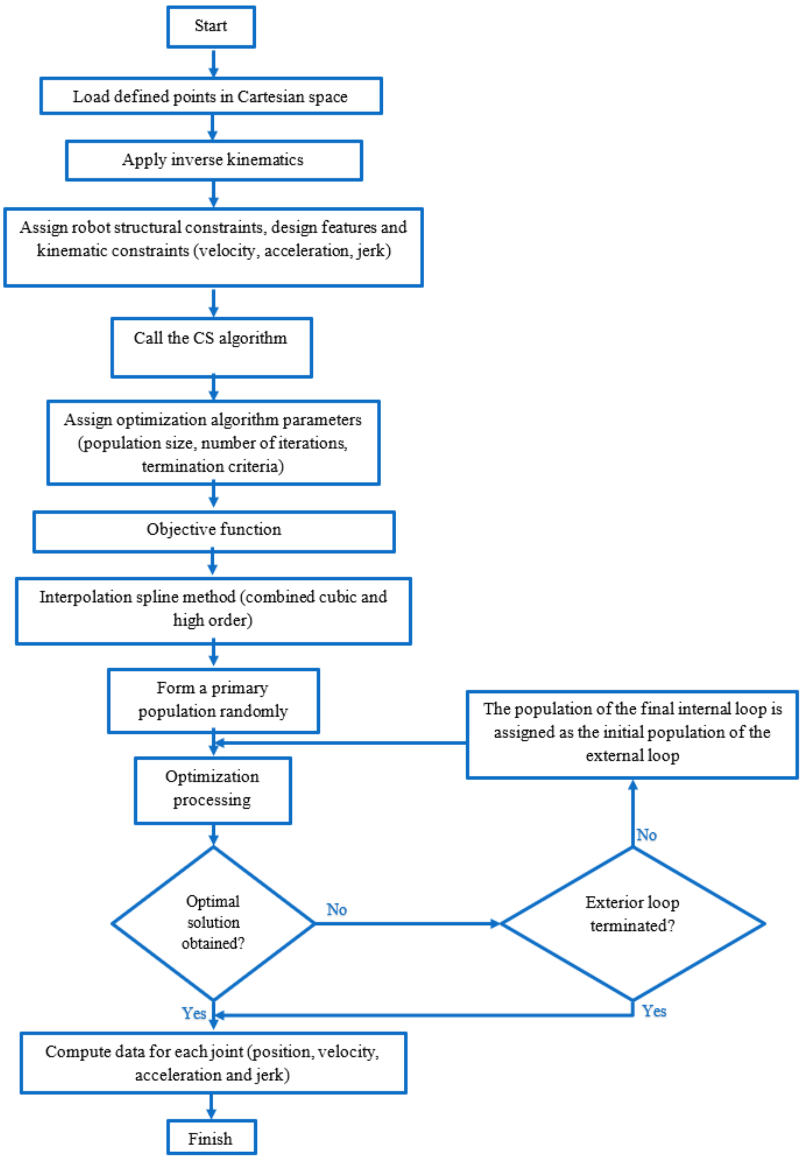

Figure 3. Flowchart of the optimal trajectory planning for a robotic arm.

Table 2. The joint via-points for trajectory planning.

Via-Points	**Joints (°)**					
	1	**2**	**3**	**4**	**5**	**6**
1	10	15	45	5	10	6
Virtual						
2	60	25	180	20	30	40
3	75	30	200	60	-40	80
4	130	-45	120	110	-60	70
5	110	-55	15	20	10	-10
6	100	-70	-10	60	50	10
7	-10	-10	100	-100	-40	30
Virtual						
8	-50	10	50	-30	10	20

Table 3. Kinematical constraints of the robot joints.

Joints No.	1	2	3	4	5	6
Velocity $(°/s)$	100	95	100	150	130	110
Acceleration $(°/s^2)$	60	60	75	70	90	80
Jerk $(°/s^3)$	60	66	85	70	75	70

Consequently, according to the selection of interpolation spline technique and objective function, the profiles of the position, velocity, acceleration and jerk for each joint are obtained with the chosen optimization algorithm between the initial and intermediate positions and also intermediate and final positions defined in the robot trajectory.

6 Simulation Results and Discussions

The parameters of optimization algorithm are selected as follows: number of nests is chosen as 20. Number of iterations is selected as 150. Discover rate of foreign eggs is set to 0.25.

The results obtained from the proposed CS algorithm are compared to the proposed optimization techniques in (Gasparetto, & Zanotto, 2007; Kucuk, 2018; Simon, & Isik, 1991) based on the used interpolation methods and the used objective functions. Also, the comparison results are comprehensively given in the tables in terms of the maximum kinematic values and their average values.

Table 4. Time intervals of time optimal trajectory planning approach.

Time interval (The interpolation methods)	Interval no.								
	h_1	h_2	h_3	h_4	h_5	h_6	h_7	h_8	h_9
Cubic spline with 7th order polynomial (s)	4.9452	3.0933	3.4937	3.9156	4.6478	4.9945	3.8972	4.3261	4.9980

To verify the effectiveness of the proposed approach, the simulation tests are implemented according to the time optimal using the aforementioned spline method. The lower and upper bounds of time interval (h_i) are set to 3 s and 5 s, respectively. After optimization with CS based on the time optimal by using the interpolation methods, the displacements, velocities, accelerations and jerks of each joint are obtained as in Figure 4. Table 4 gives the values of the consecutive time intervals (h_i) optimized with the proposed algorithm for time optimal trajectory planning based on the used interpolation method.

As can be observed from Figures 4, a motion that has the velocity, acceleration and jerk of zero at the start and end points of the trajectory is obtained based on the combination of cubic and 7th order polynomial. On the other hand, jerk continuous profiles are realized only beginning and end of the trajectory.

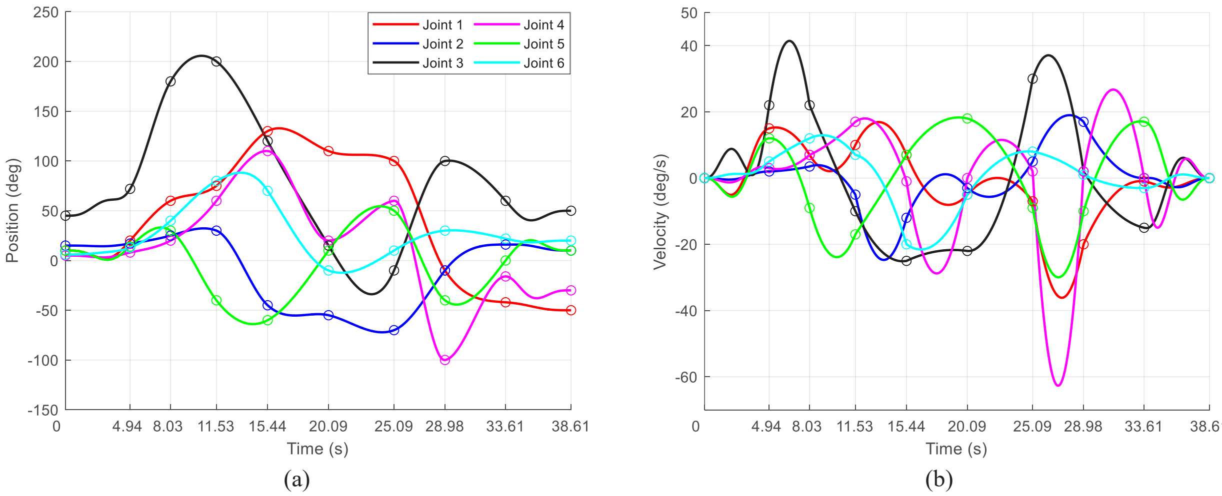

Figure 4. Resulting joint positions (a), velocities (b), accelerations (c) and jerks (d) based on the combination of cubic spline and 7th order polynomial for time optimal trajectory planning.

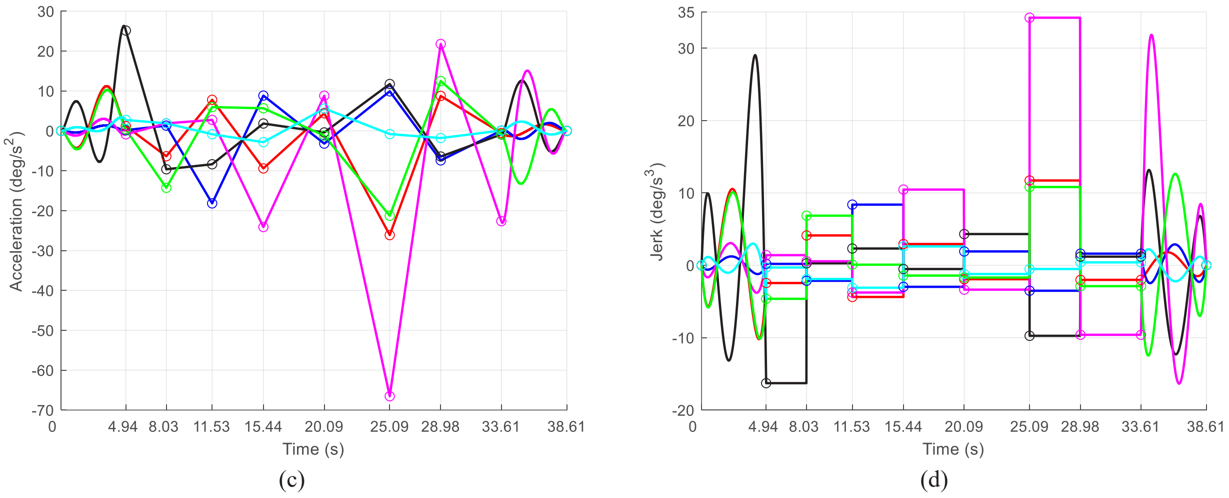

Figure 4. (continued).

From Table 5 it is noticeable that the maximum kinematic values of each joint based on the proposed algorithm are almost much lower as compared with those yielded by the algorithms in (Gasparetto, & Zanotto, 2008; Kucuk, 2018; Simon, & Isik, 1991). Also, the average values of the maximum velocities, accelerations and jerks of all joints are obtained lower compared to those obtained from (Gasparetto, & Zanotto, 2008; Kucuk, 2018; Simon, & Isik, 1991). As a result, in case of using the proposed algorithm and the combination of cubic spline and 7[th] order polynomial, the better results are provided as compared with that of (Gasparetto, & Zanotto, 2008; Kucuk, 2018; Simon, & Isik, 1991).

Table 5. Maximum joint kinematic values obtained from optimization algorithms for time optimal trajectory planning.

Algorithm	Method		Joint 1	Joint 2	Joint 3	Joint 4	Joint 5	Joint 6	Average
Proposed	Cubic + 7th order polynomial	V_{max}	16.92	18.99	41.43	26.72	18.30	12.93	**22.55**
		A_{max}	11.20	9.91	26.29	21.78	12.49	5.60	**14.54**
		J_{max}	11.72	8.38	29.04	34.20	12.65	3.01	**16.50**
Kucuk (2018)	Cubic + 7th order polynomial	V_{max}	28.36	39.49	54.53	30.03	39.22	22.13	35.62
		A_{max}	20.29	32.27	29.95	27.78	36.18	16.44	27.15
		J_{max}	17.22	24.15	29.05	24.81	29.04	11.06	22.55
Gasparetto and Zanotto (2008)	Cubic	V_{max}	25.89	20.59	45.29	45.84	29.05	22.57	31.54
		A_{max}	21.34	15.23	42.75	32.46	24.29	35.54	28.60
		J_{max}	14.22	30.16	37.50	43.56	46.03	21.52	32.17
Simon and Isik (1991)	Trigonometric	V_{max}	23.93	22.88	45.80	37.33	30.38	19.70	30.00
		A_{max}	21.34	15.23	42.75	32.46	24.29	35.54	28.60
		J_{max}	32.71	20.79	57.46	65.15	28.94	56.95	43.67

Table 6. Mean kinematic values obtained from optimization algorithms for time optimal trajectory planning.

Algorithm	Method		Joint 1	Joint 2	Joint 3	Joint 4	Joint 5	Joint 6	Average
Proposed	Cubic + 7th order polynomial	V_{mean}	8.32	5.70	15.65	13.28	11.16	6.20	10.05
		A_{mean}	4.22	2.99	6.89	8.83	5.88	2.42	5.20
		J_{mean}	3.95	2.51	5.75	8.76	4.53	1.40	4.48
Kucuk (2018)	Cubic + 7th order polynomial	V_{mean}	10.27	8.14	17.59	16.05	12.77	7.87	12.11
		A_{mean}	4.32	4.88	8.63	8.78	7.16	3.80	6.26
		J_{mean}	4.94	4.94	6.79	7.10	6.63	2.29	5.49
Gasparetto and Zanotto (2008)	Cubic	V_{mean}	13.03	9.05	23.45	21.25	16.11	9.65	15.43
		A_{mean}	7.25	6.85	12.77	10.00	12.33	6.89	11.02
		J_{mean}	8.33	8.95	14.67	28.76	16.70	9.01	14.40
Simon and Isik (1991)	Trigonometric	V_{mean}	9.84	5.64	13.42	11.89	9.21	6.12	9.35
		A_{mean}	6.29	4.88	9.94	9.57	6.61	6.16	7.24
		J_{mean}	8.61	6.24	16.01	15.38	8.39	7.58	10.37

From Table 6, the mean joint velocities, accelerations and jerks yielded by the proposed algorithm as well as their average values are much lower compared with those of (Gasparetto, & Zanotto, 2008; Kucuk, 2018; Simon, & Isik, 1991) based on each interpolation method. CS can perform better compared with those algorithms proposed by (Gasparetto, & Zanotto, 2008; Kucuk, 2018; Simon, & Isik, 1991) in terms of time optimization.

7 Conclusion

In this paper, the commonly used interpolation method for the trajectory generation of the industrial robots have been adopted in order to obtain a time optimal trajectory. The all method has been tested on PUMA robot manipulator by using both the proposed CS algorithm and the algorithms suggested by (Gasparetto, & Zanotto, 2008; Kucuk, 2018; Simon, & Isik, 1991) with the aforementioned objective function. Also, the results from the proposed algorithm have been compared with those by executing the algorithms provided in (Gasparetto, & Zanotto, 2008; Kucuk, 2018; Simon, & Isik, 1991) for each joint. The conclusions can be summarized as follows:

(1) As can be observed from the all results, the kinematic values of each joint generated by the interpolation method using the proposed algorithm meet the kinematic limits of the joint velocity, acceleration and jerk. This is crucial for dynamic trajectory planning.

(2) At the start and ending points, smooth motion trajectories with the zero jerk for each joint can be obtained in case of using the interpolation method such as the combination of cubic spline and 7th order polynomial. This smooth motion can introduce small errors while the robot is tracking the trajectory. Accordingly, it is useful to improve a control for accuracy positioning.

(3) CS optimization algorithm outperforms the algorithms proposed by previous works in terms of obtaining the mean kinematic values for both of time optimal and optimal trajectory planning.

(4) All of the average values of the maximum kinematic variables for each joint based on the aforementioned methods have been obtained lower as compared with that of previous works in case of time optimal.

(5) Having considered the used before interpolation methods, the combination of the cubic spline and 7th order polynomial provides continuous and smooth path at the initial and final via points.

(6) The simulation results have shown that the used trajectory planning methods with the proposed CS algorithm are very effective and suitable for optimal time trajectory planning.

References

Aribowo, W., & Terashima, K. (2014). Cubic Spline Trajectory Planning and Vibration Suppression of Semiconductor Wafer Transfer Robot Arm. *International Journal of Automation Technology*,8(2), 265-274. doi: 10.20965/ijat.2014.p0265.

Bobrow, J. E. (1988). Optimal robot plant planning using the minimum-time criterion. *IEEE Journal on Robotics and Automation*, 4(4), 443-450. doi:10.1109/56.811.

Bobrow, J. E., Dubowsky, S., & Gibson, J. S. (1985). Time-Optimal Control of Robotic Manipulators Along Specified Paths. *The International Journal of Robotics Research*, 4(3), 3-17. doi:10.1177/027836498500400301.

Boryga, M., & Graboś, A. (2009). Planning of manipulator motion trajectory with higher-degree polynomials use. *Mechanism and Machine Theory*, 44(7), 1400-1419. doi:10.1016/j.mechmachtheory.2008.11.003.

Chen, C.S., & Chen, S.K. (2019). Synchronization of tool tip trajectory and attitude based on the surface characteristics of workpiece for 6-DOF robot manipulator. *Robotics and Computer-Integrated Manufacturing*, 59, 13-27. doi:10.1016/j.rcim.2019.01.016.

Chen, Y., & Desrochers, A. A. (1989). Structure of minimum-time control law for robotic manipulators with constrained paths. In *1989 International Conference on Robotics and Automation* (pp. 971-976). IEEE. doi:10.1109/ROBOT.1989.100107.

Gasparetto, A, & Zanotto, V. (2007). A new method for smooth trajectory planning of robot manipulators. *Mechanism and Machine Theory*, 42(4), 455-471. doi: 10.1016/j.mechmachtheory.2006.04.002.

Gasparetto, A., & Zanotto, V. (2008). A technique for time-jerk optimal planning of robot trajectories. *Robotics and Computer-Integrated Manufacturing*, 24(3), 415-426. doi: 10.1016/j.rcim.2007.04.001.

Gasparetto, A, & Zanotto, V. (2010). Optimal trajectory planning for industrial robots. *Advances in Engineering Software*, 41(4), 548-556. doi:10.1016/j.advengsoft.2009.11.001.

Kolter, J.Z., & Andrew, Y.N. (2009). Task-space trajectories via cubic spline optimization. In *IEEE international conference on robotics and automation* (pp. 1675–82). IEEE. doi:10.1109/ROBOT.2009.5152554.

Kucuk, S. (2016). Maximal dexterous trajectory generation and cubic spline optimization for fully planar parallel manipulators. *Computer and Electrical Engineering*,56, 634-647. doi:10.1016/j.compeleceng.2016.07.012.

Kucuk, S. (2018). Optimal trajectory generation algorithm for serial and parallel manipulators. *Robotics and Computer-Integrated Manufacturing*, 48, 219-232. doi:10.1016/j.rcim.2017.04.006.

Lin, C.S., Chang, P.R., & Luh, J.Y.S. (1983). Formulation and optimization of cubic polynomial joint trajectories for industrial robots. *IEEE Transactions on Automatic Control*, 28(12), 1066-1073. doi: 10.1109/TAC.1983.1103181.

Liu, H., Lai, X., & Wu, W. (2013). Time-optimal and jerk-continuous trajectory planning for robot manipulators with kinematic constraints. *Robotics and Computer-Integrated Manufacturing*, 29(2), 309-317. doi:10.1016/j.rcim.2012.08.002.

Liu, L., Chen, C., Zhao, X., & Li, Y. (2016). Smooth trajectory planning for a parallel manipulator with joint friction and jerk constraints. *International Journal of Control Automation System*, 14, 1022-1036. doi:10.1007/s12555-014-0495-4.

Lu, S., Zhao, J., Jiang, L., & Liu, H. (2017). Time-jerk optimal trajectory planning of a 7-DOF redundant robot. *Turkish Journal of Electrical Engineering & Computer Sciences*, 25, 4211-4222. doi:10.3906/elk-1612-203.

Machmudah, A., Parman, S., Zainuddin, A., & Chacko, S. (2013). Polynomial joint angle arm robot motion planning in complex geometrical obstacles. *Applied Soft Computing*, 13(2), 1099-1109.doi: 10.1016/j.asoc.2012.09.025.

Perumaal, S.S., & Jawahar, N. (2013). Automated Trajectory Planner of Industrial Robot for Pick-and-Place Task. *International Journal of Advanced Robotic Systems*, 10(2), 1-17. doi:10.5772/53940.

Rubio, F., Llopis-Albert, C., Valero, F., & Suñer, J. L. (2016). Industrial robot efficient trajectory generation without collision through the evolution of the optimal trajectory. *Robotics and Autonomous Systems*, 86, 106-112. doi:10.1016/j.robot.2016.09.008.

Savsani, P., Jhala, R. L., & Savsani, V. J. (2013). Optimized trajectory planning of a robotic arm using teaching learning based optimization (TLBO) and artificial bee colony (ABC) optimization techniques. 2013 IEEE International Systems Conference (SysCon). doi:10.1109/syscon.2013.6549910

Savsani, P., Jhala, R. L., & Savsani, V. J. (2016). Comparative Study of Different Metaheuristics for the Trajectory Planning of a Robotic Arm. IEEE Systems Journal, 10(2), 697–708. doi:10.1109/jsyst.2014.2342292.

Shin, K., & McKay, N. (1985). Minimum-time control of robotic manipulators with geometric path constraints. *IEEE Transactions on Automatic Control*, 30(6), 531-541. doi:10.1109 / TAC.1985.1104009.

Soneji, H., & Sanghvi, R.C. (2012). Towards the improvement of Cuckoo search algorithm. In *World Congress on Information and Communication Technologies (WICT), 2012* (pp. 878-883). IEEE.

Simon, D., & Isik, C. (1991). Optimal trigonometric robot trajectories. *Robotica*, 9(4), 379–386. doi:10.1017/S0263574700000552

Yang, X. S., & Deb, S. (2009). Cuckoo search via Levy flights. In *2009 World Congress on Nature & Biologically Inspired Computing (NaBIC)* (pp. 210–214). IEEE. doi:10.1109/NABIC.2009.5393690.

Yang, X. S., & Deb, S. (2010). Engineering optimisation by cuckoo search. *International Journal of Mathematical Modelling and Numerical Optimization*, 1(4), 330–343. arXiv:1005.2908.

6th INTERNATIONAL CONFERENCE ON COMPUTATIONAL MATHEMATICS AND ENGINEERING SCIENCES

www.cmescongress.org